



# รายงานวิจัยฉบับสมบูรณ์

# สัญญาเลขที่ RSA5880012

โครงการ: การปรับปรุงสมบัติทางไจแอนต์ไดอิเล็กตริกของวัสดุเซรามิกประสิทธิภาพสูง สำหรับการประยุกต์ใช้งานเป็นตัวเก็บประจุไฟฟ้าชนิดเซรามิกและในด้านวัสดุพอลิเมอร์ คอมโพสิตค่าคงที่ ไดอิเล็กตริกสูง

Systematically improved giant-dielectric properties of novel high-performance ceramic materials for applications in ceramic-capacitors and high-dielectric polymer-ceramic composites

นายประสิทธิ์ ทองใบ มหาวิทยาลัยขอนแก่น

สหับสนุนโดยสำหักงานกองทุนสหับสนุนการวิจัยและมหาวิทยาลัยขอนแก่น

# รายงานวิจัยฉบับสมบูรณ์

โครงการ: การปรับปรุงสมบัติทางไจแอนต์ไดอิเล็กตริกของวัสดุเซรามิกประสิทธิภาพสูง สำหรับการประยุกต์ใช้งานเป็นตัวเก็บประจุไฟฟ้าชนิดเซรามิกและในด้านวัสดุพอลิเมอร์ คอมโพสิตค่าคงที่ไดอิเล็กตริกสูง

Systematically improved giant-dielectric properties of novel high-performance ceramic materials for applications in ceramic-capacitors and high-dielectric polymer-ceramic composites

สัญญาเลขที่ RSA5880012

# TABLE OF CONTENTS

	Page
Executive summary	i
Part I	1
Chapter 1 Colossal dielectric permittivity and electrical properties of	
grain boundary of $Ca_{1-3x/2}Yb_xCu_{3-y}Mg_yTi_4O_{12}$ ( $x = 0.05$ , $y=0.05$ and	1
0.30)	
Chapter 2 Improved Dielectric Properties of (Y+Mg) co-doped	
CaCu <sub>3</sub> Ti <sub>4</sub> O <sub>12</sub> Ceramics by Controlling Geometric and Intrinsic	11
Properties of Grain Boundaries	
Chapter 3 Microstructural Evolution and Strongly Enhanced	
Dielectric Response in Sn-Doped CaCu <sub>3</sub> Ti <sub>4</sub> O <sub>12</sub> /CaTiO <sub>3</sub> Ceramic	19
Composites	
Chapter 4 Significantly Improved Non-Ohmic and Giant Dielectric	
Properties of CaCu <sub>3-X</sub> Zn <sub>x</sub> Ti <sub>4</sub> O <sub>12</sub> Ceramics by Enhancing Grain	31
Boundary Response	
Chapter 5 Effects of Mg <sup>2+</sup> Doping Ions on Giant Dielectric Properties	45
and Electrical Responses of Na <sub>1/2</sub> Y <sub>1/2</sub> Cu <sub>3</sub> Ti <sub>4</sub> O <sub>12</sub> Ceramics	45
Chapter 6 Non-Ohmic Properties and Electrical Responses Of Grain	
and Grain Boundaries of Na <sub>1/2</sub> Y <sub>1/2</sub> Cu <sub>3</sub> Ti <sub>4</sub> O <sub>12</sub> Ceramics	59
Chapter 7 Enhanced Dielectric and Non-Ohmic Properties in	
CaCu <sub>3</sub> Ti <sub>4</sub> oO <sub>12</sub> /CaTiO <sub>3</sub> Nanocomposites Prepared by a Chemical	
Combustion Method	73
Chapter 8 Effects of DC Bias on Dielectric and Electrical Responses	
In (Y+Zn) Co 3 Dia Ded Perouskite Oxides	81
Chapter 9 Improved Giant Dielectric Properties of CaCu <sub>3</sub> Ti <sub>4</sub> O <sub>12</sub> via	
Simultaneously Tuning Electrical Properties of Grains and Grain	
Boundaries by F <sup>-</sup> Substitution	91
Chapter 10 Nonlinear Electrical Properties and Giant Dielectric	
Response in Na <sub>1/3</sub> Ca <sub>1/3</sub> Y <sub>1/3</sub> Cu <sub>3</sub> Ti <sub>4</sub> O <sub>12</sub> Ceramic	105
Chapter 11 Microstructural Evolution, Non-Ohmic Properties and	
Giant Dielectric Response in CaCu <sub>3</sub> Ti <sub>4-x</sub> Ge <sub>x</sub> O <sub>12</sub> Ceramics	117
Chapter 12 Preparation, Characterization, and Dielectric Properties	
of CaCuaTi <sub>4</sub> O <sub>42</sub> -Related (Na <sub>4/2</sub> Ca <sub>4/2</sub> Y <sub>4/2</sub> )Cu <sub>2</sub> Ti <sub>4</sub> O <sub>42</sub> Ceramics Using a	120

	Page
Chapter 13 Enhanced Non-Ohmic Properties and Giant Dielectric	
Response of (Sm+Zn) Co–Doped CaCu <sub>3</sub> Ti <sub>4</sub> O <sub>12</sub> Ceramics	141
Chapter 14 (Al <sup>3+</sup> , Nb <sup>5+</sup> ) Co-Doped CaCu <sub>3</sub> Ti <sub>4</sub> O <sub>12</sub> : An Extended	
Approach for Acceptor–Donor Heteroatomic Substitutions to Achieve	
High-Performance Giant-Dielectric Permittivity	151
Part II	165
Chapter 1 Investigation on Temperature Stability Performance of	100
Giant Permittivity (In+Nb) in Co–doped TiO <sub>2</sub> Ceramic: A Crucial Aspect	
for Practical Electronic Applications	167
Chapter 2 Origin(s) of apparent colossal permittivity in	107
$(\ln_{1/2} \text{Nb}_{1/2})_x \text{Ti}_{1-x} \text{O}_2$ : Clarification on the extremely induced	
Maxwell–Wagner polarization relaxation in by DC bias	179
Chapter 3 Surface Barrier Layer Effect in (In+Nb) Co-Doped TiO <sub>2</sub>	
Ceramics: An Alternative Route To Design Low Dielectric Loss	193
<b>Chapter 4</b> Colossal Permittivity in $(In_{1/2}Nb_{1/2})_xTi_{1-x}O_2$ Ceramics	
Prepared by a Glycine Nitrate Process	205
Chapter 5 High–Performance Giant-Dielectric Properties of Rutile	
TiO <sub>2</sub> Co–Doped with Acceptor–Sc <sup>3+</sup> and Donor–Nb <sup>5+</sup> Ions	215
Chapter 6 Very Low Dielectric Loss and Giant Dielectric Response	2.0
with Excellent Temperature Stability of Ga <sup>3+</sup> and Ta <sup>5+</sup> Co-Doped Rutile-	
TiO <sub>2</sub> Ceramics	229
Chapter 7 Preparation, Characterization, Electrical Properties and	
Giant Dielectric Response in (In+Nb) Co-Doped Tio <sub>2</sub> Ceramics	
Synthesized by a Urea Chemical-Combustion Method	243
Chapter 8 Preparation, Characterization, And Giant Dielectric	
Permittivity of (Y <sup>3+</sup> and Nb <sup>5+</sup> ) Co–Doped TiO <sub>2</sub> Ceramics	253
Chapter 9 Effects of Sintering Temperature on Microstructure and	
Giant Dielectric Properties of (V+Ta) Co-Doped TiO <sub>2</sub> Ceramics	265
Chapter 10 Effect of Zn <sup>2+</sup> and Nb <sup>5+</sup> Co-Doping Ions on Giant	
Dielectric Properties of Rutile-TiO <sub>2</sub> Ceramics	283

	Page
Part III	293
Chapter 1 Abnormally Enhanced Dielectric Permittivity in	
Poly(vinylidene fluoride)/Nanosized-La $_2$ NiO $_{4-\delta}$ Films	295
Chapter 2 Greatly Enhanced Dielectric Permittivity in	
$La_{1.7}Sr_{0.3}NiO_4/Poly(vinylidene\ fluoride)\ Nanocomposites\ that\ \ Retained$	
a Low Loss Tangent	305
Chapter 3 Improved Dielectric Properties of PVDF Composites by	
Employing Mg 7.5% pedNiQ4 Particles as a Filler	319
Part IV	329
Chapter 1 Effects of DC Bias on Non-Ohmic Sample–Electrode	
Contact and Grain Boundary Responses in Giant-Permittivity	
$La_{1.7}Sr_{0.3}Ni_{1-x}Mg_xO_4$ Ceramics	331
Output	343
Research Honors and Awards	347
APPENDIX	349

## **ACKNOWLEDGEMENTS**

This work was financially supported by the Thailand Research Fund (TRF) and Khon Kaen University, Thailand (Grant number RSA5880012).

The authors would like to thank the Synchrotron Light Research Institute (BL5.1 and BL5.2) (Public Organization), Nakhon Ratchasima, Thailand for XANES and XPS measurements. The authors would like to thank the National Metal and Materials Technology Center (MTEC), National Science and Technology Development Agency for providing Raman and I-V measurement facilities.

Asst.Prof.Dr. Prasit Thongbai

#### **Abstract**

Project Code: RSA5880012

**Project Title:** Systematically improved giant-dielectric properties of novel high-performance ceramic materials for applications in ceramic-capacitors and high-dielectric polymer-ceramic composites

**Investigator:** Asst.Prof.Dr. Prasit Thongbai

E-mail Address: pthongbai@kku.ac.th

**Project Period**: 3 years

In this research project, micro and nano-size ceramic powders of  $ACu_3Ti_4O_{12}$ -based (A = divalent cations or average divalent cations) and TiO<sub>2</sub>-based compounds as well as La<sub>2-x</sub>Sr<sub>x</sub>NiO<sub>4</sub> ceramic materials were prepared using a standard solid state reaction method and wet chemical methods, respectively. Phase composition and crystal structure were systematically characterized using an X-ray diffraction (XRD) technique. Microstructure analyses were done using scanning electron microscopy (SEM) and transmission electron microscopy (TEM). Valence states of any metal ions were measured by using X-ray photoelectron spectroscopy (XPS). Giant dielectric properties of sintered ceramics were systematically investigated as functions of temperature, frequency, and DC voltage bias. The effects of outer surface layers, electrode materials, and annealing in different atmospheres upon the dielectric and electrical properties of these materials were also be investigated. All important parameters required for the use of ceramics in capacitor applications were measured and further improved to achieve high-performance dielectric materials. It was found that the giant dielectric properties of ACu<sub>3</sub>Ti<sub>4</sub>O<sub>12</sub>-based ceramics have successfully been improved by several methods such as doping with suitable single-metal ions (i.e., Mg, Zn, Ge, Sn) and co-doping with metal ions (i.e., Y+Mg, Y+Zn, SM+Zn, Yb+Mg, and Al+Nb). Very high dielectric permittivity of 10<sup>3</sup>-10<sup>5</sup> with low dielectric loss tangent ( $tan\delta < 0.05$ ) were accomplished. Interestingly, excellent giant dielectric properties with very low loss tangent ( $tan\delta < 0.02$ ) and high dielectric permittivity ( $\varepsilon' \approx 10^3 - 10^5$ ) with independent of temperature over a wide range can be obtained in co-doped TiO2 ceramics (i.e., In+Nb, Y+Nb, Ga+Ta, Zn+Nb, and Sc+Nb).

Finally, high-performance dielectric ceramics were used as fillers to enhance the dielectric constant of polymer matrix composites for development of new generation flexible dielectric materials. The dielectric properties PVDF polymer can be significantly improved by incorporating with giant dielectric ceramic particles that were synthesized in this research project. Greatly enhanced dielectric permittivity of about 10<sup>3</sup> can be obtained in PVDF polymer matrix composites.

Keywords: Dielectric properties, Electrical properties, Ceramics, Composites

## บทคัดย่อ

รหัสโครงการ: RSA5880012

ชื่อโครงการ: การปรับปรุงสมบัติทางใจแอนต์ใดอิเล็กตริกของวัสดุเซรามิกประสิทธิภาพสูง สำหรับการประยุกต์ใช้งานเป็นตัวเก็บประจุไฟฟ้าชนิดเซรามิกและในด้านวัสดุพอลิเมอร์คอมโพ สิตค่าคงที่ ไดอิเล็กตริกสูง

ชื่อหักวิจัย: ผศ.ดร.ประสิทธิ์ ทองใบ

สถาบัน: มหาวิทยาลัยขอนแก่น

E-mail Address: pthongbai@kku.ac.th

ระยะเวลาโครงการ: 3 ปี

งานวิจัยนี้ ได้สังเคราะห์ผนุภาคผงเซรามิกที่มีขนาดในระดับไมโครเมตรและนาโนเมตร โดยมุ่งเน้นสังเคราะห์อนุภาคผงเซรามิก 3 กลุ่ม คือ ACu<sub>3</sub>Ti<sub>4</sub>O<sub>12</sub> (A คือ ไอออนบวกที่มีประจุ ไฟฟ้า +2 หรือกลุ่มไอออนต่างๆ ที่มีประจุไฟฟ้าเฉลี่ย +2) TiO₂ และ La₂-xSr<sub>x</sub>NiO₄ โดยการ เตรียมด้วยวิธีปฏิกิริยาสถานะของแข็งและวิธีการทางเคมีแบบเปียก องค์ประกอบเฟสและ โครงสร้างผลึกของวัสดุผงและชิ้นงานเซรามิกได้ศึกษาโดยใช้เทคนิค XRD และโครงสร้างทาง จุลภาคของวัสดุเซรามิกได้ศึกษาโดยใช้เทคนิค SEM และ TEM สถานะอิเล็กตรอนชั้นนอกสุด ของแต่ละไอออนในวัสดุเซรามิกที่สังเคราะห์ได้ถูกศึกษาโดยเทคนิค XPS ในงานวิจัยนี้ได้ศึกษา สมบัติทางใจแอนต์ใดอิเล็กตริกที่แปรตามอุณหภูมิ ความถี่ และแรงดันไฟฟ้ากระแสตรง นอกจากนี้แล้วยังได้ศึกษาอิทธิพลของผิวชั้นนอกสุดของวัสดุเซรามิก ชนิดของขั้วไฟฟ้า และ การอ่อนภายใต้บรรยากาศต่างๆ เช่น Ar หรือ  $O_2$  ที่มีต่อสมบัติทางใดอิเล็กตริกของวัสดุเซรา มิกที่สังเคราะห์ได้ และได้ทดสอบค่าพารามิเตอร์พื้นฐานต่างๆ ของวัสดุไดอิเล็กตริกที่มี ความสำคัญต่อการประยุกต์ใช้งานเป็นตัวเก็บประจุไฟฟ้า รวมทั้งได้มีการพัฒนาปรับปรุงค่า เหล่านี้เพื่อให้ได้วัสดุไดอิเล็กตริกที่มีประสิทธิภาพสูง ผลการศึกษาวิจัยพบว่า สมบัติทางไดอิเล็ก ตริกของวัสดุเซรามิกกลุ่ม ACu<sub>3</sub>Ti<sub>4</sub>O<sub>12</sub> สามารถปรับปรุงได้อย่างเป็นระบบด้วยหลายวิธีด้วยกัน เช่น การเจือด้วยไอออนเดี่ยว (เช่น Mg Zn Ge และ Sn) และการเจือด้วยคู่ไอออนต่างชนิด (เช่น Y+Mg Y+Zn SM+Zn Yb+Mg และ Al+Nb) วัสดุเซรามิกกลุ่มดังกล่าวนี้มีค่าคงที่ไดอิเล็ก ตริกได้สูงถึง 10 $^3$ -10 $^5$  และยังมีค่าแทนเจนต์ของการสูญเสียทางไดอิเล็กตริกที่ต่ำอีกด้วย (tan $\delta$ < 0.05) จากผลการศึกษาในงานวิจัยนี้ยังพบว่า วัสดุเซรามิก  ${
m TiO}_2$  สามารถปรับปรุงให้สามารถ แสดงสมบัติทางใดอิเล็กตริกที่เป็นเลิศได้โดยการเจือด้วยคู่ใอออน In+Nb Y+Nb Ga+Ta Zn+Nb และ Sc+Nb โดยวัสดุเซรามิกที่สังเคราะห์ได้มีค่าแทนเจนต์ของการสูญเสียทางไดอิเล็ก ตริกที่ต่ำมาก ( $\tan\delta < 0.02$ ) และมีค่าคงที่ไดอิเล็กตริกที่สูงมากในระดับ  $10^3$ - $10^5$  พร้อมทั้งมีการ เปลี่ยนแปลงกับอุณหภูมิเพียงเล็กน้อยเท่านั้น

งานวิจัยในส่วนสุดท้ายของโครงการได้นำวัสดุเซรามิกไจแอนต์ไดอิเล็กตริกที่มีสมบัติทาง ไดอิเล็กตริกที่เป็นเลิศมาใช้ในการปรับปรุงเพิ่มค่าคงที่ไดอิเล็กตริกของพอลิเมอร์ PVDF เพื่อ ประดิษฐ์เป็นตัวเก็บประจุไฟฟ้าที่มีความยืดหยุ่น จากการศึกษาวิจัยพบว่าสมบัติทางไดอิเล็ก ตริกของวัสดุพอลิเมอร์ PVDF สามารถปรับปรับปรุงได้อย่างมีประสิทธิภาพโดยการผสมด้วย อนุภาคเซรามิกไจแอนต์ไดอิเล็กตริก  $La_{2-x}Sr_xNiO_4$  ทำให้วัสดุผสมพอลิเมอร์ PVDF มีค่าคงที่ ไดอิเล็กตริกเพิ่มเพิ่มขึ้นจาก 10 เป็น  $10^3$ 

คำหลัก: สมบัติทางไดอิเล็กตริก; ตัวเก็บประจุไฟฟ้า; อิมพีแดนซ์

# **Executive summary**

## 1. Introduction to the research problem and its significance

Dielectric materials with ultra-high dielectric constants ( $\varepsilon' > 10^4$ ) have attracted considerable attention due to their high potential for applications in multilayer ceramic capacitors (MLCCs) [1-3]. As a result of technological progress in modern communication technology and microelectronics, investigation and development of new types of giant dielectric materials have been intensively pursued [1, 4-8]. The discovery of new materials showing very high  $\varepsilon'$  and low loss tangent (tan $\delta$ ) further stimulated significant research activity in recent years [4, 6, 9]. MLCCs can be miniaturized by replacing dielectric layers with a material having a relatively high  $\varepsilon'$ . Moreover, the value of  $\varepsilon'$  should be large to enhance the capacitance of the MLCC and increase its charge-storage efficiency [3]. Other important parameters are  $tan\delta$ , the temperature stability of  $\epsilon'$ , DC voltage dependence of  $\epsilon'$ , and the resistivity of materials [10]. The capacitance value (C) of MLCCs must have good temperature stability so that they will operate properly over a wide temperature range. For class II and III ceramic capacitors, tanδ of ceramics at 1 kHz and 25 °C must be lower than 0.025 and 0.040, respectively [10]. The value of  $\varepsilon'$  should be larger than 10<sup>3</sup> or as high as possible. The temperature coefficient of capacitance (or temperature coefficient of  $\varepsilon'$ ,  $\Delta \varepsilon'(\%)$ ) is one of the most important factors that must be considered. The demand for electronic components that can be operated at high temperatures has dramatically increased. High  $\epsilon' \sim 10^3 - 10^4$ , are usually exhibited by BaTiO<sub>3</sub>. Unfortunately, this effect is strongly temperature-dependent and thus ferroelectric MLCCs are hampered by poor temperature stability [11].

Among giant-dielectric materials,  $Ln_{2-x}Sr_xNiO_4$  (Ln = Nd, La, Sm) ceramics are most interesting. These ceramics can exhibit very high  $\epsilon'$  values of  $10^5$ - $10^6$  [3, 11].  $\epsilon'$  values of this material system are the largest compared to other materials. Such high  $\epsilon'$  is observed at relatively high frequencies, in the range of  $10^9$  Hz (GHz region) [11]. This has never been observed in other giant dielectric materials. By considering materials science coupled with the resource strategy and resource management as proposed by Krohns and co-worker serve as guidelines for development of novel materials.  $La_{2-x}Sr_xNiO_4$  ceramic (LSNO) has been judged potentially more important in the future compared to  $BaTiO_3$  and  $CaCu_3Ti_4O_{12}$  ceramics [3]. High  $tan\delta$  value of  $La_{2-x}Sr_xNiO_4$  ceramics is only one factor that has to be improved. Thus, the first part of this research work is to investigate the strategy to greatly reduce  $tan\delta$  of the  $La_{2-x}Sr_xNiO_4$  ceramic system. Substitution of metal ions and/or heat treatment of the ceramics in different atmospheres as well as other methods will be done in order to seek a suitable route to reduce  $tan\delta$ .

Most recently, Hu et al. (2013) [2] reported a novel material with excellent dielectric properties in (ln+Nb) co-doped rutile-TiO<sub>2</sub> ceramics. Ceramic with composition of (ln<sub>0.05</sub>Nb<sub>0.05</sub>)<sub>x</sub>Ti<sub>1-x</sub>O<sub>2</sub> where x = 0.1 exhibited a high  $\epsilon'$  (~6×10<sup>4</sup>) with tan $\delta$  < 0.02 (at room temperature) over a frequency range of 10<sup>2</sup>-10<sup>6</sup> Hz. Furthermore, temperature independence of  $\epsilon'$  over a wide temperature range of 80-450 K (or -193 – 177 °C) was reported for these materials. Excellent-dielectric

performance can be created by engineering the local structure within the structure of rutile-TiO $_2$ . However, the exact values of the temperature coefficient of  $\epsilon'$ , DC resistivity, the aging of dielectric properties were not reported. Moreover, several effects have never been reported. These include the effects of doping metal ions replacing the dopants of In or Nb, applied uniaxial compressive stress, sintering conditions, annealing under various atmospheres, and outer surface layer as well as current-voltage characteristics of this  $TiO_2$ -based system. These parameters and effects must be intensively studied before using these ceramics in capacitor applications. Therefore, the second part of this research work will be to intensively investigate the dielectric properties under various conditions, as proposed above.

For new generation electronic technologies, flexible polymeric dielectric materials have attracted attention because of their ease of processing, flexibility, and ultra-high breakdown voltage [12-15]. However, the  $\varepsilon'$  value of these polymers is very low compared to those of many ceramics. Recently, polymer-ceramic composites were widely investigated to enhance the value of  $\varepsilon'$  in dielectricpolymer materials. However, ε'of polymer-ceramic (i.e., BaTiO<sub>3</sub>) composites still remains low level ( $\sim$ 50) at room temperature [15]. High- $\epsilon$ ' values (60-500) were reported in polymer-ceramic composites using giant dielectric materials as a fillers These include CaCu<sub>3</sub>Ti<sub>4</sub>O<sub>12</sub>, (Li,Ti)-doped NiO, and CuO [16, 17]. However, the tanδ values of these composites were found to be very large. It is expected that this research work will produce two types of giant dielectric materials with excellent dielectric performance. These are modified-La<sub>2-x</sub>Sr<sub>x</sub>NiO<sub>4</sub> and TiO<sub>2</sub>-based compounds. Hence, the third and final part of this research work will be done under theme of highly enhanced dielectric response in polymer-ceramics composites with low tanδ. Modified-La<sub>2-x</sub>Sr<sub>x</sub>NiO<sub>4</sub> ceramics and TiO<sub>2</sub>-based compounds with excellent dielectric properties will be used as fillers in polymermatrix composites. Polyvinylidene fluoride (PVDF) will be used as a matrix since it has the highest  $\epsilon'$  among polymer-dielectric materials.

#### References

- [1] C.C. Homes, T. Vogt, S.M. Shapiro, S. Wakimoto, A.P. Ramirez, Science 293 (2001) 673-676.
- [2] W. Hu, Y. Liu, R.L. Withers, T.J. Frankcombe, L. Norén, A. Snashall, M. Kitchin, P. Smith, B. Gong, H. Chen, J. Schiemer, F. Brink, J. Wong-Leung, Nat. Mater. 12 (2013) 821-826.
- [3] S. Krohns, P. Lunkenheimer, S. Meissner, A. Reller, B. Gleich, A. Rathgeber, T. Gaugler, H.U. Buhl, D.C. Sinclair, A. Loidl, Nat. Mater. 10 (2011) 899-901.
- [4] J. Wu, C.-W. Nan, Y. Lin, Y. Deng, Phys. Rev. Lett. 89 (2002) 217601.
- [5] P. Lunkenheimer, R. Fichtl, S. Ebbinghaus, A. Loidl, Phys. Rev. B 70 (2004) 172102.
- [6] T. Park, Z. Nussinov, K. Hazzard, V. Sidorov, A. Balatsky, J. Sarrao, S.W. Cheong, M. Hundley, J.-S. Lee, Q. Jia, J. Thompson, Phys. Rev. Lett. 94 (2005) 017002.

- [7] M.C. Ferrarelli, T.B. Adams, A. Feteira, D.C. Sinclair, A.R. West, Appl. Phys. Lett. 89 (2006) 212904.
- [8] I.P. Raevski, S.A. Prosandeev, A.S. Bogatin, M.A. Malitskaya, L. Jastrabik, J. Appl. Phys. 93 (2003) 4130-4136.
- [9] M.A. Subramanian, D. Li, N. Duan, B.A. Reisner, A.W. Sleight, J. Solid State Chem. 151 (2000) 323-325.
- [10] A.J. Moulson, J.M. Herbert, Electroceramics: materials, properties, applications, 2nd ed., Wiley, West Sussex; New York, 2003.
- [11] S. Krohns, P. Lunkenheimer, C. Kant, A.V. Pronin, H.B. Brom, A.A. Nugroho, M. Diantoro, A. Loidl, Appl. Phys. Lett. 94 (2009) 122903.
- [12] Z.-M. Dang, T. Zhou, S.-H. Yao, J.-K. Yuan, J.-W. Zha, H.-T. Song, J.-Y. Li, Q. Chen, W.-T. Yang, J. Bai, Adv. Mater. 21 (2009) 2077-2082.
- [13] M. Arbatti, X. Shan, Z.Y. Cheng, Adv. Mater. 19 (2007) 1369-1372.
- [14] B.-H. Fan, J.-W. Zha, D. Wang, J. Zhao, Z.-M. Dang, Appl. Phys. Lett. 100 (2012) 012903.
- [15] Z.-M. Dang, H.-Y. Wang, H.-P. Xu, Appl. Phys. Lett. 89 (2006) 112902.
- [16] Y. Yang, B.-P. Zhu, Z.-H. Lu, Z.-Y. Wang, C.-L. Fei, D. Yin, R. Xiong, J. Shi, Q.-G. Chi, Q.-Q. Lei, Appl. Phys. Lett. 102 (2013) 042904.
- [17] D. Bhadra, M.G. Masud, S.K. De, B.K. Chaudhuri, J. Phys. D: Appl. Phys. 45 (2012) 485002.

## 2. Objectives

- 2.1 To synthesize micro and nano-size powders and their sintered ceramics of giant dielectric materials, *i.e.*, co-doped TiO<sub>2</sub> and La<sub>2-x</sub>Sr<sub>x</sub>NiO<sub>4</sub> ceramics.
- 2.2 To systematically investigate strategies for improving the overall dielectric properties of co-doped TiO<sub>2</sub> and La<sub>2-x</sub>Sr<sub>x</sub>NiO<sub>4</sub> ceramics.
- 2.3 To clarify the exact origin(s) or related possible mechanisms of the giant dielectric properties in different frequency ranges of co-doped TiO<sub>2</sub> and La<sub>2-x</sub>Sr<sub>x</sub>NiO<sub>4</sub> ceramics.
- 2.4 To seek novel giant-dielectric ceramic materials for ceramic capacitor applications and for use as a filler in flexible polymer-ceramic composites.
- 2.5 To fabricate flexible polymer-ceramic composite materials with high  $\epsilon'$  and low  $tan\delta$ .

#### 3. Methodology

# 3.1 Preparation of metal ions co-doped TiO<sub>2</sub> and La<sub>2-x</sub>Sr<sub>x</sub>NiO<sub>4</sub> powders and ceramics

Metal ion co-doped  $TiO_2$  [(**A**,**B**)-doped  $TiO_2$ , where **A** = In, Al, Ga and **B** = Nb, Sb, Ta] and **C**-doped  $La_{2-x}Sr_xNiO_4$  (**C** = Al, Zn, Sc, Cu, Mg, and In) will be prepared by different methods. A solid state reaction (SSR) method will be used to synthesize micro-size ceramic powders. Concurrently, nano-size ceramic powders will be prepared by wet-chemical (WC) methods. Each pellet of the green bodies

will be sintered in different atmospheres under various conditions. The sintered ceramics will also be annealed in Ar and O<sub>2</sub> atmospheres.

## 3.2 Fabrication of polymer-ceramic composites

Ceramic powders with different sizes obtained from SSR and WC methods and the powders that will be obtained from grinding the sintered ceramics will be used as fillers in polymer matrix composite materials. Polyvinylidene fluoride (PVDF) will be used as a polymer matrix due to its relatively high  $\epsilon'\sim10$ . PVDF-ceramic composite films with various volume fractions of ceramic fillers (0-50 vol%) will be prepared.

#### 3.3 Characterizations

The crystal structure and phase formation of samples will be characterized by an X-ray diffraction (XRD) technique. The morphologies and chemical compositions will be investigated using scanning electron microscopy (SEM) and transmission electron microscopy (TEM) with an energy dispersive X-ray (EDX) spectrometer. Densities of the sintered ceramics will be measured using an *Archimedes*'s method. Valent states of each transition metal ion will be characterized using an X-ray photoelectron spectroscopy (XPS) technique. Thermal properties and decomposition of fabricated PVDF-ceramic composites will be performed using thermogravimetric and differential thermal analysis (TG-DTA).

## 3.4 Studies of dielectric and electrical properties

The dielectric properties of all sintered ceramics will be investigated as functions of frequency ( $10^2$ – $10^7$  Hz), temperature (-70 – 220 °C), and DC bias (0 – 40 volts), and compressive stress (0 – 200 MPa). Silver paint, Ag-sputtered and Au-sputtered electrodes will be coated on both surfaces of sintered ceramics to study the effect of an electrode material. *Current–voltage* (*I-V*) measurements will be done.

# 4. Schedule for the entire project

		Year 1 Month		Year 2 Month			Year 3			
	Research activity						Mor			
		1-	5-	9-	13-	16-	21-	25-	29-	33-
		4	8	12	16	20	24	28	32	36
1	Preparation of metal ions (A,B)-									
	doped TiO <sub>2</sub>									
2	Preparation of La <sub>2-x</sub> Sr <sub>x</sub> Ni <sub>1-y</sub> C <sub>y</sub> O <sub>4</sub>									
3	Characterizations: XRD, SEM,									
	EDS, TEM, and XPS techniques.									
4	Study the dielectric and electrical									
	properties of the synthesized									
	samples.									
5	Progress report (12 month)									
6	Study the effects of doping ions.									

7	Study the effects of outer surface layer, electrode materials, annealing in different atmospheres.					
8	Progress report (24 month)					
9	Fabrication of polymer-ceramic composites using PVDF as a polymer matrix.					
10	Characterizations: SEM, EDS, and TG-DTA techniques.					
11	Study the dielectric and electrical properties.					
12	Final report (36 month)					

## 5. Expected outputs

- 5.1 High-performance dielectric properties of Ga-doped In<sub>0.05</sub>Nb<sub>0.05</sub>Ti<sub>0.9</sub>O<sub>2</sub> ceramics (Journal of the American Ceramic Society, Impact Factor 2013 = 2.428)
- 5.2 Dielectric relaxations and giant dielectric response in  $In_{0.025+x}Nb_{0.025}Ti_{0.9-x}O_2$  ceramics (Journal of Applied Physics, Impact Factor 2013 = 2.185)
- 5.3 Improved giant dielectric response and temperature stability of  $(In_{0.5}Nb_{0.5})_xTi_{1-x}O_2$  ceramics (Journal of the American Ceramic Society, Impact Factor 2013 = 2.428)
- 5.4 Strongly reduced loss tangent in high-permittivity  $La_{2-x}Sr_xNiO_4$  (x = 0.1-0.5) by doping with metal ions (Journal Alloys and Compounds, Impact Factor 2013 = 2.726)
- 5.5 Effect of Sm<sup>3+</sup> doping on the microstructure and giant dielectric response in La<sub>1.7</sub>Sr<sub>0.3</sub>NiO<sub>4</sub> (Ceramics International, Impact Factor 2013 = 2.086)
- 5.6 Giant dielectric properties of metal ions co-doped  $SnO_2$  ceramics (Materials Letters, Impact Factor 2013 = 2.269)
- 5.7 High dielectric permittivity in polymer matrix composite of  $PVDF/La_{1.7}Sr_{0.3}NiO_4$  (Composites Science and Technology, Impact Factor 2013 = 3.633)
- 5.8 Fabrication and dielectric properties of PVDF/(In, Nb)-doped  $TiO_2$  parametric composite films (Composites Part B: Engineering, Impact Factor 2013 = 2.602)
- 5.9 The origin of mechanisms contributing to the overall giant dielectric response in  $TiO_2$ -based materials (Journal Alloys and Compounds, Impact Factor 2013 = 2.726)

# 6. Budget details

Details of budgets	Year 1	Year 1	Year 3	Total
1. Honorarium				
- Principal investigator (20,000 × 12 × 3)	240,000	240,000	240,000	720,000
2. Salary for research assistant	-	-	-	-
3. Materials				
- Chemical reagent & Laboratory accessories				
<ol> <li>Starting raw materials for preparation using SSR method.</li> </ol>	60,000	30,000	15,000	105,000
Starting raw materials for preparation using     WC method	60,000	30,000	25,000	115,000
3. Ethanol and ZrO <sub>2</sub> balls	20,000	10,000	10,000	40,000
4. Alumina Crucible & Alumina sheet	10,000	-		10,000
5. N,N-dimethylformamide (DMF)	-	15,000	30,000	45,000
6. Polyvinylidene fluoride (PVDF)	-	30,000	45,000	75,000
<ol><li>Other laboratory accessories</li></ol>	20,000	20,000	10,000	50,000
- Office materials	5,000	5,000	5,000	15,000
4. Other expenses				
- Sample characterizations:				
SEM and EDS	15,000	20,000	25,000	65,000
2. TEM	15,000	25,000	15,000	55,000
3. XPS	15,000	25,000	10,000	45,000
4. TG-DTA	10,000	10,000	20,000	40,000
- Electrical measurements	30,000	40,000	50,000	120,000
5. Equipment	-	-	-	-
Total	500,000	500,000	500,000	1,500,000

#### CHAPTER 1

Colossal dielectric permittivity and electrical properties of grain boundary of  $Ca_{1-3x/2}Yb_xCu_{3-y}Mg_yTi_4O_{12}$  (x = 0.05, y=0.05 and 0.30)

#### 1.1 Introduction

The dielectric and electrical properties of CaCu<sub>3</sub>Ti<sub>4</sub>O<sub>12</sub> (CCTO) ceramics have been widely investigated in recent years [1-18]. This is because CCTO can exhibit very high dielectric permittivity (ε') of more than 10<sup>4</sup> in a frequency range below 10<sup>6</sup> Hz at over a broad temperature range. Thus, it is widely believed that CCTO ceramics may have great potential for electronic applications, especially in multilayer ceramic capacitors. The dielectric loss tangent (tanδ) values of CCTO and related ACu<sub>3</sub>Ti<sub>4</sub>O<sub>12</sub> (A=Cd, La<sub>2/3</sub>, Sm<sub>2/3</sub>,  $Y_{2/3}$ ,  $Bi_{2/3}$ ,  $Na_{1/2}Y_{1/2}$ ,  $Na_{1/2}La_{1/2}$ ,  $Na_{1/2}Yb_{1/2}$ , etc) ceramics are still larger than acceptable standard values for capacitor applications [1, 5-7, 10, 19]. Its tan  $\delta$  at 1 kHz and room temperature should as low as possible, at least less than 0.03 to prevent dissipation of stored energy. However, at some temperatures, tanδ may exceed this level and in many cases become much larger when strong AC fields are applied [20]. High tanδ in a low-frequency range observed in CCTO ceramics is usually related to the high DC conductivity ( $\sigma_{DC}$ ) of bulk ceramics, following the relation  $\tan \delta \approx \sigma_{DC} / \omega \varepsilon_0 \varepsilon'$ , where  $\varepsilon'_s$  is the dielectric permittivity at low frequencies [11]. In previous work [2, 3, 21], CCTO polycrystalline ceramics were shown to be electrically heterogeneous, consisting of semiconducting grains and insulating grain boundaries (GBs). Therefore, the primary factor that controls the overall insulating properties of the bulk ceramics is its GBs. Lowering  $\sigma_{DC}$  to reduce low-frequency tan $\delta$  can be done by enhancing GB resistance  $(R_{ab}).$ 

Substitution of  $Ln^{3+}$  lanthanide ions (e.g., Gd, Dy, La, and Yb) into Ca<sup>2+</sup> sites can effectively reduce the grain size of CCTO ceramics, resulting in an increase in GB density [4, 6, 9, 10, 12, 13, 22]. However, such reduction in  $\tan\delta$  by increasing GB layers is usually accompanied by a large decrease in  $\varepsilon'$  to values much under  $10^4$  [4, 6]. In some cases, e.g., Gd, and Y-doped CCTO [10, 12], the resulting  $\tan\delta$  was still larger than acceptable values for practical applications. It is likely that the primary advantage of  $Ln^{3+}$  ions is their ability to suppress the grain growth rate of CCTO ceramics. At sufficiently high sintering temperatures, densification of  $Ln^{3+}$ -doped CCTO ceramics is continuous, while grain growth is effectively inhibited by  $Ln^{3+}$  dopants via a GB dragging phenomenon [13].

It was reported that the macroscopic  $R_{gb}$  value of CCTO ceramics obtained from impedance spectroscopy analysis increased with  $Mg^{2+}$ doping, even though the mean grain size increased [5, 7, 8]. This indicates that the resistance of individual insulating GB layers was greatly increased. Notably,  $\epsilon'$  of  $Mg^{2+}$ –doped CCTO ceramics remained at about  $10^4$  at room temperature, while  $\tan\delta$  was decreased of about 0.05 at 1 kHz [5]. Unfortunately, this reduced  $\tan\delta$  is still higher than the standard value.

Therefore, the aim of this work is to combine of the effects of two dopants to achieve a very low  $\tan\delta$  value while retaining an  $\epsilon'$  on the order of  $10^4$ . Using a new co–doping method, Yb³+ and Mg²+ doping ions were used to simultaneously improve the overall dielectric properties of a CCTO ceramic. Yb³+ was used to control the microstructure to obtain high GB density. Mg²+ was used to retain high  $\epsilon'$  and  $R_{gb}$  values. It was found that the overall dielectric properties of CCTO ceramics can be successfully improved using this strategy.

#### 1.2 Experimental details

work. (CCTO),  $Ca_{0.925}Yb_{0.05}Cu_{3}Ti_{4}O_{12}$ this CaCu<sub>3</sub>Ti<sub>4</sub>O<sub>12</sub>  $CaCu_{2.95}Mg_{0.05}Ti_4O_{12}$  (Mg05), and  $Ca_{1-3x/2}Yb_xCu_{3-y}Mg_yTi_4O_{12}$  (x = 0.05, y=0.05 and 0.30) (referenced as YbMg05 and YbMg30 samples, respectively), were prepared using a modified sol-gel method.  $Ca(C_2H_3CO_2)_2 \cdot H_2O$ (99+%,Sigma-Aldrich),  $Cu(CH_3COO)_2 \cdot H_2O$  (99.0%, Sigma-Aldrich),  $C_{16}H_{28}O_6Ti$  (75 wt. % in isopropanol, Sigma-Aldrich),  $Mg(C_4H_6O_4)\cdot 4H_2O$  (99.999%, Sigma-Aldrich),  $Yb(CH_3CO_2)_34H_2O$ (99.9%, Sigma-Aldrich), ethylene glycol, citric acid, ethanol, and de-ionized were employed as the starting raw materials. Details of the preparation method are given elsewhere [13]. The resulting dried precursors were calcined in air at 900 °C for 10 h. The powders obtained after calcination were pressed under uniaxial compression at ≈200 MPa into disk shaped objects that were 9.5 mm in diameter and ~1.1 mm in thickness. The ceramic samples were achieved by sintering at 1070 °C for 4 h using heating and cooling rates 5 °C/min.

Crystal structure and phase composition were examined using X–ray diffraction (XRD; Philips PW3040 with Cu  $K_{\alpha}$  radiation,  $\lambda$  = 0.15406 nm). Surface morphologies of all sintered ceramics were characterized using scanning electron microscopy (SEM; SEC, SNE–4500M). Elemental distribution of Yb and Mg atoms as well as the main elements of Ca, Cu, Ti, and O in the sintered CCTO ceramics was examined a field–emission scanning electron microscopy (FE–SEM) with energy-dispersive X–ray analysis (EDX) (HITACHI SU8030, Japan). Both surfaces of the sintered ceramics were polished until smooth, washed, and dried at 150 °C overnight. The polished samples were coated by sputtering Au on surfaces for 8 min at 25 mA using a Polaron SC500 sputter coating unit. The dielectric properties were measured over the temperature range of -70–220 °C using an Agilent 4294A Precision Impedance Analyzer in the frequency range of  $10^2$ – $10^7$  Hz with an oscillation voltage of 0.5 V.

#### 1.3 Results and discussion

The phase formation and crystal structure of all the sintered ceramics were investigated using an XRD technique. As shown in Fig. 1, all the XRD patterns confirm the existence of a primary  $CaCu_3Ti_4O_{12}$  phase (JCPDS 75–2188) with no impurity phases. The diffraction peaks of all the samples are perfectly indexed to the *bcc* structure with space group Im3. It may be that Yb<sup>3+</sup> and Mg<sup>2+</sup> doping ions might be substituted for  $Ca^{2+}$  and  $Cu^{2+}$  ions in the single and co–doped ceramics, respectively. It was found that co–doping ions have an effect on the lattice parameter (a) of CCTO. a values of the CCTO, YbMg05, and YbMg30 samples were found to be 7.3921±0.0002, 7.3902±0.0025, and 7.3982±0.0011, respectively. The a value tended to decreased with increasing co–doping concentration. The ionic radii of  $Cu^{2+}$  and  $Mg^{2+}$  ions are the same ( $r_4$ =0.57 Å). Thus, the increase in the a value of the YbMg30 sample compared to that of the YbMg05 sample might have resulted from lattice distortion induced by variation in the mixed–valent structure [7].

Surface morphologies of the CCTO and co-doped ceramics are shown in Figs. 2(a-c). Grain sizes of all co-doped samples are smaller than that of the un-doped CCTO sample. A slightly abnormal grain growth can be observed in the YbMg05 sample. Large grains observed in the YbMg05 sample were reduced in size by increasing Mg<sup>2+</sup> dopant concentration. Thus, the grains of the YbMg30 sample were more uniform than

those of the YbMg05 sample. The mean grain sizes of the CCTO, YbMg05, and YbMg30 samples were calculated and found to be  $\approx$ 15.86,  $\approx$ 3.37, and  $\approx$ 2.32  $\mu$ m, respectively. Pores are also observed in the microstructure of the co-doped samples, as shown in Fig. 2(b) and (c). An Archimedes method was used to determine the relative densities of all the sintered ceramics. The relative densities of the CCTO, YbMg05, and YbMg30 samples are of about 93.05, 90.30, and 91.80%, respectively.

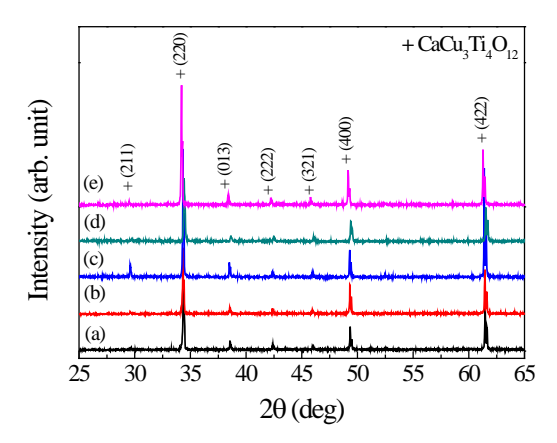
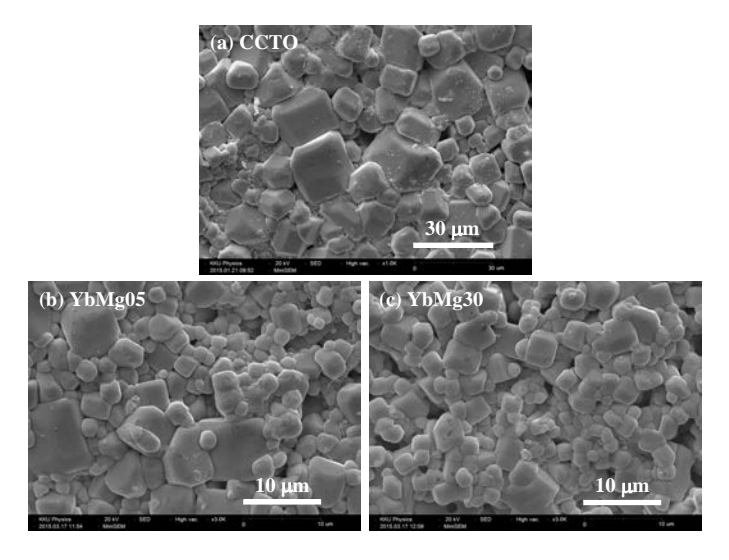
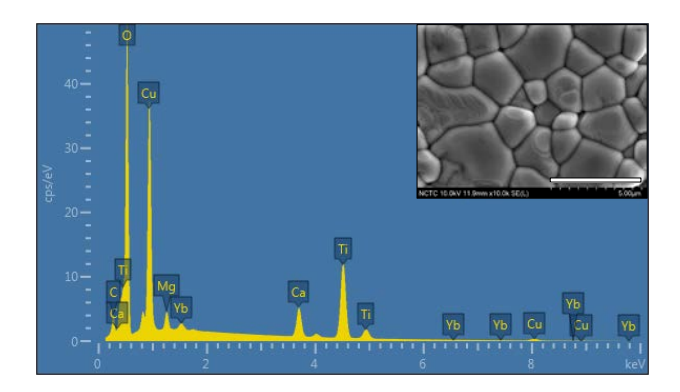


Fig. 1 XRD patterns of (a) CCTO, (b) Yb05, (c) Mg05, (d) YbMg05 and (e) YbMg30 samples.



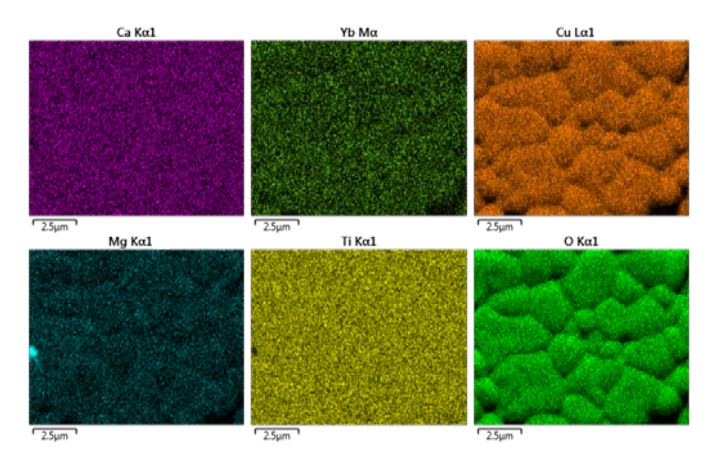
**Fig. 2** SEM images of surface microstructures of (a) CCTO, (b) YbMg05 and (c) YbMg30 samples.

Figure 3 gives the EDS spectrum of the YbMg30 sample, confirming the presence of Yb and Mg doping atoms in the ceramic sample. The main EDS–peaks for Ca, Cu, Ti, and O are also detected. To further analyze the distributions of the elements in co–doped CCTO ceramics, mapping of all elements, *i.e.*, Yb, Mg, Ca, Cu, Ti, and O, was performed. The original microstructure of the YbMg30 sample before mapping was shown in the inset of Fig. 3. As revealed in Fig. 4, the dopants were homogeneously dispersed in both the grain and grain boundary of the YbMg30 sample. Furthermore, segregation of Yb<sup>3+</sup> and Mg<sup>2+</sup> ions at any specific region (e.g., grain boundaries) was not observed.



**Fig. 3** EDS spectrum of the YbMg30 sample; inset shows the selected area for EDS testing.

L. Ni and X.M. Chen [7] reported a large increase in the mean grain size of CCTO ceramics as a result of Mg<sup>2+</sup> doping ions. This was explained as being caused by the formation of a MgO liquid phase during the sintering process, leading to a large increase the mean grain size. In our previous work [23], we found abnormal grain growth of the CCTO phase in a Mg2+-doped CCTO/CaTiO3 composite when doping with a small amount of Mg2+. Increasing Mg2+ dopant concentration resulted in a uniform microstructure with a narrow grain size distribution in both CCTO and CaTiO<sub>3</sub> phases. This may have been due to good dispersion of MgO particles in the mixed powders, leading to a uniform distribution of Mg2+ ions in the microstructure and resulting uniform grain sizes of the YbMg30 sample. By considering the effect of each doping ion (Mg2+ or Yb3+) on the grain growth mechanism of CCTO, the mean grain size of co-doped samples should increase with increasing Mg2+ content due to formation of a MgO-related liquid phase. Instead, light suppression of the grain size was observed [Figs. 2(b) and (c)]. The first consideration is that the effect of liquid phase may not be large due to low sintering temperatures used and/or short sintering times. This observation might also be attributed to the solute drag effect caused by Yb3+ doping ions [13]. It is likely that the microstructural evolution in co-doped samples cannot be well described by considering each dominant effect of Mg<sup>2+</sup> or Yb<sup>3+</sup> ion on the microstructure of CCTO ceramics. The effect of Mg<sup>2+</sup> and Yb3+ in co-doped samples and single-doped samples may be different. It is worth noting that for all co-doped ceramic systems, the regular diffusion mechanism of one doping ion may be perturbed by another one doping ion.



**Fig. 4** Element mapping of the YbMg30 sample for Ca, Yb, Cu, Mg, Ti, and O, respectively.

Figure 5 shows the frequency dependencies of the dielectric properties at 25 °C for all ceramic samples. As shown in Fig. 5(a),  $\epsilon'$  of all the samples is nearly independent of frequency from  $10^2$  to  $10^6$  Hz. In this frequency range,  $\epsilon'$  values of all the samples are in the range of  $\approx 3\times 10^3-5\times 10^5$ .  $\epsilon'$  values in the frequency range below  $10^6$  Hz of the single–doped and co–doped samples are lower than that of the un–doped CCTO sample. Under the sintering condition of 1070 °C for 4 h, the Yb05 sample has the lowest  $\epsilon'\approx 3.27\times 10^3$  at 1 kHz. As shown in the inset of Fig. 5(a), the  $\epsilon'$  values of the co–doped samples are of  $\approx 10^4$ , which is much larger than that of the Yb05 sample. In the frequency range greater than  $10^3$  Hz, the  $\epsilon'$  values of the co–doped samples are also slightly higher than the Mg05 sample. This indicates an ability of Mg²+ dopant to preserve the  $\epsilon'$  of Yb–doped CCTO ceramics.

The increase in  $\epsilon'$  of the co-doped samples is valuable only if their  $\tan\delta$  values are not enhanced as well. As illustrated in Fig. 5(b) and its inset,  $\tan\delta$  values of the co-doped samples are lower than that of the un-doped CCTO sample. Moreover,  $\tan\delta$  at 1 kHz of the YbMg05 sample is also lower than that of the Yb05 sample, but its  $\epsilon'$  value is much larger. Notably, the co-doped YbMg05 sample exhibited a high  $\epsilon' \approx 10^4$  with very low  $\tan\delta \approx 0.018$  at 25 °C and 1 kHz, while  $\tan\delta$  of the Yb05 sample was 0.027. When Mg²+doping content was increased in the co-doped sample, the  $\tan\delta$  value at 1 kHz of the YbMg30 sample was slightly increased ( $\approx 0.028$ ), while its  $\epsilon'$  was significantly increased.

According to our previous work [24], three primary mechanisms contributing to the overall  $tan\delta$  of CCTO ceramics were investigated. A high  $tan\delta$  value in a low-frequency range (<10<sup>3</sup> Hz) was mainly caused by DC conduction. An abrupt increase in  $tan\delta$  in a high-frequency range (>10<sup>5</sup> Hz) is generally resulted from the relaxation of active dipole moments that gave rise to the colossal dielectric response. The  $tan\delta$  value in a middle-frequency range originated from oscillation of ionic dipole moments and active dipole moments. As demonstrated in Fig. 5(b), high tanδ values of the un-doped CCTO and Mg05 samples in the low-frequency range are strongly dominated by the DC conduction associated with their large grain sizes (low GB density). In a low-frequency range, tanδ values of the co-doped samples are larger than that of the Yb05 sample, but lower than that of the un-doped CCTO sample. tanδ of the co-doped samples increases with increasing Mg<sup>2+</sup> doping content, which is consistent with the large low-frequency tanδ of the Mg05 sample. In the frequency range of  $10^3$ – $10^4$  Hz,  $tan\delta$  of the Yb05 sample is likely larger than those of the co-doped samples. This might be resulted from stronger lattice vibrations due to oscillation of any ions. Energy from an applied electric field is lost in overcoming inertial resistance to oscillation of ions with a specific mass. The atomic weight of Mg is much lower than that of Cu. Thus, energy used for overcoming inertial resistance to oscillate of all ions in the YbMq05 sample should be smaller than for the Yb05 sample. The larger tanδ value of the YbMg30 sample compared to the YbMg05 sample is difficult to clarify. However, this might be due to larger DC conduction in the YbMg30 sample as a result of high Mg2+ doping content just as in the case of the Mg05 sample. The largest low-frequency tanδ of the Mg05 sample resulted in an increase in  $tan\delta$  in the middle–frequency range. In this case, the effect of lattice vibrations is governed by the DC conduction effect. At 10<sup>2</sup> Hz, a tanδ value of the Yb05 sample is lowest, indicating to the ability of Yb<sup>3+</sup> to suppress the DC conduction [13].

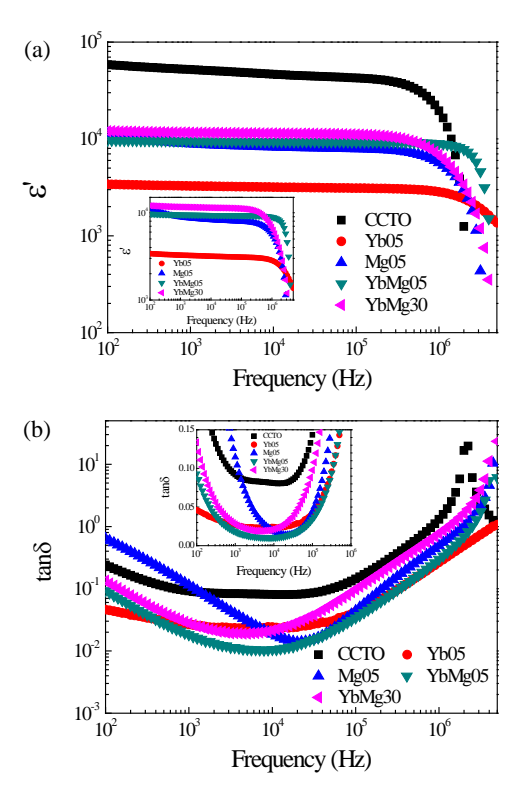


**Fig. 5** Frequency dependence of (a) ε' and (b) tanδ at 25 °C of all the samples. Their insets show enlarged views.

Therefore, it is clearly that the greatly improved dielectric performance of these co–doped samples resulted from the different roles of the Yb³+ and Mg²+ doping ions. The former dopant suppressed grain growth, yielding a small grained–microstructure. This resulted in the reduction in the DC conduction in the bulk ceramics. The latter dopant can enhance  $\epsilon'$  of the Yb–doped CCTO ceramics.

It is notable that the temperature stability of  $\epsilon'$  at 1 kHz of the co-doped samples was better than for the CCTO sample, as clearly seen in Fig. 6. Mg<sup>2+</sup> and Yb<sup>3+</sup> doping ions not only caused a large decrease in  $tan\delta$ , but also can contribute to the temperature stability of  $\epsilon'$ . The temperature dependence of  $tan\delta$  at 1 kHz of the CCTO and co-doped samples is demonstrated in the inset of Fig. 6. tanδ increases with increasing temperature, resulting from the DC conduction. The temperature coefficient of  $\epsilon'$  is another important parameter determining a dielectric material's suitability for practical capacitor applications [20, 25, 26]. Variation of  $\varepsilon'$  at 1 kHz and 25 °C ( 7万届(%)) should be in the range of ±15%. This should hold over a wide temperature range according to specific standards for ceramic capacitors. For X5R and X7R capacitors, the must be < ±15% over the ranges of -55-85 °C and -55-125 °C, respectively [20]. As shown in Fig. 7, ε' at 1 kHz of the un-doped CCTO sample was strongly dependent on temperature at temperatures higher than 80 °C. At 90 °C, // ∏ of the CCTO sample was 20.4%. As shown in the inset of Fig. 7, the temperature ranges of -70-110 °C and -70-100 °C. These ceramics have potential for application in X5R capacitors.

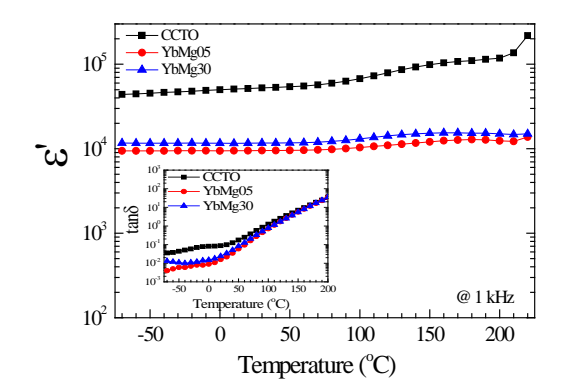


**Fig. 6** Temperature dependence of ε' for CCTO and co–doped samples; inset shows tanδ as a function of temperature.

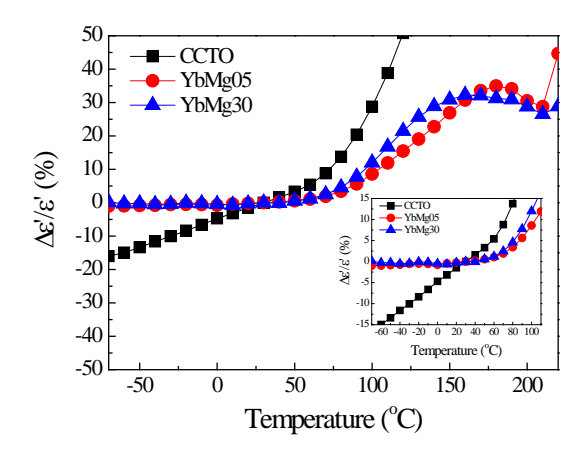


Fig. 7 Temperature coefficient of  $\epsilon'$  for CCTO, YbMg05 and YbMg30 samples. The inset shows an expanded view of  $\boxed{\text{TID}} < \pm 15\%$  in the temperature range from -70 to 110 °C.

Impedance spectroscopy was used to describe the effects of co–doping on the electrical properties of the grains and GBs. These have a close relationship to dielectric properties. The impedance data of all the ceramic samples were analyzed accounting for sample geometry by considering the ratio of area of electrode/pellet thickness.  $R_g$  and  $R_{gb}$  were determined from a nonzero intercept on the Z'–axis in the high frequency range and the diameter of a large semicircular arc in a low frequency range, respectively [3, 21]. To evaluate the values of  $R_{gb}$  at various temperatures, complex impedance ( $Z^*$ ) data were fitted to a simple equivalent circuit consisting of parallel  $R_{gb}$ – $C_{gb}$  elements using a modified equation for a  $Z^*$  plot [27]:

$$Z^* = \frac{R_{gb}}{1 + (i\omega R_{eb}C_{gb})^{\alpha}} \tag{2}$$

where  $C_{\rm gb}$  is the capacitance of GB.

 $\square$  is the an

field and  $\Box$ is constant term (0  $\leq 1$ ). According to the fitted results,  $C_{gb}$  values of the CCTO, YbMg05 and YbMg30 samples were nearly independent of temperature and found to be  $\sim$ 6.0,  $\sim$ 0.95 and  $\sim$ 1.25 nF, respectively. Changes in  $C_{gb}$  values are consistent with variation in  $\epsilon$ ' values. As shown in Fig. 8, the highest  $R_{gb}$  value is observed in the YbMg05 sample.  $R_{gb}$  values of both co-doped samples are larger than the un-doped samples. As

shown in the inset of Fig. 8,  $R_g$  of the co-doped samples increased with increasing  $Mg^{2+}$  dopant concentration.

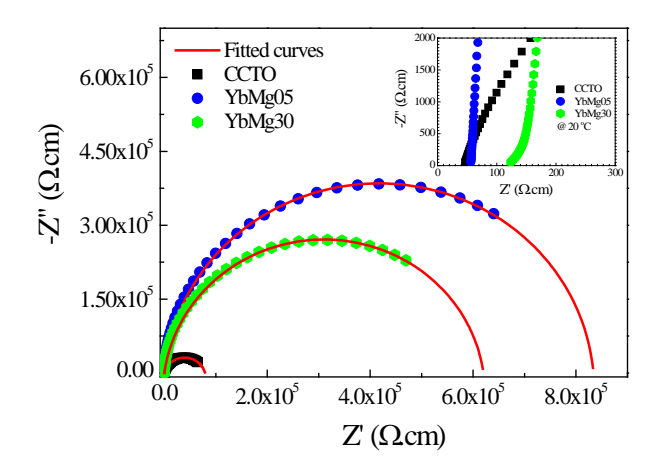


Fig. 8 Impedance complex plane (Z\*) plot at 80 °C for the CCTO, YbMg05 and YbMg30 samples. The inset shows a high CCTO, YbMg05 and YbMg30 samples.

It was also observed that variation in  $R_{\rm gb}$  values of the CCTO and co–doped samples was very consistent with changes in their  $\tan\delta$  values. This resulted from the association of low–frequency  $\tan\delta$  with DC conduction in bulk ceramics [11-13, 28]. In other words, the low–frequency  $\tan\delta$  was inversely proportional to total resistance, which is governed by  $R_{\rm gb}$  for CCTO–based compounds. Thus, it is important to note that the large increase in  $R_{\rm gb}$  is primarily due to an increase in the GB density resulting from a reduction in the mean grain size of the co–doped samples. Substitution of Yb<sup>3+</sup> can effectively reduce the grain growth through the solute drag effect thereby reducing mean grain size [13].

It was demonstrated that doping CCTO with  $Mg^{2+}$  ions can increase the resistance of individual insulating GB layers [29]. These are the two primary contributions to the significant enhancement of  $R_{gb}$  in the co–doped samples and concurrent reduction in  $\tan\delta$ . It can be seen from the fitted  $Z^*$  data that  $C_{gb}$  of the co–doped samples increased as the concentration of  $Mg^{2+}$  was increased. Thus, it is likely that another important role of  $Mg^{2+}$  is its contribution to increased  $C_{gb}$ . This may be the primary cause of the higher  $\epsilon'$  values observed in the co–doped samples than the single–doped Yb05 sample.

#### 1.4 Conclusions

The dielectric properties of CCTO ceramics were successfully improved by co–doping with Yb³+ and Mg²+ ions. The decrease in grain size of the co–doped CCTO ceramics was an important factor in reducing tan $\delta$ . Enhanced resistivity of each GB layer was due to Mg²+ doping. High values for  $\epsilon'$  (  $\approx 10^4$ ) and low values for tan $\delta$  ( $\approx 0.018-0.028$  at 1 kHz) were successfully accomplished. It is suggested that retaining high  $\epsilon'$  values may be attributed to the influence of the Mg²+ dopant on the  $C_{\rm qb}$  value.

#### References

- [1] M.A. Subramanian, D. Li, N. Duan, B.A. Reisner, A.W. Sleight, High Dielectric Constant in ACu<sub>3</sub>Ti<sub>4</sub>O<sub>12</sub> and ACu<sub>3</sub>Ti<sub>3</sub>FeO<sub>12</sub> Phases, J. Solid State Chem. 151 (2000) 323-325.
- [2] S.-Y. Chung, I.-D. Kim, S.-J.L. Kang, Strong nonlinear current–voltage behaviour in perovskite-derivative calcium copper titanate, Nat. Mater. 3 (2004) 774-778.
- [3] T.B. Adams, D.C. Sinclair, A.R. West, Influence of Processing Conditions on the Electrical Properties of CaCu<sub>3</sub>Ti<sub>4</sub>O<sub>12</sub> Ceramics, J. Am. Ceram. Soc. 89 (2006) 3129-3135.
- [4] L. Feng, X. Tang, Y. Yan, X. Chen, Z. Jiao, G. Cao, Decrease of dielectric loss in CaCu<sub>3</sub>Ti<sub>4</sub>O<sub>12</sub> ceramics by La doping, Physica Status Solidi (a) 203 (2006) R22-R24.
- [5] M. Li, G. Cai, D.F. Zhang, W.Y. Wang, W.J. Wang, X.L. Chen, Enhanced dielectric responses in Mg-doped CaCu<sub>3</sub>Ti<sub>4</sub>O<sub>12</sub>, J. Appl. Phys. 104 (2008) 074107.
- [6] S. Jin, H. Xia, Y. Zhang, Effect of La-doping on the properties of CaCu<sub>3</sub>Ti<sub>4</sub>O<sub>12</sub> dielectric ceramics, Ceram. Int. 35 (2009) 309-313.
- [7] L. Ni, X.M. Chen, Enhanced giant dielectric response in Mg-substituted CaCu<sub>3</sub>Ti<sub>4</sub>O<sub>12</sub> ceramics, Solid State Commun. 149 (2009) 379-383.
- [8] M. Li, X.L. Chen, D.F. Zhang, W.Y. Wang, W.J. Wang, Humidity sensitive properties of pure and Mg-doped CaCu<sub>3</sub>Ti<sub>4</sub>O<sub>12</sub>, Sensors and Actuators B: Chemical 147 (2010) 447-452.
- [9] R. Kashyap, R.K. Mishra, O.P. Thakur, R.P. Tandon, Structural, dielectric properties and electrical conduction behaviour of Dy substituted CaCu<sub>3</sub>Ti<sub>4</sub>O<sub>12</sub> ceramics, Ceram. Int. 38 (2012) 6807-6813.
- [10] R. Kashyap, O.P. Thakur, R.P. Tandon, Study of structural, dielectric and electrical conduction behaviour of Gd substituted CaCu<sub>3</sub>Ti<sub>4</sub>O<sub>12</sub> ceramics, Ceram. Int. 38 (2012) 3029-3037.
- [11] S. Vangchangyia, E. Swatsitang, P. Thongbai, S. Pinitsoontorn, T. Yamwong, S. Maensiri, V. Amornkitbamrung, P. Chindaprasirt, Very Low Loss Tangent and High Dielectric Permittivity in Pure-CaCu<sub>3</sub>Ti<sub>4</sub>O<sub>12</sub> Ceramics Prepared by a Modified Sol-Gel Process, J. Am. Ceram. Soc. 95 (2012) 1497-1500.
- [12] J. Boonlakhorn, P. Kidkhunthod, B. Putasaeng, T. Yamwong, P. Thongbai, S. Maensiri, Effects of Y doping ions on microstructure, dielectric response, and electrical properties of  $Ca_{1-3x/2}Y_xCu_3Ti_4O_{12}$  ceramics, J. Mater. Sci.: Mater. Electron. 26 (2015) 2329-2337.
- [13] J. Boonlakhorn, P. Thongbai, B. Putasaeng, T. Yamwong, S. Maensiri, Very high-performance dielectric properties of  $Ca_{1-3x/2}Yb_xCu_3Ti_4O_{12}$  ceramics, J. Alloys Compd. 612 (2014) 103-109.
- [14] A. Singh, S. Md Mursalin, P. Rana, S. Sen, Electrical properties of palladium-doped CaCu<sub>3</sub>Ti<sub>4</sub>O<sub>12</sub> ceramics, Applied Physics A (2015) 1-11.
- [15] R. Xue, D. Liu, Z. Chen, H. Dai, J. Chen, G. Zhao, Dielectric and Nonohmic Properties of CaCu<sub>3</sub>Ti<sub>4</sub>O<sub>12</sub>/SrTiO<sub>3</sub> Ceramics, J. Electron. Mater. 44 (2015) 1088-1094.
- [16] Y. Liu, Q. Chen, X. Zhao, Dielectric response of Sb-doped CaCu<sub>3</sub>Ti<sub>4</sub>O<sub>12</sub> ceramics, J. Mater. Sci.: Mater. Electron. 25 (2014) 1547-1552.
- [17] M. Ahmad, H. Mahfoz Kotb, Giant dielectric properties of fine-grained  $Na_{1/2}Y_{1/2}Cu_3Ti_4O_{12}$  ceramics prepared by mechanosynthesis and spark plasma sintering, J. Mater. Sci.: Mater. Electron. 26 (2015) 8939-8948.
- [18] Y. Yang, X. Wang, B. Liu, CaCu<sub>3</sub>Ti<sub>4</sub>O<sub>12</sub> ceramics from different methods: microstructure and dielectric, J. Mater. Sci.: Mater. Electron. 25 (2014) 146-151.
- [19] M. Ab Rahman, S. Hutagalung, Z. Ahmad, M. Ain, J. Mohamed, The effect of different dopant site (Cu and Ca) by magnesium on  $CaCu_3Ti_4O_{12}$  dielectric properties, J. Mater. Sci.: Mater. Electron. 26 (2015) 3947-3956.
- [20] A.J. Moulson, J.M. Herbert, Electroceramics: materials, properties, applications, 2nd ed., Wiley, West Sussex; New York, 2003.
- [21] R. Schmidt, M.C. Stennett, N.C. Hyatt, J. Pokorny, J. Prado-Gonjal, M. Li, D.C. Sinclair, Effects of sintering temperature on the internal barrier layer capacitor (IBLC) structure in  $CaCu_3Ti_4O_{12}$  (CCTO) ceramics, J. Eur. Ceram. Soc. 32 (2012) 3313-3323.
- [22] B. Shri Prakash, K.B.R. Varma, Microstructural and dielectric properties of donor doped (La<sup>3+</sup>) CaCu<sub>3</sub>Ti<sub>4</sub>O<sub>12</sub> ceramics, J. Mater. Sci.: Mater. Electron. 17 (2006) 899-907.

- [23] J. Jumpatam, B. Putasaeng, T. Yamwong, P. Thongbai, S. Maensiri, A novel strategy to enhance dielectric performance and non-Ohmic properties in Ca<sub>2</sub>Cu<sub>2-x</sub>Mg<sub>x</sub>Ti<sub>4</sub>O<sub>12</sub>, J. Eur. Ceram. Soc. 34 (2014) 2941-2950.
- [24] J. Boonlakhorn, P. Thongbai, Effect of Annealing in O<sub>2</sub> and Mechanisms Contributing to the Overall Loss Tangent of CaCu<sub>3</sub>Ti<sub>4</sub>O<sub>12</sub> Ceramics, J. Electron. Mater. 44 (2015) 3687-3695.
- [25] Y. Sun, H. Liu, H. Hao, Z. Song, S. Zhang, Structure Property Relationship in BaTiO<sub>3</sub>–Na<sub>0.5</sub>Bi<sub>0.5</sub>TiO<sub>3</sub>–Nb<sub>2</sub>O<sub>5</sub>–NiO X8R System, J. Am. Ceram. Soc. 98 (2015) 1574-1579.
- [26] A. Zeb, Y. Bai, T. Button, S.J. Milne, Temperature-Stable Relative Permittivity from  $-70^{\circ}$ C to 500°C in (Ba<sub>0.8</sub>Ca<sub>0.2</sub>)TiO<sub>3</sub>–Bi(Mg<sub>0.5</sub>Ti<sub>0.5</sub>)O<sub>3</sub>–NaNbO<sub>3</sub> Ceramics, J. Am. Ceram. Soc. 97 (2014) 2479-2483.
- [27] J. Liu, C.-G. Duan, W.-G. Yin, W. Mei, R. Smith, J. Hardy, Large dielectric constant and Maxwell-Wagner relaxation in Bi<sub>2/3</sub>Cu<sub>3</sub>Ti<sub>4</sub>O<sub>12</sub>, Phys. Rev. B 70 (2004) 144106.
- [28] S. De Almeida-Didry, C. Autret, A. Lucas, C. Honstettre, F. Pacreau, F. Gervais, Leading role of grain boundaries in colossal permittivity of doped and undoped CCTO, J. Eur. Ceram. Soc. 34 (2014) 3649-3654.
- [29] J. Boonlakhorn, P. Thongbai, Mg-doped CaCu<sub>3</sub>Ti<sub>4</sub>O<sub>12</sub> nanocrystalline powders prepared by a modified sol–gel method: Preparation, characterization, and their giant dielectric response, Jpn. J. Appl. Phys. 54 (2015) 06FJ06.

#### **CHAPTER 2**

# Improved Dielectric Properties of (Y+Mg) co-doped CaCu<sub>3</sub>Ti<sub>4</sub>O<sub>12</sub> Ceramics by Controlling Geometric and Intrinsic Properties of Grain Boundaries

#### 2.1 Introduction

Since colossal dielectric permittivity ( $\epsilon$ ') of CaCu<sub>3</sub>Ti<sub>4</sub>O<sub>12</sub> (CCTO) was first reported by Subramanian et al. [1], investigations to reduce the dielectric loss tangent ( $\tan\delta$ ) of CCTO have been extensively done [2-8]. Although CCTO can exhibit very high  $\epsilon' \sim 10^4$ , its  $\tan\delta$  is still larger than the acceptable standard value for capacitor applications. This is one of the most serious problems inhibiting the use of CCTO. Clearly, CCTO polycrystalline ceramics are electrically heterogeneous, consisting of insulating grain boundaries (GBs) and n-type semiconducting grains [9]. This is called an internal barrier layer capacitor (IBLC) structure. Such microstructure is widely accepted to be the primary cause of a material's high dielectric response. This also resulted in the formation of double Schottky barriers at the GBs [9, 10], producing the nonlinear current–voltage (or nonlinear current density–electric field, J–E) behavior of CCTO [6, 7, 9].

Generally, low–frequency  $\tan\delta$  is closely correlated to conductivity ( $\sigma_{dc}$ ) caused by long-range motion of charge carriers [6]. According to the IBLC structure, low–frequency  $\tan\delta$  can be reduced by increasing the total resistance of the bulk ceramics. This can be achieved by increasing the resistance of the insulating GBs ( $R_{gb}$ ) because the grain resistance ( $R_g$ ) of CCTO is much lower than that of the GB [11, 12]. Many strategies for reducing  $\tan\delta$  have been proposed that are based on the enhancement of GB resistance or internal interface resistance [2-4, 7, 8, 13, 14]. These can be divided into two primary groups based on whether they improve geometric or intrinsic properties of GBs [7]. The former can be achieved by controlling the microstructure to obtain a small grained microstructure with a large number of insulating GB layers [4, 7, 13, 14]. The latter is accomplished by modifying the intrinsic properties of the GBs, i.e., by increasing in the resistivity of individual GBs [3, 8, 15]. Decreasing  $\tan\delta$  and  $\sigma_{dc}$  can be accomplished by improving either the geometric or intrinsic properties of the GBs.

Usually, substitution of  $Ln^{3+}$  ions (e.g.,  $La^{3+}$ ,  $Gd^{3+}$ ,  $Y^{3+}$ ) into  $Ca^{2+}$  sites of CCTO can effectively suppress the grain growth rate, achieving a small grained microstructure [13, 14, 16, 17]. In this case,  $tan\delta$  was decreased by means of improving the geometric factors at the GBs. On the other hand, substitution of  $Mg^{2+}$  into  $Cu^{2+}$  sites caused an increase in the mean grain size or decreased GB density, but can also reduce the low-frequency  $tan\delta$  [15]. This indicated that a largely enhanced resistivity of each GB layer in Mg-doped CCTO ceramics was achieved. It is expected that co-doping CCTO with  $Ln^{3+}$  and  $Mg^{2+}$  may influence the geometric and intrinsic properties of the GBs.

In this work, a novel strategy for simultaneously tuning a ceramic microstructure and intrinsic electrical properties of GBs was explored to achieve a high-performance CCTO with a very low  $\tan\delta$ . A high  $\epsilon'$ ~8635 and very low  $\tan\delta$ ~0.013 at 1 kHz were accomplished by this method using Y³+ and Mg²+ co-doping ions.

## 2.2 Experimental details

 $CaCu_{3}Ti_{4}O_{12} \ (CCTO), \ Ca_{0.925}Y_{0.05}Cu_{3}Ti_{4}O_{12} \ (Y05), \ CaCu_{2.95}Mg_{0.05}Ti_{4}O_{12} \ (Mg05), \\ and \ Ca_{0.925}Y_{0.05}Cu_{2.95}Mg_{0.05}Ti_{4}O_{12} \ (Y-Mg05) \ were prepared using a modified sol–gel of the control of the cont$ 

method.  $Ca(C_2H_3CO_2)_2\cdot H_2O$  (99+%, Sigma–Aldrich),  $Cu(CH_3COO)_2\cdot H_2O$  (99.0%, Sigma–Aldrich),  $C_{16}H_{28}O_6Ti$  (75 wt. % in isopropanol, Sigma–Aldrich),  $Mg(C_4H_6O_4)\cdot 4H_2O$  (99.99%, Sigma–Aldrich),  $Y(CH_3CO_2)_3\cdot xH_2O$  (99.9 %, Sigma-Aldrich), ethylene glycol, citric acid, ethanol, and de–ionized water were used as starting raw materials. Details of the preparation method are given elsewhere [6]. Dried precursors were heated at 900 °C for 10 h. The powders obtained were pressed by uniaxial compression at 200 MPa into disks 9.5 mm in diameter and ~1.2 mm in thickness. The compacted powders were sintered in air at 1070 °C for 6 h using heating and cooling rates 5 °C/min.

X–ray diffraction (XRD; Philips PW3040 with Cu  $K_{\alpha}$  radiation,  $\lambda$  = 0.15406 nm) was used to characterize the phase formation in the sintered ceramics. Microstructures of the sintered ceramics were characterized using scanning electron microscopy (SEM) and energy-dispersive X-ray spectrometry (EDS) (SEC, SNE–4500M). To prepare electrodes, surfaces of the sintered ceramics were polished and then coated with Au for 8 min at 25 mA using a Polaron SC500 sputter coating unit. The dielectric properties were measured using a precision impedance analyzer (Agilent 4294A) over the frequency range of  $10^2$ – $10^7$  Hz with an oscillation voltage of 0.5 V. The measurement was performed over a temperature range from -70 to 220 °C. J–E characteristics were measured at room temperatures using a high voltage measurement unit (Keithley Model 247).  $E_b$  was defined as the electric field breakdown strength at which J = 1 mA/cm². The nonlinear coefficient ( $\alpha$ ) was calculated in the range of 1–10 mA.cm².

#### 2.3 Results and discussion

As shown in Fig. 1, a single phase of CaCu<sub>3</sub>Ti<sub>4</sub>O<sub>12</sub> (JCPDS 75–2188) can be observed in all the XRD patterns. No impurity phase was detected by this technique. The diffraction peaks in all the XRD patterns were perfectly indexed to the *bcc* structure within the space group *Im*3. Lattice parameter (*a*) values of CCTO, Y05, Mg05, and Y-Mg05 samples were of 7.391, 7.391, 7.393, and 7.395 Å, respectively. Changes in *a* may not be associated with the concentration of Mg<sup>2+</sup> due to the similarity of the ionic radii of the dopants and host ions. This slight variation might be attributed to the effect of lattice distortion induced by the variations in this mixed–valent structure [15].

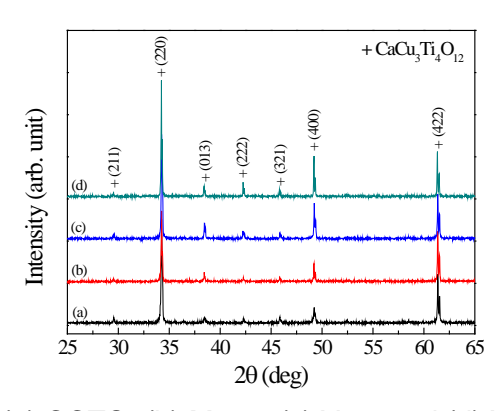
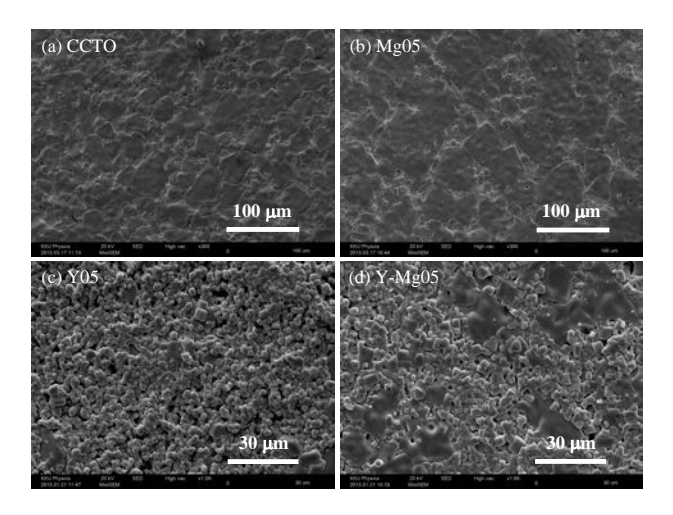


Fig. 1 XRD patterns of (a) CCTO, (b) Mg05, (c) Y05, and (d) Y-Mg05 samples.

As shown in Fig. 2, the microstructures of Y05 and Mg05 samples were very dissimilar. The former and latter exhibited strongly reduced and largely enhanced grain growth rates, respectively. The mean grain sizes of the CCTO, Y05, and Mg05 samples were approximately  $26.26\pm9.53$ ,  $2.52\pm1.07$ , and  $45.65\pm17.16$  µm, respectively. Their relative densities were about 92.8, 89.25, and 94.4%, respectively. The increase in the

mean grain size in the Mg05 sample was similar to that observed in  $CaCu_{2.85}Mg_{0.15}Ti_4O_{12}$  prepared using a solid state reaction method [15]. Its grain size increased by a factor of  $\approx 1.66$  compared to the un-doped CCTO. By doping Y³+ into Mg-doped CCTO, the grain size was greatly reduced to  $3.73\pm 1.08~\mu m$  with a relative density of  $\sim 89.1\%$ . However, a small number of large grains were also observed in the Y-Mg05 sample. The decrease in the mean grain size due to substitution of Y³+ into the ceramic arises from the solute drag effect [14, 18].



**Fig. 2** SEM images of the surface morphologies of (a) CCTO, (b) Mg05, (c) Y05, and (d) Y-Mg05 samples.

Segregation of Mg<sup>2+</sup> ions and Y<sup>3+</sup> doping ions as well as the existence of major elements in the microstructure of Y-Mg05 sample was characterized by using an SEM-EDS technique. As shown in Figs. 3(a) and (b), a mall EDS peak corresponding to Mg is likely observed in both of the large and small grains. Moreover, EDS results revealed that Mg<sup>2+</sup> ions segregated at both GBs region and within the grains. Unfortunately, Y<sup>3+</sup> ions cannot be observed. All possible EDS peaks of the major elements for Ca, Cu, Ti, and O were also detected.

A microstructure with high GB density and enhanced resistivity at individual GB layer can only be accomplished if the macroscopic total resistance of the GBs of the codoped Y-Mg05 sample is significantly larger than that of the single-doped Y05 sample. To clarify this, an impedance spectroscopy analysis was carried out. The total resistances of grains  $(R_a)$  and GBs  $(R_{ab})$  of CCTO ceramics can generally be determined from a nonzero intercept on the Z'-axis in the high frequency range and the diameter of a large semicircular arc in the low frequency range, respectively [10-12]. As shown in Fig. 4(a) and inset (1), R<sub>qb</sub> values at 80 °C of the CCTO, Y05, Mg05, and Y-Mg05 samples were of ~1.71×10<sup>4</sup>, 4.79×10<sup>5</sup>, 2.01×10<sup>5</sup>, and 1.28×10<sup>6</sup>  $\Omega$ .cm, respectively.  $R_{gb}$  of CCTO ceramics was largely increased by doping with a single-dopant, either Y3+ or Mg2+. From SEM images, increases in R<sub>ab</sub> in these two cases were primarily associated with geometric and intrinsic parameters of the GBs, respectively.  $R_{ab}$  of the Mg05 sample was significantly increased by an order of magnitude compared to that of the CCTO sample even though the GB density was decreased. This clearly indicates a great increase in resistivity of individual GB layers of the Mg05 sample. Alternatively, largely enhanced  $R_{ab}$  of the Y05 sample was dominated by the geometric parameter due to the increase in GB density. Notably, R<sub>gb</sub> of the Y-Mg05 sample was larger than that of the Y05 sample, while the

geometric properties of these two samples were not significantly different. The intrinsic factor of the GB of the Y-Mg05 sample was more dominant than that of the Y05 sample, which was improved by addition of Mg<sup>2+</sup>. Thus, in this current study, the desirable ceramic microstructure was successfully achieved in the co-doped Y-Mg05 sample. It is notable that the both single and co-doping ions have a slight effect on the electrical properties of the grains, as shown in the inset (2) of Fig. 4(a).

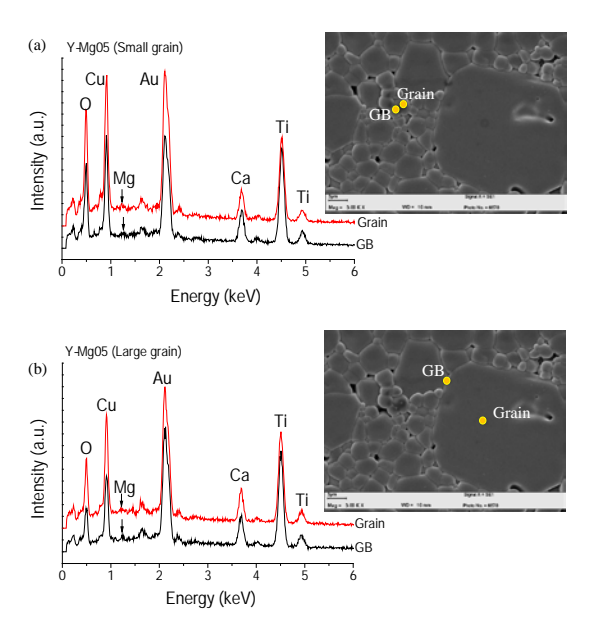


**Fig. 3** EDS spectra of the Y-Mg05 sample detected at (a) small grain and (b) large grain regions; yellow circles in the SEM images are marked as the testing EDS points.

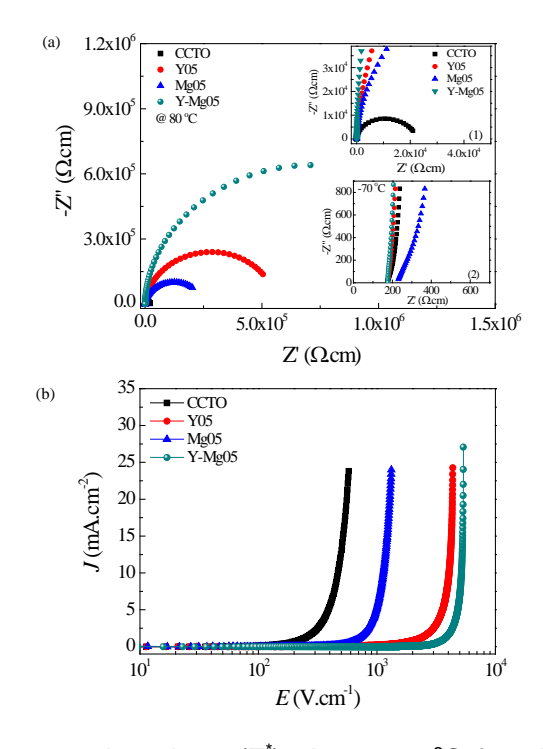


**Fig. 4** (a) Impedance complex plane (Z<sup>\*</sup>) plot at 80 °C for all the samples; insets (1) and (2) show expanded views close to the origin of Z\* plot at 80 and -70 °C, respectively. (b) *J–E* curves at room for all the samples.

CCTO can exhibit nonlinear J–E properties, which can be attributed to the creation of an electrostatic potential barrier at the GBs [9]. Generally, both the intrinsic and geometric parameters of the GBs influence the nonlinear properties [7]. As shown in Fig. 4(b), the effect of single and co-doping ions on the nonlinear properties is very consistent with the results obtained from the impedance spectroscopy analysis, even though these two measurements were conducted under different applied electric field levels.  $E_b$  values of the CCTO, Y05, Mg05, and Y-Mg05 samples were ~233.2, 2190.2, 811.3, and 3659.9 V/cm, respectively, whereas  $\alpha$  values were 3.32, 3.70, 4.85, and 6.60, respectively. These results clearly confirm that both the intrinsic and geometric parameters of the GBs of CCTO ceramics were simultaneously enhanced by co-doping with Y<sup>3+</sup> and Mg<sup>2+</sup>.

As demonstrated in Fig. 5(a) and its inset, ε' and tanδ of CCTO ceramics were decreased by both single and co-doping. However, the ε' values at 1 kHz and 20 °C of the CCTO, Y05, Mg05, and Y-Mg05 samples were still quite large, 66423, 5726, 18156, and 8634, respectively.  $tan\delta$  values were about 0.108, 0.065, 0.045, and 0.013, respectively. As shown in Fig. 2, dense ceramic microstructure was achieved in the CCTO and Mg05 samples, while residual pores were observed on the surface of the Y05 sample. Thus, the large difference in  $\varepsilon'$  values of the CCTO and Y05 samples is likely due to the effects of the GB response and porosity. Interestingly, the slightly better microstructure of the sintered Y-Mg05 sample can significantly enhance the dielectric properties compared to that of the Y05 sample. This result is similar to that reported in literature [19]. This indicates that the intrinsic properties of the GBs (e.g., the resistivity and capacitance of the GB) can be enhanced by Mg<sup>2+</sup> doping ions. Interestingly, the tanδ value of the Y-Mg05 sample was the lowest among the samples presented. It was less than 0.05 over the frequency range of 10<sup>2</sup>-10<sup>5</sup> Hz. Furthermore, ε' at 20 °C of the Y-Mg05 sample was independent of frequency over the range from 10<sup>2</sup> to 10<sup>6</sup> Hz. It is notable that the temperature stability of  $\varepsilon'$  at 1 kHz of the Y-Mg05 sample was better than for other samples, as shown in Fig. 5(b). For the CCTO, Y05, and Mg05 samples, ε' at 1 kHz largely increased as temperature higher than 100 °C. This result is similar to those observed in literature [14, 17, 20-22]. Excellent dielectric properties of CCTO with a very low  $tan\delta$  and a high  $\epsilon'$  that was independent of frequency and temperature was successfully achieved by simultaneously tuning the geometric and intrinsic properties of the GBs by co-doping with Y3+ and Mg2+, respectively.

A high  $\tan\delta$  value over a low–frequency range is generally induced by DC conduction ( $\sigma_{dc}$ ). Fig. 4(a) clearly shows that  $R_g << R_{gb}$ . Thus, the relationship between  $\tan\delta$  and  $\sigma_{dc}$  can be estimated by following equation [6]:

$$\tan \delta \approx \frac{1}{\omega \varepsilon_0 \varepsilon_s' C_0 R_{gb}} , \qquad (1)$$

where  $\mathcal{E}_s'$  is the dielectric permittivity over a low–frequency range.  $C_o$  is the empty cell capacitance. Clearly, the low–frequency  $\tan\delta$  value of the Y-Mg05 sample was very much reduced by greatly increasing  $R_{\rm gb}$ , which was accomplished by simultaneously improving both the intrinsic and geometric properties of the GBs.

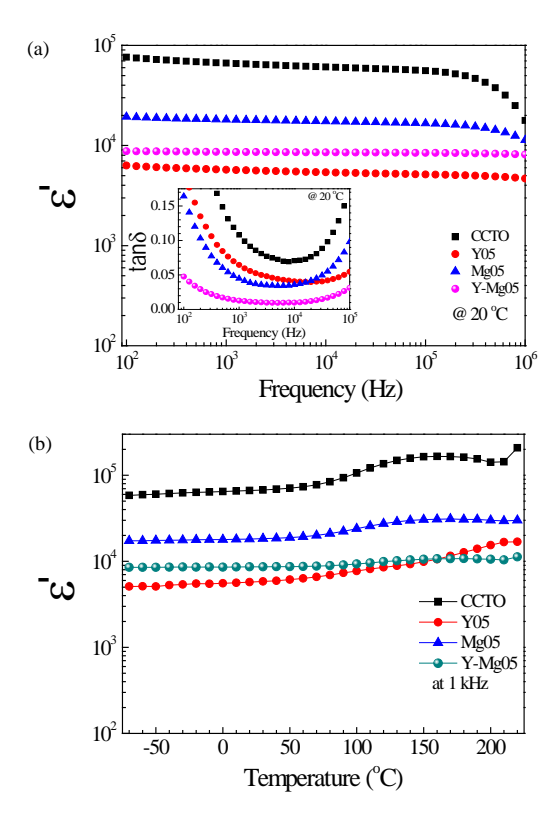


**Fig. 5** (a) Frequency dependence of  $\varepsilon'$  at 20 °C for all the samples; inset shows tanδ as a function of frequency at 20 °C. (b)  $\varepsilon'$  at 1 kHz as a function of temperature.

#### 2.4 Conclusions

A desirable CCTO microstructure of with a high GB density, greatly enhanced  $R_{gb}$  with improved overall dielectric properties was obtained by co-doping with Y³+ and Mg²+ into Ca²+ and Cu²+ sites, respectively. Significantly enhanced dielectric properties were achieved as a result of simultaneously controlling the geometric and intrinsic properties of the GBs. Excellent dielectric properties were successfully achieved in a (Y and Mg) co-doped CCTO ceramic.  $\epsilon'$  was high (~8634) and  $\tan\delta$  was very low (~0.013) with good stability over a wide range of temperatures and frequencies.

#### References

- [1] M.A. Subramanian, D. Li, N. Duan, B.A. Reisner, A.W. Sleight, High Dielectric Constant in ACu<sub>3</sub>Ti<sub>4</sub>O<sub>12</sub> and ACu<sub>3</sub>Ti<sub>3</sub>FeO<sub>12</sub> Phases, J. Solid State Chem., 151 (2000) 323-325.
- [2] E.A. Patterson, S. Kwon, C.-C. Huang, D.P. Cann, Effects of ZrO<sub>2</sub> additions on the dielectric properties of CaCu<sub>3</sub>Ti<sub>4</sub>O<sub>12</sub>, Appl. Phys. Lett., 87 (2005) 182911.
- [3] Z. Yang, L. Zhang, X. Chao, L. Xiong, J. Liu, High permittivity and low dielectric loss of the Ca<sub>1-x</sub>Sr<sub>x</sub>Cu<sub>3</sub>Ti<sub>4</sub>O<sub>12</sub> ceramics, J. Alloys Compd., 509 (2011) 8716-8719.
- [4] Y.-H. Lin, J. Cai, M. Li, C.-W. Nan, J. He, High dielectric and nonlinear electrical behaviors in TiO<sub>2</sub>-rich CaCu3Ti4O12 ceramics, Appl. Phys. Lett., 88 (2006) 172902.
- [5] W. Kobayashi, I. Terasaki, CaCu<sub>3</sub>Ti<sub>4</sub>O<sub>12</sub>/CaTiO<sub>3</sub> composite dielectrics: Ba/Pb-free dielectric ceramics with high dielectric constants, Appl. Phys. Lett., 87 (2005) 032902.
- [6] S. Vangchangyia, E. Swatsitang, P. Thongbai, S. Pinitsoontorn, T. Yamwong, S. Maensiri, V. Amornkitbamrung, P. Chindaprasirt, Very Low Loss Tangent and High Dielectric Permittivity in Pure-CaCu<sub>3</sub>Ti<sub>4</sub>O<sub>12</sub> Ceramics Prepared by a Modified Sol-Gel Process, J. Am. Ceram. Soc., 95 (2012) 1497-1500.
- [7] P. Thongbai, T. Yamwong, S. Maensiri, V. Amornkitbamrung, P. Chindaprasirt, Improved Dielectric and Nonlinear Electrical Properties of Fine-Grained CaCu<sub>3</sub>Ti<sub>4</sub>O<sub>12</sub> Ceramics Prepared by a Glycine-Nitrate Process, J. Am. Ceram. Soc., 97 (2014) 1785–1790.
- [8] J. Jumpatam, B. Putasaeng, T. Yamwong, P. Thongbai, S. Maensiri, A novel strategy to enhance dielectric performance and non-Ohmic properties in Ca<sub>2</sub>Cu<sub>2-x</sub>Mg<sub>x</sub>Ti<sub>4</sub>O<sub>12</sub>, J. Eur. Ceram. Soc., 34 (2014) 2941-2950.
- [9] S.-Y. Chung, I.-D. Kim, S.-J.L. Kang, Strong nonlinear current–voltage behaviour in perovskite-derivative calcium copper titanate, Nat. Mater., 3 (2004) 774-778.
- [10] T. Adams, D. Sinclair, A. West, Characterization of grain boundary impedances in fine- and coarse-grained CaCu<sub>3</sub>Ti<sub>4</sub>O<sub>12</sub> ceramics, Phys. Rev. B, 73 (2006) 094124.
- [11] T.B. Adams, D.C. Sinclair, A.R. West, Influence of Processing Conditions on the Electrical Properties of CaCu<sub>3</sub>Ti<sub>4</sub>O<sub>12</sub> Ceramics, J. Am. Ceram. Soc., 89 (2006) 3129-3135.
- [12] R. Schmidt, M.C. Stennett, N.C. Hyatt, J. Pokorny, J. Prado-Gonjal, M. Li, D.C. Sinclair, Effects of sintering temperature on the internal barrier layer capacitor (IBLC) structure in CaCu<sub>3</sub>Ti<sub>4</sub>O<sub>12</sub> (CCTO) ceramics, J. Eur. Ceram. Soc., 32 (2012) 3313-3323.
- [13] S.F. Shao, J.L. Zhang, P. Zheng, C.L. Wang, J.C. Li, M.L. Zhao, High permittivity and low dielectric loss in ceramics with the nominal compositions of CaCu<sub>3-x</sub>La<sub>2x/3</sub>Ti<sub>4</sub>O<sub>12</sub>, Appl. Phys. Lett., 91 (2007) 042905.
- [14] J. Boonlakhorn, P. Kidkhunthod, B. Putasaeng, T. Yamwong, P. Thongbai, S. Maensiri, Effects of Y doping ions on microstructure, dielectric response, and electrical properties of Ca<sub>1-3x/2</sub>Y<sub>x</sub>Cu<sub>3</sub>Ti<sub>4</sub>O<sub>12</sub> ceramics, J. Mater. Sci.: Mater. Electron., 26 (2015) 2329-2337.
- [15] L. Ni, X.M. Chen, Enhanced giant dielectric response in Mg-substituted CaCu<sub>3</sub>Ti<sub>4</sub>O<sub>12</sub> ceramics, Solid State Commun., 149 (2009) 379-383.
- [16] S. Jin, H. Xia, Y. Zhang, Effect of La-doping on the properties of CaCu<sub>3</sub>Ti<sub>4</sub>O<sub>12</sub> dielectric ceramics, Ceram. Int., 35 (2009) 309-313.
- [17] R. Kashyap, O.P. Thakur, R.P. Tandon, Study of structural, dielectric and electrical conduction behaviour of Gd substituted CaCu<sub>3</sub>Ti<sub>4</sub>O<sub>12</sub> ceramics, Ceram. Int., 38 (2012) 3029-3037.
- [18] M.N. Rahaman, Ceramic processing and sintering, 2nd ed., M. Dekker, New York, 2003.
- [19] M. Ab Rahman, S. Hutagalung, Z. Ahmad, M. Ain, J. Mohamed, The effect of different dopant site (Cu and Ca) by magnesium on CaCu<sub>3</sub>Ti<sub>4</sub>O<sub>12</sub> dielectric properties, J. Mater. Sci.: Mater. Electron., 26 (2015) 3947-3956.
- [20] L. Singh, U.S. Rai, K.D. Mandal, Dielectric, modulus and impedance spectroscopic studies of nanostructured  $CaCu_{2.70}Mg_{0.30}Ti_4O_{12}$  electro-ceramic synthesized by modified sol–gel route, J. Alloys Compd., 555 (2013) 176-183.
- [21] L. Singh, U.S. Rai, K.D. Mandal, N.B. Singh, Progress in the growth of CaCu<sub>3</sub>Ti<sub>4</sub>O<sub>12</sub> and related functional dielectric perovskites, Prog. Cryst. Growth Charact. Mater., 60 (2014) 15-62.
- [22] L. Sun, Z. Wang, W. Hao, E. Cao, Y. Zhang, H. Peng, Influence of Zirconium doping on microstructure and dielectric properties of  $CaCu_3Ti_4O_{12}$  synthesized by the sol–gel method, J. Alloys Compd., 651 (2015) 283-289.

#### CHAPTER 3

# Microstructural Evolution and Strongly Enhanced Dielectric Response in Sn-Doped CaCu<sub>3</sub>Ti<sub>4</sub>O<sub>12</sub>/CaTiO<sub>3</sub> Ceramic Composites

#### 3.1 Introduction

Recently, investigations to reduce the dielectric loss tangent ( $tan\delta$ ) of  $CaCu_3Ti_4O_{12}$  (CCTO) ceramics and related compounds have been intensively conducted [1-10]. Although CCTO ceramics can exhibit high dielectric permittivity values ( $\epsilon$ ') of about  $10^4$ – $10^5$ , their  $tan\delta$  values are still too large [3, 4, 11-14]. CCTO ceramics with a high  $\epsilon$ ' value and low  $tan\delta$  may be desirable for multilayer ceramic capacitors. It was found that improved dielectric and electrical properties of CCTO were obtained by deliberately creating a composite system of CCTO/CaTiO $_3$  (CTO) with the nominal chemical formula of  $Ca_2Cu_2Ti_4O_{12}$  [1, 6, 9, 15-17]. CCTO/CTO composites have very low  $tan\delta$  of  $\sim$ 0.02 compared to CCTO ceramics ( $tan\delta > 0.5$ ) [1]. Moreover, improved nonlinear current density–electric field (or non–Ohmic) properties were achieved in this composite system. Very high breakdown electric field ( $E_b$ ) and nonlinear coefficient ( $\alpha$ ) values were observed in CCTO/CTO [15].

Recently, many metal ions were substituted into Cu<sup>2+</sup> or Ti<sup>4+</sup> sites of a single phase of CCTO ceramics in order to improve their dielectric properties [2-4, 11, 18-20]. It was reported that doping CCTO with suitable ions such as Mg<sup>2+</sup> [20], Zr<sup>4+</sup> [2], and Sn<sup>4+</sup> [4] can reduce  $tan\delta$  values. Unfortunately, the reduced values of  $tan\delta$  due to substitution of these ions were still higher than the standard value for capacitor applications. This may be due to a large initial  $tan\delta$  value of CCTO. According to our previous research,  $\varepsilon'$  values of CCTO/CTO composites prepared using a nominal formula of Ca<sub>2</sub>Cu<sub>2</sub>Ti<sub>4</sub>O<sub>12</sub> were greatly enhanced by doping Zn<sup>2+</sup> and Mg<sup>2+</sup> ions into Cu<sup>2+</sup> sites. Notably, its tanδ value was still low [9, 17]. These may be desirable for capacitor applications. Simultaneously, the nonlinear current density-electric field properties of the composites were significantly improved. Using this concept, substitution of Sn<sup>4+</sup> into Ti<sup>4+</sup> sites in Ca<sub>2</sub>Cu<sub>2</sub>Ti<sub>4</sub>O<sub>12</sub> may also lead to improved dielectric properties of CCTO/CTO composites. This is because tan \u03b4 values of single phase CCTO ceramics can be reduced by Sn<sup>4+</sup> doping ions [4]. It was suggested that variation in dielectric properties of Sn-doped CCTO ceramics was attributed to intrinsic effects, existing inside the grains [4, 21]. While it is widely believed that the giant dielectric behavior of CCTO polycrystalline ceramics was attributed to the extrinsic effect of the electrical response of internal interfaces (e.g., grain boundary or domain boundary) [2, 11, 19, 22, 23]. Ribeiro et al. [21] found that the non-Ohmic properties of CCTO ceramics can be enhanced by Sn<sup>4+</sup> doping ions. Systematic investigation of the dielectric properties and electrical responses of internal interfaces of Sn<sup>4+</sup>-doped CCTO/CTO composites may provide important clues supporting the intrinsic or extrinsic model for clarifying the giant dielectric response in CCTO ceramics. To the best of our knowledge, dielectric and electrical properties of the composite system of CCTO/CTO substituted by Sn<sup>4+</sup> ions have never been reported.

Therefore, the aim of this work is to study the effects of  $Sn^{4+}$  doping ions on the microstructure and dielectric properties of CCTO/CTO composites.  $Sn^{4+}$ –doped CCTO/CTO composites were produced using a one–step process for ceramics with the nominal formula of  $Ca_2Cu_2Ti_{4-x}Sn_xO_{12}$ . Interestingly, improved dielectric properties with a strong increase in  $\epsilon'$  and slight increase in  $\tan\delta$  were achieved. However, the nonlinear electrical properties were degraded. The possible mechanisms are discussed in detail.

#### 3.2 Experimental details

Sn<sup>4+</sup>–doped CCTO/CTO composites were prepared by using a starting nominal formula of Ca<sub>2</sub>Cu<sub>2</sub>Ti<sub>4-x</sub>Sn<sub>x</sub>O<sub>12</sub> (where x=0, 0.1, 0.20, and 0.30, referenced as CCTO/CTO, Sn10, Sn20, and Sn30 composites, respectively). Ceramic powders were prepared using a conventional solid state reaction method. First, a stoichiometric mixture of CaCO<sub>3</sub> (99.95% purity), CuO (99.9% purity), SnO<sub>2</sub> (99.9% purity), and TiO<sub>2</sub> (99.9% purity) specific for each composition was ball milled in ethanol for 24 h using ZrO<sub>2</sub> balls. Second, all resulting slurries were dried and carefully ground. Third, dried mixed powders were calcined at 900 °C for 15 h. Then, the calcined powders were ground and pressed into pellets of 9.5 mm in diameter and ~1.0 mm in thickness to produce the green body. Usually, to accomplish a dense ceramic microstructure, the sintering temperatures of CCTO and CTO ceramics are of about 1050–1100 °C and ≈1300 °C, respectively. When the sintering temperature of CCTO ceramics was higher than 1100 °C, CuO becomes to decompose from CCTO lattice [24]. Thus, finally, these green body pellets were sintered in air at 1100 °C for 6 and 24 h using a heating rate of 5 °C/min.

Phase composition and crystal structures were characterized using an X-ray diffraction (XRD; Bruker, D2 phaser) technique. Scanning electron microscopy (SEM; LEO 1450VP) coupled with energy dispersive X-ray spectrometry (EDS) were used to characterize the composite microstructures. Elemental distribution in the sintered Sndoped CCTO/CTO composites were examined to reveal mapping images using a field-emission scanning electron microscopy (FE-SEM, HITACHI SU8030, Japan). For the dielectric and electrical measurements, ceramic samples were polished and coated by sputtering Au on their surfaces. The dimensions of samples used for the measurements are of about ~9.4 mm in diameter and ~0.8 mm in thickness. The dielectric properties were measured using an Agilent 4294A Precision Impedance Analyzer over the frequency range of 100 Hz to 10 MHz. The dielectric properties were investigated as a function of temperature in the range from -70 to 220 °C. The amplitude of an applied oscillation voltage was 500 mV. Current-voltage characteristics were investigated at room temperature using a high voltage measurement unit (Keithley Model 247). The electric field strength (E) and current density (J) were calculated from the applied voltage and measured current values, respectively.  $E_b$  is defined as an electric field at which J = 1mAcm<sup>-2</sup>.  $\alpha$  was calculated in the range of J = 1-10 mAcm<sup>-2</sup>.

The complex impedance ( $Z^*$ ) was calculated from the complex dielectric permittivity ( $\epsilon^*$ ) using the following relationship:

$$\varepsilon^* = \varepsilon' - i\varepsilon'' = \frac{1}{i\omega C_0 Z^*} = \frac{1}{i\omega C_0 (Z' - iZ'')} , \qquad (1)$$

where  $\varepsilon'$  and  $\varepsilon''$  are the real (dielectric constant) and imaginary parts (dielectric loss factor) of  $\varepsilon^*$ , respectively.  $\varepsilon'$  was calculated from  $\varepsilon'=C'd/\varepsilon_0S$ , where S is the area of electrode, d is the sample thickness, and  $\varepsilon_0$  is the permittivity of free space ( $\varepsilon_0=8.854\times10^{-12}$  F/m).  $\omega$  is the angular frequency of an applied AC electric field ( $\omega=2\pi f$ ) and  $i=\sqrt{-1}$ .  $C_0=\varepsilon_0S/d$  is the empty cell capacitance.

#### 3.3 Results and discussion

Fig. 1 shows the XRD patterns of the composite ceramics sintered for 6 h with nominal compositions of  $Ca_2Cu_2Ti_{4-x}Sn_xO_{12}$  (x=0-0.3). Two phases of CCTO (JCPDS 75-2188) and CTO (JCPDS 82-0231) were detected in all samples, indicating the existence of a CCTO/CTO composite system as reported in published literature [1, 9, 15-17]. Impurity phases were not observed in the XRD patterns of the composites sintered for 6 and 24 h. Generally, the composite samples can also present other phases in amount below the detection limit of the XRD analysis. As shown in Fig. 2 and EDS result, Cu-rich phase particles were observed in the microstructure of Sn<sup>4+</sup>-doped CCTO/CTO samples. However, an impurity of Sn-related phase cannot be detected in both of the XRD and EDS results. Thus, it is likely that Sn<sup>4+</sup> could substitute into Ti<sup>4+</sup> sites in CCTO and/or CTO structures. The lattice parameters (a) of the CCTO phase of CCTO/CTO, Sn10, Sn20, and Sn30 composites sintered for 6 h were found to be 7.4040, 7.4066, 7.4057, and 7.4098 Å, respectively. a values of the composites sintered for 24 h were found to be 7.3891, 7.4011, 7.3958, and 7.4075 Å, respectively. Values of a tended to increase with increasing Sn<sup>4+</sup> content. This might be due to the larger ionic radius of Sn<sup>4+</sup> (0.69 Å) compared to Ti<sup>4+</sup> (0.605 Å) [25].

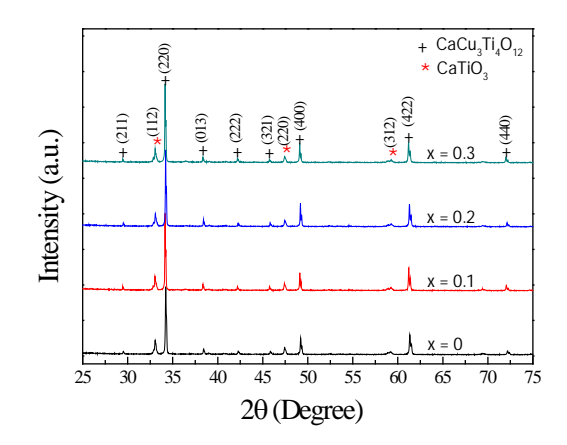
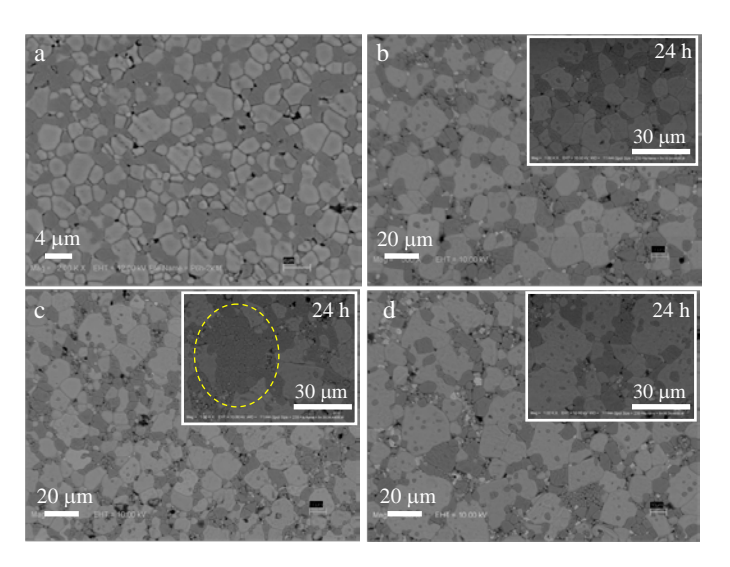


Fig. 1 XRD patterns of  $Ca_2Cu_2Ti_{4-x}Sn_xO_{12}$  (x=0-0.3) ceramics sintered for 6 h.

Figs. 2a–d show backscattered SEM images of polished surfaces of all composite samples sintered for 6 h. In each sample, at least two phases with different contrasts were observed, supporting the XRD results. Fig. 3 shows EDS spectra of the Sn30 composite measured in darker and lighter contrast regions, clearly indicating CTO and CCTO phases. This result is similar to that reported in published literature [9, 15-17]. In the lighter grains, a small intensity EDS–peak of Sn was detected as well as main EDS–peaks for Ca, Cu, Ti, and O. The EDS–peak for Sn was not observed in the darker CTO grain.

In principle, Sn<sup>4+</sup> can also substitute into CTO lattice structure. To further analyze the distribution of each element in Sn<sup>4+</sup>–doped CCTO/CTO composites, mapping of all elements was performed, as shown in Fig. 4. In Fig. 4b, it is clear that Sn<sup>4+</sup> doping ions are not homogeneously distributed in the CCTO/CTO composites. A large portion of Sn element are observed in the lighter CCTO grains, while a relatively small portion of Sn element can also be detected in the darker CTO grains, as clearly seen the rectangle area of Fig. 4b compared to that in Fig. 4a. This clearly indicated that a large portion of the Sn<sup>4+</sup> ions were substituted into the CCTO lattice structure, whereas a small portion can

substitute into the CTO lattice structure. By considering Figs. 4a and c, the darker grains are clearly confirmed to be the CTO phase, supporting the EDS result. Furthermore, CuO particles in the microstructure of the Sn30 sample (Fig. 4a) were clearly confirmed by considering the distributions of Cu and Ti, as shown in Figs. 4c and d.



**Fig. 2** Backscattered SEM images of (a) CCTO/CTO, (b) Sn10, (c) Sn20, and (d) Sn30 samples sintered for 6 h; insets of (b-d) show backscattered SEM images of the Sn10, Sn20, and Sn30 samples sintered for 24 h, respectively.

By using *in situ* synchrotron X-ray powder diffraction technique [26], it was found that the CCTO phase formation is 875 °C for a ceramic prepared by the solid state reaction method. Using the solid state reaction method, the calcination temperature of CTO phase is >1100 °C [27] to form single CTO phase. Thus, it is possible that a relatively large portion of SnO<sub>2</sub> could substitute into CCTO lattice structure in the CCTO/CTO composite powders during calcination process at 900 °C for 15 h. The residual unreacted SnO<sub>2</sub> could further substitute into CTO lattice structure during sintering the CCTO/CTO composites at 1100 °C. Note that the microstructural evolution in the composite samples sintered for 24 h is similar to that observed in the samples sintered for 6 h, as shown in the insets of Figs. 2b–d.

As shown in Fig. 2, the grain sizes of the CCTO and CTO phases in CCTO/CTO composites (both of the composites sintered for 6 and 24 h) were greatly enlarged by Sn<sup>4+</sup> doping. The mean grain sizes of the CCTO phase in the CCTO/CTO, Sn10, Sn20, and Sn30 composites sintered for 6 h were of ~3.1, ~18.0, ~17.0, and ~19.8  $\mu m$ , respectively. The mean grain sizes of the CCTO phase in the composites sintered for 24 h were of ~2.9, ~16.9, ~17.4, and ~21.5  $\mu m$ , respectively. This is completely different from that observed in the Sn–doped single phase CCTO [4, 21]. As shown in Fig. 2b–d, white spots were observed in the microstructure of the Sn10, Sn20, and Sn30 samples. This was confirmed to be an impurity (Cu–rich).

Generally, dispersion of solid particles in a polycrystalline ceramic matrix, i.e., one in which these particles are insoluble and immobile, can decrease the grain growth rate by the pinning effect. This is because grain boundary mobility was reduced. If there is a sufficient content of particles, grain boundary migration of the sintered polycrystalline ceramic will be pinned when it encounters the particles [28]. For a Ca<sub>2</sub>Cu<sub>2</sub>Ti<sub>4</sub>O<sub>12</sub> composition, the calcined powder consisted of CCTO and CTO particles with volume

fractions of ~0.66 and ~0.34, respectively [1]. The average grain sizes of the un–doped CCTO/CTO composites sintered for 6 and 24 h were nearly the same in value. According to the Zener model [28], limiting grain size ( $G_L=2\alpha r/3f$ , where  $\alpha$  is geometrical shape factor) is only proportional to inclusion particle size (r) and inversely proportional to the inclusion volume fraction (f). This result indicates that the grain growth of the CCTO matrix phase was sufficiently inhibited by (f=0.34) CTO particles.

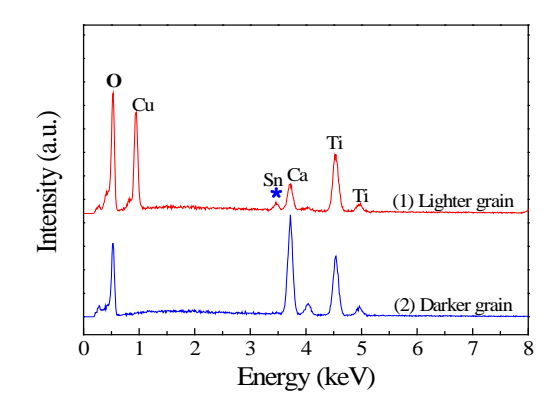
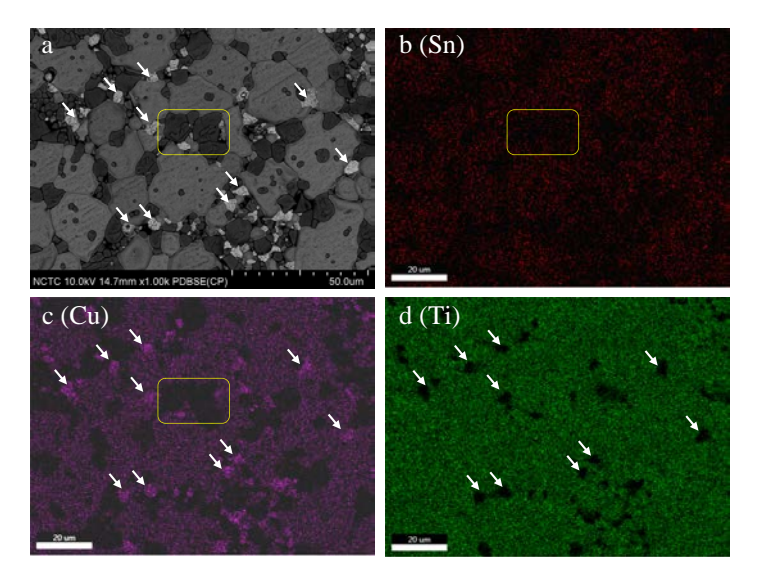


Fig. 3 EDS spectra of Sn30 sample detected at darker and lighter phases.



**Fig. 4** (a) Backscattered SEM image of Sn30 samples (b-d) Element mapping of the Sn30 sample sintered at 1100 °C for 6 h for Sn, Cu, and Ti, respectively.

It was also observed that small CTO particles (darker grains) appeared in the large CCTO grains of Sn-doped CCTO/CTO composites. This observation indicated that grain boundary mobility of Sn-doped CCTO/CTO composites cannot be pinned by CTO particles. This supports the hypothesis that liquid phase sintering may be a primary cause of the microstructural changes in Sn-doped CCTO/CTO composites. This is because enhanced grain boundary mobility due to the existence of the liquid phase in the green body during sintering process is the primary factor responsible for increasing grain growth rate of polycrystalline ceramics. In this case, grain boundaries can break away from some small particles of the CTO phase, retaining these particles internally within the CCTO grains. Normally, the grain growth of a single phase CCTO ceramic is correlated with liquid phase sintering [29]. The Cu-rich related phase is generally believed to be a source of a liquid phase during the sintering process. Therefore, the observed Cu-rich particles in

Sn–doped CCTO/CTO composites may be an important clue to explaining the large increase in the mean grain size of CCTO phase. In polycrystalline ceramics, a metal doping ion may react with a small portion of the major phase to form a eutectic liquid. The eutectic temperature of SnO $_2$ –CuO was found to be ~940  $^{\circ}$ C [30]. Thus, it is strongly suggested that the eutectic liquid phase of the SnO $_2$ –CuO system has a remarkable influence on the increase mean grain size of the CCTO phase in Sn–doped CCTO/CTO composites.

According to previous work, substitution of  $Sn^{4+}$  into a single phase CCTO caused a large decrease in the mean grain size and resulting  $\epsilon'$  values [4, 21]. The cause of the decrease in  $\epsilon'$  was suggested to be intrinsic factors inside the grains. The nanosized barrier layer capacitor model and mixed–valent structure model were proposed to describe the giant dielectric response in CCTO ceramics. In these two models, a high  $\epsilon'$  value was not strongly correlated with the electrical response at grain boundaries. In the case of Sn–doped CCTO/CTO composites, substitution of Sn<sup>4+</sup> ions into Ti<sup>4+</sup> sites in the CCTO structure can cause a decrease in  $\epsilon'$  of the CCTO phase. In the absence of the dominant electrical response of internal interfaces or grain boundaries, the effective  $\epsilon'$  of CCTO/CTO composites should decrease if the  $\epsilon'$  value of the CTO phase was not greatly enhanced by Sn<sup>4+</sup> doping.

However, in this current study,  $\varepsilon'$  of CCTO/CTO composites was greatly increased by  $Sn^{4+}$  doping, as shown in Figs. 5a and b. The  $\varepsilon'$  values at 20 °C and 1 kHz of the CCTO/CTO, Sn10, Sn20, and Sn30 samples sintered for 6 h were approximately 2173, 6057, 7968, and 10435, respectively. Concurrently,  $\varepsilon'$  values of the samples sintered for 24 h were 1863, 8457, 7097, and 13036, respectively. The discrepancy between the expected and experimental results may indicate a strong effect of Sn<sup>4+</sup> doping ions upon the enhanced dielectric response at grain boundaries in CCTO/CTO composites. Based upon the experimental results of the current study, the intrinsic effect can be excluded from possible mechanisms contributing to the enhancement of ε' values of Sn-doped CCTO/CTO composites. This observation strongly suggests that the high dielectric response in CCTO/CTO composites does not originate from intrinsic effects inside the grains. As shown in the inset of Fig. 5b, both low-frequency and high-frequency plateaus of all the composite samples were observed in a low-temperature range. These are generally assigned to be the electrical responses of the bulk grains and grain boundaries, respectively [23]. In the inset of Fig. 5a,  $tan\delta$  was slightly changed by  $Sn^{4+}$  doping ions. The values of tanδ at 20 °C and 1 kHz of the CCTO/CTO, Sn10, Sn20, and Sn30 samples sintered for 6 h were approximately 0.017, 0.019, 0.031, and 0.054, respectively. However,  $\tan\delta$  values of the samples sintered for 24 h were found to be 0.045, 0.023, 0.034, and 0.076, respectively. Notably, high- $\varepsilon'$  and low-tan $\delta$  values were achieved in the Sn<sup>4+</sup>-doped CCTO/CTO composite system.

It is worth noting that the  $\epsilon'$  value of the composites sintered for 6 h increased with increasing Sn<sup>4+</sup> doping concentration, which is well consistent with the predicted results of the internal interface model. However, for the composites sintered for 24 h, it was found that  $\epsilon'$  of the S20 sample is lower than that of the S10 sample. Generally, the dispersion of minor phase (relative to the major phase) in the matrix would play a significant role on the dielectric properties of composites and poor dispersion is likely to reduce  $\epsilon'$ . According to the microstructure analysis, the distribution of CCTO and CTO phases of all the composites sintered for 6 h was quite uniform [Figs. 2a–d]. The variation in  $\epsilon'$  is primarily

originated from the effect of doping concentration only. As shown in the inset of Fig. 2c, large aggregate of CTO grains (as indicated in the dash circle area) in the Sn20 sample sintered for 24 h was observed. This may be caused by poor mixing the starting raw materials during the ball milling process. Therefore, a lower  $\epsilon'$  value of the Sn20 sample compared to that of the Sn10 sample is caused by its inhomogeneous microstructure.

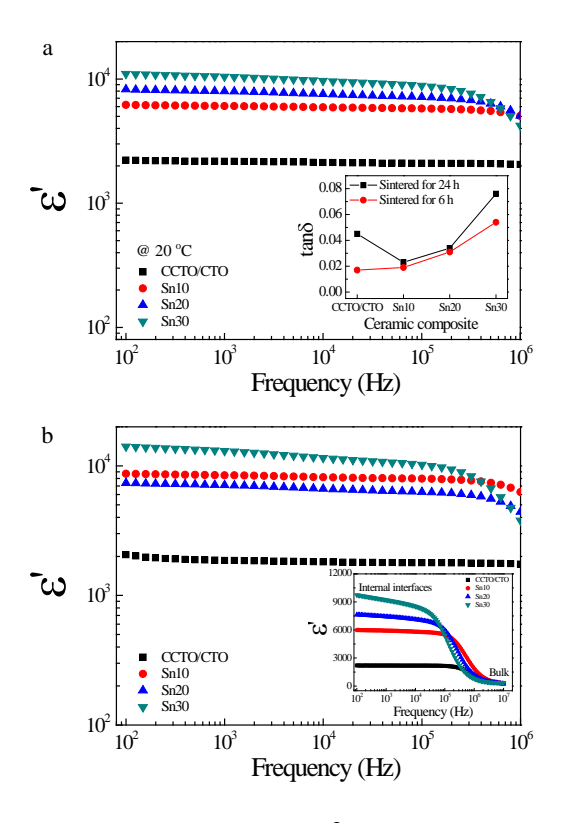
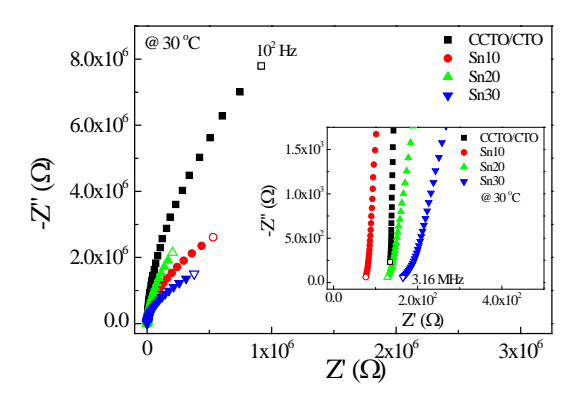


Fig. 5  $\epsilon'$  as a function of frequency at 20 °C for the composites sintered at 1100 °C for (a) 6 h and (b) 24 h. Inset of (a) shows tan $\delta$  as a function of dopant content. Inset of (b) shows the frequency dependence of  $\epsilon'$  at -70 °C

Although the grain sizes of CCTO ceramics may not be a primary factor contributing to their very high  $\varepsilon'$  values, it is still one of the most significant parameters influencing the dielectric properties of many polycrystalline ceramics. Most recent investigation revealed that variation of  $\varepsilon'$  values in CCTO ceramics has a close relationship to their mean grain size [12, 19, 22, 31-33]. Recently, we found that largely reduced grain size of CCTO ceramics did not result in a decrease in their  $\varepsilon'$  values [18]. Thus, the enhanced grain size of Sn-doped CCTO/CTO composites may be a slight effect contributing to the overall enhanced  $\varepsilon'$  values. For single phase CCTO ceramics, high  $\varepsilon'$  values were shown to correlate with the capacitance of the grain boundary ( $C_{gb}$ ) [19, 23]. Thus, the enhanced  $\varepsilon'$  values of Sn-doped CCTO/CTO composites may originate from the improved electrical response of internal interfaces.

Impedance spectroscopy was therefore used to characterize the electrical responses of the CCTO grains and internal interfaces of  $Sn^{4+}$ -doped CCTO/CTO composites. Based upon the brick-work layer model [23], the electrical structure model can be described by an equivalent circuit consisting of two parallel resistor-capacitor (RC) elements connected in series. In the current study, one RC element represents the electrical response of semiconducting grains of the CCTO phase, consisting of grain resistance ( $R_a$ ) and capacitance of grains ( $C_a$ ). The other represents the insulating layer

of internal interfaces, consisting of the resistance and capacitance of internal interfaces  $(R_{int}$  and  $C_{int})$ . It was clearly shown that CCTO-CTO and CCTO-CCTO interfaces were electrically active, indicating the presence of potential barriers [15], whereas, a CTO-CTO interface was electrically inactive [15]. Thus, the electrical response of internal interfaces in Sn-doped CCTO/CTO composite system is likely to result from CCTO-CTO and CCTO-CCTO interfaces. In general,  $R_q$  and  $R_{qb}$  (or  $R_{int}$ ) at particular temperatures can be estimated from the diameter of two semicircular arcs observed in impedance spectrum at high and low frequency ranges, respectively [23]. When only the semicircular arc at a low frequency range is observed in the measured frequency range,  $R_q$  can be estimated from a nonzero intercept on the Z' axis at high frequencies [23]. As shown in Fig. 6 and the inset, the electrical responses of the bulk grain and grain boundary are clearly demonstrated. Although the completed semicircular arcs of all the composite samples cannot be observed in the measured frequency range at 30 °C, the strong influence of Sn<sup>4+</sup> doping ions on the electrical response of internal interfaces is clearly seen. The expected diameter of the semicircular arc of CCTO/CTO composites indicating the  $R_{
m gb}$ value was largely reduced by doping with Sn<sup>4+</sup>.



**Fig. 6** Impedance complex plane (Z\*) plot at 30 °C of Ca<sub>2</sub>Cu<sub>2</sub>Ti<sub>4-x</sub>Sn<sub>x</sub>O<sub>12</sub> ceramics sintered for 6 h; open symbols indicates the data points measured at 10<sup>2</sup> Hz. Inset shows an expanded view of high frequency data close to the origin; open symbols indicates the data points measured at 3.16 MHz.

Fig. 7a shows the frequency dependence of the imaginary part (-Z") of the complex impedance at 110 °C for all composites sintered for 6 h. Relaxation peaks were observed at high temperatures, which are generally attributed to be the electrical responses of internal interfaces [11, 34]. The resistance of the internal interfaces,  $R_{int}$ , (or  $R_{qb}$ ) can be calculated from the peak height  $(Z''_{max})$  using the relationship  $Z''_{max} = R_{ph}/2$ . The peak height decreased with increasing  $Sn^{4+}$  content, indicating a reduction in  $R_{ab}$ . The decrease in R<sub>ab</sub> of a CCTO/CTO composite due to the effect of Sn<sup>4+</sup> doping ions is clearly illustrated in Fig. 7b. The diameter of a semicircle arc of the CCTO/CTO sample decreased with increasing Sn<sup>4+</sup> dopant concentration. R<sub>gb</sub> values at 110 °C of the CCTO/CTO, Sn10, Sn20, and Sn30 samples sintered for 6 h were approximately 1.05×10<sup>6</sup>, 2.01×10<sup>5</sup>,  $1.87 \times 10^5$ , and  $5.24 \times 10^4 \Omega$ , respectively.  $R_{ab}$  values of the samples sintered for 24 h were found to be  $5.45\times10^5$ ,  $1.67\times10^5$ ,  $6.63\times10^5$ , and  $4.77\times10^4$   $\Omega$ , respectively. The result achieved in the composites sintered for 6 h is consistent with the observed increase in  $tan\delta$  as the  $Sn^{4+}$  dopant concentration was increased. Reduction of  $R_{qb}$  results in the enhancement of  $tan\delta$  [19]. However, the decrease in  $tan\delta$  of the Sn10 sample compared to the CCTO/CTO sample sintered for 24 h cannot be explained by the effect of  $R_{qb}$ .

According to impedance spectroscopic analysis, the capacitance of internal interfaces (or  $C_{gb}$ ) can be calculated using the relationship  $C_{gb} = 1/2\pi f_{max}R_{gb}$ , where  $f_{max}$  is the frequency at which  $Z''_{max}$  occurred. At 110 °C,  $C_{gb}$  values of the CCTO/CTO, Sn10, Sn20, and Sn30 samples sintered for 6 h were approximately 0.38, 0.71, 0.96, and 1.21 nF, respectively.  $C_{gb}$  values of the composites sintered for 24 h were found to be 0.52, 1.07, 0.85, and 1.67 nF, respectively. These  $C_{gb}$  values of each composite sample are consistent with their  $\varepsilon'$  values, as clearly seen in the inset of Fig. 7b. A clear correlation of  $\varepsilon'$  and  $C_{gb}$  was observed. This result supports the hypothesis that an enhanced  $\varepsilon'$  value of Sn<sup>4+</sup>–doped CCTO/CTO composites is likely caused by improved electrical response at the grain boundaries.

Fig. 8 illustrates the effect of  $\mathrm{Sn^{4+}}$  on the nonlinear  $J\!-\!E$  characteristics of CCTO/CTO composites sintered for 6 h.  $\alpha$  values of the CCTO/CTO, Sn10, Sn20, and Sn30 samples were found to be 13.1, 5.68, 6.04, and 5.56, respectively, whereas,  $\alpha$  values of the composites sintered for 24 h were 9.90, 6.40, 5.66, and 6.75 respectively. The  $E_b$  value of CCTO/CTO composites sintered for 6 and 24 h was strongly reduced, as shown in Fig. 8. Clearly, the nonlinear  $J\!-\!E$  properties of CCTO/CTO composites were degraded by  $\mathrm{Sn^{4+}}$  doping. Although it is quite difficult to clarify the mechanism that affects different nonlinear  $J\!-\!E$  properties among  $\mathrm{Sn^{4+}}$ -doped CCTO/CTO composites, the different  $J\!-\!E$  properties of the un–doped CCTO/CTO and doped samples were primarily due to the greatly enlarged grain size in the CCTO phase. This can cause a decrease in the number of active CCTO–CCTO and CTO–CCTO interfaces, leading to degradation of nonlinear electrical properties.

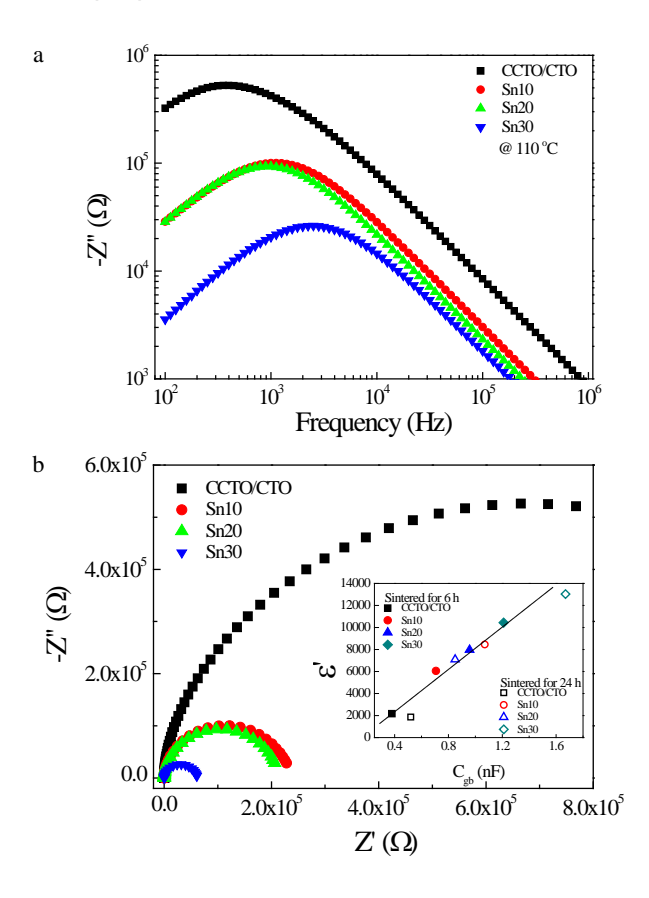


**Fig. 7** (a) Frequency dependence of -Z" of  $Ca_2Cu_2Ti_{4-x}Sn_xO_{12}$  ceramics sintered for 6 h. (b)  $Z^*$  plot at 110 °C of  $Ca_2Cu_2Ti_{4-x}Sn_xO_{12}$  ceramics sintered for 6 h; inset shows the dependence of  $\varepsilon'$  on  $C_{qb}$  for  $Ca_2Cu_2Ti_{4-x}Sn_xO_{12}$  ceramics.

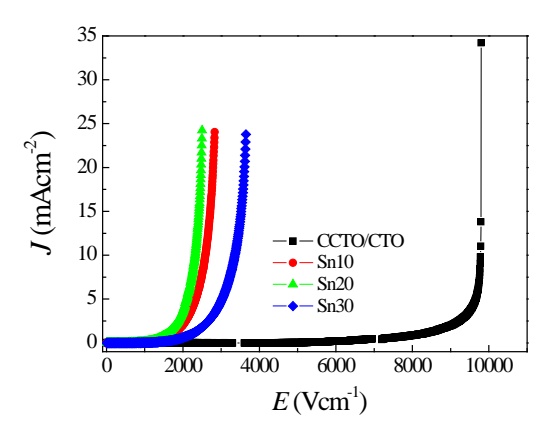


**Fig. 8** Nonlinear J–E characteristics of Ca<sub>2</sub>Cu<sub>2</sub>Ti<sub>4-x</sub>Sn<sub>x</sub>O<sub>12</sub> ceramics sintered for 6 h at room temperature.

According to our previous report for the Zn-doped CCTO/CTO composite system [9], a large increase in  $\epsilon'$  without any significant changes in the shape and mean grain size was observed. Concurrently, the nonlinear J-E properties were significantly improved by Zn<sup>2+</sup> doping. This may be dominated by the intrinsic factor of the grain boundaries rather than the geometric factor. The enhanced nonlinear J-E properties in the Zn<sup>2+</sup>-doped CCTO/CTO composite system were attributed to the improved electrical response at the grain boundaries. The electrostatic potential barrier height at the grain boundaries of CCTO/CTO could be significantly enhanced by Zn<sup>2+</sup> doping. In the case of a Sn<sup>4+</sup>-doped CCTO/CTO composite system, obviously, the geometric factor of the microstructure (i.e., grain boundaries) is the primary factor contributing to the variation in nonlinear J-E properties. It was suggested that Zn<sup>2+</sup> doping ions may improve the electrical response at the CCTO-CCTO interface, increasing the value of  $\varepsilon'$ . For CCTO ceramics, interfacial polarization at the grain boundary (i.e., CCTO-CCTO interface) is widely thought to be the origin of a giant ε' [3, 12, 23, 31]. Lower ε' value of the CCTO/CTO composite compared to CCTO ceramics is therefore due to the decrease in the CCTO-CCTO interface, while the dielectric response of the CCTO-CTO is slight. It is possible that the increase in  $\varepsilon'$ values of the Sn4+-doped CCTO/CTO composites may be attributed to the enhanced dielectric responses of CCTO-CCTO and/or CCTO-CTO interfaces as a result of Sn4+ doping ions. This greatly increased  $\varepsilon'$  was resulted from stronger interfacial polarization at internal interfaces rather than the intrinsic dielectric response inside CCTO grains. This resulted from the enlarged grain size of the CCTO phase coupled with the primary factor of enhanced electrical responses at interfaces, giving rise to increased capacitance values of the active interfaces.

According to the internal barrier layer capacitor (IBLC) model of Schottky barriers at the grain boundaries, it was proposed that double (back-to-back) Schottky potential barriers may be created at interfaces between *n*-type grains due to charge trapping at acceptor states [35]. For traditional metal oxide non-Ohmic materials, potential barriers were closely associated with oxygen enrichment at the internal interface, in which an unknown acceptor state may be induced [36]. This barrier is typically characterized as a grain boundary impedance since it is both resistive and of high capacitance. Oxygen enrichment at the CCTO-CCTO and CCTO-CTO interfaces caused by the segregation of SnO<sub>2</sub>-CuO-related liquid phase may be one of the most important factors, contributing to enhanced dielectric response at the interfaces. Improved potential barriers can increase the ability to accumulate electrical charges at the insulating interfaces, producing stronger

interfacial polarization. It is likely that, double Schottky barrier at the CCTO-CTO interface of the un–doped composite cannot be created due to the insulating nature of CTO phase. However, oxygen enrichment at this interface of the  $Sn^{4+}$ –doped CCTO/CTO composites might be compensated by lowering the cation valence (i.e.,  $Ti^{4+} \rightarrow Ti^{3+}$ ) near the surface of CTO grain. Thus, the double Schottky barrier at the CCTO-CTO interface can be induced by this way, resulting in enhanced dielectric response of the CCTO-CTO interface.

#### 3.4 Conclusions

 $\rm Sn^{4+}$ –doped CCTO/CTO composites were successfully prepared using a one–step process. Grain size in the CCTO phase of CCTO/CTO composites was significantly enlarged by  $\rm Sn^{4+}$  doping. This resulted in a strong degradation of nonlinear electrical properties. The  $\epsilon'$  value of  $\rm Sn^{4+}$ –doped CCTO/CTO composites was increased by more than a factor of 3 with a slightly changed  $\rm tan\delta$ . The influences of  $\rm Sn^{4+}$  doping on the dielectric and electrical properties of CCTO/CTO composites were reasonably explained by the extrinsic factors. This is proposed as the origin of the giant dielectric response in CCTO. The enhanced dielectric properties of CCTO/CTO composites likely originated from the improved electrical response at the internal interfaces and enlarged CCTO grain size, which were caused by substitution of  $\rm Sn^{4+}$  ions.

## References

- [1] W. Kobayashi, I. Terasaki, Appl. Phys. Lett., 87 (2005) 032902.
- [2] E.A. Patterson, S. Kwon, C.-C. Huang, D.P. Cann, Appl. Phys. Lett., 87 (2005) 182911.
- [3] S. Kwon, C.-C. Huang, E.A. Patterson, D.P. Cann, E.F. Alberta, S. Kwon, W.S. Hackenberger, Mater. Lett., 62 (2008) 633-636.
- [4] L. Ni, X.M. Chen, X.Q. Liu, Mater. Chem. Phys., 124 (2010) 982-986.
- [5] S. Kwon, D.P. Cann, Journal of Electroceramics, 24 (2010) 231-236.
- [6] J. Jumpatam, P. Thongbai, B. Kongsook, T. Yamwong, S. Maensiri, Mater. Lett., 76 (2012) 40-42.
- [7] B. Cheng, Y.-H. Lin, W. Deng, J. Cai, J. Lan, C.-W. Nan, X. Xiao, J. He, Journal of Electroceramics, 29 (2012) 250-253.
- [8] Y. Su, J. Song, R. Liu, H. Huang, Journal of Electroceramics, 30 (2013) 166-171.
- [9] J. Jumpatam, B. Putasaeng, T. Yamwong, P. Thongbai, S. Maensiri, J. Am. Ceram. Soc., 97 (2014) 2368-2371.
- [10] R. Xue, Z. Chen, H. Dai, D. Liu, T. Li, G. Zhao, Mater. Res. Bull., 66 (2015) 254-261.
- [11] Y. Liu, Q. Chen, X. Zhao, J. Mater. Sci.: Mater. Electron., 25 (2014) 1547-1552.
- [12] L. Ni, X.M. Chen, X.Q. Liu, R.Z. Hou, Solid State Commun., 139 (2006) 45-50.
- [13] M. Ahmad, E. Al-Libidi, A. Al-Jaafari, S. Ghazanfar, K. Yamada, Applied Physics A, 116 (2014) 1299-1306.
- [14] Y. Wang, L. Ni, X.M. Chen, J. Mater. Sci.: Mater. Electron., 22 (2011) 345-350.
- [15] M.A. Ramírez, P.R. Bueno, R. Tararam, A.A. Cavalheiro, E. Longo, J.A. Varela, J. Phys. D: Appl. Phys., 42 (2009) 185503.
- [16] M.A. Ramírez, R. Parra, M.M. Reboredo, J.A. Varela, M.S. Castro, L. Ramajo, Mater. Lett., 64 (2010) 1226-1228.
- [17] J. Jumpatam, B. Putasaeng, T. Yamwong, P. Thongbai, S. Maensiri, J. Eur. Ceram. Soc., 34 (2014) 2941-2950.
- [18] K. Meeporn, T. Yamwong, S. Pinitsoontorn, V. Amornkitbamrung, P. Thongbai, Ceram. Int., 40 (2014) 15897-15906.
- [19] S. De Almeida-Didry, C. Autret, A. Lucas, C. Honstettre, F. Pacreau, F. Gervais, J. Eur. Ceram. Soc., 34 (2014) 3649-3654.

- [20] M. Li, G. Cai, D.F. Zhang, W.Y. Wang, W.J. Wang, X.L. Chen, J. Appl. Phys., 104 (2008) 074107.
- [21] W.C. Ribeiro, R.G.C. Araújo, P.R. Bueno, Appl. Phys. Lett., 98 (2011) 132906.
- [22] L.F. Xu, T. Cheng, R.L. Wang, H.B. Xiao, G.Z. Liu, C.P. Yang, J. Mater. Sci.: Mater. Electron., 25 (2013) 817-823.
- [23] R. Schmidt, M.C. Stennett, N.C. Hyatt, J. Pokorny, J. Prado-Gonjal, M. Li, D.C. Sinclair, J. Eur. Ceram. Soc., 32 (2012) 3313-3323.
- [24] W. Yuan, J. Phys. D: Appl. Phys., 42 (2009) 175401.
- [25] R.D. Shannon, Acta Cryst., A32 (1976) 751-767.
- [26] X. Ouyang, S. Huang, W. Zhang, P. Cao, Z. Huang, W. Gao, J. Solid State Chem., 211 (2014) 58-62.
- [27] S. Yin, D. Chen, W. Tang, Y. Peng, Mater. Sci. Eng. B, 136 (2007) 193-196.
- [28] M.N. Rahaman, Ceramic processing and sintering, 2nd ed., M. Dekker, New York, 2003.
- [29] K.-M. Kim, S.-J. Kim, J.-H. Lee, D.-Y. Kim, J. Eur. Ceram. Soc., 27 (2007) 3991-3995.
- [30] N. Dolet, J.M. Heintz, L. Rabardel, M. Onillon, J.P. Bonnet, J. Mater. Sci., 30 (1995) 365-368.
- [31] T.B. Adams, D.C. Sinclair, A.R. West, Adv. Mater., 14 (2002) 1321-1323.
- [32] L. Liu, H. Fan, P. Fang, X. Chen, Mater. Res. Bull., 43 (2008) 1800-1807.
- [33] Y. Yang, X. Wang, B. Liu, J. Mater. Sci.: Mater. Electron., 25 (2014) 146-151.
- [34] J. Liu, C.-G. Duan, W.-G. Yin, W. Mei, R. Smith, J. Hardy, Phys. Rev. B, 70 (2004) 144106.
- [35] T. Adams, D. Sinclair, A. West, Phys. Rev. B, 73 (2006) 094124.
- [36] M.A. Ramírez, P.R. Bueno, J.A. Varela, E. Longo, Appl. Phys. Lett., 89 (2006) 212102.

## **CHAPTER 4**

## Significantly Improved Non-Ohmic and Giant Dielectric Properties of CaCu<sub>3-X</sub>Zn<sub>x</sub>Ti<sub>4</sub>O<sub>12</sub> Ceramics by Enhancing Grain Boundary Response

## 4.1 Introduction

CaCu $_3$ Ti $_4$ O $_{12}$  (CCTO) is a giant dielectric material which has been primarily studied for its potential applications in microelectronic devices, especially for multilayer ceramic capacitors. This is because CCTO exhibits giant dielectric permittivity ( $\epsilon'$ ) values of  $\approx 10^4$  [1]. CCTO polycrystalline ceramics can also exhibit non–Ohmic properties [2]. Furthermore, the optical properties of CCTO ceramics have also been widely reported in recent years [3-5]. Since, both intrinsic and extrinsic effects have been suggested as the primary cause of abnormally high  $\epsilon'$  values, the extrinsic effect of insulating (grain boundaries) barrier layer capacitor (IBLC) effect is widely accepted as the primary origin of this phenomenon [6-10]. Although the heterogeneous microstructure of CCTO polycrystalline ceramics, consisting of n-type semiconducting grains and insulating grain boundaries (GBs), was clearly shown and supports the IBLC effect well [2, 6-7], the intrinsic effect existing inside the grains of CCTO cannot be simply ignored or arbitrarily excluded [11-14].

For applications in electronic devices based on a capacitive component, the high dielectric loss tangent (tan\delta) in CCTO has been one of the most intensively studied topics in recent years [13, 15-22]. Investigations aimed at reducing tan by doping with metal ions is not only important for practical applications, but also may give an important clue to the underlying the origins of the giant dielectric response. Furthermore, enhanced nonlinear properties may be simultaneously obtained [15-16, 18, 20]. Although the improved nonlinear electrical properties of CCTO still do not meet the requirement for practical application in varistors, at least variation in properties as a result of doping ions might give an understanding of the electrical response of the GBs. This can elucidate the underlying giant dielectric response mechanism in CCTO ceramics even though the GB response might not be the primary origin of giant dielectric response.

Investigation of the dielectric properties of metal ion doped–CCTO ceramics into Cu<sup>2+</sup> sites (e.g., Ni, Mg and Zn) has been widely done. This is because the giant dielectric response and/or the nonlinear properties were found to be better than those of the undoped CCTO ceramic [13-35]. We have also demonstrated that tanδ of CCTO ceramics, prepared using a modified sol–gel method with Ca and Cu as sources of metal ions, was very low [15, 18, 36]. Although the dielectric and nonlinear electrical properties of Zn-doped CCTO ceramics, prepared by various methods, may have high potential for further improvement of its properties to achieve better dielectric–performance.

In this work, Zn–doped CCTO ceramics were synthesized using a modified sol–gel method with Ca and Cu as sources of metal ions. As expected, improved dielectric and nonlinear electrical properties were successfully achieved. High  $\epsilon'$ ~6500–7700 and low tan $\delta$ <0.05 over a wide frequency range,  $10^2$ – $10^5$  Hz, were achieved. The lowest tan $\delta$  was ~0.011 at 6.3 kHz. The nonlinear coefficient and electric field breakdown were simultaneously enhanced. Changes in properties were ascribed to the enhanced GB response.

## 4.2 Experimental details

## 2.1 Sample Preparation

A modified sol–gel method was employed to prepare  $CaCu_{3-x}Zn_xTi_4O_{12}$  (x=0, 0.05, and 0.10) ceramics. The sources of metal ions in Zn-doped CCTO ceramics were  $Ca(C_2H_3CO_2)_2$ • $H_2O$  (99+%, Sigma-Aldrich),  $Cu(CH_3COO)_2$ • $H_2O$  (99.0%, Sigma-Aldrich),  $Cu(CH_3COO)_2$ • $Uu(CH_3COO)_2$ •Uu(C

#### 2.2 Characterizations

The polished–surface morphologies were characterized using scanning electron microscopy (SEM; SEC, SNE-4500M). The phase composition and crystal structure were characterized using X–ray diffraction (XRD; Philips PW3040 with Cu K $\alpha$  radiation,  $\lambda$  = 0.15406 nm). Rietveld quantitative phase analysis was carried out using the X'Pert High Score Plus v3.0e software package by PANalytical. The diffraction patterns were collected over the range of  $2\theta$  =  $25^{\circ}$ - $65^{\circ}$  with step increase of  $0.02^{\circ}$ /min. The parameters and coefficients optimized were the zero shift, scale factor, background (with function type: polynomial), profile half

iowidth parameters (v.

site occupancies (Wyckoff) and preferred orientation parameter. X-ray Absorption Near Edge Structure (XANES) spectra of all sintered ceramics were collected at the SUT-NANOTEC-SLRI XAS beamline (BL5.2) (electron energy of 1.2 GeV; bending magnet; beam current 80–150 mA; 1.1 to 1.7×10<sup>11</sup> photon.s<sup>-1</sup>) at the Synchrotron Light Research Institute (SLRI), Nakhon Ratchasima, Thailand. Details of this characterization technique and analysis are given elsewhere [18]. The normalized XANES data were analyzed after background subtraction in the pre-edge and post–edge region using ATHENA software included in an IFEFFIT package [37].

#### 2.3 Dielectric and electrical measurements

To prepare electrodes for dielectric and electrical measurements, surfaces of the sintered  $CaCu_{3-x}Zn_xTi_4O_{12}$  ceramics were polished. Then, both surfaces sides were coated with Au using a Polaron SC500 sputter coating unit. Under this condition, the thickness of the Au electrode–layer was roughly estimated to be about 50 nm. The dielectric properties of the sintered ceramics were measured using a KEYSIGHT E4990A and Agilent 4294A Precision Impedance Analyzer with an oscillation voltage of 0.5 V. The dielectric measurements were done over the frequency and temperature ranges of  $10^2$ – $10^7$  Hz and -70 to 220 °C, respectively. Current density–electric field (J–E) characteristics were measured at room temperature (RT) using a high voltage measurement unit (Keithley 247). The  $E_b$  value was defined as the electric field breakdown at which J = 1 mA.cm<sup>-2</sup>. The nonlinear coefficient ( $\alpha$ ) was calculated in the range of 1–10 mA/cm<sup>2</sup>.

#### 4.3 Results and discussion

Before dielectric and electrical properties of the sintered ceramics were determined. the phase composition and crystal structure of the CCTO, CCTO-Zn05, and CCTO-Zn10 ceramics were investigated to ensure the samples had a single phase and exhibited a design phase structure. The experimental XRD patterns were well fitted by Rietveld refinement method. The results obtained from Rietveld refinement were summarized in Table 1. The quality of the refinement was quantified by profile residual (R<sub>p</sub>), expected residual (R<sub>exp</sub>), weighted profile residual (R<sub>wp</sub>), and goodness of fit (GOF) [38]. The details of R values in analysis of powder diffraction data using Rietveld refinement were discussed in literature [39]. From the Rietveld refinement results, low GOF values (less than 2) were obtained in all the samples, while the percentages of R<sub>exp</sub>, R<sub>wp</sub>, and R<sub>p</sub> were little high (~13 F2-123/c) torls oxtheored, be lower than 10%. The little high R-factors may be occurred by a little high of noise at background in XRD patterns [39]. Figure 1(a) shows the XRD patterns of the CCTO, CCTO-Zn05, and CCTO-Zn10 ceramics. Rietveld refinement profile fits were performed, as illustrated in Fig. 1(b-c). Accordingly, profile fits confirmed the formation of a single CCTO phase (JCPDS 75-2188) in all ceramic compositions. It is notable that all the diffraction peaks in the XRD patterns were perfectly indexed based on the bcc structure within space group Im 3. Possible impurity phases such as TiO<sub>2</sub>, CuO, Cu<sub>2</sub>O, CaTiO<sub>3</sub> or related Zn phases were not observed in the XRD patterns. The observation of a single phase of all Zn-doped CCTO samples prepared using a modified sol-gel method was similar to those observed in Zn-doped CCTO ceramics prepared via different routes such as a solid state reaction (SSR)method [14], semi-wet route [23], and solution-wet route [24]. According to the Rietveld refinement profile fits, lattice parameters (a) were ≈7.3949–7.3961 Å and are summarized in Table 1. These values are comparable to 7.391 Å for un-doped CCTO [1]. The lattice parameter of 7.3961(2) Å for the CCTO–Zn10 (x=0.1) is very consistent with  $\approx$ 7.397(4) for CaCu<sub>3-x</sub>Zn<sub>x</sub>Ti<sub>4</sub>O<sub>12</sub> ceramics with x = 0.1. [14, 29]. It is notable that the lattice parameter of Zn-doped CCTO ceramics increased with increasing Zn<sup>2+</sup> concentration. This result is similar to reported values in the literature [3, 14, 29]. The increase in the lattice parameter was likely due to a larger ionic radius of a substituted  $Zn^{2+}$  ion ( $r_4 = 0.60$ Å) compared to that of the host  $Cu^{2+}$  ion ( $r_4 = 0.57$  Å) sites [14].

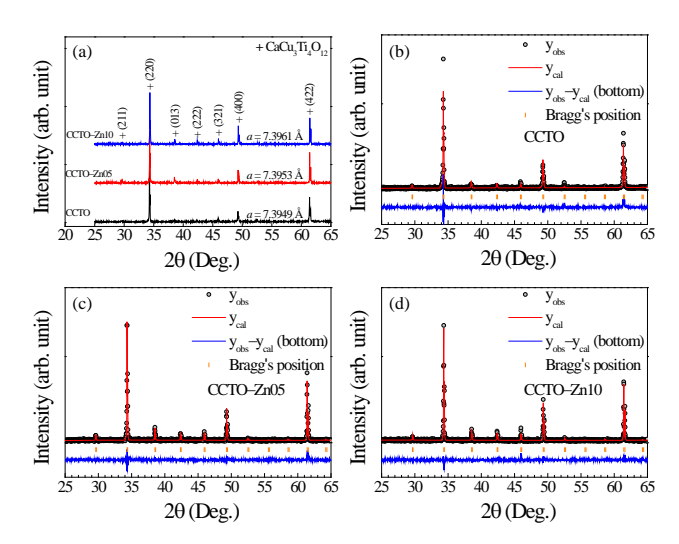


**Fig. 1** (a) XRD patterns of the CCTO, CCTO–Zn05, and CCTO–Zn10 ceramics. (b-c) Profile fits for the Rietveld refinement of the CCTO, CCTO–Zn05, and CCTO–Zn10 ceramics.

Surface morphologies of the CCTO and CCTO–Zn10 ceramics are revealed in Fig. 2. A small number of pores appeared in all the ceramics. The mean grain sizes of all samples are summarized in Table 2. It was found that the mean grain size of CCTO ceramics was greatly reduced by doping with Zn<sup>2+</sup>. This microstructural evolution was completely different from that reported by Ni and Chen [14]. The mean grain size of CCTO ceramics prepared by an SSR method (sintered at 1100 °C) was increased by doping with Zn<sup>2+</sup>. The different tendencies may have been due to the different sintering temperatures. Xu et al. [35] reported mean grain sizes of  $\approx$ 2–4  $\mu$ m for Zn–doped CCTO ceramics prepared using a sol–gel method and sintered at 1050 °C.

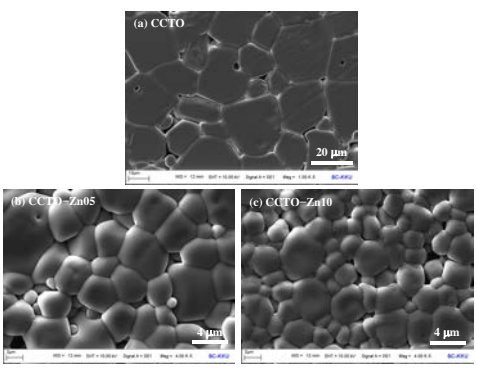


**Fig. 2** SEM images of surface morphologies of (a) CCTO, (b) CCTO–Zn05 and CCTO–Zn10 ceramics.

**Table 1.** Lattice parameter (a) and structural data obtained from the Rietveld refinement for CCTO, CCTO-Zn05, and CCTO-Zn10 ceramics sintered at 1070 °C for 6 h.

Sample	ССТО	CCTO-Zn05	CCTO-Zn10	
a (Å)	7.3949(3)	7.3953(2)	7.3961(2)	
R <sub>exp</sub> (%)	16.83	16.11	16.11	
R <sub>p</sub> (%)	17.86	14.32	13.82	
R <sub>wp</sub> (%)	21.85	17.94	17.90	
GOF	1.68	1.24	1.23	
Bond lengths (Å)		(M=Cu, Zn)		
M -O	1.9750(1)	1.9750(0)	1.9750(0)	
M -Ti	3.2020(1)	3.2020(0)	3.2030(0)	
Bond angles (°)				
O -M- O	116.693(7)	116.693(4)	116.693(4)	
O -Ti- O	89.422(5)	89.422(3)	89.422(3)	
Ti -M- Ti	109.471(4)	109.471(3)	109.471(2)	

**Table 2.** Grain size (G), ε' and tanδ at 20 °C and 1 kHz, conduction activation energies inside the grains (E<sub>g</sub>) and at GBs (E<sub>gb</sub>), Nonlinear coefficient (α), breakdown electric field ( $E_b$ ), and ratio  $Ti^{3+}/Ti^{4+}$  and  $Cu^{+}/Cu^{2+}$  of  $CaCu_{3-x}Zn_xTi_4O_{12}$  ceramics sintered at 1070 °C for 6h.

Sample	G (μm)	ε′	tanδ	E <sub>g</sub> (eV)	R <sub>gb</sub> (eV)	α	E <sub>b</sub> (V/cm)	Ti <sup>3+</sup> /Ti <sup>4+</sup> (%)	Cu <sup>+</sup> /Cu <sup>2+</sup> (%)
ССТО	25.1	66423	0.108	0.093	0.620	3.32	233	17.30	6.82
CCTO-Zn05	4.4	7696	0.017	0.088	0.652	5.80	1763	15.97	5.77
CCTO-Zn10	3.3	6554	0.016	0.092	0.662	5.62	1832	14.67	5.59

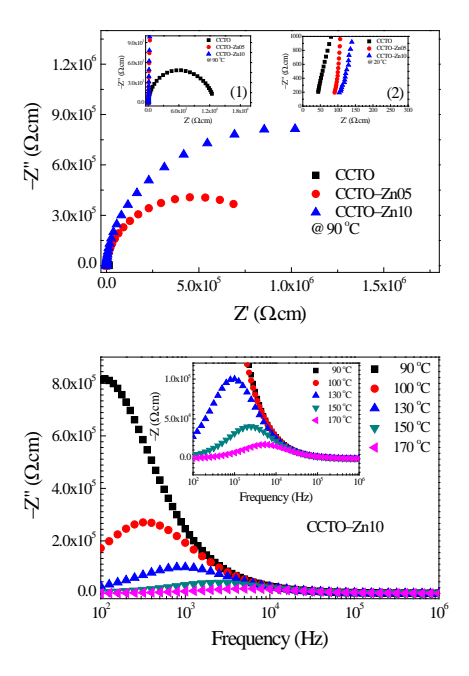


Fig. 3 (a) Impedance complex plane plot (Z\*) at 90 °C for the CCTO, CCTO-Zn05, and CCTO-Zn10 ceramics. Insets (a) and (b) show expanded views of the high-frequency data at 90 °C and 20 °C, respectively. (b) Frequency dependence of Z "Zor1the Cato at different temperature ranging from 90 °C-170 °C; its inset demonstrates an enlarged scale of the y-axis to reveal Z "peaks at high temperatures.

To study the effects of Zn<sup>2+</sup> dopant on the electrical responses of the grains and GBs of CCTO ceramics, the sintered ceramics were characterized using impedance spectroscopy at different temperatures. The diameter of a large semicircular arc (GB resistance, R<sub>gb</sub>) [6-7], cannot be evaluated at RT. Thus, the influence of Zn<sup>2+</sup> dopant on the GB properties should be studied in a high temperature range, at which Rab can be calculated. In contrast, the resistance of semiconducting grains (R<sub>q</sub>) is dominant in at low temperature. As shown in Fig. 3(a) and inset (1), R<sub>gb</sub> of all the samples can be estimated at 90 °C, while R<sub>q</sub> can easily be estimated at temperatures below 20 °C. It is notable that, at temperatures below 90 °C, the diameter of semicircle arcs in the Z\* plots for the CCTO-Zn05 and CCTO-Zn10 ceramics cannot be estimated. The R<sub>qb</sub> values at 90 °C of the CCTO, CCTO-Zn05 and CCTO-Zn10 samples were calculated and found to be  $9.71\times10^3$ ,  $8.16\times10^5$ ,  $1.63\times10^6$   $\Omega$ .cm, respectively.  $R_{ab}$  values of the CCTO-Zn05 and CCTO-Zn10 samples were increased by factors of 84 and 168, respectively, while their R<sub>g</sub> values were increased by a factor of 2 [inset (2)]. The greatly increased R<sub>gb</sub> of the CCTO-Zn05 and CCTO-Zn10 samples was likely attributable to the ability of Zn2+ doping ions to inhibit oxygen loss during sintering at high temperatures. These large increased  $R_{ab}$  values may have an influence on the greatly decreased  $tan\delta$  values of CCTO ceramics.

According to the equivalent circuit represented the IBLC structure of  $ACu_3Ti_4O_{12}$  based on the brick-work layer model, the frequency dependence of  $Z^{\prime\prime}$  can be expressed as:

$$Z''(\omega) = R_g \left[ \frac{\omega R_g C_g}{1 + (\omega R_g C_g)^2} \right] + R_{gb} \left[ \frac{\omega R_{gb} C_{gb}}{1 + (\omega R_{gb} C_{gb})^2} \right]$$
(1)

A simple relationship between  $R_{\rm gb}$  and  $Z''_{\rm max}$ ,  $Z''_{\rm max}=R_{gb}/2$ , can easily be obtained by setting  $d(\omega R_{gb}^2 C_{gb}/(1+(\omega R_{gb}C_{gb})^2))/d\omega=0$ . As demonstrated in Fig. 3(b) and its inset,  $Z''_{\rm max}$  decreased as the temperature increased, indicating a reduction of  $R_{\rm gb}$ .

To further understand the electrical properties of the GBs, the scaling behavior of Z" at different temperatures was investigated. As shown in Fig. 4 and its inset, prefect overlap of all curves at different temperatures into a single curve is observed for the CCTO–Zn10 and CCTO samples. This signifies that the relaxation process in this temperature range originated from the same mechanism.

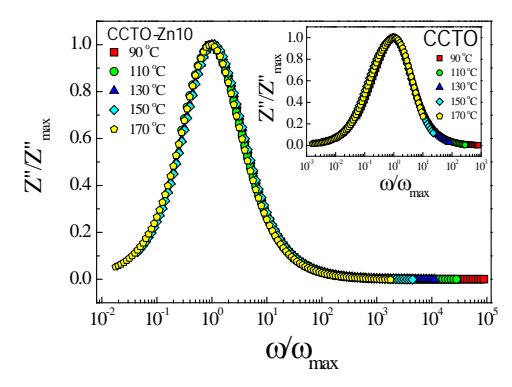


**Fig. 4** Scaling behavior of Z'' of the CCTO–Zn10 sample in the temperature range from 90 to 170 °C; its inset shows scaling behavior of Z'' of the CCTO sample.

 $R_{\rm gb}$  and  $R_{\rm g}$  values at different temperatures can be calculated. It was found that the temperature dependences of  $R_{\rm gb}$  and  $R_{\rm g}$  follow the Arrhenius law:

$$R_{g,gb} = R_0 \exp\left(\frac{E_{g,gb}}{k_B T}\right) \tag{2}$$

where  $R_0$  is pre–exponential constant term. The activation energies for conduction inside the grains (E<sub>g</sub>) and at the GBs (E<sub>gb</sub>) were calculated from the slopes of the linear fitting results. A shown in Fig. 5 and its inset, the experimental data fitted Eq. (2) well. The calculated E<sub>g</sub> values of the CCTO, CCTO–Zn05, and CCTO–Zn10 ceramics were about 0.093, 0.088, and 0.092 eV, respectively.

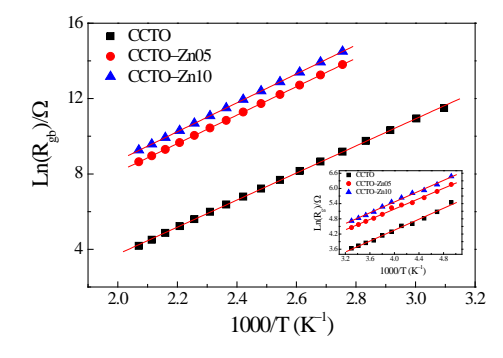


**Fig. 5** Arrhenius plots of  $R_{gb}$  of the CCTO, CCTO–Zn05, and CCTO–Zn10 ceramics. Its inset shows Arrhenius plots of  $R_g$  for these samples.

The  $E_{gb}$  values were 0.620, 0.652, and 0.662 eV, respectively.  $E_{gb}$  of CCTO ceramics was significantly changed by  $Zn^{2+}$  doping, indicating an increase in the

electrostatic potential barrier height at the GBs [40]. The  $R_{\rm gb}$  values at 20 °C can be determined from the calculated  $E_{\rm gb}$  values.  $R_{\rm gb}$  values were found to be 1.08, 142.43, and 307.57 M $\Omega$ .cm for the CCTO, CCTO–Zn05, and CCTO–Zn10 samples, respectively. The strongly increased  $R_{\rm gb}$  resulted from a combination of the effects of an increase in a number of GBs (due to small grain sizes) and the enhanced potential barrier height at the GBs.

As shown in the inset (2) of Fig. 3(a), the conduction inside the grains of CCTO ceramics was increased by doping with Zn2+ ions. This observation may be important clue to clarify the origin of the semiconducting grains of CCTO ceramics. Thus, the valence states of Ti were characterized using XANES technique. The normalized Ti K-edge XANES spectra of the CCTO, CCTO-Zn05, and CCTO-Zn10 samples, as well as the standard samples (TiO<sub>2</sub> and TiF<sub>3</sub>) are illustrated in Fig. 6(a). The overall XANES spectra of all the ceramic samples are very similar. As clearly illustrated in the inset of Fig. 6(a), the edge energy position of all ceramic samples was between the edge energy position of TiF<sub>3</sub> (Ti<sup>3+</sup>) and TiO<sub>2</sub> (Ti<sup>4+</sup>), indicating the existence of Ti<sup>3+</sup> and Ti<sup>4+</sup> in all ceramics. It was found that there is a tendency of all absorption edge energies for all samples to be closer to TiO<sub>2</sub> (Ti<sup>4+</sup>) than TiF<sub>3</sub> (Ti<sup>3+</sup>). A very slight change in edge value of Ti K-edge of all the ceramic samples was observed. These shifts were resulted from very careful XANES measurements and data analysis. Energy calibration using Ti-foil was performed throughout the experiments during the XANES measurements. Therefore, the measured spectra would have corrected edge energy, particularly the edge energy of TiO<sub>2</sub> and TiF<sub>3</sub> standards. Reasonably, it was confirmed that a very small shift of the edge value was due to the presence of Ti3+ in all samples. As illustrated in Fig. 6(b), the existence of Cu+ was confirmed by XANES spectra for Cu K-edge. The existence of a relatively small amount of Ti<sup>3+</sup> relative to larger numbers of Ti<sup>4+</sup> ions was observed in all samples. Thus, electron hopping between  $Ti^{3+}O-Ti^{4+} \leftrightarrow Ti^{4+}O-Ti^{3+}$  and  $Cu^{+}O-Cu^{2+} \leftrightarrow Cu^{2+}O-Cu^{+}$  may be the origin of n-type semiconducting grains of CCTO and Zn-doped CCTO ceramics. If this is true,  $R_{\alpha}$  should be correlated to the amount of Ti<sup>3+</sup> ions.

This hypothesis was further confirmed by quantitative analysis of XANES spectra. Quantitative analysis of different valence states in each of the samples was done using an empirical edge-shift calculation making comparisons with known standard samples. A very slight shift in the value of Ti *K*-edge due to the presence of Ti<sup>3+</sup> was confirmed [18]. The edge value can be calculated from the maximum value of the first derivative of edge region. The amount of Ti<sup>3+</sup> was calculated from eq. (3):

% of 
$$Ti^{3+}$$
 for each sample =  $\left(1 - \frac{\Delta E \text{ of sample}}{\Delta E \text{ of } Ti^{3+} \text{ and } Ti^{4+} \text{ standard}}\right) \times 100\%$  (3)

 $\Delta E$  is a difference of edge value of samples compared with a  $Ti^{3+}$  ( $TiF_3$ ) standard. The  $Ti^{3+}/Ti^{4+}$  ratios are summarized in Table 2. It was found that the  $Ti^{3+}/Ti^{4+}$  ratio decreased with increasing  $Zn^{2+}$  concentration. Similarly, the  $Cu^{+}/Cu^{2+}$  ratio decreased with increasing  $Zn^{2+}$  concentration. These are quite consistent with the slight increase in  $R_g$  for the Zn-doped CCTO ceramics [inset 2 of Fig. 3(a)]. Thus, electron hopping between  $Ti^{3+} \leftrightarrow Ti^{4+}$  and  $Cu^{+} \leftrightarrow Cu^{2+}$  sites is one of the most possible explanations for the existence of n-type semiconducting grains in CCTO ceramics. The decrease in the  $Ti^{3+}/Ti^{4+}$  and  $Cu^{+}/Cu^{2+}$  ratios of Zn-doped CCTO ceramics likely originated from a decrease in oxygen vacancies inside the grains and in the GB region. Substitution of  $Zn^{2+}$  may have an important role to suppress the formation of oxygen vacancies. Decreasing oxygen

vacancies at the GBs also had a great effect on the insulating GBs, giving rise to greatly enhanced  $R_{ob}$  values (Fig. 3(a)).

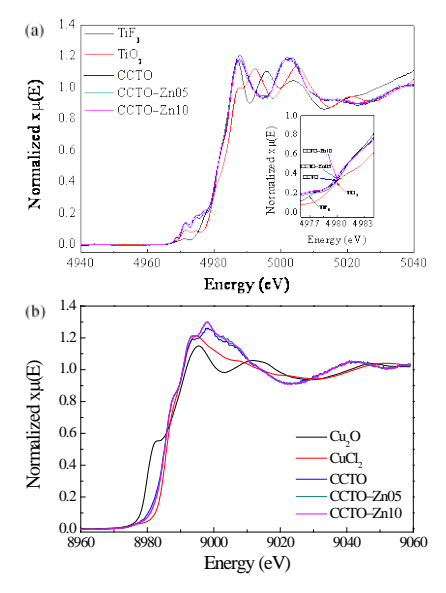


Fig. 6 (a) Normalized X-ray absorption near edge structure (XANES) spectra for Ti K-edge of the CCTO, CCTO-Zn05, and CCTO-Zn10 ceramics; inset shows expanded view close to the edge energy position of all ceramic samples. (b) Normalized X-ray absorption near edge structure (XANES) spectra for Cu K-edge of them.

For the CCTO crystal structure, the  $[TiO_6]$  distortion can cause an increase in the number of  $[TiO_5V_o^{\bullet}]$ – $[TiO_6]$  clusters in the CCTO structure. The conductivity of CCTO was originated by charge transference from  $[TiO5V_o^{\bullet}]$  to  $[CuO_4]'$ ,  $[TiO_5V_o^{\star}]$  to  $[CuO_4]^{\star}$ , or  $[CuO_4]'$  to  $[CuO_4]^{\star}$  [4]. This mechanism can also cause the existence of a  $Cu^{+}$  ions ( $[CuO_4]'$ ) in the lattice, which was well confirmed by the XANES results. Slight changes in the structural data obtaining from the Rietveld refinement may have a little effect on the conduction inside the grains. Generally, the difference in ionic radii between dopant and host ions can cause the existence of lattice strain energy. Therefore, initial segregation of  $Zn^{2+}$  ions at the GBs of CCTO can reduce the driving force for motion of GBs. Variations in the electrical properties of the grains and GBs due to  $Zn^{2+}$  dopant may have a remarkable influences on both of the non-Ohmic and dielectric properties of CCTO ceramics.

The non-linear J-E properties of  $CaCu_{3-x}Zn_xTi_4O_{12}$  ceramics were investigated at RT. As shown in Fig. 7, all the samples showed nonlinear J-E characteristics. The  $\alpha$  values of the CCTO, CCTO-Zn05, and CCTO-Zn10 ceramics were respectively 3.32, 5.80, and 5.62, while  $E_b$  values were 233, 1763, and 1832 V/cm, respectively. As can be seen in Table 2,  $E_b$  of Zn-doped CCTO ceramics had a close relationship with the mean grain size. This result is similar to those reported in literature [15-16, 35]. The significant increase in  $E_g$  was primarily caused by the geometric properties of the GBs (e.g., the number of GBs per unit of sample thickness and GB area). These were tuned by Zn<sup>2+</sup> doping. The  $\alpha$  values of Zn-doped CCTO ceramics represented in the current work are comparable to  $\alpha$  values of  $\approx$ 4.5-6.4 for Zn-doped CCTO ceramics prepared using a sol-gel method [35]. Notably, in addition to the improved dielectric properties, the nonlinear electrical properties of CCTO ceramics can be enhanced by doping with Zn<sup>2+</sup> ions.

Dielectric properties of the CCTO, CCTO-Zn05, and CCTO-Zn10 samples are shown in Fig. 8(a) and its inset. In the range of  $10^2-10^5$  Hz,  $\varepsilon'$  of the CCTO was nearly independent of frequency.  $\varepsilon'$  rapidly deceased as frequency increased from  $10^5-10^6$  Hz. Notably, ε' of Zn-doped CCTO ceramics was constant over a frequency range of 10<sup>2</sup>-10<sup>6</sup> Hz. As shown in its inset, the markedly increased  $tan\delta$  values in a high frequency range are consistent with the observed step-like decrease in  $\varepsilon'$ . The step-like decrease in  $\varepsilon'$  of the Zn-doped CCTO ceramics occurred at frequencies higher than 10<sup>6</sup> Hz. This dielectric behavior is referred to as dielectric relaxation behavior, which is usually observed in CCTO ceramics [7, 13-14, 24]. A large low-frequency tanδ value of the CCTO sample indicates a very large DC conduction in the ceramic sample, i.e., long range motion of free charges [36]. The tanδ value of CCTO ceramics was greatly reduced by doping with Zn<sup>2+</sup>, as shown in the inset of Fig. 8(a). The  $\varepsilon'$  and  $\tan\delta$  values at 1 kHz and RT are summarized in Table 2. Although ε' of Zn-doped CCTO ceramics was greatly decreased, it was still too large to be referred as a giant dielectric material or colossal permittivity material [41-42]. Interesting, very low tanδ values at 1 kHz and RT were obtained in the CCTO-Zn05 and CCTO-Zn10 samples, ≈0.017 and 0.016, respectively. The minimum tanδ values of these samples were ≈0.011 and 0.014 at 6.3 and 2.8 kHz, respectively. Furthermore, tanδ of the CCTO-Zn10 sample was lower than 0.05 over a wide frequency range of 10<sup>2</sup>-10<sup>5</sup> Hz, which is an acceptable value. Generally, a high value of low-frequency tanδ is primarily attributed to the long-range migration of charges (or DC conduction), which can be blocked by high-resistive internal insulating barriers [18, 36]. Therefore, greatly reduced low-frequency tanδ values in Zn-doped CCTO ceramics should be associated with large values of  $R_{ab}$ .

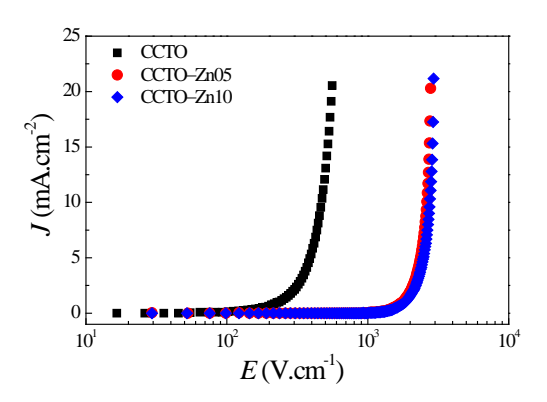


Fig. 7 J–E Characteristics of the CCTO, CCTO–Zn05, and CCTO–Zn10 ceramics.

The values of  $\varepsilon'$  at 1 kHz in the temperature range of -70–220 °C for all the samples are shown in Fig. 8(b). Open symbols signify the variation of  $\varepsilon'$  in each sample of  $\leq \pm 15\%$  compared to its value at RT. Substitution of  $Zn^{2+}$  ions into  $Cu^{2+}$  sites of CCTO ceramics improved the temperature stability of  $\varepsilon'$ . The large increase in  $\varepsilon'$  of the CCTO sample was generally observed as temperature increased [15, 20-21, 23]. This was associated with the diffusion of oxygen vacancies at the GBs [12, 43], which may cause a decrease in the GB resistance ( $R_{gb}$ ) [6]. Thus, improved dielectric properties of Zn–doped CCTO ceramics may be attributed to the ability of  $Zn^{2+}$  dopant to suppress the formation of oxygen vacancies at the GBs as well as inside the grains. The temperature coefficient values of  $\Delta\varepsilon'$  at 1 and 10 kHz for the CCTO–Zn05 and CCTO–Zn10 samples are shown in the inset of Fig. 8(b). Interestingly, at 10 kHz, the  $\Delta\varepsilon' \leq \pm 15\%$  condition ( $\Delta\varepsilon'(\%)$ ) values under the dashed line) was obtained over a wide temperature range from -70 to 150 °C, while  $\Delta\varepsilon'(\%)$ 

of the CCTO sample was very large. The decrease in oxygen vacancies at the GBs of CCTO ceramics due to substitution of  $Zn^{2+}$  had an influence on the insulating GBs, as shown in Fig. 3(a). This may suppress a strong increase in  $\epsilon'$  at high temperatures, Fig. 8(b). Furthermore, this might be an important factor contributing to enhanced  $E_b$  values (Fig. 7), even though the ceramic microstructure was clearly shown to be the primary factor. Finally, it is likely that the dielectric properties of CCTO ceramics are closely correlated with both of the ceramic microstructure and electrical properties of the GBs. Reducing grain size and enhance  $R_{gb}$  of CCTO ceramics were suggested to be one of the most suitable strategies that can cause a decrease in  $tan\delta$  and enhanced nonlinear  $J\!-\!E$  properties.

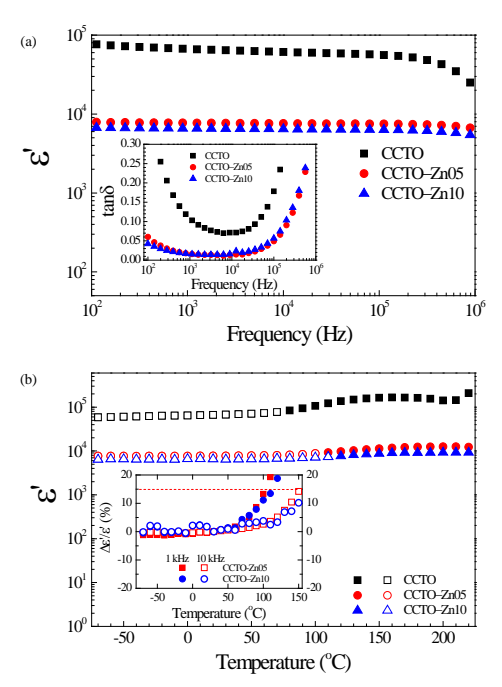


Fig. 8 (a) Frequency dependence of  $\varepsilon'$  at 20 °C for CCTO, CCTO–Zn05, and CCTO–Zn10 ceramics; inset demonstrates the frequency dependence of tan $\delta$  at 20 °C. (b) Temperature dependence of  $\varepsilon$ Zn05,1akHz of CCTO, CCTO CCTO–Zn10 ceramics; open symbols show the percentage of variation in  $\varepsilon'$  (  $\Delta$ hse  $\varepsilon$ Ahge of  $\varepsilon$ 15% compared with  $\varepsilon'$  at RT. Its inset temperature coefficient of  $\varepsilon'$  at 1 and 10 kHz.

#### 4.4 Conclusions

In summary, the effects of  $Zn^{2+}$  doping ions on the microstructural evaluation, giant dielectric, nonlinear J–E properties and microscopic properties of grains and GBs were investigated. Zn–doped CCTO ceramics were successfully prepared using a modified solgel method. The large grain size of CCTO ceramic was greatly reduced by  $Zn^{2+}$  doping and sintered at 1070 °C for 6 h. Interestingly, greatly reduced  $tan\delta$  values , ~0.016–0.017, were obtained while retaining high  $\epsilon'$  values, ~6500–7700, at 1 kHz in Zn–doped CCTO ceramics. The values of a and  $E_b$  were also enhanced significantly. As shown by impedance spectroscopy,  $R_{gb}$  of CCTO ceramics can be remarkably enhanced by doping with  $Zn^{2+}$  ions in the proper concentrations.  $R_{gb}$  is an important parameter contributing to improvement of overall dielectric and nonlinear electrical properties. The improved dielectric and nonlinear electrical properties showed the ability of  $Zn^{2+}$  doping ions to tune fine–grained microstructure and enhance the intrinsic properties of the GBs.

#### References

- [1] M.A. Subramanian, D. Li, N. Duan, B.A. Reisner, A.W. Sleight, High Dielectric Constant in ACu<sub>3</sub>Ti<sub>4</sub>O<sub>12</sub> and ACu<sub>3</sub>Ti<sub>3</sub>FeO<sub>12</sub> Phases, J. Solid State Chem. 151 (2000) 323-325.
- [2] S.-Y. Chung, I.-D. Kim, S.-J.L. Kang, Strong nonlinear current–voltage behaviour in perovskite-derivative calcium copper titanate, Nat. Mater. 3 (2004) 774-778.
- [3] L.H. Oliveira, E.C. Paris, W. Avansi, M.A. Ramirez, V.R. Mastelaro, E. Longo, J.A. Varela, X.M. Chen, Correlation Between Photoluminescence and Structural Defects in Ca<sub>1+x</sub>Cu<sub>3-x</sub>Ti<sub>4</sub>O<sub>12</sub> Systems, J. Am. Ceram. Soc. 96 (2013) 209-217.
- [4] L.H. Oliveira, A.P. de Moura, F.A. La Porta, I.C. Nogueira, E.C. Aguiar, T. Sequinel, I.L.V. Rosa, E. Longo, J.A. Varela, Influence of Cu-doping on the structural and optical properties of CaTiO<sub>3</sub> powders, Mater. Res. Bull. 81 (2016) 1-9.
- [5] A.O. Turky, M.M. Rashad, Z.I. Zaki, I.A. Ibrahim, M. Bechelany, Tuning the optical and dielectric properties of calcium copper titanate Ca<sub>x</sub>Cu<sub>3-x</sub>Ti<sub>4</sub>O<sub>12</sub> nanopowders, RSC Advances 5 (2015) 18767-18772.
- [6] T.B. Adams, D.C. Sinclair, A.R. West, Influence of Processing Conditions on the Electrical Properties of CaCu<sub>3</sub>Ti<sub>4</sub>O<sub>12</sub> Ceramics, J. Am. Ceram. Soc. 89 (2006) 3129-3135.
- [7] R. Schmidt, M.C. Stennett, N.C. Hyatt, J. Pokorny, J. Prado-Gonjal, M. Li, D.C. Sinclair, Effects of sintering temperature on the internal barrier layer capacitor (IBLC) structure in CaCu<sub>3</sub>Ti<sub>4</sub>O<sub>12</sub> (CCTO) ceramics, J. Eur. Ceram. Soc. 32 (2012) 3313-3323.
- [8] S.I.R. Costa, M. Li, J.R. Frade, D.C. Sinclair, Modulus spectroscopy of  $CaCu_3Ti_4O_{12}$  ceramics: clues to the internal barrier layer capacitance mechanism, RSC Advances 3 (2013) 7030-7036.
- [9] R. Schmidt, S. Pandey, P. Fiorenza, D.C. Sinclair, Non-stoichiometry in "CaCu<sub>3</sub>Ti<sub>4</sub>O<sub>12</sub>"
   (CCTO) ceramics, RSC Advances 3 (2013) 14580-14589.
- [10] M. Ahmadipour, M.F. Ain, Z.A. Ahmad, A Short Review on Copper Calcium Titanate (CCTO) Electroceramic: Synthesis, Dielectric Properties, Film Deposition, and Sensing Application, Nano-Micro Letters 8 (2016) 291-311.
- [11] C.H. Kim, Y.H. Jang, S.J. Seo, C.H. Song, J.Y. Son, Y.S. Yang, J.H. Cho, Effect of Mn doping on the temperature-dependent anomalous giant dielectric behavior of CaCu<sub>3</sub>Ti<sub>4</sub>O<sub>12</sub>, Phys. Rev. B 85 (2012).
- [12] L. Ni, X.M. Chen, Dielectric relaxations and formation mechanism of giant dielectric constant step in CaCu<sub>3</sub>Ti<sub>4</sub>O<sub>12</sub> ceramics, Appl. Phys. Lett. 91 (2007) 122905.
- [13] L. Ni, X.M. Chen, Enhanced giant dielectric response in Mg-substituted  $CaCu_3Ti_4O_{12}$  ceramics, Solid State Commun. 149 (2009) 379-383.
- [14] L. Ni, X.M. Chen, Enhancement of Giant Dielectric Response in CaCu<sub>3</sub>Ti<sub>4</sub>O<sub>12</sub> Ceramics by Zn Substitution, J. Am. Ceram. Soc. 93 (2010) 184-189.
- [15] J. Boonlakhorn, P. Thongbai, Mg-doped  $CaCu_3Ti_4O_{12}$  nanocrystalline powders prepared by a modified sol–gel method: Preparation, characterization, and their giant dielectric response, Jpn. J. Appl. Phys. 54 (2015) 06FJ06.
- [16] J. Boonlakhorn, B. Putasaeng, P. Kidkhunthod, P. Thongbai, Improved dielectric properties of (Y + Mg) co-doped CaCu<sub>3</sub>Ti<sub>4</sub>O<sub>12</sub> ceramics by controlling geometric and intrinsic properties of grain boundaries, Materials & Design 92 (2016) 494-498.
- [17] A. Nautiyal, C. Autret, C. Honstettre, S. De Almeida-Didry, M. El Amrani, S. Roger, B. Negulescu, A. Ruyter, Local analysis of the grain and grain boundary contributions to the bulk dielectric properties of  $Ca(Cu_{3-y}Mg_y)Ti_4O_{12}$  ceramics: Importance of the potential barrier at the grain boundary, J. Eur. Ceram. Soc. 36 (2016) 1391-1398.
- [18] J. Boonlakhorn, P. Kidkhunthod, P. Thongbai, A novel approach to achieve high dielectric permittivity and low loss tangent in CaCu<sub>3</sub>Ti<sub>4</sub>O<sub>12</sub> ceramics by co-doping with Sm<sup>3+</sup> and Mg<sup>2+</sup> ions, J. Eur. Ceram. Soc. 35 (2015) 3521-3528.
- [19] J. Boonlakhorn, P. Kidkhunthod, P. Thongbai, S. Maensiri, Colossal dielectric permittivity and electrical properties of the grain boundary of  $Ca_{1-3x/2}Yb_xCu_{3-y}Mg_yTi_4O_{12}$  (x=0.05, y=0.05 and 0.30), Ceram. Int. 42 (2016) 8467-8472.

- [20] J. Jumpatam, B. Putasaeng, T. Yamwong, P. Thongbai, S. Maensiri, A novel strategy to enhance dielectric performance and non-Ohmic properties in  $Ca_2Cu_{2-x}Mg_xTi_4O_{12}$ , J. Eur. Ceram. Soc. 34 (2014) 2941-2950.
- [21] L. Sun, R. Zhang, Z. Wang, E. Cao, Y. Zhang, L. Ju, Microstructure and enhanced dielectric response in Mg doped CaCu<sub>3</sub>Ti<sub>4</sub>O<sub>12</sub> ceramics, J. Alloys Compd. 663 (2016) 345-350.
- [22] D. Xu, K. He, R. Yu, X. Sun, Y. Yang, H. Xu, H. Yuan, J. Ma, High dielectric permittivity and low dielectric loss in sol–gel derived Zn doped CaCu<sub>3</sub>Ti<sub>4</sub>O<sub>12</sub> thin films, Mater. Chem. Phys. 153 (2015) 229-235.
- [23] L. Singh, U.S. Rai, A.K. Rai, K.D. Mandal, Sintering effects on dielectric properties of Zndoped CaCu<sub>3</sub>Ti<sub>4</sub>O<sub>12</sub> ceramic synthesized by modified sol-gel route, Electron. Mater. Lett. 9 (2013) 107-113.
- [24] L. Singh, U.S. Rai, K.D. Mandal, Dielectric properties of zinc doped nanocrystalline calcium copper titanate synthesized by different approach, Mater. Res. Bull. 48 (2013) 2117-2122.
- [25] L. Singh, I.W. Kim, B.C. Sin, K.D. Mandal, U.S. Rai, A. Ullah, H. Chung, Y. Lee, Dielectric studies of a nano-crystalline CaCu<sub>2.90</sub>Zn<sub>0.10</sub>Ti<sub>4</sub>O<sub>12</sub>electro-ceramic by one pot glycine assisted synthesis from inexpensive TiO<sub>2</sub> for energy storage capacitors, RSC Adv. 4 (2014) 52770-52784.
- [26] L. Singh, U.S. Rai, K.D. Mandal, Influence of Zn doping on microstructures and dielectric properties in CaCu<sub>3</sub>Ti<sub>4</sub>O<sub>12</sub> ceramic synthesised by semiwet route, Adv. Appl. Ceram. 111 (2012) 374-380.
- [27] L. Singh, U.S. Rai, K.D. Mandal, A. Rai, Effect of processing routes on microstructure, electrical and dielectric behavior of Mg-doped CaCu<sub>3</sub>Ti<sub>4</sub>O<sub>12</sub> electro-ceramic, Applied Physics A 112 (2013) 891-900.
- [28] L. Singh, U.S. Rai, K.D. Mandal, Dielectric, modulus and impedance spectroscopic studies of nanostructured  $CaCu_{2.70}Mg_{0.30}Ti_4O_{12}$  electro-ceramic synthesized by modified sol–gel route, J. Alloys Compd. 555 (2013) 176-183.
- [29] M. Li, G. Cai, D.F. Zhang, W.Y. Wang, W.J. Wang, X.L. Chen, Enhanced dielectric responses in Mg-doped CaCu<sub>3</sub>Ti<sub>4</sub>O<sub>12</sub>, J. Appl. Phys. 104 (2008) 074107.
- [30] M. Li, X.L. Chen, D.F. Zhang, W.Y. Wang, W.J. Wang, Humidity sensitive properties of pure and Mg-doped CaCu<sub>3</sub>Ti<sub>4</sub>O<sub>12</sub>, Sensors and Actuators B: Chemical 147 (2010) 447-452.
- [31] M.F. Ab Rahman, S.D. Hutagalung, Z.A. Ahmad, M.F. Ain, J.J. Mohamed, The effect of different dopant site (Cu and Ca) by magnesium onCaCu<sub>3</sub>Ti<sub>4</sub>O<sub>12</sub> dielectric properties, J. Mater. Sci.: Mater. Electron. 26 (2015) 3947-3956.
- [32] W. Li, S. Qiu, N. Chen, G. Du, Enhanced Dielectric Response in Mg-doped CaCu<sub>3</sub>Ti<sub>4</sub>O<sub>12</sub> Ceramics, Journal of Materials Science & Technology 26 (2010) 682-686.
- [33] L. Sun, R. Zhang, Z. Wang, E. Cao, Y. Zhang, L. Ju, Microstructure, dielectric properties and impedance spectroscopy of Ni doped CaCu<sub>3</sub>Ti<sub>4</sub>O<sub>12</sub> ceramics, RSC Advances 6 (2016) 55984-55989.
- [34] A.K. Rai, K.D. Mandal, D. Kumar, O. Parkash, Characterization of nickel doped CCTO:  $CaCu_{2.9}Ni_{0.1}Ti_4O_{12}$  and  $CaCu_3Ti_{3.9}Ni_{0.1}O_{12}$  synthesized by semi-wet route, J. Alloys Compd. 491 (2010) 507-512.
- [35] D. Xu, C. Zhang, Y. Lin, L. Jiao, H. Yuan, G. Zhao, X. Cheng, Influence of zinc on electrical and microstructural properties of CaCu<sub>3</sub>Ti<sub>4</sub>O<sub>12</sub> ceramics prepared by sol–gel process, J. Alloys Compd. 522 (2012) 157-161.
- [36] S. Vangchangyia, E. Swatsitang, P. Thongbai, S. Pinitsoontorn, T. Yamwong, S. Maensiri, V. Amornkitbamrung, P. Chindaprasirt, Very Low Loss Tangent and High Dielectric Permittivity in Pure-CaCu<sub>3</sub>Ti<sub>4</sub>O<sub>12</sub> Ceramics Prepared by a Modified Sol-Gel Process, J. Am. Ceram. Soc. 95 (2012) 1497-1500.
- [37] M. Newville, EXAFS analysis using FEFF and FEFFIT, Journal of Synchrotron Radiation 8 (2001) 96-100.
- [38] E. Silva Junior, F.A. La Porta, M.S. Liu, J. Andres, J.A. Varela, E. Longo, A relationship between structural and electronic order-disorder effects and optical properties in crystalline TiO<sub>2</sub> nanomaterials, Dalton Trans. 44 (2015) 3159-3175.
- [39] E. Jansen, W. Schäfer, G. Will, R values in analysis of powder diffraction data using Rietveld refinement, J. Appl. Crystallogr. 27 (1994) 492-496.

- [40] L. Liu, H. Fan, P. Fang, X. Chen, Sol–gel derived  $CaCu_3Ti_4O_{12}$  ceramics: Synthesis, characterization and electrical properties, Mater. Res. Bull. 43 (2008) 1800-1807.
- [41] J. Li, K. Wu, R. Jia, L. Hou, L. Gao, S. Li, Towards enhanced varistor property and lower dielectric loss of CaCu<sub>3</sub>Ti<sub>4</sub>O<sub>12</sub> based ceramics, Materials & Design 92 (2016) 546-551.
- [42] X.-g. Zhao, P. Liu, Y.-C. Song, A.-p. Zhang, X.-m. Chen, J.-p. Zhou, Origin of colossal permittivity in  $(In_{1/2}Nb_{1/2})TiO_2$  via broadband dielectric spectroscopy, Phys. Chem. Chem. Phys. 17 (2015) 23132-23139.
- [43] Q. Zheng, H. Fan, C. Long, Microstructures and electrical responses of pure and chromium-doped CaCu<sub>3</sub>Ti<sub>4</sub>O<sub>12</sub> ceramics, J. Alloys Compd. 511 (2012) 90-94.

## CHAPTER 5

# Effects of Mg<sup>2+</sup> Doping Ions on Giant Dielectric Properties and Electrical Responses of Na<sub>1/2</sub>Y<sub>1/2</sub>Cu<sub>3</sub>Ti<sub>4</sub>O<sub>12</sub> Ceramics

### 5.1 Introduction

Recently,  $CaCu_3Ti_4O_{12}$  (CCTO) has attracted considerable attention since its anomalous dielectric response was first reported by Subramanian *et al* [1]. CCTO polycrystalline ceramics are clearly shown to have an electrically heterogeneous structure consisting of semiconducting grains and insulating grain boundaries (GB), i.e., an internal barrier layer capacitor (IBLC) structure [2, 3]. Very high values of dielectric permittivity ( $\varepsilon' \approx 10^3 - 10^5$ ) were widely accepted to have originated from this special IBLC microstructure, which can be synthesized using a one–step sintering process [3]. The large dielectric loss tangent ( $tan\delta$ ) values of CCTO ceramics are unsuitable for capacitor applications. Therefore, investigation of the reduction of  $tan\delta$  in CCTO ceramics as well as other high permittivity materials in the  $ACu_3Ti_4O_{12}$  group is an important and urgent issue for supporting progress in the development of novel electronic technologies.

CCTO is one of the metal oxides in the  $ACu_3Ti_4O_{12}$  family, where A = Cd,  $Bi_{2/3}$ ,  $La_{2/3}$ ,  $Y_{2/3}$ ,  $Na_{1/2}Bi_{1/2}$ ,  $Na_{1/2}La_{1/2}$ ,  $Na_{1/2}Y_{1/2}$ ,  $Na_{1/2}Sm_{1/2}$ , and  $Na_{1/3}Ca_{1/3}Bi_{1/3}$ , among others [4-16]. In addition to CCTO ceramics, there are several short reports on the giant dielectric properties of other oxides in the  $ACu_3Ti_4O_{12}$  family. Some of these compounds exhibited good dielectric properties compared to those of CCTO. For example,  $Na_{1/2}Bi_{1/2}Cu_3Ti_4O_{12}$  ceramics exhibited good dielectric properties with high  $\epsilon'$  of 13,495 low  $tan\delta\approx0.031$  (at 10 kHz, respectively) [15]. Moreover, Liang *et al.* found high  $\epsilon'$  and low  $tan\delta$  values with good thermal stability at 10 kHz in  $Y_{2/3}Cu_3Ti_4O_{12}$ —based ceramics [12]. Although  $tan\delta$  values below 10 kHz for these  $ACu_3Ti_4O_{12}$  ceramics are quite large, they are still lower than those of CCTO ceramics. Thus, CCTO—related ceramics may have more potential for practical applications than CCTO ceramics.

CCTO [2] and other related  $ACu_3Ti_4O_{12}$  ceramics [7, 8] showed nonlinear current–voltage (current density–electric field strength, J–E) properties. The origin of nonlinear J–E behavior is likely due to the existence of Schottky barriers at the GBs [2, 17], while the origin of the high permittivity properties is still unknown. Both the extrinsic and intrinsic properties have been theorized as the source of such high permittivity behavior [3, 18-22]. The nonlinear J–E properties of  $ACu_3Ti_4O_{12}$  ceramic compounds were seldom reported [23–25].

Methods for improving the dielectric properties of  $Mg^{2+}$ -doped CCTO (M–CCTO) ceramics have been widely investigated. Li *et al.* [23, 24] reported a significant decrease in  $\tan\delta$  of M–CCTO ceramics even though the mean grain size of CCTO and M–CCTO ceramics was slightly changed. Ni and Chen reported a large increase of  $\epsilon'$  in M–CCTO ceramics in the frequency range of 1–10<sup>6</sup> Hz [19]. Surprisingly, the  $\tan\delta$  value in a low frequency range (1–10<sup>2</sup> Hz) decreased with increasing  $Mg^{2+}$  dopant concentration even, though the mean grain size of the M–CCTO ceramics increased from 21.8 to 36.2  $\mu$ m. It was further found that doping  $Mg^{2+}$  into CCTO ceramics prepared using a sol–gel method can cause a large decrease in  $\tan\delta$ , whereas  $\epsilon'$  increased significantly [25]. Therefore,  $Mg^{2+}$  is one of the most interesting dopants since it can strike a balance between high  $\epsilon'$  and low  $\tan\delta$  values. Unfortunately, improvement of other related  $ACu_3Ti_4O_{12}$  by doping with  $Mg^{2+}$  has never been reported.

In this work, the effects of  $Mg^{2+}$  doping ions on the microstructural evolution, giant dielectric properties, nonlinear J-E behavior, and electrical responses of the grain and GB of  $Mg^{2+}$ -doped  $Na_{1/2}Y_{1/2}Cu_3Ti_4O_{12}$  (M-NYCTO) ceramics were systematically investigated. The correlation between the microstructure and electrical properties was well established. Improved dielectric properties of M-NYCTO were successfully accomplished with enhanced  $\epsilon'$  and reduced  $tan\delta$  values. The mechanisms of electrical conduction inside the grain and the giant dielectric behavior of M-NYCTO are briefly discussed.

## 5.2 Experimental details

Na $_{1/2}$ Y $_{1/2}$ Cu $_{3-x}$ Mg $_x$ Ti $_4$ O $_{12}$  ceramics (where  $x=0, 0.1, 0.2, and 0.3, referred to as the NYCTO, Mg-10, Mg-20, and Mg-30 samples, respectively) were prepared using a solid–state reaction method. First, a stoichiometric mixture of the starting materials (i.e., Na<math>_2$ CO $_3$  (99.9%), Y $_2$ O $_3$  (99.99%), CuO (99.9%), MgO (99.99%), and TiO $_2$  (99.9%)) was ball–milled in ethanol for 24 h. Second, the resulting slurry was dried and calcined at 900 °C for 15 h. Then, the calcined powder was carefully ground and pressed into pellets, 9.5 mm in diameter and ~1.2 mm in thickness, by a uniaxial compression at  $\approx$ 200 MPa. Finally, these pellets were sintered at 1085 °C for 5 h.

X-ray diffraction (XRD) (PANalytical, EMPYREAN) and scanning electron microscopy (SEM) (SEC, SNE4500M) were used to respectively characterize the phase composition and microstructure of the sintered ceramics. SEM-mapping was done using field-emission scanning electron microscopy (FE-SEM) with energy-dispersive X-ray analysis (EDS) (HITACHI SU8030, Japan). X-ray Absorption Near Edge Structure (XANES) spectra were collected at the SUT-NANOTEC-SLRI XAS beamline (BL5.2) (using an electron energy of 1.2 GeV, a bending magnet, beam current of 80 - 150 mA, and 1.1 to  $1.7 \times 10^{11}$  photons s<sup>-1</sup>) at the Synchrotron Light Research Institute (SLRI). Nakhon Ratchasima, Thailand. Details of this characterization technique have been published [26]. The normalized XANES data were processed and analyzed after background subtraction in the pre-edge and post-edge region using ATHENA software included in an IFEFFIT package [27]. The chemical states of Cu and Ti were analyzed using X-ray photoelectron spectroscopy (XPS), PHI5000 VersaProbe II, ULVAC-PHI, Japan) at the SUT-NANOTEC-SLRI Joint Research Facility. Synchrotron Light Research Institute (SLRI), Thailand. The XPS spectra were fitted with PHI MultiPak XPS software using a combination of Gaussian-Lorentzian lines.

Prior to dielectric and electrical measurements, Au electrodes were sputtered onto each polished–face at a current of 25 mA for 8 min using a Polaron SC500 sputter coating unit. The dielectric properties were measured using a KEYSIGHT E4990A Impedance Analyzer over the frequency and temperature ranges of  $10^2$ – $10^7$  Hz and -70–200 °C. Each measured temperature was kept constant with a precision of  $\pm 0.1$  °C. J–E characteristics at room temperature were corrected using a high voltage measurement unit (Keithley Model 247). The breakdown electric field ( $E_b$ ) was achieved at J = 1 mA.cm<sup>-2</sup>. The nonlinear coefficient ( $\alpha$ ) was calculated using the following formula:

$$\alpha = \frac{\log(J_2/J_1)}{\log(E_2/E_1)} \tag{1}$$

where  $E_1$  and  $E_2$  are the applied electric fields, at  $J_1 = 1$  and  $J_2 = 10$  mA.cm<sup>-2</sup>, respectively. The complex impedance ( $Z^*$ ) and complex admittance ( $Y^*$ ) were calculated from the complex dielectric permittivity ( $\varepsilon^*$ ) using the following relationship:

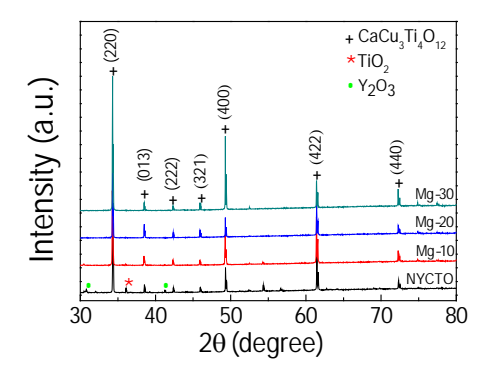
$$\varepsilon^* = \varepsilon' - i\varepsilon'' = \frac{1}{i\omega C_0 Z^*} = \frac{1}{i\omega C_0 (Z' - iZ'')}$$
 (2)

$$Y^* = Y' + iY'' = \frac{1}{Z^*} \tag{3}$$

where  $\varepsilon'$  and  $\varepsilon''$  are the real (dielectric constant) and imaginary (dielectric loss factor) components of  $\varepsilon^*$ , respectively. Y' and Y'' are the real part and imaginary parts of  $Y^*$ , respectively. Z' and Z'' are the real and imaginary parts of  $Z^*$ , respectively.  $\varepsilon'$  was calculated from  $\varepsilon' = C_p d/\varepsilon_0 A$ , where  $C_p$  is the measured capacitance, A is the electrode area, d is the sample thickness, and  $\varepsilon_0$  is the permittivity of free space ( $\mathcal{E}_0 = 8.854 \times 10^{-12}$  F/m).  $\omega$  is the angular frequency of an applied AC electric field ( $\omega = 2\pi f$ ).  $C_0 = \varepsilon_0 A/d$  is the empty cell capacitance.

### 5.3 Results and discussion

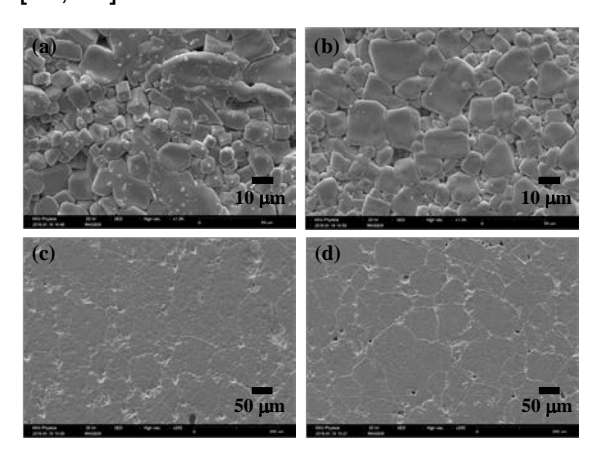
The XRD patterns of the NYCTO and M-NYCTO ceramics are shown in Fig. 1. The primary NYCTO phase was observed in all of the XRD patterns. TiO<sub>2</sub> and Y<sub>2</sub>O<sub>3</sub> impurity phases were only observed in the NYCTO sample, while a single phase of NYCTO was detected in all of the M-NYCTO samples. Incorporation of MgO particles into the starting raw materials can promote the phase formation in NYCTO ceramics. Mg<sup>2+</sup> doping ions might have an important effect on kinetically controlled metal ions diffusion as well as oxygen diffusion in NYCTO ceramics during calcination and sintering process. All of the XRD patterns indicated that the crystal structure was a perovskite-like CCTO structure (JCPDS 75–2188), which was well indexed based on *bcc* structure within space group *Im*3. The values of lattice parameters (a) were calculated by using Cohen's least mean square method. The *a values* were approximately 7.3845, 7.3852, 7.3868, and 7.3881 Å for the NYCTO, Mg-10, Mg-20, and Mg-30 samples, respectively.



**Fig. 1** XRD patterns of  $Na_{1/2}Y_{1/2}Cu_{3-x}Mg_xTi_4O_{12}$  ceramics with different dopant contents (x).

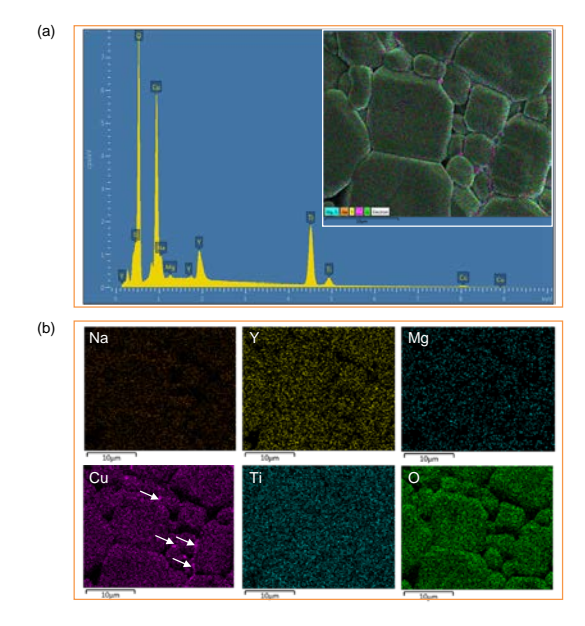
These values are comparable to those reported in literature, 7.378–7.385 Å, for NYCTO ceramics [4, 6]. It is notable that the lattice parameter tended to increase with increasing dopant concentration. This cannot be ascribed to the different ionic radii between the host and dopant ions because the ionic radii of  $Cu^{2+}$  and  $Mg^{2+}$  ions are the same ( $r_4 = 0.57$  Å). It is possible that the increase in the lattice parameter of the

M-NYCTO ceramics may have resulted from lattice distortion induced by variation in the mixed-valent structure [19, 26].



**Fig. 2** SEM images of polished surfaces of (a) NYCTO, (b) Mg-10, (c) Mg-20, and (d) Mg-30 ceramics.

The morphologies of polished surfaces for all the samples are shown in Fig. 2. Clearly, the grain size of the NYCTO ceramics was greatly enlarged by doping with  $\mathrm{Mg}^{2+}$ . This result is similar to that observed in M–CCTO ceramics, which was ascribed to the effect of a liquid phase sintering behavior [19, 26]. The mean grain sizes of the NYCTO, Mg-10, Mg-20, and Mg-30 samples were approximately equal to 11.0, 13.1, 82.4, and 88.4  $\mu m$ , respectively.



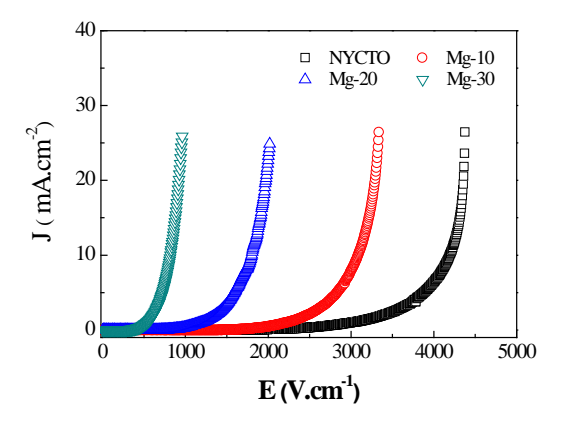
**Fig. 3** (a) EDS spectra of the Mg-10 sample; inset shows the SEM mapping image for a mixture of all elements. (b) Element mapping of the Mg-10 sample for each element, i.e., Na, Y, Mg, Cu, Ti, and O.

Fig. 3(a) shows the EDS spectrum of the Mg-10 sample detected in the selected area shown in its inset. This confirms the existence of all major elements (*i.e.*, Na, Y, Cu, Ti, and O) as well as the Mg dopant as a minor element. The image showing the mixture of all elements is shown in the inset of Fig. 3(a). Fig. 3(b) shows the SEM mapping images for each element. All of these elements are homogeneously dispersed in the

microstructure in both of the grains and GBs. Segregation of the Mg dopant in any specific region was not observed. Slight segregation of Cu along the GBs was observed (as indicated by write arrows in Cu–mapping element), which is usually observed in CCTO polycrystalline ceramics [22, 28]. It is noteworthy that both Na and Y coexisted in every grain and no single grain that contained only one or the other. This strongly indicated that the possible  $Y_{2/3}Cu_3Ti_4O_{12}$  and  $(Na,Y)Cu_3Ti_4O_{12}$  phases were not separately formed.

Fig. 4 illustrates the influence of  $Mg^{2+}$  on the nonlinear J-E characteristics of NYCTO ceramics.  $E_b$  decreased with increasing  $Mg^{2+}$  doping content.  $E_b$  values were respectively 3002, 2213, 1196, and 537 V.cm<sup>-2</sup> for the NYCTO, Mg-10, Mg-20, and Mg-30 samples, while  $\alpha$  values were about 6.79, 6.88, 5.77, and 5.40, respectively. It is reasonable to suggest that  $E_b$  was likely correlated with the volume fraction of the GB, which is inversely proportional to its mean grain size. This is similar to those observed in CCTO ceramics [2, 26]. Thus, both the intrinsic and extrinsic properties (geometric properties) of the GBs had an effect on the nonlinear J-E properties [2, 7, 17]. It is clear that the geometric factor of the GB regarding the enlarged grain size was more dominant for this case. This result confirms the origin of nonlinear J-E properties as the electrical response of the GBs. Under this sintering condition,  $Mg^{2+}$  doping ions enhanced the grain growth rate of NYCTO ceramics, giving rise to a reduction in both  $\alpha$  and  $E_b$  values.

The overall frequency dependent behaviors of the un–doped NYCTO and M–NYCTO ceramics differed slightly [Fig. 5(a)].  $\epsilon'$  was nearly independent of frequency from  $10^2$  to  $10^5$  Hz for all the samples and it significantly increased from  $\approx 14000$  to  $\approx 42000$  as Mg<sup>2+</sup> concentration increased. This is similar to that observed in M–CCTO ceramics [19, 23-26]. As revealed in Fig. 2, the enlarged grain size as a result of Mg<sup>2+</sup> doping ions is one of the most important factors contributing to the enhanced  $\epsilon'$  response. For the un–doped NYCTO sample,  $\epsilon'$  became strongly temperature dependent when the temperature was increased to values exceeding 100 °C [inset of Fig. 5(a)]. Notably, the temperature stabilities of  $\epsilon'$  for the Mg-10 and Mg-20 samples were improved to values better than that of the un–doped NYCTO sample.



**Fig. 4** Nonlinear *J–E* curves at room temperature for Na<sub>1/2</sub>Y<sub>1/2</sub>Cu<sub>3-x</sub>Mg<sub>x</sub>Ti<sub>4</sub>O<sub>12</sub> ceramics with different dopant contents (*x*).

Fig. 5(b) shows that the low–frequency  $\tan\delta$  value of the Mg-10 sample was slightly smaller than that of the NYCTO ceramic. Then, the  $\tan\delta$  values of the Mg-20 and Mg-30 samples increased to values larger than that of the NYCTO sample. The  $\tan\delta$  values at 20 °C and 1 kHz of the NYCTO, Mg-10, Mg-20 and Mg-30 samples were approximately

0.040, 0.036, 0.054 and 0.111, respectively. Furthermore,  $tan\delta$  values of the NYCTO and Mg-10 samples were smaller than 0.075 over a frequency range of  $10^2$ – $10^5$  Hz. Although many strategies have been successfully used to improve particular dielectric properties, they tend to simultaneously worsen other important dielectric properties of CCTO and  $ACu_3Ti_4O_{12}$ –related ceramics. Notably, substitution of  $Mg^{2+}$  into a NYCTO ceramic at an appropriate concentration can retain a low  $tan\delta$  value and enhance  $\epsilon'$  with good temperature stability. At  $10^2$  Hz,  $tan\delta$  values of the NYCTO, Mg-10 and Mg-20 samples were lower than 0.1, which is better than that of CCTO ceramics.

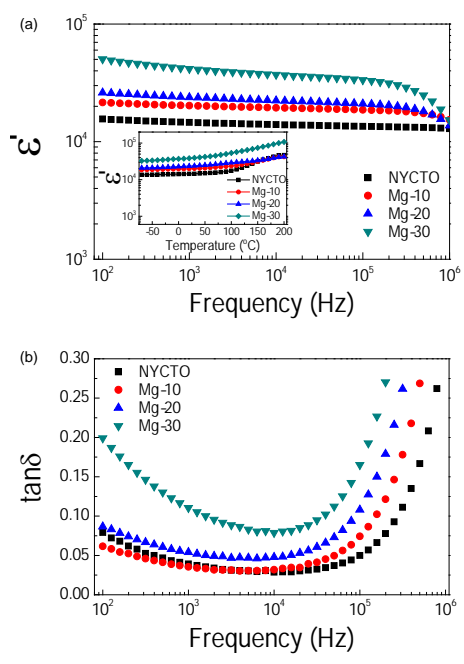
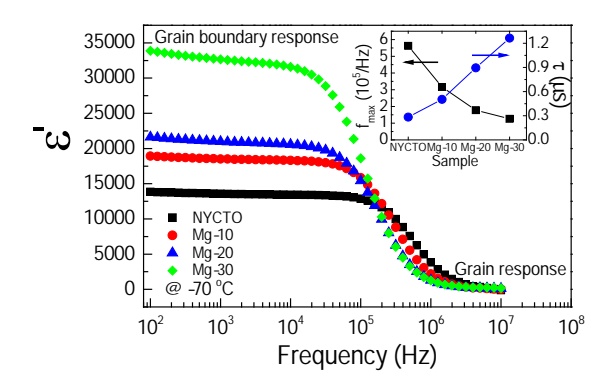


Fig. 5 (a) Dielectric permittivity (ε') at 20 °C as a function of frequency for Na<sub>1/2</sub>Y<sub>1/2</sub>Cu<sub>3-x</sub>Mg<sub>x</sub>Ti<sub>4</sub>O<sub>12</sub> ceramics with different dopant contents (x); inset shows the temperature dependence of ε' at 1 kHz. (b) Frequency dependence of tanδ at room temperature for Na<sub>1/2</sub>Y<sub>1/2</sub>Cu<sub>3-x</sub>Mg<sub>x</sub>Ti<sub>4</sub>O<sub>12</sub> ceramics.

A slight difference in dielectric behaviors was observed in a high–frequency range,  $10^5$ – $10^6$  Hz. The frequency at which the relaxation peak of  $\varepsilon''$  ( $\varepsilon''=\varepsilon'\tan\delta$ ) and corresponding rapid decrease in  $\varepsilon'$  appeared ( $f_{\text{max-relax}}$ ) shifted to lower values as Mg²+ concentration increased. This behavior was clearly observed at -70 °C [Fig. 6]. Furthermore, the electrical responses of the grain and GB became separately evident and were clearly seen in high and low frequency ranges, respectively [21, 22]. It is noteworthy that substitution of Mg²+ ions had a great effect on the GB response, but slight impact on the grain response. The inset of Fig. 6 shows that the  $f_{\text{max-relax}}$  value at -70 °C of the M–doped NYCTO ceramics decreased with increasing Mg²+ concentration, while its relaxation time ( $\tau = 1/2\pi f_{\text{max-relax}}$ ) increased. According to the Maxwell–Wagner relaxation model based on the IBLC structure [13, 20],  $f_{\text{max-relax}}$  is very sensitive to the grain resistance ( $R_g$ ) and the GB capacitance ( $C_{gb}$ ). When  $R_{gb}$ >> $R_g$  and  $C_{gb}$ >> $C_g$  (where  $C_g$  is the grain capacitance), the low–frequency dielectric permittivity ( $\varepsilon'_s$ ) and  $\tau$  can be estimated as  $\varepsilon'_s \approx C_{gb}/C_0$  and  $\tau \approx R_g C_{gb}$ , respectively.



**Fig. 6**  $f_{\text{max}}$  and τ values at -70 °C for Na<sub>1/2</sub>Y<sub>1/2</sub>Cu<sub>3-x</sub>Mg<sub>x</sub>Ti<sub>4</sub>O<sub>12</sub> ceramics with different dopant contents (x = 0-0.3).

To describe the effects of Mg<sup>2+</sup> dopant ions on the giant dielectric response in NYCTO ceramics, the electrical properties of the grain and GB were investigated. Impedance spectroscopy (IS) was employed to clarify this. In Fig. 7(a) and its inset, only the linear part of the semicircular arcs with nonzero intercept on the Z' axis was observed at 20 °C. For CCTO and ACu<sub>3</sub>Ti<sub>4</sub>O<sub>12</sub>-related ceramics, these generally describe the electrical responses of the GB (in the absence of sample-electrode contact effect) and the grain, respectively [3, 8, 9, 20, 22, 25, 26, 29-31].  $R_q$  of the NYCTO ceramics was slightly increased by doping with Mg<sup>2+</sup>, which is similar to that observed in M-CCTO ceramics [25, 26]. In the frequency range of 10<sup>2</sup>–10<sup>6</sup> Hz, it was very difficult (or perhaps impossible) to accurately determine the value of R<sub>gb</sub> at 20 °C since just few data points on the full arcs appeared in these Z\* plots. The frequency at which the maximum value of Z" appeared  $(f_{\text{max-RC}} = 1/2\pi R_{\text{gb}}C_{\text{gb}})$  was much lower than the minimum measurement frequency of the instrumentation ( $f_{\text{max-RC}}$  < 10<sup>2</sup> Hz) and the sample was too resistive (i.e., very large value of  $R_{\rm gb}$ ). Given that  $C_{\rm gb}$  was temperature independent [3, 20, 22], to increase  $f_{\rm max-RC} \rightarrow 10^2$ Hz,  $R_{\rm gb}$  must be greatly reduced by increasing its temperature. At 20 °C,  $R_{\rm gb}$  values of the un-doped NYCTO and Mg-10 samples at 20 °C were not significantly different. However, this was not true as the temperature was continuously increased [Fig. 7(b-d)] the semicircular arcs became apparent in all the samples. In Fig. 7(d), R<sub>ab</sub> of the Mg-10 and Mg-20 samples was significantly enhanced even though the volume fraction of the GB decreased due to its enlarged grain size. This indicated that substitution of Mg2+ at an appropriate concentration can cause an increase in  $R_{ob}$  values. Low tan  $\delta$  values of the NYCTO, Mg-10, and Mg-20 samples were likely associated with their high  $R_{\rm gb}$  values. The variation in  $E_b$  was not consistent with  $tan\delta$  values. This may have resulted from these two parameters being measured at different electric field strengths. It was clearly demonstrated that  $R_{\rm gb}$  of CCTO ceramics was clearly shown to correlate with oxygen vacancies at the GBs [3]. We have also found that  $R_{\rm gb}$  of Na<sub>1/2</sub>Bi<sub>1/2</sub>Cu<sub>3</sub>Ti<sub>4</sub>O<sub>12</sub> ceramics was significantly increased by annealing in O2 atmosphere [32]. Thus, it is possible that Mg<sup>2+</sup> may have a potential for exhibiting oxygen loss during the sintering process, giving rise to its  $R_{ab}$  value.

 $R_{\rm gb}$  was more than 4 orders of magnitude larger than  $R_{\rm g}$ . Thus, this suggests that the origin of giant permittivity response of all the samples was correlated with Maxwell–Wagner polarization. According to the  $Z^*$  plots, it can be seen that  $C_{\rm gb}$  of the M–NYCTO ceramics increased with increasing  $Mg^{2+}$  concentration, according to the

relationship,  $\mathcal{E}_s' \approx C_{gb}/C_0$ . Furthermore, the dielectric relaxation behavior can be well described by the Maxwell–Wagner relaxation model. The increase in  $\tau$  (or decrease in  $f_{\text{max-relax}}$ ) was attributed to the increases in  $R_{\text{g}}$  and  $C_{\text{gb}}$  values following the relationship,  $\tau \approx R_{_g}C_{_{gb}}$ .

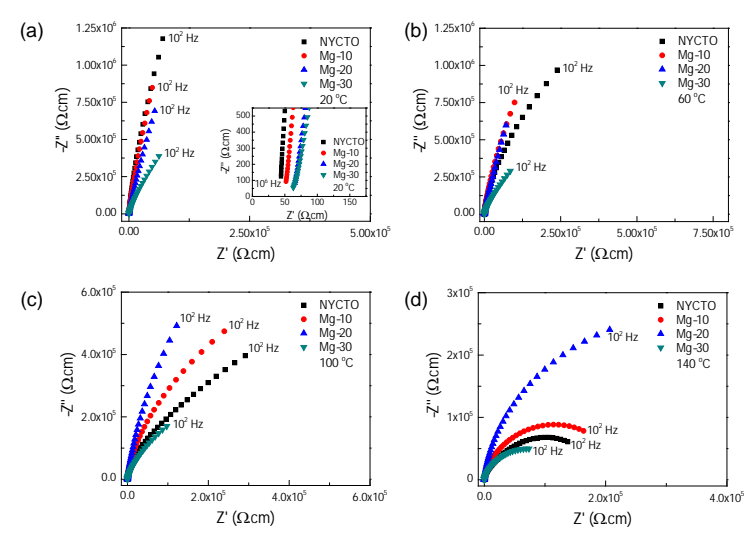


Fig. 7 Impedance complex plane (Z\*) plot at various temperatures for Na<sub>1/2</sub>Y<sub>1/2</sub>Cu<sub>3-x</sub>Mg<sub>x</sub>Ti<sub>4</sub>O<sub>12</sub> ceramics with different dopant contents (x): (a) 20 °C, (b) 60 °C, (c) 100 °C, and (d) 140 °C. Inset of (a) shows an expanded view of the Z\* plot at 20 °C in high frequency range.

According to the equivalent circuit represented the IBLC structure of  $ACu_3Ti_4O_{12}$  [13], Z" as a function of frequency can be expressed as:

$$Z''(\omega) = R_g \left[ \frac{\omega R_g C_g}{1 + (\omega R_g C_g)^2} \right] + R_{gb} \left[ \frac{\omega R_{gb} C_{gb}}{1 + (\omega R_g C_{gb})^2} \right]$$
(4)

As depicted in Fig. 8, only one electrical response in a low frequency range is dominant in the measured temperature range (-70 to 200  $^{\rm o}$ C). This apparent Z" peak should be correlated with the large semicircle [Fig. 7] and represents the electrical response of the GBs.  $R_{\rm gb}$  values at various temperatures can easily be calculated using the relationship,  $R=2Z''_{\rm max}$ , where  $Z''_{\rm max}$  is the maximum Z" value. The activation energy required for conduction of charge carriers across the potential barrier at the GB ( $E_{\rm gb}$ ) can be calculated by using the Arrhenius law [13]:

$$\sigma_{gb} = \sigma_0 \exp\left(\frac{-E_{gb}}{k_B T}\right) \tag{5}$$

where  $\sigma_{gb} = 1/R_{gb}$  is the GB conductivity and  $\sigma_0$  is pre–exponential term. In the inset of Fig. 8, the temperature dependence of  $\sigma_{gb}$  can be well fitted by Eq. (5).  $E_{gb}$  values of the NYCTO, Mg-10, Mg-20 and Mg-30 samples were 0.747, 0.765, 0.731, and 0.680 eV, respectively.  $E_{gb}$  of the Mg-10 sample significantly increased compared to the NYCTO sample. Then,  $E_{gb}$  decreased with further increases in Mg<sup>2+</sup> dopant concentration.

Generally,  $R_g$  values can be roughly estimated from the nonzero intercept of  $Z^*$  plots using linear eye guidelines [inset of Fig. 7(a)]. Alternatively,  $R_g$  can be obtained from admittance spectroscopy (AS) analysis by fitting  $Y^*$  data with the relationship [20]:

$$Y^* = \frac{(R_{gb}^{-1})(1 - \omega^2 \tau_g \tau_{gb} + i\omega \tau_{gb})}{1 + i\omega \tau}$$
 (6)

 $au_{_g}=R_{_g}C_{_g}$  ,  $au_{_{gb}}=R_{_{gb}}C_{_{gb}}$  , and  $au=R_{_g}C_{_{gb}}$  . Setting  $dY''/d\omega=0$  , the simple relationship,  $R_{\rm g}=1/2Y_{\rm max}''$  (where  $Y_{\rm max}''$  is the maximum value at the Y''-peak), is achieved. Y"-peaks of all the ceramic samples appeared in a low temperature range [Fig. 9].  $R_{\alpha}$ values and the grain conductivity ( $\sigma_b = 1/R_g$ ) obtained by IS (using linear eye guidelines) and AS (using relation  $R_{\rm g}=1/2Y_{\rm max}''$ ) were very close [insets of Figs. 9(a-d)].  $R_{\rm g}$  values can be easily calculated by using AS and this is more suitable than IS. The variation of M-NYCTO follows  $\sigma_{\rho}$  with temperature the ceramics the Arrhenius law,  $\sigma_{e} = \sigma_{0} \exp(-E_{e}/k_{B}T)$ . Good linear fits were achieved in both of the data sets obtained from these two analyses. The  $E_g$  values of all the samples were  $\approx 0.1$  eV.

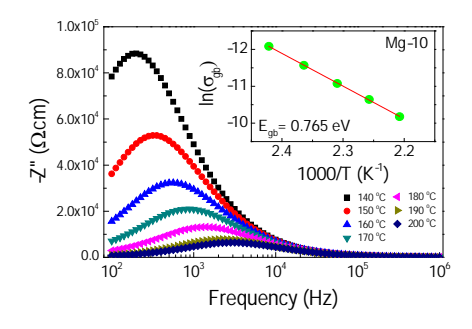


Fig. 8 Frequency dependence of Z'' at different temperatures; inset shows the Arrhenius plot for the temperature dependence of  $\sigma_{qb}$ .

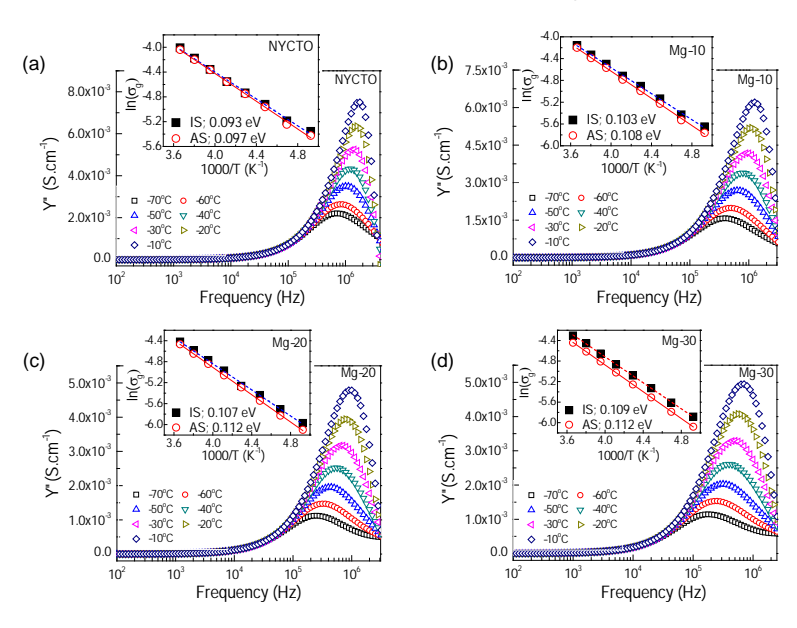
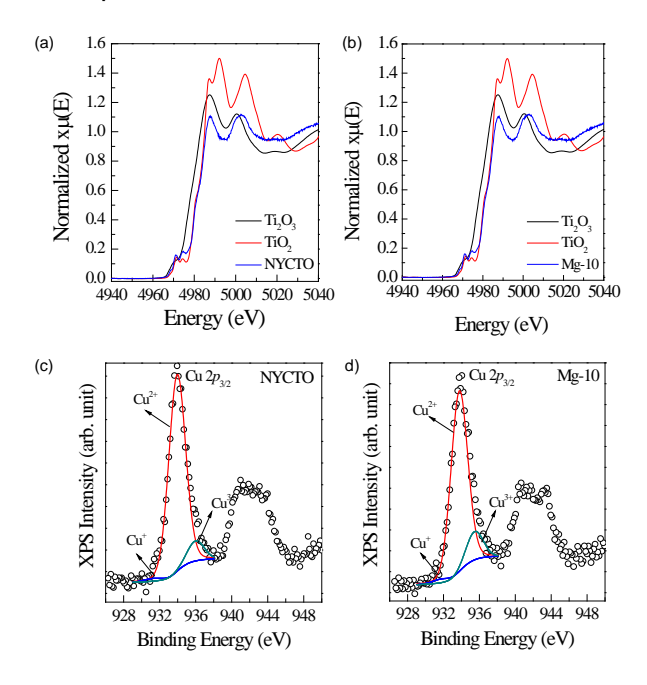


Fig. 9 Frequency dependence of Y'' at different temperatures of (a) NYCTO, (b) Mg-10, (c) Mg-20, and (d) Mg-30 ceramics; insets show their corresponding Arrhenius plots for the temperature dependence of  $\sigma_q$ .

Figs. 10(a) and (b) illustrate normalized Ti K-edge XANES spectra of the NYCTO and Mg-10 samples, respectively, as well as the standard TiO<sub>2</sub> and Ti<sub>2</sub>O<sub>3</sub> samples. The position of the edge energy of both samples was close to the TiO<sub>2</sub> standard (Ti<sup>4+</sup>). The existence of a small amount of Ti<sup>3+</sup> with a large proportion of the major Ti<sup>4+</sup>component was confirmed. The detection of a relative small amount of Ti<sup>3+</sup> was also observed in CCTO [18-20, 26] and other related compounds [5, 11]. The edge value was calculated from the maximum value of the first derivative in the edge region [26]. The ratios of Ti<sup>3+</sup>/Ti<sup>4+</sup> in the NYCTO and Mg-10 samples were determined to be 4.1% and 2.0%, respectively.



**Fig. 10** (a-b) XANES spectra for Ti *K*-edge of NYCTO and Mg-10 samples. (c-d) XPS spectra of NYCTO and Mg-10 samples.

In addition to  $Ti^{3+}$ , the presence of  $Cu^+$  and/or  $Cu^{3+}$  ions may also be a major cause of the formation of semiconducting grains in  $ACu_3Ti_4O_{12}$  ceramics [7, 19, 23]. The oxidation states of these polyvalent cations were also studied using an XPS technique. In Figs. 10(c) and d, the main peak at  $\approx 933$  eV indicated the presence of  $Cu^{2+}$  in the NYCTO structure [19, 33]. The Cu2p region was divided into three peaks using Gaussian–Lorentzian profile fitting. Small peaks at relatively higher ( $\approx 936$  eV) and lower ( $\approx 931$  eV) binding energies respectively indicated the presence of  $Cu^{3+}$  [23] and  $Cu^+$  [19]. The existence of  $Ti^{3+}$  was also detected in the XPS spectra in nearly the same amount. The ratios of  $Cu^+/Cu^{2+}$  in the NYCTO and Mg-10 samples were found to be  $\approx 1.4\%$  and  $\approx 2.1\%$ , while the ratios of  $Cu^{3+}/Cu^{2+}$  were  $\approx 9.7\%$  and  $\approx 14.9\%$ , respectively. Substitution of NYCTO with Mg<sup>2+</sup> caused an increase in both  $Cu^+$  and  $Cu^{3+}$  concentrations.

Hopping of charge carriers between  $Cu^+\leftrightarrow Cu^{2+}$ ,  $Cu^{3+}\leftrightarrow Cu^{2+}$ , and  $Ti^{3+}\leftrightarrow Ti^{4+}$  sites in the NYCTO structure may have had an effect on conductivity. From these results, the origin(s) of semiconductive grains is likely complex. Li *et al.* suggested that the presence of  $Ti^{3+}$  ions in a very low quantity would be sufficient to induce semiconducting grains in CCTO ceramics [34]. Basically, the conductivity due to hopping of charge carries should be increased by raising the  $Cu^+/Cu^{2+}$ ,  $Cu^{3+}/Cu^{2+}$ , and  $Ti^{3+}/Ti^{4+}$  ratios [35]. The increased  $R_g$  of the Mg-10 sample is only consistent with a decrease in the  $Ti^{3+}/Ti^{4+}$  ratio. Alternatively, the increase in  $Cu^+/Cu^{2+}$  and  $Cu^{3+}/Cu^{2+}$  ratios is inconsistent with an increased  $R_g$ . This

might indicate that the conduction mechanism inside the semiconducting grains of NYCTO ceramics was primarily caused by electron hopping from a  $Ti^{3+}$ –O– $Ti^{4+}$  to a  $Ti^{4+}$ –O– $Ti^{3+}$  [18, 34]. Hopping of charge carriers between complex defects,  $Cu^{4}$ –O– $Cu^{2+}$  $\leftrightarrow$ Cu<sup>2+</sup>–O–Cu<sup>3+</sup> is likely difficult due to the greatly different valance states of  $Cu^{4}$  and  $Cu^{3+}$ . The existence of  $Ti^{3+}$  and  $Cu^{4+}$  was not caused by the charge compensation, in light of the identical valence state of the host ( $Cu^{2+}$ ) and substituted ( $Mg^{2+}$ ) ions. These may have largely originated from the presence of oxygen vacancies, following  $O^{2-}$  (lattice) $\rightarrow$ 1/2 $O_{2}$ (g) + 2e $^{-}$ . Electrons enter the Ti–3d conduction band, which can be represented as  $Ti^{3+}$  in the formula,  $Na_{1/2}Y_{1/2}Cu_{3}Ti_{4-x}^{4+}Ti_{x}^{3+}O_{12-x/2}$ , giving rise to semiconductivity of the grains.

## 5.4 Conclusions

The dielectric properties of NYCTO ceramics were successfully improved by doping with  $Mg^{2+}$  ions. Substitution of  $Mg^{2+}$  can cause an increase in GB mobility, resulting in a greatly enlarged mean grain size. This was very consistent with the reduction in  $E_b$  and  $\alpha$  values.  $R_g$  of NYCTO ceramics was easily determined using admittance spectroscopy data and found to have slightly increased by  $Mg^{2+}$  doping.  $R_{gb}$  and  $E_{gb}$  values of the M–YCTO ceramic were significantly enhanced with an appropriate dopant concentration. This may be an important way to reduce  $\tan \delta$  values. XANES and XPS techniques were used to confirm the existence of  $Cu^+$ ,  $Cu^{3+}$ , and  $Ti^{3+}$  ions. The presence of  $Ti^{3+}$  ions may be the primary cause of conduction inside the grains. The  $Na_{1/2}Y_{1/2}Cu_{2.9}Mg_{0.1}Ti_4O_{12}$  ceramic exhibited low  $\tan \delta$  and enhanced  $\epsilon'$  values with good temperature stability compared to the undoped sample. The dielectric response and dielectric relaxation behavior of M–NYCTO ceramics were well described based on the IBLC model.

#### References

- [1] M.A. Subramanian, D. Li, N. Duan, B.A. Reisner, A.W. Sleight, High Dielectric Constant in ACu<sub>3</sub>Ti<sub>4</sub>O<sub>12</sub> and ACu<sub>3</sub>Ti<sub>3</sub>FeO<sub>12</sub> Phases, J. Solid State Chem. 151 (2000) 323-325.
- [2] S.-Y. Chung, I.-D. Kim, S.-J.L. Kang, Strong nonlinear current–voltage behaviour in perovskite-derivative calcium copper titanate, Nat. Mater. 3 (2004) 774-778.
- [3] T.B. Adams, D.C. Sinclair, A.R. West, Influence of Processing Conditions on the Electrical Properties of  $CaCu_3Ti_4O_{12}$  Ceramics, J. Am. Ceram. Soc. 89 (2006) 3129-3135.
- [4] M.A. Subramanian, A.W. Sleight, ACu<sub>3</sub>Ti<sub>4</sub>O<sub>12</sub> and ACu<sub>3</sub>Ru<sub>4</sub>O<sub>12</sub> perovskites: high dielectric constants and valence degeneracy, Solid State Sci. 4 (2002) 347-351.
- [5] W. Hao, J. Zhang, Y. Tan, W. Su, Giant Dielectric-Permittivity Phenomena of Compositionally and Structurally CaCu<sub>3</sub>Ti<sub>4</sub>O<sub>12</sub>-Like Oxide Ceramics, J. Am. Ceram. Soc. 92 (2009) 2937-2943.
- [6] W. Somphan, N. Sangwong, T. Yamwong, P. Thongbai, Giant dielectric and electrical properties of sodium yttrium copper titanate: Na<sub>1/2</sub>Y<sub>1/2</sub>Cu<sub>3</sub>Ti<sub>4</sub>O<sub>12</sub>, J. Mater. Sci.: Mater. Electron. 23 (2012) 1229-1234.
- [7] W. Somphan, P. Thongbai, T. Yamwong, S. Maensiri, High Schottky barrier at grain boundaries observed in Na<sub>1/2</sub>Sm<sub>1/2</sub>Cu<sub>3</sub>Ti<sub>4</sub>O<sub>12</sub> ceramics, Mater. Res. Bull. 48 (2013) 4087-4092.
- [8] L. Yang, X. Chao, Z. Yang, N. Zhao, L. Wei, Z. Yang, Dielectric constant versus voltage and non-Ohmic characteristics of Bi<sub>2/3</sub>Cu<sub>3</sub>Ti<sub>4</sub>O<sub>12</sub> ceramics prepared by different methods, Ceram. Int. 42 (2016) 2526-2533.
- [9] L. Yang, X. Chao, L. Wei, N. Zhao, Z. Yang, Dielectric responses of  $Na_{0.65}Bi_{0.45}Cu_3Ti_4O_{12}$  ceramics based on the composition design of changing the Na/Bi ratio, J. Mater. Sci.: Mater. Electron. 27 (2015) 2221-2227.

- [10] P. Kum-onsa, P. Thongbai, B. Putasaeng, T. Yamwong, S. Maensiri,  $Na_{1/3}Ca_{1/3}Bi_{1/3}Cu_3Ti_4O_{12}$ : A new giant dielectric perovskite ceramic in  $ACu_3Ti_4O_{12}$  compounds, J. Eur. Ceram. Soc. 35 (2015) 1441-1447.
- [11] P. Liang, Y. Li, Y. Zhao, L. Wei, Z. Yang, Origin of giant permittivity and high-temperature dielectric anomaly behavior in Na<sub>0.5</sub>Y<sub>0.5</sub>Cu<sub>3</sub>Ti<sub>4</sub>O<sub>12</sub> ceramics, J. Appl. Phys. 113 (2013) 224102.
- [12] P. Liang, Z. Yang, X. Chao, Z. Liu, Giant Dielectric Constant and Good Temperature Stability in Y<sub>2/3</sub>Cu<sub>3</sub>Ti<sub>4</sub>O<sub>12</sub> Ceramics, J. Am. Ceram. Soc. 95 (2012) 2218-2225.
- [13] J. Liu, C.-G. Duan, W.-G. Yin, W. Mei, R. Smith, J. Hardy, Large dielectric constant and Maxwell-Wagner relaxation in Bi<sub>2/3</sub>Cu<sub>3</sub>Ti<sub>4</sub>O<sub>12</sub>, Phys. Rev. B 70 (2004) 144106.
- [14] Z. Liu, G. Jiao, X. Chao, Z. Yang, Preparation, microstructure, and improved dielectric and nonlinear electrical properties of  $Na_{1/2}La_{1/2}Cu_3Ti_4O_{12}$  ceramics by sol–gel method, Mater. Res. Bull. 48 (2013) 4877-4883.
- [15] P. Liang, Y. Li, F. Li, X. Chao, Z. Yang, Effect of the synthesis route on the phase formation behavior and electric property of Na<sub>0.5</sub>Bi<sub>0.5</sub>Cu<sub>3</sub>Ti<sub>4</sub>O<sub>12</sub> ceramics, Mater. Res. Bull. 52 (2014) 42-49.
- [16] N. Zhao, P. Liang, L. Wei, L. Yang, Z. Yang, Synthesis and dielectric anomalies of CdCu<sub>3</sub>Ti<sub>4</sub>O<sub>12</sub> ceramics, Ceram. Int. 41 (2015) 8501-8510.
- [17] A.A. Felix, M.O. Orlandi, J.A. Varela, Schottky-type grain boundaries in CCTO ceramics, Solid State Commun. 151 (2011) 1377-1381.
- [18] L. Zhang, Z.-J. Tang, Polaron relaxation and variable-range-hopping conductivity in the giant-dielectric-constant material CaCu<sub>3</sub>Ti<sub>4</sub>O<sub>12</sub>, Phys. Rev. B 70 (2004).
- [19] L. Ni, X.M. Chen, Enhanced giant dielectric response in Mg-substituted CaCu<sub>3</sub>Ti<sub>4</sub>O<sub>12</sub> ceramics, Solid State Commun. 149 (2009) 379-383.
- [20] P. Thongbai, J. Jumpatam, B. Putasaeng, T. Yamwong, S. Maensiri, The origin of giant dielectric relaxation and electrical responses of grains and grain boundaries of W-doped  $CaCu_3Ti_4O_{12}$  ceramics, J. Appl. Phys. 112 (2012) 114115.
- [21] R. Schmidt, S. Pandey, P. Fiorenza, D.C. Sinclair, Non-stoichiometry in "CaCu<sub>3</sub>Ti<sub>4</sub>O<sub>12</sub>" (CCTO) ceramics, RSC Advances 3 (2013) 14580-14589.
- [22] R. Schmidt, M.C. Stennett, N.C. Hyatt, J. Pokorny, J. Prado-Gonjal, M. Li, D.C. Sinclair, Effects of sintering temperature on the internal barrier layer capacitor (IBLC) structure in  $CaCu_3Ti_4O_{12}$  (CCTO) ceramics, J. Eur. Ceram. Soc. 32 (2012) 3313-3323.
- [23] M. Li, G. Cai, D.F. Zhang, W.Y. Wang, W.J. Wang, X.L. Chen, Enhanced dielectric responses in Mg-doped CaCu<sub>3</sub>Ti<sub>4</sub>O<sub>12</sub>, J. Appl. Phys. 104 (2008) 074107.
- [24] M. Li, X.L. Chen, D.F. Zhang, W.Y. Wang, W.J. Wang, Humidity sensitive properties of pure and Mg-doped CaCu<sub>3</sub>Ti<sub>4</sub>O<sub>12</sub>, Sensors and Actuators B: Chemical 147 (2010) 447-452.
- [25] L. Sun, R. Zhang, Z. Wang, E. Cao, Y. Zhang, L. Ju, Microstructure and enhanced dielectric response in Mg doped CaCu<sub>3</sub>Ti<sub>4</sub>O<sub>12</sub> ceramics, J. Alloys Compd. 663 (2016) 345-350.
- [26] J. Boonlakhorn, P. Kidkhunthod, P. Thongbai, A novel approach to achieve high dielectric permittivity and low loss tangent in  $CaCu_3Ti_4O_{12}$  ceramics by co-doping with  $Sm^{3+}$  and  $Mg^{2+}$  ions, J. Eur. Ceram. Soc. 35 (2015) 3521-3528.
- [27] B. Ravel, M. Newville, ATHENA, ARTEMIS, HEPHAESTUS: data analysis for X-ray absorption spectroscopy using IFEFFIT, Journal of Synchrotron Radiation 12 (2005) 537-541.
- [28] S. Kwon, D.P. Cann, Relationship among the phase equilibria, microstructures, and dielectric properties of CaCu<sub>3</sub>Ti<sub>4</sub>O<sub>12</sub> ceramics via different sintering time, J. Mater. Sci. 44 (2009) 4117-4123.
- [29] R. Xue, G. Zhao, J. Chen, Z. Chen, D. Liu, Effect of doping ions on the structural defect and the electrical behavior of CaCu<sub>3</sub>Ti<sub>4</sub>O<sub>12</sub> ceramics, Mater. Res. Bull. 76 (2016) 124-132.
- [30] S.I.R. Costa, M. Li, J.R. Frade, D.C. Sinclair, Modulus spectroscopy of  $CaCu_3Ti_4O_{12}$  ceramics: clues to the internal barrier layer capacitance mechanism, RSC Advances 3 (2013) 7030-7036.
- [31] L. Singh, I.W. Kim, B.C. Sin, K.D. Mandal, U.S. Rai, A. Ullah, H. Chung, Y. Lee, Dielectric studies of a nano-crystalline  $CaCu_{2.90}Zn_{0.10}Ti_4O_{12}electro-ceramic by one pot glycine assisted synthesis from inexpensive <math>TiO_2$  for energy storage capacitors, RSC Adv. 4 (2014) 52770-52784.

- [32] W. Tuichai, S. Danwittayakul, T. Yamwong, P. Thongbai, Synthesis, dielectric properties, and influences oxygen vacancies have on electrical properties of  $Na_{1/2}Bi_{1/2}Cu_3Ti_4O_{12}$  ceramics prepared by a urea combustion method, J. Sol-Gel Sci. Technol. 76 (2015) 630-636.
- [33] R. Yu, H. Xue, Z. Cao, L. Chen, Z. Xiong, Effect of oxygen sintering atmosphere on the electrical behavior of CCTO ceramics, J. Eur. Ceram. Soc. 32 (2012) 1245-1249.
- [34] J. Li, M.A. Subramanian, H.D. Rosenfeld, C.Y. Jones, B.H. Toby, A.W. Sleight, Clues to the Giant Dielectric Constant of CaCu<sub>3</sub>Ti<sub>4</sub>O<sub>12</sub> in the Defect Structure of "SrCu<sub>3</sub>Ti<sub>4</sub>O<sub>12</sub>", Chem. Mater. 16 (2004) 5223-5225.
- [35] A.J. Moulson, J.M. Herbert, Electroceramics : materials, properties, applications, 2nd ed., Wiley, West Sussex; New York, 2003.

## **CHAPTER 6**

## Non-Ohmic Properties and Electrical Responses Of Grain and Grain Boundaries of Na<sub>1/2</sub>Y<sub>1/2</sub>Cu<sub>3</sub>Ti<sub>4</sub>O<sub>12</sub> Ceramics

### 6.1 Introduction

CaCu<sub>3</sub>Ti<sub>4</sub>O<sub>12</sub> (CCTO) has attracted considerable attention for both academic and technological reasons because it can exhibit unusually high values of dielectric permittivity  $(\varepsilon' \approx 10^3 - 10^5)$  with no detectable phase transition.<sup>1, 2</sup> It was reported that CCTO polycrystalline ceramic is an electrically heterogeneous structure consisting of *n*-type semiconducting grains enclosed by insulating grain boundary layer,3-5 which has an internal barrier layer capacitor (IBLC) structure. This special microstructure can easily be fabricated using a one-step sintering process. It requires no complex multistage process as most commercial IBLC's based on (Ba,Sr)TiO<sub>3</sub> ceramics.<sup>5</sup> From an applications point of view, one of the most serious impediments remaining in the use of CCTO ceramics is their high dielectric loss tangent ( $tan\delta$ ) values, especially in the low frequency range. Another point is the temperature stability of  $\varepsilon'$ . Besides, the colossal permittivity, a nonlinear current-voltage (current density-electric field strength, J-E) characteristic has been widely reported in CCTO.4, 6, 7 The origin of this non-Ohmic behavior was attributed to the existence of Schottky barriers at the grain boundaries.4 From purely academic point of view, the possible origin of giant dielectric response in CCTO ceramics has intensively been investigated. However, the exact origin of giant  $\varepsilon'$  is still unclear. Both extrinsic (e.g., IBLC model) and intrinsic (e.g., mixed valent structure and point defects) effects have been reasonably proposed. 3, 5, 8-10

CCTO is classified as a member of the ACu $_3$ Ti $_4$ O $_{12}$  family of ceramics, where A can be Ca,  $^{1\cdot3,\,5,\,7}$  Cd,  $^{1,\,11}$  Bi $_{2/3}$ ,  $^{1,\,8,\,12,\,13}$  La $_{2/3}$ ,  $^{12}$  Y $_{2/3}$ ,  $^{14\cdot16}$  Na $_{1/2}$ Bi $_{1/2}$ ,  $^{17,\,18}$  Na $_{1/2}$ La $_{1/2}$ ,  $^{19,\,20}$  Na $_{1/2}$ Y $_{1/2}$ ,  $^{21,\,22}$  Na $_{1/2}$ Sm $_{1/2}$ ,  $^{23}$  or Na $_{1/3}$ Ca $_{1/3}$ Bi $_{1/3}$ .  $^{24}$  In addition to CCTO ceramics, the colossal dielectric response and electrical properties of related–CCTO oxides in the ACu $_3$ Ti $_4$ O $_{12}$  family have been widely investigated. It was reported that some related oxides exhibited interesting dielectric properties. Na $_{1/2}$ Bi $_{1/2}$ Cu $_3$ Ti $_4$ O $_{12}$  and La–doped Na $_{1/2}$ Bi $_{1/2}$ Cu $_3$ Ti $_4$ O $_{12}$  ceramics exhibited high  $\epsilon'$  values,  $\approx 13,495$  and 10,200 at 10 kHz, respectively, while their tanō values were about 0.031 and 0.022 at 10 kHz, respectively.  $^{25,\,26}$  A high  $\epsilon'$  of 6,100–8,700 with tanō values of 0.073–0.114 at 1 kHz were achieved in Na $_{1/2}$ La $_{1/2}$ Cu $_3$ Ti $_4$ O $_{12}$  ceramics.  $^{19}$  The lowest tanō value of 0.032 was observed at 10 kHz. High  $\epsilon'$  and low tanō with good thermal stability of  $\epsilon'$  at 10 kHz were also reported for Y $_{2/3}$ Cu $_3$ Ti $_4$ O $_{12}$ , Na–doped Y $_{2/3}$ Cu $_3$ Ti $_4$ O $_{12}$ , and La–doped Y $_{2/3}$ Cu $_3$ Ti $_4$ O $_{12}$  ceramics.  $^{16,\,27,\,28}$ 

Actually,  $\tan\delta$  values of these  $ACu_3Ti_4O_{12}$  ceramics measured at frequencies lower than 10 kHz were quite large. Nevertheless, these  $\tan\delta$  values were still lower than those of CCTO ceramics. Better dielectric properties are expected by optimizing sintering conditions. Although there have been several reports on the dielectric properties of related  $ACu_3Ti_4O_{12}$  ceramic compounds, their nonlinear J–E properties were rarely reported. <sup>13, 19, 23, 29</sup> Therefore, it is valuable to optimize the dielectric properties and to study other related properties such as the non–Ohmic characteristics of similar  $ACu_3Ti_4O_{12}$  ceramics to improve their overall electrical behavior.

In this work, we systematically investigated the dielectric and nonlinear electrical properties of  $Na_{1/2}Y_{1/2}Cu_3Ti_4O_{12}$  ceramics. It was found that a high  $\epsilon'\approx 2.3\times 10^4$  at 1 kHz with good temperature stability was obtained. Interestingly, very low  $tan\delta\approx 0.03$  at a

relatively low frequency of  $10^3$  Hz was successfully achieved. Good nonlinear J–E properties were accomplished. The electrical properties of the grain and grain boundary were characterized using impedance and admittance spectroscopy analyses, respectively. The colossal dielectric properties were primarily described by interfacial polarization at the grain boundaries, while the intrinsic effect was also important as well and cannot be ignored.

### 6.2 Experimental details

In this work,  $Na_{1/2}Y_{1/2}Cu_3Ti_4O_{12}$  (NYCTO) ceramics were prepared using a conventional mixed oxide method. First, a stoichiometric mixture of  $Y_2O_3$  (99.99%),  $Na_2CO_3$  (99.9%), CuO (99.9%), and  $TiO_2$  (99.9%) was wet ball-milled in ethanol for 24 h using  $ZrO_2$  balls with diameter of  $\approx 2$  mm. Second, the mixed slurry was dried and carefully ground. Third, the dried mixed powder was calcined in air at  $1000^{\circ}$  C for 20 h. Then, the resulting calcined powder was ground to obtain a fine powder. The fine powder was pressed into pellets of 9.5 mm in diameter and  $\approx 1.2$  mm in thickness by a uniaxial compression at  $\approx 200$  MPa. Finally, these pellets were sintered in air at  $1100^{\circ}$ C for 1, 5, 10, and 20 h (referred as the NYCTO-1h, NYCTO-5h, NYCTO-10h and NYCTO-20h samples, respectively). The densities of the sintered ceramics were measured using Archimedes' method.

The phase composition and crystal structure of the sintered ceramics were characterized using an X-ray diffraction (XRD) technique (PANalytical, EMPYREAN). Scanning electron microscopy (SEM) (SEC, SNE4500M) was used to reveal the surface morphologies of the sintered ceramics. The elemental distribution in the NYCTO ceramic was examined using field-emission scanning electron microscopy (FE–SEM) with energy-dispersive X-ray analysis (EDX) (HITACHI SU8030, Japan). X-ray Absorption Near Edge Structure (XANES) spectra were collected at the SUT–NANOTEC–SLRI XAS beamline (BL5.2) (electron energy of 1.2 GeV; bending magnet; beam current 80 – 150 mA; 1.1 to  $1.7 \times 10^{11}$  photon s<sup>-1</sup>) at the Synchrotron Light Research Institute (SLRI), Nakhon Ratchasima, Thailand. Details of this characterization technique and analysis are given elsewhere.<sup>30</sup> Finally, the normalized XANES data were processed and analyzed after background subtraction in the pre–edge and post–edge region using ATHENA software included in an IFEFFIT package.<sup>31</sup>

Au was sputtered onto each surface of the sintered sample at a current of 25 mA for 8 min using a Polaron SC500 sputter coating unit. The dielectric properties were measured with а **KEYSIGHT** E4990A **Impedance** Analyzer using capacitance-dissipation factor (C<sub>p</sub>-D) mode at an oscillation voltage of 500 mV. The measurement was carried out over the frequency and temperature ranges of  $10^2 - 10^7$  Hz and -70-200 °C, respectively. Temperature was kept constant with accuracy variation of less than ±0.1 °C. Nonlinear current density-electric field strength (*J-E*) characteristics were measured using a high voltage measurement unit (Keithley Model 247) at room temperature. The breakdown electric field ( $E_b$ ) was achieved at J = 1 mA.cm<sup>-2</sup>. The nonlinear coefficient ( $\alpha$ ) was calculated using the following formula:

$$\alpha = \frac{\log(J_2/J_1)}{\log(E_2/E_1)} \,, \tag{1}$$

where  $E_1$  and  $E_2$  are the applied electric fields, at which  $J_1 = 1$  and  $J_2 = 10$  mA.cm<sup>-2</sup>, respectively. The complex impedance ( $Z^*$ ) and complex admittance ( $Y^*$ ) were calculated from the complex dielectric permittivity ( $\varepsilon^*$ ) using the following relationship:

$$\varepsilon^* = \varepsilon' - i\varepsilon'' = \frac{1}{i\omega C_0 Z^*} = \frac{1}{i\omega C_0 (Z' - iZ'')} , \qquad (2)$$

$$Y^* = Y' + iY'' = \frac{1}{Z^*} \tag{3}$$

where  $\varepsilon'$  and  $\varepsilon''$  are the real (dielectric constant) and imaginary (dielectric loss factor) components of  $\varepsilon^*$ , respectively. Y' and Y'' are the real part and imaginary parts of  $Y^*$ , respectively. Z' and Z'' are the real part and imaginary parts of  $Z^*$ , respectively.  $\varepsilon'$  was calculated from  $\varepsilon' = C_p d/\varepsilon_0 A$ , where  $C_p$  is the measured capacitance, A is the electrode area, d is the sample thickness, and  $\varepsilon_0$  is the permittivity of free space ( $\varepsilon_0 = 8.854 \times 10^{-12}$  F/m).  $\omega$  is the angular frequency of an applied AC electric field ( $\omega = 2\pi f$ ).  $C_0 = \varepsilon_0 A/d$  is the empty cell capacitance.

#### 6.3 Results and discussion

Fig. 1 shows the XRD patterns of NYCTO ceramics sintered at 1100  $^{\circ}$ C for 1–20 h. All of the XRD patterns indicated a single phase. No impurity phase was observed. These XRD patterns confirmed the formation of a CaCu<sub>3</sub>Ti<sub>4</sub>O<sub>12</sub>–like structure (JCPDS 75–2188), which was well indexed based on *bcc* structure within space group *Im*3. Lattice parameters were calculated and found to be 7.384, 7.383, 7.384 and 7.381 Å for the NYCTO–1h, NYCTO–5h, NYCTO–10h and NYCTO–20h samples, respectively. These values are quite comparable to those reported in literature, 7.378–7.385 Å.<sup>1, 22</sup> It is worth noting that impurity phases of TiO<sub>2</sub> and Y<sub>2</sub>O<sub>3</sub> were detected when the sintering temperature was decreased to 1085  $^{\circ}$ C for 5 h.

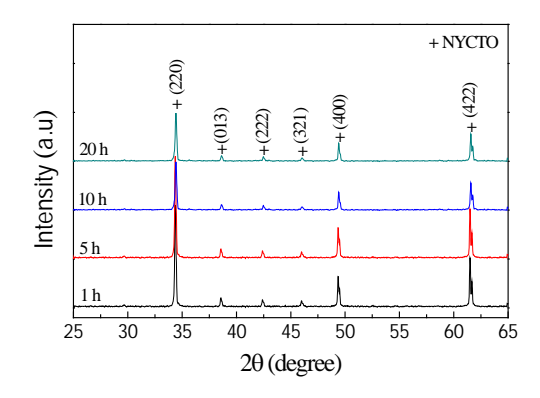
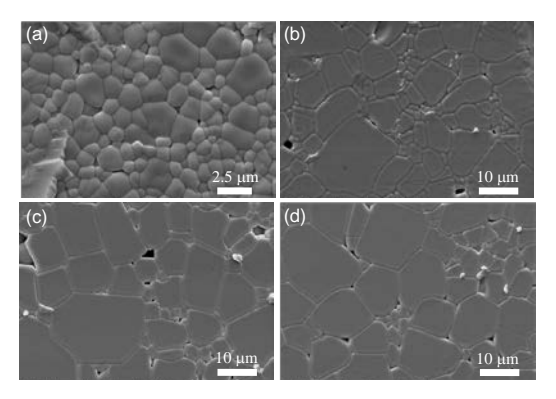


Fig. 1 XRD patterns of  $Na_{1/2}Y_{1/2}Cu_3Ti_4O_{12}$  ceramics sintered at 1100 °C for 1–20 h.

The microstructures of all polished–samples are revealed in Fig. 2. The grain size of NYCTO ceramics greatly increased as the sintering time was increased from 1 to 5 h. With a further increase in sintering time from 5 to 20 h, grain sizes of the NYCTO–5h, NYCTO–10h and NYCTO–20h changed slightly. The mean grain sizes of the NYCTO–1h, NYCTO–5h, NYCTO–10h and NYCTO–20h samples were about 1.66±0.59, 9.46±3.94

(2.74±0.8 μm for fine grains), 10.32±4.53, and 10.39±4.46 μm, respectively. The mean grain sizes of the course–grained ceramics sintered for 5–20 h are much larger than that of the fine–grained ceramic sintered for 1 h, which may be caused by the effect of liquid phase sintering mechanism. This is reasonable because the eutectic temperature between CuO and TiO<sub>2</sub> was 919 °C. $^{32-34}$  The apparent densities of the NYCTO–1h, NYCTO–5h, NYCTO–10h and NYCTO–20h samples were, respectively, 4.99, 4.97, 4.89 and 4.85 g/cm³, corresponding to the relative densities ≈96.05, 95.70, 94.16 and 93.26%, respectively (theoretical density of NYCTO was calculated to be 5.196 g/cm³). Furthermore, a small number of pores were observed. The volume fractions of porosity are ≈0.040, 0.043, 0.058 and 0.067, respectively. This resulted from a coarsening effect, which usually becomes dominant as the grain size increases with increasing sintering times. $^{35}$ 



**Fig. 2** SEM images of polished surfaces for (a) NYCTO-1h, (b) NYCTO-5h, (c) NYCTO-10h, and (d) NYCTO-20h ceramics.

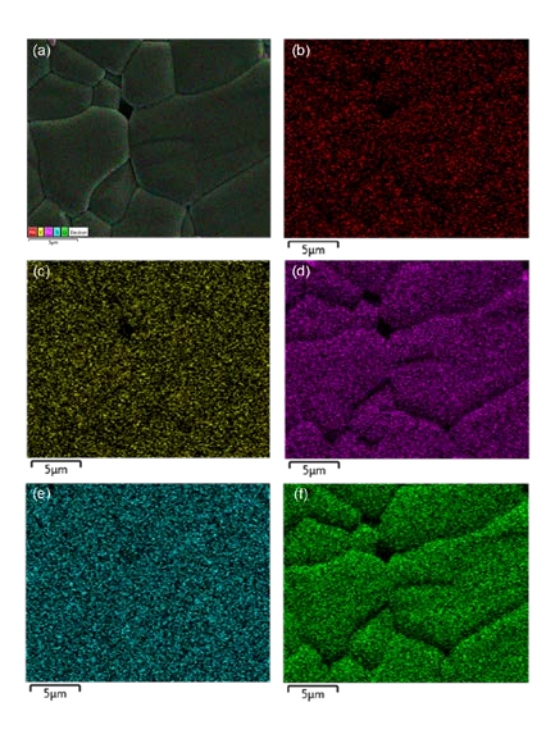


**Fig. 3** Element mapping of the Na<sub>1/2</sub>Y<sub>1/2</sub>Cu<sub>3</sub>Ti<sub>4</sub>O<sub>12</sub> ceramics sintered at 1100 °C for 10 h; (a) all elements, (b) Na, (c) Y, (d) Cu, (e) Ti, and (f) O.

To further analyze the distributions of the elements in NYCTO ceramics, mapping of all elements, *i.e.*, Na, Y, Cu, Ti and O was carried out. As shown in Fig. 3, all of the elements were homogeneously dispersed in both of the grain and grain boundary of the NYCTO–10h sample. The percentages of Na, Y, Cu and Ti measured in the selected area in Fig. 3(a) are of  $\approx$ 1.0, 8.0, 31.2 and 29.9 wt.%, respectively. Considering the starting raw materials used, mixed phases of  $Y_{2/3}Cu_3Ti_4O_{12}$  and  $(Na,Y)Cu_3Ti_4O_{12}$  may have possibly formed. However, it was found that both Na and Y coexisted in every grain. No single grain that contained only Na or only Y. This strongly indicated that only a single NYCTO phase had been formed.

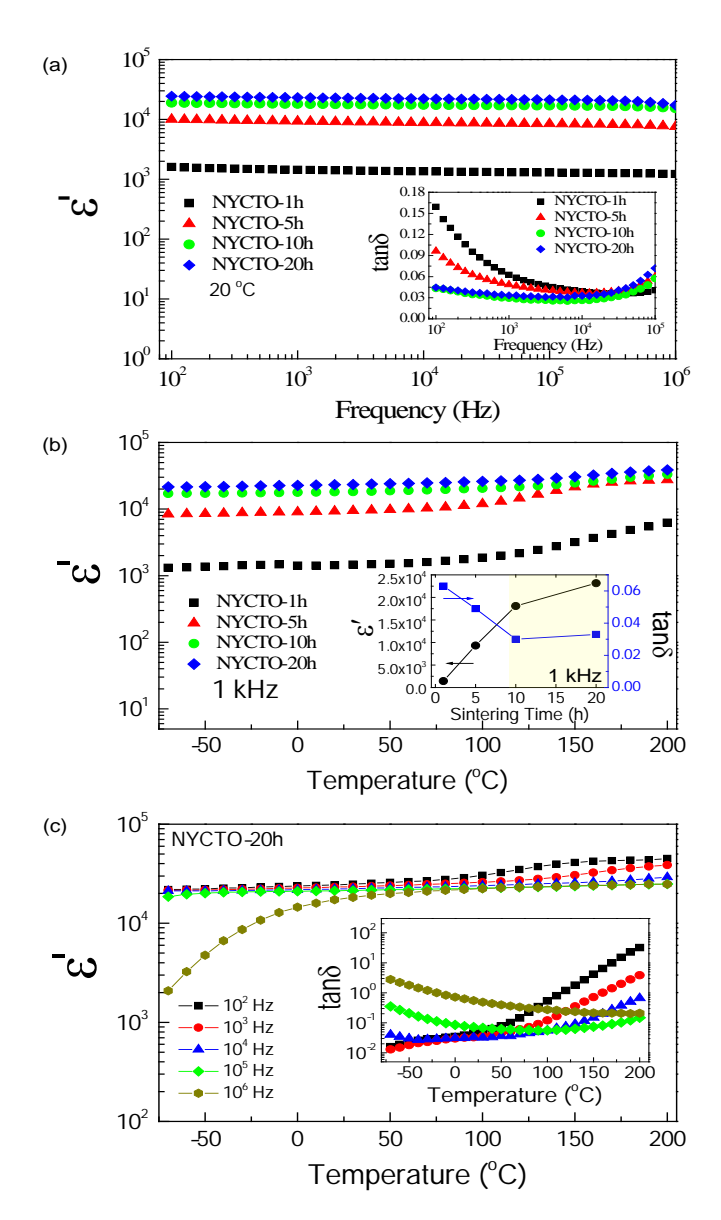


Fig. 4 (a) Dielectric permittivity (ε') at 20 °C as a function of frequency for Na<sub>1/2</sub>Y<sub>1/2</sub>Cu<sub>3</sub>Ti<sub>4</sub>O<sub>12</sub> ceramics sintered at different times; inset shows the frequency dependence of tanδ. (b) Temperature dependence of dielectric permittivity (ε') at 1 kHz for Na<sub>1/2</sub>Y<sub>1/2</sub>Cu<sub>3</sub>Ti<sub>4</sub>O<sub>12</sub> ceramics sintered at different times; inset shows ε' and tanδ for Na<sub>1/2</sub>Y<sub>1/2</sub>Cu<sub>3</sub>Ti<sub>4</sub>O<sub>12</sub> ceramics sintered at different times. (c) Temperature dependence of ε' at various frequencies for NYCTO–20h sample; inset shows tanδ as a function of temperature at different frequencies

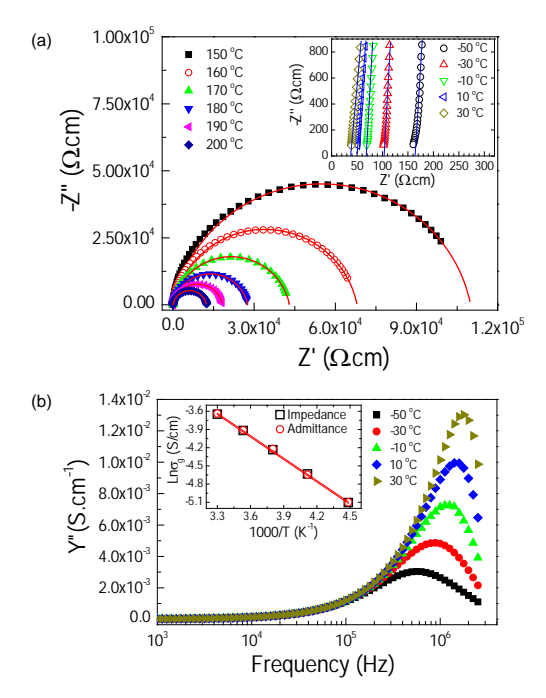


Fig. 5 (a) Impedance complex plane plot (Z\*) at different temperatures (150 to 200  $^{\circ}$ C) for NYCTO–20h sample; the red solid curves are the fitted data using Eq. (4). Inset shows an expanded view of the high–frequency data close to the origin in the temperature range from -50 to 30  $^{\circ}$ C; the blue solid lines are the eye guidelines for estimating  $R_g$ . (b) Frequency dependence of Y'' at different temperatures for NYCTO–20h sample; inset shows Arrhenius plots for the temperature dependence of  $\sigma_g$  values obtained from impedance and admittance spectroscopy analyses.

Fig. 4(a) shows the frequency dependence of  $\epsilon'$  at 20 °C for the NYCTO ceramics sintered at 1100 °C for different sintering times. The  $\epsilon'$  values of these ceramics were in the range of 1400–23000. The  $\epsilon'$  value over the frequency range of  $10^2$ – $10^6$  Hz of NYCTO ceramics was independent of frequency and increased with increasing sintering time. This result is similar to that reported in literature for CCTO ceramics, where  $\epsilon'$  usually increased with increasing sintering time  $^{36}$ . However, the increase in  $\epsilon'$  for these samples was discrete. First, the  $\epsilon'$  value significantly increased as sintering time was increased from 1 to 5 h, corresponding to a large change in their mean grain sizes [Fig. 2(a) and (b)]. Second, the  $\epsilon'$  value slightly increased from 5 to 20 h. This result was quite consistent with microstructural changes [Fig. 2(b)–(d)]. In the inset of Fig. 4(a), the low–frequency tan $\delta$  value greatly decreased with increasing sintering time from 1 to 10 h. The tan $\delta$  values of the NYCTO–10h and NYCTO–20h samples were nearly the same magnitude and were found to be lower than 0.05 over the frequency range of 100 Hz–80 kHz.

The temperature dependence of  $\epsilon'$  was also investigated, as depicted in Fig. 4(b). At temperatures above 100 °C,  $\epsilon'$  of the NYCTO-1h and NYCTO-5h samples greatly increased, whereas  $\epsilon'$  of the NYCTO-10h and NYCTO-20h samples changed little. Notably, by optimizing the sintering conditions, excellent dielectric properties of NYCTO ceramics were successfully achieved, *i.e.*, very low  $\tan\delta$  and  $\hbar$  high  $\epsilon'$  with good temperature stability.  $\tan\delta$  values (at 1 kHz and 20 °C) of the NYCTO-1h, NYCTO-5h, NYCTO-10h and NYCTO-20h samples were 0.111, 0.096, 0.030 and 0.033, respectively,

while  $\varepsilon'$  values were, respectively, 1437, 9321, 18086 and 23152. At 10<sup>2</sup> Hz, the optimized tan \delta values of NYCTO ceramics were much lower than that of CCTO ceramics. 1, 2, 6, 30 The overview effects of sintering time on the dielectric properties are clearly shown in the inset of Fig. 4(b). These good dielectric properties are in the rectangle yellow zone and can be comparable to those observed in Y<sub>2/3</sub>Cu<sub>3</sub>Ti<sub>4</sub>O<sub>12</sub> based ceramics.<sup>14-16, 27, 28</sup> Fig. 4(c) and its inset demonstrate the temperature dependences of  $\epsilon'$  and  $tan\delta$  at different frequencies (10<sup>2</sup>-10<sup>6</sup> Hz) for the NYCTO-20h sample. High-temperature dielectric dispersion is observed in the frequency range of  $10^2-10^4$  Hz, corresponding to the large increase in tanδ in a high-temperature range (>100 °C). This may be due to the effect of DC conduction in the bulk ceramic and related interfacial polarization in heterogeneous microstructure. At 10<sup>6</sup> Hz, a dramatic decrease in ε' can be observed in the temperature range from 0 to -70 °C, indicating to the dielectric relaxation behavior in NYCTO ceramics, as observed in CCTO ceramics.<sup>37</sup> The electric dipoles that give rise to giant  $\varepsilon'$  values freeze through the relaxation process in a low temperature range. Thus, there exists decay in polarization with respect to the AC applied electric field especially in a high–frequency range, which is evidenced by the drastic decrease in  $\varepsilon'(T, f)$ .

It is widely accepted that the dielectric and electrical properties of CCTO and ACu<sub>3</sub>Ti<sub>4</sub>O<sub>12</sub> ceramics strongly correlated with the electrically heterogeneous microstructure.3-5, 30 Thus, impedance spectroscopy was used to characterize the electrical responses of grains and grain boundaries. For ACu<sub>3</sub>Ti<sub>4</sub>O<sub>12</sub> ceramics, the grain boundary resistance  $(R_{gb})$  and grain resistance  $(R_g)$  can normally be evaluated from the diameter of large semicircular arc in a low frequency range and from a nonzero intercept on the Z' axis at high frequencies, respectively.3,5 As illustrated in Fig. 5(a) and its inset, the diameter of semicircle arcs and a nonzero intercept of the NYCTO-20h sample decreased with increasing temperature, indicating a reduction in  $R_{\rm gb}$  and  $R_{\rm g}$ , respectively. At any temperature,  $R_{ab}$  is much larger than  $R_{g}$  by more than 4 orders of magnitude. This clearly indicates that NYCTO ceramics are electrically heterogeneous, consisting of an insulating part of the grain boundary layers separating the semiconducting grains. Thus, the colossal permittivity of NYCTO ceramics is likely caused by an internal barrier layer capacitor (IBLC) effect. Under an applied AC electric field, an electric force (F<sub>e</sub>) acting on mobile charges inside the grains can cause accumulation of these charges at the insulating grain boundaries. This produces a strong interfacial polarization (or Maxwell–Wagner polarization), giving rise to elevated  $\varepsilon'$  values.

To obtain accurate  $R_{\rm gb}$  values at various temperatures, complex impedance (Z\*) data were fitted to a simple equivalent circuit consisting of parallel  $R_{\rm gb}C_{\rm gb}$  elements connected to  $R_{\rm g}$  in series using a modified equation for a Z\* plot,<sup>8</sup>

$$Z^* = R_g + \frac{R_{gb}}{1 + \left(i\omega R_{ab}C_{ab}\right)^{\alpha}},\tag{4}$$

where  $\alpha$  is a constant (0 < $\alpha$  ≤ 1). The capacitance of the grain ( $C_g$ ) is not accessible and the respective capacitor can simply be omitted from the circuit. The experimental data (Z\* plots) over the temperature range of 150–200 °C were well fitted by Eq. (4). The fitted results also predicted  $R_{gb}$  and  $C_{gb}$  at different temperatures.  $C_{gb}$  values of the NYCTO–1h, NYCTO–5h, NYCTO–10h and NYCTO–20h samples were slightly dependent on temperature and were found to be ~0.2, ~1.2, ~2.60, and ~3.0 nF, respectively. This was closely related to the increase in  $\epsilon$ ' of NYCTO ceramics. At the same time, the influence of the grain size on the high dielectric response in NYCTO ceramics cannot be

ignored. As shown in Fig. 6, the temperature dependence of grain boundary conductivity,  $\sigma_{gb} = 1/R_{gb}$ , follows the Arrhenius law,

$$\sigma_{gb} = \sigma_0 e^{\left(\frac{-E_{gb}}{k_B T}\right)},\tag{5}$$

where  $E_{gb}$  is the activation energy required for conduction to occur at the grain boundaries.  $E_{gb}$  values of the NYCTO-1h, NYCTO-5h, NYCTO-10h and NYCTO-20h samples were 0.654, 0.692, 0.762 and 0.746 eV, respectively. These  $E_{gb}$  values of 0.762 and 0.746 eV are higher than those values reported for CCTO ceramics ( $E_{gb} \approx 0.6$  eV).<sup>5</sup>

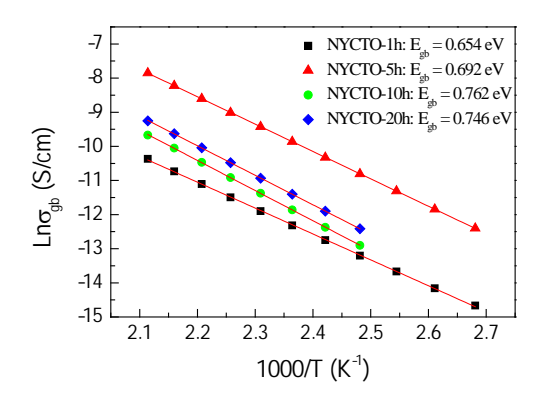


**Fig. 6** Arrhenius plots of the temperature dependence of grain boundary conductivity  $(\sigma_{gb})$  for NYCTO–20h sample; the red solid lines are the fitted data using Eq. (5).

As illustrated in the inset of Fig. 5(a),  $R_{\rm g}$  values at various temperatures can be roughly estimated from the nonzero intercept using linear eye guidelines.  $R_{\rm g}$  values of the NYCTO–20h sample at -50, -30, -10, 10 and 30 °C were estimated to be  $\approx$ 164,  $\approx$ 104,  $\approx$ 68,  $\approx$ 50 and  $\approx$ 38  $\Omega$ .cm, respectively. According to the equivalent circuit of the IBLC model, when  $R_{\rm g} << R_{\rm gb}$  and  $C_{\rm g} << C_{\rm gb}$ ,  $Y^*$  for this equivalent circuit can be simply expressed as:<sup>37</sup>

$$Y^* = \frac{(R_{gb}^{-1})(1 - \omega^2 \tau_g \tau_{gb} + i\omega \tau_{gb})}{1 + i\omega \tau},$$
(6)

where  $Y_g^* = (1+i\omega R_g C_g)/R_g$  and  $Y_{gb}^* = (1+i\omega R_{gb}C_{gb})/R_{gb}$ .  $\tau_g = R_g C_g$ ,  $\tau_{gb} = R_{gb}C_{gb}$ , and  $\tau = R_g C_{gb}$ . From Eq. (6), by setting  $dY''/d\omega = 0$ , it can be shown that  $R_g = 1/2Y_{\rm max}''$ , where  $Y_{\rm max}''$  is the maximum value at the Y''-peak. Using this relationship,  $R_g$  of the NYCTO and other ACu<sub>3</sub>Ti<sub>4</sub>O<sub>12</sub> ceramics can be easily calculated.  $R_g$  values at -50, -30, -10, 10, and 30 °C of the NYCTO-20h sample were calculated and found to be 164.62, 102.77, 68.98, 50.21 and 38.39  $\Omega$ .cm, respectively. These values are very close to those values obtained from Z\* plots using linear eye guidelines to estimate nonzero intercept value. It is interesting to show that the  $R_g$  values of IBLC's materials can be easily calculated by using an admittance spectroscopy analysis.

As shown in the inset of Fig. 5(b),  $R_{\rm g}$  values at various temperatures obtained from impedance and admittance spectroscopy analyses are nearly the same in value. The temperature dependence of the grain conductivity,  $\sigma_{\rm g}=1/R_{\rm g}$ , for the NYCTO–20h sample follows the Arrhenius law:

$$\sigma_{g} = \sigma_{0} e^{\left(\frac{-E_{g}}{k_{B}T}\right)},\tag{7}$$

where  $E_g$  is the activation energy required for conduction in grain interiors. Good linear fits were achieved in both of the data sets obtained from these two analyses [inset of Fig. 5(b)]. The  $E_g$  values of the NYCTO–20h sample were 0.107 and 0.108 eV for the data obtained from nonzero intercept and the relationship,  $R_g = 1/2Y_{\rm max}''$ , respectively. It is worth noting that the great difference in  $E_g$  and  $E_{\rm gb}$  values indicates the conductive nature of the grain compared to the grain boundary.

The valence states of Ti ions were investigated to understand the semiconductive nature of the grains in NYCTO ceramics. Fig. 7 shows normalized Ti *K*–edge XANES spectra of the NYCTO–10 sample as well as the standard TiO<sub>2</sub> and Ti<sub>2</sub>O<sub>3</sub> samples. It was found that the position of the edge energy for all samples was between the Ti<sub>2</sub>O<sub>3</sub> (Ti<sup>3+</sup>) and TiO<sub>2</sub> (Ti<sup>4+</sup>) standard samples, indicating the existence of Ti<sup>3+</sup> and Ti<sup>4+</sup> in NYCTO ceramics (Ti<sup>3+</sup>/Ti<sup>4+</sup>). There was a tendency of all absorption edge energy to be closer to the TiO<sub>2</sub> (Ti<sup>4+</sup>) standard than Ti<sub>2</sub>O<sub>3</sub> (Ti<sup>3+</sup>) standard. A relatively small amount of Ti<sup>3+</sup> was confirmed in NYCTO ceramics, just as observed in CCTO ceramics.<sup>38</sup> The edge value was calculated from the maximum value of the first derivative of the edge region. Thus, the percentage of Ti<sup>3+</sup>/Ti<sup>4+</sup> in the NYCTO–10 sample can be calculated,<sup>30</sup> and was found to be 21.6%. Therefore, the *n*–type semiconducting grains of NYCTO ceramics may be caused by electrons hopping from one Ti<sup>3+</sup>–O–Ti<sup>4+</sup> entity to another, just as occurred in CCTO ceramics.<sup>38</sup> According to the XANES result, the mixed valent states of Ti<sup>3+</sup> and Ti<sup>4+</sup> were detected in NYCTO ceramics. Thus, giant dielectric response in NYCTO ceramics can also be contributed by the mixed valent structure and point defects.<sup>9, 10, 39</sup>

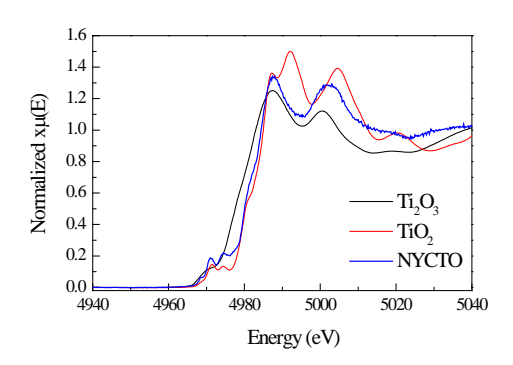


**Fig. 7** Normalized X–ray absorption near edge structure (XANES) spectra for Ti *K*–edge of NYCTO–10h sample.

Two possible mechanisms resulted in n-type semiconductivity ( $\approx$ 40  $\Omega$ .cm at room temperature) in NYCTO ceramics were proposed. The first is the classical hypothesis of an oxygen loss from the lattice according to  $O^{2-}(lattice) \rightarrow 1/2O_2(g) + 2e^-$ , where the electrons enter the Ti-3d conduction band. This is Ti<sup>3+</sup> in the formula  $Na_{1/2}Y_{1/2}Cu_3Ti_{4-x}^{4+}Ti_x^{3+}O_{12-x/2}$ . The second mechanism is based on the observation that Cu<sup>2+</sup> becomes unstable upon heating to high temperatures and reduces to Cu<sup>+</sup>. A slight amount of Cu<sup>2+</sup> is reduced to Cu<sup>+</sup> during sintering at ~1100 °C. Charge compensation follows the formula,  $3Cu^{2+} \rightarrow 2Cu^{+} + Ti^{4+}$ , *i.e.*, slight amount of excess Ti<sup>4+</sup> occupies the Cu site. Cu<sup>+</sup> can oxidize to Cu<sup>2+</sup> during cooling. Therefore, charge compensation occurs

as follows:  $Cu^+ + Ti^{4+} \rightarrow Cu^{2+} + Ti^{3+}$ . In this case, the actual formula is  $Na_{1/2}Y_{1/2}[Cu_{3-x}^{2+}Ti_{3x}^{4+}][Ti_{4-6x}^{4+}Ti_{6x}^{3+}]O_{12}$ . In both cases, residual  $Ti^{3+}$  remained in the NYCTO lattice. As suggested by Li et al., <sup>40</sup> for CCTO ceramics, very small values of x (<0.001) can be sufficient to induce n-type semiconductivity in the grains. The important clue of the second mechanism is the  $Cu_2O$  phase remaining in the sintered ceramics. <sup>41</sup> For all the NYCTO samples, this  $Cu_2O$  phase was not detected by the XRD technique [Fig. 1]. Therefore, the origin of n-type semiconducting grains of the NYCTO ceramics is likely correlated with the first mechanism due to the undetectable  $Cu_2O$  phase and the large amount of  $Ti^{3+}/Ti^{4+}$ .

Non-Ohmic characteristics of CCTO and related-ACu<sub>3</sub>Ti<sub>4</sub>O<sub>12</sub> ceramics are usually investigated to study the physical nature of electrical transport at the grain boundaries. 4, 6, 7, 13, 19, 23, 37 Unfortunately, the nonlinear properties of NYCTO ceramics have never been reported. As shown in Fig. 8, all of the NYCTO ceramics sintered at 1100 °C for different times show non-Ohmic properties. The nonlinear J-E characteristic of the NYCTO-1h sample was different from that of other samples. The E<sub>b</sub> value of the NYCTO-1h sample was much larger than those of other samples. This is consistent with its distinct microstructure [Fig. 2]. When the sintering temperature was decreased to 1085 °C for 5 h, the mean grain size slightly decreased, resulting in an increase in the  $E_b$  value (not presented). From the nonlinear J–E curves,  $\alpha$  and  $E_b$  values were calculated. The effect of sintering time on the nonlinear electrical properties can be seen in the inset of Fig. 8. In addition to the large value of  $E_b$ ,  $\alpha$  of the NYCTO-1h sample was significantly larger than those of other samples. Both  $E_b$  and  $\alpha$  values of the NYCTO-5h, NYCTO-10h and NYCTO-20h samples differed slightly. It is notable that the nonlinear properties of NYCTO ceramics were not related to  $E_{ab}$  values. This indicates that both  $\alpha$  and  $E_{b}$  are primarily dominated by the extrinsic effects, i.e., mean grain size and volume fraction of insulating grain boundaries, rather than the intrinsic effect of the grain boundary. The influence of grain size on nonlinear electrical properties of NYCTO ceramics is similar to those reported for CCTO ceramics.<sup>4, 42</sup> It is worth noting that when there were large grains in the microstructure, the non-Ohmic properties were not directly related to the average grain size. This is due to a detour of electric charges within the ceramic arising as the current avoids the fine-grained regions. This can cause a drop in the voltage across an insulating grain boundary between fine grains.<sup>42</sup> The nonlinear J-E properties of CCTO and related ACu<sub>3</sub>Ti<sub>4</sub>O<sub>12</sub> ceramics likely originated from the formation of Schottky-type potential barriers at the grain boundaries. 4, 23

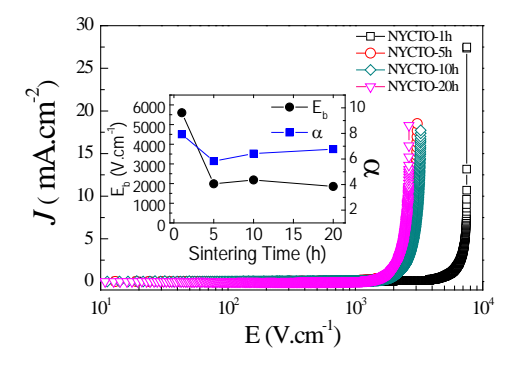


**Fig. 8** Nonlinear J-E curves at room temperature for  $Na_{1/2}Y_{1/2}Cu_3Ti_4O_{12}$  ceramics sintered at different times; inset shows electric field breakdown strength ( $E_b$ ) and

nonlinear coefficient ( $\alpha$ ) for Na<sub>1/2</sub>Y<sub>1/2</sub>Cu<sub>3</sub>Ti<sub>4</sub>O<sub>12</sub> ceramics sintered at different times.

#### 6.4 Conclusions

NYCTO ceramics were prepared by a conventional solid state reaction method sintered at 1100 °C for different times to obtain various microstructures. The mean grain size drastically increased when the sintering time was increased from 1 to 5 h and then changed little for sintering times from 5 to 20 h. All metal ions in the ceramics were randomly distributed in the microstructure. Nonlinear J-E characteristics were observed in NYCTO ceramics and found to be closely correlated with their microstructural changes. It was found that  $E_b$  of fine-grained ceramics sintered for 1 h was larger than those of the course-grained ceramics sintered for 5-20 h. The NYCTO ceramics exhibited low tanδ values of about 0.03 and very high  $\epsilon'$  values of 18000-23000 with good temperature stability. Using admittance and impedance spectroscopy analyses based on the brick-work layer model, the resistances of insulating grain boundaries and semiconducting grains at different temperatures were calculated. Using XANES technique, Ti<sup>3+</sup> was detected. The possible origin of the semiconducting grains of NYCTO ceramics was suggested to be caused by oxygen loss from the lattice during sintering process. The colossal dielectric response was caused by strong polarization at the grain boundaries, whereas the mixed valent structure and point defects were also important.

#### References

- <sup>1</sup>M. A. Subramanian and A. W. Sleight, "ACu<sub>3</sub>Ti<sub>4</sub>O<sub>12</sub> and ACu<sub>3</sub>Ru<sub>4</sub>O<sub>12</sub> perovskites: high dielectric constants and valence degeneracy," *Solid State Sci.*, **4**[3] 347-51 (2002).
- <sup>2</sup>M. A. Subramanian, D. Li, N. Duan, B. A. Reisner, and A. W. Sleight, "High Dielectric Constant in ACu<sub>3</sub>Ti<sub>4</sub>O<sub>12</sub> and ACu<sub>3</sub>Ti<sub>3</sub>FeO<sub>12</sub> Phases," *J. Solid State Chem.*, **151**[2] 323-25 (2000).
- <sup>3</sup>R. Schmidt, M. C. Stennett, N. C. Hyatt, J. Pokorny, J. Prado-Gonjal, M. Li, and D. C. Sinclair, "Effects of sintering temperature on the internal barrier layer capacitor (IBLC) structure in CaCu<sub>3</sub>Ti<sub>4</sub>O<sub>12</sub> (CCTO) ceramics," *J. Eur. Ceram. Soc.*, **32**[12] 3313-23 (2012).
- <sup>4</sup>S.-Y. Chung, I.-D. Kim, and S.-J. L. Kang, "Strong nonlinear current–voltage behaviour in perovskite-derivative calcium copper titanate," *Nat. Mater.*, **3**[11] 774-78 (2004).
- <sup>5</sup>D. C. Sinclair, T. B. Adams, F. D. Morrison, and A. R. West, "CaCu<sub>3</sub>Ti<sub>4</sub>O<sub>12</sub>: One-step internal barrier layer capacitor," *Appl. Phys. Lett.*, **80**[12] 2153 (2002).
- <sup>6</sup>J. Li, K. Wu, R. Jia, L. Hou, L. Gao, and S. Li, "Towards enhanced varistor property and lower dielectric loss of CaCu<sub>3</sub>Ti<sub>4</sub>O<sub>12</sub> based ceramics," *Materials & Design*, **92** 546-51 (2016).
- <sup>7</sup>Z.-Y. Lu, X.-M. Li, J.-Q. Wu, and M. Winter, "Voltage-Current Nonlinearity of CaCu<sub>3</sub>Ti<sub>4</sub>O<sub>12</sub> Ceramics," *J. Am. Ceram. Soc.*, **95**[2] 476-79 (2012).
- <sup>8</sup>J. Liu, C.-G. Duan, W.-G. Yin, W. Mei, R. Smith, and J. Hardy, "Large dielectric constant and Maxwell-Wagner relaxation in Bi<sub>2/3</sub>Cu<sub>3</sub>Ti<sub>4</sub>O<sub>12</sub>," *Phys. Rev. B*, **70**[14] 144106 (2004).

- <sup>9</sup>L. Ni and X. M. Chen, "Dielectric relaxations and formation mechanism of giant dielectric constant step in CaCu<sub>3</sub>Ti<sub>4</sub>O<sub>12</sub> ceramics," *Appl. Phys. Lett.*, **91**[12] 122905 (2007).
- <sup>10</sup>L. Ni and X. M. Chen, "Enhancement of Giant Dielectric Response in CaCu<sub>3</sub>Ti<sub>4</sub>O<sub>12</sub> Ceramics by Zn Substitution," *J. Am. Ceram. Soc.*, **93**[1] 184-89 (2010).
- <sup>11</sup>N. Zhao, P. Liang, L. Wei, L. Yang, and Z. Yang, "Synthesis and dielectric anomalies of CdCu<sub>3</sub>Ti<sub>4</sub>O<sub>12</sub> ceramics," *Ceram. Int.*, **41**[7] 8501-10 (2015).
- <sup>12</sup>W. Hao, J. Zhang, Y. Tan, and W. Su, "Giant Dielectric-Permittivity Phenomena of Compositionally and Structurally CaCu<sub>3</sub>Ti<sub>4</sub>O<sub>12</sub>-Like Oxide Ceramics," *J. Am. Ceram. Soc.*, **92**[12] 2937-43 (2009).
- <sup>13</sup>L. Yang, X. Chao, Z. Yang, N. Zhao, L. Wei, and Z. Yang, "Dielectric constant versus voltage and non-Ohmic characteristics of Bi<sub>2/3</sub>Cu<sub>3</sub>Ti<sub>4</sub>O<sub>12</sub> ceramics prepared by different methods," *Ceram. Int.*, **42**[2, Part A] 2526-33 (2016).
- $^{14}$ P. Liang, Z. Yang, and X. Chao, "Improved dielectric properties and grain boundary response in neodymium-doped  $Y_{2/3}Cu_3Ti_4O_{12}$  ceramics," *J. Alloys Compd.*, **678** 273-83 (2016).
- <sup>15</sup>J. Li, P. Liang, J. Yi, X. Chao, Z. Yang, and W. K. Wong-Ng, "Phase Formation and Enhanced Dielectric Response of Y<sub>2/3</sub>Cu<sub>3</sub>Ti<sub>4</sub>O<sub>12</sub> Ceramics Derived from the Sol-Gel Process," *J. Am. Ceram. Soc.*, **98**[3] 795-803 (2015).
- <sup>16</sup>P. Liang, Z. Yang, X. Chao, and Z. Liu, "Giant Dielectric Constant and Good Temperature Stability in Y<sub>2/3</sub>Cu<sub>3</sub>Ti<sub>4</sub>O<sub>12</sub> Ceramics," *J. Am. Ceram. Soc.*, **95**[7] 2218-25 (2012).
- <sup>17</sup>P. Liang, Y. Li, F. Li, X. Chao, and Z. Yang, "Effect of the synthesis route on the phase formation behavior and electric property of Na<sub>0.5</sub>Bi<sub>0.5</sub>Cu<sub>3</sub>Ti<sub>4</sub>O<sub>12</sub> ceramics," *Mater. Res. Bull.*, **52** 42-49 (2014).
- $^{18}P.$  Liang, Y. Li, X. Chao, and Z. Yang, "Pseudo-relaxor behavior in Na $_{1/2}Bi_{1/2}Cu_3Ti_4O_{12}$  ceramics," *Mater. Res. Bull.*, **60** 212-16 (2014).
- $^{19}\text{P.}$  Thongbai, T. Yamwong, and S. Maensiri, "Dielectric properties and electrical response of grain boundary of Na<sub>1/2</sub>La<sub>1/2</sub>Cu<sub>3</sub>Ti<sub>4</sub>O<sub>12</sub> ceramics," *Mater. Res. Bull.*, **47**[2] 432-37 (2012).
- $^{20}$ Z. Liu, G. Jiao, X. Chao, and Z. Yang, "Preparation, microstructure, and improved dielectric and nonlinear electrical properties of Na $_{1/2}$ La $_{1/2}$ Cu $_3$ Ti $_4$ O $_{12}$  ceramics by sol–gel method," *Mater. Res. Bull.*, **48**[11] 4877-83 (2013).
- <sup>21</sup>P. Liang, Y. Li, Y. Zhao, L. Wei, and Z. Yang, "Origin of giant permittivity and high-temperature dielectric anomaly behavior in Na<sub>0.5</sub>Y<sub>0.5</sub>Cu<sub>3</sub>Ti<sub>4</sub>O<sub>12</sub> ceramics," *J. Appl. Phys.*, **113**[22] 224102 (2013).
- <sup>22</sup>W. Somphan, N. Sangwong, T. Yamwong, and P. Thongbai, "Giant dielectric and electrical properties of sodium yttrium copper titanate: Na<sub>1/2</sub>Y<sub>1/2</sub>Cu<sub>3</sub>Ti<sub>4</sub>O<sub>12</sub>," *J. Mater. Sci.: Mater. Electron.*, **23**[6] 1229-34 (2012).
- <sup>23</sup>W. Somphan, P. Thongbai, T. Yamwong, and S. Maensiri, "High Schottky barrier at grain boundaries observed in Na<sub>1/2</sub>Sm<sub>1/2</sub>Cu<sub>3</sub>Ti<sub>4</sub>O<sub>12</sub> ceramics," *Mater. Res. Bull.*, **48**[10] 4087-92 (2013).

- <sup>24</sup>P. Kum-onsa, P. Thongbai, B. Putasaeng, T. Yamwong, and S. Maensiri, "Na<sub>1/3</sub>Ca<sub>1/3</sub>Bi<sub>1/3</sub>Cu<sub>3</sub>Ti<sub>4</sub>O<sub>12</sub>: A new giant dielectric perovskite ceramic in ACu<sub>3</sub>Ti<sub>4</sub>O<sub>12</sub> compounds," *J. Eur. Ceram. Soc.*, **35**[5] 1441-47 (2015).
- <sup>25</sup>H. Ren, P. Liang, and Z. Yang, "Processing, dielectric properties and impedance characteristics of Na<sub>0.5</sub>Bi<sub>0.5</sub>Cu<sub>3</sub>Ti<sub>4</sub>O<sub>12</sub> ceramics," *Mater. Res. Bull.*, **45**[11] 1608-13 (2010).
- <sup>26</sup>Z. Yang, H. Ren, X. Chao, and P. Liang, "High permittivity and low dielectric loss of Na<sub>0.5</sub>Bi<sub>0.5-x</sub>La<sub>x</sub>Cu<sub>3</sub>Ti<sub>4</sub>O<sub>12</sub> ceramics," *Mater. Res. Bull.*, **47**[5] 1273-77 (2012).
- <sup>27</sup>P. Liang, X. Chao, F. Wang, Z. Liu, and Z. Yang, "The Lowered Dielectric Loss and Grain-Boundary Effects in La-doped Y<sub>2/3</sub>Cu<sub>3</sub>Ti<sub>4</sub>O<sub>12</sub> Ceramics," *J. Am. Ceram. Soc.*, **96**[12] 3883-90 (2013).
- $^{28}$ P. Liang, X. Chao, and Z. Yang, "Low dielectric loss, dielectric response, and conduction behavior in Na-doped Y<sub>2/3</sub>Cu<sub>3</sub>Ti<sub>4</sub>O<sub>12</sub> ceramics," *J. Appl. Phys.,* **116**[4] 044101 (2014).
- <sup>29</sup>Y. Qiu, Z. Z. Ma, S. X. Huo, H. N. Duan, Z. M. Tian, S. L. Yuan, and L. Chen, "Giant dielectric and low voltage varistor behaviors of Ba-doped Bi<sub>1/2</sub>Na<sub>1/2</sub>Cu<sub>3</sub>Ti<sub>4</sub>O<sub>12</sub> ceramics," *J. Mater. Sci.: Mater. Electron.*, **23**[8] 1587-91 (2012).
- <sup>30</sup>J. Boonlakhorn, P. Kidkhunthod, B. Putasaeng, T. Yamwong, P. Thongbai, and S. Maensiri, "Giant dielectric behavior and electrical properties of Ca<sub>1-3x/2</sub>Lu<sub>x</sub>Cu<sub>3</sub>Ti<sub>4</sub>O<sub>12</sub> ceramics," *Applied Physics A*, **120**[1] 89-95 (2015).
- <sup>31</sup>B. Ravel and M. Newville, "ATHENA, ARTEMIS, HEPHAESTUS: data analysis for X-ray absorption spectroscopy using IFEFFIT," *Journal of Synchrotron Radiation*, **12**[4] 537-41 (2005).
- <sup>32</sup>F.-H. Lu, F.-X. Fang, and Y.-S. Chen, "Eutectic reaction between copper oxide and titanium dioxide," *J. Eur. Ceram. Soc.*, **21**[8] 1093-99 (2001).
- <sup>33</sup>L. Singh, B. C. Sin, I. W. Kim, K. D. Mandal, H. Chung, Y. Lee, and J. Varela, "A Novel One-Step Flame Synthesis Method for Tungsten-Doped CCTO," *J. Am. Ceram. Soc.*, **99**[1] 27-34 (2016).
- <sup>34</sup>S.-Y. Lee, H. E. Kim, and S.-I. Yoo, "Subsolidus Phase Relationship in the CaO–CuO–TiO<sub>2</sub> Ternary System at 950°C in Air," *J. Am. Ceram. Soc.*, **97**[8] 2416-19 (2014).
- <sup>35</sup>M. N. Rahaman, "Ceramic processing and sintering," pp. xiii, 875 p. 2nd ed. M. Dekker: New York, (2003).
- <sup>36</sup>L. Sun, Z. Wang, W. Hao, E. Cao, Y. Zhang, and H. Peng, "Influence of Zirconium doping on microstructure and dielectric properties of CaCu<sub>3</sub>Ti<sub>4</sub>O<sub>12</sub> synthesized by the solgel method," *J. Alloys Compd.*, **651** 283-89 (2015).
- <sup>37</sup>P. Thongbai, J. Jumpatam, B. Putasaeng, T. Yamwong, and S. Maensiri, "The origin of giant dielectric relaxation and electrical responses of grains and grain boundaries of Wdoped CaCu<sub>3</sub>Ti<sub>4</sub>O<sub>12</sub> ceramics," *J. Appl. Phys.*, **112**[11] 114115 (2012).
- <sup>38</sup>L. Zhang and Z.-J. Tang, "Polaron relaxation and variable-range-hopping conductivity in the giant-dielectric-constant material CaCu<sub>3</sub>Ti<sub>4</sub>O<sub>12</sub>," *Phys. Rev. B*, **70**[17] (2004).
- <sup>39</sup>Y. Wang, L. Ni, and X. M. Chen, "Effects of Nd-substitution on microstructures and dielectric characteristics of CaCu<sub>3</sub>Ti<sub>4</sub>O<sub>12</sub> ceramics," *J. Mater. Sci.: Mater. Electron.*, **22**[4] 345-50 (2011).

- $^{40}$ J. Li, M. A. Subramanian, H. D. Rosenfeld, C. Y. Jones, B. H. Toby, and A. W. Sleight, "Clues to the Giant Dielectric Constant of CaCu<sub>3</sub>Ti<sub>4</sub>O<sub>12</sub> in the Defect Structure of "SrCu<sub>3</sub>Ti<sub>4</sub>O<sub>12</sub>"," *Chem. Mater.*, **16**[25] 5223-25 (2004).
- <sup>41</sup>S. Kwon and D. P. Cann, "Relationship among the phase equilibria, microstructures, and dielectric properties of CaCu<sub>3</sub>Ti<sub>4</sub>O<sub>12</sub> ceramics via different sintering time," *J. Mater. Sci.*, **44**[15] 4117-23 (2009).
- <sup>42</sup>P. Thongbai, T. Yamwong, S. Maensiri, V. Amornkitbamrung, and P. Chindaprasirt, "Improved Dielectric and Nonlinear Electrical Properties of Fine-Grained CaCu<sub>3</sub>Ti<sub>4</sub>O<sub>12</sub> Ceramics Prepared by a Glycine-Nitrate Process," *J. Am. Ceram. Soc.*, **97**[6] 1785–90 (2014).

#### CHAPTER 7

# Enhanced Dielectric and Non-Ohmic Properties in CaCu<sub>3</sub>Ti<sub>4</sub>oO<sub>12</sub>/CaTiO<sub>3</sub> Nanocomposites Prepared by a Chemical Combustion Method

#### 7.1 Introduction

Recently,  $CaCu_3Ti_4O_{12}$  (CCTO) ceramics have been extensively investigated because of the fascinating physics underlying the origin of an ultra–high dielectric permittivity ( $\epsilon$ ') in CCTO without any detectable phase transition over a wide temperature range [1-16]. CCTO is promising for a new generation of multilayer ceramic capacitors even though the origin of the giant dielectric response in CCTO is still unclear today. According to several elegant works [2, 17], CCTO is obviously electrically heterogeneous, consisting of n–type semiconducting grains and insulating grain boundaries (GBs). Thus, the dielectric properties can be improved by tuning the electrical properties of GBs and/or other internal interfaces. The dielectric loss tangent ( $tan\delta$ ) at 1 kHz of CCTO ceramics is still too high (>0.05) [1, 5, 10, 11, 18], which is the serious problem preventing the use of CCTO in capacitor applications.

Generally, reduction in DC conductivity ( $\sigma_{dc}$ ) to decrease  $\tan\delta$  of CCTO has been carried out by increasing the resistances of GBs ( $R_{gb}$ ) or other internal interfaces [19]. Enhancement of  $R_{gb}$  can be performed by several ways such as doping CCTO with suitable metal ions to intrinsically improve electrical properties of GBs [18, 20], filling oxygen vacancies at GBs [21], or altering Ca<sup>2+</sup> and Cu<sup>2+</sup> molar ratios to produce CCTO/CaTiO<sub>3</sub> (CTO) composites [3, 7, 22, 23]. However, reduced  $\tan\delta$  of CCTO by using these methods rarely results in materials that fulfill all of the requirements of capacitor applications, *i.e.*, high  $\epsilon$ ', low  $\tan\delta$ , and good temperature stability of  $\epsilon$ '. For example, a strong decrease in  $\tan\delta$  (~0.02 at 1 kHz) observed in Ca<sub>2</sub>Cu<sub>2</sub>Ti<sub>4</sub>O<sub>12</sub> (consisting of 33.3 mol% of CCTO and 66.7 mol% of CTO) caused a large decrease in  $\epsilon$ ' (~1.8×10<sup>3</sup>) [3].

To investigate CCTO-based ceramics for use applications in electronic devices, selection of the synthesis method is one of the most important decisions, which largely determines the sintered bulk properties of CCTO ceramics. Generally, CCTO-based ceramics are prepared by the solid state reaction (SSR) method [1-3, 7, 17, 18]. However, the SSR method requires high temperatures (1000-1050 °C) and long reaction times (12-14 h) to eliminate all possible impurity phases [3, 18]. On the other hand, syntheses of ceramic powder from chemical solutions offer the possibility of closer stoichiometric control compared to the SSR method. Low-temperature chemical reactions with short reaction times are usually sufficient used to produce a pure phase [4]. The combustion method is one of the most interesting routes to produce nanocrystalline ceramics. Organic compounds like glycine, urea, citric acid, and EDTA have been widely used as fuels for gel combustion [24]. The combustion method using glycine as a fuel is one of the most attractive methods. This method was firstly reported by Chick et al. [25] which can be used effectively to prepare homogeneous nanoparticles of ceramic powders by a self-ignited combustion process. According to our previous work, a pure CCTO phase can be prepared by this method using a low sintering temperature and short reaction time [26]. The dielectric properties of CCTO ceramics can be improved by using nanocrystalline CCTO powder to form the bulk ceramics. To the best our knowledge, preparation of CCTO/CTO composites using wet chemical routes was rarely reported [22, 23]. Furthermore, syntheses of CCTO/CTO composites using a combustion method and their dielectric properties have never been reported.

Therefore, in this work, the glycine combustion method was used to synthesize nanocrystalline CCTO and CTO powders by using one–step process from the nominal chemical formula of  $Ca_2Cu_2Ti_4O_{12}$ . Dense ceramic microstructure of CCTO/CTO nanocomposites was achieved by sintering under a short reaction time for 2 h. The  $\epsilon'$  values of the sintered CCTO/CTO ceramics were significantly enhanced by factors of 4–5 compared to those ceramics prepared by SSR method, while  $tan\delta$  was still too low.

## 7.2 Experiment

 $Ca_2Cu_2Ti_4O_{12}$  (CCTO/CTO) was prepared by a chemical combustion method using glycine as a fuel. The starting raw materials used in this work consisted of  $Ca(NO_3)_2\cdot 4H_2O$  (99 %, Sigma–Aldrich),  $Cu(NO_3)_2\cdot 4H_2O$  (99.5 %, Carlo Erba),  $C_{16}H_{28}O_6Ti$  (75 wt.% in isopropanol, Sigma–Aldrich), citric acid, deionized water, and glycine. Details of the preparation method are given elsewhere [26]. Dried porous precursors were ground and calcined at 800 and 850 °C for 6 h to form CCTO and CTO phases. These powders were referred to as C1 and C2 powders, respectively. These composite powders were pressed into pellets having dimensions of 9.5 mm in diameter and ~1–2 mm in thickness by uniaxial compression at 200 MPa. Finally, these pellets were sintered in air at 1100 °C for 2, 5, 10, and 15 h. The CCTO/CTO composites sintered by using the C1 (C2) powder are abbreviated as C1S2 (C2S2), C1S5 (C2S5), C1S10 (C2S10), and C1S15 (C2S15) samples, respectively.

Scanning electron microscopy (SEM) (LEO 1450VP, UK) with an energy dispersive x–ray spectrometry (EDS) and X-ray diffraction (XRD) (Philips PW3040, the Netherlands) techniques were used to characterize the surface morphologies and phase compositions of the sintered CCTO/CTO composite ceramics, respectively. Particle size and shape of the composite powders were revealed using transmission electron microscopy (TEM) (FEI Tecnai  $G^2$ , Eindhoven, the Netherlands). Surfaces of the sintered ceramics were polished and sputtered with Au at a current of 25 mA for 8 min using a Polaron SC500 sputter coating unit. An Agilent 4294A Precision Impedance Analyzer was used to test the dielectric properties. The measurement was carried out over the frequency range from  $10^2$  to  $10^7$  Hz using an oscillation voltage of 0.5 V under the temperature range from -70 to 220 °C with step increases of 10 °C. Each temperature step was held with an accuracy of  $\pm 1$  °C. Current density–electric field (J–E) characteristics were measured at various temperatures using a high voltage measurement unit (Keithley Model 247).  $E_b$  was defined as the electric field breakdown strength at which J = 1 mA/cm². The nonlinear coefficient ( $\alpha$ ) was calculated using the following formula:

$$\alpha = \frac{\log(J_2/J_1)}{\log(E_2/E_1)} , {1}$$

where  $E_1$  and  $E_2$  are the applied electric fields, at which  $J_1 = 1$  and  $J_2 = 10$  mA.cm<sup>-2</sup>, respectively.

#### 7.3 Results and discussion

Fig. 1 shows the XRD patterns of Ca<sub>2</sub>Cu<sub>2</sub>Ti<sub>4</sub>O<sub>12</sub> powders calcined at 800 and 850 °C for 6 h. Both of the C1 and C2 powders consist of two phases of CCTO (JCPDS 75-2188) and CTO (JCPDS 82-0231). A small amount of CuO phase is still in the C1

powder. This result is similar to that reported in the literature for Ca<sub>2</sub>Cu<sub>2</sub>Ti<sub>4</sub>O<sub>12</sub> ceramics prepared by SSR method and polymer pyrolysis method [3, 7, 23]. From the nominal formula of Ca<sub>2</sub>Cu<sub>2</sub>Ti<sub>4</sub>O<sub>12</sub>, two phases of ~66.7 mol% of CTO and ~33.3 mol% of CCTO can be formed. This is because the ionic radius of Cu<sup>2+</sup> much smaller than that of Ca<sup>2+</sup>. Thus, the excess Ca<sup>2+</sup> ions cannot occupy on Cu<sup>2+</sup> lattice sites for a planar square of CuO<sub>4</sub> to form Ca(CaCu<sub>2</sub>)Ti<sub>4</sub>O<sub>12</sub> structure. Lattice parameters (a) of the CCTO phase in the C1 and C2 composite powders were calculated and found to be 7.3955 and 7.3956 Å, respectively. These values are comparable to 7.391 Å for a single CCTO phase [1]. Morphologies of the C1 and C2 powders are shown in Fig. 2. The TEM images revealed that particle size increases with increasing calcination temperature. The particles sizes of the C1 and C2 powders are of about 30-80 and 60-90 nm, respectively.

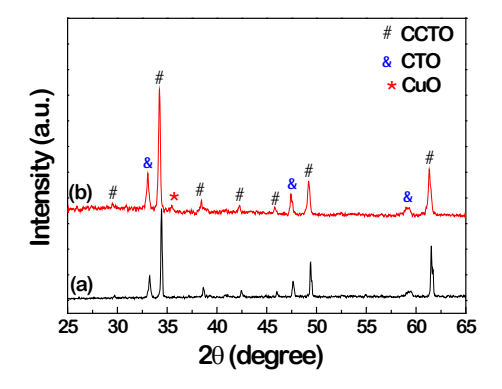


Fig. 1 XRD patterns of (a) C1 and (b) C2 powders.

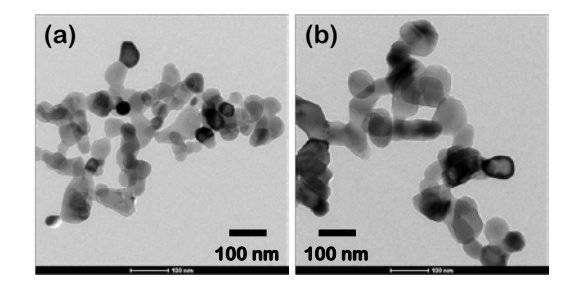
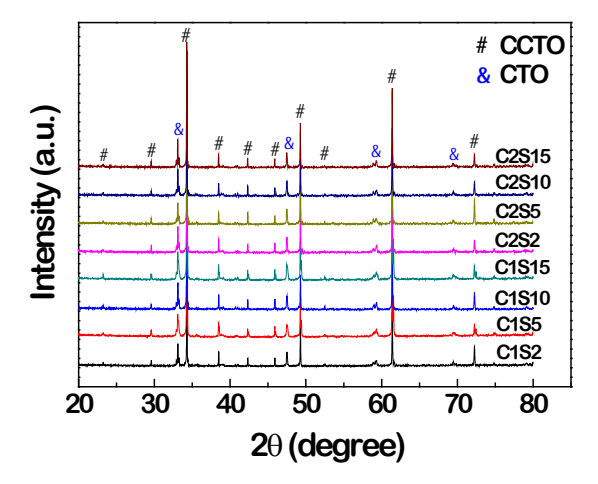


Fig. 2 TEM images of (a) C1 and (b) C2 powders.

Fig. 3 shows the XRD patterns of the sintered composite ceramics using the C1 and C2 powders as green bodies. As clearly seen, the CCTO and CTO phases are detected in all the XRD patterns. *a* values of the C1S2 (C2S2), C1S5 (C2S5), C1S10 (C2S10), and C1S15 (C2S15) samples were found to be 7.3913 (7.3924), 7.3866 (7.3904), 7.3901 (7.3904), and 7.3906 (7.3903) Å, respectively. Fig. 4 demonstrates SEM images of the C1S2 and C1S10 samples. Large and small grains are observed. According to previous works [7, 27], by using the backscattered SEM images of CCTO/CTO composites coupled with EDS technique, smooth and rough surface grains were clearly proved to be the CCTO and CTO phases, respectively. As illustrated in Fig. 5, it is clear shown that the rough surface grain (detected on point-2) is CTO phase because only EDS peaks of Ca, Ti, and O are detected. All of Ca, Cu, Ti, and O peaks are detected in the smooth surface grain (detected on point-1), indicating to be the CCTO phase. This result is similar to that reported in literature [7, 27].



**Fig. 3** XRD patterns of the ceramic composites using C1 and C2 powders and sintered under different conditions.

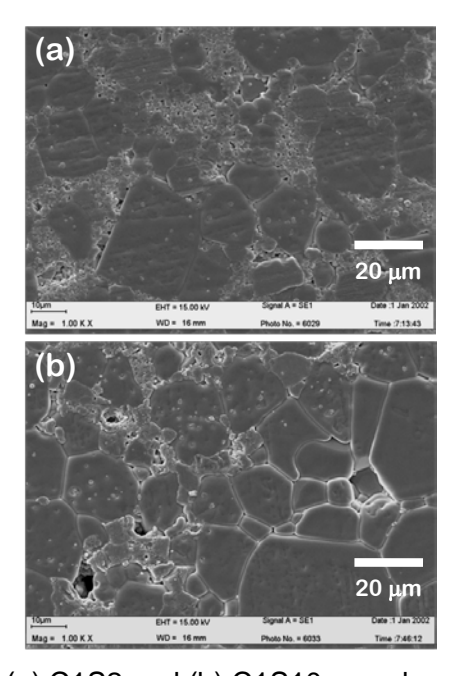
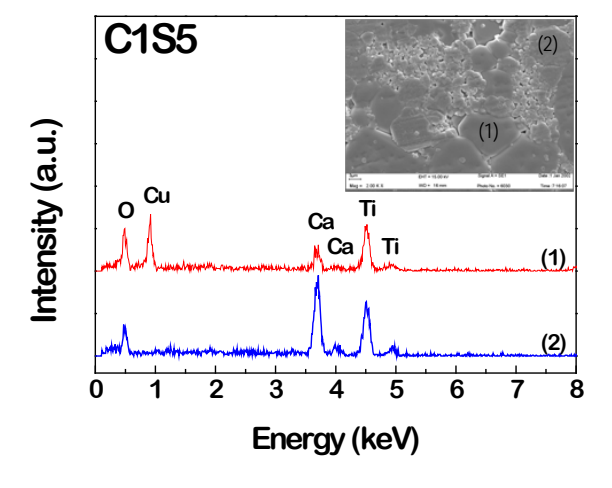
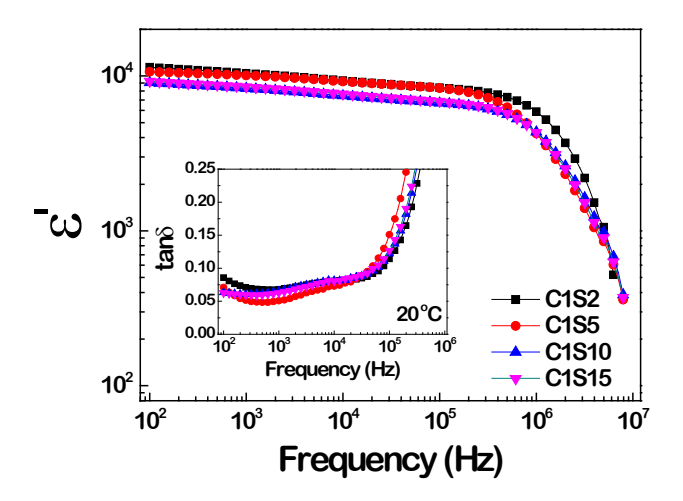


Fig. 4 SEM images of (a) C1S2 and (b) C1S10 samples.



**Fig. 5** EDS spectra of C1S5 sample at different points on the surface.

Fig. 6 demonstrates the dielectric properties as a function of frequency for the CCTO/CTO composites at 20 °C.  $\varepsilon'$  of all the samples is nearly independent on frequency in the range of  $10^2$ - $10^5$  Hz. Interestingly,  $\varepsilon'$  values of all the CCTO/CTO samples are of about  $10^4$ . These  $\varepsilon'$  values of all the CCTO/CTO samples are much larger than the  $\varepsilon'$  value of ~1800 for the CCTO/CTO composite prepared by SSR method and sintered at 1090 °C for 24 h, as first reported by Kobayashi and Terasaki [3]. Moreover, these two values are larger than the  $\varepsilon'$  value of ~1300 for the sample sintered at 1050 °C for 0.5 h sintered using a microwave sintering method [28]. Ramirez et al. [7] found  $\varepsilon'$ ~2960 at 1 kHz for CCTO/CTO ceramic sintered at 1100 °C for 3 h using a conventional furnace. According to our previous work [23],  $\varepsilon'$ ~2104 at 1 kHz was obtained in a CCTO/CTO ceramic sintered at 1050 °C for 10 h prepared by SSR method. Furthermore,  $\varepsilon'$  values of CCTO/CTO samples in this current study are also much larger than those of  $\varepsilon'$  values of CCTO/CTO composites prepared by wet chemical routes [22, 23].



**Fig. 6** Frequency dependence of ε' at 20 °C for CCTO/CTO composites fabricated by using C1 powder; inset shows tanδ as a function of frequency.

According to the previous work of Ramirez et al. [7] by using electrostatic force microscopy (EFM), CCTO–CTO and CCTO–CCTO interfaces were electrically active, indicating the presence of potential barriers. However, a CTO–CTO interface was electrically inactive. Thus, the exceptional high  $\epsilon'$  of the CCTO/CTO composites in this current study may be related to these active interfaces. As shown in the SEM images, a large internal interface area was produce in the CCTO/CTO samples due to their large grain sizes, giving rise to an increase in the capacitance value of the active internal interfaces (i.e., CCTO–CTO and CCTO–CCTO interfaces). This may be responsible for the observed high  $\epsilon'$  values of the CCTO/CTO composite ceramics presented in this work. It is worth noting that  $\tan\delta$  values are still lower than 0.1, as shown in the inset of Fig. 6. At 20 °C and 1 kHz,  $\epsilon'$  values of the C1S2 (C2S2), C1S5 (C2S5), C1S10 (C2S10), and C1S15 (C2S15) samples are of about 10407 (10203), 10085 (10248), 8324 (9888), and 8495 (7840), respectively.  $\tan\delta$  values are of about 0.068 (0.075), 0.050 (0.072), 0.065 (0.079), and 0.062 (0.056), respectively.

Fig. 7 demonstrates the temperature dependence of  $\epsilon'$  and  $\tan\delta$  at 1 kHz for the CCTO/CTO composites fabricated using the C1 powder. As clearly seen,  $\epsilon'$  is slightly dependent on temperature in the range from -70 to 100 °C. It was found that variation in  $\epsilon'$ 

at each temperature compared to the  $\varepsilon$ 'value at 25 °C was found to be less than  $\pm 15\%$  in the range of -70 to 100 °C. Notably, the C1S5 sample exhibits high low  $\tan \delta \sim 0.05$  and  $\varepsilon' \sim 10^4$  with good temperature stability. As shown in the inset,  $\tan \delta$  increases with increasing temperature when temperature was increased higher than 100 °C. This is attributed to the effect of DC conduction in the bulk ceramics. This behavior is usually observed in CCTO-based ceramics [20, 29, 30].

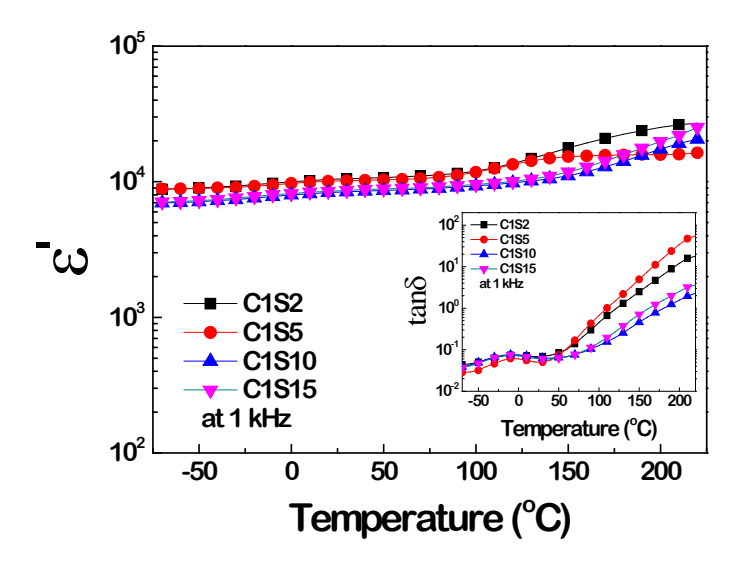


**Fig. 7** Temperature dependence of ε' at 1 kHz for CCTO/CTO composites fabricated by using C1 powder; inset shows tanδ in the temperature range of -70–220 °C.

Fig. 8 shows the nonlinear J-E characteristics of the CCTO/CTO composites prepared by a glycine combustion method. Obviously, all the composites exhibit nonlinear electrical properties. The E<sub>b</sub> values of the C1S2 (C2S2), C1S5 (C2S5), C1S10 (C2S10), and C1S15 (C2S15) samples are of about 1276.8 (1335.6), 998.6 (1039.3), 2361.6 (1538.7), and 1912.7 (2326.37) V/cm, respectively.  $\alpha$  values are of about 6.08 (5.69), 5.31 (5.15), 7.35 (6.21), and 7.03 (7.12), respectively. It is important to note that the  $E_b$  and  $\alpha$ values of the CCTO/CTO composites in this current study are lower than those of CCTO/CTO composites prepared by SSR method [27, 28, 30]. According to the microstructure analyses, large grains with sizes of about 10-40 µm were observed in the microstructure of CCTO/CTO composites prepared by a glycine combustion method, while fine grains with sizes of 2-3 μm were observed in the composites prepared by SSR method[30]. Thus, the density of active insulating internal barriers in the large grain composites is lower than that of the composites prepared by SSR method. Under the same level of applied electric field, the electric potential across the single barrier in the larger-grain CCTO/CTO composites is therefore much larger than those of the fine-grain composites. This is the primary cause of the reduction in the nonlinear properties of the CCTO/CTO composites prepared by a glycine combustion method.

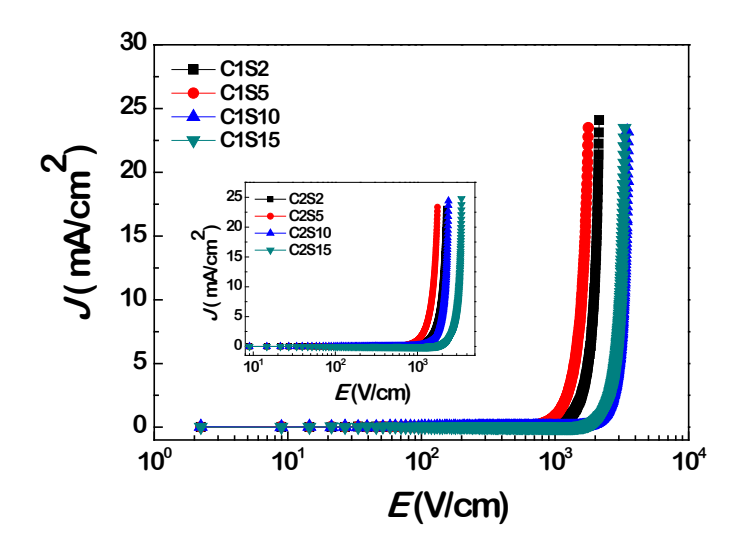


**Fig. 8** J–E curves at room temperature of CCTO/CTO composites fabricated by using C1 powder; inset shows J–E curves of CCTO/CTO composites fabricated by using C2 powder.

#### 7.4 Conclusions

In conclusion, we have successfully prepared CCTO and CTO nanoparticles with sizes of about 30-90 nm using a chemical combustion method employing glycine as fuel. The CCTO and CTO phases without impurity can be obtained using a relatively low calcination temperature of 800 °C. By using nanocrystalline powders, dense microstructure was obtained by sintering for 2 h. Notably, a low  $\tan \delta \sim 0.05$  and high  $\epsilon' \sim 1.01 \times 10^4$  with good temperature stability over a wide temperature range were achieved in the sintered CCTO/CTO composites. The nonlinear current–voltage behavior was observed in the CCTO/CTO composites. The electrical responses of CCTO–CTO and CCTO–CCTO interfaces were suggested to be the primary cause of the dielectric and nonlinear electrical properties.

#### References

- M. A. Subramanian, D. Li, N. Duan, B. A. Reisner, A. W. Sleight, J. Solid State Chem. 151, 323 (2000)
- S.-Y. Chung, I.-D. Kim, S.-J. L. Kang, Nat. Mater. 3, 774 (2004)
- 3. W. Kobayashi, I. Terasaki, Appl. Phys. Lett. 87, 032902 (2005)
- 4. J. Liu, Y. Sui, C.-g. Duan, W.-N. Mei, R. W. Smith, J. R. Hardy, Chem. Mater. 18, 3878 (2006)
- 5. L. Liu, H. Fan, P. Fang, X. Chen, Mater. Res. Bull. 43, 1800 (2008)
- 6. L. Liu, H. Fan, X. Chen, P. Fang, J. Alloys Compd. 469, 529 (2009)
- 7. M. A. Ramírez, P. R. Bueno, R. Tararam, A. A. Cavalheiro, E. Longo, J. A. Varela, J. Phys. D: Appl. Phys. **42**, 185503 (2009)
- 8. R. Sakamaki, B. Cheng, J. Cai, Y.-H. Lin, C.-W. Nan, J. He, J. Eur. Ceram. Soc. 30, 95 (2010)
- 9. R. Schmidt, M. C. Stennett, N. C. Hyatt, J. Pokorny, J. Prado-Gonjal, M. Li, D. C. Sinclair, J. Eur. Ceram. Soc. **32**, 3313 (2012)
- 10. Y. Liu, Q. Chen, X. Zhao, J. Mater. Sci.: Mater. Electron. 25, 1547 (2014)

- 11. Y. Yang, X. Wang, B. Liu, J. Mater. Sci.: Mater. Electron. 25, 146 (2014)
- 12. C. Puchmark, G. Rujijanagul, Nanoscale Research Letters 7, 7 (2012)
- 13. W. Tuichai, S. Somjid, B. Putasaeng, T. Yamwong, A. Chompoosor, P. Thongbai, V. Amornkitbamrung, S. Maensiri, Nanoscale Research Letters **8**, 1 (2013)
- 14. S. De Almeida-Didry, C. Autret, A. Lucas, C. Honstettre, F. Pacreau, F. Gervais, J. Eur. Ceram. Soc. **34**, 3649 (2014)
- 15. M. Ab Rahman, S. Hutagalung, Z. Ahmad, M. Ain, J. Mohamed, J. Mater. Sci.: Mater. Electron. **26**, 3947 (2015)
- 16. C. Masingboon, S. Maensiri, T. Yamwong, J. Nanosci. Nanotechnol. 11, 8670 (2011)
- 17. T. B. Adams, D. C. Sinclair, A. R. West, J. Am. Ceram. Soc. 89, 3129 (2006)
- 18. E. A. Patterson, S. Kwon, C.-C. Huang, D. P. Cann, Appl. Phys. Lett. 87, 182911 (2005)
- 19. S. Vangchangyia, E. Swatsitang, P. Thongbai, S. Pinitsoontorn, T. Yamwong, S. Maensiri, V. Amornkitbamrung, P. Chindaprasirt, J. Am. Ceram. Soc. **95**, 1497 (2012)
- 20. Z. Yang, L. Zhang, X. Chao, L. Xiong, J. Liu, J. Alloys Compd. 509, 8716 (2011)
- 21. R. Yu, H. Xue, Z. Cao, L. Chen, Z. Xiong, J. Eur. Ceram. Soc. 32, 1245 (2012)
- 22. J. Jumpatam, P. Thongbai, B. Kongsook, T. Yamwong, S. Maensiri, Mater. Lett. 76, 40 (2012)
- 23. P. Thongbai, B. Putasaeng, T. Yamwong, S. Maensiri, J. Alloys Compd. 509, 7416 (2011)
- 24. S. Mukherjee, M. R. Gonal, M. K. Patel, M. Roy, A. Patra, A. K. Tyagi, M. Menon, J. Am. Ceram. Soc. **95**, 290 (2012)
- 25. L. A. Chick, L. R. Pederson, G. D. Maupin, J. L. Bates, L. E. Thomas, G. J. Exarhos, Mater. Lett. 10, 6 (1990)
- 26. P. Thongbai, T. Yamwong, S. Maensiri, V. Amornkitbamrung, P. Chindaprasirt, J. Am. Ceram. Soc. **97**, 1785 (2014)
- 27. J. Jumpatam, B. Putasaeng, T. Yamwong, P. Thongbai, S. Maensiri, J. Am. Ceram. Soc. 97, 2368 (2014)
- 28. M. A. Ramírez, P. R. Bueno, J. A. Varela, E. Longo, Appl. Phys. Lett. 89, 212102 (2006)
- 29. M. Wang, B. Zhang, F. Zhou, J. Mater. Sci.: Mater. Electron. 25, 3947 (2014)
- 30. J. Jumpatam, B. Putasaeng, T. Yamwong, P. Thongbai, S. Maensiri, J. Eur. Ceram. Soc. **34**, 2941 (2014)

#### **CHAPTER 8**

#### Effects of DC Bias on Dielectric and Electrical Responses In (Y+Zn) 3 Dio Ded Kerouskite Oxides Co

#### 8.1 Introduction

response in CCTO ceramics.

The interesting dielectric properties of CaCu<sub>3</sub>Ti<sub>4</sub>O<sub>12</sub> (CCTO) perovskite oxide are its anomalous dielectric behaviors including its high dielectric permittivity (ε'~10<sup>4</sup>) without any detectable phase transition, ability to form an internal barrier layer capacitor (IBLC) structure in a one-step sintering method, and nonlinear current -voltage pr -Defination was exhibited without addition of dopants or using others [1-4]. Non special sintering steps [2, 5]. These striking features have been widely studied for potential uses in electronic applications and for understanding the underlying physical properties of CCTO ceramics [6-9].

Since the giant dielectric permittivity of CCTO was firstly reported by Subramanian et al. [1], the origin of giant  $\varepsilon'$  of CCTO ceramics has been widely investigated and is still not clearly understood. Many models were formulated to explain its abnormally large  $\varepsilon'$ values. The extrinsic origin of the IBLC model is widely accepted and was used to describe the variation of  $\varepsilon'$  with mean grain size [6, 9-15]. However, the intrinsic origin of these properties inside the grains of CCTO cannot be ignored, especially for the ±,v@lentandudti3teanecooksulashin.det@ated in CCTO [7, mixed 8]. The IBLC microstructure consists of semiconducting and insulating parts, which are attributable to the grains and grain boundaries, respectively [2, 6, 9]. Accordingly, the strong interfacial polarization or Maxwell

be produced by applying an electric field. Based on the IBLC model, microstructural characteristics are important. Therefore, the dielectric permittivity of CCTO ceramics can be changed by tuning their microstructure through adjustment of sintering conditions and/or by doping with metal ions [3, 5, 11, 16]. The control of microstructure in CCTO ceramics by substitution of metal ions into the CCTO structure has been widely investigated [8, 11, 15-21]. Substitution of various  $Ln^{3+}$  ions (where  $Ln^{3+} = Y^{3+}$ ,  $Yb^{3+}$ ,  $Sm^{3+}$ , and Gd3+) can effectively suppress the grain growth rate of CCTO ceramics, achieving a fine-grained microstructure [11, 16, 19, 20]. It was found that the  $\varepsilon'$  of CCTO can be increased by doping with Mg<sup>2+</sup> and Zn<sup>2+</sup> ions at Cu<sup>2+</sup> sites (the A' site of the AA'<sub>3</sub>M<sub>4</sub>O<sub>12</sub> structure), while tanδ was reduced (or at least remained constant) [7, 8]. Considering the microstructure of Mg<sup>2+</sup> and Zn<sup>2+</sup>-doped CCTO ceramics, improved dielectric properties are likely attributable to the modified intrinsic properties of the grain boundaries. This is because when grain sizes of Mg<sup>2+</sup> and Zn<sup>2+</sup>-doped CCTO ceramics were enlarged (or the number of grain boundaries decreased), their tanδ values were slightly changed.

Most recently, good dielectric properties (high  $\varepsilon'$  and low -loss tang  $(Ln^{3+}, Mq^{2+})$  co Ładoped YC Ort Wb covereics ported [22, 23].  $Ln^{3+}$ dopant was used to inhibit the grain growth rate and Mg2+ dopant was substituted into CCTO to enhance dielectric properties. Unfortunately, no system of  $(Ln^{3+}, Zn^{2+})$  co -doped CCTO ceramics has ever been reported. Interesting these dielectric properties may be achieved since Zn<sup>2+</sup> is one of the most effective dopants that can be used to enhance the giant dielectric response in CCTO ceramics [8, 24]. In addition to the good dielectric properties that were expected of  $(Ln^{3+}, Zn^{2+})$  co results may give some important clues to the underlying the origin of the giant dielectric

 $\delta$ ) of

-doped CC

-Wagner p

For the study of the giant dielectric response in CCTO ceramics, an impedance spectroscopy technique is usually used for separating the electrical properties of the grains and grain boundaries. The conduction activation energies inside the grains ( $E_a$ ) and at the grain boundaries ( $E_{gb}$ ) are also very important for explaining the dielectric phenomenon [3, 16, 22, 23, 25]. The  $E_{gb}$  value is closely related to the Schottky barrier height [26, 27]. To date, results of investigations on the impedance spectroscopy analysis and conduction activation energy values under an applied DC bias have rarely been reported [27]. These studies may be important for explaining the origin of the giant dielectric response in CCTO ceramics.

Thus, in this work,  $Ca_{0.925}Y_{0.05}Cu_{3-x}Zn_xTi_4O_{12}$  (x=0.05 -0.30) ceramics we prepared using a modified sol <sup>9</sup>Gefbm@thothterrestingtyed at 1055 high  $\epsilon'$  values were obtained and they increased with increasing  $Zn^{2+}$  dopant concentration, while their  $tan\delta$  values remained low. Using an impedance spectroscopy technique,  $R_{gb}$  was remarkably decreased with increasing temperature and DC bias, while the  $E_{gb}$  region was decreased by applying DC bias voltages of up to 36 V, indicating a decrease in the Schottky barrier height at the grain boundaries. The experimental results demonstrate the importance of Schottky barriers at the boundaries of semiconducting grains in controlling the high dielectric permittivity response in CCTO ceramics.

#### 8.2 Experimental details

 $Ca_{0.925}Y_{0.05}Cu_{3-x}Zn_xTi_4O_{12}$  (YZ-CCTO) ceramics, where x = 0.05-0.30, were prepared using a modified sol-gel method. Details of preparation method have been published. Ca(C<sub>2</sub>H<sub>3</sub>CO<sub>2</sub>)<sub>2</sub>•H<sub>2</sub>O (99+%, Sigma-Aldrich), Cu(CH<sub>3</sub>COO)<sub>2</sub>•H<sub>2</sub>O (99.0%, Sigma-Aldrich), Zn(CH<sub>3</sub>COO)<sub>2</sub>•2H<sub>2</sub>O (99.99%, Aldrich), Y(CH<sub>3</sub>CO<sub>2</sub>)<sub>3</sub>•xH<sub>2</sub>O (99.9%, Sigma-Aldrich), C<sub>16</sub>H<sub>28</sub>O<sub>6</sub>Ti (75 wt% in isopropanol, Sigma-Aldrich), ethylene glycol, citric acid, ethanol and de-ionized water were employed as the starting raw materials. Complete details of the preparation method are given elsewhere [11]. It is notable that ethylene glycol was used as a surfactant to prevent particle agglomeration, while citric acid was employed to enhance the solubility of the Ca, Cu, Y and Zn acetates. Ethanol was used to dissolve Ti solution. The resulting viscous gels for all compositions were dried in air at 500 °C for 15 min. The dried porous precursors were ground and calcined at 900 °C for 10 h. The calcined powders were pressed by uniaxial compression at ≈200 MPa into a pellet shape of 9.5 mm in diameter and ~1-2 mm in thickness. The Ca<sub>0.925</sub>Y<sub>0.05</sub>Cu<sub>3-x</sub>Zn<sub>x</sub>Ti<sub>4</sub>O<sub>12</sub> ceramic samples were obtained by sintering the compacted powders at 1055 °C for 6 h. These sintered ceramic samples with x = 0.05, 0.10, and 0.30were referred to as YZn05, YZn10, and YZn30 ceramics, respectively.

The phase composition and crystalline structure were characterized using an X diffractometer (PANalytical, EMPYREAN). Rietveld quantitative phase analysis was carried out using the X'Pert High Score Plus v3.0e software package by PANalytical. The diffraction patterns were collected over the range of  $2\theta$ =25°-65° with step increases of  $0.02^\circ$ /min. The surface morphologies were characterized using scanning electron microscopy (SEM; LEO 1450VP; Cambridge, UK). The chemical states of Cu and Ti were analyzed using X-ray photoelectron spectroscopy (XPS), PHI5000 VersaProbe II, ULVAC-PHI, Japan) at the SUT-NANOTEC-SLRI Joint Research Facility, Synchrotron Light Research Institute (SLRI), Thailand. The XPS spectra were fitted with PHI MultiPak XPS software using a combination of Gaussian-Lorentzian lines. Smooth surfaces were coated by Au sputtering using a Polaron SC500 sputter coating unit with electric current

~25 mA for 4 min before dielectric measurements. The dielectric properties of the sintered ceramics were measured using a KEYSIGHT E4990A Impedance Analyzer with an oscillation voltage of 0.5 V. The dielectric measurements were made over the frequency and temperature ranges of  $10^2-10^7$  Hz and -60 to 210 °C, respectively.

#### 8.3 Results and discussion

The XRD patterns of the YZn05, YZn10, and YZn30 ceramics are shown in Fig. 1. A single phase of CCTO was observed in all the sintered ceramics, which is similar to observations of pure CCTO (JCPDS 75 2018102NccatiO3,COaCO3 impurity phases or related phases of Y and Zn were detected in the XRD patterns. This may have been due to perfect substitutions of Y and Zn. It is notable that all the diffraction peaks in the XRD patterns in Fig. 1 are perfectly indexed based on the bcc structure. Rietveld refinement profile fits were performed, as illustrated in Fig. 2. Accordingly, the lattice parameters were calculated and found to be 7.3945(1), 7.3949(1) and 7.3984(1) Å for the YZn05, YZn10, and YZn30 ceramics, respectively. The increase in the value of the lattice parameter was primarily attributed to the larger ionic radius of the  $Zn^{2+}$  dopant ( $r_4$  = 0.60 Å) compared to that of the host  $Cu^{2+}$  ion ( $r_4 = 0.57$  Å). Moreover, the effect of the mixed-valence structure of Cu<sup>+</sup>/Cu<sup>2+</sup> and Ti<sup>3+</sup>/Ti<sup>4+</sup> may be another factor contributing to this observation [8, 28]. Generally, the perovskite structure (e.g., BaTiO<sub>3</sub> structure) can be considered largely flexible. For ACu<sub>3</sub>Ti<sub>4</sub>O<sub>12</sub> oxides (e.g., CaCu<sub>3</sub>Ti<sub>4</sub>O<sub>12</sub>), the structure becomes very rigid because the octahedral (TiO<sub>6</sub>) in the structure have tilted to produce square planar of CuO<sub>4</sub>. Thus, the space for the Ca<sup>2+</sup> and Cu<sup>2+</sup> cations in CCTO structure was essentially fixed. For Ca<sub>0.925</sub>Y<sub>0.05</sub>Cu<sub>3-x</sub>Zn<sub>x</sub>Ti<sub>4</sub>O<sub>12</sub>, both ionic radii of Y<sup>3+</sup> and Ca<sup>2+</sup> ions are much larger than that of Zn<sup>2+</sup> and Cu<sup>2+</sup> ions. Thus, substitution of Y<sup>3+</sup> ions into Cu<sup>2+</sup> sites may be difficult because the larger ionic radius. Conversely, it is possible that Zn<sup>2+</sup> dopant can substitute into Ca2+ sites. In this case, the lattice parameter of Ca0925Y005Cu3- $_{x}Zn_{x}Ti_{4}O_{12}$  should be reduced as  $Zn^{2+}$  doping concentration increased from x =0.05-0.30. However, it was found that the lattice parameter increased with increasing Zn<sup>2+</sup>. Therefore, it is reasonable to suggest that Y<sup>3+</sup> and Zn<sup>2+</sup> doing ions prefer to substitute into Ca<sup>2+</sup> and Cu<sup>2+</sup> sites, respectively.

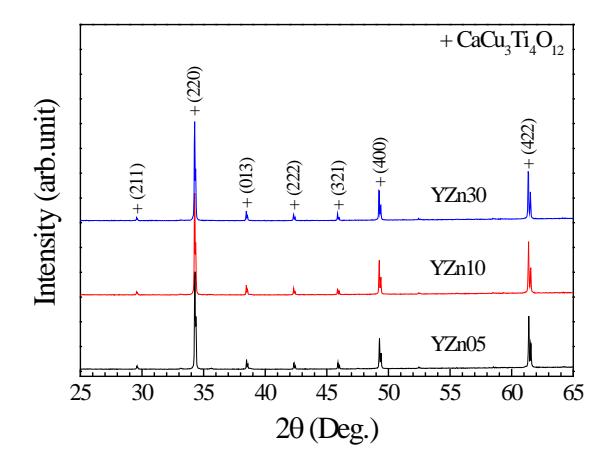


Fig. 1 XRD patterns of YZ–CCTO ceramics.

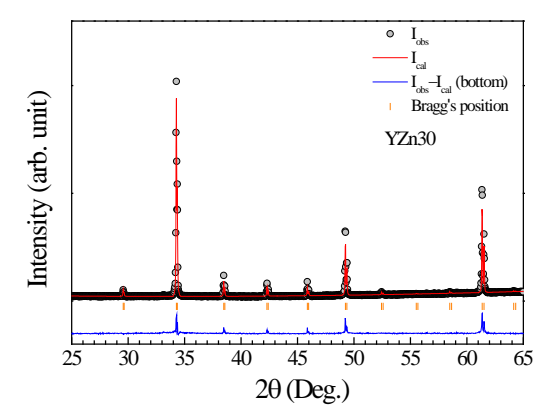


Fig. 2 Profile fits for the Rietveld refinement of the YZn30 ceramic.

Fig. 3. A small number of pores were observed in all the ceramics. Grain sizes of the YZn05, YZn10, and YZn30 ceramics are ~2 observed in all YZ -CCTO ceramics co previously reported [16], the effect of the Y3+ dopant on the reduction in the grain growth rate of CCTO ceramics was observed. The average grain sizes observed in the YZn05, YZn10, and YZn30 ceramics are similar to those reported for  $Ln^{3+}$ -doped CCTO ceramics [11, 16, 19, 20]. A strong reduction of the grain growth rate in the YZ -CCTO ceramics is likely attributable to the solute drag mechanism of the Y dopant [29]. The different ionic radii of dopant and host ions caused lattice strain. Segregation of Y3+ ions at the grain boundaries of CCTO reduced the driving force for grain boundary motion [11]. In this way, the growth of YZ €TO ceramics grains was inhibited.

Surface microstructures of the YZn05, YZn10, and YZn30 ceramics are shown in

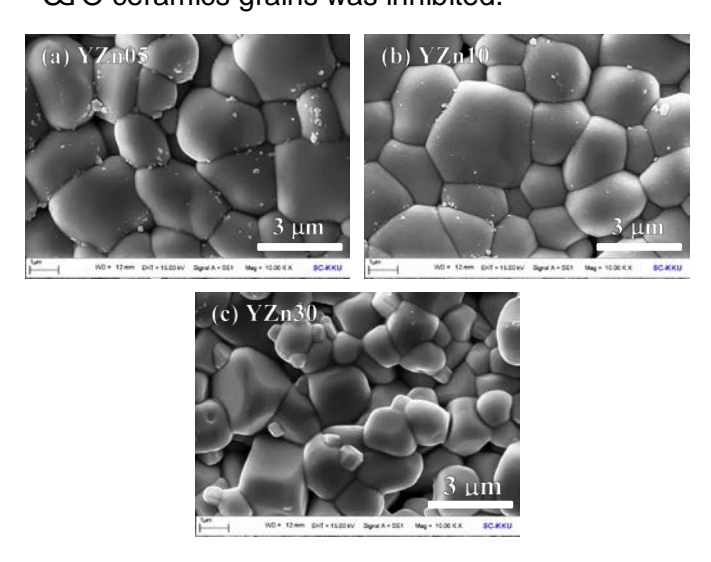


Fig. 3 SEM images of surface microstructures of (a) YZn05, (b) YZn10, and (c) YZn30 ceramics.

Frequency dependencies of ε <sup>2+</sup> increases with inc measured frequency range, it is found that ε concentration. A sudden drop in  $\varepsilon'$  values at higher frequencies for all the ceramics is observed. A significant decrease of tanδ in a low frequency range was attributed to DC conduction, which is likely associated with the electrical properties of the grain boundaries [18]. Strongly increased tanδ values in a high frequency range were consistent with the

' and tanδ are show

axis at

-CCTO

-frequency

-frequency

-frequency

observed rapid decrease in the ε' value. These signified primary polarization relaxation in CCTO ceramics [6, 11, 22, 23]. The ε 

<sup>®</sup>QatietseaYZrl05z Yzd 20, and YZn30 ceramics were 4404, 4778, and 4936, respectively, while tanδ values were 0.064, 0.048, and 0.030, respectively. The lowest tanδ value was observed in the YZn30 ceramic, which was 0.012 at 11.2 kHz. The lowest tanδ values of the YZn05 and YZn10 ceramics were 0.053 at 25.1 kHz and 0.038 at 17.8 kHz, respectively.

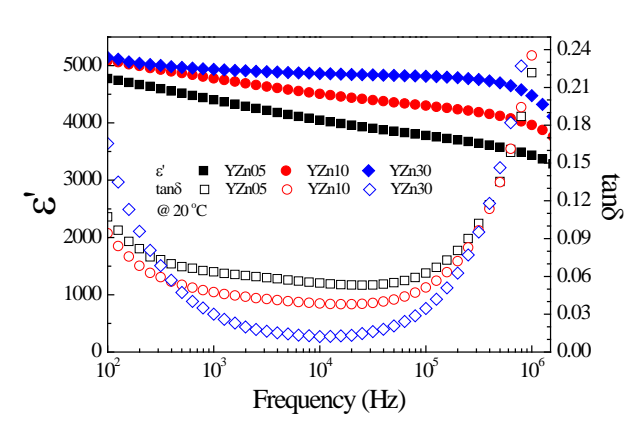


**Fig. 4** Frequency dependence of ε' (solid symbols) and tanδ (open symbols) at 20 °C for YZ–CCTO ceramics.

Generally,  $R_g$  and  $R_{gb}$  values of CCTO ceramics can be determined from Z\* plots.  $R_{gb}$  can be calculated from the diameter of a large semicircular arc in a low frequency range.  $R_g$  is usually estimated from the nonzero intercept on the Z frequencies when the measurement temperature was not too low. According to the equivalent circuit, consisting of parallel  $R_{gb}C_{gb}$  elements of the grain and grain boundary, when the semicircular arc of the grain response cannot be observed, Z\* can be expressed as:

$$Z^* = R_g + \frac{R_{gb}}{1 + (j\omega R_{gb} C_{gb})^{\alpha}}$$
 (1)

where  $C_{\text{g}}$  and  $C_{\text{gb}}$  are the capacitance values of the grain and grain boundary, respectively. ω is the angular frequency of an applied electric field. The C<sub>g</sub> value cannot be determined and the respective capacitor can simply be left out of the circuit. The experimental data was better fitted by applying a constant parameter  $\alpha$  (0 <  $\alpha$  ≤ 1). As demonstrated in Fig. 5, Z\* at 70 °C of all samples were well fitted by Eq. (1). Accordingly, R<sub>ab</sub> and C<sub>ab</sub> values were obtained. The R<sub>ab</sub> and C<sub>ab</sub> values at temperatures higher than 70 °C can also be derived from fitted data. C<sub>gb</sub> values at 70 °C of the YZn05, YZn10, and YZn30 ceramics were 0.48, 0.51, and 0.53 nF, respectively. The increases in C<sub>gb</sub> and were associated with the electrical response of the grain boundaries [16]. Rab values at 70 °C were ~2.18×10<sup>6</sup>, 2.34×10<sup>6</sup>, and 1.48×10<sup>6</sup> Ω.cm for the YZn05, YZn10, and YZn30 ceramics, respectively. As shown in the inset of Fig. 5, the Ra value of YZ ceramics changed slightly when the Zn2+ concentration was increased. It was observed that changes in the R<sub>ab</sub> value were consistent with variations in the low value (f < 500 Hz) [Fig. 4]. This indicated that the low ceramics was likely caused by DC conduction. The highest low the YZn30 ceramic was clearly consistent with its lowest R<sub>gb</sub> value.

The electrical responses of grains and grain boundaries were also investigated under an applied DC bias voltage. It is important to note that the double Schottky barriers in CCTO polycrystalline ceramics can be created at the interface between the n-type semiconducting grain and the insulating grain boundaries. This is because of charge trapping at unknown acceptor states. Trapping of charges can cause bending of the conduction band across the grain boundary [27]. As shown in Fig. 6, R<sub>ab</sub> of the YZn30 ceramic at 150 °C significantly decreased from 37.5 -30.3 k increased from 0 ā 3√2a√s, alvhöstRunchanged [Inset 1 of Fig. 6]. The decrease in R<sub>ab</sub> as a result of DC bias was reported by others [30]. The significant reduction in R<sub>ab</sub> with an increase in the DC bias is consistent with the increase in low -frequency tan value (not shown). As shown in Inset 2 of Fig. 6, the low-frequency AC conductivity (σ which is usually estimated to be equal to the DC conductivity, was significantly increased with increasing DC bias voltage. This is consistent with the reduced R<sub>qb</sub> values and increased low - Concerning to R o δ may be due the reduction in the potential barrier height at the grain boundary [27]. This is consistent with the Schottky barrier model for the grain boundary, at which the potential barrier height was reduced.

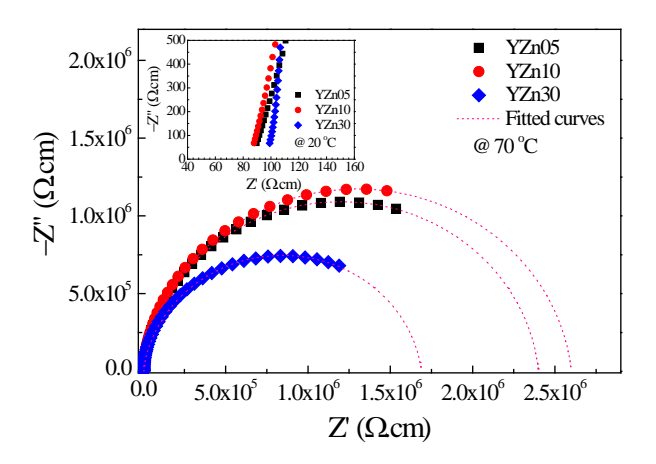


Fig. 5 Impedance complex plane (Z\*) plots of YZ–CCTO ceramics at 70 °C; inset shows high frequency Z\* plots at 20 °C.

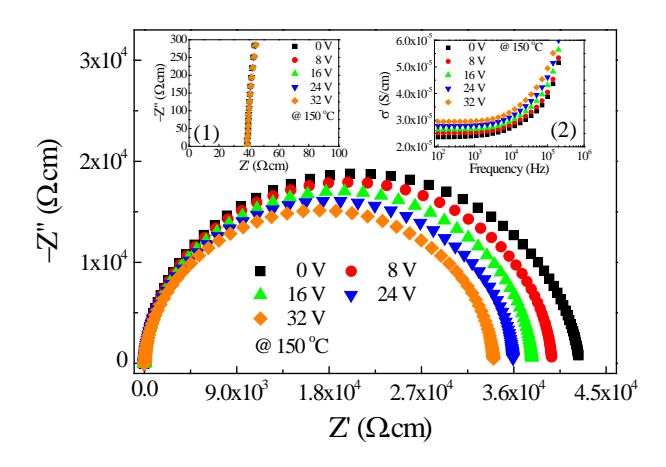
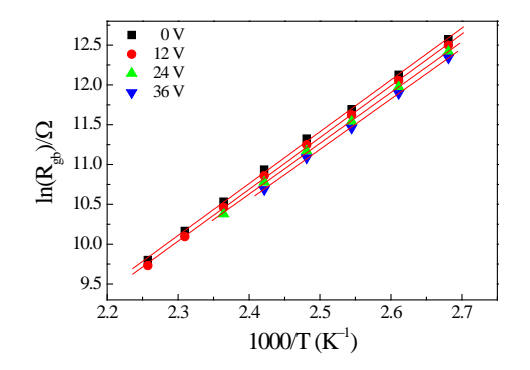


Fig. 6 Impedance complex plane (Z\*) plots for YZn30 ceramic at 150 °C under DC biases from 0–32 V. Insets (1) and (2) show expanded views of high frequency Z\* plots and AC conductivity of YZn30 ceramics, respectively.

-CCTO ce



**Fig. 7** Arrhenius plots of  $\sigma_{qb}$  as a function of DC bias voltage for the YZn30 ceramic.

The effect of DC bias on the temperature dependence of  $R_{gb}$  is demonstrated in Fig. 7.  $R_{gb}$  values at different temperatures for the YZn30 ceramic decreased with increasing DC bias. Using the Arrhenius plots of  $R_{gb}$  values,  $E_{gb}$  values at different DC bias voltages were calculated. As shown in Fig. 8, it was found the  $E_{gb}$  values of all the ceramics were reduced by applying DC bias, especially at high voltages. The DC bias reduced the potential barrier height and thus decreased  $E_{gb}$ . This result is similar to that reported by Adams *et al.* [27]. The potential barrier height of grain boundaries of the YZn30 ceramic decreased from 0.561 to 0.547 eV when the DC bias was increased from 0 to 36 V. As shown in Fig. 8, variations in the potential barrier heights of the YZn05 and YZn10 ceramics had a similar tendency. The potential barrier heights at the grain boundaries for all samples were significantly decreased with increasing DC bias. The DC bias experiment clearly showed that the grain boundary response is consistent with a Schottky barrier response Therefore, it is reasonable to suggest that YZ behavior.

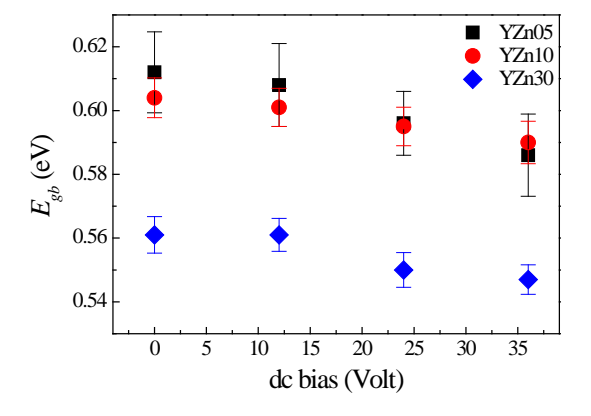


**Fig. 8** Relationship between  $E_{gb}$  values and DC bias voltage for YZ–CCTO ceramics.

According to previous works [7, 8, 20, 28, 31], hopping of charge carriers between  $Cu^+\leftrightarrow Cu^{2+}$ ,  $Cu^{3+}\leftrightarrow Cu^{2+}$ , and  $Ti^{3+}\leftrightarrow Ti^{4+}$  sites in the CCTO- type structure may have had an influence on conduction inside the grains. Thus, the origin(s) of semiconductive grains is likely complex. As demonstrated in Fig. 9, the oxidation states of polyvalent cations of YZ

—Corection of Cu2n consisted of three peaks. The main peak at a

profile fitting, the XPS spectrum of Cu2p consisted of three peaks. The main peak at a binding energy of about ≈933.95 eV can be referred to the presence as Cu<sup>2+</sup>. Another two peaks at relatively lower (≈932.32 eV) and higher (≈935.72 eV) binding energies indicated

the existence of  $Cu^+$  and  $Cu^{3+}$ , respectively. The relative amounts of  $Cu^+$ ,  $Cu^{2+}$  and  $Cu^{3+}$  were calculated and found to be 38.42, 52.93 and 8.65% respectively. It is notable that  $Ti^{3+}$  cannot be extracted from the  $Ti\ 2p$  peak, which was may be due to a small amount of  $Ti^{3+}$  ions.

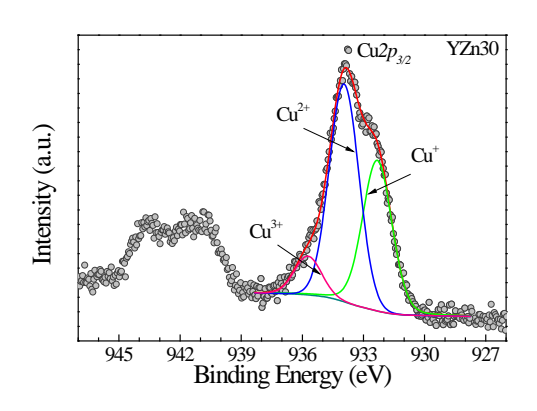


**Fig. 9** XPS spectrum of Cu 2p region of YZn30 ceramic.

#### 8.4 Conclusions

(Y+Zn) co -doped CCTO cera sol  $\frac{2}{2}$  borearthod. The lattice proceduration. The microstructure was slightly changed with varying Zn<sup>2+</sup> concentration at a sintering of 1055 °C for 6 h. High  $\epsilon' \approx 4400$   $\approx 500000$  and very -0.06 we keew tan observed in YZ -CCTO ceramics.

consistent with their changes in  $R_{gb}$ . It was found that the  $R_{gb}$  value at any temperature decreased with increasing applied DC bias voltage, while  $R_g$  did not change.  $E_{gb}$  was reduced by applying a DC bias, indicating a reduction in the Schottky barrier height at the grain boundaries. The giant dielectric response in these co  $\frac{1}{100}$  predaction can be well described by the IBLC effect based on the formation of Schottky barriers at the grain boundaries.

#### References

- [1] M.A. Subramanian, D. Li, N. Duan, B.A. Reisner, A.W. Sleight, High Dielectric Constant in ACu<sub>3</sub>Ti<sub>4</sub>O<sub>12</sub> and ACu<sub>3</sub>Ti<sub>3</sub>FeO<sub>12</sub> Phases, J. Solid State Chem., 151 (2000) 323-325.
- [2] S.-Y. Chung, I.-D. Kim, S.-J.L. Kang, Strong nonlinear current–voltage behaviour in perovskite-derivative calcium copper titanate, Nat. Mater., 3 (2004) 774-778.
- [3] D.C. Sinclair, T.B. Adams, F.D. Morrison, A.R. West,  $CaCu_3Ti_4O_{12}$ : One-step internal barrier layer capacitor, Appl. Phys. Lett., 80 (2002) 2153.
- [4] W.C. Ribeiro, R.G.C. Araújo, P.R. Bueno, The dielectric suppress and the control of semiconductor non-Ohmic feature of  $CaCu_3Ti_4O_{12}$  by means of tin doping, Appl. Phys. Lett., 98 (2011) 132906.
- [5] P. Liu, Y. Lai, Y. Zeng, S. Wu, Z. Huang, J. Han, Influence of sintering conditions on microstructure and electrical properties of CaCu<sub>3</sub>Ti<sub>4</sub>O<sub>12</sub> (CCTO) ceramics, J. Alloys Compd., 650 (2015) 59-64.

- [6] R. Schmidt, M.C. Stennett, N.C. Hyatt, J. Pokorny, J. Prado-Gonjal, M. Li, D.C. Sinclair, Effects of sintering temperature on the internal barrier layer capacitor (IBLC) structure in CaCu<sub>3</sub>Ti<sub>4</sub>O<sub>12</sub> (CCTO) ceramics, J. Eur. Ceram. Soc., 32 (2012) 3313-3323.
- [7] L. Ni, X.M. Chen, Enhanced giant dielectric response in Mg-substituted CaCu<sub>3</sub>Ti<sub>4</sub>O<sub>12</sub> ceramics, Solid State Commun., 149 (2009) 379-383.
- [8] L. Ni, X.M. Chen, Enhancement of Giant Dielectric Response in CaCu<sub>3</sub>Ti<sub>4</sub>O<sub>12</sub> Ceramics by Zn Substitution, J. Am. Ceram. Soc., 93 (2010) 184-189.
- [9] T.B. Adams, D.C. Sinclair, A.R. West, Influence of Processing Conditions on the Electrical Properties of CaCu<sub>3</sub>Ti<sub>4</sub>O<sub>12</sub> Ceramics, J. Am. Ceram. Soc., 89 (2006) 3129-3135.
- [10] R. Schmidt, S. Pandey, P. Fiorenza, D.C. Sinclair, Non-stoichiometry in "CaCu<sub>3</sub>Ti<sub>4</sub>O<sub>12</sub>" (CCTO) ceramics, RSC Advances, 3 (2013) 14580-14589.
- [11] J. Boonlakhorn, P. Thongbai, B. Putasaeng, T. Yamwong, S. Maensiri, Very high-performance dielectric properties of Ca<sub>1-3x/2</sub>Yb<sub>x</sub>Cu<sub>3</sub>Ti<sub>4</sub>O<sub>12</sub> ceramics, J. Alloys Compd., 612 (2014) 103-109.
- [12] R. Xue, D. Liu, Z. Chen, H. Dai, J. Chen, G. Zhao, Dielectric and Nonohmic Properties of CaCu<sub>3</sub>Ti<sub>4</sub>O<sub>12</sub>/SrTiO<sub>3</sub> Ceramics, J. Electron. Mater., 44 (2015) 1088-1094.
- [13] M. Ahmadipour, M.F. Ain, Z.A. Ahmad, A Short Review on Copper Calcium Titanate (CCTO) Electroceramic: Synthesis, Dielectric Properties, Film Deposition, and Sensing Application, Nano-Micro Letters, (2016) 1-21.
- [14] A. Khare, S.S. Yadava, K.D. Mandal, N.K. Mukhopadhyay, Effect of sintering duration on the dielectric properties of 0.9BaTiO<sub>3</sub>-0.1CaCu<sub>3</sub>Ti<sub>4</sub>O<sub>12</sub> nanocomposite synthesized by solid state route, Microelectron. Eng., 164 (2016) 1-6.
- [15] M. Ab Rahman, S. Hutagalung, Z. Ahmad, M. Ain, J. Mohamed, The effect of different dopant site (Cu and Ca) by magnesium on CaCu<sub>3</sub>Ti<sub>4</sub>O<sub>12</sub> dielectric properties, J. Mater. Sci.: Mater. Electron., 26 (2015) 3947-3956.
- [16] J. Boonlakhorn, P. Kidkhunthod, B. Putasaeng, T. Yamwong, P. Thongbai, S. Maensiri, Effects of Y doping ions on microstructure, dielectric response, and electrical properties of Ca<sub>1-3x/2</sub>Y<sub>x</sub>Cu<sub>3</sub>Ti<sub>4</sub>O<sub>12</sub> ceramics, J. Mater. Sci.: Mater. Electron., 26 (2015) 2329-2337.
- [17] S. De Almeida-Didry, C. Autret, A. Lucas, C. Honstettre, F. Pacreau, F. Gervais, Leading role of grain boundaries in colossal permittivity of doped and undoped CCTO, J. Eur. Ceram. Soc., 34 (2014) 3649-3654.
- [18] R. Xue, G. Zhao, J. Chen, Z. Chen, D. Liu, Effect of doping ions on the structural defect and the electrical behavior of CaCu<sub>3</sub>Ti<sub>4</sub>O<sub>12</sub> ceramics, Mater. Res. Bull., 76 (2016) 124-132.
- [19] K. He, Y. Luo, R. Yu, J. Qi, X. Sun, Y. Yang, H. Xu, J. Ma, D. Xu, Influence of  $Yb_2O_3$  on electrical and microstructural characteristics of  $CaCu_3Ti_4O_{12}$  ceramics, Mater. Res. Bull., (2014).
- [20] P. Thongbai, B. Putasaeng, T. Yamwong, S. Maensiri, Modified giant dielectric properties of samarium doped CaCu<sub>3</sub>Ti<sub>4</sub>O<sub>12</sub> ceramics, Mater. Res. Bull., 47 (2012) 2257-2263.
- [21] L. Sun, R. Zhang, Z. Wang, E. Cao, Y. Zhang, L. Ju, Microstructure and enhanced dielectric response in Mg doped CaCu<sub>3</sub>Ti<sub>4</sub>O<sub>12</sub> ceramics, J. Alloys Compd., 663 (2016) 345-350.
- [22] J. Boonlakhorn, P. Kidkhunthod, P. Thongbai, S. Maensiri, Colossal dielectric permittivity and electrical properties of the grain boundary of  $Ca_{1-3x/2}Yb_xCu_{3-y}Mg_yTi_4O_{12}$  (x=0.05, y=0.05 and 0.30), Ceram. Int., 42 (2016) 8467-8472.
- [23] J. Boonlakhorn, B. Putasaeng, P. Kidkhunthod, P. Thongbai, Improved dielectric properties of (Y + Mg) co-doped CaCu<sub>3</sub>Ti<sub>4</sub>O<sub>12</sub> ceramics by controlling geometric and intrinsic properties of grain boundaries, Materials & Design, 92 (2016) 494-498.

- [24] D. Xu, C. Zhang, Y. Lin, L. Jiao, H. Yuan, G. Zhao, X. Cheng, Influence of zinc on electrical and microstructural properties of CaCu<sub>3</sub>Ti<sub>4</sub>O<sub>12</sub> ceramics prepared by sol–gel process, J. Alloys Compd., 522 (2012) 157-161.
- [25] L. Bai, Y. Wu, L. Zhang, Influence of FeNb codoping on the dielectric and electrical properties of CaCu<sub>3</sub>Ti<sub>4</sub>O<sub>12</sub> ceramics, J. Alloys Compd., 661 (2016) 6-13.
- [26] L. Liu, H. Fan, P. Fang, X. Chen, Sol-gel derived CaCu<sub>3</sub>Ti<sub>4</sub>O<sub>12</sub> ceramics: Synthesis, characterization and electrical properties, Mater. Res. Bull., 43 (2008) 1800-1807.
- [27] T. Adams, D. Sinclair, A. West, Characterization of grain boundary impedances in fine- and coarse-grained CaCu<sub>3</sub>Ti<sub>4</sub>O<sub>12</sub> ceramics, Phys. Rev. B, 73 (2006) 094124.
- [28] M. Li, G. Cai, D.F. Zhang, W.Y. Wang, W.J. Wang, X.L. Chen, Enhanced dielectric responses in Mg-doped CaCu<sub>3</sub>Ti<sub>4</sub>O<sub>12</sub>, J. Appl. Phys., 104 (2008) 074107.
- [29] J.W. Cahn, The impurity-drag effect in grain boundary motion, Acta Metallurgica, 10 (1962) 789-798.
- [30] M. Li, X.L. Chen, D.F. Zhang, Q. Liu, C.X. Li, The effect of grain boundary resistance on the dielectric response of  $CaCu_3Ti_4O_{12}$ , Ceram. Int., 41 (2015) 14854-14859.
- [31] J. Jumpatam, A. Mooltang, B. Putasaeng, P. Kidkhunthod, N. Chanlek, P. Thongbai, S. Maensiri, Effects of  $Mg^{2+}$  doping ions on giant dielectric properties and electrical responses of  $Na_{1/2}Y_{1/2}Cu_3Ti_4O_{12}$  ceramics, Ceram. Int., 42 (2016) 16287-16295.

#### **CHAPTER 9**

# Improved Giant Dielectric Properties of CaCu<sub>3</sub>Ti<sub>4</sub>O<sub>12</sub> via Simultaneously Tuning Electrical Properties of Grains and Grain Boundaries by F<sup>-</sup> Substitution

#### 9.1 Introduction

Recently, oxide materials with giant dielectric permittivity found an important role in microelectronic devices and high–density storage applications such as capacitors and memory devices.  $^{1-4}$  One of the most interesting giant dielectric materials is CaCu<sub>3</sub>Ti<sub>4</sub>O<sub>12</sub> (CCTO) ceramics. CCTO exhibited giant dielectric permittivity ( $\epsilon' > 10^4$  at 1 kHz) over a wide temperature range from 100 to 600 K.  $^5$  The  $\epsilon'$  value of CCTO ceramics was also weakly dependent on frequency in the radio frequency range. Unfortunately, the loss tangent (tan $\delta$ ) of CCTO was still too large for practical applications in ceramic capacitors.  $^{6-}$ 

Even now, the origin of giant dielectric response is still open to scientific debate. Most research groups believe that the extrinsic origin of the internal barrier layer capacitance (IBLC) mechanism at grain boundaries (GBs) is the primary cause of the giant dielectric response in CCTO ceramics. 12, 14, 20-23 According to the IBLC mechanism, the giant dielectric response in a polycrystalline ceramic is driven by its electrically heterogeneous microstructure. This special microstructure can be fabricated using a onestep processing method that forms insulating GBs sandwiched between *n*-type semiconducting grains. The electrical responses of the grain and GB can have a remarkable influence on the dielectric properties of CCTO ceramics. 12-13, 15, 22 Moreover, due to the existence of this special microstructure, CCTO ceramics can also exhibit the non-Ohmic properties (or nonlinear current density-electric field, *J-E*). 24-25 This special behavior is believed to originate from the existence of an intrinsic potential barrier (*i.e.*, Schottky barrier) at GBs. The presence of an electrostatic barrier at the GBs of CCTO ceramic was clearly confirmed using Kervin probe force microscopy. 24

To improve the dielectric properties of CCTO ceramics, most investigations have focused on substitution of one of several doping cations into CCTO ceramics to tune the electrical properties of the grains and GBs. It has been widely demonstrated that enhancement of the GB resistance (R<sub>ab</sub>) can reduce the low-frequency tanδ value.<sup>15, 23, 26</sup> According to the space charge polarization theory (or interfacial polarization), an increase in mobile charges inside the semiconducting grains can lead to the possibility of accumulating free charges at the interface of insulating layers. This gives rise to a stronger intensity of the polarization at internal insulating interfaces, leading to an increase in  $\varepsilon'$ . The giant dielectric properties of CCTO ceramics were first reported by Subramanian et al.<sup>6</sup> There are further several reports of dopant cations substituted into CCTO ceramic such as  $Sr^{2+}$ ,  $^{23}$   $La^{3+}$ ,  $^7$   $Ni^{2+}$ ,  $^{27}$   $Mg^{2+}$ ,  $^{9}$ ,  $^{28-30}$   $Zn^{2+}$ ,  $^{31-32}$   $Ga^{3+}$ ,  $^{14}$   $Zr^{4+}$ ,  $^{33-34}$   $Sn^{4+}$ ,  $^{11}$   $Nb^{5+}$ ,  $^8$   $Ta^{5+}$   $^{12}$  and W<sup>6+</sup>. <sup>13, 35</sup> Substitution of many cations into Ca<sup>2+</sup>, Cu<sup>2+</sup> and Ti<sup>4+</sup> sites in CCTO ceramics have significant effects on the values of their  $\varepsilon'$ ,  $tan\delta$ , electrical conductivity of the GBs  $(\sigma_{ab})$  and activation energies at the GBs  $(E_{ab})$  and inside the grain  $(E_a)$ . Usually, most of these dopants can be successfully used to improve a particular dielectric property (e.g., to reduce  $\tan\delta$  or enhance  $\epsilon'$ ), while they simultaneously worsen other important dielectric properties of these materials. For example, substitution of higher cations into Ti<sup>4+</sup> sites would increase free charges inside the semiconducting grains due to the excess electron of a dopant (e.g., Nb<sup>5+</sup> or Ta<sup>5+</sup>). This can cause an increase in ε', which resulted from the

enhanced space charges at the insulating interfaces. Unfortunately, it also causes a large decrease in  $R_{\text{gb}}$ , leading to a significant increase in a low-frequency  $\tan\delta$ .<sup>8, 12</sup> Alternatively, doping CCTO with Mg<sup>2+</sup> into Cu<sup>2+</sup> sites can decrease tan $\delta$ . However, the  $\epsilon'$ value of Mg-doped CCTO was also decreased due to the decrease in free charges inside the grains, considering by the increase in R<sub>a</sub>. 9, 36

It is expected that doping CCTO with an anion can increase free charges inside the grains due to charge compensation. Substitution of F into O2 sites is electrically compensated by reduction of valance state of Ti<sup>4+</sup> to Ti<sup>3+</sup> and Cu<sup>2+</sup> to Cu<sup>+</sup>. It was clearly demonstrated that filling oxygen vacancies at the GBs can strongly increase the Rab value by annealing in an O<sub>2</sub> atmosphere. <sup>15, 20, 37</sup> Alternatively, R<sub>gb</sub> can be reduced by creating the oxygen vacancies at the grain boundaries via annealing in a N<sub>2</sub> atmosphere. Thus, it is also expected that substitution of F anions may have no effect on the insulating properties of the GBs because oxygen vacancies along the GBs are usually filled during cooling step of the sintering process. This also helps retain the insulating nature of the GBs. To the best our knowledge, there have been few reports of an anion dopant being substituted into CCTO ceramics.<sup>38</sup> The effects of an anion dopant on the microstructure and electrical properties of the grain and GB have never been reported.

In this work, a new strategy to improve the dielectric properties of CCTO ceramics was used by doping with F anions to modify the electrical responses of the grains and GBs. The effects of F<sup>-</sup> anions on the microstructural evolution and associated dielectric properties were studied and discussed. As expected, doping CCTO ceramics with F anions at  $O^{2-}$  sites resulted in improved dielectric properties via a large enhancement of  $\epsilon'$ and significant decrease in  $tan \delta$ .

#### 9.2 **Experimental Procedure**

 $CaCu_3Ti_4O_{12-x}F_x$  ceramics, where x=0, 0.05, 0.1, and 0.2 (referred to as the CCTO, F05, F10 and F20 samples, respectively), were prepared using a solid state reaction method. The starting materials used were CaCO<sub>3</sub> (Aldrich, ≥ 99.0% purity), CuO (Merck, 99% purity), CuF<sub>2</sub> (Sigma <sup>7</sup>/**ASigicha** 99.9% purity) and TiO -Aldrich, 99.9% pur First, a stoichiometric mixture of the starting materials for each composition was mixed by ball milling using zirconia (ZrO<sub>2</sub>) media in ethanol for 12 h. Second, the mixed slurries were dried and calcined at 900 °C for 15 h. Then, the calcined powders were ground and pressed into pellets with 9.5 mm in diameter and 1 compression at 200 MPa. Finally, these pellets were sintered in air at 1075 °C for 3 h.

The phase composition and crystal structure were characterized using X-ray diffraction (XRD; PANanalytical EMPYREAN). Rietveld quantitative phase analysis was done using the X'Pert High Score Plus v3.0e software package by PANalytical. The as-sintered ceramics were carefully polished to obtain smooth surfaces. The grain and GB structure of the polished- samples was formed by thermally etching at 1050 °C for 1 h. Surface morphologies of sintered ceramics were revealed using scanning electron microscopy (SEM; SEC, SNE- 4500M). Elemental distribution of the F dopant atoms and the major elements (i.e., Ca, Cu, Ti, and O) in the sintered CCTO ceramics was examined using a field-emission scanning electron microscopy (FE- SEM) with energy-dispersive X- ray analysis (EDX) (HITACHI SU8030, Japan). X-ray Absorption Near Edge Structure (XANES) spectra were collected at the SUT-NANOTEC-SLRI XAS beamline (BL5.2) (using an electron energy of 1.2 GeV, a bending magnet, beam current of 80 - 150 mA,

-2 mm in thickness

and 1.1 to  $1.7 \times 10^{11}$  photons s<sup>-1</sup>) at the Synchrotron Light Research Institute (SLRI), Nakhon Ratchasima, Thailand. Details of this characterization technique have been published. The normalized XANES data were processed and analyzed after background subtraction in the pre–edge and post–edge region using ATHENA software that is included in the IFEFFIT package. The chemical states of Cu and Ti were analyzed using X–ray photoelectron spectroscopy (XPS), PHI5000 VersaProbe II, ULVAC–PHI, Japan) at the SUT–NANOTEC–SLRI Joint Research Facility, Synchrotron Light Research Institute (SLRI), Thailand. The XPS spectra were fitted using PHI MultiPak XPS software with a combination of Gaussian–Lorentzian lines.

Before electrical measurements, both surfaces of the sintered ceramics were polished until smooth, washed, and dried at 150 °C overnight. The polished samples were coated by sputtering Au on their surfaces for 8 min at 25 mA using a Polaron SC500 sputter coating unit. The dielectric properties were measured over the temperature range of -70- 220 °C using a KEYSIGHT E4990A Impedance Analyzer in the frequency range of  $10^2$ -  $10^7$  Hz with an oscillation voltage of 0.5 V. Each measurement temperature was kept constant with a precision of  $\pm 0.1$  °C. Nonlinear J-E properties at room temperature (RT) were determined using a high voltage measurement unit (Keithley Model 247). The breakdown electric field ( $E_b$ ) was achieved at J=1 mA.cm<sup>-2</sup>. The nonlinear coefficient ( $\alpha$ ) was calculated using the following formula:

$$\alpha = \frac{\log(J_2/J_1)}{\log(E_2/E_1)}$$
 (1)

where  $E_1$  and  $E_2$  are the applied electric fields, at  $J_1 = 1$  and  $J_2 = 10$  mA.cm<sup>-2</sup>, respectively.

#### 9.3 Results and discussion

The crystal structure and phase composition of all the sintered ceramic samples were studied. Figure 1 shows the Rietveld refinement profile fits of the XRD patterns for all the samples. The profile fits confirmed the formation of a single CCTO phase (JCPDS 75–2188) in the CCTO and all F'–doped CCTO (CCTOF) ceramics. It was found that all the diffraction peaks were well indexed based on the *bcc* structure within space group  $\text{Im}\,\overline{3}$ . Impurities (e.g.,  $\text{TiO}_2$ , CuO,  $\text{Cu}_2\text{O}$  and  $\text{CaTiO}_3$ ) were not seen in the profile fits. The lattice parameters (a) of all the samples are summarized in Table 1. The *a* values of all the samples can be compared to 7.391 Å for un–doped CCTO (JCPDS 75-2188). It is notable that the *a* values of CCTOF did not change with F' dopant concentration. This result is similar to that reported in previous work with  $\text{CaCu}_3\text{Ti}_4\text{O}_{12\text{-x}}\text{F}_x$  where x=0–0.2.<sup>38</sup> The unchanged lattice parameter was likely because the ionic radii of the substituted F' anion ( $r_4$  = 1.31 Å) and the host  $\text{O}^2$ - ion ( $r_4$  = 1.38 Å) are not greatly different.<sup>40</sup>

Surface morphologies of the CCTO and CCTOF ceramics sintered at 1075  $^{\circ}$ C for 3 h are shown in Fig. 2. As can be clearly seen, there was abnormal grain growth in the microstructure of the CCTO ceramic, where the large sized grains ( $\approx 30-50~\mu m$ ) were surrounded by small grains ( $\approx 5-10~\mu m$ ). This is generally reported in literature and was ascribed to the liquid phase sintering mechanism. <sup>14, 26, 32</sup> It was found that the mean grain size of CCTO ceramics was greatly enlarged by doping with F anions. Almost all grains of the F05, F10 and F20 samples were very large ( $\approx 40-100~\mu m$ ).

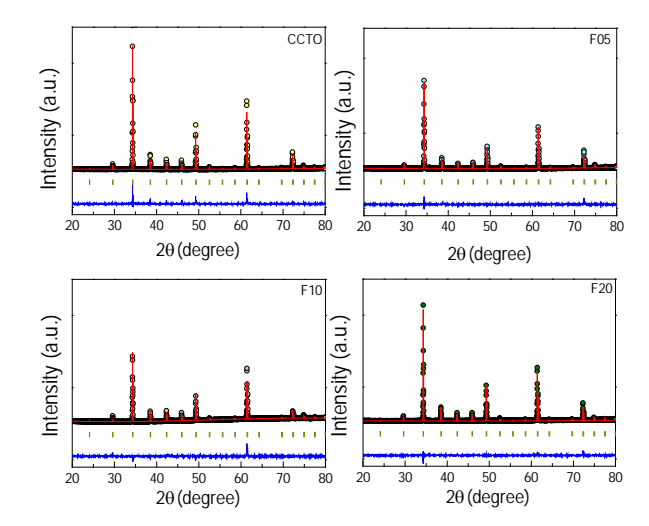


**Fig. 1** Profile fits for the Rietveld refinements of the XRD patterns of CCTO, F05, F10 and F20 samples.

**Table 1** Lattice parameter (a), dielectric permittivity ( $\epsilon$ ') and loss tangent ( $\tan \delta$ ) at RT and 1 kHz, conduction activation energies of the grain ( $E_g$ ) and grain boundary ( $E_{gb}$ ), nonlinear coefficient ( $\alpha$ ) and nonlinear breakdown electric field ( $E_b$ ).

Samples	a (Å)	ε'	$tan\delta$	$oldsymbol{\mathcal{E}}_{ extsf{g}}$	$oldsymbol{\mathcal{E}}_{gb}$	α	$E_{b}$
ССТО	7.393(2)	23,263	0.145	0.083	0.630	3.77	308.1
F05	7.393(9)	69,732	0.098	0.091	0.696	3.57	345.5
F10	7.392(7)	81,306	0.077	0.091	0.714	3.58	331.5
F20	7.393(8)	98,396	0.087	0.116	0.739	4.18	345.8

Usually, the grain growth mechanism of a polycrystalline ceramic is associated with mass transport by diffusion of ions (or atoms) across the GB layer. During sintering, the dopant directly melts and/or reacts with a small part of the major phase to form a eutectic liquid. These can cause a formation of a liquid phase in the microstructure. The liquid was present at the contact areas between the particles in the ceramic microstructure. This can contribute to promotion of the diffusion of ions. For polycrystalline ceramics, a liquid phase generally originates from a eutectic liquid. The eutectic temperature for CuO–TiO<sub>2</sub> is about 950 °C for CCTO ceramics. Although the liquid phase formed by melting of the dopant usually occurs in metallic systems, it is also possible in CCTOF ceramics. This is due to the low melting point of CuF<sub>2</sub> (836 °C). Thus, the formation of a liquid phase is likely caused by these two mechanisms. Enhancement of GB mobility resulted from the presence of the liquid phase(s) and was suggested an important factor for increasing grain growth rate in CCTOF ceramics.

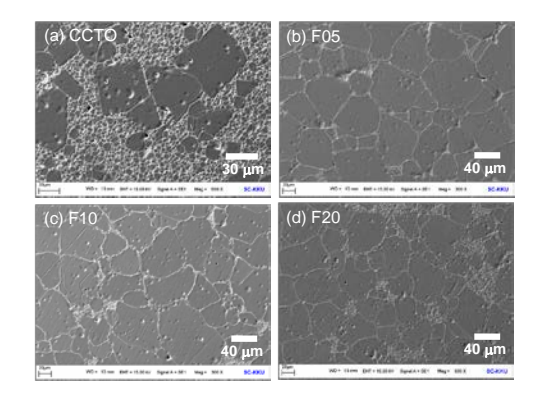


**Fig. 2** SEM images of polished surfaces of (a) CCTO, (b) F05, (c) F10 and (d) F20 samples.

Figure 3 shows the SEM mapping images of the F05 sample. This result confirms the existence of all major elements (*i.e.*, Ca, Cu, Ti, and O) and confirms the homogeneous dispersion of F<sup>-</sup> dopant in both of the grains and GBs. Segregation of the F<sup>-</sup> dopant in any specific region was not seen. In contrast, segregation of Cu was observed along the GBs, which is also generally reported in previous studies.<sup>22</sup> This result strongly confirms that the liquid phase is closely associated with a Cu–rich phase, which likely originated from melting of CuF<sub>2</sub> and the eutectic phase of CuO–TiO<sub>2</sub>.

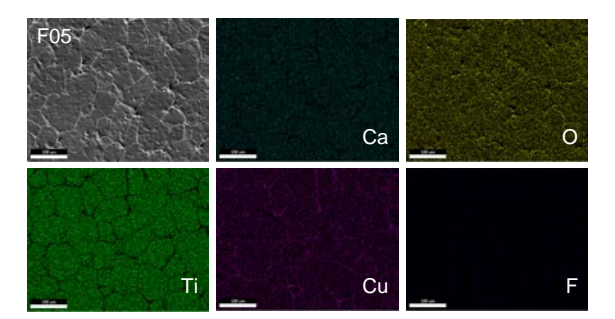


Fig. 3 Element mapping of the F05 sample for Ca, Cu, Ti, O and F.

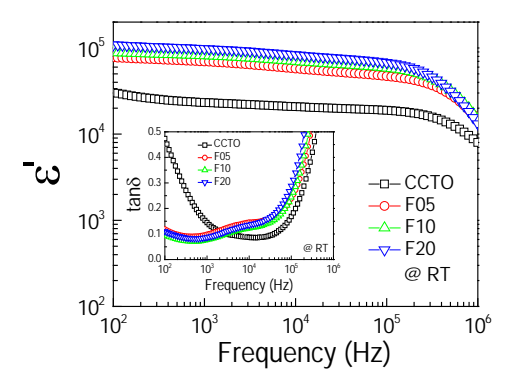


Fig. 4 Frequency dependency of dielectric permittivity ( $\epsilon$ ') at RT for CCTO, F05, F10 and F20 samples; inset show the loss tangent ( $\tan \delta$ ) as a function of frequency at RT.

The frequency dependence of the dielectric properties of all the ceramic samples is shown in Fig. 4.  $\varepsilon'$  was slightly dependent on frequency in the range of  $10^2-10^5$  Hz. Notably,  $\varepsilon'$  can be enhanced from  $\approx 10^4$  to  $\approx 10^5$  by doping with F<sup>-</sup> anions. Considering the microstructural change in CCTOF ceramics, the enlarged grain size is one of the most important parameters that increased ε'. However, the linear and continuous increase in ε' of the F-doped CCTO ceramics was not correlated with their grain sizes. ε' increased with increasing anion dopant concentration, but not for the mean grain sizes. Therefore, variation in ε' cannot be attributed to the change in the microstructure only. As illustrated in the inset of Fig. 4, a low-frequency tanδ of CCTO ceramics was greatly decreased by doping with F<sup>-</sup> anions. At 10<sup>2</sup> Hz, the tanδ of the CCTOF ceramics was reduced by a factor of 5. At frequencies higher than 10<sup>5</sup> Hz, the frequency dependent behaviors of tanδ for all of the samples were similar, i.e.,  $tan\delta$  increased with increasing frequency. This indicates the dielectric relaxation behavior of primary polarization, which will be discussed below. The  $\varepsilon'$  and tan $\delta$  values at RT and 1 kHz of all the ceramic samples are summarized in Table 1. It is notable that the low–frequency tanδ of the CCTOF ceramics was significantly reduced to < 0.1, while  $\varepsilon'$  greatly increased. Generally, this result is hard to achieve in CCTO ceramics because variations in  $tan\delta$  and  $\epsilon'$  values are usually directly proportional. The  $\epsilon'$  and  $tan\delta$  values of the CCTO and CCTOF ceramics compared to those reported in literature for both of un-doped and metal ions-doped CCTO ceramics prepared by using different method and sintered under various conditions are shown in Table 2.

The dielectric relaxation behavior of CCTO and CCTOF ceramics was studied. As shown in Fig. 5, two dielectric relaxations were observed in distinct frequency ranges. The low–frequency dielectric relaxation likely originated from the sample–electrode effect. The relatively high–frequency dielectric relaxation (*i.e.*, the primary relaxation) has widely been accepted as associated with the IBLC effect, i.e., the Maxwell–Wagner polarization relaxation. The step–like decrease in  $\varepsilon'$  and relaxation peak of  $\varepsilon''$  ( $\varepsilon''$  is the imaginary part of the complex dielectric permittivity or dielectric loss,  $\varepsilon'' = \varepsilon' \times \tan \delta$ ) shifted to a higher frequency with increasing temperature, indicating a thermally activated relaxation mechanism. The activation energy for dielectric relaxation can be calculated from the critical frequency ( $f_{max}$ ) at various temperatures at which the relaxation peak appeared as:

$$f_{\text{max}} = f_0 \exp\left(\frac{-E_a}{k_B T}\right),\tag{2}$$

where  $f_0$  is the pre–factor,  $E_a$  is the activation energy required for relaxation process, T is absolute temperature and  $k_B$  is Boltzmann constant. The frequency dependence of  $f_{\rm max}$  for all the samples obeyed the Arrhenius law in Eq. (2), inset of Fig 5(d). The  $E_a$  values of the CCTO, F05, F10 and F20 samples were about 0.096, 0.096, 0.099 and 0.115 eV, respectively. These values are comparable to the reported values of 0.103 eV, $^{32}$  0.011 eV $^{11}$  and 0.101 eV. $^{28}$  Doping CCTO with F $^-$  anions into O $^{2-}$  sites has a small influence on the dielectric–relaxation activation energy of CCTO ceramics.

**Table 2** Dielectric permittivity ( $\epsilon'$ ) and loss tangent (tan $\delta$ ) at RT and 1 kHz of un–doped CCTO and metal ion–doped CCTO ceramics doping with different ions.

Doped–CCTO ceramics (preparation method)	Sintering condition	ε'	tanδ
Ni-doped CCTO (SSR method) [44]	1040 °C / 4 h	69,833	0.073
Sn-doped CCTO (SSR method) [44]	1040 °C / 4 h	51,443	0.061
Si-doped CCTO (SSR method) [44]	1040 °C / 4 h	55,240	0.136
Al-doped CCTO (SSR method) [44]	1040 °C / 4 h	30,226	0.100
Un-doped CCTO (SSR method) [44]	1040 °C / 4 h	45,972	0.109
Un-doped CCTO (sol-gel method) [16]	1060 °C / 48 h	~42,250	~0.15
Un-doped CCTO (SSR method) [17]	1060 °C / 48 h	~100,000	~1.0
Un-doped CCTO (molten salt method) [19]	1060 °C / 1 h	~10,000	~0.15
	1060 °C / 3 h	~10,000	~0.15
Un-doped CCTO (SSR method with quenching in water) [18]	1060 °C / 3 h	~17,500	~0.085
Un-doped CCTO (SSR method) [in this work]	1075 °C for 3 h	23,263	0.145
CaCu <sub>3</sub> Ti <sub>4</sub> O <sub>11.9</sub> F <sub>0.10</sub> (SSR method) [in this work]	1075 °C for 3 h	81,306	0.077

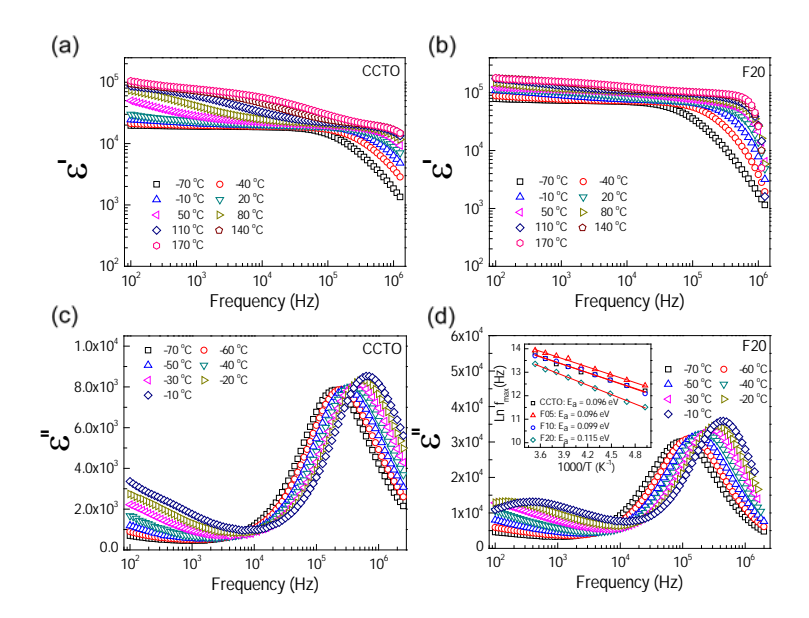


Fig. 5 Frequency dependencies of dielectric permittivity ( $\epsilon$ ') and loss tangent ( $\tan \delta$ ) at various temperatures for (a,c) CCTO and (b,d) F20 samples; inset of (d) shows Arrhenius plots of  $f_{\text{max}}$  for the dielectric relation.

To elucidate the influences of F anion dopant ions on the dielectric properties of CCTO ceramics, the grain and GB responses were studied using an impedance spectroscopy technique. Figures 6(a) and (b) show Z\* plots for all the samples at RT and

80 °C, respectively. Only the linear part of the semicircular arcs was observed at RT in the frequency range of 10<sup>2</sup>–10<sup>6</sup> Hz. A nonzero intercept on the Z' axis was observed, inset of Fig. 6(a), indicating an electrical response of the semiconducting grains. 42-43 Thus. the linear part of the semicircular arcs should be due to the electrical response of the GBs. The grain resistance  $(R_{\sigma})$  values (estimated from the nonzero intercept) of the CCTOF ceramics were smaller than that of the undoped CCTO ceramic by a factor of 2. At RT,  $R_{\rm q}$ of the CCTO sample was  $\approx 100 \,\Omega.\text{cm}$ , while  $R_q$  values of the CCTOF ceramics were nearly the same in value with  $R_{\rm q} \approx 50~\Omega.{\rm cm}$ . At RT, it is very difficult (or perhaps impossible) to accurately calculate the value of  $R_{ab}$  in the measured frequency range since just few data points on the full arcs appeared in these  $Z^*$  plots. The trend of  $R_{ab}$ values for the CCTOF ceramics cannot be determined. To obtain this, a Z\* plot at a high temperature should be performed. In Fig. 7(b), the  $R_{\rm gb}$  of each sample was estimated and found to be significantly increased by doping with  $F^-$ .  $R_{gb}$  of the CCTOF ceramics was enhanced even through the mean grain size increased compared to that of the CCTO sample. This result gives a significant clue, reflecting the largely enhanced resistance of individual GB layers. This is one of the most important factors contributing to reduction in a low-frequency tanδ in CCTOF ceramics [inset of Fig. 4]. Thus, the distribution of dopants near GBs can cause an increase in the GB resistivity, which often make great influence on the low-frequency dielectric properties,44 as clearly seen in Fig. 5. It is worth noting that all the samples were electrically heterogeneous, consisting of grains with very small  $R_g$  values and very high values of  $R_{gb}$ . Therefore, it is reasonable to suggest that the giant dielectric response in CCTOF ceramics originated from the IBLC effect.

 $R_{\rm g}$  and  $R_{\rm gb}$  values can be calculated in various temperatures. The conductivities of the grain  $(\sigma_{\rm g})$  and GB  $(\sigma_{\rm gb})$  were calculated from  $R_{\rm g}$  and  $R_{\rm gb}$ , respectively. As demonstrated in Figs. 6(c) and (d), the temperature dependencies of  $\sigma_{\rm g}$  and  $\sigma_{\rm gb}$  follow the Arrhenius law:

$$\sigma_{g/gb} = \sigma_0 \exp\left(\frac{-E_{g/gb}}{k_B T}\right),\tag{3}$$

where  $\sigma_0$  is a constant value and  $E_g$  and  $E_{gb}$  are the conduction activation energies inside the grains and GBs, respectively. The  $E_{gb}$  values of the CCTO, F05, F10 and F20 samples were about 0.630, 0.696, 0.714 and 0.739 eV, respectively. The  $E_g$  values for all the samples are summarized in Table 1.  $E_g$  slightly increased with increasing  $F^-$  dopant concentration. It was observed that the trends of variation in  $E_g$  and  $E_a$  values were similar. According to the Maxwell–Wagner polarization relaxation model, the temperature dependence at the critical frequency,  $f_{max}$ , of a thermally activated relaxation process can be expressed in term of  $R_g$ , as the following:<sup>13, 21</sup>

$$f_{\text{max}} \approx (2\pi R_g C_{gb})^{-1} \approx (2\pi C_{gb})(R_g^0)^{-1} \exp(\frac{-E_g}{k_B T}),$$
 (4)

where  $C_{gb}$  is the capacitance of GBs. From Eq. (2), the temperature dependence of  $f_{max}$  for the dielectric relaxation process in CCTO and CCTOF ceramics follows the temperature dependence of the conduction process of the grains, since  $C_{gb}$  is nearly independent of temperature. According to Eq. (2–4), the activation energies required for electrical conduction in the grain interiors and for dielectric relaxation process should be the very close. Thus, the calculated  $E_a$  and  $E_g$  values strongly confirm that the giant

dielectric response in CCTOF ceramics can be attributed to the Maxwell-Wagner polarization based on the IBLC structural model.

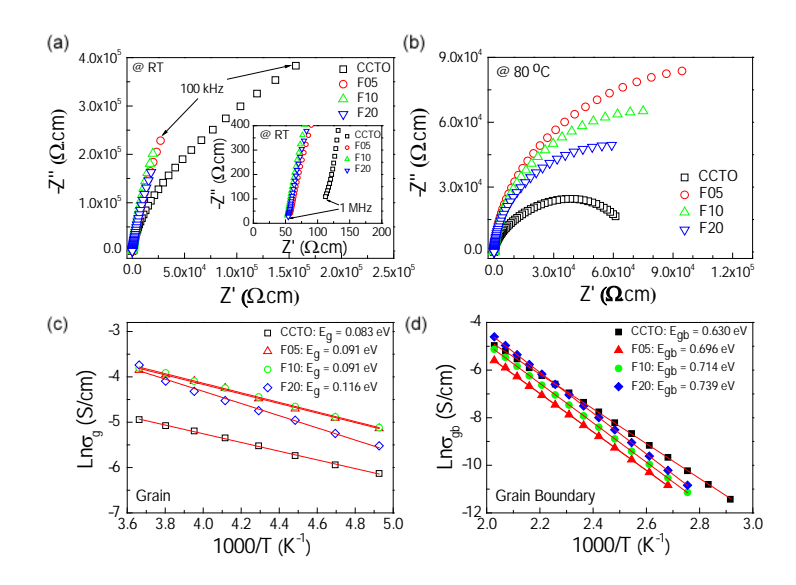


**Fig. 6** (a–b) Impedance complex plane (Z\*) plots of CCTO, F05, F10 and F20 samples at room temperature and 80  $^{\circ}$ C, respectively; inset of (a) shows an expanded view of high frequency Z\* plots at RT, revealing the nonzero intercept on Z' axis. (c–d) Arrhenius plots of  $\sigma_{g}$  and  $\sigma_{gb}$ , respectively.

As shown in the inset of Fig. 6(a),  $R_{\rm g}$  of CCTO ceramics was reduced by doping with F<sup>-</sup> anions, indicating an increase in the concentration of free charge carriers in the grain interiors. To clarify the effect of F<sup>-</sup> doping on the electrical properties of the grains, variation in valence states of Cu<sup>2+</sup> and Ti<sup>4+</sup> ions in CCTO and CCTOF samples was investigated using XPS and XANES techniques. As illustrated in Figs. 7(a) and (c), the main XPS peaks at  $\approx$ 933 eV for the CCTO and F10 samples confirm the existence of large numbers of Cu<sup>2+</sup> ions.<sup>9, 28, 32</sup> The Cu  $2p_{3/2}$  region can be divided into three peaks using Gaussian–Lorentzian profile fitting. The small XPS peaks at relatively lower and higher binding energies at  $\approx$ 931 and  $\approx$ 936 eV indicated the existence of Cu<sup>+</sup> and Cu<sup>3+</sup>, respectively.<sup>9, 28, 32</sup> The Cu<sup>+</sup>/Cu<sup>2+</sup> ratios of the CCTO and F10 samples were, respectively, about 4.26% and 5.65%, while their respective Cu<sup>3+</sup>/Cu<sup>2+</sup> ratios were 13.62% and 27.22%. Doping CCTO with F<sup>-</sup> caused an increase in both Cu<sup>+</sup> and Cu<sup>3+</sup> concentrations.

In addition to Cu<sup>+</sup> and Cu<sup>3+</sup>, the presence of Ti<sup>3+</sup> ions is usually considered a major cause of the formation of n-type semiconducting grains in CCTO ceramics. As depicted in Fig. 7(b) and (d), the primary XPS peak at  $\approx$ 458 eV for Ti<sup>4+</sup> was confirmed in all the samples. Unfortunately, the presence of Ti<sup>3+</sup> cannot be modeled using Gaussian–Lorentzian profile fitting. This may be due to a small amount of Ti<sup>3+</sup> in both the samples.<sup>2</sup> Thus, XANES was used to further investigate to the existence of Ti<sup>3+</sup>. Figure 8 shows normalized Ti K-edge XANES spectra of the CCTO and F10 samples as well as the standard TiO<sub>2</sub> (Ti<sup>4+</sup>) and Ti<sub>2</sub>O<sub>3</sub> (Ti<sup>3+</sup>) samples. It was found that the position of the edge energy of both samples was very close to the TiO<sub>2</sub> standard. As expected, a small amount of Ti<sup>3+</sup> was confirmed to exist. To obtain the ratios of Ti<sup>3+</sup>/Ti<sup>4+</sup>, the edge value was calculated from the maximum value of the first derivative in the edge region.<sup>15</sup> The ratio of

Ti<sup>3+</sup>/Ti<sup>4+</sup> can be calculated from the energy edge value.<sup>39</sup> The ratios of Ti<sup>3+</sup>/Ti<sup>4+</sup> in the CCTO and F10 samples were found to be 0.82% and 2.46%, respectively.

Substitution of  $O^{2^-}$  with  $F^-$  anions requires charge compensation, which can be achieved by reduction in cation valence ( $Cu^{2+} \rightarrow Cu^+$  and  $Ti^{4+} \rightarrow Ti^{3+}$ ). This charge compensation behavior is similar to that observed in the case of  $Y^{3+}$  doped–CCTO ceramics, which  $R_g$  of CCTO was reduced by doping with  $Y^{3+}$ . It is worth noting that the  $Cu^{3+}/Cu^{2+}$  ratio of the F10 sample was significantly increased. As shown in the SEM–mapping image for Cu dispersion, Fig. 3, segregation of Cu–rich phase along the GBs was observed. This indicated the decomposition of CuO from the CCTO lattice, creating cation vacancies. Therefore, it is possible that the increased  $Cu^{3+}/Cu^{2+}$  ratio of the F10 sample might be due to the creation of Cu vacancies.

Generally, the conductivity of n-type semiconducting grains is elevated by increasing the number of free electrons. Thus, the reduction in  $R_g$  of the CCTOF samples should be correlated with the increase in  $Cu^+/Cu^{2+}$  and  $Ti^{3+}/Ti^{4+}$  ratios over those found in the CCTO sample. For p-type semiconductor CuO ceramics, conduction is primarily caused by hole hopping between  $Cu^{3+}\leftrightarrow Cu^{2+}$ . The increase in the  $Cu^{3+}/Cu^{2+}$  ratio may also be an important cause of the reduced  $R_g$ . Form this point of view, hopping of charge carriers between  $Cu^+\leftrightarrow Cu^{2+}$ ,  $Cu^{3+}\leftrightarrow Cu^{2+}$ , and  $Ti^{3+}\leftrightarrow Ti^{4+}$  sites in the CCTO structure can result in electrical conductivity. According to our previous report, we found that the variation in  $R_g$  of  $Na_{0.5}Y_{0.5}Cu_3Ti_4O_{12}$  ceramics was only consistent with a change in the  $Ti^{3+}/Ti^{4+}$  ratio, whereas changes in  $Cu^+/Cu^{2+}$  and  $Cu^{3+}/Cu^{2+}$  ratios was not correlated to  $R_g$  values. The conduction mechanism inside the n-type semiconducting grains might be primarily attributed to electron hopping from a  $Ti^{3+}-O-Ti^{4+}$  to a  $Ti^{4+}-O-Ti^{3+}$ . Hopping of charge carriers between complex defects, i.e.,  $Cu^+-O-Cu^{2+}\leftrightarrow Cu^{2+}-O-Cu^{3+}$ , was likely difficult owing to much different valance states of  $Cu^+$  and  $Cu^{3+}$ .

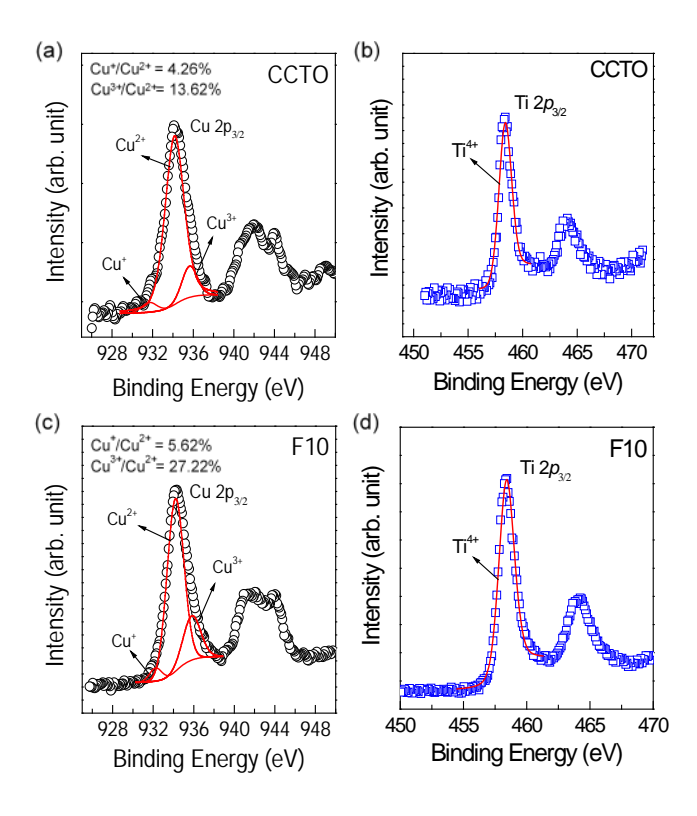


**Fig. 7** Profile XPS spectra of CCTO and F10 samples: (a,c) Ti 2*p* regions and (b,d) Cu 2*p* regions.

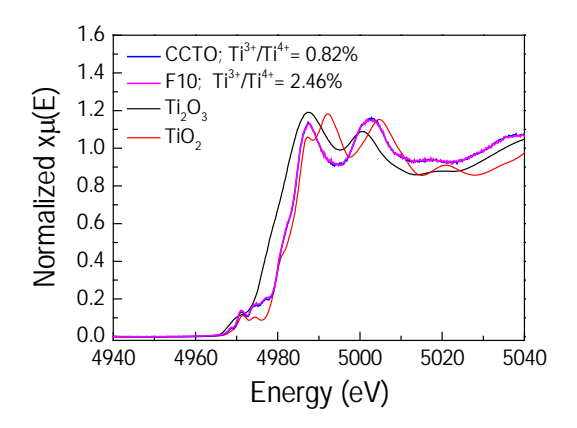


**Fig. 8** Normalized X–ray absorption near edge structure (XANES) spectra for Ti *K*–edge of the CCTO and F10 samples.

The effect of F<sup>-</sup> anions on the non–Ohmic properties of CCTO ceramics is illustrated in Fig. 9. All the samples exhibited nonlinear J-E characteristics. Accordingly,  $E_b$  and  $\alpha$ values were calculated and summarized in Table 1. According to the improved dielectric properties and the observed nonlinear electrical properties of CCTOF ceramics, it was suggested that the sample could be applied as capacitor-varistors. 48  $\alpha$  values for all the samples were not significantly different, while  $E_b$  values of the CCTOF samples were greater than that of the undoped CCTO sample, even though their grain sizes were larger than those of the CCTO sample. The volume fraction of the GB, which is inversely proportional to its mean grain size, was decreased by doping with F<sup>-</sup> anions. The increase in  $E_b$  of the CCTOF samples was consistent with their enhanced  $R_{gb}$  values over that of the CCTO sample. Although the volume fraction of the GB in the CCTOF samples was lower than that of the CCTO sample, the total resistance of their GBs ( $R_{ab}$ ) and  $E_b$  were larger. Thus, the resistivity of an individual GB layer of the CCTOF samples should much be larger than that of the CCTO sample. These results indicate that the intrinsic property (i.e., potential barrier height) of the GB of CCTO ceramics was enhanced by F doping. It was reasonably proposed that based on the n-type semiconducting grains of CCTO ceramics, the electronic energy band structure across the GB layer was equivalent to n-in.20, 49 Double Schottky potential barriers can be created at interfaces between n-type grains caused by trapping at acceptor states. This resulted in the bending of the conduction band across the GB. A potential barrier ( $\Phi_B$ ) was created at the GB sandwiched by n-type semiconducting grains.<sup>20</sup> In the absence of a DC bias,  $\Phi_B$  can be expressed as:

$$\Phi_B = \frac{qN_s^2}{8\varepsilon_0\varepsilon'N_A},\tag{5}$$

where  $N_{\rm s}$  is the acceptor (surface charge) concentration,  $\epsilon'$  is the relative permittivity of materials,  $N_{\rm d}$  is the charge carrier concentration in the semiconducting grains and q is the electronic charge. It was reported that the activation energy for conduction at the GBs has a close relationship with the potential barrier height at the GBs.<sup>10, 20</sup>  $E_{\rm gb}$  and  $\Phi_{\rm B}$  were nearly the same in value. As shown in Fig. 6(d) and Table 1, the enhanced  $E_{\rm gb}$  values indicated an increase in  $\Phi_{\rm B}$ . As demonstrated in the inset of Fig. 6(a),  $R_{\rm g}$  (or  $\sigma_{\rm g}$ ) of all the CCTOF samples was smaller than that of the CCTO sample, indicating that the charge carrier concentration in the semiconducting grains ( $N_{\rm d}$ ) of the CCTOF samples was

higher. This is responsible for the observed increase in the potential barrier height at the GBs in the CCTOF ceramic samples. Generally, it was observed that the mechanism of potential barrier formation in CCTO ceramics was also correlated with oxygen enrichment at the GBs. For this point of view, it was proposed that the GB region may possess a p-type semiconductor nature, resulting from high oxygen content and/or vacancies of metal ions along the GBs compared with the n-type semiconductor nature inside the grains. For CCTOF ceramics, the creation of oxygen vacancies may possibly be inhibited (or decreased) by F doping anions due to the lower valence state of the dopant, retaining the p-type semiconductor nature of the GBs and potential barrier height. Thus, substitution of F anions not only decreased the possibility of a reduction in  $\Phi_B$  as a result of creation of oxygen vacancies, but it also enhanced  $\Phi_B$  resulting from the creation of free charges inside the semiconducting grains.

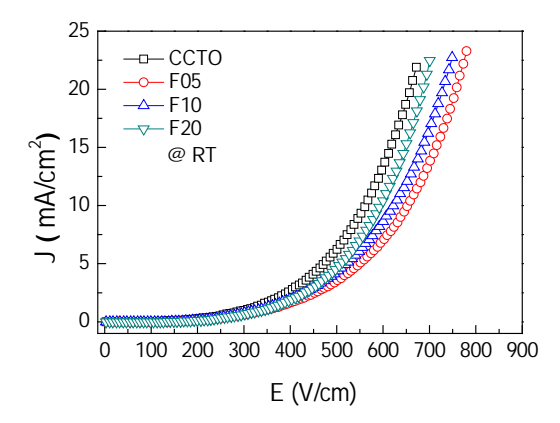


**Fig. 9** Nonlinear current density-electric field (J–E) characteristics at RT of CCTO, F05, F10 and F20 samples.

Substitution of F anions into CCTO ceramics can simultaneously improve the electrical properties of the grains and GBs. These can cause increases in both of the free charge carrier concentration inside the semiconducting grains and Schottky barrier height at the GBs, respectively. Under an applied electric field, more charges accumulated at the interface between the semiconducting grain and GB layer due to a high concentration of free charges inside the grain producing a stronger intensity of interfacial polarization (Maxwell–Wagner polarization). This gave rise to a large increase in  $\epsilon'$ . Enhanced  $\Phi_B$  resulting in  $R_{\rm gb}$  is the major cause the reduced low–frequency  $\tan\delta$ .

# 9.4 Conclusions

Significantly improved giant dielectric properties of CCTO ceramics via simultaneously tuning the electric properties of the grains and GBs was successfully done by doping CCTO with  $F^-$  anions. The grain size of CCTO ceramics was thus enlarged. The low–frequency  $\tan\delta$  of  $F^-$ –doped CCTO ceramics was greatly reduced by a factor of 5 compared to that of the undoped CCTO ceramic, which was attributed to a large increase in  $R_{gb}$  and potential barrier height at the GBs. These results were confirmed by the slight increase in electric breakdown strength of  $F^-$ –doped CCTO ceramics, even though the mean grain size was greatly increased. According to the XPS and XANES results, it was shown that the charge carrier concentration inside the semiconducting grains of  $F^-$ –doped CCTO ceramics was increased corresponding to the observed reduction in  $R_g$ .

This was responsible for the observed increase in  $\epsilon'$  from  $\approx 10^4$  to  $\approx 10^5$  at 1 kHz due to the increased intensity of interfacial polarization at the GBs. Maxwell–Wagner polarization relaxation based on the internal barrier layer capacitor model of Schottky barriers at the GBs can be used to clearly explain the variations of the giant dielectric behavior and nonlinear electrical properties of F<sup>-</sup>–doped CCTO ceramics.

### References

- 1 C. C. Homes, T. Vogt, S. M. Shapiro, S. Wakimoto and A. P. Ramirez, *Science*, 2001, **293**, 673-676.
- W. Hu, Y. Liu, R. L. Withers, T. J. Frankcombe, L. Norén, A. Snashall, M. Kitchin, P. Smith, B. Gong, H. Chen, J. Schiemer, F. Brink and J. Wong-Leung, *Nat. Mater.*, 2013, **12**, 821-826.
- 3 G. Liu, H. Fan, J. Xu, Z. Liu and Y. Zhao, RSC Advances, 2016, 6, 48708-48714.
- 4 W. Tuichai, S. Danwittayakul, S. Maensiri and P. Thongbai, *RSC Advances*, 2016, **6**, 5582-5589.
- 5 A. O. Turky, M. M. Rashad, Z. I. Zaki, I. A. Ibrahim and M. Bechelany, *RSC Advances*, 2015, **5**, 18767-18772.
- 6 M. A. Subramanian, D. Li, N. Duan, B. A. Reisner and A. W. Sleight, *J. Solid State Chem.*, 2000, **151**, 323-325.
- 7 B. Shri Prakash and K. B. R. Varma, J. Mater. Sci.: Mater. Electron., 2006, 17, 899-907.
- 8 S.-H. Hong, D.-Y. Kim, H.-M. Park and Y.-M. Kim, *J. Am. Ceram. Soc.*, 2007, **90**, 2118-2121.
- 9 M. Li, G. Cai, D. F. Zhang, W. Y. Wang, W. J. Wang and X. L. Chen, *J. Appl. Phys.*, 2008, **104**, 074107.
- 10 L. Liu, H. Fan, P. Fang and X. Chen, *Mater. Res. Bull.*, 2008, **43**, 1800-1807.
- 11 L. Ni, X. M. Chen and X. Q. Liu, *Mater. Chem. Phys.*, 2010, **124**, 982-986.
- 12 P. Thongbai, J. Jumpatam, T. Yamwong and S. Maensiri, *J. Eur. Ceram. Soc.*, 2012, **32**, 2423-2430.
- 13 P. Thongbai, J. Jumpatam, B. Putasaeng, T. Yamwong and S. Maensiri, *J. Appl. Phys.*, 2012, **112**, 114115.
- 14 J. Jumpatam, B. Putasaeng, T. Yamwong, P. Thongbai and S. Maensiri, *Ceram. Int.*, 2013, **39**, 1057-1064.
- 15 J. Boonlakhorn and P. Thongbai, *J. Electron. Mater.*, 2015, **44**, 3687-3695.
- 16 L. Liu, H. Fan, P. Fang and L. Jin, Solid State Commun., 2007, 142, 573-576.
- 17 L. Liu, H. Fan, X. Chen and P. Fang, J. Alloys Compd., 2009, 469, 529-534.
- 18 L. Liu, D. Shi, S. Zheng, Y. Huang, S. Wu, Y. Li, L. Fang and C. Hu, *Mater. Chem. Phys.*, 2013, **139**, 844-850.
- 19 Y. Huang, L. Liu, D. Shi, S. Wu, S. Zheng, L. Fang, C. Hu and B. Elouadi, *Ceram. Int.*, 2013, **39**, 6063-6068.
- 20 T. Adams, D. Sinclair and A. West, Phys. Rev. B, 2006, 73, 094124.
- 21 J. Liu, C.-G. Duan, W.-G. Yin, W. Mei, R. Smith and J. Hardy, *Phys. Rev. B*, 2004, **70**, 144106.
- 22 R. Schmidt, M. C. Stennett, N. C. Hyatt, J. Pokorny, J. Prado-Gonjal, M. Li and D. C. Sinclair, *J. Eur. Ceram. Soc.*, 2012, **32**, 3313-3323.

- 23 Z. Yang, L. Zhang, X. Chao, L. Xiong and J. Liu, *J. Alloys Compd.*, 2011, **509**, 8716-8719.
- 24 S.-Y. Chung, I.-D. Kim and S.-J. L. Kang, Nat. Mater., 2004, 3, 774-778.
- 25 M. A. Ramírez, P. R. Bueno, J. A. Varela and E. Longo, *Appl. Phys. Lett.*, 2006, **89**, 212102.
- 26 J. Boonlakhorn, P. Kidkhunthod and P. Thongbai, J. Eur. Ceram. Soc., 2015, 35, 3521-3528.
- 27 L. Sun, R. Zhang, Z. Wang, E. Cao, Y. Zhang and L. Ju, *RSC Advances*, 2016, **6**, 55984-55989.
- 28 L. Ni and X. M. Chen, Solid State Commun., 2009, 149, 379-383.
- 29 A. Nautiyal, C. Autret, C. Honstettre, S. De Almeida-Didry, M. El Amrani, S. Roger, B. Negulescu and A. Ruyter, *J. Eur. Ceram. Soc.*, 2016, **36**, 1391-1398.
- 30 M. F. Ab Rahman, S. D. Hutagalung, Z. A. Ahmad, M. F. Ain and J. J. Mohamed, *J. Mater. Sci.: Mater. Electron.*, 2015, **26**, 3947-3956.
- 31 L. Singh, I. W. Kim, B. C. Sin, K. D. Mandal, U. S. Rai, A. Ullah, H. Chung and Y. Lee, *RSC Adv.*, 2014, **4**, 52770-52784.
- 32 L. Ni and X. M. Chen, J. Am. Ceram. Soc., 2010, 93, 184-189.
- 33 W. L. Li, Y. Zhao, Q. G. Chi, Z. G. Zhang and W. D. Fei, RSC Advances, 2012, 2, 6073.
- 34 M. Gao, D. Feng, G. Yao, Y. Zhang, C. L. Chen and Y. Lin, *RSC Advances*, 2015, **5**, 92958-92962.
- 35 L. Singh, B. C. Sin, I. W. Kim, K. D. Mandal, H. Chung, Y. Lee and J. Varela, *J. Am. Ceram. Soc.*, 2016, **99**, 27-34.
- 36 J. Boonlakhorn and P. Thongbai, *Jpn. J. Appl. Phys.*, 2015, **54**, 06FJ06.
- 37 R. Yu, H. Xue, Z. Cao, L. Chen and Z. Xiong, J. Eur. Ceram. Soc., 2012, 32, 1245-1249.
- 38 A. E. Smith, T. G. Calvarese, A. W. Sleight and M. A. Subramanian, *J. Solid State Chem.*, 2009, **182**, 409-411.
- 39 M. Newville, Journal of Synchrotron Radiation, 2001, 8, 96-100.
- 40 R. D. Shannon, *Acta Cryst.*, 1976, **A32**, 751-767.
- 41 M. Li, Z. Shen, M. Nygren, A. Feteira, D. C. Sinclair and A. R. West, *J. Appl. Phys.*, 2009, **106**, 104106.
- 42 S. I. R. Costa, M. Li, J. R. Frade and D. C. Sinclair, RSC Advances, 2013, 3, 7030-7036.
- 43 R. Schmidt, S. Pandey, P. Fiorenza and D. C. Sinclair, *RSC Advances*, 2013, **3**, 14580-14589.
- 44 L. Liu, Y. Huang, Y. Li, D. Shi, S. Zheng, S. Wu, L. Fang and C. Hu, *J. Mater. Sci.*, 2012, **47**, 2294-2299.
- 45 J. Deng, X. Sun, S. Liu, L. Liu, T. Yan, L. Fang and B. Elouadi, *Journal of Advanced Dielectrics*, 2016, **06**, 1650009.
- 46 G. Li, Z. Chen, X. Sun, L. Liu, L. Fang and B. Elouadi, *Mater. Res. Bull.*, 2015, **65**, 260-265.
- 47 J. Jumpatam, A. Mooltang, B. Putasaeng, P. Kidkhunthod, N. Chanlek, P. Thongbai and S. Maensiri, *Ceram. Int.*, 2016, **42**, 16287-16295.
- 48 Y. Huang, D. Shi, Y. Li, G. Li, Q. Wang, L. Liu and L. Fang, *J. Mater. Sci.: Mater. Electron.*, 2012, **24**, 1994-1999.
- 49 L. Liu, L. Fang, Y. Huang, Y. Li, D. Shi, S. Zheng, S. Wu and C. Hu, *J. Appl. Phys.*, 2011, **110**, 094101.
- 50 M. Li and D. C. Sinclair, *J. Appl. Phys.*, 2013, **114**, 034106.

# **CHAPTER 10**

# Nonlinear Electrical Properties and Giant Dielectric Response in Na<sub>1/3</sub>Ca<sub>1/3</sub>Y<sub>1/3</sub>Cu<sub>3</sub>Ti<sub>4</sub>O<sub>12</sub> Ceramic

### 10.1 Introduction

The dielectric response of  $CaCu_3Ti_4O_{12}$  was first reported by Subramanian et al. [1].  $CaCu_3Ti_4O_{12}$  has attracted a great deal of interest owing to its exceptionally giant dielectric constant ( $\epsilon$ ') values, on the order to  $10^3$ – $10^5$ , depending on sintering duration and temperature, electrode material, cooling rate, doping ions, and preparation method [2-16]. A high  $\epsilon$ ' value was observed over a wide temperature range of 100–400 K. Usually, the loss tangent ( $tan\delta$ ) of the  $CaCu_3Ti_4O_{12}$  ceramics, over 0.05 at 1 kHz, was still too high for practical capacitor applications [17]. In addition to  $CaCu_3Ti_4O_{12}$ , isostructural  $CaCu_3Ti_4O_{12}$ –type perovskite materials (i.e., the  $ACu_3Ti_4O_{12}$  family, where  $A = La_{2/3}$ ,  $Bi_{2/3}$ ,  $Y_{2/3}$ ,  $Na_{1/2}La_{1/2}$ ,  $Na_{1/2}Bi_{1/2}$ ,  $Na_{1/2}Sm_{1/2}$ ,  $Na_{1/2}Y_{1/2}$ , and  $Na_{1/3}Ca_{1/3}Bi_{1/3}$ ) [18-27] as well as  $NaCu_3Ti_3BO_{12}$  ( $B=Nb^{5+}$ ,  $Ta^{5+}$ , and  $Sb^{5+}$ ) [28-30] have gained considerable attention because of their giant dielectric properties. Notably,  $tan\delta$  of these  $CaCu_3Ti_4O_{12}$ –related compounds are lower than that of  $CaCu_3Ti_4O_{12}$  ceramics [19-23]. These interesting properties are important for practical applications in capacitors and memory devices.

Nowadays, the origin of giant  $\epsilon'$  of CaCu<sub>3</sub>Ti<sub>4</sub>O<sub>12</sub> and related materials is still debated. The extrinsic origin of the internal barrier layer capacitance (IBLC) model is widely accepted as an explanation of the giant  $\epsilon'$  of these materials [10, 15, 20, 30-31]. The electrically heterogeneous microstructure of CaCu<sub>3</sub>Ti<sub>4</sub>O<sub>12</sub> polycrystalline ceramics consists of semiconducting grains and insulating grain boundaries (GBs). Alternatively, their intrinsic origin cannot be ignored [32-33]. In addition to a giant  $\epsilon'$  response, CaCu<sub>3</sub>Ti<sub>4</sub>O<sub>12</sub> and related ACu<sub>3</sub>Ti<sub>4</sub>O<sub>12</sub> ceramics demonstrate a nonlinear relationship between current density (J) and electric field strength (E) [8, 19-20, 34]. This behavior may be important for practical applications in varistor devices if the nonlinear coefficient and electric breakdown strength can be suitably tuned.

It is very impressive that many isostructural  $CaCu_3Ti_4O_{12}$ —type perovskite oxides partially containing  $Na^+$  in A–sites exhibit good dielectric properties. Large  $\epsilon'$  values of  $\approx 10^4$  with low  $\tan \delta$  values  $\approx 0.02-0.031$  at 10 kHz were achieved in  $Na_{1/2}Bi_{1/2}Cu_3Ti_4O_{12}$  ceramics [21, 35].  $Na_{1/2}Y_{1/2}Cu_3Ti_4O_{12}$  has been extensively investigated because it exhibits a giant  $\epsilon' \approx 10^4$  and low  $\tan \delta < 0.1$  [36]. Good dielectric properties were also achieved in  $Y_{2/3}Cu_3Ti_4O_{12}$  [23]. Most recently, the dielectric and nonlinear electrical properties of a new isostructural  $CaCu_3Ti_4O_{12}$ —type perovskite,  $Na_{1/3}Ca_{1/3}Y_{1/3}Cu_3Ti_4O_{12}$ , were investigated [19]. Its Ca–sites were occupied by  $Na^+$ ,  $Ca^{2+}$ , and  $Y^{3+}$  ions, each at a level of  $\sim 33.3$  at.%. This ceramic can exhibit a giant  $\epsilon' \approx 2.5 \times 10^4$  and low  $\tan \delta \approx 0.038$  at 1 kHz. Furthermore,  $\epsilon'$  was slightly dependent on temperature over a wide range. According to interesting dielectric properties of  $Na_{1/2}Y_{1/2}Cu_3Ti_4O_{12}$ , good giant dielectric and non–Ohmic properties of a new isostructural– $CaCu_3Ti_4O_{12}$  oxide may be achieved, with mixed valence states of  $Na^+$ ,  $Ca^{2+}$ , and  $Y^{3+}$  in the A–sites.

In this work, we synthesized a perovskite–like structure as  $(Na_{1/3}Ca_{1/3}Y_{1/3})$   $Cu_3Ti_4O_{12}$  ceramics using a conventional solid–state reaction method under different sintering conditions. The giant dielectric properties were investigated as functions of frequency, temperature and DC bias. The nonlinear current density–electric field properties were also investigated. Interestingly, the giant  $\epsilon'$  and low  $tan\delta$  values at 1 kHz were found to be

1.2×10<sup>4</sup> and 0.04, respectively. The origins of the giant dielectric response and nonlinear electrical properties are discussed in detail.

## 10.2 Experimental details

Na $_{1/3}$ Ca $_{1/3}$ Y $_{1/3}$ Cu $_3$ Ti $_4$ O $_{12}$  (NCYCTO) was prepared using a conventional solid–state reaction method. Na $_2$ CO $_3$  (99.9% purity), CaCO $_3$  (99.9% purity), Y $_2$ O $_3$  (99.99% purity), CuO (99.9% purity) and TiO $_2$  (99.9% purity) were used as the starting raw materials. First, a stoichiometric mixture of the starting materials was ball–milled in ethanol for 24 h using ZrO $_2$  balls. Second, the mixed slurry was dried and calcined at 1000 °C for 20 h. Then, the resulting calcined powder was carefully ground and pressed into pellets of 9.5 mm in diameter and ~1–2 mm in thickness by uniaxial compression. Finally the pellets were sintered at different temperatures. A dense microstructure was obtained by sintered at 1100 °C. It was found that the NCYCTO ceramics started to decompose when they were sintered at temperatures  $\geq$ 1120 °C, as was observed for Na $_{1/2}$ Sm $_{1/2}$ Cu $_3$ Ti $_4$ O $_{12}$  [27]. Thus, the sintering conditions used were 1100 °C for 10, 15 h and 1110 °C for 10 h. The sintered ceramics produced under these conditions are referred to as the NCY1, NCY2 and NCY3 samples, respectively.

Phase composition and crystal structure of the sintered ceramics were studied using X–ray diffraction (XRD; PANanalytical EMPYREAN). Scanning electron microscopy (SEM; SEC SNE4500M) was used to reveal the polished–surface morphology of the sintered NCYCTO ceramics. Valence states of Ti were characterized using an X–ray absorption near edge structure (XANES) technique. XANES spectra were collected at the SUT–NANOTEC–SLRI XAS beamline (BL5.2) at the Synchrotron Light Research Institute (SLRI), Nakhon Ratchasima, Thailand. Details of this characterization technique and analysis are given elsewhere [37]. The normalized XANES data were processed and analyzed after background subtraction in the pre–edge and post–edge regions using ATHENA software included in an IFEFFIT package [38]. Characterization of oxidation states of Cu and Ti was done using X–ray photoelectron spectroscopy (XPS; PHI5000 VersaProbe II, ULVAC–PHI, Japan) at the SUT–NANOTEC–SLRI Joint Research Facility, Synchrotron Light Research Institute (SLRI), Thailand. The experimental curves were fitted with PHI MultiPak XPS software using a combination of Gaussian–Lorentzian lines.

For dielectric and electrical measurements, surfaces of the sintered ceramics were polished and sputtered with Au at a current of 25 mA for 4 min. A KEYSIGHT E4990A and an Agilent 4294A Precision Impedance Analyzer were used to measure the dielectric properties of sintered ceramics. The measurements were done over the frequency range of  $10^2$  to  $10^7$  Hz using an oscillation voltage of 0.5 V. Dielectric properties were measured in the temperature range from -60 to 200 °C with step increases of 10 °C. Temperatures were held constant with an accuracy of  $\pm 0.1$  °C for each step. The nonlinear J-E properties were measured at room temperature (RT) using a high voltage measurement unit (Keithley Model 247). Breakdown electric field strength ( $E_b$ ) was obtained at J=1 mA.cm<sup>-2</sup>. The nonlinear coefficient ( $\alpha$ ) was calculated in the range of 1–10 mA.cm<sup>-2</sup>.

### 10.3 Results and discussion

The XRD patterns of NCYCTO ceramics sintered under different conditions are shown in the Fig. 1. All XRD patterns show a single phase with no diffraction peaks of an

impurity phase. Additionally, the lattice parameters of the NCY1, NCY2 and NCY3 samples were calculated and found to be nearly the same in value,  $\approx 7.386$  Å. The lattice parameters of CaCu<sub>3</sub>Ti<sub>4</sub>O<sub>12</sub> and Na<sub>1/2</sub>Y<sub>1/2</sub>Cu<sub>3</sub>Ti<sub>4</sub>O<sub>12</sub> ceramics were about 7.391 Å (JCPDS 75–2188) [1] and  $\approx 7.378-7.379$  Å, respectively [1, 26]. This means that the ionic radius of Ca<sup>2+</sup> in A–sites of the CaCu<sub>3</sub>Ti<sub>4</sub>O<sub>12</sub> structure was larger than that of the average ionic radius of Na<sup>+</sup> and Y<sup>3+</sup> in the Na<sub>1/2</sub>Y<sub>1/2</sub>Cu<sub>3</sub>Ti<sub>4</sub>O<sub>12</sub> structure, which randomly occupied A–sites. Reasonably, the ionic radius of NCYCTO ceramics is intermediate between the CaCu<sub>3</sub>Ti<sub>4</sub>O<sub>12</sub> and Na<sub>1/2</sub>Y<sub>1/2</sub>Cu<sub>3</sub>Ti<sub>4</sub>O<sub>12</sub> because Na<sup>+</sup> and Y<sup>3+</sup> ions in Na<sub>1/2</sub>Y<sub>1/2</sub>Cu<sub>3</sub>Ti<sub>4</sub>O<sub>12</sub> structure were partially replaced by Ca<sup>2+</sup>, leading to an enlarged lattice parameter of the NCYCTO structure.

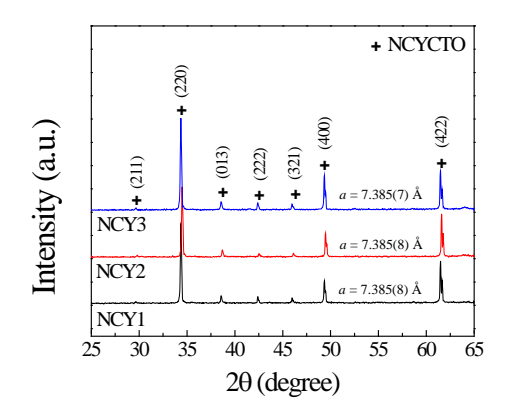
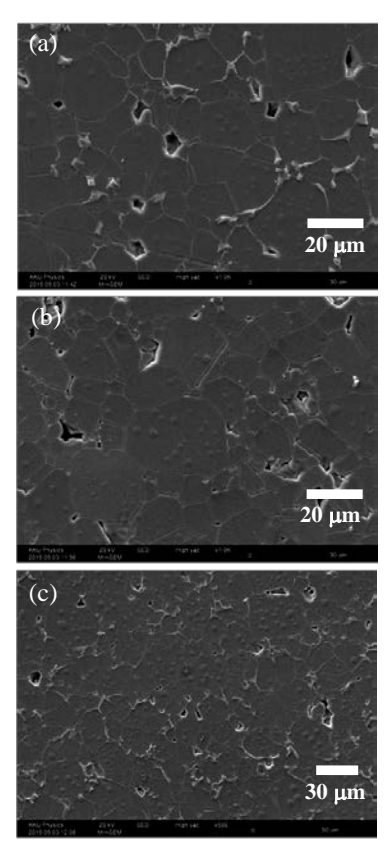


Fig. 1 XRD patterns of NCYCTO ceramics sintered under different conditions.



**Fig. 2** SEM images of polished–surfaces revealing the morphologies of (a) NCY1, (b) NCY2 and (c) NCY3 samples.

Figure 2 shows the polished-surface morphologies of NCYCTO ceramics sintered under various conditions. The average grain sizes of the NCY1, NCY2 and NCY3 samples were estimated to be ~15.9  $\pm$  5.9, ~15.1  $\pm$  6.8 and ~14.9  $\pm$  4.9  $\mu$ m, respectively. The mean grain size was slightly changed by increasing the sintering temperature from 1100 to 1110 °C. Sintering at 1100 °C for a longer time had also slight impact on the microstructure. A small number of pores were observed in all the samples. Commonly, the densification and grain growth processes in polycrystalline ceramics are primarily caused by the diffusion of atoms, ions and charged species during sintering process. For CaCu<sub>3</sub>Ti<sub>4</sub>O<sub>12</sub> ceramics, diffusion can be promoted by the presence of a liquid phase along the grain boundaries. In the current study, the large grain sizes of NCYCTO ceramics might therefore be caused by a CuO-related liquid phase, since the eutectic temperature of CuO-TiO<sub>2</sub> is ≈919 °C [16, 39]. Note that the mean grain size slightly decreased with increasing temperature from 1100-1110 °C. This is contrast to occur in CaCu<sub>3</sub>Ti<sub>4</sub>O<sub>12</sub> ceramics. It was reported that the mean grain size of CaCu<sub>3</sub>Ti<sub>4</sub>O<sub>12</sub> ceramics was reduced by creating Ca vacancies or filling oxygen vacancies during sintering process [40-41]. Thus, the grain growth of CaCu<sub>3</sub>Ti<sub>4</sub>O<sub>12</sub> and ACu<sub>3</sub>Ti<sub>4</sub>O<sub>12</sub> was likely controlled by A-site or oxygen vacancies. It is notable that Na is a kind of volatile element. Generally, Na vacancies can be easily generated at high temperatures. With increasing sintering temperature, the concentration of Na vacancy was expected to increase. Therefore, the grain growth rate of NCY3 ceramic was slightly reduced by increasing Na vacancies.

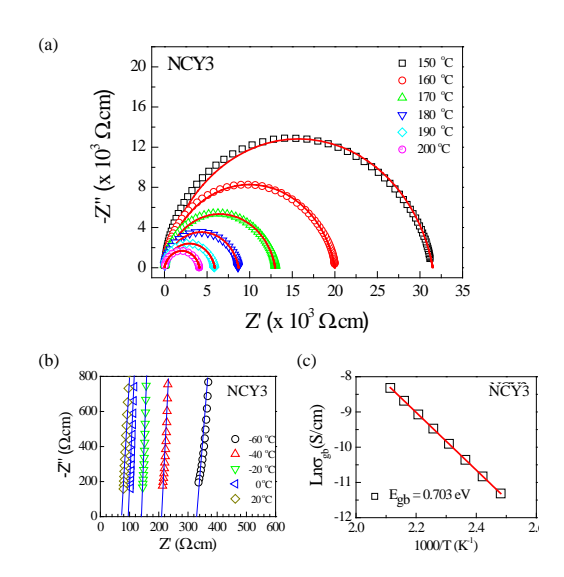


Fig. 3 (a) Impedance complex plane plots in the temperature range of 150–200  $^{\circ}$ C for the NCY3 sample; red solid curves are the fitted data using Eq. (1). (b) An expanded view of the high–frequency data close to the origin in the temperature range from -60 to 20  $^{\circ}$ C; blue solid lines are the eye guidelines for estimating  $R_{\rm g}$ . (c) Arrhenius plot of grain boundary conductivity ( $\sigma_{\rm gb}$ ) of the NCY3 sample.

The electrically heterogeneous microstructure of ACu<sub>3</sub>Ti<sub>4</sub>O<sub>12</sub> ceramics was investigated using impedance spectroscopy [8, 10, 15, 19-20, 31]. This technique may also be important for the elucidation of nonlinear properties, even though these techniques were done at different voltages. In the absence of a sample–electrode effect, the electrically heterogeneous microstructure of ACu<sub>3</sub>Ti<sub>4</sub>O<sub>12</sub> ceramics is usually explained

by an equivalent circuit consisting of two parallel resistor–capacitor (RC) elements connected in series [31, 42]. One RC element represents the electrical response of the grains and the other represents the grain boundary response. Figures 3(a) and (b) show impedance complex plane ( $Z^*$ ) plots over different temperature ranges for the NCY3 sample, and full semicircle arcs with different diameters and nonzero intercepts on the Z' axis, respectively. The decrease in diameter of the large arc indicates a reduction in GB resistance ( $R_{gb}$ ) [15, 31]. At RT, a full semicircle arc cannot be obtained in the measured frequency range ( $10^2$ – $10^7$  Hz) because of the sample's very large  $R_{gb}$  value, while the capacitance of grain boundaries ( $C_{gb}$ ) was slightly dependent on measured temperature. The grain resistance ( $R_g$ ) can generally be predicted from the nonzero intercept, as estimated by the eye blue–guidelines in Fig. 3(b) [15]. The  $Z^*$  plots of all the samples can be fitted by a simple equivalent circuit including of parallel  $R_{gb}C_{gb}$  elements joined to  $R_g$  in series using the modified equation for a  $Z^*$  plot as [42]:

$$Z^* = R_g + \frac{R_{gb}}{1 + \left(i\omega R_{gb}C_{gb}\right)^{\alpha}},\tag{1}$$

where  $\omega$  is the angular frequency of an applied electric field and  $\alpha$  is a constant value (0 <  $\alpha \le 1$ ). To fit the data, the  $C_{\rm g}$  is easy to determine and the respective capacitance can simply be omitted from the circuit. The experimental data in the temperature range between 150 to 200 °C were well fitted by equation (1). Overlapping semicircle arcs in this temperature range were not observed. This indicates that the electrical response at different temperatures is originated from the same part, *i.e.*, insulating GBs. Accurate  $R_{\rm gb}$  values were achieved by fitting Z\* data. The  $R_{\rm gb}$  values of the NCY3 sample at 150, 160, 170, 180, 190 and 200 °C were found to be 31.5, 20.0, 13.0, 8.7, 5.9 and 4.1 k $\Omega$ .cm, respectively. Additionally,  $R_{\rm g}$  increased with decreasing temperature, as shown in Fig. 3(b). The conductivities of the grain ( $\sigma_{\rm g}$ =1/ $R_{\rm g}$ ) and grain boundaries ( $\sigma_{\rm gb}$ =1/ $R_{\rm gb}$ ) at different temperatures were calculated. The temperature dependence of  $\sigma_{\rm g}$  and  $\sigma_{\rm gb}$  followed the Arrhenius law:

$$\sigma = \sigma_0 e^{\left(\frac{-E}{k_B T}\right)},\tag{2}$$

where E is the activation energy required for conduction inside the grains ( $E_g$ ) or at the GBs ( $E_{gb}$ ). As shown in Fig. 3(c), a good linear fit was achieved.  $E_{gb}$  values of the NCY1, NCY2 and NCY3 samples were, respectively, 0.692, 0.707 and 0.703 eV, while  $E_g$  values were found to be 0.102, 0.105 and 0.099 eV, respectively (data not shown). These are typical values of  $E_g$  and  $E_{gb}$  for CaCu<sub>3</sub>Ti<sub>4</sub>O<sub>12</sub> and related oxides [16, 19-20, 30, 36, 42]. Greatly different conduction activation energies between the grain and GBs confirm distinct electrical conductions in these two regions.

The NCYCTO ceramics were proved to be electrically heterogeneous, consisting of semiconducting grains and insulating GBs. The semiconducting grain property was further characterized by annealing the NCY1 sample under different oxygen partial pressure, i.e., Ar and  $O_2$  atmosphere at 950 °C for 4 h. As clearly shown in Fig. 4 and the inset, after annealing the NCY1 sample (as–sample) in Ar atmosphere (Ar–sample),  $R_{\rm gb}$  at 80 °C was greatly reduced from  $\approx 4 \times 10^5$  to  $\approx 2.9 \times 10^3 \,\Omega$ .cm. A small semicircle arc in a low frequency range was also observed, indicating to the electrode effect. Interestingly, after annealing the Ar–sample in  $O_2$  atmosphere ( $O_2$ –sample), a very large  $R_{\rm gb}$  value was restored. The

 $R_{\rm gb}$  value of the O<sub>2</sub>-sample was larger than that of the as-sample. These results confirm the existence of n-type semiconducting grains of NCYCTO ceramics.

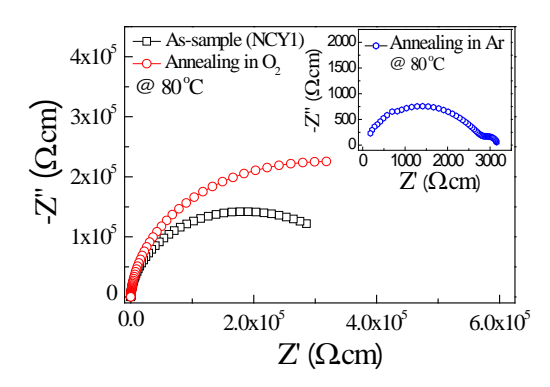


**Fig. 4** Impedance complex plane plots at 80 °C for the NCY1 sample before and after annealing in O<sub>2</sub> atmosphere; inset shows an impedance complex plane plot of the NCY1 sample after annealing in Ar atmosphere.

It is interesting to show that the  $R_{\rm g}$  values of IBLC's materials can be easily calculated using an admittance spectroscopy analysis employing the relationship,  $R_{\rm g}=1/(2Y_{\rm max}'')$ , where  $Y_{\rm max}''$  is the maximum value at the peak of the imaginary part of complex admittance ( $\dot{Y}$ ), *i.e.*, the  $\dot{Y}''$ -peak. As illustrated in Fig. 5,  $\dot{Y}''$ -peaks of the NCY3 sample as well as other samples (data not shown) appeared in the temperature range of -70 – -10 °C. As shown in the inset of Fig. 5, the  $E_{\rm g}$  value of the NCY3 sample was calculated from the slopes of the fitted line and found to be 0.104 eV. The  $R_{\rm g}$  and  $E_{\rm g}$  values of all the samples obtained from admittance and impedance spectroscopy analyses are nearly identical. To further understand the electrical properties of the GBs, the scaling behavior of  $\dot{Y}''$  for the NCY3 sample was investigated. As illustrated in Fig. 6, the overlap of all curves at different temperatures into a single curve is observed, indicating that the relaxation process at different temperatures is originated from the same mechanism.

Figure 7(a) shows normalized Ti K-edge XANES spectra of the NCY2 sample, as well as the reference standard for the Ti<sub>2</sub>O<sub>3</sub> (Ti<sup>3+</sup>) and TiO<sub>2</sub> (Ti<sup>4+</sup>) samples. The position of the edge energy of the NCY2 sample is quite far from K-edge XANES energy spectrum of the Ti<sub>2</sub>O<sub>3</sub> standard sample, but close to that of the TiO<sub>2</sub> standard sample. This result indicates the existence of small amount of Ti<sup>3+</sup> compared to level of Ti<sup>4+</sup>. Quantitative analysis of the different valence states of each of the ceramics was done using an empirical edge-shift calculation making comparisons with known standard samples. The ratio of Ti<sup>3+</sup>/Ti<sup>4+</sup> in the NCY2 sample can be calculated using the energy edge value, which was determined from the maximum value of the first derivative of the edge region [37]. The calculated ratio of Ti<sup>3+</sup>/Ti<sup>4+</sup> in the NCY2 sample was found to be  $\approx$ 3.0%. According to two plausible explanations of the origin of n-type semiconducting grains in CaCu<sub>3</sub>Ti<sub>4</sub>O<sub>12</sub> and other isostructural CaCu<sub>3</sub>Ti<sub>4</sub>O<sub>12</sub>-type oxides, the electrical conduction inside the grains was correlated with electron hopping between Ti<sup>3+</sup>  $\leftrightarrow$ Ti<sup>4+</sup> sites, but the existence of Ti<sup>3+</sup> ions in each model was proposed in different ways [15].

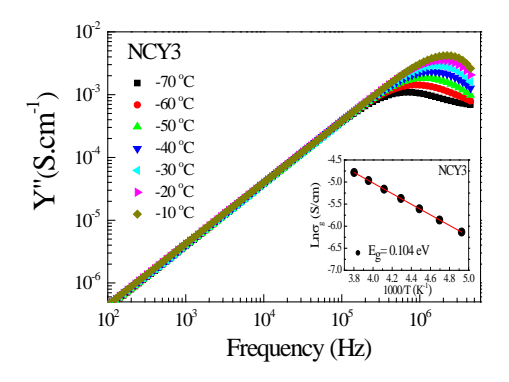


Fig. 5 Frequency dependence of Y'' at different temperatures for the NCY3 ceramic; inset shows an Arrhenius plot of grain conductivity ( $\sigma_{\alpha}$ ).

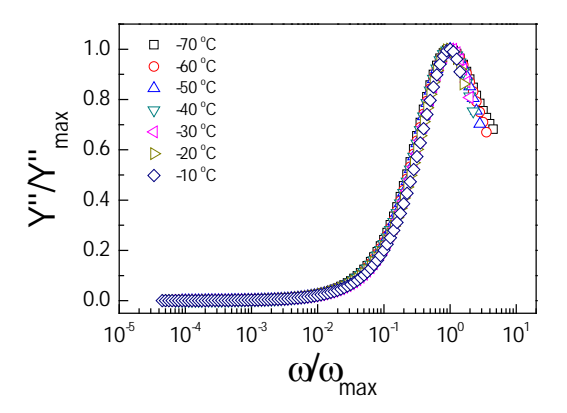


Fig. 6 Scaling behavior of Y" in the temperature range from -70 to -10 °C.

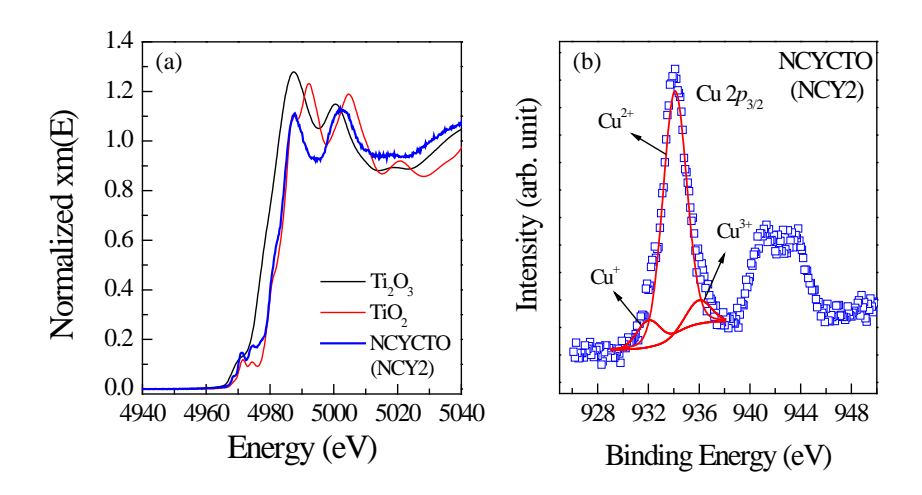
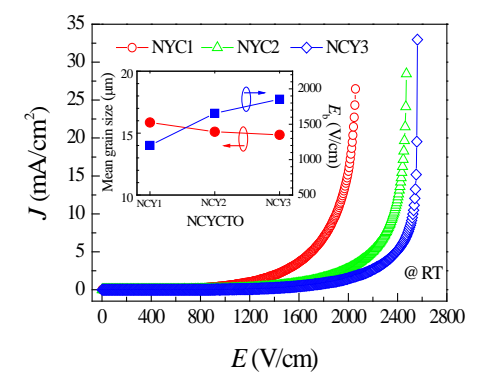


Fig. 7 (a) Normalized X-ray Absorption near-edge structure (XANES) spectra for Ti K-edge of the NCY2 sample. (b) XPS spectrum of the NCY2 sample.

Alternatively, electron hopping between  $Cu^+\leftrightarrow Cu^{2+}$  sites can also cause conduction in grains [32-33]. As shown in Fig. 7(b), the oxidation states of polyvalent cations were elucidated using an XPS technique. Three peaks were extracted from the XPS spectrum of Cu2p using Gaussian–Lorentzian profile fitting. The main peak at a binding energy of about  $\approx 934.1$  eV of the NCY2 sample was a result of the presence as  $Cu^{2+}$ . Two peaks at

relatively higher ( $\approx$ 936 eV) and lower ( $\approx$ 931 eV) binding energies indicated the presence of Cu³+ and Cu+, respectively. The calculated Cu+/Cu²+ ratio in the NCY2 sample was found to be  $\approx$ 10.5%, while the ratio of Cu³+/Cu²+ was  $\approx$ 9.2%. Conduction inside the grains may also have resulted from the presence of Cu+ and Cu³+ because the conductivity depended on the carrier concentration (*i.e.*, both of electrons and holes) and mobility of charge carriers. From the XANES and XPS results, the conduction mechanism inside the semiconducting grains of NCYCTO ceramics was primarily caused by electron hopping from Ti³+O-Ti⁴+ to Ti⁴+O-Ti³+ and Cu+O-Cu²+ to Cu²+O-Cu+. The conductivity of the grains was also enhanced by hole hopping between Cu³+O-Cu²+ to Cu²+O-Cu³+. The origin(s) of the *n*-type semiconducting grains is likely very complex. Ti³+, Cu+ and Cu³+ ions all may have significant effects on the electrical properties of grains.

Using impedance spectroscopy and investigation of polyvalent cations, NCYCTO ceramics were clearly shown to be electrical heterogeneous, consisting of semiconducting grains and insulating GBs. The non-Ohmic sample-electrode contact effect (or Schottky barrier height at the sample-electrode interface) was not observed. In contrast, the Schottky barrier height at the internal interfaces between n-type semiconducting grains and insulating GBs was observed, as clearly seen in Fig. 8. All of the samples exhibited nonlinear J-E behavior. At RT, the  $\alpha$  and E<sub>b</sub> values of the NCY1, NCY2 and NCY3 samples were found to be 4.98 and 1201 V/cm, 6.39 and 1655 V/cm and 7.4 and 1854 V/cm, respectively.  $\alpha$  and  $E_b$  values increased with increasing sintering duration and temperature. Generally, Schottky barriers can be created in ceramic oxides when there is compositional heterogeneity between the grain and GB regions. Double Schottky potential barriers at two faces of the GB can be formed by trapping charges at acceptor states. This causes bending of the conduction band across the grain boundary, creating an effective potential barrier height  $(\Phi_b)$ . This may be responsible for the observed nonlinear J-Ebehavior in NCYCTO ceramics. Generally, both the geometric and intrinsic properties of the grain and GBs influence the nonlinear properties. As demonstrated in the inset of Fig. 8, E<sub>b</sub> of NCYCTO ceramics significantly increased, while the mean grain size decreased slightly. This means that the intrinsic factor of the GB was more dominant than the geometric factor. This observation may be due to the different values of  $\Phi_b$  at the GBs of NCYCTO ceramics.



**Fig. 8** Profile fits for the Rietveld refinements of the XRD patterns of CCTO, F05, F10 and F20 samples.

The dielectric properties as functions of frequency, temperature, and DC bias are shown in Fig 9. In Fig 9(a), all of NCYCTO ceramics exhibited giant ε' values over a wide frequency range from  $10^2-10^5$  Hz. The overall frequency dependence of  $\epsilon'$  for NCYCTO ceramics was similar to that observed in most isostructural CaCu<sub>3</sub>Ti<sub>4</sub>O<sub>12</sub>-type ceramics [3, 5, 18, 28-29, 31-33, 42].  $\varepsilon'$  of the NCY2 and NCY3 samples was slightly independent of frequency over the range from  $10^2$  to  $10^5$  Hz. At RT and 1 kHz, the  $\varepsilon'$  values of the NCY1, NCY2 and NCY3 samples were found to be 11838, 12104 and 7900, respectively. It was observed that ε' of NCYCTO ceramics slightly decreased with decreasing mean grain size. According to the impedance spectroscopy analysis, the giant  $\epsilon'$  response of NCYCTO ceramics should be extrinsic in origin and primarily attributed to the IBLC effect. Alternatively, the intrinsic origin of the mixed valance states of Cu<sup>+</sup> and Ti<sup>3+</sup> cannot be ignored because this can also give rise to high  $\varepsilon'$  values in ceramic oxides [32-33]. As shown in Fig. 9(b),  $\tan \delta$  over a frequency range of  $10^2 - 10^5$  Hz was very low compared to CaCu<sub>3</sub>Ti<sub>4</sub>O<sub>12</sub> ceramics. The dramatic increase in tanδ in a high frequency range was attributed to the dielectric relaxation process, which is usually accompanied with the rapid drop in ε' in the same frequency range [19, 42]. In a low-frequency range, a high value of tanδ is usually associated with DC conduction. The tanδ values at 1 kHz for NCY1, NCY2 and NCY3 samples were found to be 0.066, 0.041 and 0.046, respectively. The  $\varepsilon'$  and tan δ values of all samples are summarized in the inset of Fig. 9(b). The temperature dependences of  $\varepsilon'$  and  $\tan\delta$  at 1 kHz are shown in Fig. 9(c). At high temperatures, both of  $\varepsilon'$  and  $\tan\delta$  greatly increased. This was caused by the effect of DC conduction in NCYCTO ceramics, which is more dominant at low frequencies. This behavior is usually observed in all isostructural CaCu<sub>3</sub>Ti<sub>4</sub>O<sub>12</sub>-type oxides [10, 13, 19-20, 32, 35, 37].

The effects of DC bias voltage on the dielectric properties of NCYCTO ceramics are depicted in Fig. 9(d) and its inset. In the frequency range of 40–300 Hz,  $\epsilon'$  increased with increasing DC bias voltage. In the frequency range of 300 Hz–10<sup>6</sup> Hz,  $\epsilon'$  was decreased by applying a DC bias voltage, while  $\tan\delta$  in the frequency range of 40– $10^6$  Hz greatly increased. These results support the IBLC model, which was proposed as the origin of the giant dielectric response in NCYCTO ceramics in the current study. Based on the IBLC model of Schottky barriers at the GBs between semiconducting grains, under an applied DC bias voltage, the barrier becomes asymmetric and  $\Phi_b$  at one side (forward bias) of GB was reduced. This may have resulted in enhanced DC conductivity because trapped charges at the GBs were released, leading to an increase in the low–frequency  $\tan\delta$ . Furthermore, it was shown that the GB capacitance per unit area was reduced by applying DC bias [43]. This can cause a decrease in  $\epsilon'$  in a wide frequency range, as clearly seen in Fig. 9(d).

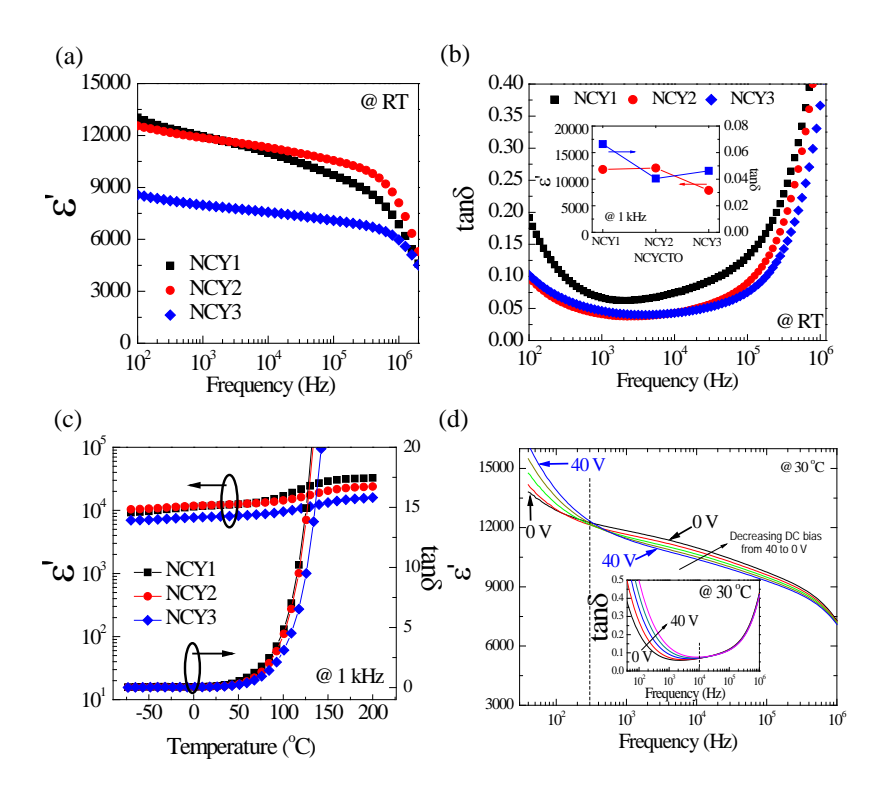


**Fig. 9** Profile fits for the Rietveld refinements of the XRD patterns of CCTO, F05, F10 and F20 samples.

### 10.4 Conclusions

Single phase of NCYCTO ceramics, an isostructural CaCu $_3$ Ti $_4$ O $_{12}$ -type oxide were successfully prepared. In these ceramics, Ca $^{2+}$  ions were replaced by Na $^+$ , Ca $^{2+}$ , and Y $^{3+}$  ions, each at a level of  $\sim 33.3$  at.%. Microstructural analysis showed that the mean grain sizes of NCYCTO ceramics were all  $\approx 15~\mu m$  when sintered at 1100-1110~°C for 10-15~h. Giant  $\epsilon'$  values and low  $\tan \delta$  were obtained in NCYCTO ceramics. The NCYCTO polycrystalline ceramics also exhibited nonlinear J-E properties. An electrically heterogeneous microstructure was confirmed using impedance spectroscopy. The origin of n-type semiconducting grains were suggested to result from the presence of Cu $^+$  and Ti $^{3+}$  ions, by XANES and XPS results. The existence of Cu $^{3+}$  may have also influenced conduction inside the grains. The giant dielectric response in NCYCTO ceramics can be well described based on the IBLC effect of Schottky barriers at the GBs between semiconducting grains.

#### References

- [1] M.A. Subramanian, D. Li, N. Duan, B.A. Reisner, A.W. Sleight, J. Solid State Chem. 151 (2000) 323-325.
- [2] S. Wu, P. Liu, Y. Lai, W. Guan, Z. Huang, J. Han, Y. Xiang, W. Yi, Y. Zeng, J. Mater. Sci.: Mater. Electron. (2016) 1-6.
- [3] X.W. Wang, P.B. Jia, X.E. Wang, B.H. Zhang, L.Y. Sun, Q.B. Liu, J. Mater. Sci.: Mater. Electron. (2016) 1-7.
- [4] P.R. Bueno, M.A. Ramírez, J.A. Varela, E. Longo, Appl. Phys. Lett. 89 (2006) 191117.

- [5] S. Krohns, P. Lunkenheimer, S.G. Ebbinghaus, A. Loidl, J. Appl. Phys. 103 (2008) 084107.
- [6] R. Xue, G. Zhao, J. Chen, Z. Chen, D. Liu, Mater. Res. Bull. 76 (2016) 124-132.
- [7] L.H. Oliveira, A.P. de Moura, F.A. La Porta, I.C. Nogueira, E.C. Aguiar, T. Sequinel, I.L.V. Rosa, E. Longo, J.A. Varela, Mater. Res. Bull. 81 (2016) 1-9.
- [8] J. Li, K. Wu, R. Jia, L. Hou, L. Gao, S. Li, Materials & Design 92 (2016) 546-551.
- [9] M.F. Ab Rahman, S.D. Hutagalung, Z.A. Ahmad, M.F. Ain, J.J. Mohamed, J. Mater. Sci.: Mater. Electron. 26 (2015) 3947-3956.
- [10] L. Sun, R. Zhang, Z. Wang, E. Cao, Y. Zhang, L. Ju, J. Alloys Compd. 663 (2016) 345-350.
- [11] X. Huang, H. Zhang, J. Li, Y. Lai, J. Mater. Sci.: Mater. Electron. (2016) 1-7.
- [12] L. Sun, Z. Wang, W. Hao, E. Cao, Y. Zhang, H. Peng, J. Alloys Compd. 651 (2015) 283-289.
- [13] L. Bai, Y. Wu, L. Zhang, J. Alloys Compd. 661 (2016) 6-13.
- [14] T. Li, H.F. He, T. Zhang, B. Zhao, Z.Q. Chen, H.Y. Dai, R.Z. Xue, Z.P. Chen, J. Alloys Compd. 684 (2016) 315-321.
- [15] T.B. Adams, D.C. Sinclair, A.R. West, J. Am. Ceram. Soc. 89 (2006) 3129-3135.
- [16] L. Singh, B.C. Sin, I.W. Kim, K.D. Mandal, H. Chung, Y. Lee, J. Varela, J. Am. Ceram. Soc. 99 (2016) 27-34.
- [17] A.J. Moulson, J.M. Herbert, *Electroceramics : materials, properties, applications.* 2nd ed.; Wiley: West Sussex; New York, 2003; p xiv, 557 p.
- [18] B. Shri Prakash, K.B.R. Varma, J. Mater. Sci.: Mater. Electron. 17 (2006) 899-907.
- [19] P. Kum-onsa, P. Thongbai, B. Putasaeng, T. Yamwong, S. Maensiri, J. Eur. Ceram. Soc. 35 (2015) 1441-1447.
- [20] P. Thongbai, T. Yamwong, S. Maensiri, Mater. Res. Bull. 47 (2012) 432-437.
- [21] Z. Yang, H. Ren, X. Chao, P. Liang, Mater. Res. Bull. 47 (2012) 1273-1277.
- [22] P. Liang, Z. Yang, X. Chao, J. Alloys Compd. 678 (2016) 273-283.
- [23] P. Liang, X. Chao, F. Wang, Z. Liu, Z. Yang, J. Am. Ceram. Soc. 96 (2013) 3883-3890.
- [24] X. Sun, C. Wang, G. Wang, C. Lei, T. Li, L. Liu, A. Feteira, J. Am. Ceram. Soc. 96 (2013) 1497-1503.
- [25] Z. Liu, X. Chao, P. Liang, Z. Yang, L. Zhi, J. Am. Ceram. Soc. 97 (2014) 2154-2163.
- [26] W. Somphan, N. Sangwong, T. Yamwong, P. Thongbai, J. Mater. Sci.: Mater. Electron. 23 (2012) 1229-1234.
- [27] W. Somphan, P. Thongbai, T. Yamwong, S. Maensiri, Mater. Res. Bull. 48 (2013) 4087-4092.
- [28] Y. Shi, W. Hao, H. Wu, L. Sun, E. Cao, Y. Zhang, H. Peng, Ceram. Int. 42 (2016) 116-121.
- [29] W. Hao, J. Zhang, Y. Tan, M. Zhao, C. Wang, J. Am. Ceram. Soc. 94 (2011) 1067-1072.
- [30] N. Sangwong, W. Somphan, P. Thongbai, T. Yamwong, S. Meansiri, Applied Physics A 108 (2012) 385-392.
- [31] R. Schmidt, M.C. Stennett, N.C. Hyatt, J. Pokorny, J. Prado-Gonjal, M. Li, D.C. Sinclair, J. Eur. Ceram. Soc. 32 (2012) 3313-3323.
- [32] L. Ni, X.M. Chen, J. Am. Ceram. Soc. 93 (2010) 184-189.
- [33] Y. Wang, L. Ni, X.M. Chen, J. Mater. Sci.: Mater. Electron. 22 (2011) 345-350.

- [34] J.Q. Wang, X. Huang, X.H. Zheng, D.P. Tang, J. Mater. Sci.: Mater. Electron. 27 (2016) 1345-1349.
- [35] H. Ren, P. Liang, Z. Yang, Mater. Res. Bull. 45 (2010) 1608-1613.
- [36] P. Liang, X. Chao, Z. Yang, J. Appl. Phys. 116 (2014) 044101.
- [37] J. Boonlakhorn, P. Kidkhunthod, P. Thongbai, J. Eur. Ceram. Soc. 35 (2015) 3521-3528.
- [38] M. Newville, Journal of Synchrotron Radiation 8 (2001) 96-100.
- [39] F.-H. Lu, F.-X. Fang, Y.-S. Chen, J. Eur. Ceram. Soc. 21 (2001) 1093-1099.
- [40] P. Thomas, K. Dwarakanath, K.B.R. Varma, J. Eur. Ceram. Soc. 32 (2012) 1681-1690.
- [41] R. Yu, H. Xue, Z. Cao, L. Chen, Z. Xiong, J. Eur. Ceram. Soc. 32 (2012) 1245-1249.
- [42] J. Liu, C.-G. Duan, W.-G. Yin, W. Mei, R. Smith, J. Hardy, Phys. Rev. B 70 (2004).
- [43] K. Mukae, K. Tsuda, I. Nagasawa, J. Appl. Phys. 50 (1979) 4475-4476.

## **CHAPTER 11**

# Microstructural Evolution, Non-Ohmic Properties and Giant Dielectric Response in CaCu<sub>3</sub>Ti<sub>4-x</sub>Ge<sub>x</sub>O<sub>12</sub> Ceramics

#### 11.1 Introduction

CaCu<sub>3</sub>Ti<sub>4</sub>O<sub>12</sub> (CCTO), the perovskite

-like ceram

has been widely investigated in recent years. CCTO has a high dielectric permittivity ( $\epsilon$ ') of ~10<sup>3</sup>-10<sup>5</sup> in the radio frequency range. Furthermore, nonlinear behavior, which is a nonlinear correlation between the current density and electric field, can also be observed in CCTO polycrystalline ceramics. Since the giant dielectric properties of CCTO ceramics were first studied, several models have been proposed to explain the giant dielectric behavior. Both intrinsic and extrinsic models have been suggested. The giant dielectric and nonlinear electrical properties are widely believed to be caused by the internal barrier layer capacitor (IBLC) structure, which can be produced by using a one

-step proces

However, special sintering steps or dopants can cause changes in these properties. The n-type semiconducting grain and insulating grain boundary (GB) can be controlled using these two methods.<sup>7</sup> The intrinsic effect that originated inside the grains cannot be simply ignored or arbitrarily excluded.<sup>13-14</sup>

The high dielectric loss tangent (tanδ) in CCTO is a significant problem that has been seriously investigated in the past few years. <sup>4-5, 15-16</sup> Investigations to reduce tanδ are not only important for practical applications, but also may give important data leading to a fundamental understanding of the origin(s) of giant dielectric behavior. Considering the nonlinear electrical properties of CCTO polycrystalline ceramics, important data about the electrical response of the GBs and thus giant dielectric response mechanism may be elucidated even though the nonlinear coefficient is still far from an acceptable value for use in varistor devices.

Many studies have used dopants to improve the dielectric and non CCTO ceramics. This is one of the most widely used methods for increasing dielectric performance. And the company dopants have been substituted into the  $Cu^{2+}$  and  $Ti^{4+}$  sites of the CCTO structure such as  $Mg^{2+}$ ,  $Zn^{2+}$ ,  $Sn^{4+}$ ,  $Zr^{4+}$  and  $W^{6+}$ ,  $S^{13}$ ,  $S^{17-23}$  Substitution of  $S^{4+}$  ions into  $S^{4+}$  sites of CCTO ceramics has rarely been reported. Moreover, the nonlinear electrical behavior of  $S^{4+}$  doped CC

microstructural evolution, deviation of the oxidation states of Cu<sup>2+</sup> and Ti<sup>4+</sup>, impedance spectroscopy analysis, giant dielectric properties and nonlinear electrical property data is lacking.

### **11.2** Experimental details

compression at ~200 MPa into pellet shapes of 9.5 mm in diameter and ~1.5 mm in thickness.

Finally, all the green bodies were sintered at 1050 °C for 6 h. The CaCu<sub>3</sub>Ti<sub>4-x</sub>Ge<sub>x</sub>O<sub>12</sub> ceramics with x = 0, 0.05, and 0.10 are referred to as the CCTO, CCTO respectively.

-Ge05 and CCTO- (

The phase composition and crystal structure were characterized using an X -ray Diffractometer (PANalytical, EMPYREAN). The diffraction spectra were collected over the 20 range of 25°-65° with a scan speed of 0.02°/min. The Rietveld refinement was done using X'Pert HighScore Plus software and compared with the crystallographic structure of CCTO. The parameters and coefficients optimized were the zero shift, scale factor, background (with function type: polynomial), profile half-width parameters (v, u, w), lattice parameter (a), atomic site occupancies (Wyckoff), and the preferred orientation parameter. Surface morphologies were characterized using scanning electron microscopy (SEM; LEO 1450VP). The densities of the sintered samples were measured using an Archimedes' method. Elemental distribution in the sintered ceramics was examined using field-emission scanning electron microscopy (FE-SEM) =ndispaersiveix(EDX) (HITACHI SU8030, Japan). X with energy -ray absorption near edge structure (XANES) spectra of all sintered ceramics were collected at the SUT-NANOTEC-SLRI XAS beamline (BL5.2) (electron energy of 1.2 GeV; bending magnet; beam current 80-150 mA; 1.1 to 1.7×10<sup>11</sup> photon.s<sup>-1</sup>) at the Synchrotron Light Research Institute (SLRI), Nakhon Ratchasima, Thailand. Details of this characterization technique and analysis are given elsewhere.<sup>25</sup> Normalized XANES data were analyzed after background subtraction in the pre-edge and postedge regions using ATHENA software included in an *IFEFFIT* package.<sup>26</sup>

Both parallel surfaces of the sintered samples were polished and carefully washed to obtain smooth and clean surfaces. All the samples were dried at 100 °C overnight. Both sides of sample surfaces were coated with Au using a Polaron SC500 sputter coating unit operated at an electric current ~25 mA for 4 min. The dielectric properties were measured using a KEYSIGHT E4990A with an oscillation voltage of 500 mV. This measurement was done in ranges of 10<sup>2</sup>-10<sup>7</sup> Hz and 60 to 210 °C. Nonlinear current density-electric field (*J-E*) characteristics were measured at room temperature (RT) using a high voltage measurement unit (Keithley 247). The rate of increase in the source voltage was 1.33 V/s. The  $E_{\rm b}$  value was defined as the electric field breakdown at which  $J = 1 \text{ mA.cm}^{-2}$ . The nonlinear coefficient ( $\alpha$ ) was calculated in the range of 1–  $10 \text{ mA/cm}^2$ .

### 11.3 Results and discussion

Fig. 1(a), the diffraction peaks of the CCTO, CCTO -Ge05, and CCTO- ( 1 21 188).a consistent with standard peaks of CCTO in the 20 range of 25°-65° (JCPDS 75 single phase was detected in all the XRD patterns with no possible impurities from CuO, Cu<sub>2</sub>O, TiO<sub>2</sub>, CaTiO<sub>3</sub> and related

-oxide Ge phases. Th

of Ge<sup>4+</sup> ions into the CCTO structure and/or some small part of a Ge phalatethrming a liquid phase during sintering and flowing along GBs during cooling.

Profile fits of the Rietveld refinement were performed, as illustrated in Figs. 1(b) quality of the refinement was quantified by the corresponding figures of merit, i.e., profile residual  $(R_p)$ , expected residual  $(R_{exp})$ , weighted profile residual  $(R_{wp})$ , and the goodness of fit (GOF).<sup>27</sup> The fitted results are summarized in Table 1. R<sub>exp</sub>, R<sub>wp</sub>, and R<sub>p</sub> values of all samples were less than 10%. The experimental XRD patterns were well fitted, which was confirmed by low GOF values  $(< 4.0 \text{ for all the samples}).^{28}$  The lattice parameter (a) was obtained from the Rietveld refinement and compared to the crystallographic CCTO structure. The calculated a values were 7.3942(1), 7.3899(2), and 7.3880(1) Å for the CCTO, CCTO respectively. A decrease in a value of the CaCu<sub>3</sub>Ti<sub>4-x</sub>Ge<sub>x</sub>O<sub>12</sub> ceramics was likely caused by the smaller ionic radius of  $Ge^{4+}$  ( $r_6 = 0.53 \text{ Å}$ ) dopant ion compared to that of the  $Ti^{4+}$  ( $r_6 = 0.605 \text{ Å}$ ) host ion.<sup>29</sup> Table 1, significant decreases in bond length between M—O and M—Cu (M=Ti, Ge) were detected. A decrease in a confirmed that  $Ge^{4+}$  ions could likely enter into the CCTO lattice.

-(d). The

-Ge05, and CCTO-

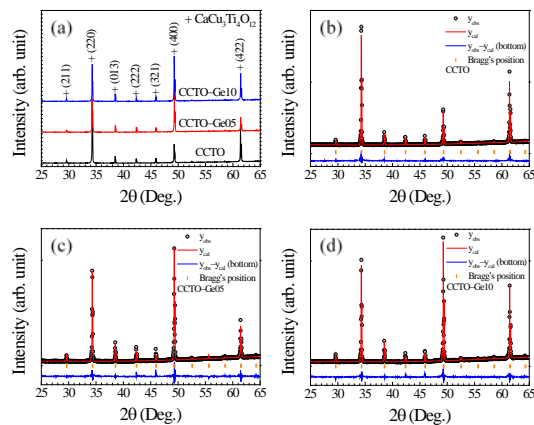


**Fig. 1** (a) XRD patterns of the CCTO, CCTO–Ge05, and CCTO–Ge10 ceramics. (b-d) Profile fits for the Rietveld refinements of the CCTO, CCTO–Ge05, and CCTO–Ge10 ceramics, respectively.

**Table 1.** Structural data obtained from the Rietveld refinement for CCTO, CCTO-Ge05, and CCTO-Ge10 ceramics.

Sample	ССТО	CCTO-Ge05	CCTO-Ge10
Lattice parameter (Å)	7.3942(1)	7.3899(2)	7.3880(1)
$R_{exp}$	3.86761	3.90774	3.89240
$R_p$	4.77845	4.52524	4.43128
$R_{wp}$	6.50429	6.52736	6.04493
GOF	2.82823	2.79013	2.41184
Bond lengths (Å)		( <b>M</b> =Ti, Ge)	
<b>M</b> —O	1.9590(0)	1.9580(0)	1.9570(0)
<b>M</b> —Cu	3.2020(0)	3.2000(0)	3.1990(0)

The microstructural evolution of CaCu<sub>3</sub>Ti<sub>4-x</sub>Ge<sub>x</sub>O<sub>12</sub> ceramics is revealed in Fig. 2. Dense microstructures of all sintered ceramics were obtained by sintering at 1050 °C for 6 h. The relative densities of the CCTO, CCTO -Ge10 cera €1**6**61005, and density of CCTO were 94.39, 95.89, and 95.75%, respectively. Highly dense ceramics were accomplished using a two  $^{4+}$ stebpplicael in mildinard naethrealt effect on the grain growth of CCTO ceramics. The grain size of CaCu<sub>3</sub>Ti<sub>4-x</sub>Ge<sub>x</sub>O<sub>12</sub> ceramics significantly increased with increasing  $Ge^{4+}$  concentration from x=0-0.10. The the CCTO, CCTO ≈6.605≈8and, 6.66T G+1 G2e10 μoveramics were respectively. The microstructural evolution in  $CaCu_3Ti_{4-x}Ge_xO_{12}$  ceramics was similar to that observed in  $Te^{4+}$ ,  $Mo^{6+}$ ,  $Ga^{3+}$ -doped CCTO ceramics. <sup>30-31</sup> This result indicates that  $Ge^{4+}$  doping ions played some important role in the grain growth mechanism of CCTO, which is generally associated with the liquid phase sintering mechanism. <sup>13, 20, 30-31</sup> Usually, the dopant directly melts and/or reacts with a small part of the major phase to form a eutectic liquid. The liquid phase was present at the contact areas between particles or grains in the microstructure. These can enhance the diffusion of ions across the GB, resulting in enhanced grain growth rate. Thus, the grain growth rate of CCTO ceramics may be activated by a Cu and/or Ge heelated liquid

eutectic temperature for CuO–TiO<sub>2</sub> is about 950 °C.

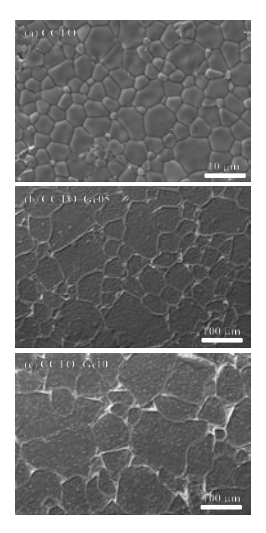


**Fig. 2** SEM images of surface morphologies of (a) CCTO, (b) CCTO–Ge05, and (c) CCTO–Ge10 ceramics.

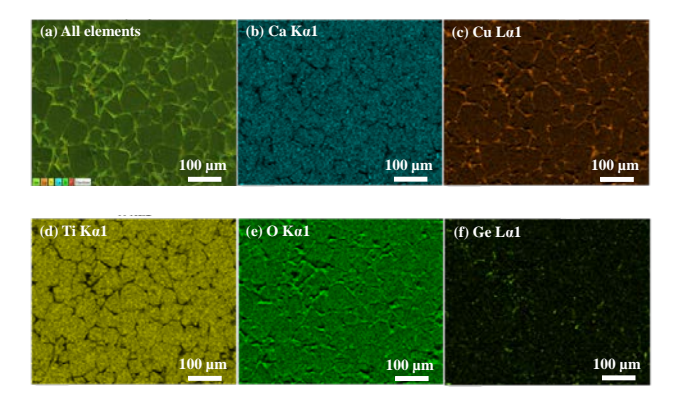


**Fig. 3** SEM mapping images of the CCTO–Ge10 ceramic sintered at 1050 °C for 3 h; (a) all elements, (b) Ca, (c) Cu, (d) Ti, (e) O, and (f) Ge.

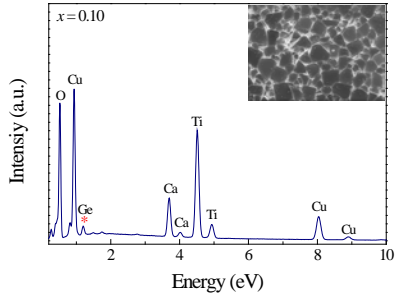


**Fig. 4** EDS spectrum of the CCTO–Ge10 ceramic; inset shows the selected area for measuring the EDS spectrum.

Figure 3 reveals the SEM mapping of the CCTO–Ge10 ceramic, showing dispersion of all major elements (*i.e.*, Ca, Cu, Ti, and O) and the Ge dopant. Segregation of Cu was observed along the GBs, which is usually reported in the literature.<sup>32</sup> Furthermore, it was found that a small portion of Ge was segregated at the GBs. These results strongly confirm that the liquid phase was closely associated with Cu and Ge–rich phases. Figure 4 and its inset show the EDS spectrum of the CCTO–Ge10 ceramic and the selected area for EDS measurement, confirming the existence of all elements (i.e., Ca, Cu, Ti, Ge, and O) in the sintered ceramic. The EDS spectra on the grains of 6

different grains were measured. The averaged percentages of Ca, Cu, Ti, and Ge were found to be ≈7.39, 36.13, 35.48 and 1.35 wt.%, respectively.

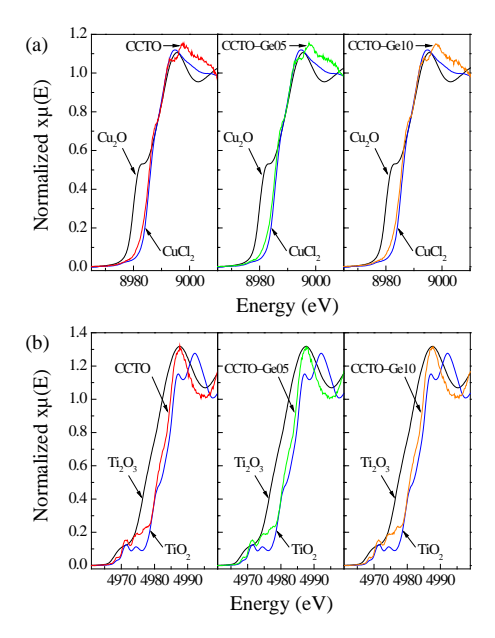


**Fig. 5** (a) Normalized XANES spectra for Cu *K*-edge for the CCTO, CCTO–Ge05, and CCTO–Ge10 ceramics and (b) Normalized XANES spectra for Ti *K*-edge.

Although the valance states of the Ge<sup>4+</sup> dopant and Ti<sup>4+</sup> host ions are the same, deviation of oxidation states for Cu<sup>2+</sup> and Ti<sup>4+</sup> may occur as a result of several factors. Sintered CaCu<sub>3</sub>Ti<sub>4-x</sub>Ge<sub>x</sub>O<sub>12</sub> ceramics were characterized using a XANES technique. Figures 5(a) and (b) demonstrate the XANES spectra, respectively, for Cu and Ti in the CCTO, CCTO ceramics. For all the samples, the Cu *K*-edge energy position was between Cu<sub>2</sub>O (Cu<sup>+</sup>) and CuCl<sub>2</sub> (Cu<sup>2+</sup>) standard samples, while the Ti *K*-edge energy position was between Ti<sub>2</sub>O<sub>3</sub> (Ti<sup>3+</sup>) and TiO<sub>2</sub> (Ti<sup>4+</sup>). These indicate that mixed oxidation states of Cu<sup>+</sup>/Cu<sup>2+</sup> and Ti<sup>3+</sup>/Ti<sup>4+</sup> occurred in all sintered ceramics. Quantitative analysis of different valence states was determined using an empirical edge—shift calculation by making comparisons with known standard samples. A slight shift in the values of Cu and Ti *K*-edge was confirmed.<sup>25, 33</sup> The maximum value of the first derivative of the edge region was used to calculate the edge value. The amount of Cu<sup>+</sup> was determined from Eq. (1):

Although the valance states of the Ge<sup>4+</sup> dopant and Ti<sup>4+</sup> host ions are the same, deviation of oxidation states for Cu<sup>2+</sup> and Ti<sup>4+</sup> may occur as a result of several factors. Sintered CaCu<sub>3</sub>Ti<sub>4-x</sub>Ge<sub>x</sub>O<sub>12</sub> ceramics were characterized using a XANES technique. Figures 5(a) and (b) demonstrate the XANES spectra, respectively, for Cu and Ti in the CCTO, CCTO ceramics. For all the samples, the Cu *K*-edge energy position was between Cu<sub>2</sub>O (Cu<sup>+</sup>) and CuCl<sub>2</sub> (Cu<sup>2+</sup>) standard samples, while the Ti *K*-edge energy position was between Ti<sub>2</sub>O<sub>3</sub> (Ti<sup>3+</sup>) and TiO<sub>2</sub> (Ti<sup>4+</sup>). These indicate that mixed oxidation states of Cu<sup>+</sup>/Cu<sup>2+</sup> and Ti<sup>3+</sup>/Ti<sup>4+</sup> occurred in all sintered ceramics. Quantitative analysis of different valence states was determined using an empirical edge—shift calculation by making comparisons with known standard samples. A slight shift in the values of Cu and Ti *K*-edge was confirmed.<sup>25, 33</sup> The maximum value of the first derivative of the edge region was used to calculate the edge value. The amount of Cu<sup>+</sup> was determined from Eq. (1):

% of 
$$Cu^+ = \left(1 - \frac{\Delta E \text{ of sample}}{\Delta E \text{ of } Cu^+ \text{ and } Cu^{2+} \text{ standard}}\right) \times 100\%$$
 (1)

 $\Delta E$  is the difference in the edge values of samples compared with a  $Cu^+$  ( $Cu_2O$ ) standard. The calculated ratios of  $Cu^+/Cu^{2+}$  for the CCTO, CCTO 6.70, and 7.04%, respectively. The  $Cu^+/Cu^{2+}$  ratio increased slightly with increasing  $Ge^{4+}$  concentration. Similarly, the  $Ti^{3+}/Ti^{4+}$  ratios can be also calculated 25, 33 and found to be 4.71, 5.83,

-Ge05, and

-Ge05, and

Ge05, and

and 5.50%, respectively. The presence of  $Cu^+$  and  $Ti^{3+}$  is similar to observations reported in the literature for CCTO and related isostructural oxides. 10, 12-14, 25, 34-35 Electron hopping between  $Ti^{3+} \leftrightarrow Ti^{4+}$  and  $Cu^{+} \leftrightarrow Cu^{2+}$  sites is one of the most possible explanations for conduction in *n*-type semiconducting grains of CaCu<sub>3</sub>Ti<sub>4-x</sub>Ge<sub>x</sub>O<sub>12</sub> ceramics. Interestingly, the Ge<sup>4+</sup> dopant had effects on the oxidation states of Cu and Ti even though charge compensation was not required due to their identical oxidation states (Ge<sup>4+</sup> and Ti<sup>4+</sup>). It is possible that increases in the Ti<sup>3+</sup>/Ti<sup>4+</sup> and Cu<sup>+</sup>/Cu<sup>2+</sup> ratios might be caused by an increase in oxygen vacancies inside the large grains, since the grain growth of CCTO ceramics was shown to be associated with the oxygen vacancies.<sup>32,34</sup>

The effects of Ge<sup>4+</sup> doping ions electrical properties of the grain and GB of CCTO ceramics were also characterized using impedance spectroscopy. The resistances of the grain and GBs ( $R_g$ and  $R_{gb}$ , respectively) can usually be estimated from the nonzero intercept on the Z' axis and the diameter of a large semicircular arc of Z\* plots, respectively. The impedance complex (Z\*) plots were fitted using a modified equation for a Z\* plot for a simple equivalent circuit consisting of parallel  $R_{gb}C_{gb}$  elements connected to  $R_g$  in series:<sup>30</sup>

$$Z^* = R_g + \frac{R_{gb}}{1 + (j\omega R_{gb} C_{gb})^{\alpha}}$$
 (2)

where  $\alpha$  is a constant parameter  $(0 < \alpha \le 1)$  and  $\omega$  is the angular frequency of an applied AC field. Usually, the grain capacitance  $(C_g)$  is not accessible and the respective capacitor can simply be removed from the circuit. At around RT, only a linear part of a large semicircle arc was observed. Consequently,  $Z^*$  plots of all the samples cannot be fitted accurately. Only  $R_g$  can be obtained from the nonzero intercept. Therefore, Z\* plots of all the samples at 80 °C were selected. Notably, Z\* plots were well fitted by Eq. (2), as illustrated in Fig. 6(a). R<sub>gb</sub> values at 80 °C for the CCTO,  $^{3}$ ,G  $^{2}$ 050 $\times$   $^{1}$ 10 $^{4}$  Gramics were 1.15 $\times$ 10

respectively. The  $Ge^{4+}$  dopant has a strong effect on the  $R_{gb}$  value, which remarkably increased with increasing  $Ge^{4+}$  content.  $R_{gb}$  increased even though a number of insulating GB layer decreased (or the mean grain size increased). Theoretically, when doping Ge<sup>4+</sup> ions into Ti<sup>4+</sup> sites, charge compensation is not required. Thus, the intrinsic properties (e.g., the potential barrier height) of the GBs should not be altered. A change in  $R_{\rm gb}$  may have resulted from geometric parameters of the GB such as thickness. The increase in  $R_{\rm gb}$  was likely caused by segregation of Cu and/or Ge-rich phases along the GBs, as revealed in Figs. 2 and 3(c) and (f). As shown in the inset of Fig. 6(a), the  $R_{\rm g}$  of CCTO ceramics was slightly reduced by doping with  ${\rm Ge}^{4+}$  ions, corresponding to a small increase in the Cu<sup>+</sup>/Cu<sup>2+</sup> and Ti<sup>3+</sup>/Ti<sup>4+</sup> ratios. Substitution of Ge<sup>4+</sup> into CCTO ceramics not only increased  $R_{\rm gb}$ , but also decreased  $R_{\rm g}$  and the free charge carriers inside the grains.

Fig. 6(b), Z\* plots at higher temperatures of all ceramics were well fitted by Eq. (2). R<sub>gb</sub> values at different temperatures could be obtained. According to our previous work,  $^{35-36}$   $R_{\rm g}$  can easily be calculated from the frequency dependence of Y", the imaginary part of admittance complex (Y\*).  $R_g \approx 1/Y''_{\text{max}}$ , where  $Y''_{\text{max}}$  is the maximum value at the Y''-peak.  $R_g$  values at various temperatures obtained from the impedance and admittance analyses were nearly the same in value. Figs. 7(a)–(c), the Y"–peaks at temperatures below 0 °C for the CCTO, CCTO <sup>5</sup>-GLEU 10 leteramAircshindere observed in the fr

temperatures, the Y"-peaks shifted out of the upper limit of the measured frequency range. The magnitude of the Y"-peak increased with increasing temperature, indicating a decrease in  $R_{\rm g}$ . Variation in  $R_{\rm gb}$  and  $R_{\rm g}$  for all the samples followed the Arrhenius law:

$$R_{g,gb} = R_0 \exp(E_{g,gb} / k_B T) \tag{3}$$

where  $E_g$  and  $E_{gb}$  are the activation energies for conduction inside the grains and at the GBs, kexanouhe Titizale advestant the transfer constant and respectively.  $R_0$  is a pre absolute temperature, respectively. Fig. 7(d) and its inset, the temperature dependencies of  $R_{gb}$  and  $R_g$  were linearly fitted by Eq. (3). The activation energies were calculated from the slopes of these linear relationships.  $E_g$  of the CCTO, CCTO 97, 91, and 96 meV, respectively.  $E_g$  of  $CaCu_3Ti_{4-x}Ge_xO_{12}$  ceramics slightly changed with

variation in the  $Ge^{4+}$  content. This result was closely associated with a slight decrease in  $R_g$ .

-Ge05, and

-Ge05, and CCTO- (

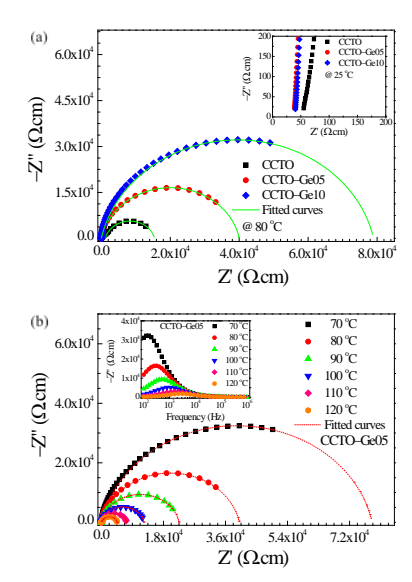
Alternatively,  $E_{gb}$  was enhanced by  $Ge^{4+}$  doping.  $E_{gb}$  values were 450, 658, and 633 meV, respectively. This result may have been caused by the segregation of Cu and/or Ge-rich phases along the GBs.

According to the increase in both of  $R_{\rm gb}$  and  $E_{\rm gb}$  of  $CaCu_3Ti_{4-x}Ge_xO_{12}$  ceramics, the influence of  $Ge^{4}$  on the enhanced nonlinear  $J-\bar{E}$  properties was expected, even though these two properties were measured at different voltage levels. As shown in the inset (1) of Fig. 8, all the samples exhibited nonlinear J-E characteristics, confirming a close correlation between the electrically heterogeneous IBLC structure and nonlinear J-E behavior. The  $\alpha$  values of the CCTO, CCTO

-Ge05, and

while the E<sub>b</sub> values were 72.8, 268.8, and 242.7 V.cm<sup>-1</sup>, respectively. Usually, an increase in the GB density is the primary factor for enhancement of nonlinear J-E properties. 7, 16, 25 However, the values of  $E_b$  and  $\alpha$  of  $CaCu_3Ti_{4-x}Ge_xO_{12}$  ceramics were enhanced even though the GB density was reduced due to its enlarged grain size. A larger total resistance of a sample with fewer insulating layers indicated that the average resistance of individual insulating layers in the CCTO **CCTO** 

-Ge05, and -Ge10 ceramics was much larger in t



(a) Impedance complex plane (Z\*) plots at 80 °C for the CCTO, CCTO-Ge05, and Fig. 6 CCTO-Ge10 ceramics; inset shows an enlarged view of Z\* plots at 25 °C close to the origin, revealing a nonzero intercept on Z' axis. (b) Z\* plots of the CCTO-Ge05 ceramic in the temperature range of 70

According to the impedance spectroscopy analysis and investigation of nonlinear electrical properties, it was clearly shown that CaCu<sub>3</sub>Ti<sub>4-x</sub>Ge<sub>x</sub>O<sub>12</sub> ceramics were electrically heterogeneous, comprised of insulating GBs and semiconducting grains. Thus, the giant dielectric response and tan \delta can be controlled by tuning the properties of the grains and GBs. The frequency dependence of ε' and tanδ of the CaCu<sub>3</sub>Ti<sub>4-x</sub>Ge<sub>x</sub>O<sub>12</sub> ceramics with different in microstructures is demonstrated in Fig. 8 and inset (2). The low

-frequency

frequency. Interestingly, substitution of  $Ge^{4+}$  ions not only enhanced the  $\varepsilon'$  response, but enabled a  $\frac{2}{2}$ depèndence ofapid decrease in  $\varepsilon'$  at stable frequency frequencies higher than 10<sup>5</sup> Hz and the corresponding rapid increase in tanδ were caused by dielectric relaxation. <sup>13, 17</sup> The  $\varepsilon'$  values at 1 kHz and RT of the CaCu<sub>3</sub>Ti<sub>4-x</sub>Ge<sub>x</sub>O<sub>12</sub> with x=0, 0.05, and 0.10 were, respectively, 69029, 107667, and 108165, while tanδ values were 0.600, 0.068, and 0.064, respectively. This significant increase of  $\varepsilon'$  is quite consistent with IBLC model since an enhanced  $\varepsilon'$  value was related to an increase in the mean grain size. Another important reason for this is the increase free charges inside the grains (in Cu<sup>+</sup>/Cu<sup>2+</sup> and Ti<sup>3+</sup>/Ti<sup>4+</sup> ratios). Under an applied electric field, more charge carriers inside the semiconducting grains moved and were eventually trapped at the GBs. This caused an increase in the interfacial polarization intensity, giving rise to an enhanced  $\varepsilon'$  value.

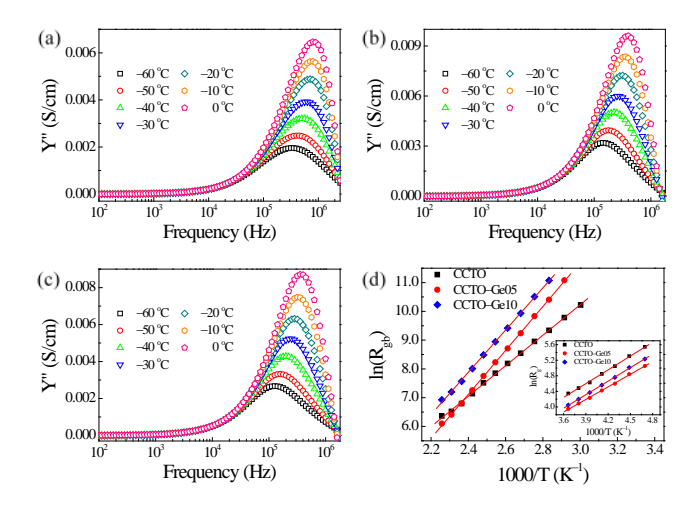


**Fig. 7** (a-c) Frequency dependence of Y" at different temperatures for the CCTO, CCTO–Ge05, and CCTO–Ge10 ceramics. (b) Arrhenius plots of  $R_{gb}$  for all the samples; inset demonstrates the Arrhenius plots of  $R_{g}$ .

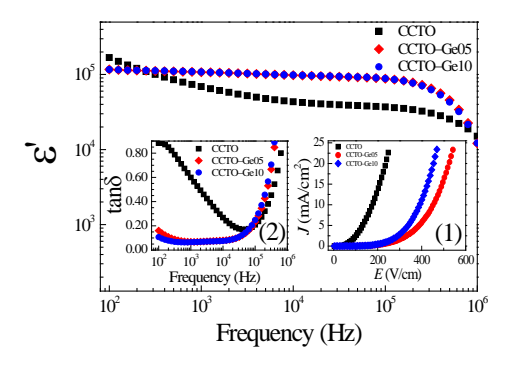


**Fig. 8** Frequency dependence of ε' at 25 °C for the CCTO, CCTO–Ge05, and CCTO–Ge10 ceramics; insets (1) and (2) show tanδ as a function of frequency and J –E characteristics at RT.

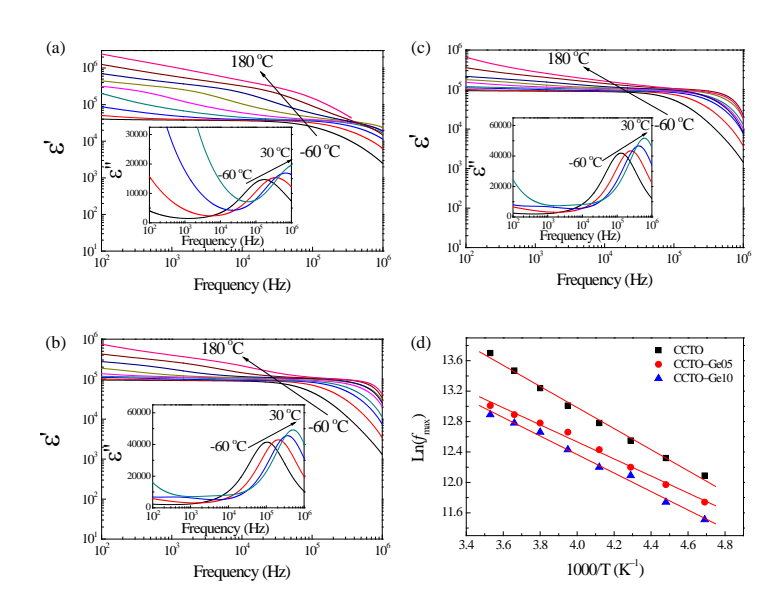


Fig. 9 Frequency dependence of  $\varepsilon'$  at different temperatures (-60 to 180 °C) of (a) CCTO, (b) CCTO–Ge05, and (c) CCTO–Ge10 ceramics; insets show their tan $\delta$  values. (c) Arrhenius plot for the relaxation frequency  $(f_{\text{max}})$ .

Interestingly, tanó values of the CCTO by a factor of 10 compared to that of the un values of un general case, the enhanced low insulating GB layers as the mean grain size incre

-radoped CCTO ce <sup>37</sup>doped ସେପୀ ଡ ceramics ir -frequency

insulating GB layers as the mean grain size increased, giving rise to a decrease in  $R_{\rm gb}$ . A significant reduction in tan $\delta$  in the CCTO enhancement of  $R_{\rm gb}$ .  $^{16, 30, 39}$ 

-Ge05 and

-Ge05 and

The frequency dependencies of  $\varepsilon'$  and  $\varepsilon''$  (the imaginary part of the complex dielectric permittivity,  $\varepsilon'' = \varepsilon' \times \tan \delta$ ) at different temperatures were studied. Figs. 9(a -c), a strong of  $\varepsilon'$  as a function of temperature in the range of -60 <sup>o</sup>C180as observed in the dielectric spectra of the CCTO ceramic. This was less dominant in the CCTO -Ge10 ceramics, indicating a greater temperature stability of  $\varepsilon'$ . Obviously, two dielectric relaxations were observed in distinct frequency ranges, i.e.,  $10^4$ – $10^5$  Hz and  $10^5$ – $10^6$  Hz. The low-frequency dielectric relaxation is likely attributed to the sample-electrode effect. The rapid decrease in  $\varepsilon'$  in a high frequency range and corresponding  $\varepsilon''$  peak (inset figures) shifted to higher frequencies as temperature was increased, indicating a thermally activated dielectric relaxation behavior. The activation energy  $(E_a)$  required for the relatively high -freguency calculated from the temperature dependence of the critical frequency  $(f_{\text{max}})$  (the frequency at which the relaxation  $\varepsilon''$  peak appeared) following:

$$f_{\text{max}} = f_0 \exp\left(\frac{-E_a}{k_B T}\right),\tag{4}$$

where  $f_0$  is a constant value. As depicted in Fig. 9(d), the frequency dependence of  $f_{\rm max}$  for all the ceramics followed the Arrhenius law (Eq. 4). The  $E_a$  values of the CCTO, CCTO —Ge05 and CCTO —Ge05 and TGe10endsamicchawge ih20he9 $E_{\rm g}$  and 96 meV and  $E_a$  values were similar. According to the Maxwell —Wagner possed on the IBLC structure, the temperature dependence of  $f_{\rm max}$  can be expressed in terms of  $R_{\rm g}$ . Therefore, the similar values of  $E_a$  and  $E_g$  indicated that the giant dielectric response in these ceramics was extrinsic in origin and related to their electrically IBLC microstructures. Substitution of Ge<sup>4+</sup> into Ti<sup>4+</sup> sites can simultaneously improve the giant dielectric and nonlinear electrical properties of CCTO ceramics. The improved dielectric properties were attributed to a combination causes including an enlarged grain size, increased free charge carriers, and segregation of liquid at the GBs. The last cause can also enhance the nonlinear electrical properties.

# 11.4 Conclusions

The CaCu<sub>3</sub>Ti<sub>4-x</sub>Ge<sub>x</sub>O<sub>12</sub> ceramics with x=0-0.10 were synthesized using a solid state reaction method. A pure phase of CCTO was confirmed in all the sintered ceramic samples. All sintered ceramics had a highly dense microstructure. Doping CCTO with Ge<sup>4+</sup> caused an increase in the mean grain size, which was primarily due to the liquid phase sintering, revealed by SEM mapping elements in the surface morphology. Significantly enhanced  $R_{\rm gb}$  coupled with a slightly decreased  $R_{\rm g}$  was achieved. Enhancement of  $\varepsilon'$  from  $6.90\times10^4$  to  $1.08\times10^5$  while reducing tan $\delta$  by one order of magnitude was achieved. The nonlinear electrical properties of CCTO were enhanced by doping with Ge<sup>4+</sup> ions. The enhanced giant dielectric properties were ascribed to the enlarged grain size, increased free charge carriers, and segregation of liquid at the GBs.

### References

<sup>1</sup>M. A. Subramanian, D. Li, N. Duan, B. A. Reisner, and A. W. Sleight, "High Dielectric Constant in ACu<sub>3</sub>Ti<sub>4</sub>O<sub>12</sub> and ACu<sub>3</sub>Ti<sub>5</sub>FeO<sub>12</sub> Phases," *J. Solid State Chem.* **151** [2] 323-5 (2000).

<sup>2</sup>L. Liu, H. Fan, P. Fang, and X. Chen, "Sol–gel derived CaCu<sub>3</sub>Ti<sub>4</sub>O<sub>12</sub> ceramics: Synthesis, characterization and electrical properties," *Mater. Res. Bull.* **43** [7] 1800-7 (2008).

- <sup>3</sup>L. Liu, Y. Huang, Y. Li, D. Shi, S. Zheng, S. Wu, L. Fang, and C. Hu, "Dielectric and non-Ohmic properties of CaCu<sub>3</sub>Ti<sub>4</sub>O<sub>12</sub> ceramics modified with NiO, SnO<sub>2</sub>, SiO<sub>2</sub>, and Al<sub>2</sub>O<sub>3</sub> additives," *J. Mater. Sci.* **47** [5] 2294-9 (2012).
- <sup>4</sup>L. Sun, R. Zhang, Z. Wang, E. Cao, Y. Zhang, and L. Ju, "Microstructure and enhanced dielectric response in Mg doped CaCu<sub>3</sub>Ti<sub>4</sub>O<sub>12</sub> ceramics," *J. Alloys Compd.* **663** 345-50 (2016).
- <sup>5</sup>A. Nautiyal, C. Autret, C. Honstettre, S. De Almeida-Didry, M. El Amrani, S. Roger, B. Negulescu, and A. Ruyter, "Local analysis of the grain and grain boundary contributions to the bulk dielectric properties of Ca(Cu<sub>3-y</sub>Mg<sub>y</sub>)Ti<sub>4</sub>O<sub>12</sub> ceramics: Importance of the potential barrier at the grain boundary," *J. Eur. Ceram. Soc.* **36** [6] 1391-8 (2016).
- <sup>6</sup>X. W. Wang, P. B. Jia, X. E. Wang, B. H. Zhang, L. Y. Sun, and Q. B. Liu, "Calcining temperature dependence on structure and dielectric properties of CaCu<sub>3</sub>Ti<sub>4</sub>O<sub>12</sub> ceramics," *J. Mater. Sci.: Mater. Electron.* 1-7 (2016).
- <sup>7</sup>S.-Y. Chung, I.-D. Kim, and S.-J. L. Kang, "Strong nonlinear current–voltage behaviour in perovskite-derivative calcium copper titanate," *Nat. Mater.* **3** [11] 774-8 (2004).
- <sup>8</sup>R. Schmidt, S. Pandey, P. Fiorenza, and D. C. Sinclair, "Non-stoichiometry in "CaCu<sub>3</sub>Ti<sub>4</sub>O<sub>12</sub>" (CCTO) ceramics," *RSC Advances* **3** [34] 14580-9 (2013).
- <sup>9</sup>S. I. R. Costa, M. Li, J. R. Frade, and D. C. Sinclair, "Modulus spectroscopy of CaCu<sub>3</sub>Ti<sub>4</sub>O<sub>12</sub> ceramics: clues to the internal barrier layer capacitance mechanism," *RSC Advances* **3** [19] 7030-6 (2013).
- <sup>10</sup>W. Hao, H. Wu, P. Xu, Y. Shi, S. Yang, M. Wang, L. Sun, E. Cao, and Y. Zhang, "Influence of Sb-doping on dielectric properties of NaCu<sub>3</sub>Ti<sub>3</sub>TaO<sub>12</sub> ceramics and relevant mechanism(s)," *Ceram. Int.* **43** [4] 3631-8 (2017).
- <sup>11</sup>Y. Liu, W. Wang, J. Huang, F. Tang, C. Zhu, and Y. Cao, "Dielectric properties of giant permittivity NaCu<sub>3</sub>Ti<sub>3</sub>NbO<sub>12</sub> ceramics," *Ceram. Int.* **39** 9201–6 (2013).
- <sup>12</sup>W. Hao, J. Zhang, Y. Tan, M. Zhao, and C. Wang, "Giant Dielectric Permittivity Properties and Relevant Mechanism of NaCu<sub>3</sub>Ti<sub>3</sub>SbO<sub>12</sub> Ceramics," *J. Am. Ceram. Soc.* **94** [4] 1067-72 (2011).
- <sup>13</sup>L. Ni, and X. M. Chen, "Enhancement of Giant Dielectric Response in CaCu<sub>3</sub>Ti<sub>4</sub>O<sub>12</sub> Ceramics by Zn Substitution," *J. Am. Ceram. Soc.* **93** [1] 184-9 (2010).
- <sup>14</sup>Y. Wang, L. Ni, and X. M. Chen, "Effects of Nd-substitution on microstructures and dielectric characteristics of CaCu<sub>3</sub>Ti<sub>4</sub>O<sub>12</sub> ceramics," *J. Mater. Sci.: Mater. Electron.* **22** [4] 345-50 (2011).
- <sup>15</sup>L. Sun, R. Zhang, Z. Wang, E. Cao, Y. Zhang, and L. Ju, "Microstructure, dielectric properties and impedance spectroscopy of Ni doped CaCu<sub>3</sub>Ti<sub>4</sub>O<sub>12</sub> ceramics," *RSC Advances* **6** [61] 55984-9 (2016).
- <sup>16</sup>J. Boonlakhorn, B. Putasaeng, P. Kidkhunthod, and P. Thongbai, "Improved dielectric properties of (Y + Mg) co-doped CaCu<sub>3</sub>Ti<sub>4</sub>O<sub>12</sub> ceramics by controlling geometric and intrinsic properties of grain boundaries," *Materials & Design* **92** 494-8 (2016).
- <sup>17</sup>L. Ni, X. M. Chen, and X. Q. Liu, "Structure and modified giant dielectric response in CaCu<sub>3</sub>(Ti<sub>1-x</sub>Sn<sub>x</sub>)<sub>4</sub>O<sub>12</sub> ceramics," *Mater. Chem. Phys.* **124** [2-3] 982-6 (2010).
- <sup>18</sup>L. Sun, Z. Wang, W. Hao, E. Cao, Y. Zhang, and H. Peng, "Influence of Zirconium doping on microstructure and dielectric properties of CaCu<sub>3</sub>Ti<sub>4</sub>O<sub>12</sub> synthesized by the sol–gel method," *J. Alloys Compd.* **651** 283-9 (2015).
- <sup>19</sup>P. Thongbai, J. Jumpatam, B. Putasaeng, T. Yamwong, and S. Maensiri, "The origin of giant dielectric relaxation and electrical responses of grains and grain boundaries of W-doped CaCu<sub>3</sub>Ti<sub>4</sub>O<sub>12</sub> ceramics," *J. Appl. Phys.* **112** [11] 114115 (2012).
- <sup>20</sup>L. Singh, B. C. Sin, I. W. Kim, K. D. Mandal, H. Chung, Y. Lee, and J. Varela, "A Novel One-Step Flame Synthesis Method for Tungsten-Doped CCTO," *J. Am. Ceram. Soc.* **99** [1] 27-34 (2016).
- <sup>21</sup>W. L. Li, Y. Zhao, Q. G. Chi, Z. G. Zhang, and W. D. Fei, "Enhanced performance of core-shell-like structure Zr-doped CaCu<sub>3</sub>Ti<sub>4</sub>O<sub>12</sub> ceramics prepared by a flame synthetic approach," *RSC Advances* **2** [14] 6073 (2012).
- <sup>22</sup>L. Singh, I. W. Kim, B. C. Sin, K. D. Mandal, U. S. Rai, A. Ullah, H. Chung, and Y. Lee, "Dielectric studies of a nano-crystalline CaCu<sub>2.90</sub>Zn<sub>0.10</sub>Ti<sub>4</sub>O<sub>12</sub>electro-ceramic by one pot glycine assisted synthesis from inexpensive TiO<sub>2</sub> for energy storage capacitors," *RSC Adv.* **4** [95] 52770-84 (2014).

- <sup>23</sup>M. F. Ab Rahman, S. D. Hutagalung, Z. A. Ahmad, M. F. Ain, and J. J. Mohamed, "The effect of different dopant site (Cu and Ca) by magnesium onCaCu<sub>3</sub>Ti<sub>4</sub>O<sub>12</sub> dielectric properties," *J. Mater. Sci.: Mater. Electron.* **26** [6] 3947-56 (2015).
- <sup>24</sup>F. Amaral, L. C. Costa, M. A. Valente, and F. Henry, "Dielectric relaxation and morphologic properties of CaCu<sub>3</sub>Ti<sub>4</sub>O<sub>12</sub> doped with GeO<sub>2</sub>," *J. Non-Cryst. Solids* **355** [43-44] 2160-4 (2009).
- <sup>25</sup>J. Boonlakhorn, P. Kidkhunthod, and P. Thongbai, "A novel approach to achieve high dielectric permittivity and low loss tangent in  $CaCu_3Ti_4O_{12}$  ceramics by co-doping with  $Sm^{3+}$  and  $Mg^{2+}$  ions," *J. Eur. Ceram. Soc.* **35** [13] 3521-8 (2015).
- <sup>26</sup>M. Newville, "EXAFS analysis using FEFF and FEFFIT," J Synchrotron Radiat 8 [Pt 2] 96-100 (2001).
- <sup>27</sup>E. Silva Junior, F. A. La Porta, M. S. Liu, J. Andres, J. A. Varela, and E. Longo, "A relationship between structural and electronic order-disorder effects and optical properties in crystalline TiO<sub>2</sub> nanomaterials," *Dalton Trans.* **44** [7] 3159-75 (2015).
- <sup>28</sup>R. A. Young, and D. B. Wiles, "Profile shape functions in Rietveld refinements," *J. Appl. Crystallogr.* **15** [4] 430-8 (1982).
- <sup>29</sup>R. D. Shannon, "Revised effective ionic radii and systematic studies of interatomic distances in halides and chalcogenides," *Acta Cryst.* **32** [5] 751-67 (1976).
- <sup>30</sup>P. Thongbai, B. Putasaeng, T. Yamwong, V. Amornkitbamrung, and S. Maensiri, "Liquid phase sintering behavior and improvement of giant dielectric properties by modifying microstructure and electrical response at grain boundaries of CaCu<sub>3</sub>Ti<sub>4-x</sub>Mo<sub>x</sub>O<sub>12</sub> ceramics," *J. Alloys Compd.* **582** [0] 747-53 (2014).
- <sup>31</sup>J. Jumpatam, B. Putasaeng, T. Yamwong, P. Thongbai, and S. Maensiri, "Enhancement of giant dielectric response in Ga-doped CaCu<sub>3</sub>Ti<sub>4</sub>O<sub>12</sub> ceramics," *Ceram. Int.* **39** [2] 1057-64 (2013).
- <sup>32</sup>A. A. Felix, V. D. N. Bezzon, M. O. Orlandi, D. Vengust, M. Spreitzer, E. Longo, D. Suvorov, and J. A. Varela, "Role of oxygen on the phase stability and microstructure evolution of CaCu<sub>3</sub>Ti<sub>4</sub>O<sub>12</sub> ceramics," *J. Eur. Ceram. Soc.* **37** [1] 129-36 (2017).
- <sup>33</sup>J. Boonlakhorn, P. Kidkhunthod, B. Putasaeng, and P. Thongbai, "Significantly improved non-Ohmic and giant dielectric properties of CaCu<sub>3-x</sub>Zn<sub>x</sub>Ti<sub>4</sub>O<sub>12</sub> ceramics by enhancing grain boundary response," *Ceram. Int.* **43** [2] 2705-11 (2017).
- <sup>34</sup>R. Yu, H. Xue, Z. Cao, L. Chen, and Z. Xiong, "Effect of oxygen sintering atmosphere on the electrical behavior of CCTO ceramics," *J. Eur. Ceram. Soc.* **32** [6] 1245-9 (2012).
- <sup>35</sup>J. Jumpatam, A. Mooltang, B. Putasaeng, P. Kidkhunthod, N. Chanlek, P. Thongbai, and S. Maensiri, "Effects of Mg<sup>2+</sup> doping ions on giant dielectric properties and electrical responses of Na<sub>1/2</sub>Y<sub>1/2</sub>Cu<sub>3</sub>Ti<sub>4</sub>O<sub>12</sub> ceramics," *Ceram. Int.* **42** [14] 16287-95 (2016).
- <sup>36</sup>J. Jumpatam, W. Somphan, J. Boonlakhorn, B. Putasaeng, P. Kidkhunthod, P. Thongbai, and S. Maensiri, "Non-Ohmic Properties and Electrical Responses of Grains and Grain Boundaries of Na<sub>1/2</sub>Y<sub>1/2</sub>Cu<sub>3</sub>Ti<sub>4</sub>O<sub>12</sub> Ceramics," *J. Am. Ceram. Soc.* n/a-n/a (2016).
- <sup>37</sup>S. De Almeida-Didry, C. Autret, A. Lucas, C. Honstettre, F. Pacreau, and F. Gervais, "Leading role of grain boundaries in colossal permittivity of doped and undoped CCTO," *J. Eur. Ceram. Soc.* **34** [15] 3649-54 (2014).
- <sup>38</sup>P. Thongbai, B. Putasaeng, T. Yamwong, and S. Maensiri, "Current–voltage nonlinear and dielectric properties of CaCu<sub>3</sub>Ti<sub>4</sub>O<sub>12</sub> ceramics prepared by a simple thermal decomposition method," *J. Mater. Sci.: Mater. Electron.* **23** [3] 795-801 (2012).
- <sup>39</sup>T. B. Adams, D. C. Sinclair, and A. R. West, "Influence of Processing Conditions on the Electrical Properties of CaCu<sub>3</sub>Ti<sub>4</sub>O<sub>12</sub> Ceramics," *J. Am. Ceram. Soc.* **89** [10] 3129-35 (2006).

# **CHAPTER 12**

Preparation, Characterization, and Dielectric Properties of CaCu<sub>3</sub>Ti<sub>4</sub>O<sub>12</sub>-Related (Na<sub>1/3</sub>Ca<sub>1/3</sub>Y<sub>1/3</sub>)Cu<sub>3</sub>Ti<sub>4</sub>O<sub>12</sub> Ceramics Using a Simple Sol-Gel Method

## 12.1 Introduction

Over the past few years, the giant dielectric properties of a series of isostructural CaCu<sub>3</sub>Ti<sub>4</sub>O<sub>12</sub> (CCTO)–type perovskites have been widely investigated [1-21]. This is because CCTO and CCTO-related oxides exhibit very high dielectric permittivity ( $\varepsilon'$ ) values of 10<sup>4</sup> over a wide temperature range. Such high  $\varepsilon'$  values were found to be stable with temperature in the range of 100–400 K. These oxides were believed to be a promising material for capacitor applications. Furthermore, the physical characteristics explaining the giant dielectric response in polycrystalline CCTO ceramics is still unclear. Nevertheless, it is widely believed that the internal barrier layer capacitor (IBLC) effect based on Maxwell-Wagner polarization (or interfacial polarization) at the grain boundaries (GBs) is the primary cause of the giant dielectric response in CCTO and related oxides [22-25]. This IBLC model was confirmed by impedance spectroscopy and microprobe analyses [26, 27]. The microstructure consisted of n-type semiconducting grains and insulating GBs. However, the intrinsic effect cannot be ignored [28, 29]. In addition to the giant dielectric properties, CCTO and related ceramics can also exhibit non-Ohmic properties [14, 27].

Unfortunately, a high loss tangent ( $\tan\delta$ >0.05 at 1 kHz) of CCTO and related ceramics is still unsuitable for capacitor applications [4, 6, 10, 12, 29]. Therefore, investigation to reduce the  $\tan\delta$  of CCTO ceramics is still a challenge. Doping CCTO and related oxides with suitable ions is a generally used method to improve their dielectric properties. Interestingly, a reduction in  $\tan\delta$  values to less than 0.05 was achieved by doping with ions such as La<sup>3+</sup> [30], and Mg<sup>2+</sup> [14].

Except for CCTO, the family of  $ACu_3Ti_4O_{12}$  related-oxides (where A = Cd,  $Na_{1/2}La_{1/2}$ ,  $Na_{1/2}Bi_{1/2}$ ,  $Na_{1/2}Y_{1/2}$ ,  $Na_{1/3}Ca_{1/3}Bi_{1/3}$ ,  $Bi_{2/3}$ ,  $Na_{1/3}Ca_{1/3}Y_{1/3}$ ) can exhibit improved giant  $\varepsilon'$  and non-Ohmic properties [1, 2, 10, 13, 17, 20, 22, 31]. The giant dielectric response was widely ascribed to the IBLC effect. Another sub-family of ACu<sub>3</sub>Ti<sub>4</sub>O<sub>12</sub> materials, in which the A-site was randomly occupied by +1, +2 and +3 valence charged ions, each at a level about at.%, of ~33.3 was reported. Good dielectric properties  $[Na_{1/3}^{+}Ca_{1/3}^{2+}Ln_{1/3}^{3+}]Cu_{3}Ti_{4}O_{12}$ , where  $Ln_{3}^{+}$  can be Bi and Y, were reported [10, 13, 31]. For example, low tan $\delta$  (~0.038) and a high  $\varepsilon'$  values (~2.5×10<sup>4</sup>) were obtained in (Na<sub>1/3</sub>Ca<sub>1/3</sub>Bi<sub>1/3</sub>)Cu<sub>3</sub>Ti<sub>4</sub>O<sub>12</sub> ceramics [10]. Additionally, several chemical solution routes and control of sintering conditions for synthesis of CCTO and related oxides have been widely used to significantly improve their dielectric properties [6, 17, 20, 32]. A shorter reaction time and lower temperature were sufficient for their synthesis due to the homogeneity of the starting materials at an atomic scale. Improved dielectric properties of CCTO ceramics prepared using a sol–gel method were studied by Sun et al. [33]. They reported a high  $\epsilon'$  value of about  $1.8\times10^4$  with a low  $tan\delta\sim0.03$  at 1 kHz and RT. Unfortunately,  $[Na^+_{1/3}Ca^{2+}_{1/3}Ln^{3+}_{1/3}]Cu_3Ti_4O_{12}$  ceramics prepared via a chemical route have never been reported.

In the work,  $(Na_{1/3}Ca_{1/3}Y_{1/3})Cu_3Ti_4O_{12}$  (NCYCTO) ceramics were prepared using a simple sol–gel method. Their phase formation, microstructure, dielectric response, and electrical properties were systematically investigated. It was found that the highest  $\varepsilon'$  value of this ceramic system was  $2.5\times10^4$  and a low  $\tan\delta$  values of  $\sim$ 0.04 were measured at 1 kHz. The origin of the giant dielectric response and nonlinear electrical properties are discussed.

# 12.2 Experimental details

NCYCTO ceramics were prepared using a simple sol-gel method (SSG). First, stoichiometric amount of each starting material, i.e.. NaCH<sub>3</sub>COO. (CH<sub>3</sub>CO<sub>2</sub>)<sub>3</sub>Y.H<sub>2</sub>O, Ca(C<sub>2</sub>H<sub>3</sub>CO<sub>2</sub>)<sub>2</sub>.H<sub>2</sub>O, and Cu(CH<sub>3</sub>COO)<sub>2</sub>.H<sub>2</sub>O were dissolved in an aqueous solution of citric acid (5 wt%) and ethylene glycol with constant stirring at RT. Second, C<sub>16</sub>H<sub>28</sub>O<sub>6</sub>Ti was dissolved in the above solution under continued stirring. After that, ethanol was added drop wise into the solution at 150°C until it formed a viscous gel. Then, the gel was dried in air at 350 °C for 40 min. Samples of the resulting porous and dried precursor were ground and calcined at 800, 850 and 900°C for 6 h (referred to as the C800, C850, and C900 powders, respectively). All calcined powders were carefully re-ground and pressed into pellets, ~1.0 mm in thickness and 9.5 mm in diameter, by uniaxial compression at about 200 MPa. Finally, these pellets were sintered in air at 1080°C for 4, 8 and 16 h.

The crystal structure and phase composition of the calcined powders and sintered ceramics were measured using an X-ray diffraction (XRD) technique (PANalytical, EMPYREAN). Scanning electron microscopy (SEM) (SEC, SNE4500M) was used to reveal the microstructure of the sintered ceramics. Before the surface morphology measurements, the as-sintered ceramics were carefully polished and thermally etched at 1040°C for 20 minutes. The distribution of elements, i.e., Na, Ca, Y, Cu, Ti and O, in the sintered NCYCTO ceramic was investigated using field-emission scanning electron microscopy (FE-SEM) with energy-dispersive X-ray analysis (EDX) (HITACHI SU5030, Japan). X-ray Absorption Near Edge Structure (XANES) spectra were measured at the SUT-NANOTEC-SLRI XAS beamline (BL5.2), the Synchrotron Light Research Institute (SLRI), Nakhon Ratchasima, Thailand. Details of this characterization technique and analysis are given elsewhere [14]. The normalized XANES data were corrected and analyzed after background subtraction in the pre-edge and post-edge region using ATHENA software included in an IFEFFIT package [34]. The sintered ceramics were also characterized using X-ray photoelectron spectroscopy (XPS), PHI5000 VersaProbe II, ULVAC-PHI, Japan) at the SUT-NANOTEC-SLRI Joint Research Facility, Synchrotron Light Research Institute (SLRI), Thailand. The XPS spectra were fitted with PHI MultiPak XPS software using Gaussian-Lorentzian lines.

For dielectric measurements, Au electrodes were made by sputtering Au on each pellet face at a current of 30 mA for 8 min using a Polaron SC500 sputter coating unit. The dielectric properties were measured using a KEYSIGHT E4990A Impedance Analyzer using a capacitance–dissipation factor mode. An oscillation voltage of 500 mV was used. The measurements were done over the frequency and temperature ranges of  $10^2$ – $10^7$  Hz and -70–200 °C, respectively. Each measured temperature was kept constant with an accuracy of less than  $\pm 0.1$  °C. The dielectric properties under DC bias voltage were measured in the range of 0–40 V at RT. Nonlinear current density–electric field strength (J–E) characteristics were investigated using a high voltage measurement unit (Keithley Model 247) at RT. The breakdown electric field (E<sub>b</sub>) and nonlinear coefficient ( $\alpha$ ) were obtained at J = 1 mA.cm<sup>-2</sup> and calculated in the range of at J = 1–10 mA.cm<sup>-2</sup>, respectively.

### 12.3 Results and discussion

The XRD patterns of NCYCTO powders prepared using the SSG method and calcined at different temperatures are illustrated in the Fig.1. A primary phase of NCYCTO is detected in the XRD patterns of all powders. These XRD patterns confirm the formation of a CCTO-like phase (JCPDS card no. 75–2188). All the diffraction peaks are well indexed based on the body-centered cubic structure within space group  $Im\bar{3}$ . A small amount of a CuO impurity phase is observed in all powders. The lattice parameters of the C800, C850, and C900 powders were 7.389, 7.388, and 7.387 Å, respectively. These values are between the corresponding values of CCTO (7.391 Å) [1] and Na<sub>1/2</sub>Y<sub>1/2</sub>Cu<sub>3</sub>Ti<sub>4</sub>O<sub>12</sub> (7.381–7.387 Å) [2, 13, 31]. This is due to the difference in the ionic radii of the A–sites. A Ca<sup>2+</sup> ion (0.99 Å) is larger than that of the average Na<sup>+</sup> (0.95 Å) and Y<sup>3+</sup> (0.93 Å) ions. Na<sup>+</sup>, Ca<sup>2+</sup> and Y<sup>3+</sup> ions randomly occupied the A–site of the ACu<sub>3</sub>Ti<sub>4</sub>O<sub>12</sub> structure.

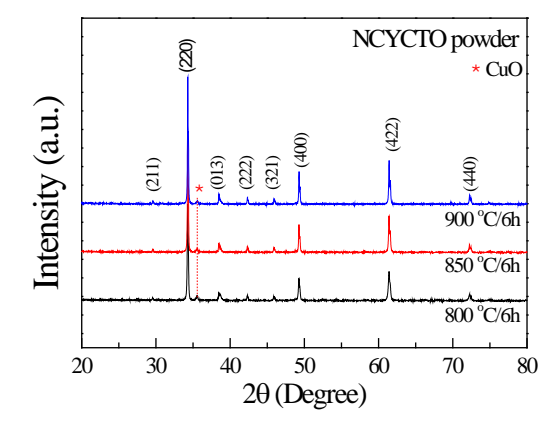
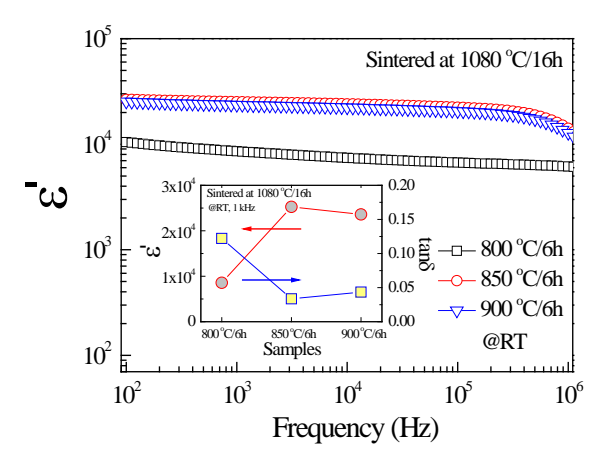


Fig. 1 XRD patterns of C800, C850, and C900 powders.

Figure 2 shows the dielectric properties of the NCYCTO ceramics sintered at  $1080\,^{\circ}\text{C}$  for 16 h using powders that were calcined at different temperatures. The inset of Fig. 2 shows  $\epsilon'$  and  $\tan\delta$  values measured at 1 kHz and RT for the sintered ceramics. The  $\epsilon'$  ( $\tan\delta$ ) values of the sintered NCYCTO ceramics using the C800, C850, and C900 powders are about  $8.6\times10^3$  (0.122),  $2.5\times10^4$  (0.034) and  $2.4\times10^4$  (0.046), respectively. These interesting dielectric properties are achieved in the sintered ceramics using C850 and C900 powders. The C850 powder was further used to prepare ceramic samples sintered at  $1080\,^{\circ}\text{C}$  for 4, 8 and 16 h (referred to as the NCY\_4h, NCY\_8h and NCY\_16h ceramics, respectively) since its bulk ceramic has the best dielectric properties. It is notable that the dielectric properties of the NCYCTO ceramic prepared using the SSG method is better that those of NCYCTO ceramics prepared by a conventional solid state reaction method [13, 31]. The influences of sintering time on the dielectric and electrical properties of NCYCTO ceramics were studied as follows.



**Fig. 2** Frequency dependence of  $\varepsilon'$  at RT of NCYCTO ceramics sintered at 1080 °C for 16 h fabricated from the C800, C850, and C900 powders; inset shows the summarized values  $\varepsilon'$  and  $\tan\delta$  at 1 kHz and RT.

Figure 3 shows the Rietveld refinement profile fit of the C850 powder and all sintered ceramics, confirming the presence of a primary phase of NCYCTO, which has a CCTO-like structure [1, 2]. According to the Rietveld refinement, lattice parameters of the NCY\_4h, NCY\_8h, and NCY\_16h ceramics are 7.387, 7.382 and 7.381 Å, respectively. These values are very close to that obtained in NCYCTO prepared using a solid state reaction method (for 7.387 Å) [31].

Figure 4(a) shows a TEM image of NCYCTO particles calcined at 850 °C for 6h. The particle sizes are about 100–300 nm. The surface morphologies of the NCYCTO ceramics sintered at  $1080^{\circ}$ C for different sintering times are shown in Fig. 4(b)–4(d). The average grain sizes of the NCY\_4h, NCY\_8h and NCY\_16h ceramics are estimated to be  $6.7\pm2.9$ ,  $7.1\pm3.6$  and  $14.5\pm6.9$  µm, respectively. For a CCTO polycrystalline ceramic, grain growth is usually described by a liquid phase sintering mechanism [7]. The eutectic temperature of CuO–TiO<sub>2</sub> is about  $\approx950^{\circ}$ C [6]. Therefore, this liquid phase can appear during sintering process,

giving rise to an increased grain growth rate. This mechanism can be responsible for the observed enlargement of the mean grain size of the NCYCTO ceramics. Segregation of some particles with irregular shape is observed along the GBs, especially for the NCY\_4h ceramic.

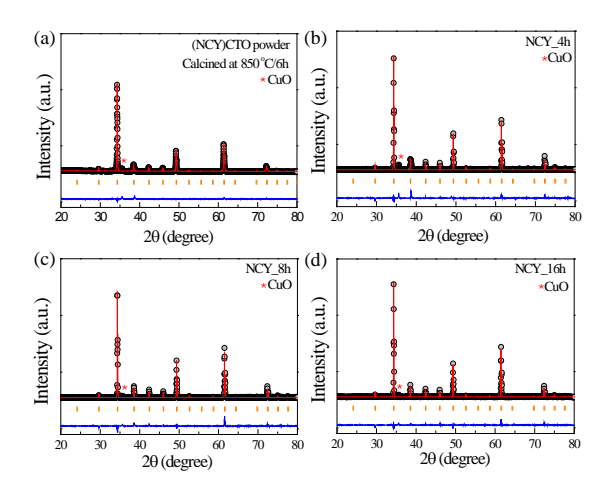
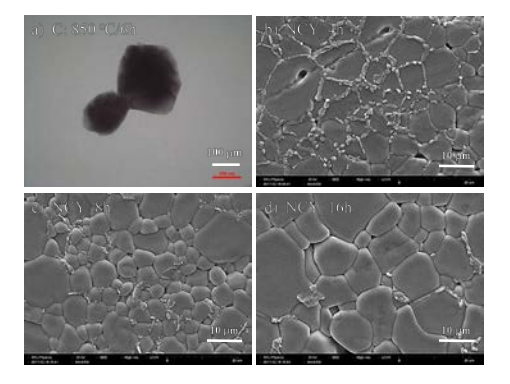


Fig. 3 Profile fits for Rietveld refinements of (a) C850 powder, (b) NCY\_4h, (c) NCY\_8h, and (d) NCY\_16h samples.



**Fig. 4** (a) TEM image of C850 powder. (b)-(d) SEM images of polished surfaces of NCY\_4h, NCY\_8h, NCY\_16h samples, respectively.

Figure 5(a) shows the EDS spectrum of the NCY\_16h ceramic measured in a selected area [its inset], confirming the existence of all ions of interest in NCYCTO. SEM mapping images of Na, Ca, Y, Cu, Ti and O of the NCY\_16h ceramic are shown in Fig. 5(b), revealing a homogeneous dispersion of each element in the microstructure. As illustrated in the inset of Fig. 5(a), slight segregation of a CuO-rich phase is observed. This confirms that the particles with irregular shapes observed in the NCYCTO ceramics are from the CuO-rich phase, corresponding to the XRD result.

The frequency dependence of the dielectric properties at RT of NCYCTO ceramics sintered at 1080°C for different sintering times is shown in Fig. 6. In the range of  $10^2$  to  $10^5$  Hz, the  $\varepsilon'$  values all the ceramic samples are independent of

frequency. The  $\varepsilon'$  values at RT and 1 kHz of the NCY\_4h, NCY\_8h and NCY\_16h ceramics are about  $9.2\times10^3$ ,  $1.3\times10^4$  and  $2.5\times10^4$ , respectively. Here, it is observed that  $\varepsilon'$  increased with increasing average grain size. It is notable that these values are larger than those obtained in NCYCTO ceramics prepared using a solid state reaction method [13, 31]. The enhanced dielectric response can usually be associated with a change in microstructure, according to the IBLC model. The effective dielectric constant,  $\varepsilon'_{eff}$ , can be expressed as [35]:

$$\varepsilon_{eff}' = \frac{\varepsilon_{gb} d_g}{t_{gb}} \tag{1}$$

where  $\varepsilon_{gb}$ ,  $d_g$ , and  $t_{gb}$  are the dielectric constant of the GB, the average grain size, and the GB thickness, respectively.

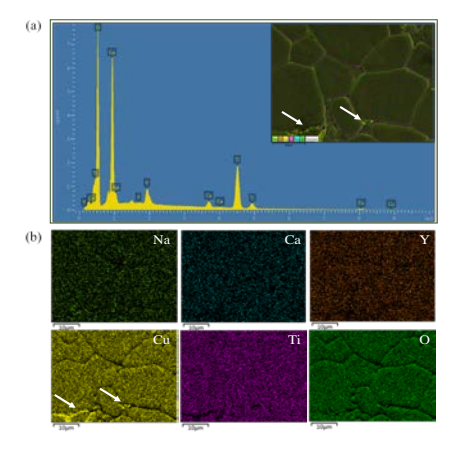


**Fig. 5** (a) EDS spectra of the NCY\_16h sample; inset shows the selected area for SEM mapping. (b) Elemental mapping of the NCY\_16h sample, i.e., Na, Ca, Y, Cu, Ti, and O.

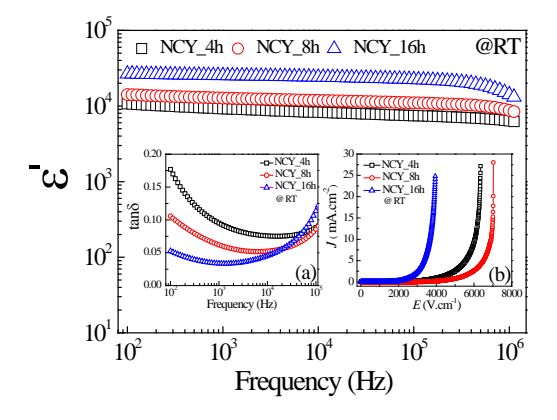


**Fig. 6** ε' at RT as a function of frequency for NCY\_4h, NCY\_8h and NCY\_16h samples. Inset (a) shows the  $tan\delta$  values as a function of frequency at RT. Inset (b) shows nonlinear J-E characteristics at RT of all samples.

As shown in inset (a) of Fig. 6,  $\tan\delta$  in a low frequency range of all ceramics is greatly increased with decreasing frequency. This behavior may have been caused by either DC conductivity or related interfacial polarization of the heterogeneous microstructure [35]. At RT and 1 kHz, the  $\tan\delta$  values of the NCY\_4h, NCY\_8h and NCY\_16h samples are 0.095, 0.062 and 0.034, respectively.  $\varepsilon'$  increases with sintering time, while  $\tan\delta$  is reduced. High  $\varepsilon'$  with good frequency stability and low  $\tan\delta$  is successfully achieved in the NCY\_16h sample. This indicates that the NCY\_16h sample may have potential use for capacitor applications.

As illustrated in inset (b) of Fig. 6, all of the NCYCTO ceramics prepared using the SSG method exhibit nonlinear J–E characteristics. The  $\alpha$  values of the NCY\_4h, NCY\_8h, and NCY\_16h ceramics at RT are, respectively, 5.85, 7.91, and 6.60, while the  $E_b$  values are  $4.1\times10^3$ ,  $5.2\times10^3$ , and  $2.6\times10^3$  V/cm, respectively. It is now widely accepted the nonlinear properties of CCTO and related compounds are likely caused by the formation of Schottky barriers at the GBs sandwiched by semiconducting grains [7, 14, 27].

As shown in Fig. 7(a), the  $Z^*$  plots in the temperature range of 150 to 200 °C are well fitted by the following modified equation corresponding to an equivalent circuit as demonstrated in the inset (2) of Fig. 7(a) [22]:

$$Z^* = R_g + \frac{R_{gb}}{1 + \left(i\omega R_{gb}C_{gb}\right)^{\alpha}} \tag{2}$$

where  $\alpha$  is a constant value (0< $\alpha$ ≤1),  $C_g$  (R<sub>g</sub>) and  $C_{gb}$  (R<sub>gb</sub>) are the capacitance (resistance) of grains and GBs, respectively. The  $C_g$  is not accessible and the respective capacitor can simply be omitted from the circuit. This result confirms that the microstructure of NCYCTO ceramics is electrically heterogeneous. In the inset (1) of Fig. 7(a), the temperature dependencies of GB conductivity ( $\sigma_{gb}$ ) follows the Arrhenius law:

$$\sigma_{gb} = \sigma_0 \exp\left(\frac{-E_{gb}}{k_B T}\right) \tag{3}$$

where  $\sigma_0$  is a constant value,  $E_{\rm gb}$  is the conduction activation energies at the GB,  $k_{\rm B}$  is the Boltzmann constant and T is the absolute. The  $E_{\rm gb}$  values of the NCY\_4h, NCY\_8h and NCY\_16h ceramics were calculated from the slopes of fitted data and found to be 0.677, 0.782, and 0.797 eV, respectively.  $E_{\rm gb}$  significantly increases with increasing sintering times. These values are higher than 0.514–0.703 eV for NCYCTO ceramics prepared using a solid state reaction method [13, 31].

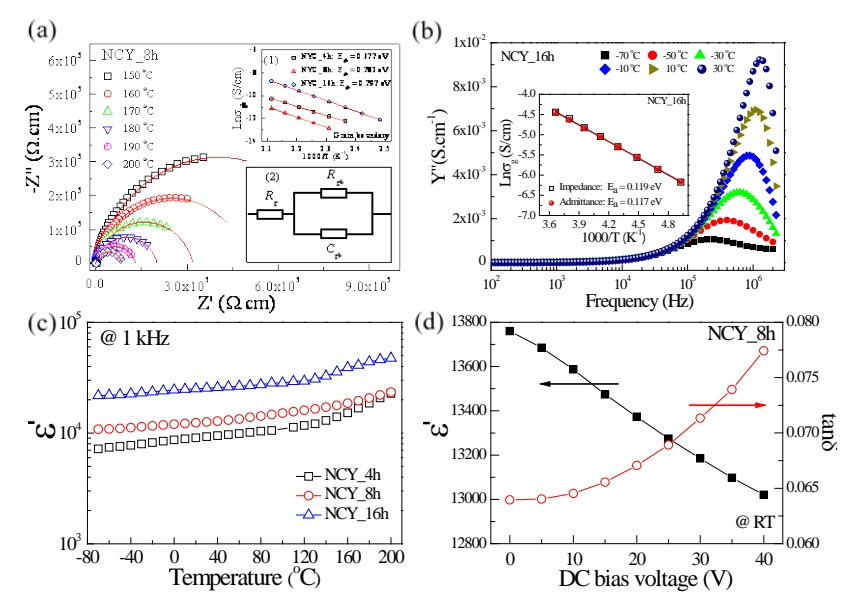


**Fig. 7** (a)  $Z^*$  plots for NCY\_8h sample at different temperatures (150 to 200 °C); the red solid curves are the fitted data using Eq. (2). Inset (1) of (a) shows Arrhenius plots of  $\sigma_{gb}$ ; the red solid lines are the fitted data using Eq. (4). Inset (2) of (a) shows an equivalent circuit corresponding to Eq. (2). (b) Frequency dependence of Y'' at different temperatures for the NCY\_16h sample; inset shows Arrhenius plots for the temperature dependence of  $\sigma_g$  values obtained from impedance and admittance spectroscopy analyses. (c) Temperature dependence of  $\varepsilon'$  at 1 kHz for NCYCTO ceramics. (d)  $\varepsilon'$  and tan $\delta$  values at 1 kHz and RT for the NCY\_8h sample under DC bias voltages.

 $R_{\rm g}$  values in a low temperature range can easily be calculated from the admittance spectroscopy analysis. As shown in Fig. 7(b), Y''-peaks of the NCY\_16h ceramic appear in a low temperature range. Accordingly,  $R_{\rm g}$  can be calculated from the relation,  $R_{\rm g}$  =1/(2  $Y''_{\rm max}$ ), where  $Y''_{\rm max}$  is the maximum value at the peak of the imaginary part of complex admittance (Y\*) [36]. As shown in the inset of Fig. 7(b), the temperature dependence of the grain conductivity follows the Arrhenius law:

$$\sigma_{g} = \sigma_{0} \exp\left(\frac{-E_{g}}{k_{B}T}\right) \tag{4}$$

where  $E_{\rm g}$  is the conduction activation energies inside the grains. The experimental data obtained from the impedance and admittance spectroscopy analyses are well fitted using equation (4). Accordingly, the  $E_{\rm g}$  values obtained from these analyses are 0.119 and 0.117 eV, respectively.

The temperature dependence of  $\varepsilon'$  at 1 kHz of NCYCTO ceramics is demonstrated in Fig. 7(c).  $\varepsilon'$  slightly increases from -70 to 120 °C and then strongly increases at temperatures higher than 120 °C. This may have been caused by effect of DC conductivity, which is a one of factors corresponded to AC

high  $\tan\delta$  values [4, 35]. Figure 7(d) shows the effects of DC bias voltage on the dielectric properties, i.e.,  $\epsilon'$  and  $\tan\delta$  values of the NCY\_8h ceramic at RT.  $\epsilon'$  decreases with increasing applied DC bias voltage, while  $\tan\delta$  greatly increases. This result may be associated with variation in the Schottky barrier height at the GBs as a result of applied DC bias [26]. With increasing DC bias voltage, the amount of accumulated charges is decreased because some charges can cross the insulating GBs. Consequently, the intensity of interfacial polarization at the GBs is reduced, giving rise to a decreased dielectric response [31]. Simultaneously, the DC conductivity increases due to the long range movement of free charges. A high loss  $\tan\delta$  associated with the reduction in  $\epsilon'$  value is obtained under an increased DC bias voltage.

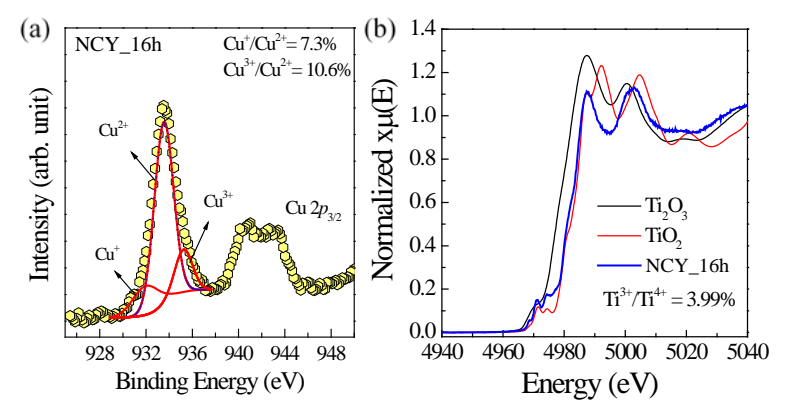


**Fig. 8** (a) XPS spectrum of Cu *2p* region for the NCY\_16h sample. (b) Normalized XANES spectra for Ti *K*-edge of the NCY\_16h sample.

To explain the electrical conductivity of *n*-type semiconducting grains in the NCYCTO ceramic, the reactions of polyvalent cations ( $Cu^{2+} \rightarrow Cu^{+}$  and  $Ti^{4+} \rightarrow$ Ti<sup>3+</sup>) were investigated using XPS and XANES techniques. For the CCTO and A<sub>2/3</sub>Cu<sub>3</sub>Ti<sub>4</sub>O<sub>12</sub> related ceramics, the presence of Cu<sup>+</sup> and Ti<sup>3+</sup> ions can cause formation of *n*-type semiconducting grains [25, 28, 29]. Figure 8(a) shows the XPS spectrum of Cu 2p of the NCY\_16h sample. Three peaks are extracted from the XPS spectrum of Cu 2p using Gaussian-Lorentzian profile fitting. The highest peak, with a binging energy 933.51 eV, is ascribed to Cu<sup>2+</sup> [28, 29]. The peaks at 931.43 and 935.26 eV indicate the presence of Cu<sup>+</sup> and Cu<sup>3+</sup>, respectively [28, 37]. The ratios of  $Cu^+/Cu^{2+}$  and  $Cu^{3+}/Cu^{2+}$  are found to be 7.3% and 10.6%, respectively. Thus, the presence of Cu<sup>+</sup> and Cu<sup>3+</sup> has an effect on the electrical conductivity of grains. The presence of Cu3+ might be associated with the segregation of a Cu-rich phase along the GBs [37], as shown in Fig. 4(d). According to the XPS results, Ti3+ is difficult to detect, which may have been due to its low concentration. The XANES spectrum was further used to confirm the presence of Ti<sup>3+</sup> to clearly describe electrical conductivity in the grain interiors. Fig. 8(b) illustrates XANES spectra of the NCY\_16h sample, as well as the standard samples, i.e., Ti<sub>2</sub>O<sub>3</sub> (Ti<sup>3+</sup>) and TiO<sub>2</sub> (Ti<sup>4+</sup>). The edge energy of the NCY\_16h sample is observed to closely match the TiO2 standard. The presence of a small amount of Ti3+ is confirmed. The maximum value of the first derivative in the edge region is used to calculate the  $Ti^{3+}/Ti^{4+}$  ratio, which is 3.99%. It is reasonably to infer that electron hopping between  $Ti^{3+} \leftrightarrow Ti^{4+}$  lattice sites may have also influenced the electrical conductivity of grains. The nature of electrical conductivity in grains is still complex. Nevertheless, it is reasonable to conclude that  $Cu^+$ ,  $Cu^{3+}$  and  $Ti^{3+}$  ions have an effect on this property.

## 12.4 Conclusions

NCYCTO nanoparticles were successfully synthesized using a simple sol–gel method. Dense microstructure of sintered ceramics was obtained by employing NCYCTO nanoparticles. Na, Ca, Y, Cu, Ti, and O were well dispersed in the microstructure, indicating the formation of single phase. A high dielectric permittivity of  $2.52\times10^4$  and low loss tangent of about 0.034 (at 1 kHz) were accomplished by optimization of preparation parameters. Good nonlinear J–E properties with  $E_b$ =5,160 V/cm and  $\alpha$ =7.91 were also achieved. Through investigation of the DC bias dependence of the dielectric properties and using impedance spectroscopy, the giant dielectric response was attributed to the IBLC effect. It is suggested that the semiconducting grains of NCYCTO ceramics were induced by the presence of Cu<sup>+</sup>, Cu<sup>3+</sup>, and Ti<sup>3+</sup> ions.

#### References

- 1. M.A. Subramanian, D. Li, N. Duan, B.A. Reisner, A.W. Sleight, J. Solid State Chem. 151, 323-325 (2000)
- 2. M.A. Subramanian, A.W. Sleight, Solid State Sci. 4, 347-351 (2002)
- 3. L. Liu, H. Fan, L. Wang, X. Chen, P. Fang, Philos. Mag. 88, 537-545 (2008)
- 4. Q. Zheng, H. Fan, C. Long, J. Alloys Compd. 511, 90-94 (2012)
- 5. R. Löhnert, H. Bartsch, R. Schmidt, B. Capraro, J. Töpfer, A. Feteira, J. Am. Ceram. Soc. 98, 141-147 (2015)
- 6. L. Singh, B.C. Sin, I.W. Kim, K.D. Mandal, H. Chung, Y. Lee, J. Varela, J. Am. Ceram. Soc. 99, 27-34 (2016)
- 7. J. Jumpatam, B. Putasaeng, T. Yamwong, P. Thongbai, S. Maensiri, Mater. Res. Bull. 77, 178-184 (2016)
- 8. A. Nautiyal, C. Autret, C. Honstettre, S. De Almeida-Didry, M. El Amrani, S. Roger, B. Negulescu, A. Ruyter, J. Eur. Ceram. Soc. 36, 1391-1398 (2016)
- 9. R. Löhnert, B. Capraro, S. Barth, H. Bartsch, J. Müller, J. Töpfer, J. Eur. Ceram. Soc. 35, 3043-3049 (2015)
- 10. P. Kum-onsa, P. Thongbai, B. Putasaeng, T. Yamwong, S. Maensiri, J. Eur. Ceram. Soc. 35, 1441-1447 (2015)
- 11. S. Wu, P. Liu, Y. Lai, W. Guan, Z. Huang, J. Han, Y. Xiang, W. Yi, Y. Zeng, J. Mater. Sci.: Mater. Electron. 1-6 (2016)
- 12. X.W. Wang, P.B. Jia, X.E. Wang, B.H. Zhang, L.Y. Sun, Q.B. Liu, J. Mater. Sci.: Mater. Electron. 1-7 (2016)

- 13. Y. Liu, X. Zhao, C. Zhang, J. Mater. Sci.: Mater. Electron. 27, 11757-11761 (2016)
- 14. J. Boonlakhorn, P. Kidkhunthod, P. Thongbai, J. Eur. Ceram. Soc. 35, 3521-3528 (2015)
- 15. W. Wan, C. Liu, H. Sun, Z. Luo, W.-X. Yuan, H. Wu, T. Qiu, J. Eur. Ceram. Soc. 35, 3529-3534 (2015)
- 16. M.A. Ponce, M.A. Ramirez, F. Schipani, E. Joanni, J.P. Tomba, M.S. Castro, J. Eur. Ceram. Soc. 35, 153-161 (2015)
- 17. J. Li, P. Liang, J. Yi, X. Chao, Z. Yang, J. Am. Ceram. Soc. 98, 795-803 (2015)
- 18. Z. Xu, H. Qiang, J. Mater. Sci.: Mater. Electron. 28, 376-380 (2017)
- 19. Z. Xu, H. Qiang, Y. Chen, Z. Chen, Mater. Chem. Phys. 191, 1-5 (2017)
- 20. Z. Liu, Z. Yang, X. Chao, J. Mater. Sci.: Mater. Electron. 1-11 (2016)
- 21. L. Liu, H. Fan, X. Chen, P. Fang, J. Alloys Compd. 469, 529-534 (2009)
- 22. J. Liu, C.-G. Duan, W.-G. Yin, W. Mei, R. Smith, J. Hardy, Phys. Rev. B 70, 144106 (2004)
- 23. W. Hao, H. Wu, P. Xu, Y. Shi, S. Yang, M. Wang, L. Sun, E. Cao, Y. Zhang, Ceram. Int. 43, 3631-3638 (2017)
- 24. Y. Shi, W. Hao, H. Wu, L. Sun, E. Cao, Y. Zhang, H. Peng, Ceram. Int. 42, 116-121 (2016)
- 25. W. Hao, J. Zhang, Y. Tan, M. Zhao, C. Wang, J. Am. Ceram. Soc. 94, 1067-1072 (2011)
- 26. T. Adams, D. Sinclair, A. West, Phys. Rev. B 73, 094124 (2006)
- 27. S.-Y. Chung, I.-D. Kim, S.-J.L. Kang, Nat. Mater. 3, 774-778 (2004)
- 28. L. Ni, X.M. Chen, X.Q. Liu, Mater. Chem. Phys. 124, 982-986 (2010)
- 29. L. Ni, X.M. Chen, Solid State Commun. 149, 379-383 (2009)
- 30. S.F. Shao, J.L. Zhang, P. Zheng, C.L. Wang, J.C. Li, M.L. Zhao, Appl. Phys. Lett. 91, 042905 (2007)
- 31. J. Jumpatam, W. Somphan, B. Putasaeng, N. Chanlek, P. Kidkhunthod, P. Thongbai, S. Maensiri, Mater. Res. Bull. 90, 8-14 (2017)
- 32. W. Li, L. Tang, F. Xue, Z. Xin, Z. Luo, G. Du, Ceram. Int. 43, 6618-6621 (2017)
- 33. L. Sun, Z. Wang, Y. Shi, E. Cao, Y. Zhang, H. Peng, L. Ju, Ceram. Int. 41, 13486-13492 (2015)
- 34. B. Ravel, M. Newville, Journal of Synchrotron Radiation 12, 537-541 (2005)
- 35. J. Wu, C.-W. Nan, Y. Lin, Y. Deng, Phys. Rev. Lett. 89, 217601 (2002)
- 36. J. Jumpatam, W. Somphan, J. Boonlakhorn, B. Putasaeng, P. Kidkhunthod, P. Thongbai, S. Maensiri, J. Am. Ceram. Soc. 100, 157-166 (2017)
- 37. M. Li, G. Cai, D.F. Zhang, W.Y. Wang, W.J. Wang, X.L. Chen, J. Appl. Phys. 104, 074107 (2008)

# **CHAPTER 13**

# Enhanced Non-Ohmic Properties and Giant Dielectric Response of (Sm+Zn) Co-Doped CaCu<sub>3</sub>Ti<sub>4</sub>O<sub>12</sub> Ceramics

#### 13.1 Introduction

In recent years, the electrical and dielectric properties of CaCu<sub>3</sub>Ti<sub>4</sub>O<sub>12</sub> (CCTO) ceramics have been widely studied, especially with regard to their dielectric and nonlinear current-voltage properties [1-26]. CCTO is well known as a giant dielectric or colossal permittivity material. Very high dielectric permittivities (ε'~10<sup>3</sup>–10<sup>5</sup>) in the frequency range of  $10^2 - 10^5$  Hz are usually reported. Furthermore, nonlinear current-voltage characteristics were also observed in CCTO polycrystalline ceramics [1, 7, 8, 27, 28]. These two important properties are essential for capacitor and varistor applications [29]. Besides the applications point of view, the fascinating giant dielectric response with no detectable phase transition and correlated nonlinear electrical properties of CCTO ceramics have attracted attention of researchers seeking to clarify the origin of these phenomena. Both intrinsic and extrinsic origins have been proposed [2-5, 24, 30, 31]. Many research studies reported close correlation between the microstructure and electrical properties of CCTO ceramics, indicating an extrinsic effect [1-3, 24]. According to the internal barrier layer capacitor (IBLC) model, the effect is widely believed to be the exact origin of both the giant dielectric and nonlinear electrical properties. Nevertheless, the intrinsic effect cannot be simply ignored [4, 5].

Although the origin of these properties is still open to scientific debate, it has been clearly shown that CCTO polycrystalline ceramics electrically consist of semiconducting grains and insulting grain boundaries (GBs) [1-3, 8]. As such, their dielectric and electrical properties can be controlled by tuning their microstructure. Usually, enhancing GB layers, hence increasing the total GB resistance ( $R_{gb}$ ) by reducing the mean grain size, is a general approach for obtaining a low dielectric loss tangent ( $tan\delta$ ) and improving a ceramic's nonlinear electrical properties. However, this is not always true. In the case of Nb or Ta doped-CCTO ceramics, although their mean grain sizes were significantly reduced,  $tan\delta$  values were increased. This is because the resistivity of individual GB layers was greatly reduced, resulting in a large decrease in  $R_{gb}$ . Controlling the ceramic microstructure while retaining (or intrinsically enhancing) individual GB layers may be one of the most suitable routes.

According to our previous work [8], improved dielectric and nonlinear electrical properties of Sm³+ doped-CCTO ceramics were achieved (compared to the un-doped CCTO ceramic) by reducing their mean grain size. However, the resulting low-frequency tanδ was still very large (≈0.2 at 10² Hz). This may have resulted from a low resistivity of individual GB layers. Moreover, a dense ceramic microstructure could not be obtained, which may have resulted from the dominant effect of a solute drag mechanism. This is unsuitable for practical applications. Substitution of Zn²+ into CCTO ceramics can improve microstructure [5] and enhance electrical properties [7]. Therefore, in the current work, (Sm+Zn) co–doped CCTO ceramics were successfully prepared using a modified sol–gel method. The effect of co-dopants on ceramic microstructure, dielectric and nonlinear electrical properties were investigated and discussed in detail.

## 13.2 Experimental details

A modified sol–gel method was used to prepare  $CaCu_3Ti_4O_{12}$  and  $Ca_{0.925}Sm_{0.05}Cu_{3-x}Zn_xTi_4O_{12}$  ceramics. Starting raw materials consisted of  $Ca(C_2H_3CO_2)_2\cdot H_2O$  (>99%, Sigma-Aldrich),  $Cu(CH_3COO)_2\cdot H_2O$  (99.0%, Sigma-Aldrich),  $C_{16}H_{28}O_6Ti$  (75 wt% in

isopropanol, Sigma-Aldrich),  $(CH_3CO_2)_3Sm \cdot xH_2O$  (99.9%, Sigma-Aldrich),  $Zn(CH_3COO)_2 \cdot 2H_2O$  (99.99%, Sigma-Aldrich), ethylene glycol, citric acid, ethanol, and de–ionized water. Details of the preparation method are given in elsewhere [27]. To obtain a main phase of CCTO, all dried precursors were calcined at 900 °C for 10 h. Compacted powders (~9.5 mm in diameter and ~1.5–2.0 mm in thickness) were sintered at 1070 °C for 6 h. The sintered  $Ca_{0.925}Sm_{0.05}Cu_{3-x}Zn_xTi_4O_{12}$  ceramics with x=0, 0.05 and 0.10 are referred to as the Sm05, SmZn05, and SmZn10 ceramics, respectively.

To study their phase composition and crystal structure, X–ray Diffractometry (PANalytical, EMPYREAN, XRD) was used to collect the diffraction patterns of each sample over a 2θ range of 20°–80° with a scan speed of 0.02°/point. The XRD patterns were analyzed with a Rietveld refinement method using the X'Pert High Score Plus v3.0e software package by PANalytical. The surface morphologies were characterized using scanning electron microscopy (SEC, SNE-4500M, SEM).

Au was coated on both sides of the polished-surface of sintered ceramics using a Polaron SC500 sputter coating unit with electric current of ~25 mA for 4 min. Their dielectric properties were measured using a KEYSIGHT E4990A Impedance Analyzer with an oscillation voltage of 500 mV in the frequency and temperature ranges of  $10^2-10^6$  Hz and -60 °C to 210 °C, respectively. Nonlinear current density–electric filed (J–E) characteristics were measured at room temperature (RT) using a high voltage measurement unit (Keithley 247).  $E_b$  was defined as the electric field breakdown at which  $J = 1 \text{ mA/cm}^2$ . The nonlinear coefficient ( $\alpha$ ) was calculated in the range of 1–10 mA/cm<sup>2</sup>.

## 13.3 Results and discussion

The crystalline structure of the CCTO, Sm05, SmZn05, and SmZn10 ceramics was studied using an XRD technique. In Fig. 1, the XRD patterns of all the samples are well fitted using the Rietveld refinement method. Accordingly, the structural data obtained from the Rietveld refinement for CCTO, Sm05, SmZn05, and SmZn10 ceramics are summarized in Table 1. Good R-factors, which were lower than 5.95%, were observed in all of the XRD patterns. The goodness of fit (GOF) values were also very low (<1.76). A main phase of CCTO was observed in all the sintered ceramics. No CaO, CaTiO<sub>3</sub>, CuO, Cu<sub>2</sub>O, TiO<sub>2</sub>, or related Sm/Zn oxide phases were detected in any of the XRD spectra. These XRD patterns were perfectly indexed based on the body-centered cubic structure. In Table 1, the lattice parameter (a) values of all of the sintered ceramics were comparable to those reported in literature for un-doped CCTO (≈7.392 Å) and  $CaCu_{2.85}Zn_{0.15}Ti_4O_{12}$  ( $\approx$ 7.395 Å) ceramics [5]. The a value of the Sm05 (x = 0) ceramic was slightly larger than that of the un-doped CCTO ceramic, which was similar to that reported in the literature [8]. The a value of the Ca<sub>0.925</sub>Sm<sub>0.05</sub>Cu<sub>3-x</sub>Zn<sub>x</sub>Ti<sub>4</sub>O<sub>12</sub> ceramics tended to increase with increasing x from 0 to 0.1. This may be primarily attributed to a larger ionic radius of the  $Zn^{2+}$  ( $r_4 = 0.60 \text{ Å}$ ) dopant ion compared to that of the  $Cu^{2+}$  ( $r_4 = 0.60 \text{ Å}$ ) 0.57 Å) host ion [32], while the ionic radii of Ca<sup>2+</sup> and Sm<sup>3+</sup> are not different significantly [8]. The charge compensated defects, which occurred in the co-doped ceramics, may also have an effect on the increased value of a [4, 5].

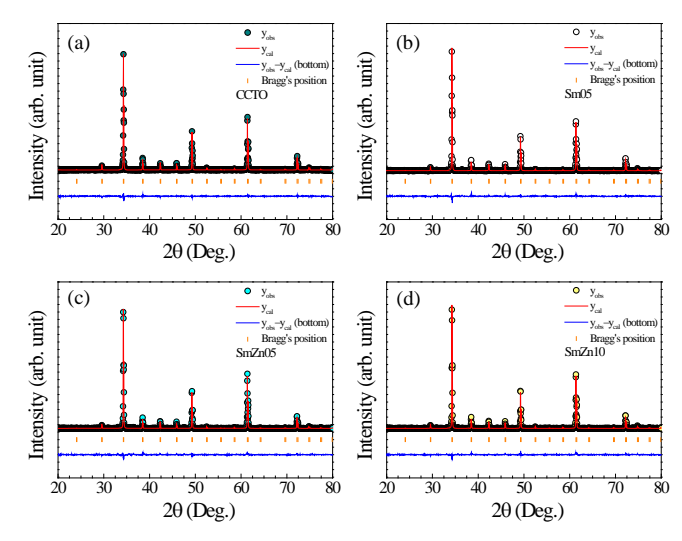


Fig. 1 Rietveld profile fits of the (a) CCTO, (b) Sm05, (c) SmZn05, and (d) SmZn10 ceramics.

**Table 1.** Structural data obtained from the Rietveld refinement for CCTO, Sm05, SmZn05, and SmZn10 ceramics.

Sample	ССТО	Sm05	SmZn05	SmZn10
a (Å)	7.392(3)	7.393(3)	7.394(6)	7.395(0)
R <sub>exp</sub> (%)	4.12	4.49	4.11	4.12
R <sub>p</sub> (%)	3.38	4.61	3.85	3.51
R <sub>wp</sub> (%)	4.36	5.95	5.26	4.54
GOF	1.12	1.76	1.64	1.22

**Table 2.** Grain size, ε' and tanδ at 1 kHz and 20 °C, resistances inside the grains (R<sub>g</sub>) and at GBs (R<sub>gb</sub>) at 20 °C, conduction activation energies inside the grains (E<sub>g</sub>) and at GBs (E<sub>gb</sub>), breakdown electric field (E<sub>b</sub>), and nonlinear coefficient (α) of CCTO, Sm05, SmZn05 and SmZn10 ceramics.

Sampl e	G (μm)	ε′	tanδ	$R_g$ ( $\Omega$ .cm	$R_{gb}$ (M $\Omega$ .cm	E <sub>g</sub> (eV )	E <sub>gb</sub> (eV)	E <sub>b</sub> (V/cm)	α
ССТО	25.6±10.7	66423	0.108	43	1.08	0.95	0.620	233.2	3.29
Sm05	3.4±0.9 *8.1±2.3	16489	0.399	42	0.44	0.56	0.542	476.7	3.20
SmZn0 5	3.7±1.4	7588	0.099	54	14.00	0.65	0.587	2586.2	4.28
SmZn1 0	2.0±0.6	5313	0.041	69	89.55	0.70	0.615	4601.3	6.41

<sup>\*</sup> The mean grain size determined from large grains.

For an AA' $_3$ M $_4$ O $_{12}$  perovskite structure, MO $_6$  (e.g., TiO $_6$  for CCTO structure) has a tilted octahedral structure, resulting in formation of a square planar coordination for the A' ion (e.g., Cu for CCTO structure) [33]. Compared to BaTiO $_3$  and its isostructural perovskite structures, the CCTO structure and related oxides are very rigid. Therefore, the space for the Ca $^{2+}$  and Cu $^{2+}$  cations in the CCTO structure is essentially fixed. It is widely reported that many related A $_{2/3}$ Cu $_3$ Ti $_4$ O $_{12}$  (A = La $^{3+}$ , Sm $^{3+}$ , Y $^{3+}$ , etc) ceramics can be synthesized and their cell parameters are very close to that of the CCTO structure [33]. Thus, the A-site in an AA' $_3$ M $_4$ O $_{12}$  structure (e.g., Ca $^{2+}$  in the CCTO structure) can only be occupied by these A $^{3+}$  ions. Considering the greatly disparate sizes of Ca $^{2+}$  ( $r_{12}$  = 1.34 Å) and Cu $^{2+}$  ( $r_4$  = 0.57 Å) and an essentially fixed structure, Zn $^{2+}$  preferentially substitutes for Cu $^{2+}$  due to their similar ionic radii, while Sm $^{3+}$  can be substituted only into Ca $^{2+}$  sites.

The frequency dependence of  $\varepsilon'$  and  $\tan\delta$  of all of the samples is illustrated in Fig. 2 and its inset. All of the ceramics exhibited giant dielectric properties. The  $\epsilon'$  or capacitance was nearly independent of frequency in the range of 10<sup>2</sup>-10<sup>5</sup> Hz, which is similar to results reported in literature for CCTO and related oxides [2-5, 21, 22, 34, 35]. The  $\varepsilon'$  and  $\tan\delta$ values of the Sm05, SmZn05 and SmZn10 ceramics were lower than that of the CCTO ceramic over the measured frequency range. However, the frequency stability of  $\epsilon'$  of these single-doped and co-doped ceramics was greater than that of the un-doped CCTO ceramic, especially in a high frequency range. The low-frequency  $tan\delta$  value of the singledoped Sm05 ceramic was much higher than that of the un-doped CCTO ceramic, while simultaneous substitution of Sm and Zn dopants into CCTO ceramics caused a great decrease in  $tan\delta$  over the measured frequency range. Notably,  $tan\delta$  at  $10^2$  Hz of the SmZn10 ceramic was much lower than that of the CCTO ceramic by a factor of at least 3. Alternatively, the increase in  $tan\delta$  in a high frequency range was associated with the primary polarization relaxation process that gave rise to the giant dielectric response in CCTO ceramics [4-6]. Simultaneous co-doping of CCTO with (Sm+Zn) dopants can also significantly reduce the high-frequency tanδ by extending the relaxation frequency to higher frequencies. For capacitor applications, the  $\varepsilon'$  and  $\tan\delta$  values at 1 kHz are considered. These values are summarized in Table 2.

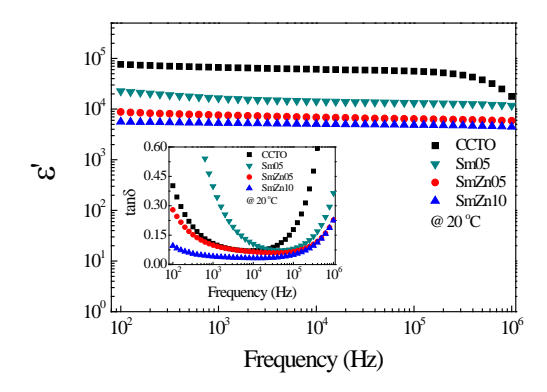


**Fig. 2** Frequency dependence of  $\epsilon'$  at 20 °C for the CCTO, Sm05, SmZn05, and SmZn10 ceramics. Inset shows the frequency dependence of tanδ.

The effect of Sm single-dopant and (Sm+Zn) co-dopants on the nonlinear J–E properties was clearly observed, as shown in Fig. 3. All of the sintered ceramics exhibited nonlinear properties with different electric breakdown strengths.  $E_b$  and  $\alpha$  values were calculated from the J–E curves and summarized in Table 2. The  $\alpha$  values of the CCTO, Sm05, SmZn05, and SmZn10 ceramics were found to be 3.29, 3.20, 4.28, and 6.41,

whereas the  $E_b$  values were 233.2, 476.7, 2586.2, and 4601.3 V/cm, respectively. The  $\alpha$  values of the co-doped ceramics continuously increased compared to those of the undoped CCTO and single-doped CCTO ceramics, while  $E_b$  was greatly enhanced by (Sm+Zn) co–doping. In addition to improved dielectric properties, their nonlinear electrical properties were simultaneously enhanced. The formation of a Schottky barrier was considered the origin of the nonlinear electrical behavior [2].

According to the IBLC model of Schottky barriers at the GBs [2], the giant dielectric response and nonlinear electrical properties of CCTO ceramics originate in the GB region. Therefore, the electrical responses of the GBs and grains were further studied using an impedance spectroscopy technique to describe the origin of the enhanced dielectric and nonlinear properties of the (Sm+Zn) co-doped CCTO ceramics. At RT, a large semicircular arc of all Z\* plots, in which its diameter is equal to the R<sub>ab</sub> value [2], could not be observed for any of the ceramics due to limitations of the measured frequency range. As illustrated in Fig. 4 and its insets, a large semicircular arc of all the ceramics can be seen at 80 °C. R<sub>ab</sub> of the Sm05 ceramic was slightly smaller than that of the CCTO ceramic. This indicates that doping CCTO ceramics with only Sm3+ cannot improve the electrical properties of the GBs, and hence the dielectric properties were not improved either. Clearly, R<sub>ab</sub> of the CCTO ceramics was greatly enhanced by co-doping with (Sm+Zn). This result is very consistent with its remarkably reduced tanδ value and strongly enhanced nonlinear electrical properties [27, 34]. It is notable that the grain resistance (R<sub>g</sub>), which can be estimated from the nonzero intercept [2], slightly increased with increasing co-dopant concentration. The R<sub>g</sub> values of the CCTO and Sm05 ceramics are nearly the same in value. These improved properties were largely controlled by the GBs. The contributions of the intrinsic and extrinsic factors of the GBs were further studied as follows.

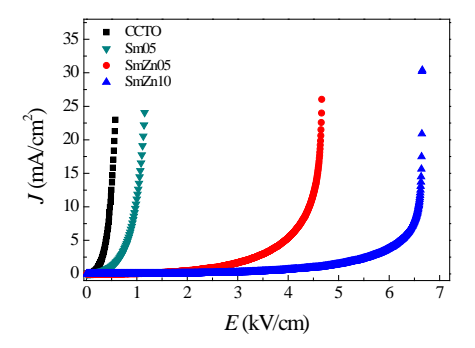


Fig. 3 J–E characteristics of the CCTO, Sm05, SmZn05, and SmZn10 ceramics.

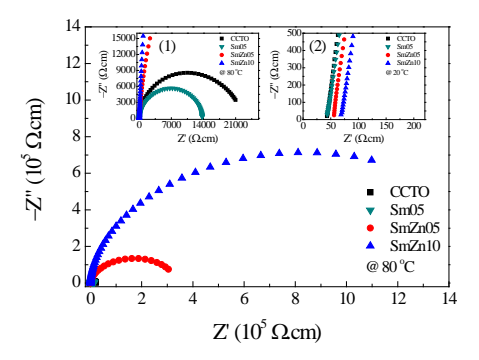


Fig. 4 Impedance complex plane (Z\*) plots of the CCTO, Sm05, SmZn05, and SmZn10 ceramics at 80 °C. Inset (1) shows its expanded view and inset (2) shows an expanded view of the high-frequency data close to the origin at 20 °C.

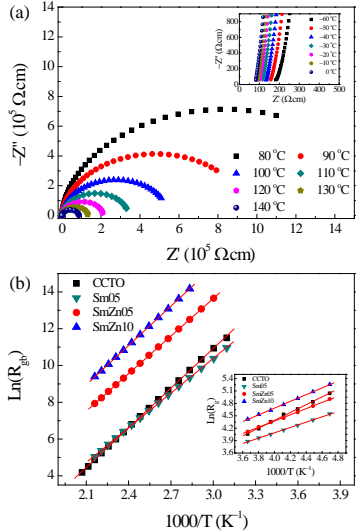
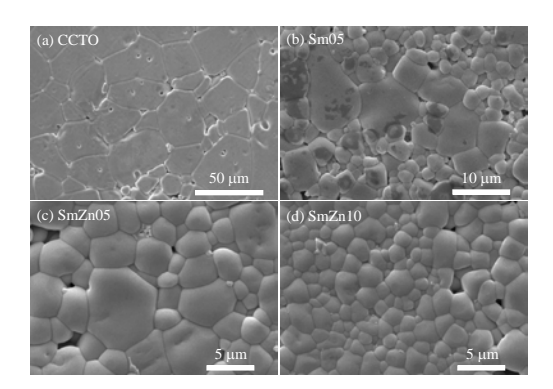


Fig. 5 (a) Z\* plots of the SmZn10 ceramic in the temperature range of 80 °C–140 °C; inset shows an expanded view of the high-frequency data close to the origin (–60 to 0 °C. (b) Arrhenius plots showing the temperature dependence of R<sub>gb</sub>: inset shows Arrhenius plots depicting the temperature dependence of R<sub>g</sub>.



**Fig. 6** SEM images of surface morphologies for (a) CCTO, (b) Sm05, (c) SmZn05, and (d) SmZn10 ceramics.

The intrinsic parameters (i.e., the conduction activation energies) of the grains and GBs were investigated to clearly demonstrate whether intrinsic and/or extrinsic factors had a stronger effect on the observed improvement in the dielectric and nonlinear electrical properties. As shown in Fig. 5(a), the large semicircular arc of the  $Z^*$  plot and associated  $R_{gb}$  decreased with increasing temperature, indicating a thermally activated conduction process. Additionally,  $R_g$  decreased as temperature increased [inset of Fig. 5(a)]. As shown in Fig. 5(b) and its inset, the temperature dependencies of  $R_g$  and  $R_{gb}$  obey the Arrhenius law:

$$R_{g,gb} = R_0 \exp(E_{g,gb} / k_B T),$$
 (1)

where  $E_g$  and  $E_{gb}$  are the activation energies for conduction inside the grains and at the GBs, respectively.  $R_0$  is a pre  $k_{\rm B}x_{\rm B}$  when  $k_{\rm B}x_{\rm B}$  and  $k_{\rm B}x_{\rm B}$  when  $k_{\rm B}x_{\rm B}$  and  $k_{\rm B}x_{\rm B}$  was then  $k_{\rm B}x_{\rm B}$  was the fitted lines and summarized in Table 2. Both of  $k_{\rm B}x_{\rm B}$  values of

ceramics, in which  $E_{gb}$  was greatly reduced [6]. According to the calculated  $E_{gb}$  values,  $R_{gb}$  at about RT was determined and listed in Table 2. The reduction in  $\tan\delta$  and improved nonlinear electrical properties at RT were confirmed as arising from a strongly enhanced  $R_{gb}$ .

Generally, the macroscopic view of the electrical properties of the GBs is determined by the intrinsic and extrinsic properties (geometric factors) of the GBs. As shown in Table 2,  $E_{gb}$  values of the co-doped ceramics were slightly lower than that of un-doped CCTO ceramics. Usually,  $E_{gb}$  of CCTO ceramics is closely related to the potential barrier height at the GBs [3]. Therefore, it can be deduced that the intrinsic properties of the GBs in the co-doped ceramics were slightly changed. Nevertheless,  $\tan\delta$  and nonlinear parameters were strongly improved, which may be due to the extrinsic factors of the GBs that were correlated with microstructural changes.

To clarify this, the microstructures of all sintered ceramics were revealed, as shown in Fig. 6. The average grain sizes of all the ceramics are listed in Table 2. The grain size of the CCTO ceramic is very large [Fig. 6(a)], with an average of ≈25.6 μm. A small number of pores was observed both inside the grains and at the GBs of the CCTO ceramic indicating abnormal grain growth [36]. Interestingly, the mean grain size of CCTO ceramics was strongly reduced by doping with Sm3+ [Fig. 6(b)]. This may have resulted from the solute drag effect in the co-doped ceramics, in which segregation of Sm dopant at the GBs inhibited the motion of GBs [8, 36]. It is notable that abnormal grain growth behavior was also observed in the Sm05 ceramic. According to previous studies [7, 34], when Zn-doped CCTO ceramics were sintered at ≤1070 °C, their mean grain size was reduced by doping with Zn<sup>2+</sup>. As shown in Figs. 6(c) and (d), the mean grain size of the (Sm+Zn) co-doped CCTO ceramics decreased with increasing Zn dopant concentration. Therefore, it is reasonable to suggest that both Sm3+ and Zn2+ dopants inhibited grain growth in CCTO ceramics. It is important to note that the microstructure of the SmZn10 ceramic was denser than that of the Sm single-doped CCTO ceramic, as reported in the literature [8]. This may have been due to the ability of the Zn2+ dopant to enhance the densification rate of CCTO ceramics [5]. A fine grained microstructure with small number of pores was observed in the SmZn10 ceramic. As a result, the density of active insulating GB layers perpendicular to the direction of the applied electric field was increased. This is the most important factor contributing to the enhanced total R<sub>qb</sub> values. It is clear that the improved dielectric and nonlinear electrical properties of the co-doped CCTO ceramics were achieved by controlling their microstructure through inclusion of co-dopants. Additionally, a decrease in  $\varepsilon'$  of the (Sm+Zn) co-doped ceramics is very consistent with the observed reduction in the grain size, as predicted by the IBLC model. Therefore, the influence of the geometric parameters of the microstructure had a stronger effect on the dielectric and nonlinear properties of (Sm+Zn) co-doped CCTO than that of the intrinsic properties of GBs.

#### 13.4 Conclusions

We successfully improved the non–Ohmic and giant dielectric properties of CCTO ceramics by simultaneously controlling their microstructure and retaining the intrinsic electrical properties of the GBs via co-doping with (Sm+Zn) ions. Doping CCTO with Sm can inhibit its grain growth rate, while the simultaneous substitution of Sm and Zn can provide a dense microstructure. A fine grained, dense microstructure was successfully accomplished. Notably, enhanced nonlinear properties and a reduced  $\tan \delta$  value of  $\approx 0.041$  with a high  $\epsilon' > 10^3$  were achieved using a co-doping concept. The improved dielectric and nonlinear properties resulted from the IBLC effect.

#### References

- [1] S.-Y. Chung, I.-D. Kim, S.-J.L. Kang, Strong nonlinear current–voltage behaviour in perovskite-derivative calcium copper titanate, Nat. Mater. 3(11) (2004) 774-778.
- [2] T. Adams, D. Sinclair, A. West, Characterization of grain boundary impedances in fine- and coarse-grained CaCu<sub>3</sub>Ti<sub>4</sub>O<sub>12</sub> ceramics, Phys. Rev. B 73(9) (2006) 094124.
- [3] L. Liu, H. Fan, P. Fang, X. Chen, Sol-gel derived  $CaCu_3Ti_4O_{12}$  ceramics: Synthesis, characterization and electrical properties, Mater. Res. Bull. 43(7) (2008) 1800-1807.
- [4] L. Ni, X.M. Chen, Enhanced giant dielectric response in Mg-substituted CaCu<sub>3</sub>Ti<sub>4</sub>O<sub>12</sub> ceramics, Solid State Commun. 149(9-10) (2009) 379-383.
- [5] L. Ni, X.M. Chen, Enhancement of Giant Dielectric Response in CaCu<sub>3</sub>Ti<sub>4</sub>O<sub>12</sub> Ceramics by Zn Substitution, J. Am. Ceram. Soc. 93(1) (2010) 184-189.
- [6] P. Thongbai, J. Jumpatam, T. Yamwong, S. Maensiri, Effects of Ta<sup>5+</sup> doping on microstructure evolution, dielectric properties and electrical response in CaCu<sub>3</sub>Ti<sub>4</sub>O<sub>12</sub> ceramics, J. Eur. Ceram. Soc. 32(10) (2012) 2423-2430.
- [7] D. Xu, C. Zhang, Y. Lin, L. Jiao, H. Yuan, G. Zhao, X. Cheng, Influence of zinc on electrical and microstructural properties of CaCu<sub>3</sub>Ti<sub>4</sub>O<sub>12</sub> ceramics prepared by sol–gel process, J. Alloys Compd. 522 (2012) 157-161.
- [8] P. Thongbai, B. Putasaeng, T. Yamwong, S. Maensiri, Modified giant dielectric properties of samarium doped CaCu<sub>3</sub>Ti<sub>4</sub>O<sub>12</sub> ceramics, Mater. Res. Bull. 47(9) (2012) 2257-2263.
- [9] W. Wan, C. Liu, H. Sun, Z. Luo, W.-X. Yuan, H. Wu, T. Qiu, Low-toxic gelcasting of giant dielectric-constant  $CaCu_3Ti_4O_{12}$  ceramics from the molten salt powder, J. Eur. Ceram. Soc. 35(13) (2015) 3529-3534.
- [10] M.A. Ponce, M.A. Ramirez, F. Schipani, E. Joanni, J.P. Tomba, M.S. Castro, Electrical behavior analysis of n-type CaCu<sub>3</sub>Ti<sub>4</sub>O<sub>12</sub> thick films exposed to different atmospheres, J. Eur. Ceram. Soc. 35(1) (2015) 153-161.
- [11] R. Löhnert, B. Capraro, S. Barth, H. Bartsch, J. Müller, J. Töpfer, Integration of CaCu<sub>3</sub>Ti<sub>4</sub>O<sub>12</sub> capacitors into LTCC multilayer modules, J. Eur. Ceram. Soc. 35(11) (2015) 3043-3049.
- [12] M. Ahmad, H. Mahfoz Kotb, Giant dielectric properties of fine-grained  $Na_{1/2}Y_{1/2}Cu_3Ti_4O_{12}$  ceramics prepared by mechanosynthesis and spark plasma sintering, J. Mater. Sci.: Mater. Electron. 26(11) (2015) 8939-8948.
- [13] J. Li, P. Liang, J. Yi, X. Chao, Z. Yang, Phase Formation and Enhanced Dielectric Response of  $Y_{2/3}Cu_3Ti_4O_{12}$  Ceramics Derived from the Sol–Gel Process, J. Am. Ceram. Soc. 98(3) (2015) 795-803.
- [14] R. Xue, Z. Chen, H. Dai, D. Liu, T. Li, G. Zhao, Effects of rare earth ionic doping on microstructures and electrical properties of  $CaCu_3Ti_4O_{12}$  ceramics, Mater. Res. Bull. 66 (2015) 254-261.
- [15] R. Löhnert, H. Bartsch, R. Schmidt, B. Capraro, J. Töpfer, A. Feteira, Microstructure and Electric Properties of CaCu<sub>3</sub>Ti<sub>4</sub>O<sub>12</sub> Multilayer Capacitors, J. Am. Ceram. Soc. 98(1) (2015) 141-147.
- [16] J. Jumpatam, P. Thongbai, Enhanced dielectric and non-ohmic properties in  $CaCu_3Ti_4O_{12}/CaTiO_3$  nanocomposites prepared by a chemical combustion method, J. Mater. Sci.: Mater. Electron. 27(11) (2016) 12085-12090.
- [17] A. Nautiyal, C. Autret, C. Honstettre, S. De Almeida-Didry, M. El Amrani, S. Roger, B. Negulescu, A. Ruyter, Local analysis of the grain and grain boundary contributions to the bulk dielectric properties of  $Ca(Cu_{3-y}Mg_y)Ti_4O_{12}$  ceramics: Importance of the potential barrier at the grain boundary, J. Eur. Ceram. Soc. 36(6) (2016) 1391-1398.
- [18] L. Singh, B.C. Sin, I.W. Kim, K.D. Mandal, H. Chung, Y. Lee, J. Varela, A Novel One-Step Flame Synthesis Method for Tungsten-Doped CCTO, J. Am. Ceram. Soc. 99(1) (2016) 27-34.
- [19] X.W. Wang, P.B. Jia, X.E. Wang, B.H. Zhang, L.Y. Sun, Q.B. Liu, Calcining temperature dependence on structure and dielectric properties of CaCu<sub>3</sub>Ti<sub>4</sub>O<sub>12</sub> ceramics, J. Mater. Sci.: Mater. Electron. (2016) 1-7.
- [20] Y. Liu, X. Zhao, C. Zhang, Dielectric and impedance characteristics of  $Na_{1/3}Ca_{1/3}Y_{1/3}Cu_3Ti_4O_{12}$  ceramic prepared by solid-state reaction method, J. Mater. Sci.: Mater. Electron. 27(11) (2016) 11757-11761.

- [21] S. Wu, P. Liu, Y. Lai, W. Guan, Z. Huang, J. Han, Y. Xiang, W. Yi, Y. Zeng, Effect of Ba<sup>2+</sup> doping on microstructure and electric properties of calcium copper titanate (CaCu<sub>3</sub>Ti<sub>4</sub>O<sub>12</sub>) ceramics, J. Mater. Sci.: Mater. Electron. (2016) 1-6.
- [22] X. Huang, H. Zhang, J. Li, Y. Lai, Influence of different dopant sites by lanthanum on the dielectric properties of CaCu<sub>3</sub>Ti<sub>4</sub>O<sub>12</sub> ceramics, J. Mater. Sci.: Mater. Electron. (2016) 1-7.
- [23] J.Q. Wang, X. Huang, X.H. Zheng, D.P. Tang, Structure and electric properties of CaCu<sub>3</sub>Ti<sub>4</sub>O<sub>12</sub> ceramics prepared by rapid sintering, J. Mater. Sci.: Mater. Electron. 27(2) (2016) 1345-1349.
- [24] J. Jumpatam, B. Putasaeng, T. Yamwong, P. Thongbai, S. Maensiri, Microstructural evolution and strongly enhanced dielectric response in Sn-doped CaCu<sub>3</sub>Ti<sub>4</sub>O<sub>12</sub>/CaTiO<sub>3</sub> ceramic composites, Mater. Res. Bull. 77 (2016) 178-184.
- [25] R. Xue, G. Zhao, J. Chen, Z. Chen, D. Liu, Effect of doping ions on the structural defect and the electrical behavior of CaCu<sub>3</sub>Ti<sub>4</sub>O<sub>12</sub> ceramics, Mater. Res. Bull. 76 (2016) 124-132.
- [26] H.M. Kotb, M.A. Mohamad, Electrical and dielectric properties of Na<sub>1/2</sub>La<sub>1/2</sub>Cu<sub>3</sub>Ti<sub>4</sub>O<sub>12</sub> ceramics prepared by high energy ball-milling and conventional sintering, Chinese Physics B 25(12) (2016) 128201.
- [27] J. Boonlakhorn, P. Kidkhunthod, P. Thongbai, A novel approach to achieve high dielectric permittivity and low loss tangent in  $CaCu_3Ti_4O_{12}$  ceramics by co-doping with  $Sm^{3+}$  and  $Mg^{2+}$  ions, J. Eur. Ceram. Soc. 35(13) (2015) 3521-3528.
- [28] J. Li, K. Wu, R. Jia, L. Hou, L. Gao, S. Li, Towards enhanced varistor property and lower dielectric loss of CaCu<sub>3</sub>Ti<sub>4</sub>O<sub>12</sub> based ceramics, Materials & Design 92 (2016) 546-551.
- [29] A.J. Moulson, J.M. Herbert, Electroceramics : materials, properties, applications, 2nd ed., Wiley, West Sussex; New York, 2003.
- [30] Q. Zheng, H. Fan, C. Long, Microstructures and electrical responses of pure and chromium-doped CaCu<sub>3</sub>Ti<sub>4</sub>O<sub>12</sub> ceramics, J. Alloys Compd. 511(1) (2012) 90-94.
- [31] L. Liu, H. Fan, X. Chen, P. Fang, Electrical properties and microstructural characteristics of nonstoichiometric CaCu<sub>3x</sub>Ti<sub>4</sub>O<sub>12</sub> ceramics, J. Alloys Compd. 469(1-2) (2009) 529-534.
- [32] R.D. Shannon, Revised Effective Ionic Radii and Systematic Studies of Interatomie Distances in Halides and Chaleogenides, Acta Cryst. A32 (1976) 751-767.
- [33] M.A. Subramanian, A.W. Sleight, ACu<sub>3</sub>Ti<sub>4</sub>O<sub>12</sub> and ACu<sub>3</sub>Ru<sub>4</sub>O<sub>12</sub> perovskites: high dielectric constants and valence degeneracy, Solid State Sci. 4(3) (2002) 347-351.
- [34] J. Boonlakhorn, P. Kidkhunthod, B. Putasaeng, P. Thongbai, Significantly improved non-Ohmic and giant dielectric properties of CaCu<sub>3-x</sub>Zn<sub>x</sub>Ti<sub>4</sub>O<sub>12</sub> ceramics by enhancing grain boundary response, Ceram. Int. 43(2) (2017) 2705-2711.
- [35] W. Hao, H. Wu, P. Xu, Y. Shi, S. Yang, M. Wang, L. Sun, E. Cao, Y. Zhang, Influence of Sb-doping on dielectric properties of NaCu<sub>3</sub>Ti<sub>3</sub>TaO<sub>12</sub> ceramics and relevant mechanism(s), Ceram. Int. 43(4) (2017) 3631-3638.
- [36] M.N. Rahaman, Ceramic processing and sintering, 2nd ed., M. Dekker, New York, 2003.

# **CHAPTER 14**

(Al<sup>3+</sup>, Nb<sup>5+</sup>) Co–Doped CaCu<sub>3</sub>Ti<sub>4</sub>O<sub>12</sub>: An Extended Approach for Acceptor– Donor Heteroatomic Substitutions to Achieve High–Performance Giant– Dielectric Permittivity

#### **14.1 Introduction**

Since the giant dielectric behavior of the most studied CaCu<sub>3</sub>Ti<sub>4</sub>O<sub>12</sub> (CCTO) ceramics was reported by Subramanian et al. [1], many giant-dielectric oxides have been extensively investigated. Giant-dielectric oxides that can exhibit unusually high dielectric permittivities ( $\varepsilon'$ ) of  $\approx 10^3 - 10^6$  without detectable ferroelectric phase transitions found in CCTO and its isostructural-type perovskites [1-17], Zr-doped SrTiO<sub>3</sub> [18], La<sub>2-x</sub>Sr<sub>x</sub>NiO<sub>4</sub> [19], SnO<sub>2</sub>-Zn<sub>2</sub>SnO<sub>4</sub> [20], PZN-PZT/Ag [21] and  $\mathbf{A} = \mathbf{F}_{1/2} \mathbf{B}_{1/2} \mathbf{O}_3$  ( $\mathbf{A} = \mathbf{B} \mathbf{a}$ , Sr, Ca;  $\mathbf{B} = \mathbf{N} \mathbf{b}$ , Ta, Sb) [22], among others. In addition to their potential applications in electronic and high energydense storage devices, the origins of giant-dielectric behavior have also been intensively studied in detail. Many elegant models were proposed to describe the giant-dielectric properties of these oxides such as the internal barrier layer capacitor (IBLC) [23], surface barrier layer capacitor (SBLC) [24], and small polaron hopping models [19] as well as the non-Ohmic sample-electrode contact model [25]. Actually, the origin(s) of the giant-dielectric responses of these materials is still open to scientific debate. Based on the applications point of view, unacceptably high values of the dielectric loss tangent (tan $\delta$ ) of these giantdielectric oxides is considered the most serious problem. A large high temperature value of the temperature coefficient, i.e., variation of  $\varepsilon'$  or capacitance (at 1 kHz) at any temperature compared to room temperature (RT), is one of the most difficult parameters to improve. Generally, if a parameter can be successfully improved, other dielectric parameters are simultaneously was worsened.

Recently, a newly discovered (In3+, Nb5+) co-doped rutile TiO2 ceramic can exhibit a low tan $\delta$  ( $\approx 0.02$ ) and very high  $\epsilon'$  ( $\approx 6 \times 10^4$ ) with good frequency and temperature stability [26]. Simultaneously, a new elegant model, i.e., the electron-pinned defect-dipole (EPDD) model, was proposed to explain the underlying mechanisms of the high dielectric performance of INTO ceramics. In this EPDD model, free electrons in the TiO<sub>2</sub> structure are produced by doping with Nb5+. Under an applied electric field, such localized electrons were freely polarized in triangular shaped  $In_2^{3+}V_o^{\bullet\bullet}Ti^{3+}$  defect complexes of the  $In^{3+}$  defect environments. However, it was further suggested that the giant-dielectric behavior in INTO ceramics originated from the IBLC and/or SBLC effects [27, 28]. Although a controversy about the origin of the giant-dielectric response of INTO currently exists, the acceptor-donor co-doping concept can successfully be used to achieve high-performance giant-dielectric properties in other co-doped TiO<sub>2</sub> systems such as (Al<sup>3+</sup>, Nb<sup>5+</sup>) [29], (Mg<sup>2+</sup>, Nb<sup>5+</sup>) [30] and (Ga<sup>3+</sup>, Ta<sup>5+</sup>) [28], among others. Interestingly, this strategy for obtaining high  $\varepsilon'$  values while retaining a very low tanδ can be applied to SnO<sub>2</sub> ceramics by co-doping them with (Al<sup>3+</sup>, Nb<sup>5+</sup>) [31]. Enhanced  $\varepsilon'$  values of  $\approx 10^3$  with low tan $\delta$  values  $\approx 0.03$  at 1 kHz and RT were achieved in an  $Al_{0.03}Nb_{0.05}Sn_{0.92}O_2$  ceramic. However, to achieve a highly dense microstructure with a very high  $\epsilon'$  value in these co-doped  $TiO_2$  and  $SnO_2$  ceramics, high sintering temperatures of 1400-1500°C were employed [26, 29, 31].

In the current work, we have successfully used the co–doping concept to significantly improve the dielectric properties of CaCu<sub>3</sub>Ti<sub>4</sub>O<sub>12</sub> prepared using a mixed oxide method and sintering at a relatively low temperature of 1090 °C. Through optimization of dopant concentration and sintering conditions, high-performance giant–dielectric properties of CaCu<sub>3</sub>Ti<sub>4</sub>O<sub>12</sub> ceramics were obtained by co–doping for substitution (Al<sup>3+</sup>, Nb<sup>5+</sup>) into TiO<sub>6</sub> octahedral sites. The possible origin of the giant-dielectric properties is systematically investigated and discussed in detail.

# 14.2 Experimental details

Co–doped  $CaCu_3Ti_{4-x}(Nb_{1/2}AI_{1/2})_xO_{12}$ , where x=0.025-0.2, as well as single-doped  $CaCu_3Ti_{3.975}Nb_{0.025}O_{12}$  (Nb025) and  $CaCu_3Ti_{3.975}AI_{0.025}O_{12}$  (Al025) ceramics were prepared via a solid state reaction method. The starting raw materials consisted of  $CaCO_3$  (99.0%), CuO (99.9%),  $TiO_2$  (99.99%),  $AI_2O_3$  (99.99%) and  $Nb_2O_5$  (99.99%). First, a stoichiometric mixture of the starting materials corresponding to each doping composition was mixed by wet–ball milling in ethanol for 24 h. Second, the mixed raw materials were dried at 80 °C for 24 h to remove ethanol from the media. Third, the resulting dried precursors were ground and calcined at 850 °C for 12 h. Then, the resulting calcined powders were ground and pressed by uniaxial compression at  $\approx$ 180 MPa into pellet shaped disks, 9.5 mm in diameter and  $\approx$ 1.2 mm in thickness. These pellets were sintered at 1050–1090 °C for 3–36 h using a heating rate 2 °C/min followed by natural cooling in a furnace to room temperature (RT).

The phase composition and crystal structure of these ceramics were characterized using X-ray Diffractometry (PANalytical, EMPYREAN). The diffraction spectra were collected over the 20 range of 25°-65° with s step size of 0.02°/min. The Rietveld refinement was carried out using X'Pert HighScore Plus software and compared with the crystallographic structure of CCTO. Surface morphologies were characterized using scanning electron microscopy (SEM; LEO 1450VP). The distribution of all elements used in the sintered ceramics was examined using field-emission scanning electron microscopy (FE-SEM) with -ratis/peansiallysisX (EDX) (HITACHI SU8030, Japan). X-ray energy Absorption Near Edge Structure (XANES) and X-ray photoelectron spectroscopy (XPS) spectra were collected at the SUT-NANOTEC-SLRI XAS and beamline (BL5.2) (electron energy of 1.2 GeV; bending magnet; beam current 80-150 mA; 1.1 to 1.7×10<sup>11</sup> photon.s<sup>-1</sup>) and BL5.1 XPS machine (PHI5000 VersaProbe II, ULVAC-PHI) at the SUT-NANOTEC-SLRI at the Synchrotron Light Research Institute (SLRI), Nakhon Ratchasima, Thailand. Details of this characterization technique and analysis are given elsewhere [8].

To measure dielectric and electrical properties, both surface sides of the sintered samples were carefully polished to obtain smooth and clean surfaces. After that, all the samples were dried overnight at 100 °C. Both top and bottom sample surfaces were coated by Au sputtering using a Polaron SC500 sputter coating unit with an electric current ~25 mA for 4 min. The dielectric properties of the sintered ceramics were measured using a KEYSIGHT E4990A unit with an oscillation voltage of 500 mV. These measurements were done in range of 40  $^{6}$ 10 Hz and  $^{9}$ 60 Nto all the ar current density—electric field (*J*–*E*) characteristics were measured at room temperature (RT) using a high voltage measurement unit (Keithley 247). The rate of increase in source voltage was 1.33 V/s. The  $E_b$  value was defined as the electric field breakdown at which J = 1 mA.cm<sup>-2</sup>. The nonlinear coefficient ( $\alpha$ ) was calculated in the range of 1–10 mA/cm<sup>2</sup>.

# 14.3 Results and discussion

Typical ε' and tanδ values at 103 Hz and RT for the co-doped CaCu<sub>3</sub>Ti<sub>4-</sub>  $_x(Nb_{1/2}AI_{1/2})_xO_{12}$  (x = 0.025-0.2) sintered under different conditions are shown in Fig. 1. Both  $\varepsilon'$  and  $\tan\delta$  values remarkably changed, irrespective of the sintering time or co-dopant concentration. All of co-doped samples exhibited very large  $\varepsilon'$ values (>10<sup>4</sup>). This is similar to that observed in a pure CCTO ceramic, since very high  $\varepsilon'$  values can easily be produced, but it is usually accompanied by quite large  $tan\delta$  values, especially in a low frequency range ( $\leq 10^3$  Hz) [1, 8, 10, 23, 25]. Therefore, the composition and sintering optimization should first focus on the reduction of tanδ. Substitution of CCTO with high concentrations of co-dopants (x  $\geq$  0.1) likely gives rise to very high tan $\delta$  > 0.1. Low tan $\delta$  < 0.1 values were obtained in the co-doped ceramics with  $x \le 0.05$ . These interesting dielectric properties can be comparable to those reported in literature [32-35]. The ceramic compositions with  $x \le 0.05$  can be further optimized by sintering at 1090 °C for 18 h. Interestingly, low tan \delta values can also be achieved even at frequencies as low as 40 Hz (as represented in Fig. 4). This is very hard to accomplish in CCTO-based ceramics. Thus, the co-doped  $CaCu_3Ti_{4-x}(Nb_{1/2}AI_{1/2})_xO_{12}$  ceramics with x = 0.025and 0.05 sintered under this condition (referred to as the NA025 and NA05 ceramics, respectively) were selected to further investigate the underlying mechanisms of the origin of the significantly improved dielectric response.

**Table 1.** Lattice parameter (a), grain size (G) and relative density ( $\rho$ ).

Sample	a (Å)	G (μm)	ρ (%)
Nb025	7.395(2)	20.2±7.5	96.2
AI025	7.390(7)	129.6±52.3	93.5
NA025	7.392(8)	35.1±15.5	94.1
NA05	7.393(0)	34.6±21.9	93.3

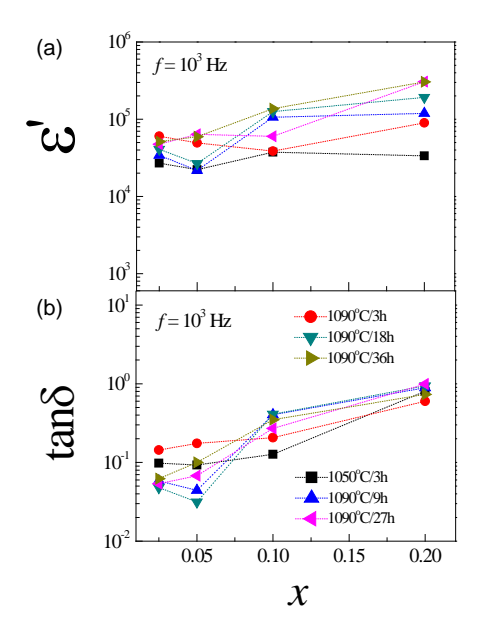


**Fig. 1** (a-b) ε' and tanδ values at  $10^3$  Hz for CaCu<sub>3</sub>Ti<sub>4-x</sub>(Nb<sub>1/2</sub>Al<sub>1/2</sub>)<sub>x</sub>O<sub>12</sub> (x = 0.025-0.20) sintered under various conditions.

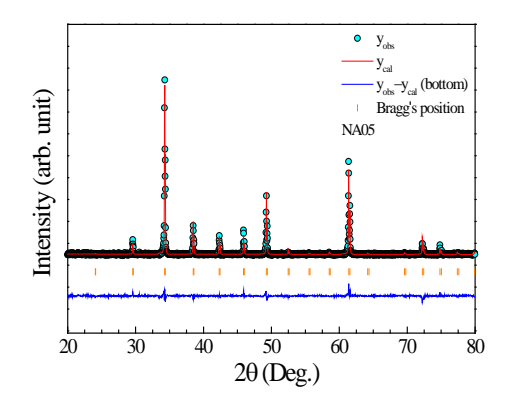
The diffraction peaks of all single-doped (Nb025 and Al025) and co-doped (NA025 and NA05) ceramics were consistent with standard peaks of CCTO (JCPDS 75 2016BasA wasodeterot€duin the Al025 ceramic, as shown in Fig. S1(a) (Supplementary Information). No impurities (i.e., CuO, Cu<sub>2</sub>O, TiO<sub>2</sub>, CaTiO<sub>3</sub> and related sintered ceramics. This might have been due to the complete substitution of Nb and Al dopants into the co-doped ceramics. The profile fits of the Rietveld refinement of the co-doped NA05 ceramic and other single-doped and co-doped NA025 ceramics are demonstrated in Fig. 2 and Fig. S1(b quality of the refinement was quantified by several parameters [Table S1 (Supplementary Information)]. Accordingly, lattice parameter (a) values were obtained. The a values of the Nb025 and Al025 ceramics were slightly larger and smaller, respectively, than that of CCTO ceramic. This may have been due to the larger and smaller ionic radii of Nb5+ and Al3+ dopants than that of the host Ti4+ ions. The a values of the co-doped ceramics were between the corresponding values for the single-doped ceramics.

Fig. 3 reveals the effects of  $Al^{3+}$  or  $Nb^{5+}$  single-dopant and  $(Al^{3+} + Nb^{5+})$  co-dopants on the microstructural evolution of CCTO ceramics. Obviously, doping CCTO ceramics with  $Al^{3+}$  and/or  $Nb^{5+}$  has remarkable influences on their microstructures. The relative densities of all the ceramics were higher than 93%, as can be seen in Table 1. The mean grain size of a pure CCTO ceramic sintered at  $1090\,^{\circ}$ C for 18 h was very large and found to be  $\approx 55.1\,\mu m$  [Fig. S2, Supplementary Information]. A greatly reduced mean grain size of the Nb025 ceramic ( $\approx 20.2\,\mu m$ ) is similar to that reported in the literature for  $Nb^{5+}/Ta^{5+}$  doped-CCTO ceramics [36, 37]. Substitution of  $Al^{3+}$  into CCTO resulted in a large increase in the mean grain size ( $\approx 129.6\,\mu m$ ), which is consistent with the results of

-oxide Nb/Al pha

-d), respectively.

Rahman *et al.* [38]. The grain size of CCTO was enlarged to  $\approx$ 100  $\mu$ m by adding a small amount of Al<sub>2</sub>O<sub>3</sub> (0.01 wt%).



**Fig. 2** Profile fits for the Rietveld refinement of co-doped NA05 ceramic.

Obviously,  $Al^{3+}$  and  $Nb^{5+}$  dopants have distinct roles in grain growth as well as enhancement and inhibition mechanisms of CCTO ceramics, respectively. Alternatively, the mean grain sizes of the co–doped NA025 ( $\approx$ 35.1 µm) and NA05 ( $\approx$ 34.6 µm) ceramics were between the mean grain sizes of the single–doped Al025 and Nb025 ceramics and not much different that of the un–doped CCTO ceramic. Interestingly, simultaneous substitution of both  $Al^{3+}$  and  $Nb^{5+}$  ions can balance the driving and restorative forces for grain boundary (GB) migration. Therefore, the microstructure of CCTO ceramics was slightly changed by co–doping with  $Al^{3+}$  and  $Nb^{5+}$  ions. Microstructural analyses revealed good dispersion of the major elements (*i.e.*, Ca, Cu, Ti, and O) and the Al and Nb dopants in the co–doped ceramics [Fig. S3, Supplementary Information]. No segregation of Cu or the dopants was observed. The EDS spectrum of the NA05 ceramic and the related measurement area are illustrated in Fig. S4 and its inset (Supplementary Information), confirming the presence of Ca, Cu, Ti, O, Al, and Nb.

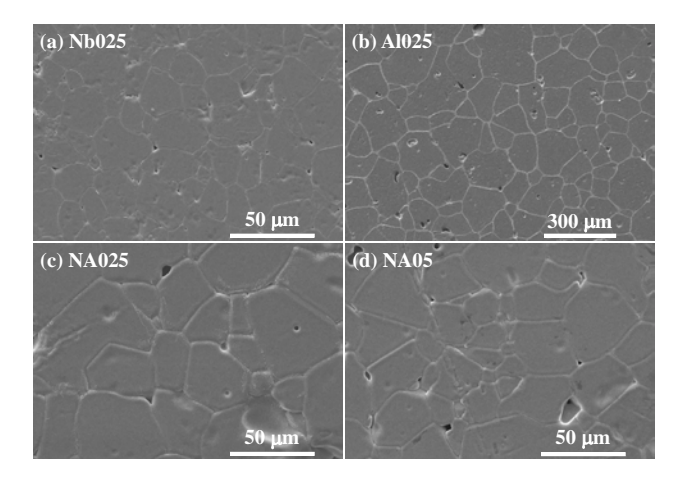


Fig. 3 SEM images of (a) single-doped Nb025, (b) single-doped Al025, (c) co-doped NA025, and (d) co-doped NA05 ceramics.

Fig. 4 shows  $\varepsilon'$  and  $\tan\delta$  as a function of frequency (40–10<sup>6</sup> Hz) at RT for all of the ceramics. The  $\varepsilon'$  values of the single-doped Al025 and Nb025 ceramics are larger than those of the co-doped NA025 and NA05 ceramics. Nevertheless,  $\varepsilon'$ values of both co-doped ceramics are still too large (>10<sup>4</sup>). Furthermore, their  $\varepsilon'$ values has more frequency-stability than those of the single-doped ceramics. Interestingly, over the measured frequency range, the  $tan\delta$  values of both co-doped ceramics are much lower than those of the single-doped ceramics as well as the un-doped CCTO ceramic (tan $\delta \approx 0.17$  at 40 Hz). The  $\epsilon'$  and tan $\delta$ values at 1 kHz and RT of all ceramics examined are listed in Table 2. Very high tanδ values of CCTO ceramics usually appear in the low and high frequency ranges [4, 5, 8, 11, 36], which are associated with high DC conductivity and a dielectric relaxation phenomenon, respectively [39]. Such a very large value of a low frequency  $tan\delta$  is unsuitable for practical applications [40]. Notably, low frequency  $tan\delta$  values of the co-doped ceramics were still very low. The  $tan\delta$ value at 40 Hz of the NA05 ceramic was ≈0.05. The frequency dependent behavior of tanδ for the co-doped ceramics is similar to those observed in (In<sup>3+</sup>, Nb<sup>5+</sup>) and (Ga<sup>3+</sup>, Ta<sup>5+</sup>) co-doped TiO<sub>2</sub> ceramics [26, 28], for which a low frequency  $tan\delta$  was still too low. This is one of the important features of the high-performance giant-dielectric properties of co-doped TiO<sub>2</sub> systems that has never been obtained in other giant dielectric oxides [2, 6-9, 13, 19, 22, 36]. Besides low  $tan\delta$  and high  $\epsilon'$  values,  $\epsilon'$  of the co-doped CCTO ceramics was much more temperature-stable than that of the pure and single-doped CCTO ceramics, as shown in the inset of Fig. 4.

Based on the EPDD or IBLC/SBLC models for  $A^{3+}/Nb^{5+}$  co-doped  $TiO_2$  ceramics, it was postulated that role of  $A^{3+}$  dopant (A = In, Ga, or Al, *etc*) was to produce complex defect clusters for confining free electrons or forming internal insulating interfaces for blocking electrons, respectively [26-28]. For  $Al^{3+}/Nb^{5+}$  co-doped CCTO ceramics, the role of  $Nb^{5+}$  dopant was not to promote the giant dielectric response because the  $\epsilon'$  value of CCTO-based materials was already high ( $\approx 10^3 - 10^5$ ). Furthermore, doping CCTO with only  $Al^{3+}$  or  $Nb^{5+}$  cannot reduce  $tan\delta$  to values lower than the un-doped or co-doped ceramics. Thus, reduction of  $tan\delta$  should be promoted by  $Al^{3+}$  and  $Nb^{5+}$  dopants acting in unison.

**Table 2.**  $\epsilon'$  and  $\tan\delta$  (at 1 kHz and RT), activation energies for conduction at the grain  $(E_g)$  and GB  $(E_{gb})$ , grain resistance  $(R_g)$  and GB resistance  $(R_{gb})$  and nonlinear properties  $(\alpha \text{ and } E_b)$  at RT.

Sample	ε'	tanδ	E <sub>g</sub> (eV)	E <sub>gb</sub> (eV)	$R_g$ ( $\Omega$ .cm)	$R_{gb}$ ( $\Omega$ .cm)	α	E <sub>b</sub> (V/cm)
Nb025	4.8×10 <sup>5</sup>	0.566	0.083	0.353	30±0.6	1.03×10 <sup>4</sup>	3.10	21.7
AI025	2.1×10 <sup>5</sup>	0.129	0.100	0.619	38±0.3	1.34×10 <sup>6</sup>	4.36	210.3
NA025	4.1×10 <sup>4</sup>	0.058	0.086	0.781	45±0.5	3.69×10 <sup>8</sup>	5.40	620.3
NA05	2.9×10 <sup>4</sup>	0.045	0.090	0.817	66±0.8	1.17×10 <sup>9</sup>	5.76	723.3

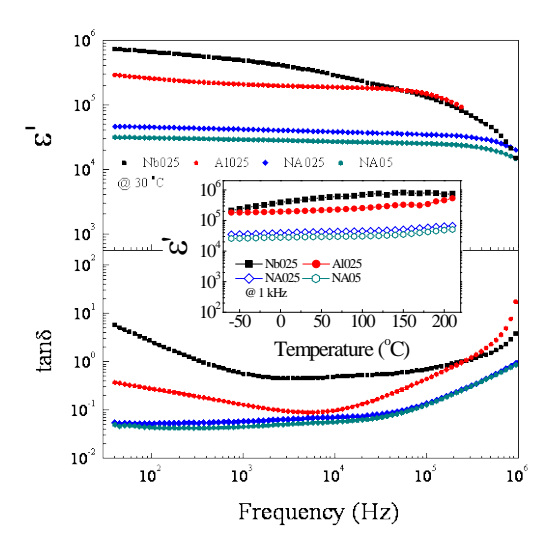


Fig. 4 Frequency dependence of  $\epsilon'$  and  $\tan\delta$  at RT for CCTO, single-doped and co-doped CCTO ceramics; inset shows the temperature dependence of  $\epsilon'$  at 1 kHz.

The possible mechanisms were clarified using impedance spectroscopy (IS). Fig. 5(a) and its insets, both the single– and co–doped ceramics are electrically heterogeneous, consisting of semiconducting grains and insulating GBs, which is indicated by the nonzero intercept and large semicircular arc on the Z\* plot, respectively [23]. This is a general feature of the RT–Z\* plots of CCTO–based ceramics [8, 11, 14, 23, 36, 37, 39]. The semiconducting grains are likely associated with the presence of Cu<sup>+</sup> and Ti<sup>3+</sup> ions, which were, respectively, detected by XPS and XANES techniques [Fig. S5, Supplementary Information]. A significant decrease in the low frequency tanδ value of the co–doped ceramics can be described by the greatly enhanced GB resistance (R<sub>gb</sub>). R<sub>gb</sub> values of both co–doped ceramics were much larger than those of the single–doped ceramics [Fig. 5(a) and inset (2)]. The grain resistance (R<sub>g</sub>) values at -60°C [inset (1) of Fig. 5(a)] as well as at RT [Table 2] of the co–doped ceramics were larger than that of the single–doped ceramics. Figs. 5(b) and (c) illustrate the temperature

dependencies of  $R_g$  and  $R_{gb}$ , following to the Arrhenius law. Over a wide temperature range, both  $R_g$  and  $R_{gb}$  values of the co–doped ceramics were significantly higher than those of the single–doped ceramics. The conduction activation energies inside the grains  $(E_g)$  and at the GBs  $(E_{gb})$  were calculated and summarized in Table 2.  $E_g$  values of both single– and co–doped ceramics were slightly changed, while  $E_{gb}$  values of both co–doped ceramics were significantly larger than those of the single–doped ceramics. Considering the significantly increased values of  $R_{gb}$  and  $E_{gb}$  for the co–doped ceramics, the electrical properties of the GBs of CCTO ceramics were improved by co–doping with  $Al^{3+}$  and  $Nb^{5+}$ .

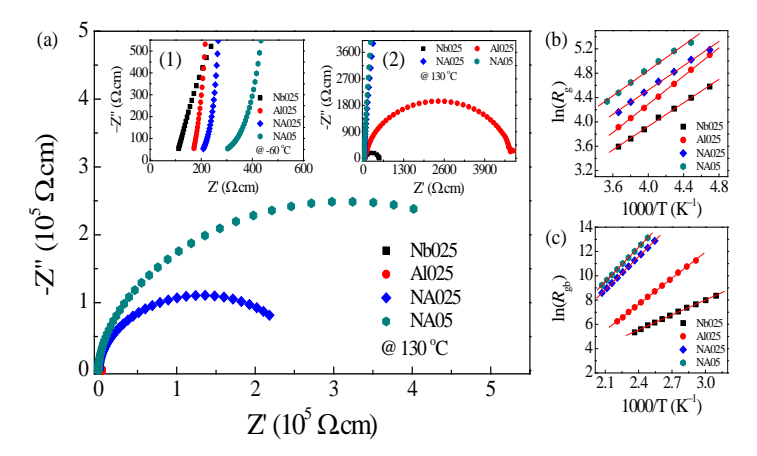
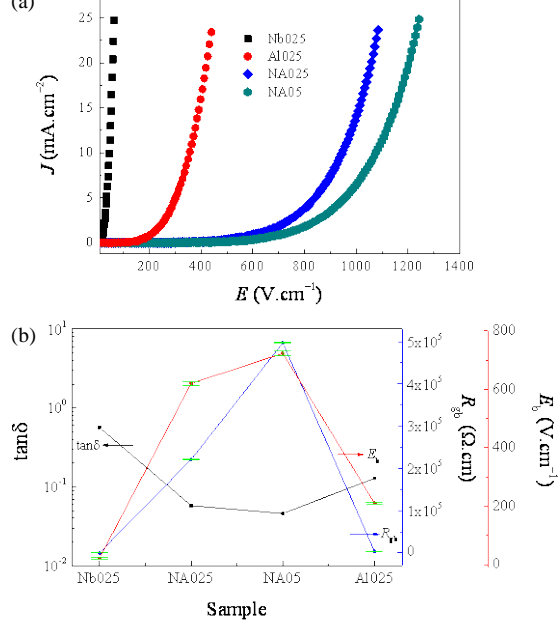


Fig. 5 (a) Impedance complex (Z\*) plane plot at 140 °C for CCTO, single-doped and co-doped CCTO ceramics; insets show an expanded view of the high frequency data close to the origin, revealing (1) the nonzero intercept on the Z' axis at 30 °C, and, (2) Z\* plane plot of the single-doped Al025 and Nb025 ceramics at 140 °C. (b-c) Arrhenius plots of the grain and GB resistance data.

Given that  $E_{gb}$  was independent of temperature over the measured range,  $R_{gb}$  values at RT for all the ceramics were calculated and summarized in Table 2. Obviously, low  $\tan\delta$  values at RT of the co-doped ceramics should be associated with their very large  $R_{gb}$  values ( $10^8-10^9~\Omega.cm$ ), corresponding to the IBLC model of Schottky barriers at the GBs. In a low-frequency range, a high  $\tan\delta$  value is associated with DC conductivity ( $\sigma_{dc}=1/R_{gb}$ ). When  $R_g << R_{gb}$ , the relationship between  $\tan\delta$  and  $\sigma_{dc}$  can be estimated by following equation  $\tan\delta \approx \left(\omega\epsilon_0\epsilon'_sC_0R_{gb}\right)^{-1}$ , where  $\epsilon'_s$  is a low-frequency dielectric permittivity.  $C_o$  is the empty cell capacitance. Clearly, the low-frequency  $\tan\delta$  value at RT of the co-doped CCTO ceramics is very much reduced by greatly increasing  $R_{gb}$ . Low  $\tan\delta$  values of CCTO-ceramics as a result of their large  $R_{gb}$  values were reported in literature [32, 33, 35]. Furthermore, the large decrease in the  $R_{gb}$  of the single-doped Nb025 and Al025 ceramics is similar to that observed in TiO<sub>2</sub>-based ceramics

such as (Nb $^{5+}$  or Ta $^{5+}$ ) [36, 37, 41] and Sc $^{3+}$  doped-CCTO [42] ceramics, respectively.



**Fig. 6** (a) Nonlinear J–E characteristics of single and co–doped CCTO ceramics. (b) Correlation between tan $\delta$  (at 1 kHz and RT), R<sub>gb</sub>, and E<sub>b</sub> of single and co–doped CCTO ceramics.

According to the XPS and XANES results, the lowest  $R_g$  value of the Nb025 ceramics was likely due to its large  $Cu^+/Cu^{2+}$  and  $Ti^{3+}/Ti^{4+}$  ratios [Table S2, *Supplementary Information*], which were primarily caused by the presence of oxygen vacancies and doping with Nb<sup>5+</sup> ions. The relatively large  $R_g$  values of both co–doped ceramics may have resulted from their small  $Cu^+/Cu^{2+}$  ratios. Generally, substitution of  $Al^{3+}$  for  $Ti^{4+}$  does not produce free electrons. Thus, the large  $Cu^+/Cu^{2+}$  ratio of the Al025 ceramic should be correlated to the presence of oxygen vacancies during sintering. Although the presence of  $Cu^+$  can possibly originate from some portion of  $Al^{3+}$  doping ions being substituted into  $Cu^{2+}$  sites, the concentration of  $Al^{3+}$  doping ions was very low compared to the large ratio of  $Cu^+/Cu^{2+}$  found. According to the XPS and XANES analysis, it is likely that conduction in CCTO–based oxides is very complex because electron hopping can occur in both  $Ti^{3+}$ –O– $Ti^{4+}$  and  $Cu^+$ –O– $Cu^{2+}$ .

Generally, the nonlinear electrical properties of CCTO-based ceramics are attributed to the formation of Schottky barriers at the GBs [23]. As illustrated in 6(a), the nonlinear J–E characteristics are observed in all ceramics. A greatly reduced  $E_b$  value of the Nb025 ceramic was similar to that previously reported for Nb<sup>5+</sup>/Ta<sup>5+</sup> doped–CCTO, while the J–E characteristics of the Al025 ceramic were similar to those observed in Sc<sup>3+</sup> doped–CCTO [37, 41, 42]. Doping CCTO with either of +5 or +3 ions caused a decrease in a potential barrier height at the GBs [41, 42], resulting in a decrease in the macroscopic parameter of  $E_b$ . Surprisingly, simultaneously doping CCTO with these +5 and +3 ions can cause increases in

both the  $E_b$  and  $\alpha$  values, as listed in Table 2. Greatly improved dielectric and nonlinear properties of the co-doped ceramics might have resulted from the enhanced electrical properties of the GBs via co-doping with Al3+ and Nb5+. This hypothesis is illustrated in Fig. 6(b). Lowering the tanδ value of the co-doped ceramics is inversely related to remarkable increases in R<sub>ab</sub> and E<sub>b</sub>. We found that  $\varepsilon'$  (at RT and  $10^2-10^5$  Hz) of the co-doped ceramics decreased with increasing applied DC bias from 0-40 V, while the low frequency tanδ was increased [Fig. S6. Supplementary Information]. Furthermore, the dielectric properties of the co-doped ceramics were not changed by sputter coating with Ag instead of Au [Fig. S7(a), Supplementary Information]. On the contrary, the dielectric properties of the single-doped Nb025 ceramic were significantly changed, especially in the low frequency range [Fig. S7(b), Supplementary Information]. Thus, the effect of the sample-electrode interface can be excluded from the total polarization in the co-doped ceramics. These findings support the IBLC model of Schottky barriers at the GBs as the primary origin of the high performance giant-dielectric properties of the (Al<sup>3+</sup> + Nb<sup>5+</sup>) co-doped CCTO ceramics [23].

The significantly improved giant dielectric properties and enhanced nonlinear electrical properties were likely caused by an improved electronic structure at the GBs as a result of  $(Al^{3+} + Nb^{5+})$  co-dopants. In the absence of a DC bias, a potential barrier height  $(\Phi_B)$  at the GBs can be expressed as [23]:

$$\Phi_B = \frac{qN_s^2}{8\varepsilon_0 \varepsilon' N_d},\tag{1}$$

where  $\epsilon'$  is the relative permittivity of materials and q is the electronic charge.  $N_{\rm S}$  and  $N_{\rm d}$  are the acceptor (surface charge) and charge carrier concentrations in the n-type semiconducting grains, respectively. Variations in the  $R_{\rm gb}$ ,  $E_{\rm b}$  and  $E_{\rm gb}$  values of CCTO-based ceramics were directly associated with a change in  $\Phi_B$ . Largely decreased values of  $R_{\rm gb}$  and  $E_{\rm b}$ , and thus  $\Phi_B$ , for the single-doped Nb025 ceramic, may also have been associated with a large amount of  $N_{\rm d}$  (a low value of  $R_{\rm g}$ ). The  $E_{\rm b}$  values of the Al025 and un-doped CCTO ceramics ( $E_{\rm b}\approx 240$  V/cm) were slightly different, which is similar to that observed in a Sc³+ doped-CCTO (in Ti⁴+ site) [42]. A secondary Cu₂O phase was detected in the Al025 ceramic, indicating that the Al³+ ions occupied both Cu²+ and Ti⁴+ sites. Self-compensation by some Al³+ ions in each site occurred in the Al025 ceramic because Al³+ ions are an electron donor in Cu²+ sites and simultaneously an acceptor in Ti⁴+ sites.

According to the IS, XPS, and XANSE results, the first reason for the increase in  $\Phi_B$  of the co-doped ceramics is a reduction of  $N_{\rm d}$ , which was indicated by a significant increase in the R<sub>g</sub>. This can be achieved only if  $N_{\rm s}$  can be held constant or increased. No Cu<sub>2</sub>O was observed in either of the co-doped ceramics, indicating that most of the Al<sup>3+</sup> occupied the Ti<sup>4+</sup> sites. Therefore, self-compensation between Al<sup>3+</sup> and Nb<sup>5+</sup> occurred, retaining the active acceptor states at the GBs. Additionally, a low Cu<sup>+</sup>/Cu<sup>2+</sup> ratio observed in the co-doped

ceramics compared to that of the single–doped ceramics suggested fewer oxygen vacancies and lower number of free electrons ( $N_d$ ). Consequently, the  $\Phi_B$  and related  $E_{gb}$  values can be increased by reducing  $N_d$  coupled with retaining the  $N_s$  concentration. The results presented in this work demonstrate the importance of electronic structure at the GBs in controlling the dielectric and nonlinear electrical properties of CCTO ceramics, supporting the IBLC model of Schottky barriers at GBs between n-type semiconducting grains.

# 14.4 Conclusions

By optimization of dopant concentration and sintering condition, improved giant–dielectric properties of CCTO can be obtained by using a newly acceptor–donor co-doping approach. (Al³+, Nb⁵+) co–doped CCTO ceramics exhibited largely temperature and frequency independent dielectric properties. A very high dielectric permittivity of  $\approx 2.9 - 4.1 \times 10^4$  and a low  $\tan \delta \approx 0.045 - 0.058$  were accomplished. Doping (Al³+, Nb⁵+) into the TiO<sub>6</sub> octahedral sites of CCTO ceramics can greatly reduce  $\tan \delta$  compared to those of the Al³+ or Nb⁵+ single–doped CCTO ceramics. This can also cause great increases in  $R_{gb}$  and  $E_{gb}$  as well as in non–Ohmic properties. The importance of GB properties was demonstrated to control the nonlinear electrical and giant-dielectric properties of CCTO ceramics, supporting the IBLC model of Schottky barriers. We believed the findings of this research can give comprehensive guidance with a simple strategy to achieve usable dielectric properties for practical design of electronic applications.

# References

- [1] M.A. Subramanian, D. Li, N. Duan, B.A. Reisner, A.W. Sleight, High Dielectric Constant in ACu<sub>3</sub>Ti<sub>4</sub>O<sub>12</sub> and ACu<sub>3</sub>Ti<sub>3</sub>FeO<sub>12</sub> Phases, J. Solid State Chem. 151(2) (2000) 323-325.
- [2] Y. Shi, W. Hao, H. Wu, L. Sun, E. Cao, Y. Zhang, H. Peng, High dielectric-permittivity properties of NaCu<sub>3</sub>Ti<sub>3</sub>Sb<sub>0.5</sub>Nb<sub>0.5</sub>O<sub>12</sub> ceramics, Ceram. Int. 42(1, Part A) (2016) 116-121.
- [3] A. Nautiyal, C. Autret, C. Honstettre, S. De Almeida-Didry, M. El Amrani, S. Roger, B. Negulescu, A. Ruyter, Local analysis of the grain and grain boundary contributions to the bulk dielectric properties of  $Ca(Cu_{3-y}Mg_y)Ti_4O_{12}$  ceramics: Importance of the potential barrier at the grain boundary, J. Eur. Ceram. Soc. 36(6) (2016) 1391-1398.
- [4] L. Singh, B.C. Sin, I.W. Kim, K.D. Mandal, H. Chung, Y. Lee, J. Varela, A Novel One-Step Flame Synthesis Method for Tungsten-Doped CCTO, J. Am. Ceram. Soc. 99(1) (2016) 27-34.
- [5] R. Löhnert, H. Bartsch, R. Schmidt, B. Capraro, J. Töpfer, A. Feteira, Microstructure and Electric Properties of CaCu<sub>3</sub>Ti<sub>4</sub>O<sub>12</sub> Multilayer Capacitors, J. Am. Ceram. Soc. 98(1) (2015) 141-147.
- [6] J. Li, P. Liang, J. Yi, X. Chao, Z. Yang, Phase Formation and Enhanced Dielectric Response of  $Y_{2/3}Cu_3Ti_4O_{12}$  Ceramics Derived from the Sol–Gel Process, J. Am. Ceram. Soc. 98(3) (2015) 795-803.
- [7] P. Kum-onsa, P. Thongbai, B. Putasaeng, T. Yamwong, S. Maensiri,  $Na_{1/3}Ca_{1/3}Bi_{1/3}Cu_3Ti_4O_{12}$ : A new giant dielectric perovskite ceramic in  $ACu_3Ti_4O_{12}$  compounds, J. Eur. Ceram. Soc. 35(5) (2015) 1441-1447.

- [8] J. Boonlakhorn, P. Kidkhunthod, P. Thongbai, A novel approach to achieve high dielectric permittivity and low loss tangent in  $CaCu_3Ti_4O_{12}$  ceramics by co-doping with  $Sm^{3+}$  and  $Mg^{2+}$  ions, J. Eur. Ceram. Soc. 35(13) (2015) 3521-3528.
- [9] Q. Zheng, H. Fan, C. Long, Microstructures and electrical responses of pure and chromium-doped CaCu<sub>3</sub>Ti<sub>4</sub>O<sub>12</sub> ceramics, J. Alloys Compd. 511(1) (2012) 90-94.
- [10] X.W. Wang, P.B. Jia, X.E. Wang, B.H. Zhang, L.Y. Sun, Q.B. Liu, Calcining temperature dependence on structure and dielectric properties of CaCu<sub>3</sub>Ti<sub>4</sub>O<sub>12</sub> ceramics, J. Mater. Sci.: Mater. Electron. (2016) 1-7.
- [11] S. Wu, P. Liu, Y. Lai, W. Guan, Z. Huang, J. Han, Y. Xiang, W. Yi, Y. Zeng, Effect of Ba<sup>2+</sup> doping on microstructure and electric properties of calcium copper titanate (CaCu<sub>3</sub>Ti<sub>4</sub>O<sub>12</sub>) ceramics, J. Mater. Sci.: Mater. Electron. (2016) 1-6.
- [12] R. Löhnert, B. Capraro, S. Barth, H. Bartsch, J. Müller, J. Töpfer, Integration of CaCu<sub>3</sub>Ti<sub>4</sub>O<sub>12</sub> capacitors into LTCC multilayer modules, J. Eur. Ceram. Soc. 35(11) (2015) 3043-3049.
- [13] W. Wan, C. Liu, H. Sun, Z. Luo, W.-X. Yuan, H. Wu, T. Qiu, Low-toxic gelcasting of giant dielectric-constant  $CaCu_3Ti_4O_{12}$  ceramics from the molten salt powder, J. Eur. Ceram. Soc. 35(13) (2015) 3529-3534.
- [14] J.Q. Wang, X. Huang, X.H. Zheng, D.P. Tang, Structure and electric properties of  $CaCu_3Ti_4O_{12}$  ceramics prepared by rapid sintering, J. Mater. Sci.: Mater. Electron. 27(2) (2016) 1345-1349.
- [15] M. Ahmad, H. Mahfoz Kotb, Giant dielectric properties of fine-grained  $Na_{1/2}Y_{1/2}Cu_3Ti_4O_{12}$  ceramics prepared by mechanosynthesis and spark plasma sintering, J. Mater. Sci.: Mater. Electron. 26(11) (2015) 8939-8948.
- [16] M.F. Ab Rahman, S.D. Hutagalung, Z.A. Ahmad, M.F. Ain, J.J. Mohamed, The effect of different dopant site (Cu and Ca) by magnesium on CaCu<sub>3</sub>Ti<sub>4</sub>O<sub>12</sub> dielectric properties, J. Mater. Sci.: Mater. Electron. 26(6) (2015) 3947-3956.
- [17] J. Jumpatam, P. Thongbai, T. Yamwong, S. Maensiri, Effects of Bi<sup>3+</sup> doping on microstructure and dielectric properties of CaCu<sub>3</sub>Ti<sub>4</sub>O<sub>12</sub>/CaTiO<sub>3</sub> composite ceramics, Ceram. Int. 41, Supplement 1 (2015) S498-S503.
- [18] Z. Wang, M. Cao, Q. Zhang, H. Hao, Z. Yao, Z. Wang, Z. Song, Y. Zhang, W. Hu, H. Liu, Dielectric Relaxation in Zr-Doped SrTiO<sub>3</sub> Ceramics Sintered in N<sub>2</sub> with Giant Permittivity and Low Dielectric Loss, J. Am. Ceram. Soc. 98(2) (2015) 476-482.
- [19] X.Q. Liu, G. Liu, P.P. Ma, G.J. Li, J.W. Wu, X.M. Chen, Giant dielectric response with reduced loss in ceramics with nominal composition of  $La_{1.5}S_{r0.5}NiO_4$ -SiO<sub>2</sub>, Journal of Electroceramics (2016).
- [20] G.-Z. Zang, H.-H. Liu, J.-F. Lei, X.-F. Wang, L.-B. Li, J.-X. Cao, G.-R. Li, Origin of the High Permittivity and Varistor Behavior in  $SnO_2$ – $Zn_2SnO_4$  Composite Ceramics, J. Am. Ceram. Soc. 98(7) (2015) 2112-2116.
- [21] M. Zheng, Y. Hou, X. Fan, M. Zhu, Novel Core—Shell Nanostructure in Percolative PZN-PZT/Ag Ferroelectric Composites, J. Am. Ceram. Soc. 98(2) (2015) 543-550.

= Ba, Sr, and Ca) pe

- [22] S. Ke, H. Fan, H. Huang, Dielectric relaxation in A<sub>2</sub>FeNbO<sub>6</sub> (A ceramics, Journal of Electroceramics 22(1-3) (2007) 252-256.
- [23] T. Adams, D. Sinclair, A. West, Characterization of grain boundary impedances in fine- and coarse-grained  $CaCu_3Ti_4O_{12}$  ceramics, Phys. Rev. B 73(9) (2006) 094124.
- [24] C.C. Wang, L.W. Zhang, Surface-layer effect in  $CaCu_3Ti_4O_{12}$ , Appl. Phys. Lett. 88(4) (2006) 042906.

- [25] P. Lunkenheimer, R. Fichtl, S. Ebbinghaus, A. Loidl, Nonintrinsic origin of the colossal dielectric constants in CaCu<sub>3</sub>Ti<sub>4</sub>O<sub>12</sub>, Phys. Rev. B 70(17) (2004) 172102.
- [26] W. Hu, Y. Liu, R.L. Withers, T.J. Frankcombe, L. Norén, A. Snashall, M. Kitchin, P. Smith, B. Gong, H. Chen, J. Schiemer, F. Brink, J. Wong-Leung, Electron-pinned defect-dipoles for high-performance colossal permittivity materials, Nat. Mater. 12(9) (2013) 821-826.
- [27] J. Li, F. Li, C. Li, G. Yang, Z. Xu, S. Zhang, Evidences of grain boundary capacitance effect on the colossal dielectric permittivity in (Nb + In) co-doped TiO<sub>2</sub> ceramics, Sci Rep 5 (2015) 8295.
- [28] W. Tuichai, N. Thongyong, S. Danwittayakul, N. Chanlek, P. Srepusharawoot, P. Thongbai, S. Maensiri, Very low dielectric loss and giant dielectric response with excellent temperature stability of Ga<sup>3+</sup> and Ta<sup>5+</sup> co-doped rutile-TiO<sub>2</sub> ceramics, Materials & Design 123 (2017) 15-23.
- [29] G. Liu, H. Fan, J. Xu, Z. Liu, Y. Zhao, Colossal permittivity and impedance analysis of niobium and aluminum co-doped TiO<sub>2</sub> ceramics, RSC Advances 6(54) (2016) 48708-48714.
- [30] C. Yang, M.-Y. Tse, X. Wei, j. hao, Colossal permittivity of (Mg+Nb) co-doped TiO<sub>2</sub> ceramics with low dielectric loss, Journal of Materials Chemistry C 10.1039/C7TC01020F (2017).
- [31] Y. Song, X. Wang, X. Zhang, X. Qi, Z. Liu, L. Zhang, Y. Zhang, Y. Wang, Y. Sui, B. Song, Colossal dielectric permittivity in (Al -dolble) cotile SnO<sub>2</sub> ceramics with low loss at room temperature, Appl. Phys. Lett. 109(14) (2016) 142903.
- [32] J. Jumpatam, W. Somphan, B. Putasaeng, N. Chanlek, P. Kidkhunthod, P. Thongbai, S. Maensiri, Nonlinear electrical properties and giant dielectric response in  $Na_{1/3}Ca_{1/3}Y_{1/3}Cu_3Ti_4O_{12}$  ceramic, Mater. Res. Bull. 90 (2017) 8-14.
- [33] L. Sun, R. Zhang, Z. Wang, E. Cao, Y. Zhang, L. Ju, Microstructure, dielectric properties and impedance spectroscopy of Ni doped CaCu<sub>3</sub>Ti<sub>4</sub>O<sub>12</sub> ceramics, RSC Advances 6(61) (2016) 55984-55989.
- [34] L. Sun, Z. Wang, W. Hao, E. Cao, Y. Zhang, H. Peng, Influence of Zirconium doping on microstructure and dielectric properties of CaCu<sub>3</sub>Ti<sub>4</sub>O<sub>12</sub> synthesized by the sol–gel method, J. Alloys Compd. 651 (2015) 283-289.
- [35] L. Sun, R. Zhang, Z. Wang, E. Cao, Y. Zhang, L. Ju, Microstructure and enhanced dielectric response in Mg doped CaCu<sub>3</sub>Ti<sub>4</sub>O<sub>12</sub> ceramics, J. Alloys Compd. 663 (2016) 345-350.
- [36] S.-H. Hong, D.-Y. Kim, H.-M. Park, Y.-M. Kim, Electric and Dielectric Properties of Nb-Doped CaCu<sub>3</sub>Ti<sub>4</sub>O<sub>12</sub> Ceramics, J. Am. Ceram. Soc. 90(7) (2007) 2118-2121.
- [37] P. Thongbai, J. Jumpatam, T. Yamwong, S. Maensiri, Effects of Ta<sup>5+</sup> doping on microstructure evolution, dielectric properties and electrical response in CaCu<sub>3</sub>Ti<sub>4</sub>O<sub>12</sub> ceramics, J. Eur. Ceram. Soc. 32(10) (2012) 2423-2430.
- [38] M.F.A. Rahman, M.J. Abu, S.A. Karim, R.A. Zaman, M.F. Ain, Z.A. Ahmad, J.J. Mohamed, Microwave dielectric properties of CaCu<sub>3</sub>Ti<sub>4</sub>O<sub>12</sub>-Al<sub>2</sub>O<sub>3</sub> composite, AIP Conf. Proc. 1756(1) (2016) 020007.
- [39] J. Boonlakhorn, P. Thongbai, Effect of Annealing in O<sub>2</sub> and Mechanisms Contributing to the Overall Loss Tangent of CaCu<sub>3</sub>Ti<sub>4</sub>O<sub>12</sub> Ceramics, J. Electron. Mater. 44(10) (2015) 3687-3695.
- [40] A.J. Moulson, J.M. Herbert, Electroceramics: materials, properties, applications, 2nd ed., Wiley, West Sussex; New York, 2003.
- [41] S.-Y. Chung, J.-H. Choi, J.-K. Choi, Tunable current-voltage characteristics in polycrystalline calcium copper titanate, Appl. Phys. Lett. 91(9) (2007) 091912.
- [42] S.-Y. Chung, S.-I. Lee, J.-H. Choi, S.-Y. Choi, Initial cation stoichiometry and current-voltage behavior in Sc-doped calcium copper titanate, Appl. Phys. Lett. 89(19) (2006) 191907.

## CHAPTER 1

Investigation on Temperature Stability Performance of Giant Permittivity (In+Nb) in Co-doped TiO<sub>2</sub> Ceramic: A Crucial Aspect for Practical Electronic Applications

# 1.1 Introduction

Recently, a large number of giant-dielectric materials with very high dielectric permittivities ( $\varepsilon' > 10^3$ ) have been discovered. They are considered potentially useful in electronic applications such as capacitors and memory devices or in high energy-dense storage applications. These giant-dielectric materials are derived from CaCu<sub>3</sub>Ti<sub>4</sub>O<sub>12</sub> and related compounds, 1-3 Ln<sub>2-x</sub>Sr<sub>x</sub>NiO<sub>4</sub> (Ln = Nd, La, Sm), 4-7 NiO-based oxides, 8  $AFe_{1/2}B_{1/2}O_3$  (A=Ba, Sr, Ca; B=Nb, Ta, Sb), 9, 10 LuFe<sub>2</sub>O<sub>4</sub>, 11 as well as BaTiO<sub>3</sub>/Ni composite materials. 12 Unfortunately, the tanδ values of these materials are usually larger than 0.1 in a low frequency range, which are higher than the standard values for capacitor applications. This is a significant impediment to practical electronic applications using these materials. To the best of our knowledge, the temperature stability of  $\varepsilon'$  ( $\Delta \varepsilon' / \varepsilon'_{RT}$  (%)) or temperature coefficient of capacitance ( $\Delta C/C_{RT}$  (%)) of these giant dielectric materials is more a difficult problem to solve. 13-15 Large increases in  $\varepsilon'$  (at 1 kHz) at high temperatures are usually due to DC conduction in the materials and the electrical response of grain boundaries. This is one of the most important parameters used for developing dielectric materials for practical applications in electronic devices. For example, in X7R capacitors,  $\Delta \varepsilon'/\varepsilon'_{RT}$  of a dielectric material used must be less than  $\pm 15\%$ over the temperature range of -55 to 125 °C. 16

Most recently, Hu *et al.*  $(2013)^{17}$  reported excellent dielectric properties in a (In+Nb) co–doped rutile–TiO<sub>2</sub> (IN-T) ceramic system. A  $(In_{0.5}Nb_{0.5})_xTi_{1-x}O_2$  ceramic with x=0.1, exhibited a very low  $tan\delta\approx0.02$  and an especially high  $\epsilon'\sim6\times10^4$  that was frequency independent over the range of  $10^2-10^6$  Hz. Notably,  $\epsilon'$  was independent of temperature over a wide temperature range of 80–450 K (-193–177 °C). This excellent dielectric performance was attributed to deliberately introduce large defect–dipole clusters containing highly localized electrons. Using this novel and elegant model, the complex stoichiometry of  $(In_x^{3+}Nb_x^{5+}Ti_x^{3+})Ti_{1-3x}^{4+}O_{2-x/2}$  produced defect clusters, in which the electrons created by  $Nb^{5+}$  doping ions resulting in the reduction of  $Ti^{4+}$  to  $Ti^{3+}$  are contained by the presence of  $In^{3+}$ . Without  $In^{3+}$ , electrons would be delocalized and lead to high DC conductivity and  $tan\delta$  values. In the other words, this excellent dielectric performance in IN-T ceramics can be created by engineering the local structure within the rutile– $TiO_2$  structure.

Generally, the existence of dielectric relaxation in any temperature range is usually accompanied by a rapid change in  $\epsilon'$  and the appearance of a strong  $\tan\delta$  peak. Although the relaxation phenomena in a dielectric can give some important clues to clarify the origin of the dielectric response,  $\epsilon^{7,-10,-11,-17,-20-22}$  it may be undesirable for practical applications due to the resulting large changes in dielectric properties. In pioneering work,  $\epsilon^{17}$  two primary dielectric relaxations were observed in IN–T ceramics. The main dielectric relaxation was due to freezing electrons in defect–dipoles. This resulted in a giant  $\epsilon'$  that was observed in the temperature range of 10–40 K with activation energies of 0.015–0.02 eV. Another relaxation caused by an extrinsic effect was observed in the

range of 450–720 K.<sup>17</sup> Thus, a  $\varepsilon'$  plateau between these two relaxations should be independent of temperature from 50 to 450 K if no other dielectric relaxation occurs between these two relaxations. However, a set of small  $\tan\delta$ –peaks ( $\approx$ 240–360 K) likely appeared in the loss spectra of 10%IN–T (Fig. 2(a) of Ref. <sup>17</sup>). This might be another relaxation that occurred at an ambient RT. Although the maximum  $\tan\delta$  value at the relaxation peak was kept low (<0.02),<sup>17</sup> the  $\varepsilon'$  values in the vicinity of this relaxation might be greatly changed, giving rise to a large value of  $\Delta\varepsilon'/\varepsilon'_{RT}$ (%). The appearance of this ambient RT–relaxation was further confirmed by Zhao *et al.*<sup>20</sup> This dielectric relaxation (DR3 in Fig. 3(a) of Ref. <sup>20</sup>) was clearly observed in the temperature range of 200–280 K for 5%IN–T.

It is very important to investigate the effect of such ambient RT-dielectric relaxations on the temperature–stability of IN–T ceramics because of the great importance for this parameter for practical applications in electronic devices. To the best our knowledge, the exact values of  $\Delta\epsilon'/\epsilon'_{RT}$  of IN–T ceramics and other co–doped TiO $_2$  systems have never been reported and discussed from this point of view. Thus, the aim of this work is to study the temperature dependent behavior of IN–T ceramics at two very different dopant levels. This will allow study of the influence of ambient–RT dielectric relaxation on the dielectric properties over a standard temperature range for capacitor applications. We found that substitution of (In+Nb) co–doping ions into TiO $_2$  at a high concentration can greatly enhance  $\epsilon'$  and while successfully achieving a low tan $\delta$  value. However, its temperature stability below RT was simultaneously worsened. By reducing the co–dopant concentration, excellent  $\epsilon'$  temperature stability was accomplished.

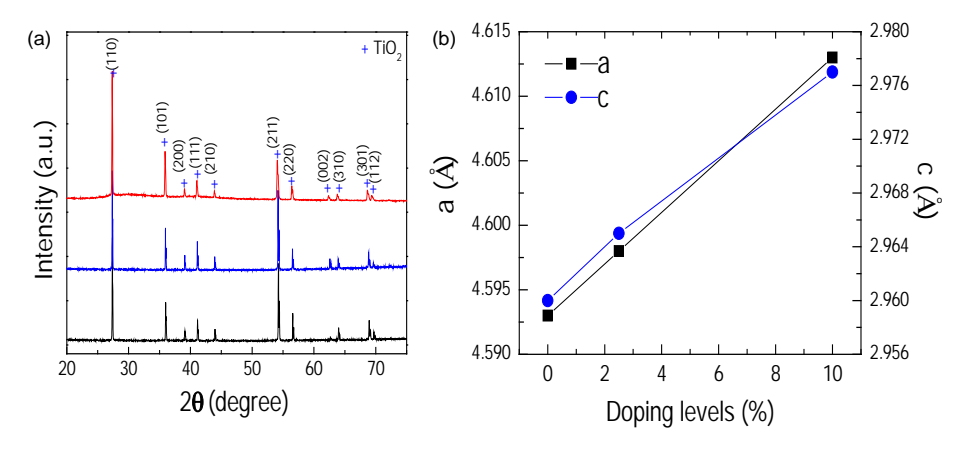
# 1.2 Experimental details

 $(In_{0.5}Nb_{0.5})_xTi_{1-x}O_2$  ceramics with x=0, 0.025, and 0.10 were prepared using a solid state reaction (SSR) method. This ceramics were referenced as 0%IN–T, 2.5%IN–T, and 10%IN–T samples, respectively.  $TiO_2$  (Sigma–Aldrich, >99.9% purity),  $Nb_2O_5$  (Sigma–Aldrich, 99.99% purity), and  $In_2O_3$  (Sigma–Aldrich, 99.99% purity) were used as the starting raw materials. First, a stoichiometric mixture of the starting materials was ball–milled in ethanol for 24 h using  $\approx$ 2.0 mm diameter  $ZrO_2$  balls. The mixed powder was ground and pressed into pellets (without a binder) of 9.5 mm in diameter and  $\approx$ 1.2 mm in thickness by uniaxial compression at  $\approx$ 200 MPa. Finally, these pellets were sintered at different temperatures (1400–1550  $^{\circ}$ C) for 1–10 h.

X–ray diffraction (XRD; Bruker, D 2phaser) was used to characterize the phase composition and crystal structures of the sintered IN–T ceramics. The microstructure and elemental distribution in the TINO ceramic were examined using a field–emission scanning electron microscopy (FE–SEM) with energy-dispersive X–ray analysis (EDX) (HITACHI SU8030, Japan). Before electrical measurements, Au was sputtered onto each pellet face at a current of 25 mA for 8 min using a Polaron SC500 sputter coating unit (Sussex, UK). The capacitance and dispassion factor (D or  $\tan\delta$ ) of the ceramic samples were measured using an Agilent 4294A Precision Impedance Analyzer over the frequency and temperature ranges of  $10^2$ – $10^6$  Hz and -70–220 °C, respectively.

#### 1.3 Results and discussion

Fig. 1(a) shows the XRD patterns of all sintered IN–T ceramics. A main phase of rutile–TiO $_2$  (JCPDS 21–1276) was observed in all samples with no impurity phase. The diffraction peaks in all XRD patterns were perfectly indexed based on a tetragonal structure. Lattice parameters were calculated from the diffraction peaks and found to be a=4.593 Å and c=2.960 Å, a=4.598 Å and c=2.965Å, and a=4.613 Å and c=2.977 Å for the 0%IN–T, 2.5%IN–T, and 10%IN–T samples, respectively. As shown in Fig. 1(b), both the a and c parameters increased with increasing co–dopant concentration. The a and c values of the 0%IN–T sample were nearly the same as the sample in values for retile–TiO $_2$  (JCPDS 21–1276) with a=4.593 Å and c=2.959 Å. It is important to note that a and c values of the 10%IN–T sample were very close to the values reported by Hu et a1.17 with a≈4.615 Å and c≈2.980 Å for 10% (In+Nb) co–doped TiO $_2$  ceramic (see Fig. S7 of Supplementary information of Ref. 17). The enlarged lattice parameters are likely due to the larger ionic radii of In<sup>3+</sup> and Nb<sup>5+</sup> over that of Ti<sup>4+</sup>. This clearly indicates that both In<sup>3+</sup> and Nb<sup>5+</sup> doping ions can be substituted into the rutile–TiO $_2$  structure.



(a) XRD pattern of (In<sub>0.5</sub>Nb<sub>0.5</sub>)<sub>x</sub>Ti<sub>1-x</sub>O<sub>2</sub> ceramics with x=0, 0.025, and 0.10.
 (b) Variation of lattice parameters of (In<sub>0.5</sub>Nb<sub>0.5</sub>)<sub>x</sub>Ti<sub>1-x</sub>O<sub>2</sub> ceramics with co-dopant concentration (x).

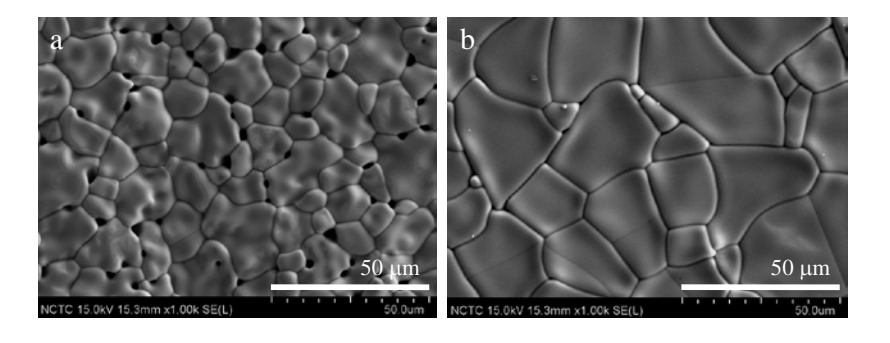


**Fig. 2** SEM images of surface morphologies of  $(In_{0.5}Nb_{0.5})_xTi_{1-x}O_2$  ceramics with (a) x=0.10 and (b) x=0.025.

Fig. 2 shows the microstructure of the 10%IN-T and 2.5%IN-T samples. It was found that the grain size of IN-T ceramics decreased with increasing co-dopant concentration. The estimated grain sizes of the 0%IN-T, 2.5%IN-T, and 10%IN-T

samples were of  $\approx 50-100$ ,  $\approx 25-50$ , and  $\approx 10-20~\mu m$ , respectively. This indicates that the grain growth rate of TiO<sub>2</sub> was inhibited by In<sup>3+</sup> and Nb<sup>5+</sup> dopant ions. Furthermore, residual pores were only observed in the microstructure of the 10%IN–T sample. These pores were homogeneously distributed throughout the microstructure and appeared at the grain boundaries and triple junctions between grains, indicating normal grain growth characteristic. Note that, the abnormal grain growth was not observed in all the samples.

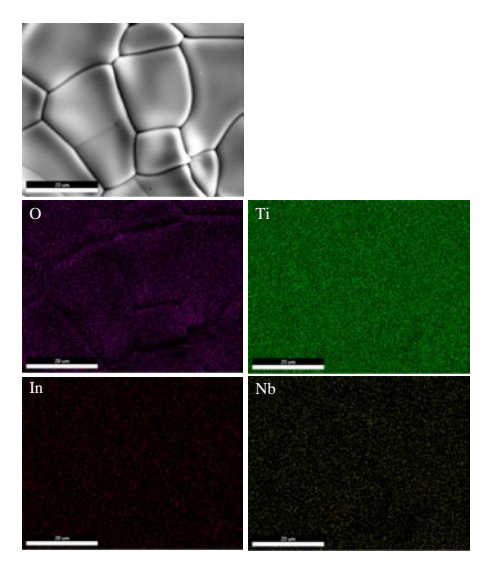


**Fig. 3** Element mapping of the  $(In_{0.5}Nb_{0.5})_xTi_{1-x}O_2$  ceramic with x=0.025 sintered at 1550 °C for 1 h.

Usually, inhomogeneous distribution of dopants is one of the most common factors that result in abnormal grain growth.<sup>28</sup> Thus, it is likely that both In<sup>3+</sup> and Nb<sup>5+</sup> doping ions were homogeneously distributed in the TiO<sub>2</sub>. To further analyze the distributions of the elements in co–doped TiO<sub>2</sub> ceramics, mapping of all elements, *i.e.*, Ti, O, In, and Nb, was performed. As shown in Fig. 3, the dopants were homogeneously dispersed in both the grain and grain boundary of the 2.5%IN–T sample. This was similar to that observed in the 10%IN–T sample. Segregation of In<sup>3+</sup> and Nb<sup>5+</sup> ions at any specific region, such as grain boundaries, was not observed.

It was clearly demonstrated that high– $\epsilon'$  with low–tan $\delta$  values in co–doped TiO $_2$  will be achieved only if two types of defects caused by In $^{3+}$  and Nb $^{5+}$  dopants overlapped or were separated by less than 5 Å. $^{17, 18}$  From the microstructural analysis, the distribution of In $^{3+}$  and Nb $^{5+}$  dopants was very homogenous at the microscopic level. However, the overlap of defect dipoles cannot be completely confirmed. The existence of strongly correlated defect dipoles that give rise to the high–dielectric performance of IN–T ceramics is likely justified by considering their apparent dielectric parameters. As shown in Fig. 4(a) and its inset, the 10%IN–T sample exhibited a high– $\epsilon'$ , on the order of  $10^4$ – $10^5$ , with a low–frequency tan $\delta$  value <0.1. At  $10^2$  Hz and 30 °C,  $\epsilon'$  and tan $\delta$  values were about  $5.1\times10^4$  and 0.03, respectively, confirming strongly correlated defect dipoles. It is notable that these values are comparable to  $\epsilon'\approx6.1\times10^4$  and tan $\delta\approx0.02$  for the 10%IN–T ceramic reported. Slight differences in  $\epsilon'$  and tan $\delta$  values may have been due to different sintering conditions, which was demonstrated by Li *et al.*<sup>26</sup> In the temperature range from -60 to 150 °C,  $\epsilon'$  was very slightly dependent on frequency between  $10^2$ – $10^6$  Hz. The dielectric relaxation, which is usually characterized by a steplike decrease in  $\epsilon'$ , was not

observed in these dielectric spectra. In the inset of Fig. 4(a), broad  $\tan\delta$  peaks were observed in the temperature range of -30 to 30 °C, signifying that dielectric relaxation occurred. As is clearly illustrated in Fig. 4(b), steplike decreases in  $\epsilon$ ′ and  $\tan\delta$  peaks were simultaneously observed in the temperature range from -60 to 50 °C for the 10%IN–T sample sintered at 1500 °C for 5 h. The existence of this ambient RT dielectric relaxation is consistent with both the 5% and 10%IN–T ceramics sintered at 1400 °C for 10 h.<sup>17, 20</sup>

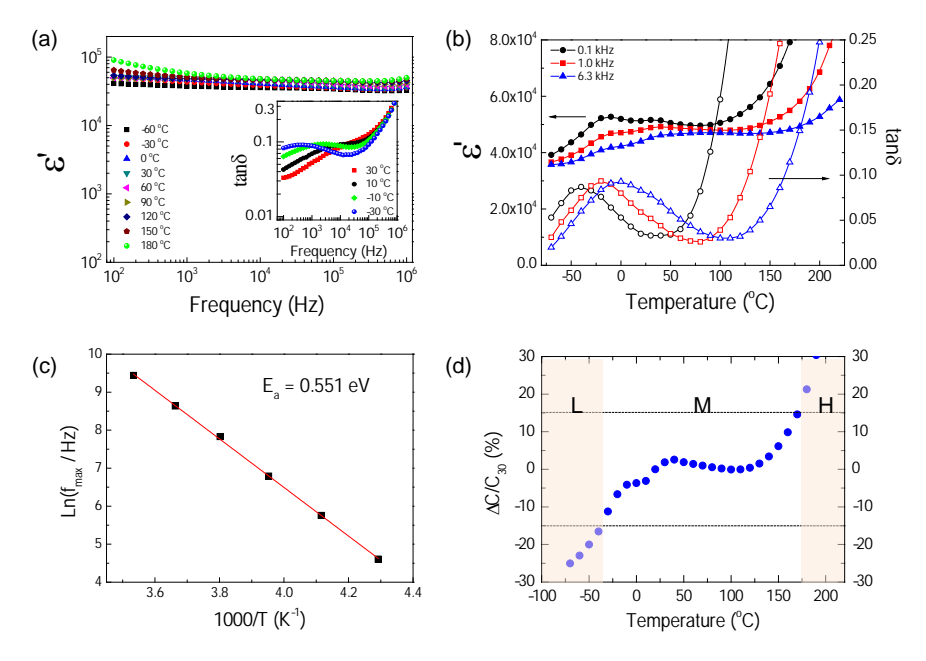


**Fig. 4** (a) Frequency dependence of ε' at various temperatures ranging from -60 to 180 °C for the  $(In_{0.5}Nb_{0.5})_xTi_{1-x}O_2$  ceramic with x=0.1; inset shows tanδ at different temperatures. (b) Temperature dependence of ε' and tanδ at various frequencies for the  $(In_{0.5}Nb_{0.5})_xTi_{1-x}O_2$  ceramic with x=0.1. (c) Arrhenius plot of  $f_{max}$  for dielectric relaxation in (a) and (b). (d) Temperature coefficient of capacitance value at 1 kHz of the  $(In_{0.5}Nb_{0.5})_xTi_{1-x}O_2$  ceramic with x=0.1.

It was found that the temperature dependence of the frequency at which the  $tan\delta$  peak appeared ( $f_{max}$ ) follows the Arrhenius equation:

$$f_{\text{max}} = f_0 \exp(-E_a / k_B T) , \qquad (1)$$

where  $f_0$  is the pre–factor,  $E_a$  is the activation energy required for the relaxation process,  $k_B$  is the Boltzmann constant, and T is absolute temperature. As shown in Fig. 4(c), a good linear fit was achieved. This result indicates a non–polaron type relaxation due to a hopping motion of localized carriers.  $^{17,\ 21}$   $E_a$  was calculated from the slope of the fitted line and found to be 0.551 eV for the 10%IN–T sample. In Fig 4(b),  $\epsilon'$  of the 10%IN–T sample rapidly decreased at temperatures under 0 °C, while  $\epsilon'$  was still too large ( $\approx$ 4×10<sup>4</sup>). This resulted in a very large temperature coefficient that is undesirable for electronic applications, especially X–R type capacitors. As shown in Fig. 4(d), large values of the temperature coefficient in high and low temperature ranges (zones H and L, respectively) were clearly caused by R<sub>H</sub> and R<sub>M</sub>, respectively. The condition,  $\Delta$ C/C<sub>RT</sub> < ±15%, of the 10%IN–T sample was only achieved in the temperature range of -30 to 170 °C (zone M).

Despite measurements over a limited temperature range (-70–220  $^{\circ}$ C) in the current study, it is likely that there are at least three temperature regions in which dielectric relaxations occurred in the IN–T ceramic system: low (<-70  $^{\circ}$ C), middle (an ambient RT, -60 to 50  $^{\circ}$ C), and high–temperature (>170  $^{\circ}$ C). The dielectric relaxations that occurred in these ranges are hereafter referred to as R<sub>L</sub>, R<sub>M</sub>, and R<sub>H</sub>, respectively. To study dielectric relaxations in IN–T ceramics, the complex electric modulus (M\*) was calculated from the complex dielectric permittivity ( $\epsilon$ \*) as follows:

$$M^* = M' + jM'' = 1/\epsilon^* = 1/(\epsilon' - j\epsilon''), \tag{2}$$

where M' and M'' are the real and imaginary parts of M\*.  $\varepsilon'$  and  $\varepsilon''$  are the real (dielectric permittivity) and imaginary parts of  $\varepsilon^*$ . The frequency dependence of M" at various temperatures was investigated. At -20 °C [Fig. 5(a)], for the 10%IN-T sample, only one M" peak was observed at ≈10<sup>3</sup> Hz. A tail (a drastic increase in M") in the high frequency range may signify another M" peak corresponding to a low temperature dielectric response. However, this M" peak could not be observed even at the lowest measurement temperature (-70 °C). This is not surprising, as reported by Zhao et al.20, two low-temperature dielectric relaxations occurred in the case of 5%IN-T in the temperature range of 10-180 K (-260 to -93 °C). These two relaxations were also observed in the 0.5% (Ga+Nb) co-doped TiO<sub>2</sub> ceramic in the same temperature range.<sup>29</sup> Nevertheless, these low-temperature relaxations, R<sub>1</sub>, are beyond the scope of the current study. At 20 °C [Fig. 5(b)], the apparent M" peak shifted to a higher frequency. This set of relaxation peaks of M" is very consistent with the tanδ peaks of the ambient RT dielectric relaxation [inset of Fig. 4(a)]. As demonstrated in Fig. 6(a), the frequencies at which M" and tanδ peaks appeared at 0 °C are nearly in the same in position. This relaxation peak of M" was clearly identified as R<sub>M</sub>.

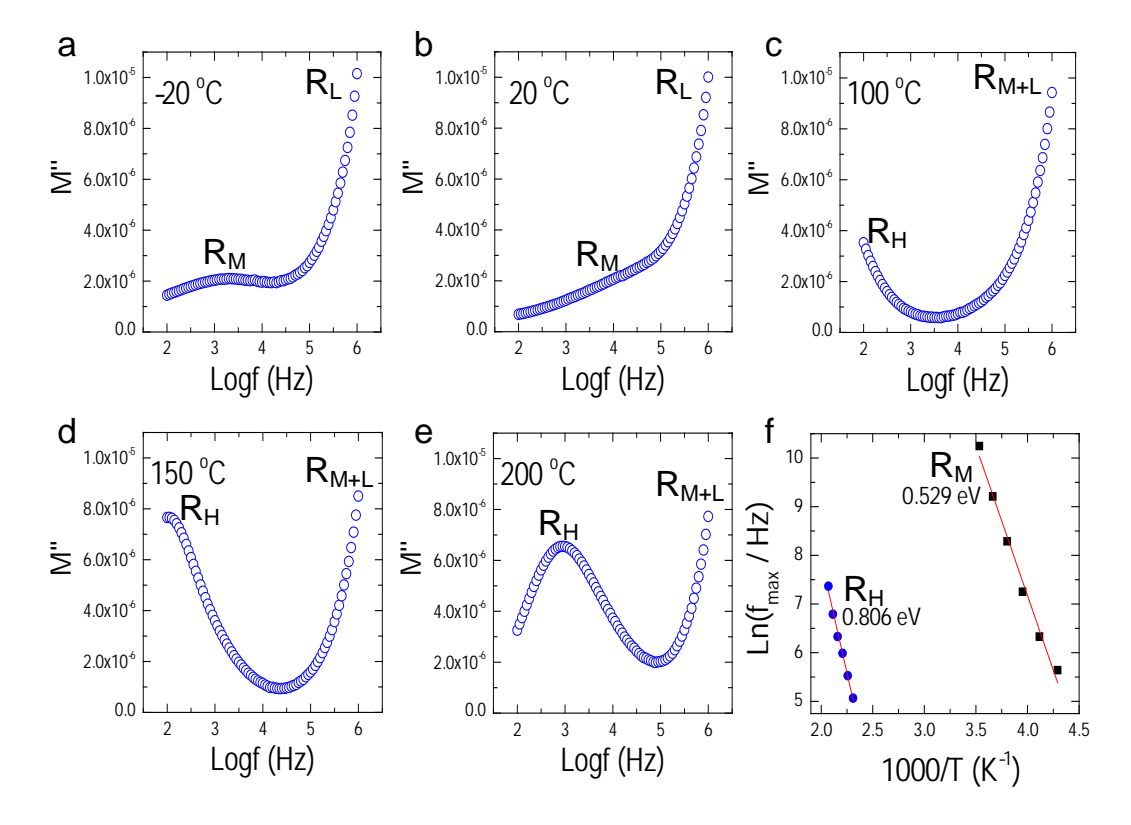
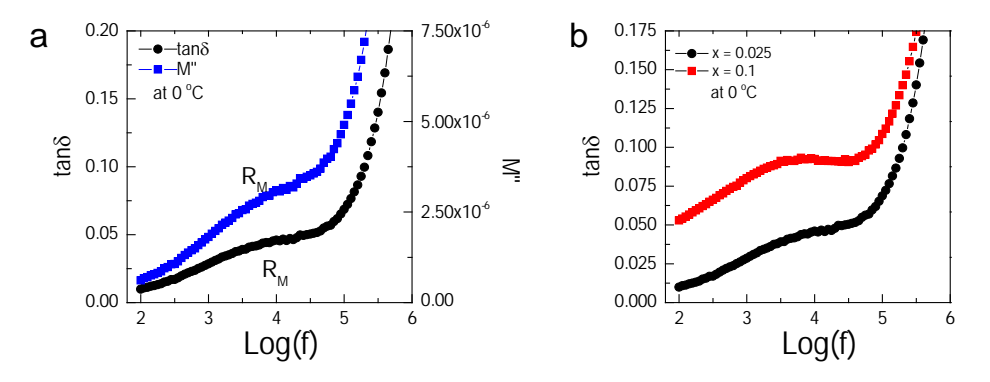


Fig. 5 (a–e) M" plots vs. of frequency at different temperatures. (f) Arrhenius plots for  $R_H$  and  $R_M$ .

When the temperature was increased to 100  $^{\circ}$ C [Fig. 5(c)], no peak was observed. A tail in the low frequency range began to appear, which might have been R<sub>H</sub>. M" relaxation peaks appeared in a high temperature range (150–200  $^{\circ}$ C), as shown in Figs. 5(d)–(e). The M" peak of R<sub>H</sub> shifted to a high frequency as temperature was increased. The existence of R<sub>H</sub> is reported in literature.<sup>17</sup> In the current study, only M" peaks of R<sub>M</sub> and R<sub>H</sub> were observed in the 10%IN–T sample. The temperature dependences of these M" peaks follow the Arrhenius equation, as is shown in Fig. 5(f). The relaxation activation energies for R<sub>M</sub> and R<sub>H</sub> of the 10%IN–T sample were, respectively, about 0.529 and 0.806 eV. It is observed that the activation energies of R<sub>M</sub> obtained from tan $^{\circ}$  and M" were very close.

Considering  $R_M$  of the 10%IN–T sample, an application of this  $TiO_2$ –based material system in electronic devices might be difficult due to the temperature instability of  $\epsilon'$  in the vicinity of  $R_M$ . As shown in Fig. 6(b),  $R_M$ , which was indicated by a  $tan\delta$  peak, was also observed in the 2.5%IN–T sample. The  $tan\delta$  peak intensity and  $tan\delta$  values over the measured frequency range of the 2.5%IN–T sample were lower than those of the 10%IN–T sample. In the point of view of application, these impressive dielectric properties (i.e., low  $tan\delta$  and frequency–independent  $high-\epsilon'$ ) of the IN–T material system are of little value if this problem with  $R_M$  cannot be resolved.



**Fig. 6** (a) Frequency dependence of  $\tan\delta$  and M" at 0 °C for 2.5% IN–T. (b) Frequency dependence of  $\tan\delta$  at 0 °C for 2.5% IN–T and 10% IN–T ceramics.

The temperature–dependence of  $\epsilon'$  for 2.5% and 10%IN–T samples with significantly different dopant contents was determined. In Fig. 7(a),  $\epsilon'$  values of both samples seem to be independent of temperature over the range of -70 to 200 °C. However, careful inspection of the inset of Fig. 7(a) revealed large variations in  $\epsilon'$  for both samples as temperature was increased to more than 180 °C (>450 K). It is still impressive that  $\epsilon'$  greater than 10<sup>4</sup> with temperature independence to 180 °C is a notable achievement. In contrast to the 10%IN–T sample, the  $\epsilon'$  value of the 2.5%IN–T sample in a low temperature range was very slightly dependent on temperature. Notably, it was found that  $\epsilon'$  and tan $\delta$  of the 2.5%IN–T sample (at 30 °C and 10<sup>2</sup> Hz) were, respectively,  $\approx$ 1.57×10<sup>4</sup> and  $\approx$ 0.006. This extremely low tan $\delta$  value is especially impressive when compared to

higher dopant content IN-T ceramics<sup>17, 20</sup> or other co-doped TiO<sub>2</sub> systems<sup>23, 25, 29</sup> as well as giant dielectric materials.<sup>1, 8</sup>

As seen in Fig. 7(b), the temperature coefficient of the 2.5%IN–T sample was as low as  $\pm 7$  over a temperature range from -70 to 180 °C. This is satisfactory for X8R capacitor applications, in which  $\epsilon'$  of dielectric layers must not vary with temperature more than  $\pm 15\%$  at temperatures between -55 and 150 °C. Compared to other X8R–based dielectric materials,  $^{30\text{-}32}$  the more impressive properties of the 2.5%IN–T sample standout due to its much higher  $\epsilon'$  and extremely low tan $\delta$  values.

We now turn to briefly discuss the possible origin of  $R_M$  and  $R_H$  in the IN–T ceramic system to further develop better dielectric materials. The activation energies for  $R_M$  and  $R_H$  of the 10%IN–T sample were calculated and found to be  $\approx 0.529-0.552$  and 0.806 eV, respectively. Unfortunately, activation energy values of the 2.5%IN–T sample could not be calculated since only shoulder of M''relaxation peak was observed. Generally, the movement of oxygen vacancies in metal oxides occur at high temperatures and the required activation energies are generally quite high, e.g., 0.91 eV for BaTiO $_3$  ceramic and 0.84-1.26 eV for un–doped rutile TiO $_2$ . The activation energy of  $R_H$  is comparable to the values for the motion of oxygen vacancies. Thus,  $R_H$  is likely associated with oxygen vacancies. The slightly lower activation energy of the 10%IN–T ample may have been due to a greater number of oxygen vacancies caused by substitution of  $In^{3+}$  ions.

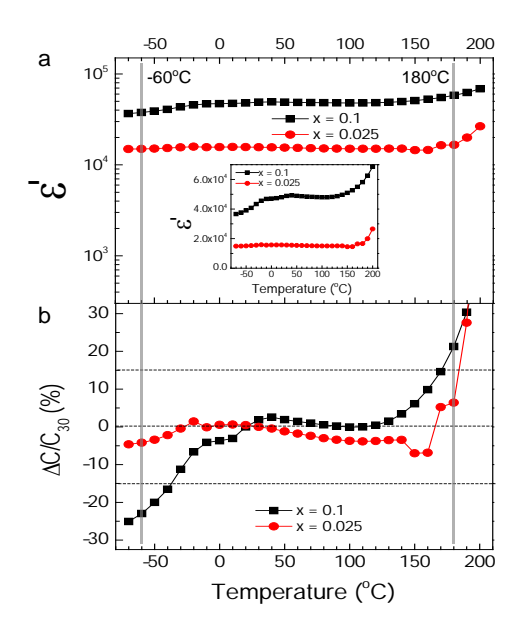


Fig. 7 (a) Temperature dependence of  $\varepsilon'$  at 1 kHz; inset shows  $\varepsilon'$ -temperature plots on a linear scale to clearly reveal the variation of  $\varepsilon'$  over the measured temperature range. (b) Temperature coefficient of capacitance ( $\Delta$ C/C<sub>30</sub>) at 1 kHz for 2.5% IN-T and 10% IN-T ceramics.

The activation energy of  $R_{\rm M}$  was much larger than activation energies of  $\approx 0.015-0.02$  eV for polarization of free electrons in triangular shaped  $In_2^{3+}V_o^{\bullet\bullet}Ti^{3+}$  defect complexes, which was suggested as the primary polarization giving rise to high dielectric performance of IN–T ceramics. Interfacial polarization may be an important factor contributing to  $R_{\rm M}$ . The activation energy of  $R_{\rm M}$  is typically in the range of relaxation activation energy for

electrical responses at the grain boundary, e.g., 0.55-0.6 eV for  $CaCu_3Ti_4O_{12}^{3, 34}$  and 0.439eV for Li and Ti co-doped NiO.<sup>8</sup> Doping Nb<sup>5+</sup> into TiO<sub>2</sub> can generate free electrons by reducing  $Ti^{4+}$  to  $Ti^{3+}$  as follows:

$$2TiO_2 + Nb_2O_5 \xrightarrow{4TiO_2} 2Ti'_{Ti} + 2Nb^{\bullet}_{Ti} + 8O_O + 1/2O_2,$$
 (3)

$$Ti^{4+} + e \rightarrow Ti^{3+}. \tag{4}$$

Substitution of TiO<sub>2</sub> with In<sup>3+</sup> required oxygen vacancies for charge compensation following the relation:

$$In_2O_3 \xrightarrow{2TiO_2} 2In'_{Ti} + V_O^{\bullet \bullet} + 3O_O.$$
 (5)

Accordingly, several point defects were introduced in the rutile structure of co–doped samples. Two special local structures can be formed, triangular  $In_2^{3+}V_0^{\bullet\bullet}Ti^{3+}$  and diamond  $Nb_2^{5+}Ti^{3+}A_{Ti}$  (A=In<sup>3+</sup>, Ti<sup>3+</sup>, or Ti<sup>4+</sup>) shapes.<sup>17, 18</sup> In principle, low  $\tan\delta$  coupled with high  $\epsilon'$  values can be obtained only in the cases of triangular and diamond shaped intrinsic–defect complexes that overlap or are strongly correlated. In practice, complete overlapping of these two local structures is difficult (or perhaps impossible) to accomplished. Non–overlapped (or isolated)  $Nb_2^{5+}Ti^{3+}A_{Ti}$  defect dipoles produce delocalized electrons, which is similar to the case of  $Nb^{5+}$ –doped  $TiO_2$ . Other free electrons are usually generated by oxygen loss during sintering process as follows:<sup>20</sup>

$$O_O^x \to \frac{1}{2}O_2 + V_O^{\bullet \bullet} + 2e'$$
 (6)

Under an applied electric field, hopping electrons are blocked by an insulating grain boundary and/or other internal interfaces, producing an additional interfacial polarization. Thus,  $R_M$  may have originated through interfacial polarization relaxation. With decreasing (In+Nb) co–dopant concentration, the number of delocalized electrons from the  $Nb_2^{5+}Ti^{3+}A_{Ti}$  defect was possibly reduced. This can cause a decrease in interfacial polarization intensity. In the 2.5%IN–T sample, an additional  $\epsilon'$  value contributing from interfacial polarization should be less than that of the 10%IN–T sample. The deviation of the  $\epsilon'$  value at RT (contributed to by  $R_L+R_M$ ) from the  $\epsilon'$  value in a relatively low–temperature range (arising from  $R_L$  alone) should be smaller in the case of the 2.5%IN–T sample. This resulted in lower values of the temperature coefficient at temperatures below RT.

As shown in Fig. 7(b), the positive and negative temperature coefficient values of both samples in the high and low temperature ranges, respectively, resulted from  $R_H$  and  $R_M$ . In the range of RT-150 °C, a significant difference in temperature dependent behaviors of the 2.5% and 10%IN-T samples appeared. Negative and positive coefficients were obtained in the 2.5% and 10% IN-T samples, respectively. A small positive coefficient of the 10%IN-T sample is similar to that reported earlier. Interestingly, the negative value of the 2.5%IN-T sample has never been reported for co-doped  $TiO_2$  materials and is similar to that of pure  $TiO_2$ , which was attributed to the dominant effect of ionic polarization. However, the ionic polarization has never given rise to a  $\varepsilon'$  value of more than  $10^3$  at RT. This result means that in addition to several dominant effects (i.e., electron-pinned defect-dipoles,  $^{17}$  polaron hopping polarization,  $^{20,29}$  interfacial

polarization,  $^{20}$  and surface barrier layer  $^{29}$  as well as the gradient in  $Ti^{3+}$  concentration distribution  $^{27}$ ), the dominant effect of ionic-like polarization caused by the introduction of various point defects may be another key factor that has a significant influence on the dielectric properties of co-doped  $TiO_2$  materials. Intensive experimental and theoretical investigations are needed on this important topic.

### 1.4 Conclusions

IN–T ceramics were successfully synthesized using a SSR method. Highly dispersed  $ln^{3+}$  and  $Nb^{5+}$  doping ions in the microstructure of IN–T ceramics were achieved. Substitution of these two ions resulted in an expansion of lattice parameters for both of a and c values. It was found that  $\Delta C/C_{RT}$  values in low temperature (below RT) and high temperature (>150 °C) ranges of IN–T ceramics were primarily affected by  $R_{M}$  and  $R_{H}$ , respectively.  $R_{H}$  was associated with the movement on oxygen vacancies and found to be independent of dopant content. The  $R_{M}$  effect was dependent on co–dopant concentration and originated from interfacial polarization of delocalized charges. Highly co–doped 10%(In+Nb) substituted in  $TiO_{2}$  resulted in extremely high  $\epsilon'$  values with very low tan $\delta$ , but failed to exhibit improved  $\Delta C/C_{RT}$  values below RT due to the strong interfacial polarization effect. When the co–dopant content was decreased to 2.5%(In+Nb), the interfacial polarization effect was slight, leading a low  $\Delta C/C_{RT}$  value of less than 5% in the temperature range from RT to -70 °C. Notably, a very high  $\epsilon'$  value of  $1.57\times10^4$  and an ultra–low tan $\delta$  of  $\approx 0.006$  with an excellent temperature coefficient of less than  $\pm7\%$  in the range of -70–180 °C were achieved.

#### References

- 1. M. A. Subramanian, D. Li, N. Duan, B. A. Reisner and A. W. Sleight, *J. Solid State Chem.*, 2000, **151**, 323-325.
- 2. P. Lunkenheimer, R. Fichtl, S. Ebbinghaus and A. Loidl, *Phys. Rev. B*, 2004, **70**, 172102.
- 3. L. Liu, H. Fan, P. Fang and X. Chen, *Mater. Res. Bull.*, 2008, **43**, 1800-1807.
- 4. T. Park, Z. Nussinov, K. Hazzard, V. Sidorov, A. Balatsky, J. Sarrao, S. W. Cheong, M. Hundley, J.-S. Lee, Q. Jia and J. Thompson, *Phys. Rev. Lett.*, 2005, **94**, 017002.
- 5. S. Krohns, P. Lunkenheimer, C. Kant, A. V. Pronin, H. B. Brom, A. A. Nugroho, M. Diantoro and A. Loidl, *Appl. Phys. Lett.*, 2009, **94**, 122903.
- 6. P. Thongbai, T. Yamwong and S. Maensiri, *Mater. Lett.*, 2012, **82**, 244-247.
- 7. X. Q. Liu, B. W. Jia, W. Z. Yang, J. P. Cheng and X. M. Chen, *J. Phys. D: Appl. Phys.*, 2010, **43**, 495402.
- 8. Y.-H. Lin, M. Li, C.-W. Nan, J. Li, J. Wu and J. He, Appl. Phys. Lett., 2006, 89, 032907.
- 9. I. P. Raevski, S. A. Prosandeev, A. S. Bogatin, M. A. Malitskaya and L. Jastrabik, *J. Appl. Phys.*, 2003, **93**, 4130-4136.
- 10. Y. Y. Liu, X. M. Chen, X. Q. Liu and L. Li, Appl. Phys. Lett., 2007, 90, -.
- 11. N. Ikeda, H. Ohsumi, K. Ohwada, K. Ishii, T. Inami, K. Kakurai, Y. Murakami, K. Yoshii, S. Mori, Y. Horibe and H. Kito, *Nature*, 2005, **436**, 1136-1138.
- 12. C. Pecharromán, F. Esteban-Betegón, J. F. Bartolomé, S. López-Esteban and J. S. Moya, *Adv. Mater.*, 2001, **13**, 1541-1544.

- 13. J. Boonlakhorn, P. Thongbai, B. Putasaeng, T. Yamwong and S. Maensiri, *J. Alloys Compd.*, 2014, **612**, 103-109.
- 14. Z. Yang, L. Zhang, X. Chao, L. Xiong and J. Liu, *J. Alloys Compd.*, 2011, **509**, 8716-8719.
- 15. Y. Li, P. Liang, X. Chao and Z. Yang, Ceram. Int., 2013, 39, 7879-7889.
- 16. A. J. Moulson and J. M. Herbert, *Electroceramics : materials, properties, applications*, Wiley, West Sussex; New York, 2nd edn., 2003.
- W. Hu, Y. Liu, R. L. Withers, T. J. Frankcombe, L. Norén, A. Snashall, M. Kitchin, P. Smith,
   B. Gong, H. Chen, J. Schiemer, F. Brink and J. Wong-Leung, *Nat. Mater.*, 2013, 12, 821-826.
- 18. C. C. Homes and T. Vogt, *Nat. Mater.*, 2013, **12**, 782-783.
- 19. J. Wu, C.-W. Nan, Y. Lin and Y. Deng, *Phys. Rev. Lett.*, 2002, **89**, 217601.
- 20. X.-g. Zhao, P. Liu, Y.-C. Song, A.-p. Zhang, X.-m. Chen and J.-p. Zhou, *Phys. Chem. Chem. Phys.*, 2015, **17**, 23132-23139.
- 21. C. Wang, N. Zhang, Q. Li, Y. Yu, J. Zhang, Y. Li and H. Wang, *J. Am. Ceram. Soc.*, 2015, **98**, 148-153.
- 22. S. Tangwancharoen, P. Thongbai, T. Yamwong and S. Maensiri, *Mater. Chem. Phys.*, 2009, **115**, 585-589.
- 23. Z. Li, J. Wu and W. Wu, *Journal of Materials Chemistry C*, 2015, **3**, 9206-9216.
- 24. Z. Gai, Z. Cheng, X. Wang, L. Zhao, N. Yin, R. Abah, M. Zhao, F. Hong, Z. Yu and S. Dou, *Journal of Materials Chemistry C*, 2014, **2**, 6790-6795.
- 25. X. Cheng, Z. Li and J. Wu, Journal of Materials Chemistry A, 2015, 3, 5805-5810.
- 26. J. Li, F. Li, Y. Zhuang, L. Jin, L. Wang, X. Wei, Z. Xu and S. Zhang, *J. Appl. Phys.*, 2014, **116**, 074105.
- 27. W. Hu, K. Lau, Y. Liu, R. L. Withers, H. Chen, L. Fu, B. Gong and W. Hutchison, *Chem. Mater.*, 2015, **27**, 4934-4942.
- 28. M. N. Rahaman, Ceramic processing and sintering, M. Dekker, New York, 2nd edn., 2003.
- 29. W. Dong, W. Hu, A. Berlie, K. Lau, H. Chen, R. L. Withers and Y. Liu, *ACS Applied Materials & Interfaces*, 2015, DOI: 10.1021/acsami.5b07467.
- 30. Y. Sun, H. Liu, H. Hao, Z. Song and S. Zhang, J. Am. Ceram. Soc., 2015, 98, 1574-1579.
- 31. J. Jumpatam, B. Putasaeng, T. Yamwong, P. Thongbai and S. Maensiri, *J. Eur. Ceram. Soc.*, 2014, **34**, 2941-2950.
- 32. G. Yao, X. Wang, T. Sun and L. Li, J. Am. Ceram. Soc., 2011, 94, 3856-3862.
- 33. W. L. Warren, K. Vanheusden, D. Dimos, G. E. Pike and B. A. Tuttle, *J. Am. Ceram. Soc.*, 1996, **79**, 536-538.
- 34. T. B. Adams, D. C. Sinclair and A. R. West, *J. Am. Ceram. Soc.*, 2006, **89**, 3129-3135.

## **CHAPTER 2**

Origin(s) of apparent colossal permittivity in  $(In_{1/2}Nb_{1/2})_xTi_{1-x}O_2$ : Clarification on the extremely induced Maxwell–Wagner polarization relaxation in by DC bias

#### 2.1 Introduction

Recently, Hu *et al.*<sup>1</sup> reported a notably high–dielectric performance with an extreme high dielectric permittivity ( $\varepsilon'\approx6\times10^4$ ) and an ultra–low dielectric loss tangent ( $\tan\delta\approx0.02$ ) over a frequency range of  $10^2-10^6$  Hz in ( $\ln^{3+}+Nb^{5+}$ ) co–doped rutile– $TiO_2$  (IN–T) ceramics. By comparing this with previously reported colossal permittivity materials such as  $CaCu_3Ti_4O_{12}$  (CCTO),<sup>2-4</sup>  $Ba(Fe_{1/2}Nb_{1/2})O_3$ ,<sup>5-6</sup> and co–doped  $NiO^7$  ceramics, the temperature stability of IN–T was much better than in these ceramics.<sup>8</sup> The frequency–independent  $\varepsilon'$  of IN–T ceramics was reported to be slightly dependent of temperature over a wide range of 80–450 K.<sup>1</sup> Large defect–dipole clusters containing highly localized electrons produced by the complex stoichiometry of  $(\ln_x^{3+}Nb_x^{5+}Ti_x^{3+})Ti_{1-3x}^{4+}O_{2-x/2}$  proved to be the origin of these excellent dielectric properties.<sup>1</sup>

In pioneering work, two primary dielectric relaxations were observed in IN-T ceramics. The primary low-temperature dielectric relaxation (10-50 K) that gives rise to temperature-independent colossal permittivity over wide range was due to freezing electrons in defect-dipoles. Another relaxation caused by an extrinsic effect was observed in the range of 450-720 K. Other work reported that there are at least additional two dielectric relaxations that also occur in the temperature ranges of 50–150 K and 200–300 K. These relaxations were attributed to polaron hopping and interfacial polarization (or space-charge polarization or Maxwell-Wagner polarization), respectively.8-10 Most recently, it was demonstrated that the sample-electrode interface has a remarkable effect on the colossal permittivity of IN-T ceramics and (Ga+Nb) co-doped TiO<sub>2</sub> ceramics. 10-12 This means that there are several factors that have significant influences on the dielectric properties of TiO<sub>2</sub>-based materials. Even though the electron-pinned defect-dipole model has been a novelty reasonable model for describing the origin of the high-performance dielectric properties of IN-T ceramics, Maxwell-Wagner polarization at the grain boundaries (GB) (i.e., the internal barrier layer capacitor effect, IBLC) was also proposed as their exact origin, 11, 13-17 creating significant confusion. Thus, the origin of high performance dielectric properties of TiO<sub>2</sub>-based ceramics must be clarified.

The relaxation phenomenon in a dielectric material is generally undesirable for practical applications due to the resulting large changes in dielectric properties. However, it may give some important clues about the underlying mechanism governing the intriguing dielectric behavior in different temperature and frequency ranges.<sup>1, 9, 18-19</sup> Investigation of dielectric relaxation can elucidate possible sources of polarization in a particular frequency range.<sup>8-9, 18</sup>

From the point of view of capacitor applications, the DC voltage bias-dependence of  $\epsilon'$  is one of the most important parameters used to justify the use dielectric materials for low or high-voltage application. From an academic point of view, the effects of DC bias on the electrical and colossal dielectric properties may also give some important clues to understanding the overall dielectric responses in these materials, just as the investigation of dielectric relaxation. Usually, in the case that accumulated charges at the sample-electrode contact or where internal interfaces are the primary polarization source,

these charges would be stress-induced by applying a DC bias. Eventually, if the applied DC bias is sufficient high, the accumulated charges could become induced-mobile charges and move across the electrostatic potential barrier at these interfaces, giving rise to the DC conductivity ( $\sigma_{dc}$ ) and correlated low-frequency  $\tan\delta$  values. Concurrently, DC bias also can cause a decrease in the amount of accumulated charges, leading to a decrease in the intensity of Maxwell-Wagner polarization and  $\epsilon'$ . For CuO and La<sub>2-x</sub>Sr<sub>x</sub>NiO<sub>4</sub> ceramics that their colossal dielectric responses were dominated by the non-Ohmic sample-electrode effect, <sup>22, 24</sup> the low-frequency  $\epsilon'$  values at room temperature (RT) can easily be reduced by applying DC bias at 0–4 and 0–1.5 V, respectively. A low-frequency  $\epsilon'$  value (at 200 °C) caused by the sample-electrode effect for a CCTO ceramic was decreased by applying DC bias at 0–2 V.<sup>21</sup> For the effect of DC bias on the GB response in CCTO ceramics, variations in dielectric and electrical properties were dependent on their microstructures (e.g., mean grain size and grain size distribution). It had a great effect on the coarse-grained CCTO ceramic (grain size  $\approx$ 100 µm), but it had no effect on the small-grained CCTO ceramic ( $\approx$ 5 µm) in the range of 0–15 V DC bias.

Unfortunately, systematical investigation of the effects of DC bias and consequently resulting dielectric relaxation on the colossal dielectric response and electrical properties of bulk IN–T ceramics has never been reported. Thus, the main objective of this work is to study the influence of DC bias to clarify the origin of the colossal dielectric properties of IN–T ceramics and to design material for practical application. We found that the strong polarization relaxation of the IN–T ceramic with high concentration of co–dopants was easily induced in a low frequency range as a result of applied a DC bias. In contrast, the dielectric properties at 1 kHz of the IN–T ceramic with low concentration of co–dopants was slightly dependent on DC bias in the range of 0–40 V. The high  $\epsilon'$  value in a high frequency range was not changed by applying a DC bias, indicating the DC bias independence of the primary polarization in IN–T ceramics. The possible sources of polarizations in different frequency ranges are discussed and clarified.

## 2.2 Experimental details

 $(\ln_{1/2} \text{Nb}_{1/2})_x \text{Ti}_{1-x} O_2$  ceramics with x = 0.05 and 0.1 (abbreviated as the 5%IN–T and 10%IN–T ceramics, respectively) as well as a Nb–doped TiO<sub>2</sub> (Ti<sub>0.975</sub>Nb<sub>0.025</sub>O<sub>2</sub>, 2.5%N–T) ceramic were prepared using a solid state reaction method. TiO<sub>2</sub> (>99.9% purity), Nb<sub>2</sub>O<sub>5</sub> (99.99% purity), and In<sub>2</sub>O<sub>3</sub> (99.99% purity) were used as the starting raw materials. Details of the preparation method are given elsewhere.<sup>8</sup> The 5%IN–T and 10%IN–T ceramics were obtained by sintering at 1500 °C for 5 h. The sintering condition of pure–TiO<sub>2</sub> and the Nb–doped TiO<sub>2</sub> ceramics was 1400 °C for 5 h.

X-ray diffraction (XRD; Bruker, D 2phaser) was used to characterize the phase composition and crystal structures of all the sintered ceramics. Rietveld quantitative phase analysis was carried out using the X'Pert High Score Plus v3.0e software package by PANalytical. The microstructure and elemental distribution in the IN-T ceramic were examined using a field-emission scanning electron microscopy (FE-SEM) with energy-dispersive X-ray analysis (EDX) (HITACHI SU8030, Japan). The chemical states of Ti were analyzed using X-ray photoelectron spectroscopy (XPS), PHI5000 VersaProbe II, ULVAC-PHI, Japan) at the SUT-NANOTEC-SLRI Joint Research Facility, Synchrotron Light Research Institute (SLRI), Thailand. The XPS spectra were fitted with PHI MultiPak

XPS software using a combination of Gaussian–Lorentzian lines. Before electrical measurements, Au was sputtered onto each pellet face (did not polish) at a current of 25 mA for 8 min using a Polaron SC500 sputter coating unit (Sussex, UK). The dielectric properties were measured under an AC oscillation voltage of 0.5 V using Agilent 4294A Precision Impedance Analyzer and KEYSIGHT E4990A Impedance Analyzer over the frequency range of  $10^2–10^6$  Hz. Dielectric measurements were performed under different DC bias levels.

## 2.3 Results and discussion

The XRD patterns of the sintered pure–TiO<sub>2</sub>, 2.5%N–T, 5%IN–T and 10%IN–T ceramics are given in Fig. 1. All the XRD patterns show the main phase of rutile–TiO<sub>2</sub> (JCPDS 21–1276) with a tetragonal structure without impurity phase. Lattice parameters (a and c) were calculated from Rietveld refinement profile fits. a and c values of the TiO<sub>2</sub>, 2.5%N–T, 5%IN–T and 10%IN–T ceramics were found to be 4.592(2) and 2.959(6) Å, 4.595(6) and 2.962(6) Å, 4.599(2) and 2.965(8) Å and 4.601(4) and 2.967(3) Å, respectively. The a and c values of the 10%IN–T ceramic are comparable to values reported in literature,  $a\approx$ 4.615 Å and  $c\approx$ 2.980 Å, for the 10%(In+Nb) sample.¹ Both a and c parameters of the 2.5%N–T, 5%IN–T and 10%IN–T ceramics were larger than those of sintered pure–TiO<sub>2</sub> ceramic and retile–TiO<sub>2</sub> with a=4.593 Å and c=2.959 Å (JCPDS 21–1276). It was also observed that both a and c parameters increased with increasing doping concentration. The enlargement in the lattice parameters is attributed to the larger ionic radii of In<sup>3+</sup> and Nb<sup>5+</sup> than those of the host Ti<sup>4+</sup> ion. This clearly indicates that both In<sup>3+</sup> and Nb<sup>5+</sup> doping ions entered into the rutile–TiO<sub>2</sub> lattice structure.

The insets of Fig. 1 show the microstructure of the 5%IN-T and 10%IN-T ceramics, revealing GB and grain structures, with mean grain sizes of  $\approx 27.3\pm 5.8$  and  $\approx 22.8\pm 4.7$  µm, respectively. Residual pores were also observed in the microstructure of the 10%IN-T ceramic, while they did not appear in the pure-TiO<sub>2</sub>, Nb-doped TiO<sub>2</sub> and 5%IN-T ceramics. To further analyze the distributions of all elements in the 10%IN-T ceramic, mapping of Ti, O, In, and Nb elements was performed. As shown in Fig. 2, the dopants were homogeneously dispersed in both the grain and GB. No segregation of  $In^{3+}$  and  $Nb^{5+}$  ions at any specific region was observed.

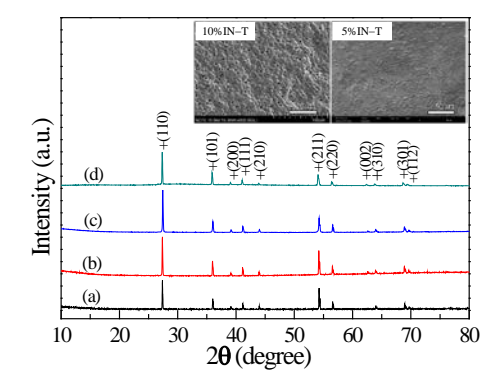


**Fig. 1** XRD patterns of the (a) pure–TiO<sub>2</sub>, (b) Nb–doped TiO<sub>2</sub>, (c) 5%IN–T and (d) 10%IN–T ceramics; inset reveals surface morphologies of the 5%IN–T and 10%IN–T ceramics.

The oxidation states of polyvalent cations of the 10%IN–T ceramic were identified by an XPS spectrum, Fig. 3. Using Gaussian–Lorentzian profile fitting, the XPS spectrum of Ti2p consisted of two peaks. The main peak at a binding energy of about  $\approx$ 458.80 eV can be referred to as the presence as Ti<sup>4+</sup>.<sup>1, 16-17, 25</sup> Another peak at relatively lower binding energy of  $\approx$ 457.35 eV indicated the existence of Ti<sup>3+</sup>.<sup>1, 16-17</sup> The Ti<sup>3+</sup>/Ti<sup>4+</sup> ratio was about 4.29%. Substitution of Nb<sup>5+</sup> into TiO<sub>2</sub> can produce free electrons by reducing Ti<sup>4+</sup> to Ti<sup>3+</sup> as follows:

$$2TiO_2 + Nb_2O_5 \xrightarrow{4TiO_2} 2Ti'_{Ti} + 2Nb^{\bullet}_{Ti} + 8O_O + 1/2O_2,$$
 (1)

$$Ti^{4+} + e \to Ti^{3+}$$
. (2)

Very high  $\epsilon'$  of IN-T ceramics should be correlated with the produced free electrons that can be considered as sources of the polarization at any microscopic regions (e.g., GBs, Domain boundary, outer surface and sample-electrode interface) and/or at a local structure (e.g., detect clusters).

Without an applied DC bias, the 10%IN-T ceramic exhibited excellent dielectric properties with  $\varepsilon' \approx 4.9 \times 10^4$  and  $\tan \delta \approx 0.052$  at  $10^3$  Hz and RT, Fig. 4(a) and its inset.  $\varepsilon'$  was slightly dependent on frequency from  $10^2-10^6$  Hz. The values of  $\varepsilon'$  and  $\tan \delta$  are comparable to those published in the literature. These excellent dielectric properties may have originated from either the electron–pinned defect–dipoles or strong interfacial polarization effect. The exact origin will be discussed hereafter.

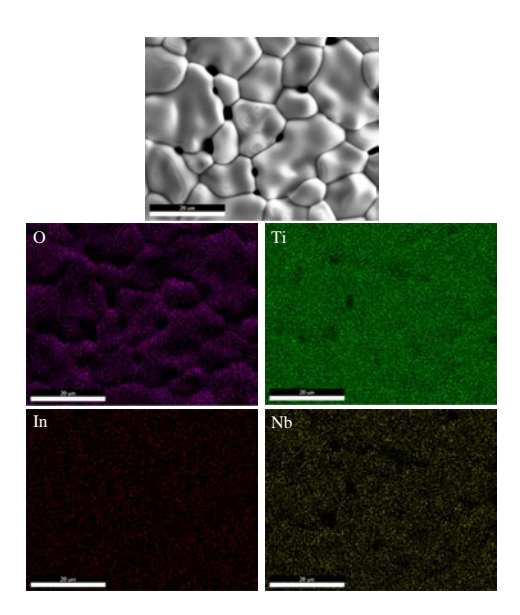
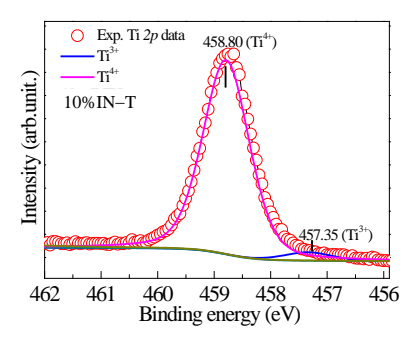


Fig. 2 SEM image and element mapping of the 10%IN-T ceramic.

As illustrated in Fig. 4(a),  $\varepsilon'$  in a frequency range of  $10^2$ – $10^3$  Hz of the 10%IN–T ceramic increased with increasing DC bias from 0 to 20 V using step increases of 5 V/step. When the DC bias was increased to 25 V, an overload limited measurement (OLM) was occurred. This is generally due to large current leakage passing through the bulk sample. A drastically increased  $\varepsilon'$  was observed in a low frequency range when DC bias increased from 15 to 20 V. Either of hopping charge transport of free charges or strong Maxwell–Wagner–polarization (or space charge polarization) relaxation induced by DC bias may have been the primary cause of this observation.<sup>26</sup> In the former case,

hopping conduction usually leads to the typical power–law frequency dependencies of the Universal Dielectric Response (UDR), in which there are characteristic signatures in the frequency dependences of the complex conductivity and permittivity that follow the relationships,  $\sigma' = \sigma_0 v^s$  and  $\epsilon' \propto v^{s-1}$  (s < 1), respectively. <sup>26</sup> In the latter case, a high plateau in the  $\epsilon'$  value in a low–frequency range coupled with a relaxation tan $\delta$  peak are usually observed. <sup>7, 26-27</sup>



**Fig. 3** XPS spectrum of the 10%IN–T ceramic for Ti 2*p* region.

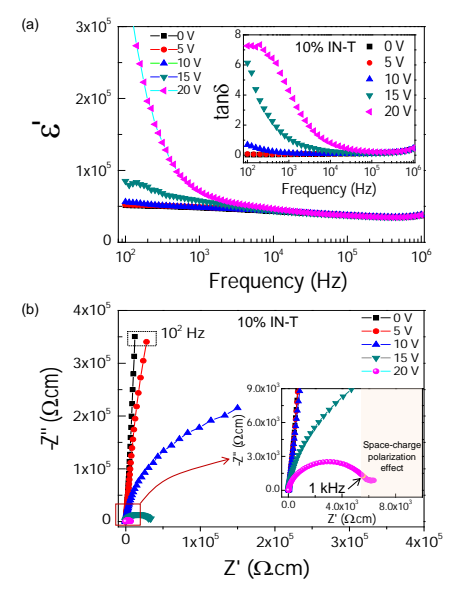


Fig. 4 (a) Effect of DC bias (0–20 V) on ε' at RT for the 10%IN–T ceramic in a frequency range of 10²–10<sup>6</sup> Hz and inset demonstrates the influence of DC bias on tanδ. (b) RT–impedance complex plane (Z\*) plot as a function of DC bias (0–20 V) for the 10%IN–T ceramic and the inset is an enlarged view of Z\* plot near the origin.

Inset of Fig. 4(a), a low–frequency  $\tan\delta$  peak appeared when DC bias was 20 V, while the plateau of  $\epsilon'$  was not observed. The disappearance of the  $\epsilon'$  plateau may have been due to the frequency at which the step–like decrease in  $\epsilon'$  (or at which the  $\epsilon''$ –peak appeared) was lower than the frequency of  $\tan\delta$ –peak by value of  $1/\tau \left(\sqrt{\epsilon_s'/\epsilon_\infty'}-1\right)$  Hz, where  $\epsilon_s'$  and  $\epsilon_\infty'$  are respectively the  $\epsilon'$  values in a low and high frequency ranges, and  $\tau$  is the relaxation time. Thus, it is likely that a strong low–frequency Maxwell–Wagner polarization was created by applying a DC bias. It is noteworthy that  $\epsilon'$  of the 10%IN–T ceramic at frequencies higher than  $10^4$  Hz was independent of DC bias (0–20 V). This

indicates that the DC bias has no effect on the primary source of the polarization that gives rise to the high-dielectric performance in IN-T ceramics.

To clarify the possible origins of the additional Maxwell–Wagner polarization and the primary polarization, an impedance spectroscopy analysis under different DC bias voltages was performed. Without an applied DC bias, only a linear part of arc with a high–frequency near–zero intercept is observed from Z\* plot at RT, Fig. 4(b). This is similar to that reported by Hu et al. They suggested that the complex impedance at RT contained only one constituent intra–grain contribution, which was considered to be the source of the primary polarization. Such a resistance was roughly estimated to be >100 M $\Omega$ .cm. This value is consistent with the result reported by Wu *et al.*, in which the resistance estimated from large semicircle arc of the (Nb<sub>0.5</sub>In<sub>0.5</sub>)<sub>0.01</sub>Ti<sub>0.99</sub>O<sub>2</sub> ceramic was found to be  $\approx$ 1500 M $\Omega$ .cm. They suggested that this very high resistance value was attributed to the GB response, at which primary polarization occurred. This is a significant controversy concerning primary polarization, which must be clarified.

The diameter of a semicircle arc was dramatically decreased by increasing the applied DC bias. The resistance of the 10%IN-T ceramic was reduced by 3 and 4 orders of magnitude after applying a 15 and 20 V DC bias, respectively [inset of Fig. 4(b)]. At 20 V DC bias, the corresponding resistance was as low as  $\approx 6 \times 10^3$   $\Omega$ .cm. Furthermore, a low-frequency tail was observed. This may be attributed to the interfacial effect, which is consistent with the variations in  $\varepsilon'$  and tan $\delta$  values [Fig. 4(a)]. Besides a large semicircle arc, a nonzero intercept on Z' axis was observed, corresponding to the electrical response of a semiconducting part with resistance of 15–20  $\Omega$ .cm (does not shown). Thus, the observed large semicircle arc should be due to the electrical response of insulating part(s) (e.g., another phase, a resistive outer-surface layer, grain boundaries and/or domain boundaries). For a coarse-grained CCTO ceramic (grain size ≈100 µm), the GB resistance ( $R_{\rm gb}$ ) was greatly reduced by increasing DC bias from 0 to 15 V. The GB capacitance ( $C_{\rm gb}$ ), which was related to  $\epsilon'$  value, was also significantly decreased.<sup>20</sup> For a fine-grained CCTO ceramic (grain size ≈5 μm), its R<sub>ab</sub> value slightly decreased from 4  $M\Omega$  (no DC bias) to  $\approx 2.5$   $M\Omega$  at 4 V and remained constant up to 15 V DC bias. By considering the grain size of ≈22.8 µm for the 10%IN-T ceramic, it is possible that R<sub>ab</sub> could be reduced by applying DC bias at 15-20 V. However, the primary dielectric response in the 10%IN-T ceramic was not changed, just as reported in the case of a coarse-grained CCTO ceramic.

When the DC bias was increased to 25 V, OLM occurred due to large current leakage. This situation indicated that there were a large number of induced-mobile charges that passed through the bulk ceramics into the circuit. After that, for 24 h, the dielectric properties of the 10%IN–T ceramic were measured again at RT without an applied DC bias (hereafter referred as the 10%IN–T\_A1 sample). Fig. 5(a), an additional  $\epsilon'$  plateau for the 10%IN–T\_A1 sample was observed in a low-frequency range. Concurrently, the step-like decrease in  $\epsilon'$  and corresponding  $\tan\delta$ -peak shifted to a high frequency range [Fig. 5(b)]. After a large number of mobile charges were produced by applying a DC bias at 25 V, the dominant effect of the induced–Maxwell–Wagner polarization was extended to a higher frequency range. Generally, when the distance between the adjacent barriers in a dielectric is shortened and/or the density of mobile charges in the conductive part is sufficiently large, the frequency range of sensitivity for the Maxwell–Wagner polarization (or space–charge polarization) can usually be extended

to a higher frequency range. The latter cause is there responsible for the observed movement of the induced–Maxwell–Wagner polarization to higher frequency range. A large semicircle arc in a low–frequency range of an insulating part (at which space–charge polarization has been induced) and another electrical response of an insulating part with smaller semicircle arc were observed [Fig. 5(c)]. A nonzero intercept did not change after the situation of OLM existed, Fig. 5(d). Now, there are at least three electrical responses in the 10%IN–T ceramic, *i.e.*, (1) grains, (2) GBs and (3) unknown insulating part(s). Among these, at least two insulating parts contain in the large semicircle arc of the 10%IN–T ceramic. The nonzero intercept and a relatively small semicircle arc can be assigned to be electrical responses of the semiconducting grains and GBs, respectively.

An unknown insulating part(s) with very large resistance compared to  $R_{\text{gb}}$  might be caused by trapped–charges at the sample–electrode contact. The  $\epsilon'$  value contributed by the polarization at sample–electrode contact can be completely eliminated by annealing the sample–electrode contact at 200–300 °C.<sup>22, 29</sup> To further clarify the possible origin of the large induced–Maxwell–Wagner polarization, the 10%IN–T\_A1 sample was annealed in air at 200 °C for 0.5 h (referred as the 10%IN–T\_A2 sample). Annealing had a slight influence on the low–frequency values of  $\epsilon'$  and tan $\delta$  [Fig. 5(a) and (b)]. Fig. 5(c), the large induced–Maxwell–Wagner polarizations of the 10%IN–T\_A1 and 10%IN–T\_A2 samples were not too different significantly. These results clearly indicate that the sample–electrode contact has a slight effect, but it cannot still be ignored.

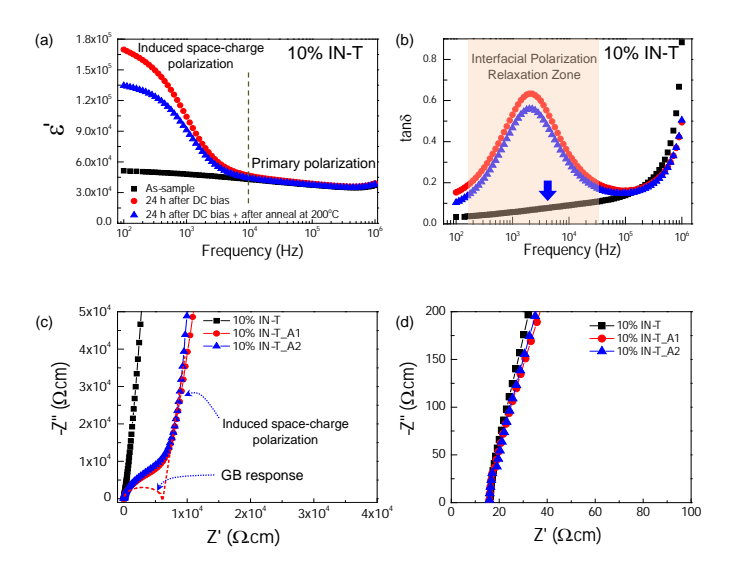
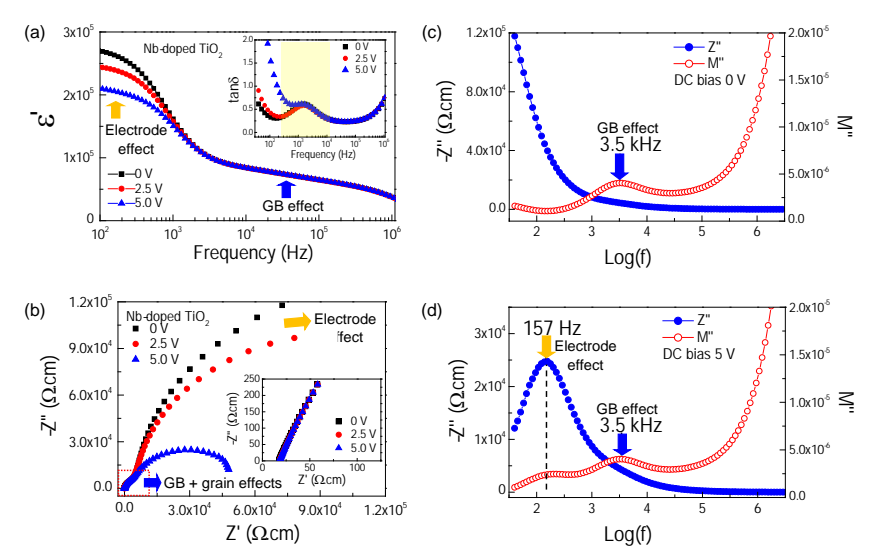


Fig. 5 Effects of aging (24 h) and annealing (at 200  $^{\circ}$ C in air for 0.5 h) of the 10%IN–T ceramic on (a)  $\epsilon'$  and (b)  $\tan\delta$  values at RT in a frequency range of  $10^2$ – $10^6$  Hz without DC bias. (c)  $Z^*$  plots at RT for untreated, aged, and annealed samples measured without DC bias. The dashed red line is the eye guideline for estimating  $R_{gb}$ . (d) An expanded view of the high–frequency data close to the origin for  $Z^*$  plots of Fig. (c), revealing the nonzero intercept on Z' axis.

To clearly show the effects of DC bias on the electrical responses of the GBs and non–Ohmic sample–electrode contact of  $TiO_2$ –based ceramics, the dielectric and electrical properties of the single–doped 2.5%N–T ceramic were investigated at RT as a function of DC bias. Fig. 6(a), two colossal dielectric responses are observed in the frequency range of  $10^2$ – $10^6$  Hz. The low–frequency colossal dielectric response (LFCDR)

was significantly reduced by DC bias, whereas the relatively high–frequency dielectric response did not change. A nonzero intercept with two semicircle arcs are observed in  $Z^*$  plot [Fig. 6(b) and its inset]. At least three electrical responses were confirmed to exist in the 2.5%N–T ceramic. The diameter of a large semicircle arc was remarkably decreased by DC bias, while a relatively small semicircle arc and nonzero intercept did not change. These are generally assigned as the electrical responses of the sample–electrode contact, GBs and grains, respectively. The effects of DC bias on electrical response of sample–electrode contact and associated colossal dielectric properties of the 2.5%N–T ceramic are similar to those observed in other colossal dielectric materials such as CuO, CCTO and  $La_{2-x}Sr_xNiO_4$  ceramics.  $^{21-22, 24}$  It is notable that the relaxation frequency of  $tan\delta$  peak did not change [inset of Fig. 6(a)]. Only low–frequency  $tan\delta$  was greatly increased by DC bias. These results indicate the unique characteristic of the sample–electrode effect, which was easily degraded by releasing trapped charges at the non–Ohmic contact during applying DC bias.



**Fig. 6** (a) Effect of DC bias (0-5 V) on  $\epsilon'$  at RT for the Nb–doped TiO<sub>2</sub> ceramic in a frequency range of  $10^2$ – $10^6$  Hz; inset demonstrates the influence of DC bias on  $\tan\delta$ . (b)  $Z^*$  plot at RT as a function of DC bias (0-5 V) for the Nb–doped TiO<sub>2</sub> ceramic; inset is an enlarged view of  $Z^*$  plot near the origin, revealing the nonzero intercept due to the grain response. (c–d) Combined Z'' and M'' spectroscopic plots at RT for the Nb–doped TiO<sub>2</sub> ceramic without and with 5 V DC bias, respectively.

To further confirm each of these electrical responses in the 2.5%N–T ceramic, combined Z" and M" spectroscopic plots at RT were performed under 0 and 5 V DC bias, Figs. 6(c) and (d). Without DC bias, a single M" peak is observed at  $f_{\text{max-phase2}} \approx 3.5$  kHz. Another M" peak shifts to above the upper frequency limit ( $f_{\text{max-phase1}} > 10$  MHz), indicating that this phase is very conductive, corresponding to the nonzero intercept [inset of Fig. 6(b)]. Such a phase 1 was reasonably assigned as the semiconducting grain.  $f_{\text{max-phase3}}$  of a Debye–type peaks in Z" plot occurred below the lower measuring frequency limit of the instrumentation (<40 Hz). Increasing temperature measurement is usually performed to decrease resistance value for moving  $f_{\text{max-phase3}}$  into the measured frequency range, regrading to the general relationship  $f_{\text{max}} = 1/2\pi RC$ . In this current study, the resistance of

phase 3 was reduced by applying DC bias (5 V), moving  $f_{\text{max-phase3}}$  in Z" plot as well as in M" plot into the frequency at 157 Hz [Fig. 6(d)]. Phase 3 is presumably correlated to an electrode effect. It is important to note that the M"-peak height and  $f_{\text{max-phase2}}$  did not change before and after applied 5 V DC bias, indicating unchanged C and R values, respectively. This phase can be referred as the insulating GBs.

Now, it is clearly to distinguish the LFCDR mechanisms between the 10%IN–T and 2.5%N–T ceramics. The LFCDR in the former case was greatly induced to exist by DC bias. For the latter case, it already appeared and was then destroyed by DC bias. Generally, the non–Ohmic sample–electrode contact is created at the interface between semiconductive ceramic surface and conductive–metal electrode. The existence of semiconducting grains of the 10%IN–T ceramic has been confirmed, but the effect of non–Ohmic sample–electrode contact was not dominant (the LFCDR unappeased for without DC bias). This means that the outer surface region facing with the metal–electrode may not be semiconductor, but quite insulator.

At RT, an OLM did not occur in the 5%IN-T ceramic even at 40 V DC bias, indicating very high resistances of outer-surface layer and/or insulating GBs compared to that of the 10%IN-T ceramic, Fig. 7(a). Obviously, the LFCDR can also be induced. The induced polarization relaxation, i.e., a step-like decrease in  $\varepsilon'$  and corresponding relaxation  $tan\delta$ -peak, shifts to a high frequency as DC bias increased [Fig. 7(a) and its inset]. The primary dielectric response still did not change, just as observed in the 10%IN-T ceramic. After the dielectric properties of the 5%IN-T ceramic was measured at RT under 40 V DC bias, this sample was immediately measured again without DC bias. It was found that the dielectric properties before and after applied DC bias at 40 V were nearly the same in value, as illustrated in Fig. 8(a) and its inset. As shown in Fig. 8(b), at 40 V DC bias, two semicircle arcs of the insulating parts were separated. The  $R_{ab}$  value corresponding to a small semicircle arc at higher frequencies was estimated to be ≈150 kΩ.cm. This result implies that if the applied 40 V DC bias has also affected to the electrical properties of the GBs, without DC bias the RT-value of  $R_{\rm gb}$  for the 5%IN-T ceramic should be at least as large as 150 k $\Omega$ .cm. Note that the impedance spectra under DC bias of the 5%IN-T and 10%IN-T ceramics are very similar. In IN-T ceramics, the inhomogeneous dielectric behavior can be rather pronounced:  $R_{ab}$  and  $R_{a}$  can differ by a factor of up to ≈10<sup>4</sup>. The conduction activation energy associated with either grain or GB conduction processes was expected to differ by up to a factor of >10. Thus, the IBLC can suitably be used to describe the very large  $\varepsilon'$  value in IN–T ceramics.

To reveal the dielectric and electrical behavior of the 5%IN-T ceramic after OLM occurred, the dielectric measurement under different DC bias voltages was carried out at higher temperatures. At 50 °C, the dielectric properties can be measured only in the range of 0–35 V, OLM occurred when the DC bias was adjusted to 40 V. The frequency dependence of  $\epsilon'$  at 50 °C under applying DC bias (0–35 V) for the 5%IN-T ceramic is demonstrated in Fig. 7(b). For any voltage level of DC bias, the induced step-like decrease in  $\epsilon'$  shifted to a high frequency when temperature was increased from RT to 50 °C. Additionally, a linear increase in  $\epsilon'$  in a frequency range below 100 Hz was dominant, corresponding to the large increase in  $\tan\delta$  as frequency decreased [inset of Fig. 7(b)]. The relaxation  $\tan\delta$ –peak is not observed, which is likely due to great effect of DC conduction. The energy loss ( $\tan\delta$ ) due to the dielectric relaxation phenomena was concealed by very high energy loss contributing from the DC conductivity ( $\sigma_{dc}$ ).

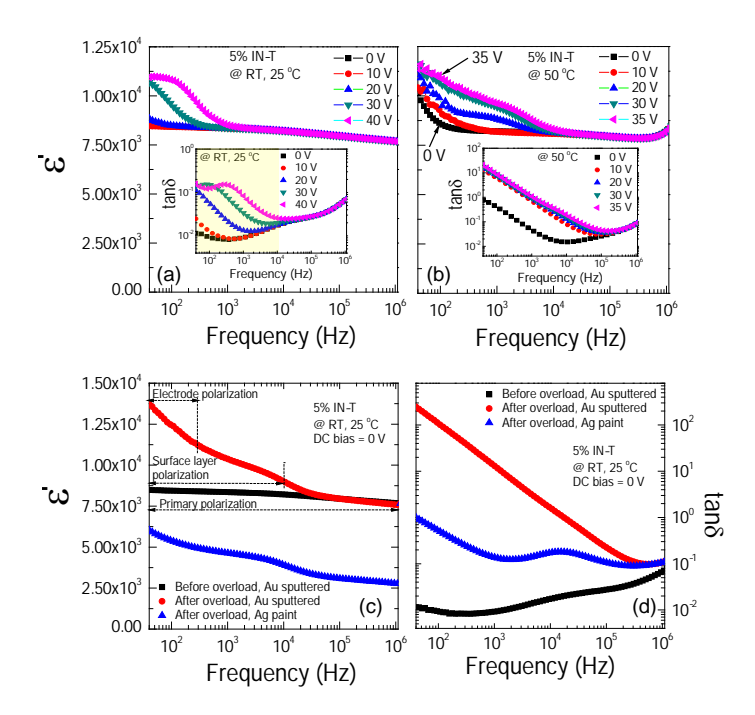


**Fig. 7** (a–b) Frequency dependence of ε' under different DC bias voltages for the 5%IN–T ceramic at RT ( $\approx$ 25 °C) and 50 °C, respectively; their insets illustrate the effect of DC bias on tanδ at RT ( $\approx$ 25 °C) and 50 °C. (c–d) ε' and tanδ at RT without DC bias (0 V) of the as–fired 5%IN–T ceramic sample and the 5%IN–T ceramic samples after an overload limited DC bias measurement using Au–sputtered and Ag paint electrodes.

The dielectric properties at RT without DC bias of the 5%IN-T ceramic before and after OLM with different types of electrodes are depicted in Figs. 7(c) and (d). After OLM occurred at 50 °C, for 15 h, an additional ε' plateau at RT for the 5%IN-T ceramic with Au-sputtered electrode was observed in a low-frequency range, while the primary dielectric response did not change. The step-like decrease in  $\varepsilon'$  was observed at  $\approx 10^4$  Hz. The overall dielectric behavior of the 5%IN-T ceramic after overload took place is quite similar to that observed in the 10%IN-T ceramic. By replacing Au sputtered electrode with Ag paint electrode (a sample thickness did not change and the outer surface layer was not removed), a dielectric spectrum over a measured frequency rage is similar to that obtained from Au-sputtered electrode, but the magnitude of the dielectric response was lower [Fig. 7(c)]. The difference in magnitudes of the dielectric responses between the samples with Au sputtered and Aq paint electrodes is primarily due to different methods for electrode preparation. Although an electrode was fabricated from the same metal, the dielectric response of the sample with sputtered electrode is usually larger.<sup>30</sup> This means that the induced-LFCDR in the frequency range of 40-10<sup>4</sup> Hz may primarily correlated with other source (e.g., the interface between resistive outer-surface layer and conductive inner core), whereas the electrode polarization effect cannot be ignored.

Two different dielectric behaviors between the 5%IN–T and 10%IN–T ceramics were observed. First, in the low–frequency range of 40–300 Hz, a linear increase in  $\varepsilon'$  appeared, indicating another source of polarization. Second, the induced–relaxation peak of  $\tan\delta$  was not observed. These results indicate a strong dominant effect of DC

conductivity, which is usually related to electrode effect. A low-frequency  $\tan\delta$  of the 5%IN-T ceramic using Ag paint electrode is much lower than that of the ceramic using Au sputtered electrode by about 2 orders of magnitude. Furthermore, a relaxation  $\tan\delta$ -peak is observed. These mean that the interface resistance ( $R_e$ ) of the ceramic with Ag paint electrode was much larger than that of the ceramic with Au-sputtered electrode. After OLM, it is possible that some free charges have trapped at the sample-electrode interface. This produced the electrode polarization, which is generally accompanied with very larger  $\tan\delta$  value.

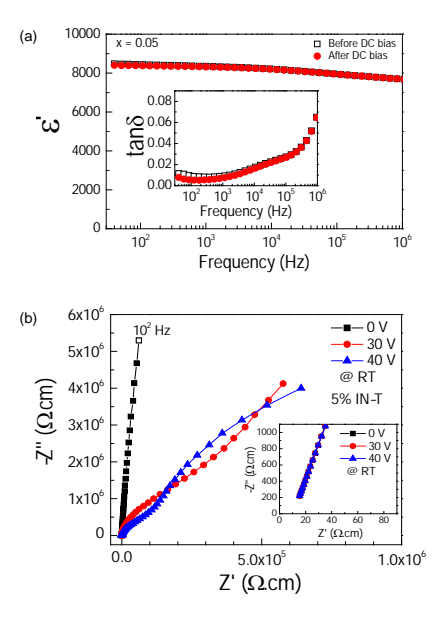


Fig. 8 (a) ε' of the 5%IN–T ceramic before and after applied DC bias at 40 V (measured at RT without DC bias); inset shows tanδ before and after applied DC bias at 40 V. (b) RT–impedance complex plane (Z\*) plot under DC bias at 0, 30 and 40 V for the 5%IN–T ceramic; inset shows a nonzero intercept near the origin.

To confirm the dielectric response of each source of polarization in the 5%IN–T ceramic, combined Z'' and M'' spectroscopic plots at RT were used to describe. As shown in Fig. 9(a), without DC bias, Z'' and M'' peaks of an insulating phase(s) are not observed because they are at < 40 Hz. The M'' peak of semiconducting phase is at > 10 MHz, which is clearly assigned to the semiconducting grains. Careful inspection suggests that there is an intermediate component phase (referred to as phase 1) presented with  $f_{\text{max}}$  between  $10^4$  – $10^5$  Hz, as indicated by a M'' shoulder–peak in a dash rectangle area. At 30 V DC bias, another M'' peak became to appear with  $f_{\text{max}} = 95.5$  Hz (does not shown), while Z'' peak still disappeared. As demonstrated in Fig. 9(b), with increasing DC bias to 40 V,  $f_{\text{max}}$  of a low–frequency M'' peak shifted to 330 Hz (referred to as phase 2). Interestingly, Z'' peak was not observed and expected to exist at  $f_{\text{max}} < 40$  Hz (referred to as phase 3). These results indicate that there are two insulating interfaces in the 5%IN–T ceramic, which were occurred by applying by DC bias.

As discussed early in Fig. 7, after OLM occurred, the electrical response of sample–electrode contact was much dominant than that of the outer–surface layer effect. As shown in Fig. 9(c), both of Z'' and M'' peaks appear in nearly the same frequency with  $f_{\rm max}$  between  $10^4$  – $10^5$  Hz, indicating that only phase 1 appeared in the measured frequency range after OLM. By replacing Au sputtered electrode with Ag paint electrode,

both of the peak–height and peak position ( $f_{\rm max}$ ) of the M" peak for a phase 1 did not change. Notably, low–frequency Z" and M" peaks become to occur at nearly the same with  $f_{\rm max}\approx 40$ –50 Hz. Obviously, phase 3 cam be assigned as the electrical response of sample–electrode contact, i.e., the electrode effect. Thus, a phase 2 can be reasonably to the resistive outer–surface layer response. It is possible that after OLM occurred at 50 °C, the insulating properties of the resistive outer–surface was degraded and eventually less dominant. After that, both surface sides of the 5%IN–T ceramic were removed by polishing. As depicted in Fig. 9(e), the low–frequency electrode response and a phase 1 were still observed. This strongly confirm that a phase 1 was the GBs. When Au sputtered electrode was used, only the electrode effect can be observed, Fig. 9(f).

According to the experimental results in this current study, it was suggested that the primary polarization that gave rise to high  $\epsilon'$  of IN–T ceramics was likely attributed to the interfacial polarizations. On the other hand, it was found that the most important factor contributing to very low  $\tan\delta$  value (<0.05) is the resistive outer–surface layer. The resistive outer–surface was not only able to prevent the DC conduction through the ceramic sample, but also inhibited the formation of non–Ohmic sample–electrode contact, which is usually accompanied with a large  $\tan\delta$  value in a low–frequency range. This gave rise to the high performance dielectric properties in IN–T ceramics. From the point of view of capacitor applications, according to our previous work, co–doping TiO<sub>2</sub> with a high concentration of In+Nb (10%) caused a decrease in the temperature stability of  $\epsilon'$  and low co–doping concentration was suggested. In this current study, we also suggested that substitution of In+Nb co–dopants into TiO<sub>2</sub> with a low concentration can cause the DC bias intendance of the dielectric properties. Although the thickness of the resistive outer–surface layer cannot be calculated, this work provide the important alternative method to achieve the high dielectric performance in the N–T ceramic system.

Finally, it should be noted that this work is not to discredit the possibility of the electron pinned–defect dipole model being generated by essentially designing complex defects in a rutile–structure. The discussion is based on the experimental results that were obtained in our synthesized IN–T ceramics. Actually, the special structure of complex defects may also possibly existed in our IN–T ceramics, but did not dominate. Instead, the observed semiconducting grains might be originated by a very large amount of free charges existing during sintering step at a very high temperature of  $1500^{\circ}$ C. In this case, exceed free electrons cannot be captured by the triangular shaped  $In_2^{3+}V_o^{\bullet\bullet}Ti^{3+}$  defect complexes.

## 2.4 Conclusions

The origin of the high–performance dielectric properties and optimized composition of the co–doped  $TiO_2$  ceramics for suitably using in practical applications were successfully achieved by studying the influences of DC bias on colossal dielectric responses. According to the analogous study of the DC bias effect in the Nb single–doped  $TiO_2$  ceramics, the unique characteristics under DC bias for the dielectric responses contributing from the electrode and GB effects were clearly demonstrated. The low–frequency  $\epsilon'$  and  $tan\delta$  of IN–T ceramics were strongly induced by applying DC bias and had been removed by immediately applying no DC bias. It was demonstrated that the induced–polarization can be permanently appeared without DC bias by applying DC bias over the overload limited measurement. All of cases, the primary polarization still

unchanged. The permanent induced–polarizations were originated from the dielectric responses of the non–Ohmic sample–electrode contact and resistive outer–surface layer. Excellent dielectric performance of the IN–T ceramics was shown to be primality attributed to the existence of resistive outer–surface layer, while the colossal dielectric response was originated from the interfacial polarization at the insulating GBs.

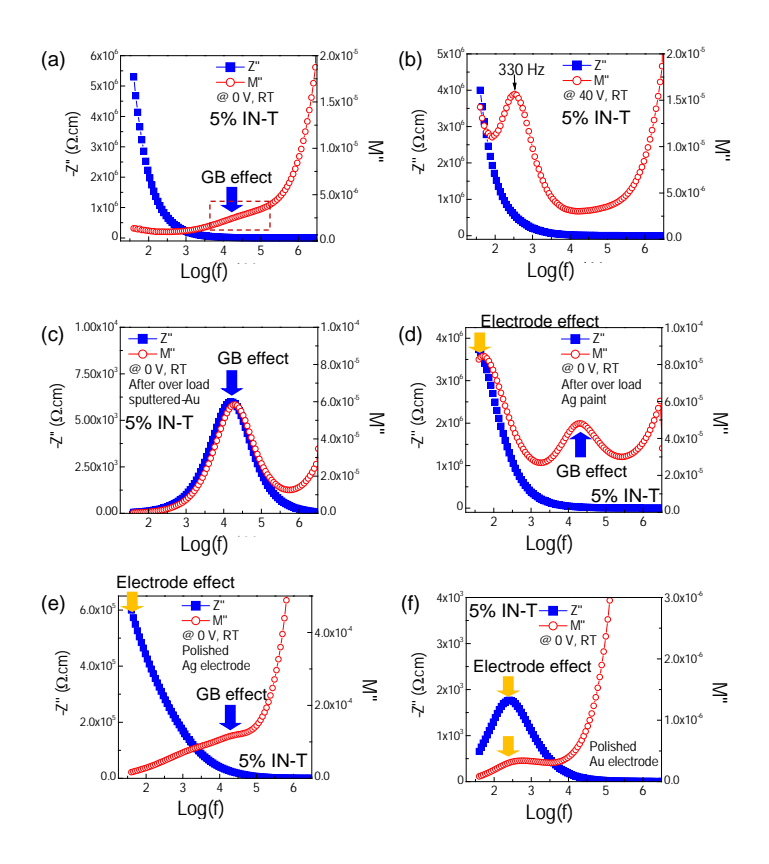


Fig. 9 (a–b) Combined Z" and M" spectroscopic plots at RT for the as–fired 5%IN–T ceramic sample under 0 and 40 V DC bias, respectively. (c–d) Combined Z" and M" spectroscopic plots at RT without DC bias (0 V) for the 5%IN–T ceramic samples after an overload limited DC bias measurement using Au–sputtered and Ag paint electrodes, respectively. (e–f) Combined Z" and M" spectroscopic plots at RT without DC bias (0 V) for the polished 5%IN–T ceramic samples using Au–sputtered and Ag paint electrodes, respectively.

## References

- 1 W. Hu, Y. Liu, R. L. Withers, T. J. Frankcombe, L. Norén, A. Snashall, M. Kitchin, P. Smith, B. Gong, H. Chen, J. Schiemer, F. Brink and J. Wong-Leung, *Nat. Mater.*, 2013, **12**, 821-826.
- 2 L. Singh, I. W. Kim, B. C. Sin, K. D. Mandal, U. S. Rai, A. Ullah, H. Chung and Y. Lee, *RSC Adv.*, 2014, **4**, 52770-52784.
- 3 J. Li, K. Wu, R. Jia, L. Hou, L. Gao and S. Li, *Materials & Design*, 2016, **92**, 546-551.
- 4 M. Gao, D. Feng, G. Yao, Y. Zhang, C. L. Chen and Y. Lin, *RSC Advances*, 2015, **5**, 92958-92962.
- 5 Z. Wang, Y. F. Wen, H. J. Li, M. R. Fang, C. Wang and Y. P. Pu, *J. Alloys Compd.*, 2016, **656**, 431-438.

- 6 H. Yang, Y. Yang, Y. Lin, J. Zhu and F. Wang, Ceram. Int., 2012, 38, 1745-1749.
- 7 J. Wu, C.-W. Nan, Y. Lin and Y. Deng, *Phys. Rev. Lett.*, 2002, **89**, 217601.
- 8 W. Tuichai, S. Danwittayakul, S. Maensiri and P. Thongbai, *RSC Advances*, 2016, **6**, 5582-5589.
- 9 X.-g. Zhao, P. Liu, Y.-C. Song, A.-p. Zhang, X.-m. Chen and J.-p. Zhou, *Phys. Chem. Chem. Phys.*, 2015, **17**, 23132-23139.
- 10 W. Dong, W. Hu, A. Berlie, K. Lau, H. Chen, R. L. Withers and Y. Liu, *ACS Applied Materials & Interfaces*, 2015, **7**, 25321-25325.
- 11 Y. Q. Wu, X. Zhao, J. L. Zhang, W. B. Su and J. Liu, *Appl. Phys. Lett.*, 2015, **107**, 242904.
- 12 T. Nachaithong, P. Thongbai and S. Maensiri, J. Eur. Ceram. Soc., 2017, 37, 655-660.
- 13 J. Li, F. Li, Y. Zhuang, L. Jin, L. Wang, X. Wei, Z. Xu and S. Zhang, *J. Appl. Phys.*, 2014, **116**, 074105.
- 14 J. Li, F. Li, C. Li, G. Yang, Z. Xu and S. Zhang, Sci Rep, 2015, 5, 8295.
- 15 Y. Song, X. Wang, Y. Sui, Z. Liu, Y. Zhang, H. Zhan, B. Song, Z. Liu, Z. Lv, L. Tao and J. Tang, *Scientific Reports*, 2016, **6**, 21478.
- 16 Y. Song, X. Wang, X. Zhang, Y. Sui, Y. Zhang, Z. Liu, Z. Lv, Y. Wang, P. Xu and B. Song, *Journal of Materials Chemistry C*, 2016, **4**, 6798-6805.
- 17 G. Liu, H. Fan, J. Xu, Z. Liu and Y. Zhao, RSC Advances, 2016, 6, 48708-48714.
- 18 C. Wang, N. Zhang, Q. Li, Y. Yu, J. Zhang, Y. Li and H. Wang, *J. Am. Ceram. Soc.*, 2015, **98**, 148-153.
- 19 Y. Y. Liu, X. M. Chen, X. Q. Liu and L. Li, Appl. Phys. Lett., 2007, 90, -.
- 20 T. Adams, D. Sinclair and A. West, Phys. Rev. B, 2006, 73, 094124.
- 21 M. Li, D. C. Sinclair and A. R. West, *J. Appl. Phys.*, 2011, **109**, 084106.
- 22 M. Li, A. Feteira and D. C. Sinclair, *J. Appl. Phys.*, 2009, **105**, 114109.
- 23 P. Thongbai, T. Yamwong and S. Maensiri, *Appl. Phys. Lett.*, 2009, **94**, 152905.
- 24 K. Meeporn, N. Chanlek and P. Thongbai, *RSC Advances*, 2016, **6**, 91377-91385.
- 25 J. Li, Z. Xu, F. Li, X. Zhu and S. Zhang, RSC Advances, 2016, 6, 20074-20080.
- 26 P. Lunkenheimer, S. Krohns, S. Riegg, S. G. Ebbinghaus, A. Reller and A. Loidl, *The European Physical Journal Special Topics*, 2010, **180**, 61-89.
- 27 R. Schmidt, M. C. Stennett, N. C. Hyatt, J. Pokorny, J. Prado-Gonjal, M. Li and D. C. Sinclair, *J. Eur. Ceram. Soc.*, 2012, **32**, 3313-3323.
- 28 K.-C. Kao, *Dielectric phenomena in solids : with emphasis on physical concepts of electronic processes*. Academic Press: Amsterdam; Boston, 2004; p xvii, 581 p.
- 29 M. Li, Z. Shen, M. Nygren, A. Feteira, D. C. Sinclair and A. R. West, *J. Appl. Phys.*, 2009, **106**, 104106.
- 30 S. Krohns, P. Lunkenheimer, S. G. Ebbinghaus and A. Loidl, *J. Appl. Phys.*, 2008, **103**, 084107.

## **CHAPTER 3**

# Surface Barrier Layer Effect in (In+Nb) Co-Doped TiO<sub>2</sub> Ceramics: An Alternative Route To Design Low Dielectric Loss

#### 3.1 Introduction

A large number of giant-dielectric materials with very high dielectric permittivities (ε'≈10<sup>3</sup>-10<sup>6</sup>) have been investigated because giant-dielectric materials are considered potentially useful in various electronic applications as well as in high energy-dense storage applications. 1-14 Recently, Hu et al. 15 reported (In+Nb) co-doped rutile-TiO<sub>2</sub> ceramics as a novel material with excellent dielectric performance. The dielectric permittivity (ε') of (In<sub>0.5</sub>Nb<sub>0.5</sub>)<sub>x</sub>Ti<sub>1-x</sub>O<sub>2</sub> (INTO) ceramics increased with increasing dopant concentration (x), while the dielectric loss tangent  $(\tan \delta)$  remained very low. Temperature independence of  $\epsilon'$  over the range of 80–450 K was reported for this material. This discovery stimulated research in the field of giant dielectric materials based on TiO2 for application in high-performance capacitors due to its abundance and low toxicity. 16-26 According to the nominal composition of  $(In_{0.5}Nb_{0.5})_xTi_{1-x}O_2$ , the complex stoichiometry of  $(\ln_x^{3+} \text{Nb}_x^{5+} \text{Ti}_x^{3+}) \text{Ti}_{1-3x}^{4+} \text{O}_{2-x/2}$  produced defect clusters, giving rise to very high  $\epsilon'$  values. The electrons created by the reduction of Ti<sup>4+</sup> to Ti<sup>3+</sup> resulting from Nb<sup>5+</sup> doping ions were confined by the presence of In<sup>3+</sup> in a rutile structure. 15-16 Without In<sup>3+</sup> doping ions. electrons would delocalize and lead to very high tanδ values, usually larger than 1.0 at low frequencies. This mechanism was referred to as the electron-pinned defect-dipole (EPDD) model.

It was found that the electrode effect has slight influence on the overall dielectric response of INTO ceramics.<sup>15</sup> This was characterized by using different electrode materials, i.e., sputtered-Au and Ag-painted electrodes. High  $\varepsilon'$  and low tan $\delta$  values of INTO ceramics were obtained by using these two types of electrode materials. Most recently, Wu et al. found that extremely frequency-dependent  $\varepsilon'$  in a low frequency range (1 mHz-1 kHz) with very high tanδ value was observed in the INTO sample that was prepared by cutting sample from the core part of the sintered block.<sup>27</sup> Notably, after annealing in air, a largely frequency-independent giant  $\varepsilon'$  value over a wide frequency range was achieved. Very low tanδ was also obtained. It was suggested that the extremely high  $\varepsilon'$  in a low-frequency range was caused by the electrode effect, i.e., the existence of a non-Ohmic sample-electrode contact. Accordingly, the greatly decreased tanδ value was attributed to a large increase in the grain boundary resistance.<sup>27</sup> Indeed, the surface barrier layer capacitor (SBLC) effect may have also an effect on the reduction in  $tan\delta$  in this case. Unfortunately, the SBLC effect on a  $tan\delta$  value of INTO ceramics has never been reported. Besides the EPDD model, the internal barrier layer capacitor (IBLC) effect was also widely proposed as the exact origin, 23, 27-29 creating significant confusion. In addition to the EPDD and IBLC models, several factors have significant influences on the dielectric properties of TiO<sub>2</sub>-based materials, including the electrode effect (for Ga+Nb co-doped TiO<sub>2</sub>) and polaron hopping polarization (for INTO and Ga+Nb co-doped TiO<sub>2</sub>) as well as a gradient distribution in Ti<sup>3+</sup> concentration (for Al+Nb co-doped TiO<sub>2</sub>).<sup>18-</sup> 19, 30

To achieve ultra-high  $\varepsilon'$  values in TiO<sub>2</sub>-based ceramics, long sintering times ( $\geq$ 10 h) at high temperatures ( $\geq$ 1400 °C) were required when using a conventional solid state reaction (CSSR) method.<sup>15, 18-23, 27-32</sup> By using fine nano-powders, ultra-high  $\varepsilon'$  values of

INTO ceramics may be accomplished by sintering for very short times. Furthermore, fine nano-powders obtained via a wet chemical route usually offer the possibility of closer stoichiometric control and good dispersion of dopants.<sup>1</sup> Unfortunately, since the giant dielectric properties of INTO ceramics were discovered, the giant dielectric behavior of INTO prepared by wet chemical routes has rarely been reported.<sup>33</sup>

In this work, a simple sol-gel method was used to synthesize INTO ceramics to obtain dense INTO ceramics with good dispersion of co-dopants. The effects of SBLC and non-Ohmic sample-electrode contact on the giant dielectric properties of INTO ceramics were investigated. High performance giant-dielectric INTO ceramics were successfully accomplished by eliminating the electrode effect coupled with creating a resistive outer-surface layer to create a blocking effect.

## 3.2 Experimental details

 $(In_{0.5}Nb_{0.5})_xTi_{1-x}O_2$  (INTO) ceramics with x=0.005, 0.01, 0.015, and 0.025 were prepared by a simple sol–gel method.  $C_{16}H_{28}O_6Ti$  (Sigma–Aldrich),  $In_3N_3O_9\cdot xH_2O$  (Sigma–Aldrich, 99.999%), NbCl<sub>5</sub> (Sigma–Aldrich, >99.9%), deionized water, and citric acid were used as the starting raw materials. First, stoichiometric amounts of  $C_{16}H_{28}O_6Ti$ ,  $In_3N_3O_9\cdot xH_2O$ , and NbCl<sub>5</sub> were dissolved in 50 mL of an aqueous solution of citric acid with constant stirring at 130 °C until a viscous gel was obtained. Second, the gel was dried at 350 °C for 30 min. Then, all dried gels were calcined at 1000 °C for 6 h. Next, the calcined powders were pressed into pellets with 9.5 mm in diameter and ~1.2 mm in thickness. Finally, these pellets were sintered at 1500 °C for 1 h using a heating rate of 2 °C/min followed by natural furnace cooling to room temperature. The densities of the sintered ceramics were measured using Archimedes' method.

X–ray diffraction (XRD) (PANalytical, EMPYREAN) and scanning electron microscopy (SEM) (SEC, SNE4500M) were used to characterize the phase composition and microstructure of INTO ceramics. The elemental distribution in the INTO ceramics was examined using field–emission scanning electron microscopy (FE–SEM) with energy–dispersive X–ray analysis (EDX) (HITACHI SU8030, Japan). X–ray Absorption Near Edge Structure (XANES) spectra were collected at the SUT–NANOTEC–SLRI XAS beamline (BL5.2) (electron energy of 1.2 GeV; bending magnet; beam current 80-150 mA; 1.1 to  $1.7 \times 10^{11}$  photon s<sup>-1</sup>) at the Synchrotron Light Research Institute (SLRI), Nakhon Ratchasima, Thailand. Details of this characterization technique and analysis were given elsewhere. The normalized XANES data were processed and analyzed after background subtraction in the pre–edge and post–edge region using ATHENA software included in an IFEFFIT package. The superposition of the pre–edge and post–edge region using ATHENA software included in an IFEFFIT package.

To prepare electrodes for dielectric measurement, all as–sintered ceramics were carefully polished to obtain smooth surfaces. Both sides of surfaces were coated with Au at a current of 25 mA for 8 min using a Polaron SC500 sputter coating unit. This set of polished samples was referred to as the "P1–samples". The dielectric properties were measured using a KEYSIGHT E4990A Impedance Analyzer over frequency and temperature ranges of  $40-10^6$  Hz and -70-220 °C, respectively. To study the effect of a surface layer on the dielectric properties, the initial electrode of all P1–samples was removed (sample thickness was decreased from  $\approx 1.23$  to  $\approx 1.14$  mm for the x=0.005 sample) and then annealed in air at 1200 °C for 1 h. Both sides of the surface were

sputtered with Au under the same condition. This set of samples was referred to as the "annealed–samples". Finally, a thin layer of the outer surfaces of the annealed–samples was removed (sample thickness was reduced from ≈1.14 to ≈1.09 mm) and the samples coated with Au. The last set of samples was referred to as the "P2–samples". The effect of sample thickness on the apparent dielectric properties was also investigated using Ag paint as an electrode material.

#### 3.3 Results and discussion

Figures 1(a) and (b) show SEM images of  $(\ln_{0.5} \text{Nb}_{0.5})_x \text{Ti}_{1-x} \text{O}_2$  powders with x=0.01 and 0.015, respectively. Particle sizes were nearly spherical and about 100–300 nm in diameter. Figure 1(c) shows the XRD patterns of INTO powders and sintered ceramics. The main phase of rutile— $\text{TiO}_2$  (JCPDS 21–1276) was observed in all samples with no impurities. This indicates that both  $\ln^{3+}$  and  $\ln^{5+}$  dopants can likely be substituted into the rutile— $\text{TiO}_2$  structure. The diffraction peaks in all XRD patterns were perfectly indexed based on a tetragonal structure. These results are similar to those reported for ( $\ln^{5+} \text{Nb}$ ) co—doped  $\text{TiO}_2$  ceramics that were prepared by a CSSR method.  $\ln^{5+} \text{Ns}_2$  The lattice parameters ( $\ln^{5+} \text{Ns}_2$  and  $\ln^{5+} \text{Ns}_2$  values) did not change when the dopant concentration was increased. This may have been due to the small amount of dopants used.

As shown in Fig. 2, the microstructure of sintered ceramics was dense. The mean grain size of  $(In_{0.5}Nb_{0.5})_xTi_{1-x}O_2$  ceramics slightly decreases as the dopant concentration increased. The relative densities of the  $(In_{0.5}Nb_{0.5})_xTi_{1-x}O_2$  ceramics with x=0.005, 0.01, 0.015, and 0.025 were approximately 97.6, 91.5, 92.9, and 94.4 %, respectively. The distributions of all the elements in  $(In_{0.5}Nb_{0.5})_xTi_{1-x}O_2$  ceramics were characterized using an SEM–mapping technique. As revealed in Figs. 2(a–c), the dopants were homogeneously dispersed in the microstructure.

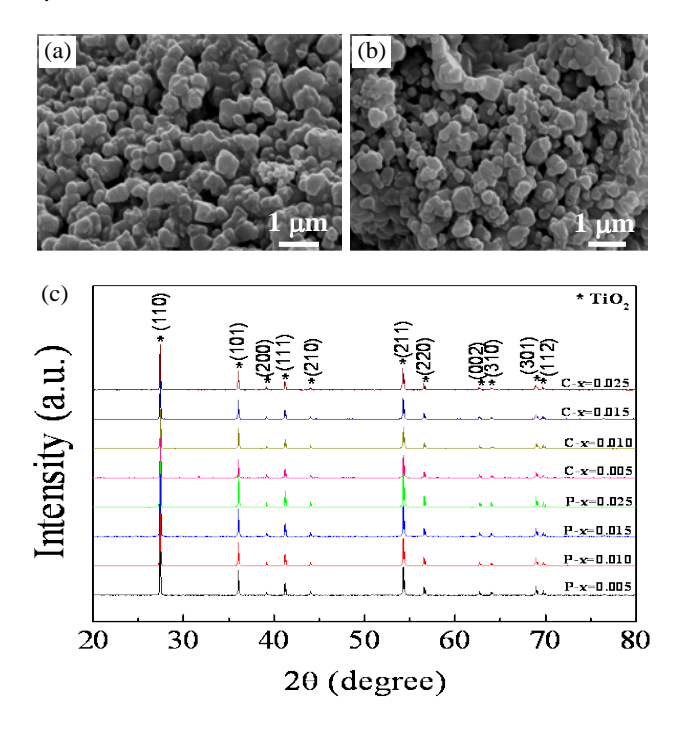


**Fig. 1** SEM images of INTO powders with (a) x=0.01 and (b) x=0.015. (c) XRD patterns of INTO powders and sintered ceramics: P and C denote powder and sintered ceramics, respectively.

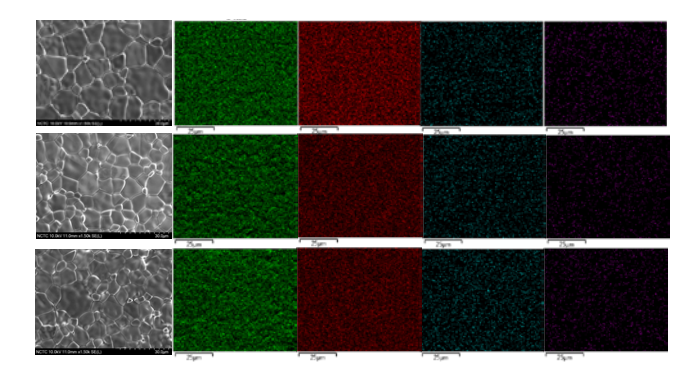
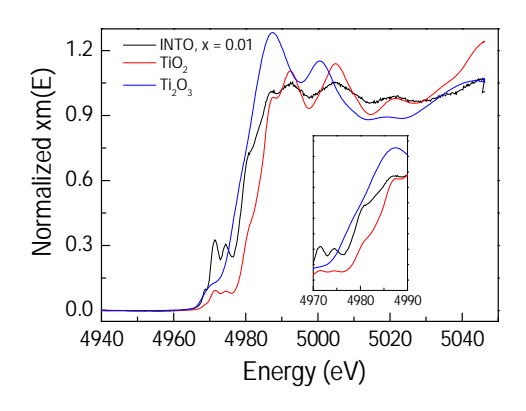


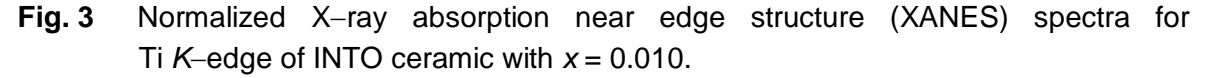
Fig. 2 Element mapping of INTO ceramics with (a) x = 0.010, (b) x = 0.015, and (c) x = 0.025.

Figure 3 demonstrates normalized Ti K-edge XANES spectra of the INTO ceramic with x = 0.01 as well as the standard samples of  $Ti_2O_3$  ( $Ti^{3+}$ ) and  $TiO_2$  ( $Ti^{4+}$ ). As clearly shown in the inset, the edge energy position is between  $Ti_2O_3$  and  $TiO_2$ , but close to  $TiO_2$  standard. This indicates the existence of a relatively small amount of  $Ti^{3+}$  compared to that of the major component of  $Ti^{4+}$ . A very small variation in the edge energy value of Ti K-edge was detected. Energy calibration using Ti-foil was carried out throughout the experiments during the XANES measurements. The measured spectra would have corrected edge energy, particularly the edge energy of  $TiO_2$  and  $Ti_2O_3$  standards. Therefore, a very small shift of the edge value was confirmed to be caused by the existence of  $Ti^{3+}$  the INTO ceramic. Quantitative analysis of different oxidation states was performed using an empirical edge-shift calculation making comparisons with known standard samples. The maximum value of the first derivative of edge region was used to calculate the edge value. The amount of  $Ti^{3+}$  can be calculated:

% of 
$$Ti^{3+}$$
 for each sample =  $\left(1 - \frac{\Delta E \text{ of sample}}{\Delta E \text{ of } Ti^{3+} \text{ and } Ti^{4+} \text{ standard}}\right) \times 100\%$ , (1)

where,  $\Delta E$  is a difference of edge value of a sample compared with a Ti<sup>3+</sup> standard. Surprisingly, the ratio of Ti<sup>3+</sup>/Ti<sup>4+</sup> in the INTO ceramic with x=0.01 was found to be 25.41%, which is much larger than the theoretical value. The amount of Ti<sup>3+</sup> should be  $\approx$ 0.5%. Such a high Ti<sup>3+</sup>/Ti<sup>4+</sup> ratio was likely caused by the existence of oxygen vacancies following the O<sup>2-</sup>(*lattice*)  $\rightarrow$  1/2O<sub>2</sub>(g) + 2e<sup>-</sup>. The existence of a larger amount of Ti<sup>3+</sup> should have a great influence on the dielectric properties of the sintered INTO ceramics.





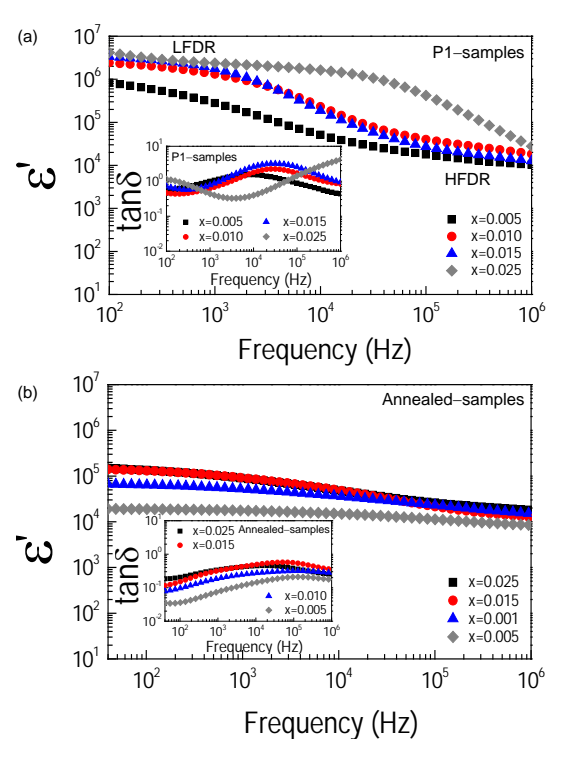
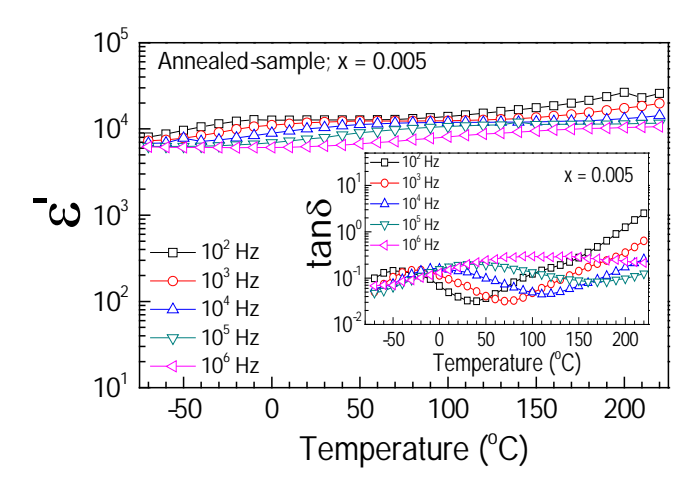


Fig. 4 RT frequency dependence of  $\epsilon'$  of INTO ceramics: (a) P1-samples and (b) annealed-samples. Insets show their  $\tan\delta$  values as a function of frequency at RT.

The dielectric properties at room temperature (RT) of the P1-samples are shown in Fig. 4(a) and its inset. In the low frequency range, ε' increases with increasing co-dopant concentrations from x=0.005 to 0.025. At 1 kHz,  $\epsilon'$  values of the INTO ceramics with  $x=0.005, 0.01, 0.015, \text{ and } 0.025 \text{ were about } 2.8\times10^5, 1.3\times10^6, 1.8\times10^6, \text{ and } 2.4\times10^6,$ respectively. These values are very much larger than for the pure-TiO2 ceramic (ε'≈250).16 tanδ values in a low-frequency range are quite large, > 0.1, over a measured frequency range [inset of Fig. 4(a)]. This extremely enhanced  $\varepsilon'$  value is much larger than those of other giant dielectric materials such as CaCu<sub>3</sub>Ti<sub>4</sub>O<sub>12</sub> 9, 14, 35 and La<sub>2-x</sub>Sr<sub>x</sub>NiO<sub>4</sub>. 36 There are at least two giant dielectric responses observed in the P1-samples. Low and high-frequency plateaus corresponding to ε'≈10<sup>6</sup>-10<sup>7</sup> and ≈10<sup>4</sup>, respectively are seen in Fig. 4(a). A step-like decrease in  $\varepsilon'$  between the first and second plateaus was observed and tended to shift to higher frequencies as the co-dopant concentration was increased. This was accompanied by a movement of the relaxation  $tan\delta$ -peak [inset of Fig. 4(a)]. The dielectric response of the second plateau was still too large (≈10<sup>4</sup>). A comprehensive study on the origin of the low-frequency dielectric response (LFDR) will be discussed in the last section. However, the origin of the primary polarization that gives rise to a largely temperature— and frequency-independent giant  $\varepsilon'$  value, which was indicated by the relatively high-frequency dielectric response (HFDR), is beyond to scope of this work. Nowadays, EPDD and IBLC models have been widely used to describe the primary giant-dielectric response in co-doped TiO2 ceramics. According to the EPDD model, the giant dielectric response was resulted from the formation of large defect dipole clusters in

the grain interiors, in which free electrons were confined in the special local–structure.  $^{15, 19, 21-22, 33}$  For the IBLC model, the giant dielectric response in INTO and other co–doped  $TiO_2$  ceramics was thought to be caused by the interfacial polarization at insulating grain boundaries.  $^{23-24, 26-28, 37}$ 

After annealing the P1-samples in air, the overall giant dielectric properties of the INTO ceramics were significantly altered [Fig. 4(b)]. The first plateau corresponding to the LFDR was not observed in the annealed INTO ceramic with x=0.005, while the first plateau of other samples with higher dopant concentration remarkably decreased from  $10^6 - 10^7$  to  $10^{5}$ . This indicated that annealing can cause frequency-dependent  $\varepsilon'$  value in the range of  $10^2-10^6$  Hz. As shown in the inset of Fig. 4(b),  $tan\delta$  of all the annealed samples was largely reduced compared to that of the P1-samples. It is worth noting that the low-frequency tanδ values of other giant dielectric materials such as CaCu<sub>3</sub>Ti<sub>4</sub>O<sub>12</sub>, La<sub>1.6</sub>Sr<sub>0.4</sub>NiO<sub>4</sub>, (Li+Ti) co-doped NiO, and A<sub>2</sub>FeNbO<sub>6</sub> (A=Ba, Sr. and Ca) ceramics are usually too large ( $tan\delta >> 0.1$  at 1 kHz), 3, 5, 13-14, 35-36 According to previous work, using an oxalate chemical solution combined with spark plasma sintering (SPS), a 1.0% INTO ceramic exhibited a high  $\varepsilon' \approx 0.9 \times 10^4$  and  $\tan \delta \approx 0.2$  at RT and 40 Hz. 33 Interestingly, the annealed INTO ceramic with x=0.005 exhibited a frequency-independent  $\varepsilon'$  value of  $\approx 1.9 \times 10^4$  with a very low  $\tan \delta \approx 0.035$  at 40 Hz. Furthermore, as shown in Fig. 5,  $\varepsilon'$  of the annealed INTO ceramics with x=0.005 was slight dependent of temperature, while  $tan\delta$  at 1 kHz was lower than 0.1 over a wide temperature range [inset of Fig. 5]. This indicated that a simple sol-gel route is an effective wet chemical route for preparing high performance INTO ceramics.



**Fig. 5** Temperature dependence of  $\varepsilon'$  at different frequencies for annealed INTO samples with x = 0.005.

As shown in Fig. 6(a), the giant LFDR of the P1 and P2-samples was likely associated with the electrode effect. This is because the giant LFDR and the related large value of  $\tan\delta$  can be almost completely eliminated by annealing. Then, it can be deliberately recreated by removing the outer surfaces of the annealed-sample, at while the grain boundary response cannot be vanished or be recovered by removing outer surface layers. Furthermore,  $\epsilon'$  of the P2-sample is larger than that of the P1-sample. A step-like decrease in  $\epsilon'$  of the P2-sample shifts to higher frequency, indicating the stronger polarization intensity. Actually, the frequency dependence of  $\epsilon'$  and  $\tan\delta$  value of

the P2–sample are very similar to that reported in previous work for 5%(In+Nb) co–doped ceramic, Fig. 4 of Ref <sup>39</sup>. This giant  $\varepsilon'$  was described as the electrode effect.

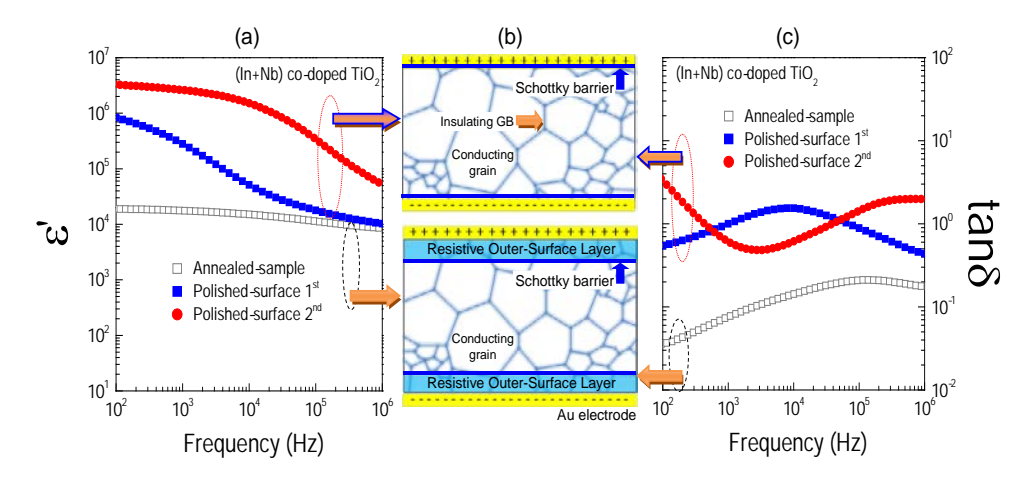


Fig. 6 Frequency dependence of (a)  $\varepsilon'$  and (c)  $\tan\delta$  at RT for the P1, annealed and P2-INTO samples with x=0.005. (b) Schematic images for the effects of Schottky barriers at the interfaces between sample–electrode and resistive outer surface–conductive inner core on the dielectric properties.

As shown in Fig. 7, the electrode effect in the INTO ceramic with x = 0.005 was confirmed. By using Ag–paint electrode, the apparent  $\varepsilon'$  value decreased with decreasing sample thickness. This observation can be explained by roughly assuming the same depletion–layer contribution to the measured capacitance in all sample thickness. To calculate  $\varepsilon'$ , the measured capacitance ( $C_p$ ) value was divided by the empty capacitance ( $C_0 = \varepsilon_0 A/d$ ), which was larger for a thinner sample (smaller d value). As a result, a lower apparent  $\varepsilon'$  value was achieved in a thinner sample.

Generally, there are at least two types of polarization artifacts related to Schottky barriers near the surface region. These are referred to as the electrode and SBLC effects. The former is related to the formation of Schottky barriers between a semiconducting sample surface and metal electrodes used. This results in a non-Ohmic sample-electrode contact. The Schottky barrier height primarily depends on the different work functions between the metal electrode and electron affinity of the semiconductor. The latter effect can usually occur between a resistive outer-surface layer and a semiconducting inner core. In this case, the Schottky barrier height due to the electrode effect cannot be formed. In the current study, the semiconducting surface (as well as the inner core) caused by the existence of Ti3+ in the P1-INTO ceramics was confirmed by a XANES technique [Fig. 3]. Thus, the Schottky barrier height can be formed at the interface between the Au electrode and semiconducting surface of the P1-sample. After annealing, the electrode effect disappeared because the semiconducting surface had become a resistive surface, which was primarily due to filling of oxygen vacancies on the surface. The Schottky barrier height cannot be formed at the interface between an insulating surface and Au-electrode.

We now turn to discuss the greatly reduced  $\tan\delta$  value in the annealed–sample. After the outer surface of the annealed sample was removed,  $\tan\delta$  greatly increased [Fig. 6(c)]. At 40 Hz,  $\tan\delta$  of the P2–sample increased by two orders of magnitude. The very low  $\tan\delta$ 

value of the annealed–sample was primarily attributed to the highly resistive outer–surface layer. If such a reduced  $tan\delta$  value was dominated by an enhanced grain boundary resistance ( $R_{gb}$ ) as a result of annealing, further removing surface material would not change the  $tan\delta$  value. Based on the experimental results in the current work, a low  $tan\delta$  value in the annealed sample cannot be due to the blocking effect of insulating grain boundaries. Instead, the SBLC effect is a key factor for obtaining a low  $tan\delta$  value. According to the first report, the strong electrode effect was not observed in the INTO ceramic prepared by a solid state reaction method. A resistive outer surface, i.e., SBLC effect, was not found. This may be due to the small amount of tandata in the sintered samples. Different preparation methods may result in homogeneous distribution of dopants and/or other defects in the INTO ceramic. Schematic images for the effects of Schottky barriers at the interfaces between sample–electrode and resistive outer surface–conductive inner core on the dielectric properties of INTO ceramics prepared by a simple sol–gel method were clearly shown in Fig. 6(b).

Although investigation on possible origins of the primary polarization contributing to the giant  $\varepsilon'$  is beyond the scope of this work, such large  $\tan\delta$  values of the P1 and P2-samples can be reasonably described by the EPDD or IBLC effect. For EPDD effect, substitution of Nb<sup>5+</sup> into TiO<sub>2</sub> can produce free electrons by reducing Ti<sup>4+</sup> to Ti<sup>3+</sup>, following the relations  $2TiO_2 + Nb_2O_5 \xrightarrow{4TiO_2} 2Ti'_{Ti} + 2Nb_{Ti}^{\bullet} + 8O_O + 1/2O_2$  and  $Ti^{4+} + e \rightarrow Ti'^{3+}$ . Doping TiO<sub>2</sub> with In<sup>3+</sup> requires oxygen vacancies for charge compensation,  $In_2O_3 \xrightarrow{2TiO_2} 2In'_{Ti} + V_O^{\bullet \bullet} + 3O_O$ . High  $\epsilon'$  and low tan $\delta$  can be obtained when triangular shaped  $In_2^{3+}V_O^{\bullet\bullet}Ti^{3+}$  and diamond shaped  $Nb_2^{5+}Ti^{3+}A_{Ti}$  (A=In<sup>3+</sup>, Ti<sup>3+</sup>, or Ti<sup>4+</sup>) intrinsic defect complexes are strongly correlated or overlapped. 15 Thus, if the EPDDs can be formed in our INTO samples, a large tanδ value of the P1-samples can be ascribed to high concentration of excess free electrons as detected in the XANES spectrum. For the IBLC effect, conduction of free charges in a semiconducting grain was inhibited by insulating grain boundaries, which consisted of an amorphous crystalline structure and/or relatively complete oxidation regions.<sup>27</sup> In this case, a large tanδ value of the P1-samples was ascribed to a small value of R<sub>ab</sub>≈2500 Ω.cm, which was calculated from an impedance spectroscopy (not presented).

In the current study, an alternative route to achieve low  $tan\delta$  in INTO ceramics was clearly shown and can be easily performed. The SBLC effect was suggested to be one of the most important factors contributing to the apparent low  $tan\delta$  values in INTO ceramics. We believe that this work provides comprehensive guidance for improvement of dielectric properties of INTO ceramics by creating resistive outer–surface layer and/or inhibiting the formation of non–Ohmic sample–electrode contact. Furthermore, this investigation may open a new outer–surface design approach for other co–doped  $TiO_2$  ceramic systems and dielectric films.

## 3.4 Conclusion

INTO ceramics were successfully prepared using a simple sol–gel method. A dense microstructure with homogeneous dispersion of In<sup>3+</sup> and Nb<sup>5+</sup> co–doping ions in rutile–TiO<sub>2</sub> ceramics was obtained using a short sintering time for 1 h. The presence of Ti<sup>3+</sup> in INTO ceramics was confirmed by a XANES technique. The Ti<sup>3+</sup>/Ti<sup>4+</sup> ratio was found

to be larger than the theoretical value based on the concentration of the Nb<sup>5+</sup> dopant, which may have been due to the existence of oxygen vacancies during sintering at high temperature. An extremely high low–frequency  $\epsilon'$  response ( $\epsilon' \approx 10^6 - 10^7$ ) caused by the formation of high Schottky barriers at the sample–electrode contact, which can be eliminated by annealing in air. This can improve dielectric properties with a very low  $\tan \delta \approx 0.035$  and a high  $\epsilon'$  value of  $\approx 1.9 \times 10^4$  with small temperature and frequency dependencies. It was suggested that the SBLC effect may be one of the most important factors contributing to the apparent low  $\tan \delta$  and frequency–independent  $\epsilon'$ . We believe that this work provides comprehensive guidance for the improvement of dielectric properties of  $TiO_2$ –based ceramics by eliminating the non–Ohmic sample–electrode contact and forming resistive outer surface layers.

#### References

- <sup>1</sup>J. Liu, Y. Sui, C.-g. Duan, W.-N. Mei, R. W. Smith, and J. R. Hardy, "CaCu<sub>3</sub>Ti<sub>4</sub>O<sub>12</sub>: Low Temperature Synthesis by Pyrolysis of an Organic Solution," *Chem. Mater.* **18** [16] 3878-82 (2006).
- <sup>2</sup>C. C. Wang, and L. W. Zhang, "Surface-layer effect in CaCu<sub>3</sub>Ti<sub>4</sub>O<sub>12</sub>," *Appl. Phys. Lett.* **88** [4] 042906 (2006).
- <sup>3</sup>S. Ke, H. Fan, and H. Huang, "Dielectric relaxation in A<sub>2</sub>FeNbO<sub>6</sub> (A perovskite ceramics," *Journal of Electroceramics* **22** [1-3] 252-6 (2007).
- = Ba, Sr,
- <sup>4</sup>L. Liu, H. Fan, P. Fang, and L. Jin, "Electrical heterogeneity in CaCu<sub>3</sub>Ti<sub>4</sub>O<sub>12</sub> ceramics fabricated by sol–gel method," *Solid State Commun.* **142** [10] 573-6 (2007).
- <sup>5</sup>P. Thongbai, S. Tangwancharoen, T. Yamwong, and S. Maensiri, "Dielectric relaxation and dielectric response mechanism in (Li, Ti)-doped NiO ceramics," *J. Phys.: Condens. Matter* **20** [39] 395227 (2008).
- <sup>6</sup>L. Liu, H. Fan, P. Fang, and X. Chen, "Sol–gel derived CaCu<sub>3</sub>Ti<sub>4</sub>O<sub>12</sub> ceramics: Synthesis, characterization and electrical properties," *Mater. Res. Bull.* **43** [7] 1800-7 (2008).
- <sup>7</sup>M. Li, A. Feteira, and D. C. Sinclair, "Relaxor ferroelectric-like high effective permittivity in leaky dielectrics/oxide semiconductors induced by electrode effects: A case study of CuO ceramics," *J. Appl. Phys.* **105** [11] 114109 (2009).
- <sup>8</sup>Q. Zheng, H. Fan, and C. Long, "Microstructures and electrical responses of pure and chromium-doped CaCu<sub>3</sub>Ti<sub>4</sub>O<sub>12</sub> ceramics," *J. Alloys Compd.* **511** [1] 90-4 (2012).
- <sup>9</sup>L. Singh, U. S. Rai, and K. D. Mandal, "Dielectric, modulus and impedance spectroscopic studies of nanostructured CaCu<sub>2.70</sub>Mg<sub>0.30</sub>Ti<sub>4</sub>O<sub>12</sub> electro-ceramic synthesized by modified sol–gel route," *J. Alloys Compd.* **555** 176-83 (2013).
- <sup>10</sup>J. Boonlakhorn, P. Kidkhunthod, and P. Thongbai, "A novel approach to achieve high dielectric permittivity and low loss tangent in CaCu<sub>3</sub>Ti<sub>4</sub>O<sub>12</sub> ceramics by co-doping with Sm<sup>3+</sup> and Mg<sup>2+</sup> ions," *J. Eur. Ceram. Soc.* **35** [13] 3521-8 (2015).
- <sup>11</sup>J. Shi, H. Fan, X. Liu, Y. Ma, and Q. Li, "Bi deficiencies induced high permittivity in lead-free BNBT–BST high-temperature dielectrics," *J. Alloys Compd.* **627** 463-7 (2015).
- $^{12}$ Z. Liu, H. Fan, and M. Li, "High temperature stable dielectric properties of  $(K_{0.5}Na_{0.5})_{0.985}Bi_{0.015}Nb_{0.99}Cu_{0.01}O_3$  ceramics with core-shell microstructures," *Journal of Materials Chemistry C* **3** [22] 5851-8 (2015).
- <sup>13</sup>J. Li, K. Wu, R. Jia, L. Hou, L. Gao, and S. Li, "Towards enhanced varistor property and lower dielectric loss of CaCu<sub>3</sub>Ti<sub>4</sub>O<sub>12</sub> based ceramics," *Materials & Design* **92** 546-51 (2016).

- <sup>14</sup>L. Sun, R. Zhang, Z. Wang, E. Cao, Y. Zhang, and L. Ju, "Microstructure and enhanced dielectric response in Mg doped CaCu<sub>3</sub>Ti<sub>4</sub>O<sub>12</sub> ceramics," *J. Alloys Compd.* **663** 345-50 (2016).
- <sup>15</sup>W. Hu, Y. Liu, R. L. Withers, T. J. Frankcombe, L. Norén, A. Snashall, M. Kitchin, P. Smith, B. Gong, H. Chen, J. Schiemer, F. Brink, and J. Wong-Leung, "Electron-pinned defect-dipoles for high-performance colossal permittivity materials," *Nat. Mater.* **12** [9] 821-6 (2013).
- <sup>16</sup>C. C. Homes, and T. Vogt, "Colossal permittivity materials: Doping for superior dielectrics," *Nat. Mater.* **12** [9] 782-3 (2013).
- <sup>17</sup>C. Wang, N. Zhang, Q. Li, Y. Yu, J. Zhang, Y. Li, and H. Wang, "Dielectric Relaxations in Rutile TiO<sub>2</sub>," *J. Am. Ceram. Soc.* **98** [1] 148-53 (2015).
- <sup>18</sup>W. Hu, K. Lau, Y. Liu, R. L. Withers, H. Chen, L. Fu, B. Gong, and W. Hutchison, "Colossal Dielectric Permittivity in (Nb+Al) Codoped Rutile TiO<sub>2</sub> Ceramics: Compositional Gradient and Local Structure," *Chem. Mater.* **27** [14] 4934-42 (2015).
- <sup>19</sup>X.-g. Zhao, P. Liu, Y.-C. Song, A.-p. Zhang, X.-m. Chen, and J.-p. Zhou, "Origin of colossal permittivity in (In<sub>1/2</sub>Nb<sub>1/2</sub>)TiO<sub>2</sub> via broadband dielectric spectroscopy," *Phys. Chem. Chem. Phys.* **17** [35] 23132-9 (2015).
- <sup>20</sup>W. Tuichai, P. Srepusharawoot, E. Swatsitang, S. Danwittayakul, and P. Thongbai, "Giant dielectric permittivity and electronic structure in (Al + Sb) co-doped TiO<sub>2</sub> ceramics," *Microelectron. Eng.* **146** 32-7 (2015).
- <sup>21</sup>Z. Li, J. Wu, and W. Wu, "Composition dependence of colossal permittivity in (Sm<sub>0.5</sub>Ta<sub>0.5</sub>)<sub>x</sub>Ti<sub>1-x</sub>O<sub>2</sub> ceramics," *Journal of Materials Chemistry C* **3** [35] 9206-16 (2015).
- <sup>22</sup>X. Cheng, Z. Li, and J. Wu, "Colossal permittivity in ceramics of TiO<sub>2</sub> Co-doped with niobium and trivalent cation," *Journal of Materials Chemistry A* **3** [11] 5805-10 (2015).
- <sup>23</sup>J. Li, F. Li, Y. Zhuang, L. Jin, L. Wang, X. Wei, Z. Xu, and S. Zhang, "Microstructure and dielectric properties of (Nb -dopectrutile TiO<sub>2</sub> ceramics," *J. Appl. Phys.* **116** [7] 074105 (2014).
- <sup>24</sup>G. Liu, H. Fan, J. Xu, Z. Liu, and Y. Zhao, "Colossal permittivity and impedance analysis of niobium and aluminum co-doped TiO<sub>2</sub> ceramics," *RSC Advances* **6** [54] 48708-14 (2016).
- <sup>25</sup>J. Li, Z. Xu, F. Li, X. Zhu, and S. Zhang, "SiO<sub>2</sub>-Ti<sub>0.98</sub>In<sub>0.01</sub>Nb<sub>0.01</sub>O<sub>2</sub> composite ceramics with low dielectric loss, high dielectric permittivity and an enhanced breakdown electric field," *RSC Advances* **6** [24] 20074-80 (2016).
- <sup>26</sup>Y. Song, X. Wang, X. Zhang, Y. Sui, Y. Zhang, Z. Liu, Z. Lv, Y. Wang, P. Xu, and B. Song, "The contribution of doped-Al to the colossal permittivity properties of Al<sub>x</sub>Nb<sub>0.03</sub>Ti<sub>0.97-x</sub>O<sub>2</sub> rutile ceramics," *J. Mater. Chem. C* (2016).
- <sup>27</sup>Y. Q. Wu, X. Zhao, J. L. Zhang, W. B. Su, and J. Liu, "Huge low-frequency dielectric response of (Nb,In)-doped TiO<sub>2</sub> ceramics," *Appl. Phys. Lett.* **107** [24] 242904 (2015).
- <sup>28</sup>J. Li, F. Li, C. Li, G. Yang, Z. Xu, and S. Zhang, "Evidences of grain boundary capacitance effect on the colossal dielectric permittivity in (Nb + In) co-doped TiO<sub>2</sub> ceramics," *Sci Rep* **5** 8295 (2015).
- <sup>29</sup>Y. Song, X. Wang, Y. Sui, Z. Liu, Y. Zhang, H. Zhan, B. Song, Z. Liu, Z. Lv, L. Tao, and J. Tang, "Origin of colossal dielectric permittivity of rutile Ti<sub>0.9</sub>In<sub>0.05</sub>Nb<sub>0.05</sub>O<sub>2</sub>: single crystal and polycrystalline," *Scientific Reports* **6** 21478 (2016).
- <sup>30</sup>W. Dong, W. Hu, A. Berlie, K. Lau, H. Chen, R. L. Withers, and Y. Liu, "Colossal Dielectric Behavior of Ga+Nb Co-Doped Rutile TiO<sub>2</sub>," *ACS Applied Materials & Interfaces* **7** [45] 25321-5 (2015).
- <sup>31</sup>W. Tuichai, S. Danwittayakul, S. Maensiri, and P. Thongbai, "Investigation on temperature stability performance of giant permittivity (In + Nb) in co-doped TiO<sub>2</sub> ceramic: a crucial aspect for practical electronic applications," *RSC Advances* **6** [7] 5582-9 (2016).

- <sup>32</sup>J. Li, F. Li, Z. Xu, Y. Zhuang, and S. Zhang, "Nonlinear I–V behavior in colossal permittivity ceramic: (Nb+In) co-doped rutile TiO<sub>2</sub>," *Ceram. Int.* **41, Supplement 1** S798-S803 (2015).
- <sup>33</sup>H. Han, P. Dufour, S. Mhin, J. H. Ryu, C. Tenailleau, and S. Guillemet-Fritsch, "Quasi-intrinsic colossal permittivity in Nb and In co-doped rutile TiO<sub>2</sub> nanoceramics synthesized through a oxalate chemical-solution route combined with spark plasma sintering," *Phys. Chem. Chem. Phys.* **17** [26] 16864-75 (2015).
- <sup>34</sup>B. Ravel, and M. Newville, "ATHENA, ARTEMIS, HEPHAESTUS: data analysis for X-ray absorption spectroscopy using IFEFFIT," *Journal of Synchrotron Radiation* **12** [4] 537-41 (2005).
- <sup>35</sup>W. L. Li, Y. Zhao, Q. G. Chi, Z. G. Zhang, and W. D. Fei, "Enhanced performance of core-shell-like structure Zr-doped CaCu<sub>3</sub>Ti<sub>4</sub>O<sub>12</sub> ceramics prepared by a flame synthetic approach," *RSC Advances* **2** [14] 6073 (2012).
- <sup>36</sup>A. Chouket, O. Bidault, V. Optasanu, A. Cheikhrouhou, W. Cheikhrouhou-Koubaa, and M. Khitouni, "Enhancement of the dielectric response through Al-substitution in La<sub>1.6</sub>Sr<sub>0.4</sub>NiO<sub>4</sub> nickelates," *RSC Adv.* **6** [29] 24543-8 (2016).
- $^{37}$ T. Nachaithong, P. Thongbai, and S. Maensiri, "Colossal permittivity in  $(In_{1/2}Nb_{1/2})_xTi_{1-x}O_2$  ceramics prepared by a glycine nitrate process," *J. Eur. Ceram. Soc.* **37** [2] 655-60 (2017).
- <sup>38</sup>M. Li, Z. Shen, M. Nygren, A. Feteira, D. C. Sinclair, and A. R. West, "Origin(s) of the apparent high permittivity in CaCu<sub>3</sub>Ti<sub>4</sub>O<sub>12</sub> ceramics: clarification on the contributions from internal barrier layer capacitor and sample-electrode contact effects," *J. Appl. Phys.* **106** [10] 104106 (2009).
- <sup>39</sup>D. A. Crandles, S. M. M. Yee, M. Savinov, D. Nuzhnyy, J. Petzelt, S. Kamba, and J. Prokeš, "Electrode effects in dielectric spectroscopy measurements on (Nb+In) co-doped TiO<sub>2</sub>," *J. Appl. Phys.* **119** [15] 154105 (2016).

## **CHAPTER 4**

## Colossal Permittivity in $(ln_{1/2}Nb_{1/2})_xTi_{1-x}O_2$ Ceramics Prepared by a Glycine Nitrate Process

#### 4.1 Introduction

Recently, the excellent dielectric properties of newly discovered (In+Nb) co-doped rutile–TiO $_2$  (INTO) ceramics were reported [1]. This INTO ceramic system exhibited a high dielectric permittivity of  $\varepsilon'\approx 2-6\times 10^4$  that depended on co-dopant concentration.  $\varepsilon'$  of the INTO ceramics increased with increasing co-dopant concentration from 0.05 to 10%, while the lowest dielectric loss tangent (tan $\delta$ ) of the 10% INTO ceramic was  $\approx 0.02$  at room temperature (RT) over a wide frequency range. Importantly,  $\varepsilon'$  was nearly independent of temperature in the range of 80–450 K [1]. Consequently, INTO ceramics have greatly stimulated research in the field of colossal dielectric materials for applications in both high–energy–density storage applications and high–performance capacitors [1-17]. Considering its resource strategy and resource management [18, 19], TiO $_2$  is suitable for replacing conventional ferroelectric–based capacitive materials since TiO $_2$  is abundant and has low toxicity.

A newly proposed model has been developed to describe the excellent dielectric performance of TiO<sub>2</sub>-based ceramics, which can be applied to other ceramic oxides [1]. large defect clusters caused by the complex stoichiometry  $(\ln_x^{3+} \text{Nb}_x^{5+} \text{Ti}_x^{3+}) \text{Ti}_{1-3x}^{4+} \text{O}_{2-x/2}$  was proposed as the origin of very high  $\varepsilon'$  values. Accordingly, free electrons are created by the reduction of Ti<sup>4+</sup> to Ti<sup>3+</sup> resulting from Nb<sup>5+</sup> dopant ions. The electrons produced from this are confined within complex defect clusters in the rutile structure, which were formed by doping with In<sup>3+</sup>. Without In<sup>3+</sup> doping ions, even though very high  $\varepsilon'$  values can be achieved, electrons cannot be confined and the  $tan\delta$  value is large [18]. This mechanism was referred to the electron-pinned defect-dipole (EPDD) model. It was further found that there were many factors that can contribute to the overall dielectric response in TiO<sub>2</sub>-based ceramics over wide frequency and temperature ranges. These include electron hopping [5, 17], interfacial polarization at internal interfaces (i.e., internal barrier layer capacitor (IBLC) effect) [3, 7, 12, 14, 20, 21], and non-Ohmic sample-electrode contact [5, 14].

Substitution of (In+Nb) ions at high concentrations (i.e.,  $\geq 10$  at.%) was accompanied with a dominant interfacial effect, just as observed in a single Nb–doped TiO<sub>2</sub> ceramic. This is undesirable for capacitor applications [1]. The INTO ceramics that were substituted with small amounts of (In+Nb) had a lower  $\epsilon'$  compared to the 10%INTO ceramic, while their  $\tan \delta$  values were higher [1]. Such larger  $\tan \delta$  values were associated with the frequency dependence of  $\epsilon'$  of lower doping content INTO ceramics. This likely signifies the interfacial effect. Thus, it is hypothesized that the interfacial effect at some interfaces may be dominant when the dopant content is very low. Investigation of the colossal dielectric properties of INTO ceramics with low–dopant content should be performed. Although the first reported results revealed that the surface barrier layer capacitor (SBLC) effect has slight influence on the overall dielectric response of INTO ceramics [1], it was further found that annealing an INTO ceramic in air had a significant effect on the low–frequency  $\epsilon'$  value [14]. This was suggested to be caused by the effect of a non–Ohmic sample–electrode contact.

To obtain INTO ceramics with more homogeneous dispersion of In<sup>3+</sup> and Nb<sup>5+</sup> co-dopant ions, wet chemical routes should be used instead of a solid state reaction (SSR) method for preparing the materials. It is expected that the fine powders obtained

can also offer the possibility of closer stoichiometric control and good dispersion of dopants [22, 23]. Furthermore, the highly-dense sintered ceramics would be achieved by using fine nano-sized powders. For future applications, the study of preparation methods to fabricate a fine INTO powder is one of the most important issues that should be addressed. If INTO ceramics are to be used in electronic device applications, selection of an effective preparation method is one of the most important issues that needs to be addressed.

Unfortunately, investigation of the colossal dielectric properties of INTO ceramics prepared by wet chemical routes has rarely been reported [16]. Among the wet chemical methods, the glycine nitrate process (GNP) is one of the most attractive methods and it is classified as a combustion process using glycine as a fuel. The GNP method can be effectively used to prepare homogeneous nanoparticles of ceramic powders using a self–ignited combustion process [22, 24-27]. Hence, the first objective of this work is to provide a new wet chemical route for synthesizing INTO ceramics with homogeneous dispersion of dopants. It is expected that good dielectric properties of INTO ceramics can be achieved. The second objective is to investigate the colossal dielectric properties of INTO ceramics that contain low concentrations of co–dopants in order to clarify the possible origin(s) of the colossal dielectric properties. Interfacial effect at some interfaces may be dominant when the dopant content is very low.

## 4.2 Experimental details

 $(ln_{1/2}Nb_{1/2})_xTi_{1-x}O_2$  ceramics with x=0.005, 0.010, and 0.015 (referred as the 0.5%INTO, 1.0%INTO, and 1.5%INTO ceramics, respectively) were prepared using a combustion method with glycine as fuel.  $C_{16}H_{28}O_6Ti$  (Sigma–Aldrich),  $ln_3N_3O_9\cdot xH_2O$  (Sigma–Aldrich, 99.999%), NbCl $_5$  (Sigma–Aldrich, >99.9%), deionized water, citric acid, and glycine were used as the starting raw materials. First,  $ln_3N_3O_9\cdot xH_2O$  and NbCl $_5$  were dissolved in an aqueous solution of citric acid with constant stirring at RT. Second, a  $C_{16}H_{28}O_6Ti$  solution was dropped into the metal ion solution above under constant stirring until a clear and transparent solution was obtained. Then, glycine powder was added into the mixed solution with stirring at 150 °C until a viscous gel was obtained. Finally, the gel was dried at 350 °C for 1 h using heating rate 1 °C/min. All resulting dried porous precursors were ground and calcined at 1000 °C for 6 h. The powders were pressed into pellets 9.5 mm in diameter and ~1.2 mm in thickness by uniaxial compression at  $\approx$ 200 MPa. Finally, these pellets were sintered in air at 1400 °C for 6 h with heating rate 2 °C/min.

The microstructure and elemental distribution in the as–sintered INTO ceramics were examined using field–emission scanning electron microscopy (FE–SEM) with energy–dispersive X–ray analysis (EDX) (HITACHI SU8030, Japan). X–ray diffraction (XRD) (PANalytical, EMPYREAN) was used to characterize the phase composition and crystal structure of the samples. To reveal the surface morphologies, the as–sintered INTO ceramics were carefully polished to obtain smooth surfaces. Then, an obvious grain and grain boundary structure of the polished–samples was obtained by thermally etching the samples at 1200 °C for 0.5 h. Scanning electron microscopy (SEM) (SEC, SNE4500M) was used to revealed surface morphologies.

Before electrical measurements, Au was sputtered onto each pellet face at a current of 25 mA for 8 min using a Polaron SC500 sputter coating unit (Sussex, UK). The capacitance ( $C_p$ ) and dispassion factor (D or  $tan\delta$ ) of the ceramic samples were corrected using a KEYSIGHT E4990A Impedance Analyzer over the frequency and temperature

ranges of 40 Hz $-10^7$  Hz and -50-200 °C, respectively. The nonlinear current density–electric field (J-E) behavior at RT was measured using a high voltage measurement unit (Keithley Model 247).

## 4.3 Results and discussion

The XRD patterns of all INTO powders and sintered INTO ceramics are represented in Fig. 1. A main phase of rutile– $TiO_2$  with a tetragonal structure (JCPDS 21-1276) is clearly indexed in all samples with no impurity phases. Lattice parameters of the 0.5%INTO, 1.0%INTO, and 1.5%INTO ceramics were found to be a=4.592 Å and c=2.960 Å, a=4.595 Å and c=2.961Å, and a=4.594 Å and c=2.961 Å, respectively. The a and c values of all the samples were nearly the same as the values for rutile– $TiO_2$  (JCPDS 21–1276), a=4.593 Å and c=2.959 Å. These calculated values are comparable to those reported in the literature for the ( $Nb_{0.5}In_{0.5}$ ) $_{0.01}Ti_{0.99}O_2$  [16]. The slight difference in lattice parameter values between pure rutile– $TiO_2$  and the co–doped samples was likely due to a small amount of dopant ions.

The calcined INTO powders were characterized using transmission electron microscopy, revealing nanoparticles with sizes of ≈100–300 nm (data not shown). Surface morphologies of the polished–surfaces of the INTO ceramics are shown in Fig. 2. Dense microstructure with obvious grain and grain boundary structures are observed. Grain sizes of INTO ceramics were slightly changed by variation in co–dopant concentrations. The distributions of the elements in INTO ceramics (*i.e.*, Ti, O, In, and Nb) were characterized using an SEM–mapping technique. It was found that the dopants were homogeneously dispersed in the microstructure (data not shown).

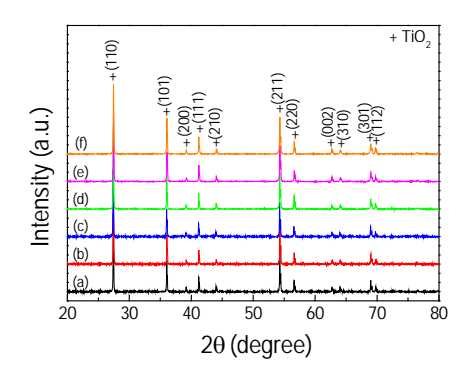


Fig. 1 XRD patterns of  $(In_{1/2}Nb_{1/2})_xTi_{1-x}O_2$  (a-c) powders and (d-f) sintered ceramics; (a,d) x=0.005, (b,e) x=0.010, and (c,f) x=0.015.

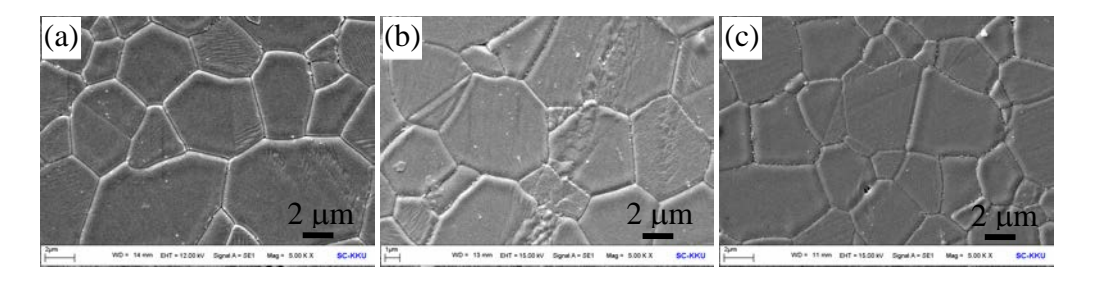
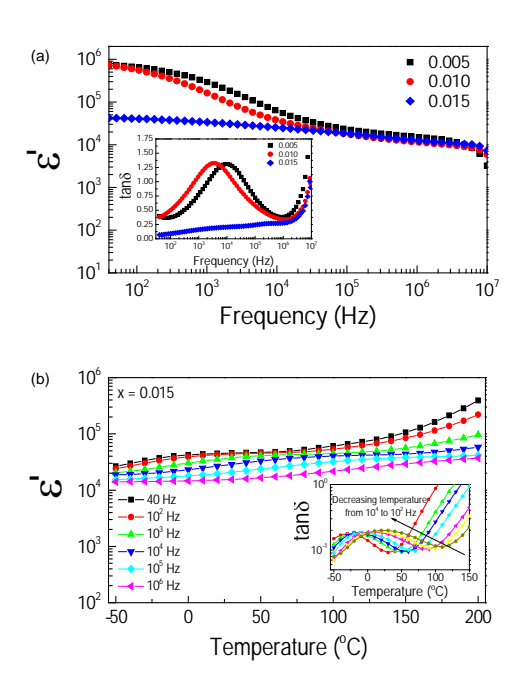


Fig. 2 SEM images of polished surfaces of  $(In_{1/2}Nb_{1/2})_xTi_{1-x}O_2$  ceramics with (a) x=0.005, (b) x=0.010, and (c) x=0.015.

The dielectric properties at RT of the as-sintered INTO ceramics are shown in Fig. 3(a). All of the INTO ceramics exhibited very high  $\varepsilon'$  values of about  $10^4$ – $10^6$  over a wide frequency range. Two distinct behaviors for frequency dependence of ε' were observed in a low frequency range.  $\varepsilon'$  of the 1.5%INTO ceramic was slightly dependent on frequency in the range of 40 to  $10^7$  Hz, while  $\varepsilon'$  values of the 0.5% and 1.0%INTO ceramics were strongly dependent on frequency. This indicates an additional polarization within in these ceramics. As shown in the inset of Fig. 3(a), tanδ of the 1.5%INTO ceramic was very low over a wide frequency range. This is consistent with the frequency independence of  $\varepsilon'$ observed in the 1.5%INTO ceramic. A strong tanδ relaxation peak was observed in the 0.5% and 1.0%INTO ceramics, corresponding to a step-like decrease in their ε' values in the frequency range of 10<sup>3</sup>–10<sup>4</sup> Hz. This dielectric relaxation behavior is generally caused by extrinsic effects such as the electrical response of grain boundary, domain boundary, or sample-electrode contact [13, 28-30]. If one of these factors can be proved to be the primary contributor to the colossal permittivity over a measured frequency range (40 to 10<sup>7</sup> Hz), other factors may be responsible for further polarization relaxation in a low-frequency range of 10<sup>3</sup>–10<sup>4</sup> Hz. The origins of the primary and additional dielectric responses will be discussed as an impedance spectroscopy (IS) analysis in the next part.



**Fig. 3** (a) Frequency dependence of  $\varepsilon'$  at RT for  $(In_{1/2}Nb_{1/2})_xTi_{1-x}O_2$  ceramics with x=0.005–0.015; inset shows  $tan\delta$  as a function of frequency. (b) Temperature dependence of  $\varepsilon'$  at various frequencies for the  $(In_{1/2}Nb_{1/2})_xTi_{1-x}O_2$  ceramic with x=0.015; inset shows the temperature dependence of  $tan\delta$  in the frequency range o

It is worth noting that the 1.5%INTO ceramic prepared using a GNP method exhibited good dielectric properties with  $\varepsilon'\approx42,376$  and  $\tan\delta\approx0.06$  at RT and 40 Hz. Although an impressive dielectric performance of TiO<sub>2</sub>-based ceramics was reported and stimulated research activity in the field of colossal ceramic materials, there were few investigations of preparation methods using wet chemical routes [16]. It was reported that a nano-1.0%INTO ceramic prepared using an oxalate chemical-solution combined with spark plasma sintering (SPS) exhibited high  $\varepsilon'\approx0.9\times10^4$  and  $\tan\delta\approx0.2$  at 40 Hz and RT

[16]. Thus, the GNP method may be one of the most interesting wet chemical routes for preparing INTO ceramics. Usually,  $\tan\delta$  values of colossal permittivity materials in such a low frequency range are very large. For a  $CaCu_3Ti_4O_{12}$  ceramic prepared by a SPS method,  $\tan\delta\approx10$  was obtained at 40 Hz [31], and values of  $\tan\delta>0.2$  were obtained in a  $CaCu_3Ti_4O_{12}$  ceramic prepared by a SSR method [32-34]. For co-doped NiO,  $\tan\delta$  values at  $10^2$  Hz were larger than 0.5 [35]. At  $10^3$  Hz,  $\tan\delta$  values of  $Ba(Fe_{1/2}Nb_{1/2})O_3$  were larger than 0.2–5 [36, 37]. A small low  $\tan\delta$  value in a low frequency range indicates little DC conduction in bulk ceramics [35]. These very high  $\tan\delta$  values in a low-frequency range of several colossal permittivity materials are generally associated with the resistance of insulating grain boundaries [3].

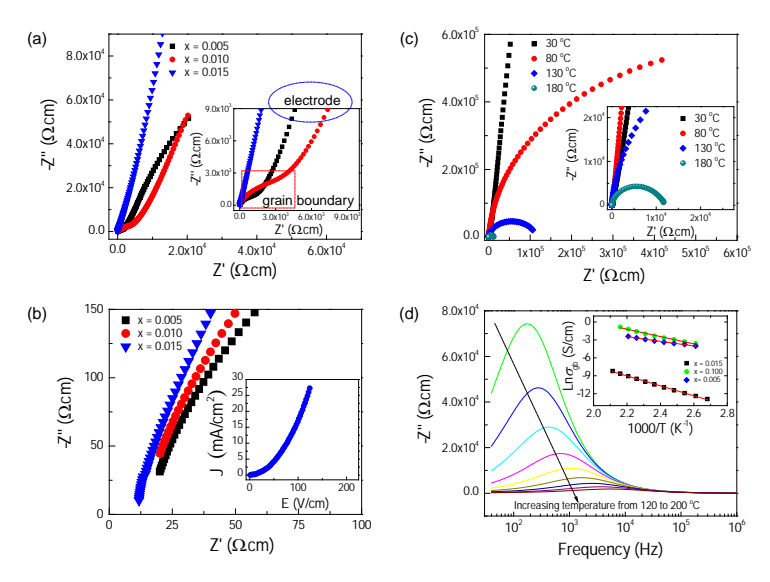


**Fig. 4** (a) Impedance complex plane (Z\*) plots at RT for  $(In_{1/2}Nb_{1/2})_xTi_{1-x}O_2$  ceramics with x=0.005–0.015; inset gives an expanded view close to the origin, revealing the grain boundary response. (b) Expanded view of the high–frequency data of Z\* plots in Figure 4(a), revealing the nonzero intercept of the grain response; inset shows the nonlinear J–E behavior of the  $(In_{1/2}Nb_{1/2})_xTi_{1-x}O_2$  ceramic with x=0.015.

The temperature dependence of  $\epsilon'$  in the 1.5%INTO ceramic at various frequencies is illustrated in Fig. 3(b). The  $\epsilon'$  value was slightly dependent on temperature in the range from -50 to 150 °C compared to those of other colossal permittivity materials [30, 35, 36]. At temperatures higher than 150 °C, the  $\epsilon'$  value was strongly dependent on temperature, especially in a low frequency range. This may have been caused by an increase in DC conduction, which resulted from the long distance movement of free charge carriers [35]. These charges can accumulate at any insulating interfaces under an applied electric field. This can cause an increase in the interfacial polarization, increasing the  $\epsilon'$  value [13]. Dielectric relaxation in the frequency and temperature ranges of 40–10<sup>4</sup> Hz and -50–150 °C was observed in the 1.5%INTO ceramic. This was confirmed by the appearance  $\tan\delta$  peaks, as shown in the inset of Fig. 3(b). This result is similar to those reported in the literature [13, 38]. This dielectric relaxation was likely attributed to the electrical response(s) of internal insulating interfaces between grains (i.e., grain boundaries) [13] and/or between resistive–outer surface layers and a conductive inner core [6].

The electrical responses of grain and grain boundaries of the sintered INTO ceramics were investigated using IS to clarify the origins of the primary and additional polarizations contributing to the overall colossal dielectric responses. As shown in Fig. 4(a) and its inset, only the linear portion of an arc is observed in the Z\* plot of the 1.5%INTO ceramic, while Z\* plots of 0.5% and 1.0%INTO ceramics showed a linear response of an arc in a low-frequency range and semicircular arcs (as depicted by the red rectangle in the inset). The nonzero intercept on the Z' axis was observed for all the ceramics, Fig. 4(b). This indicates that there exists a semiconducting part in all the INTO ceramics, which is usually referred to the semiconducting grains [3, 14, 29, 39, 40]. The grain resistance ( $R_a$ ) values at RT of all the ceramics were ≈10-20 Ω.m, which are comparable to those reported in the literature [14]. Three electrical responses from the high to low-frequency range of the semiconducting grains, insulating grain boundary (and/or resistive-outer surface layer) and sample-electrode contact were clearly confirmed in the 0.5% and 1.0%INTO ceramics. Fig. 5(a) and its inset, a full semicircle arc is clearly evident in the Z\* plot of the 1.5%INTO ceramic as temperature was increased. No overlapping arcs were observed in the Z\* plot, indicating the electrical response of only an insulating portion. Only two primary electrical responses, i.e., semiconducting grains and insulating grain boundaries coupled with a resistive-outer surface layer, were confirmed in the 1.5%INTO ceramic. In Fig. 4(a), the grain boundary resistance ( $R_{ob}$ ) at RT of INTO ceramics increased with increasing co-dopant concentration. This is very consistent with that reported by Y. Song et al. [20], which reported that the  $R_{\rm qb}$  value of  ${\rm Al}_x{\rm Nb}_{0.03}{\rm Ti}_{0.97-x}{\rm O}_2$  ceramics increased with increasing  $Al^{3+}$  content from x = 0.01 to 0.03.

The conductivity of the grain boundary ( $\sigma_{\rm gb}$ =1/ $R_{\rm gb}$ ) at each temperature was calculated from the Z"-frequency plots, Fig. 5(b). the apparent Z" peak shifted to higher frequencies with increasing temperature, indicating a thermally activated electrical response. According to the results in Figs. 4 and 5, this set of apparent Z" peaks can be considered the electrical response of the grain boundaries. At the maximum value of Z" ( $Z''_{\rm max}$ ), it can be shown that  $R = 2Z''_{\rm max}$ . As shown in the inset of Fig. 5(b), the temperature dependence of  $\sigma_{\rm gb}$  for all the INTO ceramics follows the Arrhenius law,

$$\sigma_{gb} = \sigma_0 \exp\left(\frac{-E_{gb}}{k_B T}\right),\tag{1}$$

where  $\sigma_0$  is a constant value,  $E_{\rm gb}$  is the activation energy required for conduction across the grain boundaries. From Eq. (1), the  $E_{\rm gb}$  values of the 1.5%, 1.0% and 0.5%INTO ceramics were 0.717, 0.429 and 0.275 eV, respectively. The  $E_{\rm gb}$  value decreased with decreasing co–dopant concentration. For  ${\rm Al}_x{\rm Nb}_{0.03}{\rm Ti}_{0.97\text{-}x}{\rm O}_2$  ceramics [20], the  $E_{\rm gb}$  value was reduced from 0.69 to 0.31 eV by decreasing the  ${\rm Al}^{3+}$  concentration (x) from x=0.03 to 0.01. The  ${\rm Al}^{3+}$  doping ions could be considered as an acceptor dopant, which captured the electrons that were produced by  ${\rm Nb}^{5+}$  doping ions [20]. In the current study, the primary cause for enhancement of both of  $R_{\rm gb}$  (at RT) and  $E_{\rm gb}$  values was an increase in  ${\rm ln}^{3+}$  doping only. This result supports the importance of the role of +3 ions to promote the insulating properties of all co–doped  ${\rm TiO}_2$  based ceramics [20]. These  $E_{\rm gb}$  values are comparable to values of 0.35 eV for 10%INTO ceramics prepared by an SSR method [12] can also be comparable to 0.65(7) eV for the 1.0%INTO ceramic prepared using an oxalate chemical–solution route combined with a SPS method [16] It is important to note that the temperature dependence of  $\sigma_{\rm gb}$  of all the INTO ceramics follows the Arrhenius law. This is not consistent with in the case of single Nb–doped  ${\rm TiO}_2$ , in which temperature

dependence of conductivity follows the Mott-VRH law and is related to a small polaron mechanism [1].

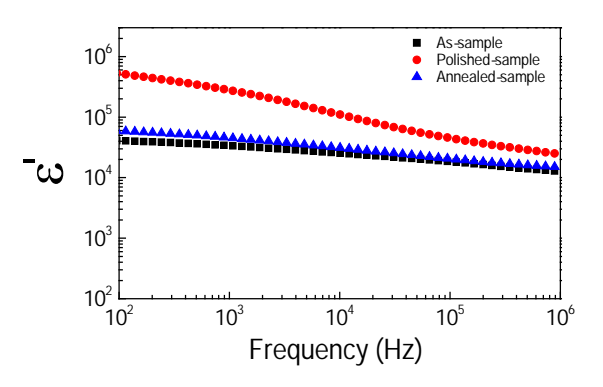


Fig. 5 Dielectric properties of various sintered ceramics.

Generally,  $R_{\alpha}$  and the grain capacitance ( $C_{\alpha}$ ) values of INTO and other colossal permittivity materials are very low [12, 20]. The corresponding relaxation frequency  $(f_{\text{max}}=1/2\pi R_{\text{q}}C_{\text{q}})$  of the M" peak (imaginary part of the complex modulus, M') usually appear in a very low temperature range (<100 K), which cannot be done in this current study. Nevertheless, the origin of the colossal permittivity in INTO ceramics is unlikely correlated with strong polarization inside the grains for the EPDD mechanism [1]. There are two primary reasons supporting this hypothesis. First for the EPDD model, free electrons in INTO ceramics are created by substitution of Nb5+ following the relationships,  $2TiO_2 + Nb_2O_5 \xrightarrow{4TiO_2} 2Ti'_{Ti} + 2Nb_{Ti}^{\bullet} + 8O_O + 1/2O_2$  and  $Ti^{4+} + e \rightarrow Ti^{3+}$ . Free electrons can be confined in highly correlated  $In_2^{3+}V_0^{\bullet\bullet}Ti^{3+}$  defect clusters inside the grains, giving rise to high  $\varepsilon'$  and low tan $\delta$  values. Accordingly, the  $R_g$  and  $E_g$  values of INTO ceramics should be very large. However, the existence of semiconducting grains with very low  $R_{\alpha}$ values was confirmed by IS. Second, non-Ohmic properties of varistor oxides and CaCu<sub>3</sub>Ti<sub>4</sub>O<sub>12</sub> polycrystalline ceramics are usually ascribed to the existence of a Schottky barrier at the insulating grain boundaries, which is sandwiched by n-type semiconducting grains. Inset of Fig. 4(b), the 1.5%INTO ceramics exhibited a nonlinear J-E characteristic, indicating the formation of a Schottky barrier at the grain boundary. Based on the EPDD model, this nonlinear behavior cannot occur due to the insulating character of the grains and grain boundaries. Considering IS analysis and nonlinear J-E behavior, the colossal permittivity in INTO ceramics prepared by a GNP method may be extrinsic in its origin(s), resulting from the IBLC and SBLC effects.

Generally, the colossal low–frequency dielectric response resulting from the electrode effect would be dominant when  $R_{\rm gb}$  is greatly reduced to a level smaller that  $R_{\rm e}$  [40]. In contrast, when adjusting resistances so that  $R_{\rm gb}>>R_{\rm e}>>R_{\rm g}$ , the electrode effect did not appear. Thus, the electrode effect cannot be dominant in the 1.5%INTO ceramic due to its very large  $R_{\rm gb}$  value. In the 0.5% and 1.0%INTO ceramics,  $R_{\rm gb}$  values at RT were too small (but still larger than their  $R_{\rm g}$  values). Consequently, the electrode effect was very dominant. An additional large  $\epsilon'$  value in a low–frequency range was clearly confirmed to originate from the electrode effect. The electrode effect can be dominant in the 1.5%INTO ceramic when the outer surfaces of the as–sintered sample were removed, which will be discussed below.

Fig. 6 shows the SBLC effect on the dielectric properties of the 1.5%INTO ceramic. After dielectric properties of the as-fired sample were measured, both sides of the electrodes and outer surface layers of the pellet were removed by polishing them with SiC paper (referred as the polished-sample). The polished-sample was coated by Au sputtering. It was found that  $\varepsilon'$  of the polished–sample was enhanced by about one order of magnitude. At 1 kHz, the  $\varepsilon'$  value increased from  $3.36\times10^4$  to  $2.77\times10^5$ , contradicting reports in the literature [1]. This result indicates that sample-electrode contact has a great impact on the overall dielectric response in the INTO ceramic system. Furthermore, it was found that  $tan\delta$  was also significantly increased over the measured frequency range. After that, the surfaces and electrodes of the polished-sample were removed. Then, this sample was annealed in air at 1200 °C for 30 min (referred as the annealed-sample). An Au sputtered electrode was made for dielectric measurements. Interestingly,  $\varepsilon'$  almost completely recovered to its initial value, strongly supporting the SBLC's contribution to the colossal dielectric properties in INTO ceramics in a low frequency range. After annealing in air, the surfaces of the 1.5%INTO ceramic were re-oxidized. As a result, free charges on the surfaces might be reduced by filling oxygen vacancies with oxygen ions during the annealing process. Although the formation of SBLC on the surfaces may be difficult to explain, it is clear that different types of defects on surfaces of the INTO ceramic had distinct effects on the SBLC mechanism. It is possible that after the polishing process, the large increase observed in  $\varepsilon'$  of the polished-sample may have been largely due to the dominant effect of sample-electrode contact. This is generally caused by the difference in work functions between the Au electrode and the surface of the ceramic sample [14]. After annealing, the outer surface layer became a system of fully insulating layers. Thus, the sample-electrode contact effect cannot be produced. The formation of insulating layers also caused a decrease in tan . It is important to note this SBLC effect has never been observed in INTO ceramics prepared by a SSR method [1]. It should be noted that this work is not to discredit the possibility of the EPDD effect being generated by essentially designing complex defects in a rutile-structure. The discussion is based on the experimental results that were obtained in INTO ceramics prepared by a GNP method. As suggested by Han et al. [16], different preparation methods may result in difference in homogeneous distribution of dopants and/or other defects in the INTO ceramic. This might lead to the different mechanisms contributing to the colossal permittivity of INTO ceramics. Therefore, systematic investigation is needed in this area and further work should be carefully done.

### 4.4 Conclusions

We successfully prepared (In+Nb) co–doped TiO $_2$  ceramic nanoparticles with very low dopant concentrations using a GNP method. Highly dense microstructure of the sintered ceramics was obtained. It was found that both of the In $_1$  and Nb $_2$  doping ions were homogeneously dispersed in the microstructure. (In $_1$ /2Nb $_1$ /2) $_{0.015}$ Ti $_{0.985}$ O $_2$  exhibited a high  $\epsilon$ ' $\approx$ 42,376 and low tan $_2$ 0.06 at 40 Hz and RT. By considering impedance spectroscopy analysis and nonlinear J-E characteristic, the colossal dielectric response at RT in the INTO ceramics should be primarily attributed to the IBLC effect. Space–charge polarization due to the formation of non–Ohmic sample–electrode contact was observed when the co–dopant concentrations were  $\leq$ 1.0 mol $_2$ 0 because the R $_3$ 0 value was smaller than  $_3$ 1 the INTO ceramics prepared using the GNP method.

### References

- [1] W. Hu, Y. Liu, R.L. Withers, T.J. Frankcombe, L. Norén, A. Snashall, M. Kitchin, P. Smith, B. Gong, H. Chen, J. Schiemer, F. Brink, J. Wong-Leung, Electron-pinned defect-dipoles for high-performance colossal permittivity materials, Nat. Mater. 12 (2013) 821.
- [2] Z. Gai, Z. Cheng, X. Wang, L. Zhao, N. Yin, R. Abah, M. Zhao, F. Hong, Z. Yu, S. Dou, A colossal dielectric constant of an amorphous TiO<sub>2</sub>:(Nb, In) film with low loss fabrication at room temperature, J. Mater. Chem. C 2 (2014) 6790.
- [3] J. Li, F. Li, Y. Zhuang, L. Jin, L. Wang, X. Wei, Z. Xu, S. Zhang, Microstructure and dielectric properties of (Nb -dop+)ctrutile TiO<sub>2</sub> ceramics, J. Appl. Phys. 116 (2014) 074105.
- [4] X. Cheng, Z. Li, J. Wu, Colossal permittivity in ceramics of TiO<sub>2</sub> co-doped with niobium and trivalent cation, J. Mater. Chem. A 3 (2015) 5805.
- [5] W. Dong, W. Hu, A. Berlie, K. Lau, H. Chen, R.L. Withers, Y. Liu, Colossal dielectric behavior of Ga+Nb co-doped rutile TiO<sub>2</sub>, ACS Appl. Mater. Interfaces 7 (2015) 25321.
- [6] W. Hu, K. Lau, Y. Liu, R.L. Withers, H. Chen, L. Fu, B. Gong, W. Hutchison, Colossal dielectric permittivity in (Nb+Al) co-doped rutile TiO<sub>2</sub> Ceramics: Compositional Gradient and Local Structure, Chem. Mater. 27 (2015) 4934.
- [7] J. Li, F. Li, C. Li, G. Yang, Z. Xu, S. Zhang, Evidences of grain boundary capacitance effect on the colossal dielectric permittivity in (Nb + In) co-doped TiO<sub>2</sub> ceramics, Sci. Rep. 5 (2015) 8295.
- [8] J. Li, F. Li, Z. Xu, Y. Zhuang, S. Zhang, Nonlinear I–V behavior in colossal permittivity ceramic: (Nb+In) co-doped rutile TiO<sub>2</sub>, Ceram. Int. 41 (2015) S798.
- [9] Z. Li, J. Wu, W. Wu, Composition dependence of colossal permittivity in  $(Sm_{0.5}Ta_{0.5})_xTi_{1-x}O_2$  ceramics, J. Mater. Chem. C 3 (2015) 9206.
- [10] W. Tuichai, P. Srepusharawoot, E. Swatsitang, S. Danwittayakul, P. Thongbai, Giant dielectric permittivity and electronic structure in (Al+Sb) co-doped TiO<sub>2</sub> ceramics, Microelectron. Eng. 146 (2015) 32.
- [11] C. Wang, N. Zhang, Q. Li, Y. Yu, J. Zhang, Y. Li, H. Wang, Dielectric relaxations in rutile TiO<sub>2</sub>, J. Am. Ceram. Soc. 98 (2015) 148.
- [12] Y. Song, X. Wang, Y. Sui, Z. Liu, Y. Zhang, H. Zhan, B. Song, Z. Liu, Z. Lv, L. Tao, J. Tang, Origin of colossal dielectric permittivity of rutile Ti<sub>0.9</sub>In<sub>0.05</sub>Nb<sub>0.05</sub>O<sub>2</sub>: single crystal and polycrystalline, Sci. Rep. 6 (2016) 21478.
- [13] W. Tuichai, S. Danwittayakul, S. Maensiri, P. Thongbai, Investigation on temperature stability performance of giant permittivity (In + Nb) in co-doped TiO<sub>2</sub> ceramic: a crucial aspect for practical electronic applications, RSC Adv. 6 (2016) 5582.
- [14] Y.Q. Wu, X. Zhao, J.L. Zhang, W.B. Su, J. Liu, Huge low-frequency dielectric response of (Nb,In)-doped TiO<sub>2</sub> ceramics, Appl. Phys. Lett. 107 (2015) 242904.
- [15] Z. Li, J. Wu, D. Xiao, J. Zhu, W. Wu, Colossal permittivity in titanium dioxide ceramics modified by tantalum and trivalent elements, Acta. Mater. 103 (2016) 243.
- [16] H. Han, P. Dufour, S. Mhin, J.H. Ryu, C. Tenailleau, S. Guillemet-Fritsch, Quasi-intrinsic colossal permittivity in Nb and In co-doped rutile  ${\rm TiO_2}$  nanoceramics synthesized through a oxalate chemical-solution route combined with spark plasma sintering, Phys. Chem. Chem. Phys. 17 (2015) 16864.
- [17] X.G. Zhao, P. Liu, Y.C. Song, A.P. Zhang, X.M. Chen, J.P. Zhou, Origin of colossal permittivity in (In<sub>1/2</sub>Nb<sub>1/2</sub>)TiO<sub>2</sub> via broadband dielectric spectroscopy, Phys. Chem. Chem. Phys. 17 (2015) 23132.
- [18] C.C. Homes, T. Vogt, Colossal permittivity materials: Doping for superior dielectrics, Nat. Mater. 12 (2013) 782.
- [19] S. Krohns, P. Lunkenheimer, S. Meissner, A. Reller, B. Gleich, A. Rathgeber, T. Gaugler, H.U. Buhl, D.C. Sinclair, A. Loidl, The route to resource-efficient novel materials, Nat. Mater. 10 (2011)
- [20] Y. Song, X. Wang, X. Zhang, Y. Sui, Y. Zhang, Z. Liu, Z. Lv, Y. Wang, P. Xu, B. Song, The contribution of doped-Al to the colossal permittivity properties of Al<sub>x</sub>Nb<sub>0.03</sub>Ti<sub>0.97-x</sub>O<sub>2</sub> rutile ceramics, J. Mater. Chem. C 4 (2016) 6798.
- [21] G. Liu, H. Fan, J. Xu, Z. Liu, Y. Zhao, Colossal permittivity and impedance analysis of niobium and aluminum co-doped TiO<sub>2</sub> ceramics, RSC Adv. 6 (2016) 48708.

- [22] M.N. Rahaman, Ceramic processing and sintering, 2nd ed., M. Dekker, New York, (2003).
- [23] L. Singh, U.S. Rai, K.D. Mandal, N.B. Singh, Progress in the growth of CaCu<sub>3</sub>Ti<sub>4</sub>O<sub>12</sub> and related functional dielectric perovskites, Prog. Cryst. Growth Charact. Mater. 60 (2014) 15.
- [24] P. Thongbai, T. Yamwong, S. Maensiri, V. Amornkitbamrung, P. Chindaprasirt, Improved dielectric and nonlinear electrical properties of fine-grained CaCu<sub>3</sub>Ti<sub>4</sub>O<sub>12</sub> ceramics prepared by a glycine-nitrate process, J. Am. Ceram. Soc. 97 (2014) 1785.
- [25] L. Singh, I.W. Kim, B.C. Sin, K.D. Mandal, U.S. Rai, A. Ullah, H. Chung, Y. Lee, Dielectric studies of a nano-crystalline  $CaCu_{2.90}Zn_{0.10}Ti_4O_{12}$ electro-ceramic by one pot glycine assisted synthesis from inexpensive  $TiO_2$  for energy storage capacitors, RSC Adv. 4 (2014) 52770.
- [26] P. Blennow, K.K. Hansen, L.R. Wallenberg, M. Mogensen, Synthesis of Nb-doped SrTiO<sub>3</sub> by a modified glycine-nitrate process, J. Eur. Ceram. Soc. 27 (2007) 3609.
- [27] Z. Lei, Q. Zhu, S. Zhang, Nanocrystalline scandia-doped zirconia (ScSZ) powders prepared by a glycine–nitrate solution combustion route, J. Eur. Ceram. Soc. 26 (2006) 397.
- [28] T.T. Fang , C.P. Liu, Evidence of the internal domains for inducing the anomalously high dielectric constant of  $CaCu_3Ti_4O_{12}$ , Chem. Mater. 17 (2005) 5167.
- [29] M. Li, Z. Shen, M. Nygren, A. Feteira, D.C. Sinclair, A.R. West, Origin(s) of the apparent high permittivity in CaCu<sub>3</sub>Ti<sub>4</sub>O<sub>12</sub> ceramics: clarification on the contributions from internal barrier layer capacitor and sample-electrode contact effects, J. Appl. Phys. 106 (2009) 104106.
- [30] W. Li, R.W. Schwartz, A. Chen, J. Zhu, Dielectric response of Sr doped CaCu<sub>3</sub>Ti<sub>4</sub>O<sub>12</sub> ceramics, Appl. Phys. Lett. 90 (2007) 112901.
- [31] R. Kumar, M. Zulfequar, T.D. Senguttuvan, Structural and impedance spectroscopic studies of spark plasma sintered CaCu<sub>3</sub>Ti<sub>4</sub>O<sub>12</sub> dielectric ceramics: an evidence of internal resistive barrier effect, J. Mater. Sci: Mater. Electron (2016).
- [32] J. Li, K. Wu, R. Jia, L. Hou, L. Gao, S. Li, Towards enhanced varistor property and lower dielectric loss of CaCu<sub>3</sub>Ti<sub>4</sub>O<sub>12</sub> based ceramics, Materials & Design 92 (2016) 546.
- [33] L. Bai, Y. Wu, L. Zhang, Influence of FeNb codoping on the dielectric and electrical properties of CaCu<sub>3</sub>Ti<sub>4</sub>O<sub>12</sub> ceramics, J. Alloys. Compd. 661 (2016) 6.
- [34] A.K. Thomas, K. Abraham, J. Thomas, K.V. Saban, Structural and dielectric properties of A-and B-sites doped CaCu<sub>3</sub>Ti<sub>4</sub>O<sub>12</sub> ceramics, Ceram. Int. 41 (2015) 10250.
- [35] J. Wu, C.W. Nan, Y. Lin, Y. Deng, Giant dielectric permittivity observed in Li and Ti doped NiO, Phys. Rev. Lett. 89 (2002) 217601.
- [36] H. Yang, Y. Yang, Y. Lin, J. Zhu, F. Wang, Preparation and electrical properties of (1-x)Ba(Fe<sub>0.5</sub>Nb<sub>0.5</sub>)O<sub>3</sub>-xBaTiO<sub>3</sub> ceramics, Ceram. Int. 38 (2012) 1745.
- [37] P.K. Patel, K.L. Yadav, H. Singh, A.K. Yadav, Origin of giant dielectric constant and magnetodielectric study in Ba(Fe<sub>0.5</sub>Nb<sub>0.5</sub>)O<sub>3</sub> nanoceramics, J. Alloys. Compd. 591 (2014) 224.
- [38] J. Li, Z. Xu, F. Li, X. Zhu, S. Zhang, SiO<sub>2</sub>-Ti<sub>0.98</sub>In<sub>0.01</sub>Nb<sub>0.01</sub>O<sub>2</sub> composite ceramics with low dielectric loss, high dielectric permittivity and an enhanced breakdown electric field, RSC Adv. 6 (2016) 20074.
- [39] R. Schmidt, M.C. Stennett, N.C. Hyatt, J. Pokorny, J. Prado-Gonjal, M. Li, D.C. Sinclair, Effects of sintering temperature on the internal barrier layer capacitor (IBLC) structure in  $CaCu_3Ti_4O_{12}$  (CCTO) ceramics, J. Eur. Ceram. Soc. 32 (2012) 3313.
- [40] M. Li, D.C. Sinclair, A.R. West, Extrinsic origins of the apparent relaxorlike behavior in CaCu<sub>3</sub>Ti<sub>4</sub>O<sub>12</sub> ceramics at high temperatures: A cautionary tale, J. Appl. Phys. 109 (2011) 084106.

# **CHAPTER 5**

# High–Performance Giant-Dielectric Properties of Rutile TiO<sub>2</sub> Co–Doped with Acceptor–Sc<sup>3+</sup> and Donor–Nb<sup>5+</sup> Ions

### 5.1 Introduction

Since the giant dielectric behavior of the most studied CaCu<sub>3</sub>Ti<sub>4</sub>O<sub>12</sub> (CCTO) ceramics was reported by Subramanian et al. [1], giant dielectric oxides have been extensively investigated. Giant dielectric oxides that can exhibit unusual high dielectric permittivities ( $\epsilon$ ') of  $\approx 10^3 - 10^6$  without detectable ferroelectric phase transitions concluded of CCTO and its isostructural-type perovskites [1-6], CuO [7], La<sub>2-x</sub>Sr<sub>x</sub>NiO<sub>4</sub> [8-10], Bi-deficiencies BNBT-BST [11], and  $\mathbf{A} \mathbf{F} \mathbf{e}_{1/2} \mathbf{B}_{1/2} \mathbf{O}_3$  ( $\mathbf{A} = \mathbf{B} \mathbf{a}$ , Sr, Ca;  $\mathbf{B} = \mathbf{N} \mathbf{b}$ , Ta, Sb) [12-13] among others. In addition to the potential applications in electronic and high energy-dense storage devices, the origins of giant dielectric behavior of each oxide have also been studied in detail. Many elegant models were proposed to describe the giant dielectric behavior of these oxides such as the internal barrier layer capacitor (IBLC) [5, 14-15], surface barrier layer capacitor (SBLC) [16-17], polaronic stacking fault defect [18] and small polaron hopping models [9-10] as well as the non-Ohmic sample-electrode contact model [2, 17]. Based on the applications point of view, unacceptably high values of the dielectric loss tangent (tanδ) of these giant dielectric oxides is considerable to be the most serious problem. A large high-temperature value of the temperature coefficient, i.e., variation of  $\epsilon'$  or capacitance (at 1 kHz) at any temperature compared to that value at room temperature (RT), is one of the most difficult parameters to improve. Generally, if a parameter can be successfully improved, other dielectric parameters are simultaneously was worsened.

Interestingly, a newly discovered co-doped rutile TiO<sub>2</sub> ceramic can exhibit a low tanδ value and extremely high  $\varepsilon'$  that is stable with temperature over a wide range. This material is likely to enable further development in electronic devices as well as being used in energy-storage devices. Substitution of 10% In3++Nb5+ into rutile-TiO2 (INTO) can produce a very high  $\epsilon' \approx 6 \times 10^4$  and low  $\tan \delta \approx 0.02$  [19]. It was shown that  $\epsilon'$  decreased with decreasing co-doping concentration, while tanδ at 1 kHz tended to increase. Accordingly, a new model, i.e., the electron-pinned defect-dipole (EPDD) model, was proposed to describe the high dielectric performance of INTO ceramics. It suggests that free electrons, which were produced by doping with Nb5+, can be confined in In3+-defect environments [19]. Therefore, under an applied electric field, such localized electrons were freely polarized in triangular shaped  $In_2^{3+}V_O^{\bullet\bullet}Ti^{3+}$  defect complexes in the rutile structure. It was further suggested that the giant dielectric behavior in INTO ceramics was attributed to the IBLC effect [14, 20-23], rather than being explained by the EPDD model. Thus, the origin of the giant dielectric response in INTO ceramics as well as the other co-doped TiO<sub>2</sub>-based systems is still open to scientific debate. Nevertheless, this discovery has greatly stimulated research in the field of giant dielectric constant materials [15-17, 20-33].

Most recently, the complete characterization details (*i.e.*, the phase composition and crystal structure, microstructural analysis, variation in oxidation states and the presence of defects) and the dielectric and electrical properties of other co–doped TiO<sub>2</sub> systems such as Ga<sup>3+</sup>+Nb<sup>5+</sup> [16], Bi<sup>3+</sup>+Nb<sup>5+</sup> [25], Al<sup>3+</sup>+Ta<sup>5+</sup> [29], Al<sup>3+</sup>+Nb<sup>5+</sup> [26], Er<sup>3+</sup>+Nb<sup>5+</sup> [31], Zn<sup>2+</sup>+Nb<sup>5+</sup> [32] and Sm<sup>3+</sup>+Nb<sup>5+</sup> [33] co–doped TiO<sub>2</sub> ceramics were investigated. All of these experimental results are very interesting and have an importance for further development of giant dielectric oxides for use in practical applications. Unfortunately, the temperature

coefficient values and details of analysis of these co-doped TiO<sub>2</sub> systems were seldom reported. Furthermore, the DC bias dependence upon the dielectric response, which is an important parameter, was lacking [30].

For the point of view of applications, there is an ongoing need for a new high–performance donor–acceptor co–doped  $TiO_2$  system. Although Cheng et al. [25] reported the giant dielectric constant properties of  $TiO_2$  co–doped with  $Nb^{5+}$  and various trivalent cation acceptors including  $Bi^{3+}$ ,  $Pr^{3+}$ ,  $Dy^{3+}$ ,  $Sm^{3+}$ , and  $Gd^{3+}$  among others, only the  $Bi^{3+}+Nb^{5+}$  co–doped  $TiO_2$  ceramic system was presented in detail. Among these, only the  $Bi^{3+}+Nb^{5+}$  co–doped  $TiO_2$  type–ceramic can exhibit a low $\delta$  value ( $tan\delta < 0.1$ ), while other co–dopants had very large  $tan\delta$  values. Importantly, except for  $tan\delta$  values. As demonstrated by Hu et al. [26], high  $tan\delta$  and low  $tan\delta$  values of the  $tan\delta$  values. Thus, other excellent dielectric properties of any donor–acceptor co–doped  $tan\delta$  system may be obtained by tuning sintering conditions as well as dopant concentrations.

In the current study, the composition and sintering optimizations, structural and microstructural analyses, and the dielectric and electrical properties as functions of frequency, temperature and DC bias of the Sc<sup>3+</sup>+Nb<sup>5+</sup> co-doped rutile-TiO<sub>2</sub> (ScNTO) are represented. High-performance giant-dielectric properties of this ScNTO system can be achieved by optimizing sintering conditions doping concentrations.

# 5.2 Experimental details

 $(Sc_{0.5}Nb_{0.5})_xTi_{1-x}O_2$  (ScNTO) ceramics, where x=0.1, 0.025, 0.05, and 0.10, were prepared using a solid state reaction (SSR) method. These ceramic compounds are referred to as 1%ScNTO, 2.5%ScNTO, 5%ScNTO and 10%ScNTO ceramics, respectively. Rutile-TiO<sub>2</sub> (Sigma–Aldrich, >99.9% purity), Nb<sub>2</sub>O<sub>5</sub> (Sigma–Aldrich, 99.99% purity), and Sc<sub>2</sub>O<sub>3</sub> (Sigma–Aldrich, 99.9% purity) were used as the starting raw materials. Complete details of the preparation of co–doped TiO<sub>2</sub> by the SSR method are given elsewhere [30]. The ceramic samples were obtained by sintering compacted powder at different temperatures from 1300 to 1500 °C for 1–10 h.

Phase composition and crystal structure of these samples were characterized using X-ray diffraction (PANalytical, EMPYREAN). Scanning electron microscopy (SEM) (SEC, SNE4500M) was used to reveal the microstructure of the sintered ceramics. Mapping the distribution of each type of ion in the ScNTO ceramics was performed using field-emission scanning electron microscopy (FE-SEM) with energy-dispersive X-ray analysis (EDS) (HITACHI SU8030, Japan). Raman spectra of sintered ceramics were collected with a UV-vis Raman System (NT-MDT Ntegra Spectra). The oxidation states in ScNTO ceramics were analyzed using X-ray photoelectron spectroscopy (XPS), PHI5000 VersaProbe II, ULVAC-PHI, Japan) at the SUT-NANOTEC-SLRI Joint Research Facility, Synchrotron Light Research Institute (SLRI), Thailand. The XPS spectra were fitted with PHI MultiPak XPS software using Gaussian-Lorentzian lines. Two parallel electrodes were fabricated by sputter coating with Au. The capacitance and dissipation factor (D, tanδ) were measured using a KEYSIGHT E4990A Impedance Analyzer over the frequency and temperature ranges of 40–10<sup>7</sup> Hz and -60–210 °C,

respectively. Each measurement temperature was kept constant with a precision of  $\pm 0.1$  °C.

### 5.3 Results and discussion

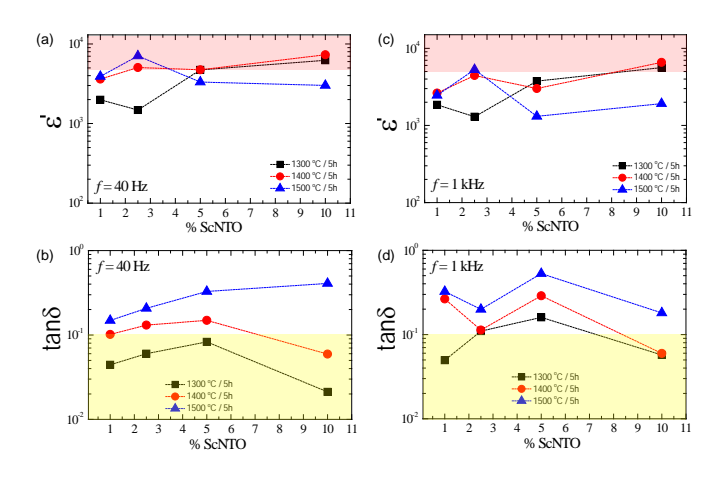


**Fig. 1** ε' and tanδ values at 40 Hz (a–b) and 1 kHz (c–d) for (Sc+Nb) co–doped TiO<sub>2</sub> ceramics with various co–dopant contents.

Fig. 1 illustrates typical room temperature  $\varepsilon'$  and  $\tan\delta$  measured at 40 Hz and 1 kHz for the ScNTO ceramics with various co-dopant concentrations sintered at 1300-1500 °C for 5 h. Both  $\varepsilon'$  and  $\tan\delta$  remarkably change, irrespectively of the co-doping concentration or sintering temperature. According to the composition and sintering optimizations, the ScNTO ceramics that can exhibit high  $\epsilon'$  (>5000) and low tan $\delta$  (<0.1) values, as represented in the respective the red and yellow zones, were classified as potential giant-dielectric materials. For the 1%, 2.5% and 5%ScNTO ceramics sintered at 1300 °C for 5 h, although their tanδ values at 40 Hz were very low as shown in the yellow zone of Fig. 1(b), their  $\varepsilon'$  values were also lower than 5000 in the frequency range of 40–10<sup>3</sup> Hz [Figs. 1(a) and (c)]. For all ceramic compositions sintered at 1500 °C for 5 h, tanδ was very large. It was found that the tan $\delta$  and  $\epsilon'$  values of the 10%ScNTO ceramics sintered at 1300 and 1400 °C were respectively in the yellow and red zones, indicating that this ceramic composition can be optimized by sintering at these conditions. It is clearly demonstrated that sintering process should be one of key methods to control the dielectric properties of the ScNTO ceramics. This behavior is similar to that observed in CCTO ceramics [3, 5, 34]. Throughout this work, we therefore focused on only the 10%ScNTO ceramics. Furthermore, the effects of sintering time were also taken into account.

It is noteworthy that when high–dielectric performance was achieved, a unique feature of the dielectric properties of the ScNTO ceramics was observed. Comparing to those of other giant dielectric materials such as CCTO or  $La_{2-x}Sr_xNiO_4$  [8-10, 18, 35], the  $tan\delta$  value in a low frequency (e.g., at 40 Hz) of the ScNTO ceramics was lower than the value measured at higher frequency. For almost all other giant dielectric oxides, it is usually observed that  $tan\delta$  at 100 Hz is much higher than that at 1 kHz by at least a factor of 2 and as much as one order of magnitude [8, 35]. This clearly was caused by a large DC current leakage.

Fig. 2 shows the XRD patterns of the TiO<sub>2</sub> and 10%ScNTO sintered under different conditions. A main phase of rutile-TiO<sub>2</sub> (JCPDS 21-1276) with a tetragonal structure was detected in all ceramic samples. No impurity phase was observed. The lattice parameters, a and c, were calculated from the XRD patterns. The a and c values of the TiO2 were 4.593 and 2.959 Å, respectively. The a values of the 10%ScNTO ceramics sintered at 1300 °C for 5 h and 1400 °C for 1, 5 and 10 h were respectively found to be 4.603, 4.600, 4.606 and 4.608 Å, while their c values were 2.972, 2.968, 2.975 and 2.978 Å, respectively. The a value of TiO<sub>2</sub> slightly increased by co-doping with 10%Sc+Nb. Interestingly, c values of the 10%ScNTO ceramics were significantly larger than that of TiO<sub>2</sub>. According to the previous work [19], the a value of TiO<sub>2</sub> slightly increased by doping with Nb<sup>5+</sup>, which was due to the small difference in the ionic radii in Ti<sup>4+</sup> ( $r_6 = 0.605 \text{ Å}$ ) and Nb<sup>5+</sup> ( $r_6 = 0.64$  Å). The obvious enhancement of the c value was attributed to the larger ionic radius of  $Sc^{3+}$  ( $r_6 = 0.745 \text{ Å}$ ) compared to that of  $Ti^{4+}$  [36]. This result is consistent with that reported in the literature for the INTO ceramic system, in which the c value increased with increasing In3+ dopant concentration [19, 30]. It is likely that the acceptor dopants were preferentially substituted into the rutile structure along the c-axis. With detection of no impurity phase and increased values of lattice parameters, substitution of Sc<sup>3+</sup> and Nb<sup>5+</sup> doping ions into the rutile-TiO<sub>2</sub> structure is likely.

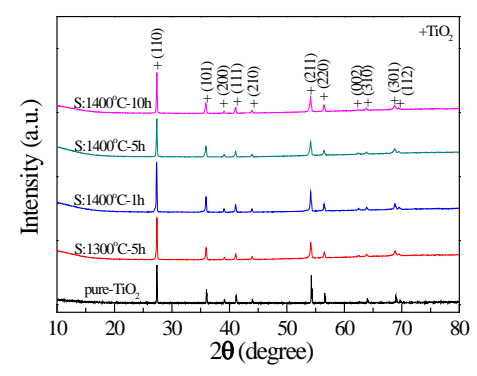


**Fig. 2** XRD patterns of TiO<sub>2</sub> and 10%ScNTO ceramics sintered under different conditions.

The microstructure of the 10%ScNTO ceramics sintered under various conditions is revealed in Fig. 3. All the ceramic samples had highly dense microstructure with no pores. Obvious grains and grain boundaries (GBs) were observed. The mean grain sizes of the ceramics sintered at 1300 °C for 5 h and 1400 °C for 1, 5 and 10 h were  $\approx\!\!4.1, \approx\!\!6.9, \approx\!\!13.5$  and  $\approx\!16.8~\mu m$ , respectively. The mean grain size of the ceramic sintered at 1500 °C for 5 h was  $\approx\!\!38.4~\mu m$ . The grain size significantly increased with increasing sintering time and temperature. The dispersion of all elements in ScNTO ceramics was investigated using SEM mapping images, as shown in Fig. 4. Both Sc and Nb dopants, as well as the primary elements, were homogeneously dispersed in the microstructure.

Fig. 5 shows XPS spectra of the 10%ScNTO ceramic. As demonstrated in Fig. 5(a), the fitted Sc 2*p* peaks at 401.36 and 406.23 eV were evident, confirming the presence of Sc<sup>3+</sup> [37]. Generally, substitution of acceptor ions such as Sc<sup>3+</sup> into TiO<sub>2</sub> is requires oxygen vacancies for charge compensation following the relation:

$$Sc_2O_3 \xrightarrow{2TiO_2} 2Sc'_{Ti} + V_O^{\bullet \bullet} + 3O_O$$
 (1)

To confirm the presence of oxygen vacancies, the XPS spectrum of O 1s profiles was corrected, Fig. 5(b). According to the Gaussian–Lorentzian profile fitting, four peaks were obtained. The main peak at 529.5 eV was ascribed to an oxygen lattice in the bulk Ti–O bond [15, 19, 31]. Three peaks at 530.9, 532.0 and 533.3 eV were assigned to oxygen lattices of other cation–oxygen bonds (i.e., Sc–O and Nb–O bonds), oxygen vacancies and surface hydroxyl (OH), respectively [15, 19, 25, 31].

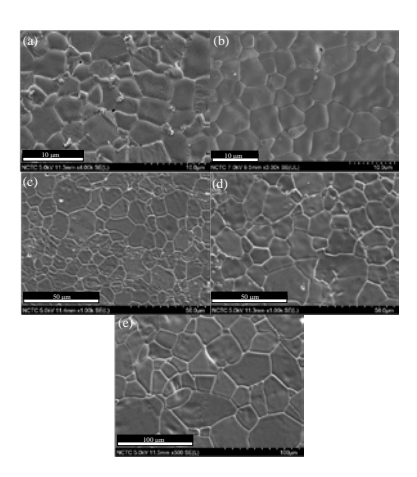
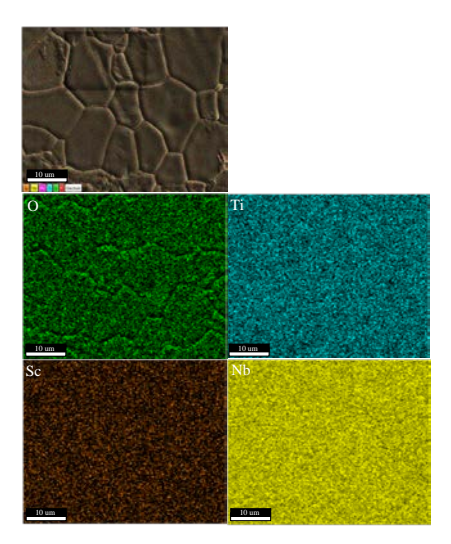


Fig. 3 SEM images of polished–surfaces of 10%ScNTO ceramics sintered under various conditions: (a) 1300 °C for 5 h, (b) 1400 °C for 1 h, (c) 1400 °C for 5 h, (c) 1400 °C for 10 h and (d) 1500 °C for 5 h.



**Fig. 4** Elemental mapping of the 10%ScNTO ceramic sintered at 1400 °C for 5 h.

In Fig. 5(c), the XPS result shows that the binding energies of Nb 3d electrons were 209.5 and 206.74 eV for 3 $d_{3/2}$  and 3 $d_{5/2}$ , respectively. The splitting of the spin–orbit was  $\approx$ 2.76 eV, corresponding to the case of Nb<sup>5+</sup> doped TiO<sub>2</sub> materials [19]. According to the profile fitting, an additional 3 $d_{5/2}$  peak with relatively low–binding energy at  $\approx$ 204.3 eV was not found. This clearly confirms the presence of only Nb<sup>5+</sup> in the ScNTO ceramics [19]. Generally, free electrons in a rutile–TiO<sub>2</sub> ceramic can be produced by doping with electron–donors such as Ta<sup>5+</sup> or Nb<sup>5+</sup>. This resulted in reduction of Ti<sup>4+</sup> to Ti<sup>3+</sup>, following the relationship:

$$2TiO_{2} + Nb_{2}O_{5} \xrightarrow{4TiO_{2}} 2Ti'_{Ti} + 2Nb^{\bullet}_{Ti} + 8O_{O} + 1/2O_{2},$$

$$Ti^{4+} + e \to Ti^{3+}.$$
(2)

To confirm this, the XPS spectrum of Ti 2p was measured. As illustrated in Fig. 5(d), the peak position of the Ti  $2p_{3/2}$  was observed at a binding energy of 458.25 eV, corresponding to the presence of Ti<sup>4+</sup>. Another peak at a relatively lower binding energy of 457.17 eV was achieved by fitting the experimental results, confirming the presence of Ti<sup>3+</sup> in the ScNTO ceramics [19, 38]. The Ti<sup>3+</sup>/Ti<sup>4+</sup> ratio of the 10%ScNTO ceramic was found to be 4.29%, which is approximately the theoretical value.

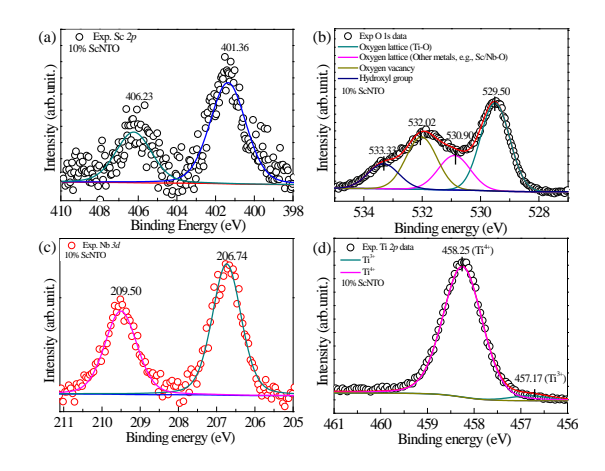


**Fig. 5** XRS spectra of the 10%ScNTO ceramic sintered at 1400  $^{\circ}$ C for 5 h; (a) Sc 2p, (b) O 1s, (c) Nb 3d and (d) Ti 2p.

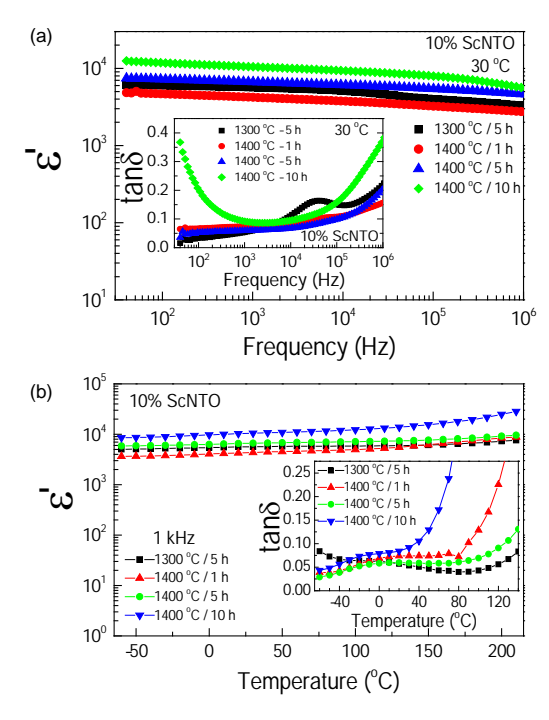


**Fig. 6** (a) Frequency dependence of  $\epsilon'$  at 30 °C for 10%ScNTO ceramics sintered under various conditions; inset shows  $\tan\delta$  at 30 °C over the measured frequency range. (b) Temperature dependence of  $\epsilon'$  at 1 kHz for 10%ScNTO ceramics sintered under different conditions; inset shows  $\tan\delta$  at 1 kHz as a function of temperature.

The dielectric properties of ScNTO ceramics are shown in Fig. 6. All the 10%ScNTO ceramics sintered under various conditions exhibited very high  $\epsilon'$  values over wide frequency and temperature ranges. In Fig. 6(a),  $\epsilon'$  was nearly independent of frequency over the range of  $10^2-10^5$  Hz. In this frequency range, the  $\epsilon'$  values of the 10%ScNTO ceramics were in the range of 4800–12500, while very low  $\tan\delta$  values of  $\approx$ 0.016–0.035 at 40 Hz were achieved [inset of Fig. 6(a)]. The low–frequency  $\tan\delta$  of the 10%ScNTO ceramic sintered at 1400 °C for 10 h was very large and greatly increased with decreasing frequency  $(\tan\delta\approx$ 0.37 at 40 Hz). This was likely caused by a large DC conduction in the ceramic [39]. Sintering at high temperature for a long time usually produces more oxygen vacancies and associated free electrons following the relationship:

$$O_O^x \to \frac{1}{2}O_2 + V_O^{\bullet \bullet} + 2e'. \tag{4}$$

The presence of oxygen vacancies at the GBs and/or outer surfaces can cause a decrease in the resistivity, thus insulting parts of the system. Through further optimization, sintering the ScNTO ceramic for long times reduced the dielectric performance of the ScNTO system. The temperature dependencies of the dielectric properties at 1 kHz of the 10%ScNTO ceramics are shown in Fig. 6(b). As can be clearly seen,  $\epsilon'$  of all the samples was slightly dependent on temperature in the range from -60 to 210 °C. The ε' value of the 10%ScNTO ceramic sintered at 1400 °C for 10 h was likely more dependent on temperature than for other samples. This is consistent with the highest low-frequency  $tan\delta$  value and high DC conduction, which is usually dominant at high temperatures. As illustrated in the inset of Fig. 6(b), the tanδ value of the ceramic sintered for 10 h was dramatically enhanced with increasing temperatures over 40 °C. Notably, the tanδ value of the ceramics sintered at 1300 and 1400 °C for 5 h were too low even though temperature was increased to be greater than 100 °C. This has never been accomplished in CCTO and other giant dielectric constant materials. Although the mechanism of the giant dielectric response in co-doped TiO<sub>2</sub> may be similar to co-doped NiO, the giant dielectric properties of co-doped TiO<sub>2</sub> are likely better that that of co-doped NiO ceramics [39-40].

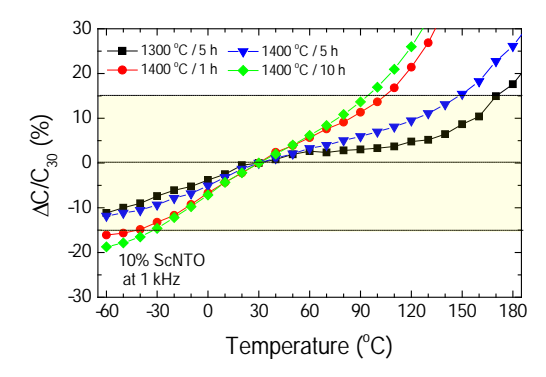
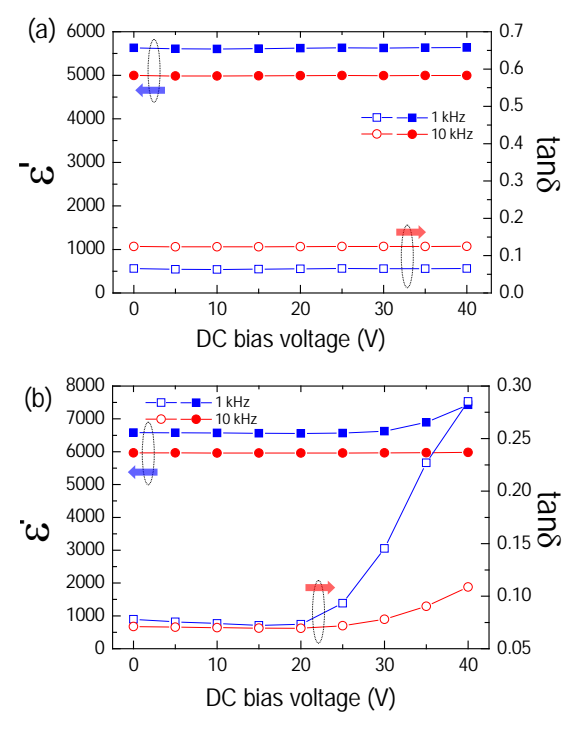


Fig. 7 Temperature coefficient of capacitance values at 1 kHz compared to that at 30 °C for 10%ScNTO ceramics sintered under various conditions.

For practical applications in electronic devices, the temperature coefficient of the temperature–dependence of  $\varepsilon'$  (calculated at 1 kHz) should be less than ±15% (compared to room temperature) for X–R type capacitors. As shown in Fig. 6(b),  $\varepsilon'$  values of all the samples were likely slightly dependent on temperature over the measured temperature range. The behavior of the temperature coefficient is revealed in Fig. 7(a). Unfortunately,

variation in  $\epsilon'$  as the temperature of the ceramics sintered at 1400 °C for 1 and 10 h was very large when carefully consider their temperature coefficient values. As temperatures higher than 90 °C, the temperature coefficient rapidly increased to values greater than  $\pm 15\%$ , making it unsuitable for practical applications. It is interesting that the temperature coefficients of the ceramics sintered at 1300 and 1400 °C for 5 h were less than  $\pm 15\%$  in the temperature ranges from -60–170 °C and -60–150 °C, respectively. These values are satisfactory for X8R capacitor applications, in which  $\epsilon'$  of dielectric layers used must not vary with temperature more than  $\pm 15\%$  at temperatures between -55 and 150 °C. Inset of Fig. 6(b), it is important to note that high tan $\delta$  values in high temperatures (especially above 120 °C) of the ScNTO ceramics sintered at 1400 °C will restrict the application as X8R capacitors. Notably, low tan $\delta$  and high  $\epsilon'$  values with the excellent temperature coefficient of the ScNTO ceramics can be accomplished by optimizing the co–dopant concentrations and sintering conditions. These good dielectric properties are difficult to achieve in other giant dielectric materials other than co–doped TiO<sub>2</sub> based ceramics.



**Fig. 8** Room temperature DC bias–dependence of ε' and tanδ at 1 and 10 kHz for 10%ScNTO ceramics sintered at (a) 1300 °C for 5 h and (b) 1400 °C for 5 h.

The DC bias dependence of the dielectric properties of the 10%ScNTO ceramics was also investigated to further evaluate their high–performance giant–dielectric properties. For capacitor applications, the dielectric properties of the material used should be stable with an applied DC bias or at least change very little. Figs. 8(a) and (b) show the effect of DC bias on the dielectric properties of the 10%ScNTO ceramics sintered at 1300 and 1400 °C for 5 h, respectively. The  $\epsilon'$  and  $\tan\delta$  values at 1 and 10 kHz of the sample sintered at 1300 °C were independent of DC bias over the range of 0–40 V [Fig. 8(a)]. At a 40 V DC bias,  $\epsilon'$  and  $\tan\delta$  values at 1 kHz were changed slightly by  $\approx$ 0.11% and  $\approx$ 0.47%, respectively. As illustrated in Fig. 8(b), the dielectric properties of the sample sintered 1400 °C were independent of DC bias only over the range of 0–20 V. With increasing DC bias voltage higher than 20 V,  $\tan\delta$  greatly increased. Usually, the electrostatic potential barriers, i.e., double Schottky barriers, can be created at interfaces between n–type grains

caused by trapping at acceptor states, leading to the bending of the conduction band across the GB [3, 41]. A potential barrier height ( $\Phi_b$ ) was created at the GB layer. Under an applied DC bias voltage, the barrier becomes asymmetric and  $\Phi_b$  at one side of GB was reduced. This may have resulted in an increase in DC conductivity, resulting in an increase in the low–frequency tan $\delta$ . Sintering the ScNTO ceramic at a lower temperature can result in the best dielectric properties. Comparing the dielectric properties of other co–doped TiO<sub>2</sub> materials (e.g., In+Nb, Ga+Nb, Al+Nb, Al+Ta, Bi+Nb) [16, 19, 25-26, 29], it is very impressive the show that high–performance giant–dielectric properties of the ScNTO ceramics can be achieved using a low sintering temperature and a short time (1300 °C for 5 h).

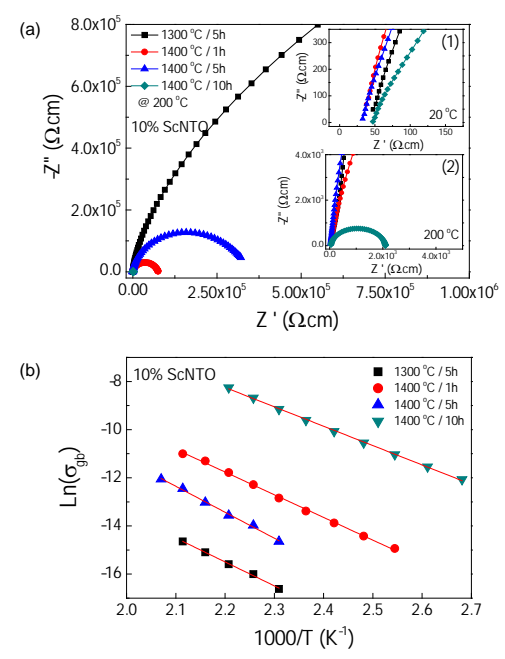


**Fig. 9** (a) Impedance complex plane (Z\*) plots at 200 °C for 10%ScNTO ceramics sintered under different conditions; insets (1) and (2) show expanded views of the impedance data at high frequencies at 20 and 200 °C, respectively. (b) Arrhenius plot of the temperature dependence of GB conductivity ( $\sigma_{gb}$ ) for 10%ScNTO ceramics.

To achieve a better understanding of the giant dielectric properties of the ScNTO ceramics, an impedance spectroscopy was used to separate the electrical responses of individual parts of the ScNTO ceramics. At approximately room temperature, only a linear portion of a large semicircle arc (does not show) with a nonzero intercept [inset (1) of Fig. 9(a)] was observed in  $Z^*$  plots, indicating insulating and semiconducting parts [5]. The effect of sintering conditions on the electrical properties of the GBs could not be determined due to the lack of a complete semicircular arc. Therefore,  $Z^*$  plots at a high temperature must be used. As demonstrated in Fig. 9(a) and inset (2), a large semicircle arc (at 200 °C) for each sample are clearly observed in  $Z^*$  plots. Obviously, the sintering conditions have a remarkable influence on the total resistance of insulating parts ( $R_i$ ). This can originate from the GBs and/or outer surface layer.  $R_i$  significantly decreased with increasing sintering temperature from 1300 to 1400 °C. However,  $R_i$  cannot be correlated to the sintering time (fixed sintering temperature at 1400 °C).  $R_i$  of the sample sintered for 5 h was larger than that of the samples sintered for 1 and 10 h. Alternatively, the resistance of semiconducting grains ( $R_0$ ), which is usually calculated from the nonzero

intercept, of all the samples were very close due to use of the same concentration of Nb<sup>5+</sup> dopant. It was observed that  $R_i$  was associated with the high–temperature coefficient of  $\epsilon'$ . The 10%ScNTO ceramics with low a  $R_i$  value exhibited an  $\epsilon'$  value with poor temperature stability. Conversely, for the ceramics with a high  $R_i$  value, the temperature stability of  $\epsilon'$  was excellent. According to the impedance spectroscopy analysis, it is reasonable to suggest that the giant dielectric properties of the 10%ScNTO ceramics can be attributed to the interfacial polarization effect, rather than EPDD due to the presence of semiconducting grains.  $R_i$  values of the samples sintered at 1300 and 1400 °C for 5 h were still too large (>10<sup>5</sup>  $\Omega$ .cm) even at 200 °C. Thus, the high–performance giant–dielectric properties of these samples can be well described by the large  $R_i$  values.

It was also found that the temperature dependence of the conductivity of the insulating parts  $(\sigma_i=1/R_i)$  obeys the Arrhenius law,

$$\sigma_i = \sigma_0 \exp\left(\frac{-E_i}{k_R T}\right),\tag{5}$$

where  $\sigma_0$  is a constant value,  $E_i$  is the activation energy required for conduction in the insulating region. The  $E_i$  values of the ceramics sintered at 1300 °C for 5 h and 1400 °C for 1, 5 and 10 h were found to be 0.857, 0.831, 0.931 and 0.663 eV, respectively. It was observed that the conduction activation energy of the 10%ScNTO ceramics was significantly larger than that of the conduction activation energy at the GB of CCTO ceramics ( $E_{\rm gb}\approx 0.47-0.74$  eV) [3, 34-35, 42].  $E_i$  values of the ScNTO ceramics can be comparable to  $E_{\rm gb}$  values of the un–doped Ba(Fe<sub>0.5</sub>Nb<sub>0.5</sub>)O<sub>3</sub> ceramics (0.88–0.95 eV) [43-44]. The large  $E_i$  value of the ScNTO ceramics is also considered as another important factor for obtaining high–performance of the giant dielectric properties of the 10%ScNTO ceramics.

### 5.4 Conclusions

Acceptor and donor (Sc³+Nb⁵+) co–doped TiO₂ ceramics were successfully synthesized using a solid state reaction method. By optimizing the dopant concentration and sintering conditions, high  $\epsilon'$  and low  $\tan\delta$  values were achieved in 10% (Sc³+Nb⁵+) co–doped TiO₂ sintered at 1300 and 1400 °C for 5 h. These ceramics can exhibited very low  $\tan\delta\approx0.016$ –0.035 and high  $\epsilon'\approx10^3$ –10⁴ values with excellent temperature stabilities of  $\epsilon'$  at 1 kHz.  $\Delta\epsilon'(T)/\epsilon'_{RT} < \pm15\%$  was obtained over the temperature range from -60 to 150 °C, meeting the requirement for use in X8R capacitors. Furthermore, these  $\epsilon'$  and  $\tan\delta$  values were independent of applied DC bias over the range of 0–40 V. The (Sc³+Nb⁵+) co–doped TiO₂ ceramics were electrically heterogeneous, consisting of semiconducting grains and ultra-high resistant insulating layers. The observed high–performance giant–dielectric properties were attributed to interfacial polarization at insulating layers. The excellent temperature stability of  $\epsilon'$  and low  $\tan\delta$  resulted from veryhigh total resistance of the insulating layers and a very large value for conduction activation energy compared to other giant dielectric materials.

= Ba, Sr,

### References

- [1] M.A. Subramanian, D. Li, N. Duan, B.A. Reisner, A.W. Sleight, High Dielectric Constant in ACu<sub>3</sub>Ti<sub>4</sub>O<sub>12</sub> and ACu<sub>3</sub>Ti<sub>3</sub>FeO<sub>12</sub> Phases, J. Solid State Chem. 151 (2000) 323-325.
- [2] P. Lunkenheimer, R. Fichtl, S. Ebbinghaus, A. Loidl, Nonintrinsic origin of the colossal dielectric constants in CaCu<sub>3</sub>Ti<sub>4</sub>O<sub>12</sub>, Phys. Rev. B 70 (2004) 172102.
- [3] L. Liu, H. Fan, P. Fang, X. Chen, Sol–gel derived CaCu<sub>3</sub>Ti<sub>4</sub>O<sub>12</sub> ceramics: Synthesis, characterization and electrical properties, Mater. Res. Bull. 43 (2008) 1800-1807.
- [4] L. Singh, I.W. Kim, B.C. Sin, K.D. Mandal, U.S. Rai, A. Ullah, H. Chung, Y. Lee, Dielectric studies of a nano-crystalline CaCu<sub>2.90</sub>Zn<sub>0.10</sub>Ti<sub>4</sub>O<sub>12</sub>electro-ceramic by one pot glycine assisted synthesis from inexpensive TiO<sub>2</sub> for energy storage capacitors, RSC Adv. 4 (2014) 52770-52784.
- [5] R. Schmidt, M.C. Stennett, N.C. Hyatt, J. Pokorny, J. Prado-Gonjal, M. Li, D.C. Sinclair, Effects of sintering temperature on the internal barrier layer capacitor (IBLC) structure in CaCu<sub>3</sub>Ti<sub>4</sub>O<sub>12</sub> (CCTO) ceramics, J. Eur. Ceram. Soc. 32 (2012) 3313-3323.
- [6] Y. Shi, W. Hao, H. Wu, L. Sun, E. Cao, Y. Zhang, H. Peng, High dielectric-permittivity properties of NaCu<sub>3</sub>Ti<sub>3</sub>Sb<sub>0.5</sub>Nb<sub>0.5</sub>O<sub>12</sub> ceramics, Ceram. Int. 42 (2016) 116-121.
- [7] M. Li, A. Feteira, D.C. Sinclair, Relaxor ferroelectric-like high effective permittivity in leaky dielectrics/oxide semiconductors induced by electrode effects: A case study of CuO ceramics, J. Appl. Phys. 105 (2009) 114109.
- [8] A. Chouket, O. Bidault, V. Optasanu, A. Cheikhrouhou, W. Cheikhrouhou-Koubaa, M. Khitouni, Enhancement of the dielectric response through Al-substitution in La<sub>1.6</sub>Sr<sub>0.4</sub>NiO<sub>4</sub> nickelates, RSC Adv. 6 (2016) 24543-24548.
- [9] K. Meeporn, N. Chanlek, P. Thongbai, Effects of DC bias on non-ohmic sample-electrode contact and grain boundary responses in giant-permittivity La<sub>1.7</sub>Sr<sub>0.3</sub>Ni<sub>1-x</sub>Mg<sub>x</sub>O<sub>4</sub> ceramics, RSC Advances 6 (2016) 91377-91385.
- [10] J. Wang, G. Liu, B.W. Jia, X.Q. Liu, X.M. Chen, Giant dielectric response and polaronic hopping in Al-substituted  $A_{5/3}Sr_{1/3}NiO_4$  (A=La, Nd) ceramics, Ceram. Int. 40 (2014) 5583-5590.
- [11] J. Shi, H. Fan, X. Liu, Y. Ma, Q. Li, Bi deficiencies induced high permittivity in lead-free BNBT–BST high-temperature dielectrics, J. Alloys Compd. 627 (2015) 463-467.
- [12] I.P. Raevski, S.A. Prosandeev, A.S. Bogatin, M.A. Malitskaya, L. Jastrabik, High dielectric permittivity in  $AFe_{1/2}B_{1/2}O_3$  nonferroelectric perovskite ceramics (A=Ba, Sr, Ca; B=Nb, Ta, Sb), J. Appl. Phys. 93 (2003) 4130-4136.
- [13] S. Ke, H. Fan, H. Huang, Dielectric relaxation in  $A_2$ FeNbO $_6$  (A perovskite ceramics, Journal of Electroceramics 22 (2007) 252-256.

Journal of Materials Chemistry C 4 (2016) 6798-6805.

- [14] Y. Song, X. Wang, X. Zhang, Y. Sui, Y. Zhang, Z. Liu, Z. Lv, Y. Wang, P. Xu, B. Song, The contribution of doped-Al to the colossal permittivity properties of Al<sub>x</sub>Nb<sub>0.03</sub>Ti<sub>0.97-x</sub>O<sub>2</sub> rutile ceramics,
- [15] G. Liu, H. Fan, J. Xu, Z. Liu, Y. Zhao, Colossal permittivity and impedance analysis of niobium and aluminum co-doped TiO<sub>2</sub> ceramics, RSC Advances 6 (2016) 48708-48714.
- [16] W. Dong, W. Hu, A. Berlie, K. Lau, H. Chen, R.L. Withers, Y. Liu, Colossal Dielectric Behavior of Ga+Nb Co-Doped Rutile TiO<sub>2</sub>, ACS Applied Materials & Interfaces 7 (2015) 25321-25325.
- [17] T. Nachaithong, P. Thongbai, S. Maensiri, Colossal permittivity in  $(In_{1/2}Nb_{1/2})_xTi_{1-x}O_2$  ceramics prepared by a glycine nitrate process, J. Eur. Ceram. Soc. 37 (2017) 655-660.
- [18] P.R. Bueno, R. Tararan, R. Parra, E. Joanni, M.A. Ramírez, W.C. Ribeiro, E. Longo, J.A. Varela, A polaronic stacking fault defect model for CaCu<sub>3</sub>Ti<sub>4</sub>O<sub>12</sub> material: an approach for the origin of the huge dielectric constant and semiconducting coexistent features, J. Phys. D: Appl. Phys. 42 (2009) 055404.
- [19] W. Hu, Y. Liu, R.L. Withers, T.J. Frankcombe, L. Norén, A. Snashall, M. Kitchin, P. Smith, B. Gong, H. Chen, J. Schiemer, F. Brink, J. Wong-Leung, Electron-pinned defect-dipoles for high-performance colossal permittivity materials, Nat. Mater. 12 (2013) 821-826.
- [20] J. Li, F. Li, C. Li, G. Yang, Z. Xu, S. Zhang, Evidences of grain boundary capacitance effect on the colossal dielectric permittivity in (Nb + In) co-doped TiO<sub>2</sub> ceramics, Sci Rep 5 (2015) 8295.
- [21] J. Li, F. Li, Z. Xu, Y. Zhuang, S. Zhang, Nonlinear I–V behavior in colossal permittivity ceramic: (Nb+In) co-doped rutile TiO<sub>2</sub>, Ceram. Int. 41, Supplement 1 (2015) S798-S803.

- [22] Y.Q. Wu, X. Zhao, J.L. Zhang, W.B. Su, J. Liu, Huge low-frequency dielectric response of (Nb,In)-doped TiO<sub>2</sub> ceramics, Appl. Phys. Lett. 107 (2015) 242904.
- [23] Y. Song, X. Wang, Y. Sui, Z. Liu, Y. Zhang, H. Zhan, B. Song, Z. Liu, Z. Lv, L. Tao, J. Tang, Origin of colossal dielectric permittivity of rutile Ti<sub>0.9</sub>In<sub>0.05</sub>Nb<sub>0.05</sub>O<sub>2</sub>: single crystal and polycrystalline, Scientific Reports 6 (2016) 21478.
- [24] J. Li, F. Li, Y. Zhuang, L. Jin, L. Wang, X. Wei, Z. Xu, S. Zhang, Microstructure and dielectric properties of (Nb -do/pred crutile TiO<sub>2</sub> ceramics, J. Appl. Phys. 116 (2014) 074105.
- [25] X. Cheng, Z. Li, J. Wu, Colossal permittivity in ceramics of TiO<sub>2</sub> Co-doped with niobium and trivalent cation, Journal of Materials Chemistry A 3 (2015) 5805-5810.
- [26] W. Hu, K. Lau, Y. Liu, R.L. Withers, H. Chen, L. Fu, B. Gong, W. Hutchison, Colossal Dielectric Permittivity in (Nb+Al) Codoped Rutile TiO<sub>2</sub> Ceramics: Compositional Gradient and Local Structure, Chem. Mater. 27 (2015) 4934-4942.
- [27] W. Tuichai, P. Srepusharawoot, E. Swatsitang, S. Danwittayakul, P. Thongbai, Giant dielectric permittivity and electronic structure in (Al + Sb) co-doped TiO<sub>2</sub> ceramics, Microelectron. Eng. 146 (2015) 32-37.
- [28] J. Li, Z. Xu, F. Li, X. Zhu, S. Zhang, SiO<sub>2</sub>-Ti<sub>0.98</sub>In<sub>0.01</sub>Nb<sub>0.01</sub>O<sub>2</sub> composite ceramics with low dielectric loss, high dielectric permittivity and an enhanced breakdown electric field, RSC Advances 6 (2016) 20074-20080.
- [29] Z. Li, J. Wu, D. Xiao, J. Zhu, W. Wu, Colossal permittivity in titanium dioxide ceramics modified by tantalum and trivalent elements, Acta Mater. 103 (2016) 243-251.
- [30] W. Tuichai, S. Danwittayakul, S. Maensiri, P. Thongbai, Investigation on temperature stability performance of giant permittivity (In + Nb) in co-doped TiO<sub>2</sub> ceramic: a crucial aspect for practical electronic applications, RSC Advances 6 (2016) 5582-5589.
- [31] M.-Y. Tse, X. Wei, J. Hao, High-performance colossal permittivity materials of (Nb + Er) codoped  $TiO_2$  for large capacitors and high-energy-density storage devices, Phys. Chem. Chem. Phys. 18 (2016) 24270-24277.
- [32] X. Wei, W. Jie, Z. Yang, F. Zheng, H. Zeng, Y. Liu, J. Hao, Colossal permittivity properties of Zn,Nb co-doped TiO<sub>2</sub> with different phase structures, Journal of Materials Chemistry C 3 (2015) 11005-11010.
- [33] Z. Li, J. Wu, W. Wu, Composition dependence of colossal permittivity in  $(Sm_{0.5}Ta_{0.5})_xTi_{1-x}O_2$  ceramics, Journal of Materials Chemistry C 3 (2015) 9206-9216.
- [34] Y. Huang, D. Shi, Y. Li, G. Li, Q. Wang, L. Liu, L. Fang, Effect of holding time on the dielectric properties and non-ohmic behavior of CaCu<sub>3</sub>Ti<sub>4</sub>O<sub>12</sub> capacitor-varistors, J. Mater. Sci.: Mater. Electron. 24 (2012) 1994-1999.
- [35] J. Boonlakhorn, P. Kidkhunthod, P. Thongbai, A novel approach to achieve high dielectric permittivity and low loss tangent in  $CaCu_3Ti_4O_{12}$  ceramics by co-doping with  $Sm^{3+}$  and  $Mg^{2+}$  ions, J. Eur. Ceram. Soc. 35 (2015) 3521-3528.
- [36] R.D. Shannon, Revised Effective Ionic Radii and Systematic Studies of Interatomie Distances in Halides and Chaleogenides, Acta Cryst. A32 (1976) 751-767.
- [37] Y. Zhang, C. Zhang, Y. Lin, D.-B. Xiong, D. Wang, X. Wu, D. He, Influence of  $Sc^{3+}$  doping in B-site on electrochemical performance of  $Li_4Ti_5O_{12}$  anode materials for lithium-ion battery, J. Power Sources 250 (2014) 50-57.
- [38] L.R. Sheppard, J. Holik, R. Liu, S. Macartney, R. Wuhrer, Tantalum Enrichment in Tantalum-Doped Titanium Dioxide, J. Am. Ceram. Soc. 97 (2014) 3793-3799.
- [39] J. Wu, C.-W. Nan, Y. Lin, Y. Deng, Giant Dielectric Permittivity Observed in Li and Ti Doped NiO, Phys. Rev. Lett. 89 (2002) 217601.
- [40] Y. Li, L. Fang, L. Liu, Y. Huang, C. Hu, Giant dielectric response and charge compensation of Li- and Co-doped NiO ceramics, Mater. Sci. Eng. B 177 (2012) 673-677.
- [41] L. Liu, H. Fan, L. Wang, X. Chen, P. Fang, Dc-bias-field-induced dielectric relaxation and ac conduction in CaCu<sub>3</sub>Ti<sub>4</sub>O<sub>12</sub> ceramics, Philos. Mag. 88 (2008) 537-545.
- [42] L. Liu, D. Shi, S. Zheng, Y. Huang, S. Wu, Y. Li, L. Fang, C. Hu, Polaron relaxation and non-ohmic behavior in  $CaCu_3Ti_4O_{12}$  ceramics with different cooling methods, Mater. Chem. Phys. 139 (2013) 844-850.

- [43] Y. Huang, D. Shi, L. Liu, G. Li, S. Zheng, L. Fang, High-temperature impedance spectroscopy of  $BaFe_{0.5}Nb_{0.5}O_3$  ceramics doped with  $Bi_{0.5}Na_{0.5}TiO_3$ , Applied Physics A 114 (2014) 891-896.
- [44] X. Sun, J. Deng, S. Liu, T. Yan, B. Peng, W. Jia, Z. Mei, H. Su, L. Fang, L. Liu, Grain boundary defect compensation in Ti-doped  $BaFe_{0.5}Nb_{0.5}O_3$  ceramics, Applied Physics A 122 (2016) 864.

### **CHAPTER 6**

# Very Low Dielectric Loss and Giant Dielectric Response with Excellent Temperature Stability of Ga<sup>3+</sup> and Ta<sup>5+</sup> Co-Doped Rutile-TiO<sub>2</sub> Ceramics

### 6.1 Introduction

Various giant-dielectric ceramics with unusual highly dielectric permittivities  $(\varepsilon' \approx 10^3 - 10^6)$  in the radio frequency range have been widely reported in recent years. These materials may be potentially useful in many applications, e.g., ceramic capacitors and high energy-dense storage devices. The giant-dielectric ceramics that have been widely investigated include CaCu<sub>3</sub>Ti<sub>4</sub>O<sub>12</sub> (CCTO) and other isostructural-type perovskites [1-3], CuO [4], NiO-based oxides [5-6], La<sub>2-x</sub>Sr<sub>x</sub>NiO<sub>4</sub> [7], and AFe<sub>1/2</sub>B<sub>1/2</sub>O<sub>3</sub> (A=Ba, Sr, Ca; B=Nb, Ta, Sb) [8]. Usually, at least two important parameters are out of the standard acceptable range for practical applications and are difficult to simultaneously improve. The first parameter is a large low-frequency loss tangent (tan $\delta > 0.05$ ). The temperature stability of  $\varepsilon'$ ,  $\Delta \varepsilon'(T)/\varepsilon'_{RT}$  (%), is the second parameter. To the best our knowledge, the temperature stability of all above giant dielectric materials was much more difficult to resolve than that of high tanδ. According to the EIA standards, for the X7R and X8R temperature specifications for capacitor applications,  $\Delta \varepsilon'(T)/\varepsilon'_{RT}$  of a dielectric material must be  $<\pm15\%$  over the temperature ranges of -55 - 125 °C and -55 - 150 °C, respectively [9]. It is usually found that most strategies used to improve a particular dielectric parameter simultaneously worsen other important dielectric parameters.

Most recently, very high performance dielectric properties were reported in  $In^{3+}$  and  $Nb^{5+}$  co-doped rutile-TiO<sub>2</sub> (INTO) ceramics [10]. A largely temperature and frequency-independent giant permittivity ( $\varepsilon'\approx6\times10^4$ ) with a very low  $tan\delta\approx0.02$  was observed in a  $(In_{1/2}Nb_{1/2})_{0.1}Ti_{0.9}O_2$  (10%INTO) ceramic. A new model was proposed as follows. Free electrons were produced by substitution of  $Nb^{5+}$ , resulting in the reduction of  $Ti^{4+}$  to  $Ti^{3+}$ . These free electrons were localized in the  $In^{3+}$  ion environment [10]. This mechanism is referred as the electron-pinned defect-dipole (EPDD) model. This development has stimulated research in the field of the high-performance giant-dielectric materials [11-25], since  $TiO_2$  is abundant and nontoxic.

For  $TiO_2$ -based giant dielectric ceramics, the electrode effect has a slight influence on the overall dielectric response of INTO ceramics [10], but it has an impact on the dielectric properties of (Ga+Nb) co-doped  $TiO_2$  [13]. In addition to the EPDD model, the internal barrier layer capacitor (IBLC) model based on the interfacial polarization the grain boundary (GB) effect was proposed as the origin of the high-performance giant-dielectric properties of co-doped  $TiO_2$  ceramics [11, 19-23]. A significant controversy concerning the origin of the giant  $\epsilon'$  of NITO as well as other co-doped  $TiO_2$  ceramics currently exists. Furthermore, several phenomena have been observed in  $TiO_2$ -based materials [13-14], such as polaron hopping polarization (for INTO and Ga+Nb co-doped  $TiO_2$ ) and a gradient distribution in  $Ti^{3+}$  concentration (for Al+Nb co-doped  $TiO_2$ ), which have significant influences on the dielectric responses in different temperature ranges.

Most recently, the giant dielectric properties of  $(A^{3+}_{0.5}Ta_{0.5})_xTi_{1-x}O_2$  ( $A^{3+}$  = AI, Sm, Bi, Fe, In, Dy, Ga, Gd, Yb, or Sc) ceramic systems have been investigated. These co–doped  $TiO_2$  ceramics can exhibit very high  $\varepsilon'$  values of  $1.9\times10^4-1.4\times10^5$  [18]. In regard to  $(A^{3+}_{0.5}Ta_{0.5})_xTi_{1-x}O_2$  with  $A^{3+}$  = AI, there were no further details about other  $(A^{3+}_{0.5}Ta_{0.5})_xTi_{1-x}O_2$  ceramics. Crystal structure, microstructure analysis, dielectric spectra as a functions of frequency and temperature and electrical properties of the grains and GBs as well as the valance states of metal ions were unreported. Nevertheless, 12.5% (AI+Ta) co–doped  $TiO_2$  ceramics exhibited interesting dielectric properties with  $\varepsilon'\approx37,600$  and  $tan\delta\approx0.054$  at 1 kHz and 20 °C [18]. However, a strong  $\varepsilon'$  peak near 0 °C was observed in this co–doped  $TiO_2$  system. This might give rise to an unacceptably high–temperature coefficient, which is unsuitable for practical applications. Although a

giant– $\epsilon'$  of INTO ceramics was found to be slightly dependent on temperature, careful inspection revealed that  $\Delta\epsilon'(T)/\epsilon'_{RT}$  was as high as >20% when the temperature was lower than -40 °C or higher than 180 °C [24]. It is very important to completely understand the temperature dependent behavior of the dielectric properties for further reducing the temperature coefficient of all co–doped TiO<sub>2</sub> ceramics. Alternatively, it is also vitally important to perform an ongoing search for new donor/acceptor co–doped TiO<sub>2</sub> ceramics of this class to further optimize their performance.

In this paper, we reported the synthesis and dopant–concentration optimization, structural analysis, microstructure and characterization of the dielectric properties of  $Ga^{3+}$  and  $Ta^{5+}$  co–doped rutile  $TiO_2$  (GTTO) ceramics. Notably, excellent dielectric properties (very low  $tan\delta$ , high  $\epsilon'$  and good temperature stability over a wide range) were successfully accomplished using heat–treated GTTO. The effect of DC bias on the dielectric properties was also studied to optimize the ceramic samples for practical use. Obviously, the insulating GBs and resistive thin outer–surface layers have a remarkable influence on the high–performance giant dielectric properties of GTTO ceramics. It is strongly believed the findings of this research can give comprehensive guidance with a simple strategy to achieve usable dielectric properties of  $TiO_2$ –based ceramics for practical design in electronic applications.

# 6.2 Experimental and theoretical calculation details

A conventional solid state reaction method was used to synthesize  $(Ga_{0.5}Ta_{0.5})_xTi_{1-x}O_2$  (GTTO), where x=0, 0.025, 0.05, and 0.10 (referred to as  $TiO_2$ , 2.5%GTTO, 5.0%GTTO, and 10%GTTO samples, respectively) as well as the single-doped  $Ga_{0.025}Ti_{0.975}O_2$  (2.5%GTO) and  $Ta_{0.025}Ti_{0.975}O_2$  (2.5%TTO) ceramics. The starting raw materials consisted of TiO<sub>2</sub> (Sigma-Aldrich, >99.9% purity), Ta<sub>2</sub>O<sub>5</sub> (Sigma-Aldrich, 99.99% purity), and Ga<sub>2</sub>O<sub>3</sub> (Sigma-Aldrich, 99.99% purity). First, a stoichiometric mixture of the starting materials corresponding to each doping composition was carefully mixed by wet-ball milling in ethanol for 24 h using ≈2.0 mm diameter ZrO₂ balls. Second, the ethanol media was evaporated at 100 °C, until a dried mixed powder was achieved. Third, the resulting dried powder was ground and sieved several times. Then, fine mixed powder was pressed into pellets (without a binder) of ≈9.5 mm in diameter and ≈1.2 mm in thickness by uniaxial compression at ≈180 MPa. Finally, all of pellets for all doping compositions were sintered at different temperatures from 1300 to 1500 °C for 5 h using a heating rate 2 °C/min followed by natural furnace cooling to room temperature (RT).

X-ray diffraction (PANalytical, EMPYREAN) and scanning electron microscopy (SEM) (SEC, SNE4500M) were employed to respectively characterize the phase composition and surface morphologies of the sintered ceramics. SEM-mapping was performed using field-emission scanning electron microscopy (FE-SEM) with energy-dispersive X-ray analysis (EDS) (HITACHI SU8030, Japan) to reveal elemental distribution in the GTTO ceramics. Raman spectra of the polished pellets were collected on a UV-vis Raman System (Horiba Jobin-Yvon T64000). The chemical states in GTTO ceramics were analyzed using X-ray photoelectron spectroscopy (XPS), PHI5000 VersaProbe II, ULVAC-PHI, Japan) at the SUT-NANOTEC-SLRI Joint Research Facility, Synchrotron Light Research Institute (SLRI), Thailand. The XPS spectra were fitted with PHI MultiPak XPS software using a combination of Gaussian and Lorentzian lines.

Before dielectric measurements, all of the sintered ceramics were well polished and further thermally treated at 1200 °C for 1 h to eliminate the electrode effect and to obtain low  $\tan\delta$  values [20]. Each pellet face of all samples was coated with Au electrodes by passing a current of 25 mA for 8 min using a Polaron SC500 sputter coating unit (Sussex, UK). The dielectric properties were measured under an AC oscillation voltage of 500 mV using a KEYSIGHT E4990A Impedance Analyzer over the frequency and temperature ranges of  $10^2 - 10^7$  Hz and -70 - 220 °C, respectively. Each measured temperature was

kept constant with a precision of  $\pm 0.1$  °C. Dielectric measurements were also performed under different DC bias levels (0–40 V).

To gain deep insight into the structural nature of these materials, the most preferable configuration of the GTTO ceramics was determined using density functional theory implemented in the Vienna *Ab initio* Simulation Package (VASP) code [26]. The pseudopotential used in the current study was based on the projector augmented wave approach [27]. Under the LDA+U formalism [28-29] with U=7.5 eV, the 600 eV plane wave energy cutoff was tested for total energy convergence. Moreover, the 2×2×2 and 3×3×3 k–point samplings of the reciprocal lattice space with the Monkhorst–Pack scheme [30] were employed for relaxed and static calculations, respectively.

### 6.3 Results and discussion

The XRD patterns of the ceramic samples sintered at 1400 °C for 4 h are illustrated in Fig. 1(a). Clearly, a main phase of rutile–TiO<sub>2</sub> (JCPDS 21–1276) with a tetragonal structure was observed in all of the ceramic samples. Except for the single–doped 2.5%GTO ceramic, no impurity phase was observed, Fig. 1(b). Lattice parameters (a and c values) were obtained from Rietveld refinement profile fits (data not shown) and summarized in Table 1. Both the a and c values of the single–doped GTO and TTO as well as co–doped GTTO ceramics were larger than those of the un–doped TiO<sub>2</sub> ceramic. This indicates that both Ga<sup>3+</sup> and Ta<sup>5+</sup> doping ions entered into the rutile–TiO<sub>2</sub> lattice structure. The effect of sintering temperature on the phase composition and crystal structure of the 2.5%GTTO ceramic is shown in Fig. 1(c). There was no impurity phase in all the XRD patterns. The a and c values of the 2.5%GTTO ceramics sintered at 1300, 1400 and 1500 °C were summarized in Table 1. The a values for all sintering temperatures are nearly the same in magnitude, whereas, the c values are the same.

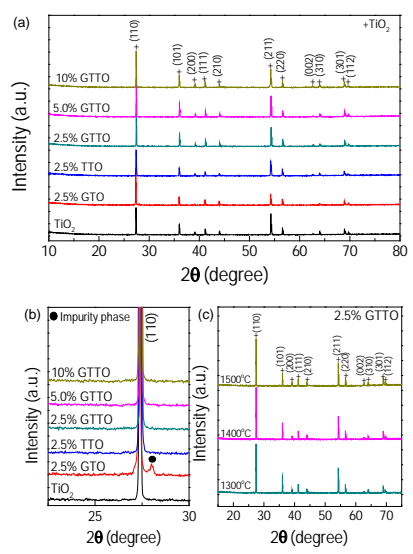


**Fig. 1** (a–b) XRD patterns of TiO<sub>2</sub>, Ga doped–TiO<sub>2</sub>, Ta doped–TiO<sub>2</sub>, and (Ga+Ta) co–doped TiO<sub>2</sub> ceramics sintered at 1400 °C for 5 h. (a) and (b) represent, respectively, the XRD patterns in a wide range scale and narrow range scale, revealing the existence a second phase. (c) XRD patterns of 2.5%(Ga+Ta) co–doped TiO<sub>2</sub> ceramics sintered at different temperatures (1300–1500 °C) for 5 h.

Fig. 2 shows the microstructures of the  $TiO_2$ , single-doped and co-doped ceramics sintered at 1400 °C for 5 h. All of the ceramic samples had a highly dense microstructure without porosity. The mean grain sizes of the  $TiO_2$ , 2.5%GTO and 2.5%TTO were  $\approx$ 20.5,  $\approx$ 19.0 and  $\approx$ 8.3  $\mu$ m, respectively. Substitution of  $Ga^{3+}$  into  $TiO_2$  had no significant effect on

the microstructure. Instead, doping  $TiO_2$  with  $Ta^{5+}$  caused a substantial decrease in the mean grain sizes. This result is similar to that observed in Ta–doped CCTO ceramics, in which a major role of the  $Ta^{5+}$  dopant was its ability to inhibit GB mobility [31]. The mean grain sizes of the 2.5%GTTO, 5.0%GTTO and 10%GTTO ceramics were  $\approx$ 11.6,  $\approx$ 16.0 and  $\approx$ 16.9  $\mu$ m, respectively. The mean grain sizes of all co–doped GTTO ceramics were smaller than that of the un–doped  $TiO_2$  ceramic. At a low co–doping concentration (2.5 mol%), the effect of  $Ta^{5+}$  on the grain growth was dominant. With increasing co–doping concentration, the microstructure of the co–doped  $TiO_2$  ceramics was governed by the effect of  $Ga^{3+}$ . Considering the mean grain sizes of the single–doped 2.5%GTO ( $\approx$ 19.0  $\mu$ m) and 2.5%TTO ( $\approx$ 8.3  $\mu$ m) ceramics, the driving and restorative forces for the GB migration in the co–doped 2.5%GTTO ceramic, which were respectively caused by  $Ga^{3+}$  and  $Ta^{5+}$  dopants, were likely balanced. This is because the mean grain size of  $\approx$ 11.6  $\mu$ m is close to the average value of these two single–doped ceramics.

**Table 1** Lattice parameters (*a* and *c*) of all samples sintered at different temperatures for 4 h.

Sample	Lattice parameters (Å)	
•	a	С
Sintered at 1400 °C		-
TiO <sub>2</sub>	4.593(2)	2.960(4)
2.5%GTO	4.594(8)	2.962(1)
2.5%TTO	4.601(5)	2.966(7)
2.5%GTTO	4.597(7)	2.964(1)
5.0%GTTO	4.598(9)	2.965(8)
10%GTTO	4.596(6)	2.965(9)
Sintered at 1300 °C	,	, ,
2.5%GTTO	4.597(3)	2.964(1)
Sintered at 1500 °C	. ,	. ,
2.5%GTTO	4.598(4)	2.964(1)

Doping  ${\rm TiO_2}$  with  ${\rm Ga^{3+}}$  ions may require oxygen vacancies for charge compensation, following the relation:

$$Ga_2O_3 \xrightarrow{2TiO_2} 2Ga'_{Ti} + V_O^{\bullet \bullet} + 3O_O.$$
 (1)

Thus, the grain growth of GTTO ceramics was likely dominated by the diffusion of oxygen ions. To confirm the presence of oxygen vacancies, Raman spectra of the GTTO ceramics were corrected compared to a pure TiO2 ceramic, since the Raman spectra of TiO<sub>2</sub>-based ceramics are usually sensitive to oxygen vacancies [14, 32]. As illustrated in Fig. 3(a), the strongest peaks of  $A_{1a}$  and  $E_{a}$  modes were observed in all ceramic samples. These are usually associated with O-Ti-O bonds and are caused by oxygen atom liberation along the c-axis [14]. Fig. 3(b), the Raman peaks of  $A_{1a}$  ( $\approx$ 611–619 cm<sup>-1</sup>) and  $E_{\rm g}$  ( $\approx$ 445–448 cm<sup>-1</sup>) of GTTO ceramics significantly shifted to higher and lower wave numbers, respectively, as the Ga<sup>3+</sup> and Ta<sup>5+</sup> co-dopant concentration increased from 0 (pure rutile-TiO<sub>2</sub>) to 10 mol%. It was shown that the position of the  $E_0$  mode shifted from 447 to 443 cm<sup>-1</sup> as the [O]/[Ti] ratio in a rutile-TiO<sub>2</sub> decreased from 2.0 to 1.99 [32]. Therefore, the shifting  $E_g$  peak position strongly confirms that the oxygen vacancy concentration was increased by increasing  $Ga^{3+}$  concentration, following to eq. (1). Shifting of the A<sub>1q</sub> peak position can clearly describe the effect of dopants on the Ti-O bond due to the different ionic radii of the host and dopant ions. The Raman results confirmed that Ga3+ and Ta5+ can be substituted into the rutile-TiO2 structure, supporting the XRD results.

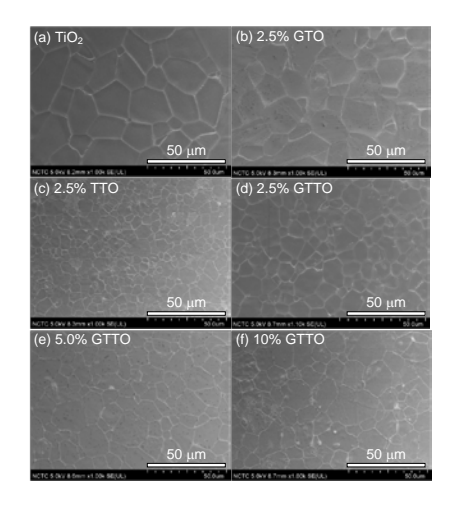


**Fig. 2** SEM images of polished–surfaces of (a) TiO<sub>2</sub>, (b) 2.5%GTO, (c) 2.5%TTO, (d) 2.5%GTTO, (e) 5.0%GTTO, and (f) 10%GTTO ceramics sintered at 1400 °C for 5 h.

The influence of sintering temperature on the microstructural evolution of the 2.5%GTTO ceramic was studied, since the concentration of oxygen vacancies can also be enhanced by increasing sintering temperature. Given a fixed co-dopant concentration, the number of oxygen vacancies and their diffusion rate should be increased by increasing sintering temperature. As expected, the mean grain size of the 2.5%GTTO ceramic increased from 10.6 to 22.5  $\mu$ m as sintering temperature was increased from 1300 to 1500 °C, Fig. 4(a-c). Mapping images of Ti, Ga and Ta elements are shown in Fig. 4(d-f). In the measureable resolution, both the dopants Ga and Ta dopants as well as Ti were homogeneously dispersed in the microstructure. Unfortunately, the dispersion of dopants at the GBs cannot be identified because the resolution is not sufficiently high

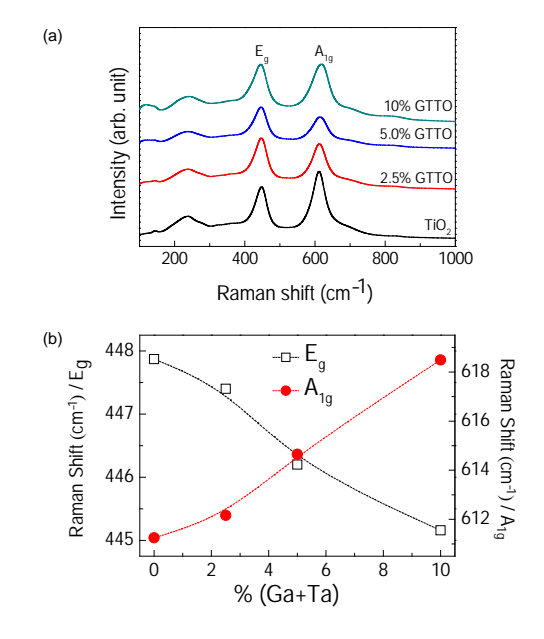


**Fig. 3** (a) Raman spectra of TiO<sub>2</sub> and (Ga+Ta) co-doped TiO<sub>2</sub> ceramics sintered at 1400 °C for 5 h. (b) Raman shift of E<sub>g</sub> and A<sub>1g</sub> modes of GTTO ceramics as a function of (Ga+Ta) co-dopant concentrations.

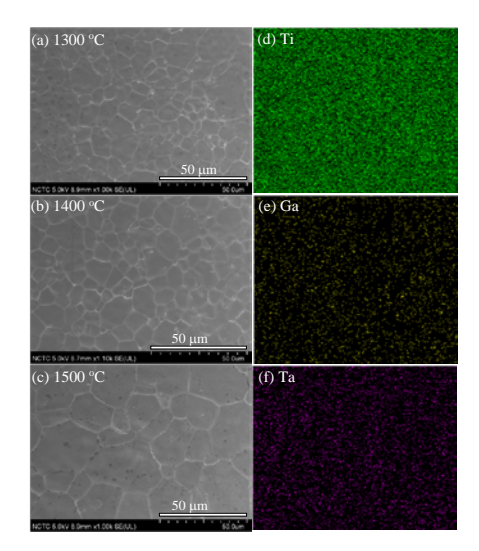


**Fig. 4** (a–c) SEM images of polished–surfaces of 2.5%GTTO ceramics sintered at 1300, 1400 and 1500 °C for 5 h. (d–f) Element mapping of the 2.5%GTTO sintered at 1500 °C for 5 h.

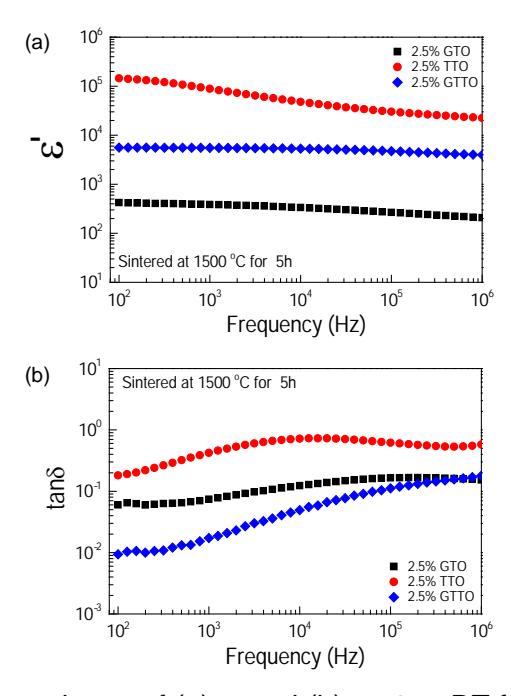


**Fig. 5** Frequency dependence of (a)  $\varepsilon'$  and (b) tanδ at RT for the 2.5%GTO, 2.5%TTO, and 2.5%GTTO ceramics sintered at 1500 °C for 5 h.

High performance giant dielectric properties were only obtained in the co–doped GTTO ceramics. The dielectric properties at RT of the co–doped 2.5%GTTO ceramic compared to those of the single–doped 2.5%GTO and 2.5%TTO ceramics are presented in Figs. 5(a) and (b). Although an ultrahigh  $\epsilon'$  value ( $\approx\!10^5$  at 1 kHz) can be achieved in the 2.5%TTO ceramic, a very high tan $\!\delta$  (> 0.1) was also obtained. Creation of electrons by reducing  $\mathrm{Ti}^{4+}$  to  $\mathrm{Ti}^{3+}$  in a rutile–TiO $_2$  ceramic is usually performed by doping with electron–donor ions (e.g.,  $\mathrm{Ta}^{5+}$ ), following the relationship:

$$2TiO_2 + Ta_2O_5 \xrightarrow{4TiO_2} 2Ti'_{Ti} + 2Ta^{\bullet}_{Ti} + 8O_O + 1/2O_2$$
, (2)

$$Ti^{4+} + e \to Ti^{3+}$$
. (3)

In this case, interfacial polarization due to free electrons trapped at some defects or interfaces was probably responsible for the observed giant dielectric properties [21]. The

2.5%GTO ceramic exhibited a low  $\tan \delta \approx 0.07$  at 1 kHz, and a low  $\epsilon'$  value ( $\approx 400$ ) was also obtained. The dielectric properties of  $TiO_2$  were not balanced by only doping with either  $Ga^{3+}$  or  $Ta^{5+}$  ions. A largely frequency–independent  $\epsilon'$  and low  $\tan \delta$  of  $TiO_2$  were simultaneously achieved by co–doping with acceptor–donor ions of  $Ga^{3+}$  and  $Ta^{5+}$ . These good dielectric parameters of the (Ga+Ta) co–doped  $TiO_2$  system can be comparable to those of (In+Nb) [10, 20, 24], (Zn+Nb) [33], (AI+Nb) [14] and (Ga+Nb) [13] co–doped  $TiO_2$  systems. All of these co–doped  $TiO_2$  systems exhibited high  $\epsilon' > 10^3$  with very low  $\tan \delta < 0.05$  at RT and 1 kHz. The mechanism of the giant dielectric response in GTTO ceramics is likely similar to that observed in co–doped NiO ceramics. However, the dielectric properties of the GTTO ceramics are better that those of co–doped NiO ceramics [5-6, 34].

The relationship between giant dielectric properties and microstructure is usually observed, especially for CCTO ceramics [1, 31, 35]. Unfortunately, this relationship has never been observed or reported for co–doped TiO $_2$  ceramics. As shown in Figs. 6(a–b), the  $\epsilon'$  values of the 2.5%GTTO and 5.0%GTTO ceramics increased with increasing sintering temperature from 1300 to 1500 °C, indicating the grain size dependence of  $\epsilon'$  in GTTO ceramics. For the 2.5%GTTO ceramics, in the frequency range below  $10^4$  Hz,  $\tan\delta$  tended to decrease as sintering temperature was increased. This is in contrast to CCTO ceramics, in which both  $\epsilon'$  and  $\tan\delta$  usually increased with increasing sintering temperature. At  $10^2$  Hz and RT, the  $\epsilon'$  values of the 2.5% and 5.0%GTTO ceramics were, respectively,  $5.6 \times 10^3$  and  $3.8 \times 10^4$ , while  $\tan\delta$  values were 0.009 and 0.036, respectively. For several co–doped TiO $_2$  ceramics [11, 14, 36], the sintering conditions have an effect on the dielectric properties. The increase in  $\epsilon'$  of the GTTO ceramics is similar to that observed in CCTO ceramics [1, 37].

The  $\epsilon'$  and  $\tan\delta$  values at 1 kHz and RT for the GTTO ceramics with different co–dopant concentrations sintered under various temperatures are shown in Figs. 6(c–d). The co–dopant concentrations and sintering temperatures were simultaneously optimized. Good dielectric properties (i.e., high  $\epsilon'>10^3$  with  $\tan\delta<0.1$ ) of GTTO ceramics with low dopant concentrations ( $\leq 5$  mol%) were accomplished by sintering at 1400 and 1500 °C. For 10%GTTO ceramic, good dielectric properties could be obtained by sintering at 1400 °C. Sintering condition of 1300 °C for 5 h was unsuitable for the GTTO ceramic system.

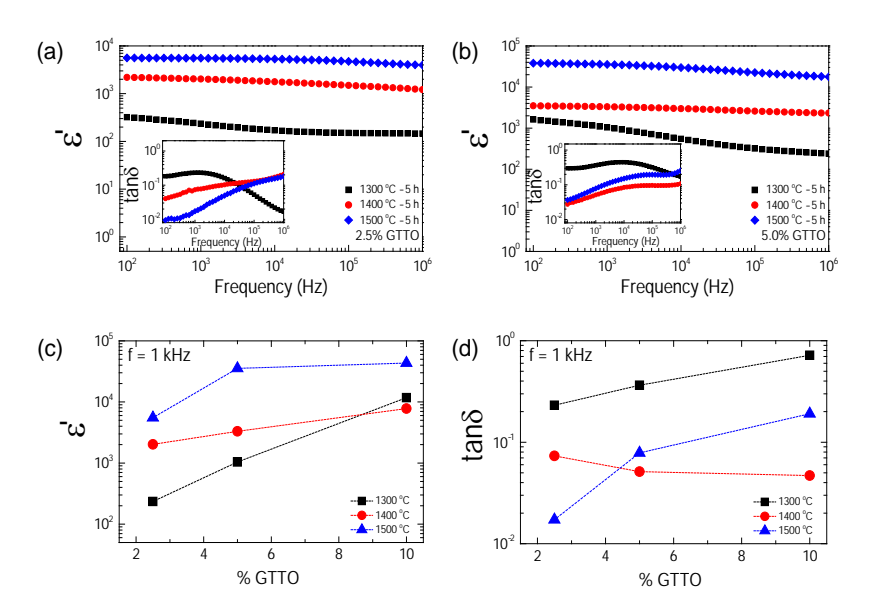


**Fig. 6** (a–b) Frequency dependence of ε' at RT for the 2.5%GTTO and 5.0%GTTO ceramics sintered at 1300–1500 °C for 5 h. The insets of (a) and (b) show tanδ values at RT of the 2.5%GTTO and 5.0%GTTO ceramics. (c–d) Dielectric

properties ( $\epsilon'$  and  $\tan\delta$ , respectively) at RT and 1 kHz for (Ga+Ta) co-doped TiO<sub>2</sub> as a function of dopant content sintered at different temperatures for 5 h.

Very high  $\varepsilon'$  values in the range of  $10^3$ – $10^5$  with low tan $\delta$ <0.1 at 1 kHz and RT were notably achieved in the GTTO system. Actually, these good dielectric properties can also achieved CCTO and related isostructural-ACu<sub>3</sub>Ti<sub>4</sub>O<sub>12</sub> doping/co-doping with suitable metal ions such as Sr<sup>2+</sup>, Yb<sup>3+</sup> and Y<sup>3+</sup>+Mg<sup>2+</sup> [35, 38-39]. However, excellent dielectric-temperature stability (especially at temperatures higher than 125 °C) has never been accomplished in these CCTO-based ceramics. The 2.5%GTTO ceramic sintered at 1500 °C for 5 h exhibited the best temperature coefficient of capacitance or  $\varepsilon'$ . Fig. 7(a),  $\varepsilon'$  values at 1 kHz – 1 MHz of the 2.5%GTTO ceramic seem to be independent of temperature from -70 to 220 °C. The temperature coefficients at different temperatures  $(\Delta \varepsilon'(T)/\varepsilon'_{RT})$  were calculated to identify the high-performance giant-dielectric properties of GTTO ceramics. Inset of Fig. 7(a), the temperature coefficient of GTTO ceramics was still lower than ±15% even though at temperatures higher than 150 °C. At 10 kHz,  $\Delta \varepsilon'(200^{\circ}C)/\varepsilon'_{RT} = 6.26\%$ . At 1 kHz,  $\Delta \varepsilon'(180^{\circ}C)/\varepsilon'_{RT} < 15\%$ . This is much better than those of other giant dielectric materials such as CCTO, CuO, NiO-based oxides,  $La_{2-x}Sr_xNiO_4$  and  $AFe_{1/2}B_{1/2}O_3$  [4, 6-8, 38-39].

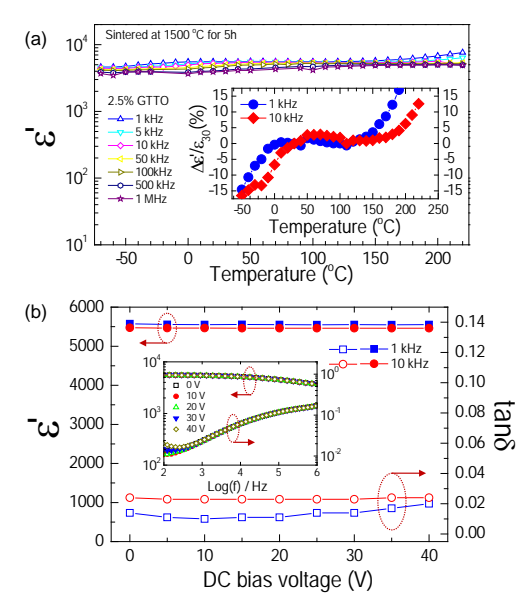
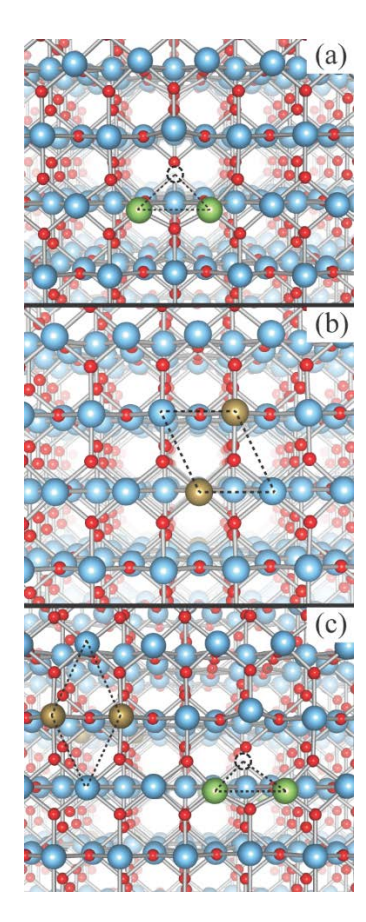


Fig. 7 (a) Temperature dependence of  $\epsilon'$  at selected frequencies for the 2.5%GTTO ceramic sintered at 1500 °C for 5 h. The inset shows the temperature coefficient of  $\epsilon'$  at 1 kHz for the 2.5%GTTO ceramic. (b) DC bias voltage dependence of capacitance at selected frequencies for the 2.5%GTTO ceramic. The inset shows frequency dependence of  $\epsilon'$  at RT under different DC voltage levels.

Fig. 7(b), the  $\varepsilon'$  and  $\tan\delta$  values at the selected frequencies of 1 and 10 kHz were nearly independent of DC bias voltage in the range of 0–40 V. At 40 V DC bias,  $\varepsilon'$  and  $\tan\delta$  values were slightly changed by  $\approx$ 0.23% and  $\approx$ 3.0%, respectively. This observation reflects another view of the high–performance dielectric permittivity of GTTO ceramics. Usually, the electrostatic potential barriers can be created at interfaces between n–type grains and interfaces between a resistive outer–surface layer and a semiconducting inner core. The barrier becomes asymmetric and the potential barrier height at one side of GB was reduced under an applied DC bias [1, 40]. This can cause an increase in the low–frequency  $\tan\delta$  value and reduction in  $\varepsilon'$  value. Thus, the DC bias independence of dielectric properties may be due to very large value of the potential barrier height at the internal interfaces. Inset of Fig. 7(b),  $\varepsilon'$  was independent of DC bias over the frequency range of  $10^2$ – $10^6$  Hz, while  $\tan\delta$  at  $10^2$  Hz was slightly increased by increasing DC bias.

This may have been caused by the release of trapped electrons from an internal interface as a result of applying a DC bias. Oxygen ions and/or other change species were forced and accumulated the surface layer–electrode interface.

To investigate the local defects of the GTTO ceramics, first-principles calculations were done. Based on the results of Raman spectra (Fig. 3), we firstly created one oxygen vacancy and then replaced two Ti atoms with two Ga atoms in rutile TiO2. This structure is defined as 2GaVoTiO2 (Vo stands for the oxygen vacancy). In the present work, several initial configurations of GaVoTiO2 were setup. For each configuration, we allowed all atoms to relax fully with no symmetry constraints. Based on our total energy calculations, we found that the most stable form of 2GaV<sub>0</sub>TiO<sub>2</sub> was a triangular form as presented in Fig. 8(a). Also, we investigated the most preferable structure for the case of 2Ti atoms substituted by 2Ta atoms in TiO2 and this is referred to as 2TaTiO2. According to the stable structure of 2TaTiO2, we found that 2Ta atoms preferentially form a diamond shaped structure as shown in Fig. 8(b). We used the most stable configurations of GaV<sub>o</sub>TiO<sub>2</sub> and 2TaTiO<sub>2</sub> to further investigate the lowest energy configuration of the GTTO ceramics, by placing the 2GaVo triangular and 2Ta diamond defects into the TiO2 structure simultaneously. When the 2GaVo triangular and 2Ta diamond defects were present in TiO<sub>2</sub>, three possible cases were considered in the present study, (a) a 2Ta diamond shape was placed near the Vo triangular defect, (b) the 2Ta diamond shape was placed near 2Ga atoms with a triangular defect, and (c) the 2Ta diamond defect and 2GaV<sub>o</sub> triangular shape were placed rather far from each other. On the basis of total energy, our results revealed that case (c) resulted in the lowest total energy. The 2GaV<sub>o</sub> triangular defect does not prefer to be close to the 2Ta diamond defect as shown in Fig. 8(c). These findings suggest that there is a rather small coupling between the 2GaV<sub>o</sub> triangular and 2Ta diamond defects. Consequently, the giant dielectric permittivity in the GTTO ceramics should come mainly from the interfacial polarization at the internal insulating layers (i.e., IBLC and/or surface barrier layer capacitor (SBLC) effects) rather than EPDD effect.



**Fig. 8** The lowest energy configurations of (a) 2GaV<sub>o</sub>TiO<sub>2</sub> triangular complex (b) 2TaTiO<sub>2</sub> diamond defect, and (c) triangular and diamond defects of (Ga+Ta) co-doped TiO<sub>2</sub> ceramics. Green, light blue, brown, and red spheres denote Ga, Ti, Ta and O, respectively. The oxygen vacancy or V<sub>o</sub> is represented by dotted spheres.

To clarify the origins of the high-performance giant-dielectric properties of GTTO ceramics, the electrical responses were investigated using impedance spectroscopy. In Fig. 9(a) and its inset, large semicircle arcs and nonzero intercept on the Z' axis are observed in Z\* plot of the 2.5%GTTO ceramic. These indicate the existence of insulating and semiconducting components, respectively [2, 19]. The diameter of the large semicircle arc significantly decreased with increasing temperature, while the nonzero intercept slightly decreased in the temperature range from 150 to 210°C. The nonzero intercept is usually considered a result of the electrical response of the semiconducting grains [2, 19, 25, 41]. The large semicircle arc may result from the combined effects of many parts such as the GBs and resistive outer-surface layers. The relatively high resistivity of GBs may correlate to the amorphous crystalline structure and a relatively complete oxidation of GB regions (compared to the grains) [20]. According to our previous work [25], after annealing the In+Nb co-doped TiO2 in air, the semiconducting surface had become a resistive surface. This was primarily caused by filling of oxygen vacancies on the surface. The formation of resistive thin outer-surface layers may also be due to other mechanisms. Careful investigation is needed to clarify the exact origin of the resistive thin outer-surface layers. The grain resistance  $(R_{\rm q})$  values, which were estimated from the nonzero intercept [41], were ≈35 Ω.cm. This is comparable to other co-doped TiO<sub>2</sub> ceramics [19, 25]. At 150 °C, the total resistance of the insulating components ( $R_i$ ) of the 2.5%GTTO ceramic was as large as ≈1.2×10<sup>6</sup> Ω.cm. while the total resistance of CCTO ceramics, which primarily governed by the GB resistance, was much lower than this value [1, 35]. Thus, the especially good temperature stability of the  $\varepsilon'$  value of the 2.5%GTTO ceramic likely resulted from a very high  $R_i$  value even at high temperatures.

The conductivity of the insulating parts ( $\sigma_i$ =1/ $R_i$ ) at different temperatures can be calculated from the Z"-frequency plots, Fig. 9(b), at the maximum value of Z" ( $Z''_{max}$ ),  $R=2Z''_{max}$ . In the inset of Fig. 9(b), the temperature dependence of  $\sigma_i$  follows the Arrhenius law:

$$\sigma_i = \sigma_0 \exp\left(\frac{-E_i}{k_B T}\right),\tag{4}$$

where  $\sigma_0$  is a constant value,  $E_i$  is the activation energy required for conduction in the insulating region. The  $E_i$  value of the 2.5%GTTO ceramic was 0.909 eV. This is much larger than that of the conduction activation energy at the GB for CCTO ceramics ( $E_{\rm gb} \approx 0.47-0.74$  eV) [1, 31, 35, 37, 42]. The  $E_i$  value of the GTTO ceramic is comparable to  $E_{\rm gb}$  values of the Ba(Fe<sub>1/2</sub>Nb<sub>1/2</sub>)O<sub>3</sub> ceramics (0.88–0.95 eV) [43-44]. The temperature–variation of  $\sigma_i$  of GTTO ceramics obeys the Arrhenius law. This is not consistent with the case of single Nb–doped TiO<sub>2</sub>, in which the temperature dependence of conductivity follows the Mott–VRH law and is related to a small polaron mechanism [10].

As shown in Fig. 10(a), the position of the Ti  $2p_{3/2}$  is clearly observed in both of the 5.0% and 10%GTTO ceramics with the same binding energy of  $\approx$ 458.4 eV, corresponding to the presence of Ti<sup>4+</sup> [10]. Additionally, another peak was observed at a relatively lower binding energy of  $\approx$ 457.1 eV, indicating the presence of Ti<sup>3+</sup> [10, 45]. The Ti<sup>3+</sup>/Ti<sup>4+</sup> ratios of the 5% and 10%GTTO ceramics were about 1.31 and 2.12%, respectively. These values are smaller than those of the theoretical ratios of individual dopants (2.5 and 5% for Ta<sup>5+</sup>). According to the first report of INTO ceramics [10], the Ti<sup>3+</sup>/Ti<sup>4+</sup> ratio of the 10%INTO

sample obtained from the XPS result ( $\approx$ 5.87%) was very close to the theoretical value for 5%Nb<sup>5+</sup>–doped TiO<sub>2</sub>. The concentration of Ti<sup>3+</sup> detected in the 10%INTO ceramic was larger than that of the 10%GTTO ceramic by a factor of  $\approx$ 3, while the  $\epsilon'$  values of these two systems were not greatly different ( $\epsilon' \approx 6 \times 10^4$  and  $4.3 \times 10^4$  for the 10%INTO and GTTO ceramics, respectively). This confirms that the origin of the high–performance giant–dielectric properties of the GTTO ceramic system cannot be attributed to the EPDD model.

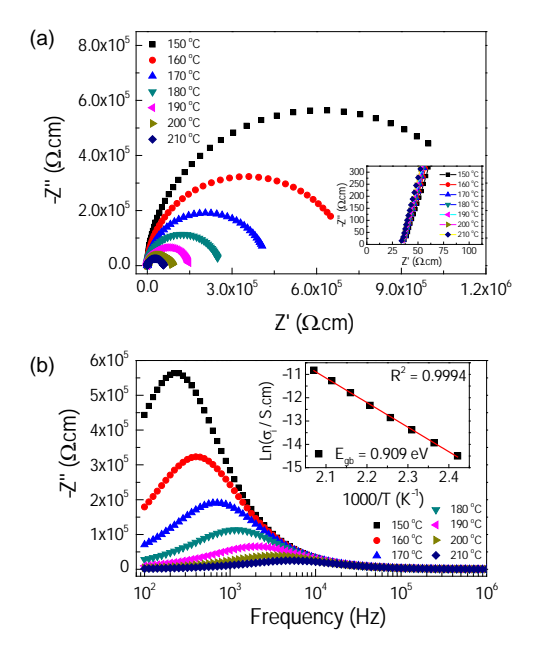


**Fig. 9** (a) Impedance complex plane (Z\*) plots in the temperature range of 150–210 °C of 2.5%GTTO ceramic sintered at 1500 °C for 5 h; inset shows an expanded view of the high frequency data close to the origin. (b) Frequency dependence of -Z" at various temperatures of 2.5%GTTO ceramic; inset shows the Arrhenius plots of the conductivity of insulating components (σ<sub>i</sub>).

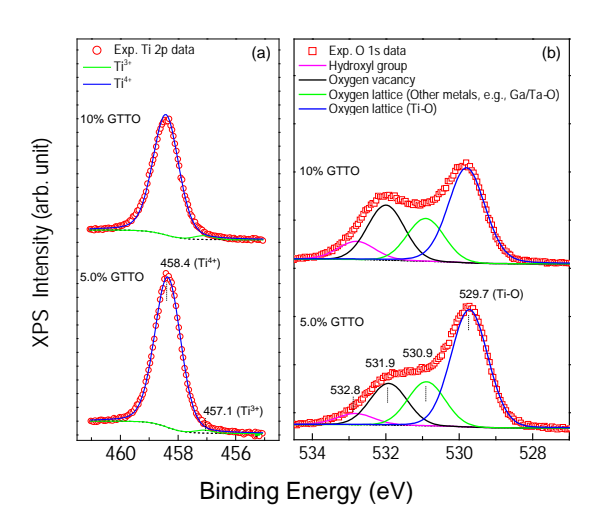


**Fig. 10** Valence states of (Ga+Ta) co–doped TiO₂ form XPS spectra (open circles) and corresponding fitted results (solid lines) of the 5%GTTO and 10%GTTO ceramics sintered at 1500 °C for 5 h; (a) Ti 2p and (b) O 1s.

As shown in Fig. 10(a), the position of the Ti  $2p_{3/2}$  is clearly observed in both of the 5.0% and 10%GTTO ceramics with the same binding energy of  $\approx$ 458.4 eV, corresponding to the presence of Ti<sup>4+</sup> [10]. Additionally, another peak was observed at a relatively lower

binding energy of  $\approx$ 457.1 eV, indicating the presence of Ti³+ [10, 45]. The Ti³+/Ti⁴+ ratios of the 5% and 10%GTTO ceramics were about 1.31 and 2.12%, respectively. These values are smaller than those of the theoretical ratios of individual dopants (2.5 and 5% for Ta⁵+). According to the first report of INTO ceramics [10], the Ti³+/Ti⁴+ ratio of the 10%INTO sample obtained from the XPS result ( $\approx$ 5.87%) was very close to the theoretical value for 5%Nb⁵+–doped TiO₂. The concentration of Ti³+ detected in the 10%INTO ceramic was larger than that of the 10%GTTO ceramic by a factor of  $\approx$ 3, while the  $\epsilon$ ′ values of these two systems were not greatly different ( $\epsilon$ ′  $\approx$ 6×10⁴ and 4.3×10⁴ for the 10%INTO and GTTO ceramics, respectively). This confirms that the origin of the high–performance giant–dielectric properties of the GTTO ceramic system cannot be attributed to the EPDD model.

The O 1s profiles in the 5% and 10%GTTO ceramics are shown in Fig. 10(b). Using Gaussian–Lorentzian profile fitting, four components were obtained: a main peak at 529.8 eV and three higher–energy peaks at 530.9–532.8 eV. The main peak can be ascribed to the oxygen lattice as the bulk Ti–O bond [10]. The peaks at 530.9, 531.9 and 532.8 were ascribed to oxygen lattices of other metal ions (i.e., Ga–O and Ta–O), oxygen vacancies and surface hydroxyl (OH), respectively [10, 19]. Substitution of Ta<sup>5+</sup> did not induce oxygen vacancies, whereas doping TiO<sub>2</sub> with acceptor ions such as Ga<sup>3+</sup> is generally required oxygen vacancies for charge compensation, as required by eq. (1). Fig. 11(a), specifically, Ta 4f was observed as two peaks; 4 f<sub>7/2</sub> at 26.2 eV and 4 f<sub>5/2</sub> at 28.2 eV. This result is consistent with the typical result for Ta 4f, which indicated the presence of Ta<sup>5+</sup> in the GTTO ceramics [45-46]. In Fig. 11(b), the fitted Ga 2p3/2 peak located at around 1118.0 eV can be ascribed to Ga<sup>3+</sup> [47].

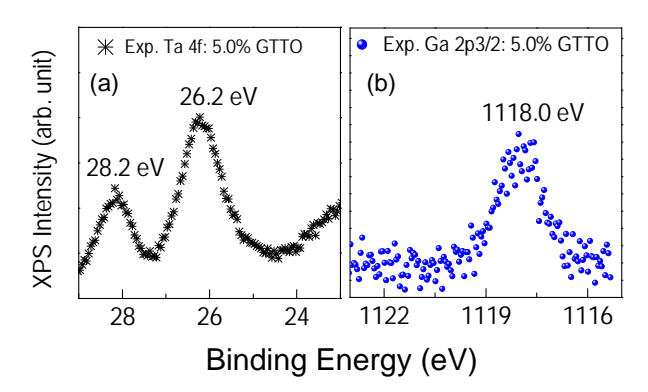


**Fig. 11** XPS spectra of the 5%GTTO ceramic sintered at 1500  $^{\circ}$ C for 5 h; (a) Ta 4f and (b) Ga 2p.

### 6.4 Conclusions

 $(Ga_{0.5}Ta_{0.5})_xTi_{1-x}O_2$  ceramics with different co–dopant concentrations, as well as Ga or Ta single–doped  $TiO_2$  ceramics, were successfully prepared using a conventional mixed oxide method. A highly dense microstructure was obtained in all sintered ceramics. The grain sizes of  $(Ga_{0.5}Ta_{0.5})_xTi_{1-x}O_2$  increased with increasing co–dopant concentrations and sintering temperatures. High  $\epsilon'\approx5.5\times10^3-3.5\times10^4$  and very low  $\tan\delta\approx0.017-0.079$  at 1 kHz were achieved. Interestingly, good temperature stability of  $\epsilon'$   $(\Delta\epsilon'(T)/\epsilon'_{RT} < \pm15\%$  over a wide temperature range) was obtained in the  $(Ga_{0.5}Ta_{0.5})_{0.025}Ti_{0.975}O_2$  ceramic. Furthermore, it was found that the dielectric properties were independent of DC over the range of 0–40 V. The  $(Ga_{0.5}Ta_{0.5})_{0.025}Ti_{0.975}O_2$  ceramic exhibited extremely large resistivity values. Examination of the possible formation of defect structures was performed using a first–principles study. A slight coupling between the 2Ta diamond and  $2GaV_0$  triangular shapes was indicated, indicating a slight EPDD effect. The origin of the high–performance giant–dielectric properties was attributed to interfacial polarization at the very highly resistive insulating layers.

= Ba, Sr, a

## References

- [1] L. Liu, H. Fan, P. Fang, X. Chen, Sol-gel derived CaCu<sub>3</sub>Ti<sub>4</sub>O<sub>12</sub> ceramics: Synthesis, characterization and electrical properties, Mater. Res. Bull. 43 (2008) 1800-1807.
- [2] R. Schmidt, M.C. Stennett, N.C. Hyatt, J. Pokorny, J. Prado-Gonjal, M. Li, D.C. Sinclair, Effects of sintering temperature on the internal barrier layer capacitor (IBLC) structure in CaCu<sub>3</sub>Ti<sub>4</sub>O<sub>12</sub> (CCTO) ceramics, J. Eur. Ceram. Soc. 32 (2012) 3313-3323.
- [3] J. Li, K. Wu, R. Jia, L. Hou, L. Gao, S. Li, Towards enhanced varistor property and lower dielectric loss of CaCu<sub>3</sub>Ti<sub>4</sub>O<sub>12</sub> based ceramics, Materials & Design 92 (2016) 546-551.
- [4] M. Li, A. Feteira, D.C. Sinclair, Relaxor ferroelectric-like high effective permittivity in leaky dielectrics/oxide semiconductors induced by electrode effects: A case study of CuO ceramics, J. Appl. Phys. 105 (2009) 114109.
- [5] Y. Liu, W. Wang, J. Huang, C. Zhu, C. Wang, Y. Cao, High dielectric permittivity of Li and Sc co-doped NiO ceramics, J. Mater. Sci.: Mater. Electron. 25 (2014) 1298-1302.
- [6] J. Wu, C.-W. Nan, Y. Lin, Y. Deng, Giant Dielectric Permittivity Observed in Li and Ti Doped NiO, Phys. Rev. Lett. 89 (2002) 217601.
- [7] A. Chouket, O. Bidault, V. Optasanu, A. Cheikhrouhou, W. Cheikhrouhou-Koubaa, M. Khitouni, Enhancement of the dielectric response through Al-substitution in La<sub>1.6</sub>Sr<sub>0.4</sub>NiO<sub>4</sub> nickelates, RSC Adv. 6 (2016) 24543-24548.
- [8] S. Ke, H. Fan, H. Huang, Dielectric relaxation in A<sub>2</sub>FeNbO<sub>6</sub> (A ceramics, Journal of Electroceramics 22 (2007) 252-256.
- [9] A.J. Moulson, J.M. Herbert, *Electroceramics : materials, properties, applications*. 2nd ed.; Wiley: West Sussex; New York, 2003; p xiv, 557 p.
- [10] W. Hu, Y. Liu, R.L. Withers, T.J. Frankcombe, L. Norén, A. Snashall, M. Kitchin, P. Smith, B. Gong, H. Chen, J. Schiemer, F. Brink, J. Wong-Leung, Electron-pinned defect-dipoles for high-performance colossal permittivity materials, Nat. Mater. 12 (2013) 821-826.
- [11] J. Li, F. Li, Y. Zhuang, L. Jin, L. Wang, X. Wei, Z. Xu, S. Zhang, Microstructure and dielectric properties of (Nb -dop+dcautile TiO<sub>2</sub> ceramics, J. Appl. Phys. 116 (2014) 074105.
- [12] X. Cheng, Z. Li, J. Wu, Colossal permittivity in ceramics of TiO<sub>2</sub> Co-doped with niobium and trivalent cation, Journal of Materials Chemistry A 3 (2015) 5805-5810.
- [13] W. Dong, W. Hu, A. Berlie, K. Lau, H. Chen, R.L. Withers, Y. Liu, Colossal Dielectric Behavior of Ga+Nb Co-Doped Rutile TiO<sub>2</sub>, ACS Applied Materials & Interfaces 7 (2015) 25321-25325.
- [14] W. Hu, K. Lau, Y. Liu, R.L. Withers, H. Chen, L. Fu, B. Gong, W. Hutchison, Colossal Dielectric Permittivity in (Nb+Al) Codoped Rutile TiO<sub>2</sub> Ceramics: Compositional Gradient and Local Structure, Chem. Mater. 27 (2015) 4934-4942.
- [15] J. Li, F. Li, Z. Xu, Y. Zhuang, S. Zhang, Nonlinear I–V behavior in colossal permittivity ceramic: (Nb+In) co-doped rutile TiO<sub>2</sub>, Ceram. Int. 41, Supplement 1 (2015) S798-S803.
- [16] W. Tuichai, P. Srepusharawoot, E. Swatsitang, S. Danwittayakul, P. Thongbai, Giant dielectric permittivity and electronic structure in (Al + Sb) co-doped TiO<sub>2</sub> ceramics, Microelectron. Eng. 146 (2015) 32-37.
- [17] J. Li, Z. Xu, F. Li, X. Zhu, S. Zhang, SiO<sub>2</sub>-Ti<sub>0.98</sub>In<sub>0.01</sub>Nb<sub>0.01</sub>O<sub>2</sub> composite ceramics with low dielectric loss, high dielectric permittivity and an enhanced breakdown electric field, RSC Advances 6 (2016) 20074-20080.
- [18] Z. Li, J. Wu, D. Xiao, J. Zhu, W. Wu, Colossal permittivity in titanium dioxide ceramics modified by tantalum and trivalent elements, Acta Mater. 103 (2016) 243-251.
- [19] G. Liu, H. Fan, J. Xu, Z. Liu, Y. Zhao, Colossal permittivity and impedance analysis of niobium and aluminum co-doped TiO<sub>2</sub> ceramics, RSC Advances 6 (2016) 48708-48714.
- [20] Y.Q. Wu, X. Zhao, J.L. Zhang, W.B. Su, J. Liu, Huge low-frequency dielectric response of (Nb,In)-doped TiO<sub>2</sub> ceramics, Appl. Phys. Lett. 107 (2015) 242904.
- [21] Y. Song, X. Wang, Y. Sui, Z. Liu, Y. Zhang, H. Zhan, B. Song, Z. Liu, Z. Lv, L. Tao, J. Tang, Origin of colossal dielectric permittivity of rutile Ti<sub>0.9</sub>In<sub>0.05</sub>Nb<sub>0.05</sub>O<sub>2</sub>: single crystal and polycrystalline, Scientific Reports 6 (2016) 21478.
- [22] J. Li, F. Li, C. Li, G. Yang, Z. Xu, S. Zhang, Evidences of grain boundary capacitance effect on the colossal dielectric permittivity in (Nb + In) co-doped TiO<sub>2</sub> ceramics, Sci Rep 5 (2015) 8295.
- [23] Y. Song, X. Wang, X. Zhang, Y. Sui, Y. Zhang, Z. Liu, Z. Lv, Y. Wang, P. Xu, B. Song, The contribution of doped-Al to the colossal permittivity properties of Al<sub>x</sub>Nb<sub>0.03</sub>Ti<sub>0.97-x</sub>O<sub>2</sub> rutile ceramics, Journal of Materials Chemistry C 4 (2016) 6798-6805.

- [24] W. Tuichai, S. Danwittayakul, S. Maensiri, P. Thongbai, Investigation on temperature stability performance of giant permittivity (In + Nb) in co-doped TiO<sub>2</sub> ceramic: a crucial aspect for practical electronic applications, RSC Advances 6 (2016) 5582-5589.
- [25] T. Nachaithong, P. Thongbai, S. Maensiri, Colossal permittivity in  $(In_{1/2}Nb_{1/2})_xTi_{1-x}O_2$  ceramics prepared by a glycine nitrate process, J. Eur. Ceram. Soc. 37 (2017) 655-660.
- [26] G. Kresse, J. Furthmüller, Efficiency of ab-initio total energy calculations for metals and semiconductors using a plane-wave basis set, Computational Materials Science 6 (1996) 15-50.
- [27] P.E. Blöchl, Projector augmented-wave method, Phys. Rev. B 50 (1994) 17953-17979.
- [28] D.M. Ceperley, B.J. Alder, Ground State of the Electron Gas by a Stochastic Method, Phys. Rev. Lett. 45 (1980) 566-569.
- [29] S.L. Dudarev, G.A. Botton, S.Y. Savrasov, C.J. Humphreys, A.P. Sutton, Electron-energy-loss spectra and the structural stability of nickel oxide: An LSDA+U study, Phys. Rev. B 57 (1998) 1505-1509.
- [30] H.J. Monkhorst, J.D. Pack, Special points for Brillouin-zone integrations, Phys. Rev. B 13 (1976) 5188-5192.
- [31] P. Thongbai, J. Jumpatam, T. Yamwong, S. Maensiri, Effects of Ta<sup>5+</sup> doping on microstructure evolution, dielectric properties and electrical response in CaCu<sub>3</sub>Ti<sub>4</sub>O<sub>12</sub> ceramics, J. Eur. Ceram. Soc. 32 (2012) 2423-2430.
- [32] J.C. Parker, R.W. Siegel, Calibration of the Raman spectrum to the oxygen stoichiometry of nanophase TiO<sub>2</sub>, Appl. Phys. Lett. 57 (1990) 943-945.
- [33] X. Wei, W. Jie, Z. Yang, F. Zheng, H. Zeng, Y. Liu, J. Hao, Colossal permittivity properties of Zn,Nb co-doped TiO<sub>2</sub> with different phase structures, Journal of Materials Chemistry C 3 (2015) 11005-11010.
- [34] Y. Li, L. Fang, L. Liu, Y. Huang, C. Hu, Giant dielectric response and charge compensation of Li- and Co-doped NiO ceramics, Mater. Sci. Eng. B 177 (2012) 673-677.
- [35] J. Boonlakhorn, P. Thongbai, B. Putasaeng, T. Yamwong, S. Maensiri, Very high-performance dielectric properties of Ca<sub>1-3x/2</sub>Yb<sub>x</sub>Cu<sub>3</sub>Ti<sub>4</sub>O<sub>12</sub> ceramics, J. Alloys Compd. 612 (2014) 103-109.
- [36] W. Tuichai, S. Danwittayakul, N. Chanlek, P. Thongbai, S. Maensiri, High-performance giant-dielectric properties of rutile TiO<sub>2</sub> co-doped with acceptor-Sc<sup>3+</sup> and donor-Nb<sup>5+</sup> ions, J. Alloys Compd. 703 (2017) 139-147.
- [37] Y. Huang, D. Shi, Y. Li, G. Li, Q. Wang, L. Liu, L. Fang, Effect of holding time on the dielectric properties and non-ohmic behavior of  $CaCu_3Ti_4O_{12}$  capacitor-varistors, J. Mater. Sci.: Mater. Electron. 24 (2012) 1994-1999.
- [38] Z. Yang, L. Zhang, X. Chao, L. Xiong, J. Liu, High permittivity and low dielectric loss of the Ca<sub>1-x</sub>Sr<sub>x</sub>Cu<sub>3</sub>Ti<sub>4</sub>O<sub>12</sub> ceramics, J. Alloys Compd. 509 (2011) 8716-8719.
- [39] J. Boonlakhorn, B. Putasaeng, P. Kidkhunthod, P. Thongbai, Improved dielectric properties of (Y + Mg) co-doped CaCu<sub>3</sub>Ti<sub>4</sub>O<sub>12</sub> ceramics by controlling geometric and intrinsic properties of grain boundaries, Materials & Design 92 (2016) 494-498.
- [40] L. Liu, H. Fan, L. Wang, X. Chen, P. Fang, Dc-bias-field-induced dielectric relaxation and ac conduction in CaCu3Ti4O12 ceramics, Philos. Mag. 88 (2008) 537-545.
- [41] R. Schmidt, S. Pandey, P. Fiorenza, D.C. Sinclair, Non-stoichiometry in "CaCu<sub>3</sub>Ti<sub>4</sub>O<sub>12</sub>" (CCTO) ceramics, RSC Advances 3 (2013) 14580-14589.
- [42] L. Liu, D. Shi, S. Zheng, Y. Huang, S. Wu, Y. Li, L. Fang, C. Hu, Polaron relaxation and non-ohmic behavior in CaCu<sub>3</sub>Ti<sub>4</sub>O<sub>12</sub> ceramics with different cooling methods, Mater. Chem. Phys. 139 (2013) 844-850.
- [43] Y. Huang, D. Shi, L. Liu, G. Li, S. Zheng, L. Fang, High-temperature impedance spectroscopy of BaFe<sub>0.5</sub>Nb<sub>0.5</sub>O<sub>3</sub> ceramics doped with Bi<sub>0.5</sub>Na<sub>0.5</sub>TiO<sub>3</sub>, Applied Physics A 114 (2014) 891-896.
- [44] X. Sun, J. Deng, S. Liu, T. Yan, B. Peng, W. Jia, Z. Mei, H. Su, L. Fang, L. Liu, Grain boundary defect compensation in Ti-doped BaFe<sub>0.5</sub>Nb<sub>0.5</sub>O<sub>3</sub> ceramics, Applied Physics A 122 (2016) 864.
- [45] L.R. Sheppard, J. Holik, R. Liu, S. Macartney, R. Wuhrer, Tantalum Enrichment in Tantalum-Doped Titanium Dioxide, J. Am. Ceram. Soc. 97 (2014) 3793-3799.
- [46] K. Obata, H. Irie, K. Hashimoto, Enhanced photocatalytic activities of Ta, N co-doped TiO<sub>2</sub> thin films under visible light, Chem. Phys. 339 (2007) 124-132.
- [47] X. Liu, M. Khan, W. Liu, W. Xiang, M. Guan, P. Jiang, W. Cao, Synthesis of nanocrystalline Ga–TiO<sub>2</sub> powders by mild hydrothermal method and their visible light photoactivity, Ceram. Int. 41 (2015) 3075-3080.

# CHAPTER 7

Preparation, Characterization, Electrical Properties and Giant Dielectric Response in (In+Nb) Co-Doped Tio<sub>2</sub> Ceramics Synthesized by a Urea Chemical-Combustion Method

### 7.1 Introduction

(In+Nb) co-doped TiO<sub>2</sub> (INTO) is a giant dielectric material, i.e., a material that can exhibit very high dielectric permittivity ( $\epsilon'>10^4$ ), that has been intensively investigated since a successfully new strategy to improve the giant dielectric properties of TiO<sub>2</sub> was reported by Hu *et al* [1]. Substitution of In<sup>3+</sup> and Nb<sup>5+</sup> ions into TiO<sub>2</sub> can greatly increase  $\epsilon'$  with retaining low loss tangent (tanδ). Furthermore, the dielectric properties of INTO ceramics were slightly dependent on frequency ( $10^2-10^6$  Hz) and temperature ( $\approx80-450$  K) [1, 2]. These are the basic important parameters that must be considered before designing dielectric materials for practical application in electronic devices [3, 4]. The INTO material is the promising giant dielectric material because TiO<sub>2</sub> is abundance and low toxicity [2, 5-12].

According to the nominal composition of  $(In_{0.5}Nb_{0.5})_xTi_{1-x}O_2$ , the  $\epsilon'$  value increased with increasing co-doping concentration, while  $tan\delta$  was kept too low. The complex stoichiometry of  $(In_x^{3+}Nb_x^{5+}Ti_x^{3+})Ti_{1-3x}^{4+}O_{2-x/2}$  was proved to be existed [1]. This produced defect clusters, in which the strong polarization occurred, giving rise to very high  $\epsilon'$  values. The electron–pinned defect–dipole (EPDD) model was reasonably proposed. In this elegant model, the electrons were created by the reduction of  $Ti^{4+}$  to  $Ti^{3+}$  resulting from  $Nb^{5+}$  doping ions. These electrons were confined by the presence of  $In^{3+}$  in a rutile structure [1]. It was observed that, without  $In^{3+}$  dopant ions, free electrons in  $Nb^{5+}$  or  $Ta^{5+}$  doped  $TiO_2$  ceramics can delocalize and lead to very high low-frequency  $tan\delta$  values, usually larger than 0.1 at low frequencies [1, 13-15]. Besides the EPDD model, the internal barrier layer capacitor (IBLC) and/or surface barrier layer capacitor (SBLC) effects were proposed as the exact origin of the high-performance giant-dielectric properties [9, 12, 13, 16-21], creating significant confusion.

Generally, fine nano-powders obtained via a wet chemical route usually offer a higher possibility of closer stoichiometric control than by the solid state reaction method and offer good dispersion of dopants [19]. The investigation of preparation routes to fabricate a fine INTO powder is one of the most important issues, which should be addressed. To investigate INTO ceramics for use in electronic devices, the selection of an effective preparation route is one of the most important decisions required. Unfortunately, since the giant dielectric properties of INTO were discovered, the giant dielectric behavior of INTO prepared by wet chemical routes has rarely been reported [19, 20, 22].

In this work, a urea chemical-combustion route was therefore used to synthesize INTO nanocrystalline ceramics. It is interesting that the sintered INTO ceramics fabricated by nanocrystalline powders can exhibit good dielectric properties. High  $\epsilon' > 10^4$  and low  $\tan \delta < 0.1$  were obtained. The origin of the giant dielectric behavior was discussed in details.

### 7.2 Experimental details

 $(In_{0.5}Nb_{0.5})_vTi_{1.v}O_2$  powders with x=0.01 and 0.015 (referred to as P1 and P2 powders, respectively) were prepared by a chemical combustion method using urea as fuel. The starting raw materials concluded of In<sub>3</sub>N<sub>3</sub>O<sub>9</sub>·xH<sub>2</sub>O (Sigma-Aldrich, 99.999%), NbCl<sub>5</sub> (Sigma-Aldrich, >99.9%), C<sub>16</sub>H<sub>28</sub>O<sub>6</sub>Ti (75 wt.% in isopropanol, Sigma-Aldrich), deionized water, citric acid, and urea. First, In<sub>3</sub>N<sub>3</sub>O<sub>9</sub>·xH<sub>2</sub>O and NbCl<sub>5</sub> were dissolved in aqueous solution of citric acid (2.5 wt%) with constant stirring at room temperature. Second, C<sub>16</sub>H<sub>28</sub>O<sub>6</sub>Ti solution was dropped into the metal ion solution above under constant stirring. After this step, a transparent and clear solution was observed. Third, 0.5 g of urea powder was mixed into the metal ion solution with constant stirring at 150 °C until a viscous gel was obtained. Then, the gel was dried at 350 °C for 1 h. The resulting dried porous precursors were ground and calcined at 1000 °C for 6 h to form a pure phase of rutile-TiO<sub>2</sub>. Next, the P1 and P2 powders were pressed into pellets having dimensions of 9.5 mm in diameter and ~1.5 mm in thickness by uniaxial compression at 200 MPa. Finally, these pellets were sintered in air at 1400 °C for 2 and 6 h with heating rate 2 °C/mic. The  $(In_{0.5}Nb_{0.5})_xTi_{1-x}O_2$  ceramics with x=0.01 sintered for 2 and 6 h were referred to as the INTO-1 and INTO-2 ceramics, respectively. The (In<sub>0.5</sub>Nb<sub>0.5</sub>)<sub>x</sub>Ti<sub>1-x</sub>O<sub>2</sub> ceramics with x= 0.015 sintered for 2 and 6 h were referred to as the INTO-3 and INTO-4 ceramics, respectively.

The phase composition and crystal structure of the  $(In_{0.5}Nb_{0.5})_xTi_{1-x}O_2$  powders and sintered ceramics were characterized by an X-ray diffraction technique (XRD) PANalytical, EMPYREAN). Transmission electron microscopy (TEM, ZEISS EM902) was used to reveal the  $(In_{0.5}Nb_{0.5})_xTi_{1-x}O_2$  nanoparticles. Surface morphologies of the sintered  $(In_{0.5}Nb_{0.5})_xTi_{1-x}O_2$  ceramics were revealed by scanning electron microscopy (SEM) (SEC, SNE4500M). The elemental distribution on the microstructure was examined using a field–emission scanning electron microscopy (FE–SEM) with energy-dispersive X–ray analysis (EDX) (HITACHI SU8030, Japan). For dielectric measurement, each pellet face was polished and sputtered with Au at a current of 25 mA for 8 min using a Polaron SC500 sputter coating unit. The dielectric properties were measured using a KEYSIGHT E4990A Impedance Analyzer over the frequency range from 40 to  $10^6$  Hz using an oscillation voltage of 0.5 V. The dielectric properties were measured over the temperature range from -60 to 200 °C with a step increase of 10 °C. Each temperature step was held with an accuracy of  $\pm 1$  °C.

## 7.3 Results and discussion

Figure 1 shows the XRD patterns of all INTO powders and sintered INTO ceramics, which were synthesized by a urea chemical-combustion method. The experimental XRD patterns were well fitted by Rietveld refinement method. Accordingly, a main phase of rutile–TiO<sub>2</sub> with a tetragonal structure (JCPDS 21-1276) is confirmed in both P1 and P2 powders as well as in all sintered ceramics is observed. No impurity phase is detected. According to the Rietveld refinement profile fits, lattice parameters (*a* and *c*) were achieved and summarized in Table 1. The *a* and *c* values of all the samples are close to the values for rutile–TiO<sub>2</sub> (JCPDS 21–1276), *a*=4.593 Å and *c*=2.959 Å. These calculated values are comparable to those reported in the literature for the (Nb<sub>0.5</sub>In<sub>0.5</sub>)<sub>0.01</sub>Ti<sub>0.99</sub>O<sub>2</sub> [1, 2]. Lattice parameters of the P2 powder are slightly larger than that of the P1 powder. This might associated with the slight increase in co–doping concentration from 1.0 to 1.5 %. As shown in Table 1, slight changes in lattice parameters caused by processing conditions

might be attributed to several factors such as oxygen vacancies and/or lattice distortion induced by the variation of mixed-valent structure.

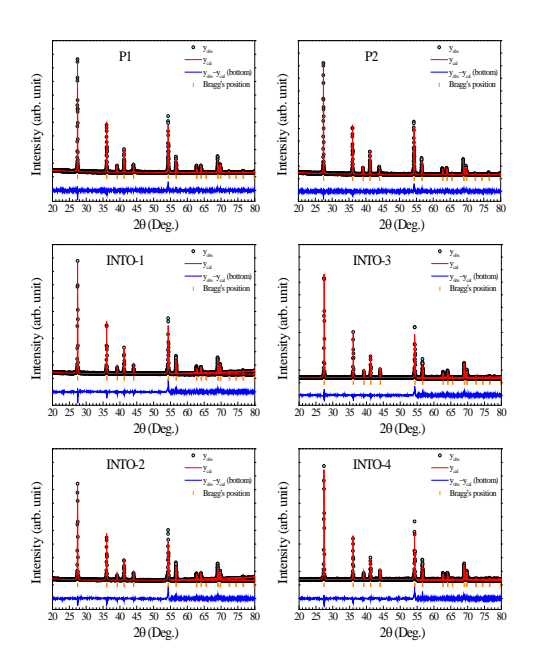


Fig. 1 Profile fits for the Rietveld refinement of INTO powders and sintered ceramics.

**Table 1** Lattice parameters of INTO powders and sintered ceramics.

Sample	Lattice parameter (Å)	
	а	С
P1	4.594(0)	2.959(4)
P2	4.594(8)	2.959(6)
INTO-1	4.593(2)	2.961(0)
INTO-2	4.594(3)	2.961(5)
INTO-3	4.593(7)	2.961(6)
INTO-4	4.593(6)	2.961(2)

The calcined INTO powders were revealed using TEM technique. Nanocrystalline INTO powders with nearly spherical shape and particle sizes are of ≈200–300 nm were obtained as shown in the inset of Fig. 2(b). These fine powders were used to fabricate the green body (compacted powder) of INTO for sintering. The surface morphologies of the polished–surfaces of the sintered INTO ceramics are illustrated in Fig. 2. Obvious grain and grain boundary structures with small amount of pores are observed. All ceramic samples are quite dense. Two important features are observed. First, it is likely that a grain size of INTO ceramics prepared by a urea chemical-combustion method tends to increase with increasing sintering temperature from 2 to 6 h. This means that the sintering

conditions may have an effect on the microstructure of INTO ceramics, just as observed in  $CaCu_3Ti_4O_{12}$  (CCTO)-based ceramics [23-27]. Second, grain sizes of INTO ceramics are slightly changed by increasing concentration of co-dopants. This behavior is quite different from that of CCTO ceramics [28, 29]. The dispersion of In and Nb dopants as well as the major elements of Ti and O in INTO ceramics were revealed by SEM–mapping technique. As shown in Fig. 3, both In and Nb dopants were homogeneously dispersed throughout in the microstructure.

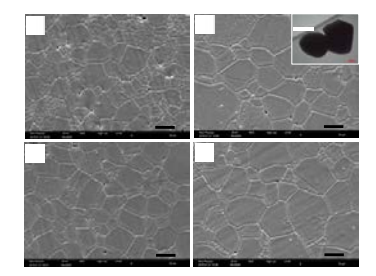


**Fig. 2** SEM images of polished-surface morphologies of (a) INTO-1, (b) INTO-2, (c) INTO-3, and (d) INTO-4 ceramics; inset reveals TEM image of INTO particles for the P1 powder.

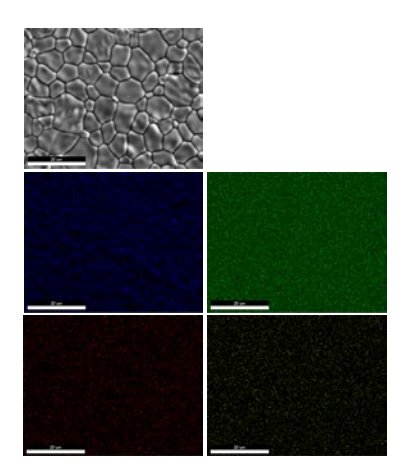
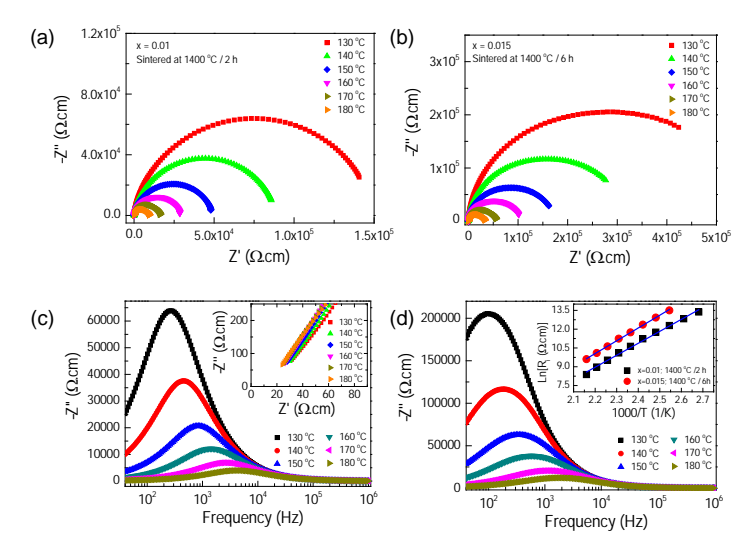


Fig. 3 SEM image and SEM mapping of all elements in INTO-1 ceramic.

The electrical properties of the sintered INTO ceramics were investigated using impedance spectroscopy at various temperatures to clarify the possible origin(s) of the giant dielectric behavior. As demonstrated in Figs. 4(a) and (b), large semicircle arcs can be observed in the Z\* plot in the temperature range of 130-180 °C for the INTO-1 and INTO-4 ceramics. Usually, the large semicircle arc can be assigned as the electrical responses of insulating part such as grain boundary or other insulating phases [13, 30]. The diameter of the semicircle arc decreases with increasing temperature, indicating to the decrease in the resistance of insulating phase. As depicted in the inset of Fig. 4(c), the nonzero intercept on the Z' axis was observed. This can be assigned as the electrical response of the semiconducting grains [19]. The resistance of the semiconducting grains  $(R_g)$  was estimated about 20  $\Omega$ .cm and very slightly decreased as temperature increased. Thus, it is reasonable to suggest that the giant dielectric response in the INTO ceramics prepared by a urea chemical-combustion method is primarily originated from the interfacial polarization at the interface between semiconducting and insulating phases [12, 30]. It is important to note that this work is not to discredit the EPDD model, at which the giant dielectric response in INTO ceramics was proposed to be caused by essentially

designing complex defects in a rutile–TiO<sub>2</sub> structure. The interpretation of the results is purely based on the experimental results.



**Fig. 4** (a-b) Impedance complex plane plot (Z\*) at different temperatures from 130 to 180 °C for INTO-1 and INTO-4 ceramics. (c-d) Frequency dependence of -Z" at different temperatures. Inset of (c) reveals an expanded view of the high frequency data close to the origin of the INTO-1 ceramic. Inset of (d) shows Arrhenius plot for conduction in the insulating phase.

The resistance of the insulating phase ( $R_i$ ) at each temperature was calculated from the Z''-frequency plots. As demonstrated in Figs. 4(c) and (d), the apparent Z'' peak shifted to lower frequencies with decreasing temperature. This behavior indicates to a thermally activated electrical response.  $R_i$  can be calculated from the At the maximum value of Z'' ( $Z''_{max}$ ), i.e.,  $R_i = 2Z''_{max}$  [30]. Therefore, with increasing temperature, the decrease in  $Z''_{max}$  indicates to the decrease in  $R_i$ , corresponding to the decrease in diameter of the semicircle arc. It is also observed that, the temperature dependence behavior of  $R_i$  for the INTO ceramics follows the Arrhenius law [inset of Fig. 4(d)],

$$R_i = R_0 \exp\left(\frac{E_i}{k_B T}\right),\tag{1}$$

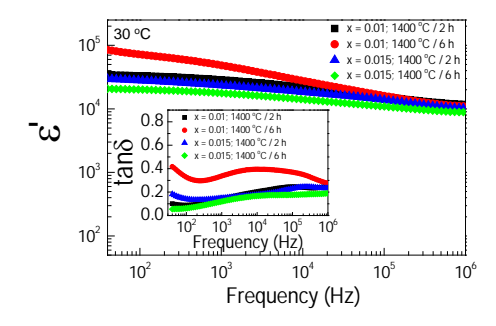
where  $R_0$  is a constant value,  $E_i$  is the activation energy required for conduction in the insulating phase. The  $E_i$  values of the INTO-1, INTO-2, INTO-3, and INTO-4 ceramics can be calculated from Eq. (1) and found to be 0.823, 0.750, 0.774 and 0.880 eV, respectively. These  $E_{\rm gb}$  values are comparable to values of 0.35 eV for 10%INTO ceramics prepared by an SSR method [17]. These values can also be comparable to 0.65(7) and 0.717 eV for the 1.0%INTO ceramic prepared using an oxalate chemical–solution route combined with a SPS method and 1.5%INTO ceramic prepared by a glycine nitrate process, respectively [22]. Furthermore, the  $E_i$  values are close to the activation energies of insulating part of about 0.663-0.931 eV and 0.909 eV for the (Sc+Nb) and (Ga+Ta) codoped TiO<sub>2</sub> ceramics, respectively [18, 21]. The conduction activation energies of the grain boundaries of CCTO and Ba(Fe<sub>0.5</sub>Nb<sub>0.5</sub>)O<sub>3</sub>-based ceramics [31-35] can also be comparable to 0.750-0.880 eV of the INTO ceramics that were prepared by a urea chemical-combustion route.

Fig. 5 shows the dielectric properties as a function of frequency at 30 °C of the INTO ceramics. Very high  $\varepsilon'$  values of about  $10^4$ – $10^6$  are observed in all the INTO ceramics sintered at 1400 °C for 2 and 6 h. These high ε' values appear over a wide frequency range from 40 to  $10^6$  Hz.  $\varepsilon'$  of the INTO-4 (x=0.015, sintered at 1400 °C for 6 h) ceramic was slightly dependent on frequency in the range of 40 to  $10^6$  Hz, while  $\varepsilon'$  values of the INTO-2 (x=0.01, sintered at 1400 °C for 6 h) ceramic was strongly dependent on frequency. The strong frequency dependence of  $\epsilon'$  of the INTO-2 ceramic may be associated with the sample electrode effect. At 40 Hz and 30 °C, the ε' values of the INTO-1, INTO-2, INTO-3, and INTO-4 ceramics are of 3.43×10<sup>4</sup>, 8.48×10<sup>4</sup>, 2.96×10<sup>4</sup>, and  $2.07 \times 10^4$ , respectively. As shown in the inset, tan  $\delta$  of the INTO-2 ceramic was the largest over the measured frequency range. This is consistent with its largest  $\varepsilon'$  value. The tan $\delta$ values of the INTO-1, INTO-2, INTO-3, and INTO-4 ceramics are 0.101, 0.417, 0.182, and 0.054, respectively. The sintering condition has a remarkable influence on the giant dielectric properties of the INTO ceramics that were synthesized by a urea chemicalcombustion method. This observation is usually observed in other giant dielectric materials (e.g., co-doped NiO, Ba(Fe<sub>0.5</sub>Nb<sub>0.5</sub>)O<sub>3</sub>, and CCTO ceramics as well as other codoped TiO<sub>2</sub> systems [6, 9, 18, 21, 36-40]. Thus, the giant dielectric response in the INTO ceramics is likely extrinsic in origin. According to the impedance spectroscopy, the interfacial polarization at the interface between semiconducting and insulating phases may be responsible for this observed giant dielectric response. Substitution of Nb5+ into TiO<sub>2</sub> can generally produce free electrons as follows [1]:

$$2TiO_2 + Nb_2O_5 \xrightarrow{4TiO_2} 2Ti'_{Ti} + 2Nb^{\bullet}_{Ti} + 8O_O + 1/2O_2,$$
 (2)

$$Ti^{4+} + e \rightarrow Ti^{3+}. \tag{3}$$

Thus, the conduction mechanism inside semiconducting grains of INTO ceramics is attributed to electron hopping between  $Ti^{3+} \leftrightarrow Ti^{4+}$ . It is important to note that the origin of the giant dielectric behavior in INTO ceramics is quite similar to that observed in (Al+Nb) co-doped SnO<sub>2</sub> and (Li+Ti, Co) co-doped NiO ceramics, in which the primary role of Nb<sup>5+</sup> and Li<sup>+</sup> doping ions is to produce free charges inside the semiconducting grains [39, 41, 42]. All of these giant dielectric materials exhibited very large  $\epsilon'$  values of  $10^3$ - $10^5$ . However, it is unlikely similar to that observed in single and co-doped ATiO<sub>3</sub> ceramics [43, 44].



**Fig. 5** Frequency dependence of dielectric permittivity ( $\epsilon$ ') at 30 oC fro INTO ceramics; inset shows  $\tan \delta$  as a function of frequency at 30 °C.

Among these ceramic samples, the INTO-4 ceramic prepared using a urea chemical-combustion method shows the best dielectric properties with  $\epsilon' \approx 2.07 \times 10^4$  and  $\tan \delta \approx 0.054$  at 40 Hz and 30 °C. Impressive dielectric properties of all TiO<sub>2</sub>-based ceramics were

reported and stimulated research activity in the field of colossal ceramic materials. However, there were few investigations of preparation methods using wet chemical routes [19, 20, 22]. By using an oxalate chemical–solution combined with spark plasma sintering (SPS), a (1%In+Nb) co-doped TiO<sub>2</sub> ceramic exhibited high  $\varepsilon'\approx0.9\times10^4$  and  $\tan\delta\approx0.2$  at 40 Hz and RT [22]. According to our previous work, the (1.5%In+Nb) co-doped TiO<sub>2</sub> ceramic prepared by a glycine nitrate process can exhibit  $\varepsilon'\approx42,376$ and  $\tan\delta\approx0.06$  at room temperature and 40 Hz [19]. Therefore, the urea chemical-combustion route can be one of the most interesting wet chemical routes for preparing INTO ceramics. Generally, low-frequency  $\tan\delta$  values of other giant dielectric materials are very high, which is undesirable for electronic applications. In the case of CCTO ceramics prepared by a SPS method, very large values of  $\tan\delta>0.2$  were obtained in CCTO-based ceramics [23-25, 45, 46]. Very unacceptably high  $\tan\delta$  values in a low–frequency range are generally associated with the resistance of insulating grain boundaries.

#### 7.4 Conclusions

We have successfully synthesized a pure rutile phase of  $In_{0.5}Nb_{0.5})_xTi_{1-x}O_2$  (x=0.01 and 0.015) nanocrystalline powders using a urea chemical-combustion method. Dense microstructure with small amount of pores and good dispersion of In and Nb doping ions were observe in sintered ceramics. It was also found that a grain size tended to increase with increasing sintering time. Interestingly, the  $(In_{1/2}Nb_{1/2})_{0.015}Ti_{0.985}O_2$  ceramic sintered at 1400 °C for 6 h exhibited a low tan $\delta$  value of  $\approx$ 0.054 with high  $\epsilon$ ' of  $\approx$  2.07×10<sup>4</sup>. The semiconducting and insulating phases were clearly confirmed. High dielectric response and low tan $\delta$  can be well described based on the electrically heterogeneous microstructure.

## References

- 1. W. Hu, Y. Liu, R.L. Withers, T.J. Frankcombe, L. Norén, A. Snashall, M. Kitchin, P. Smith, B. Gong, H. Chen, J. Schiemer, F. Brink, J. Wong-Leung, Nat. Mater. 12, 821-826 (2013)
- 2. W. Tuichai, S. Danwittayakul, S. Maensiri, P. Thongbai, RSC Advances 6, 5582-5589 (2016)
- 3. A.J. Moulson, J.M. Herbert, Electroceramics: materials, properties, applications, 2nd ed., Wiley, West Sussex; New York, 2003.
- 4. Z. Wang, M. Cao, Q. Zhang, H. Hao, Z. Yao, Z. Wang, Z. Song, Y. Zhang, W. Hu, H. Liu, J. Am. Ceram. Soc. 98, 476-482 (2015)
- 5. C. Wang, N. Zhang, Q. Li, Y. Yu, J. Zhang, Y. Li, H. Wang, J. Am. Ceram. Soc. 98, 148-153 (2015)
- 6. W. Hu, K. Lau, Y. Liu, R.L. Withers, H. Chen, L. Fu, B. Gong, W. Hutchison, Chem. Mater. 27, 4934-4942 (2015)
- 7. Z. Li, J. Wu, W. Wu, Journal of Materials Chemistry C 3, 9206-9216 (2015)
- 8. X. Cheng, Z. Li, J. Wu, Journal of Materials Chemistry A 3, 5805-5810 (2015)
- 9. J. Li, F. Li, Y. Zhuang, L. Jin, L. Wang, X. Wei, Z. Xu, S. Zhang, J. Appl. Phys. 116, 074105 (2014)
- 10. G. Liu, H. Fan, J. Xu, Z. Liu, Y. Zhao, RSC Advances 6, 48708-48714 (2016)
- 11. J. Li, Z. Xu, F. Li, X. Zhu, S. Zhang, RSC Advances 6, 20074-20080 (2016)
- 12. Y. Song, X. Wang, X. Zhang, Y. Sui, Y. Zhang, Z. Liu, Z. Lv, Y. Wang, P. Xu, B. Song, Journal of Materials Chemistry C 4, 6798-6805 (2016)
- 13. W. Tuichai, S. Danwittayakul, N. Chanlek, P. Srepusharawoot, P. Thongbai, S. Maensiri, RSC Advances 7, 95-105 (2017)
- 14. B. Shang, P. Liang, F. Li, X. Chao, L. Wei, Z. Yang, J. Alloys Compd. 704, 64-69 (2017)
- 15. F. Li, B. Shang, P. Liang, L. Wei, Z. Yang, J. Electron. Mater. 45, 5178-5184 (2016)

- 16. J. Li, F. Li, C. Li, G. Yang, Z. Xu, S. Zhang, Sci Rep 5, 8295 (2015)
- 17. Y. Song, X. Wang, Y. Sui, Z. Liu, Y. Zhang, H. Zhan, B. Song, Z. Liu, Z. Lv, L. Tao, J. Tang, Scientific Reports 6, 21478 (2016)
- 18. W. Tuichai, S. Danwittayakul, N. Chanlek, P. Thongbai, S. Maensiri, J. Alloys Compd. 703, 139-147 (2017)
- 19. T. Nachaithong, P. Thongbai, S. Maensiri, J. Eur. Ceram. Soc. 37, 655-660 (2017)
- 20. T. Nachaithong, P. Kidkhunthod, P. Thongbai, S. Maensiri, J. Am. Ceram. Soc. 10.1111/jace.14688, (2017)
- 21. W. Tuichai, N. Thongyong, S. Danwittayakul, N. Chanlek, P. Srepusharawoot, P. Thongbai, S. Maensiri, Materials & Design 123, 15-23 (2017)
- 22. H. Han, P. Dufour, S. Mhin, J.H. Ryu, C. Tenailleau, S. Guillemet-Fritsch, Phys. Chem. Chem. Phys. 17, 16864-75 (2015)
- 23. W. Wan, C. Liu, H. Sun, Z. Luo, W.-X. Yuan, H. Wu, T. Qiu, J. Eur. Ceram. Soc. 35, 3529-3534 (2015)
- 24. L. Singh, B.C. Sin, I.W. Kim, K.D. Mandal, H. Chung, Y. Lee, J. Varela, J. Am. Ceram. Soc. 99, 27-34 (2016)
- 25. J. Li, P. Liang, J. Yi, X. Chao, Z. Yang, J. Am. Ceram. Soc. 98, 795-803 (2015)
- 26. X.J. Luo, Y.S. Liu, C.P. Yang, S.S. Chen, S.L. Tang, K. Bärner, J. Eur. Ceram. Soc. 35, 2073-2081 (2015)
- 27. M.F. Ab Rahman, S.D. Hutagalung, Z.A. Ahmad, M.F. Ain, J.J. Mohamed, J. Mater. Sci.: Mater. Electron. 26, 3947-3956 (2015)
- 28. A. Nautiyal, C. Autret, C. Honstettre, S. De Almeida-Didry, M. El Amrani, S. Roger, B. Negulescu, A. Ruyter, J. Eur. Ceram. Soc. 36, 1391-1398 (2016)
- 29. J. Boonlakhorn, B. Putasaeng, P. Kidkhunthod, P. Thongbai, Materials & Design 92, 494-498 (2016)
- 30. M. Li, D.C. Sinclair, J. Appl. Phys. 114, 034106 (2013)
- 31. L. Liu, D. Shi, S. Zheng, Y. Huang, S. Wu, Y. Li, L. Fang, C. Hu, Mater. Chem. Phys. 139, 844-850 (2013)
- 32. L. Liu, H. Fan, P. Fang, X. Chen, Mater. Res. Bull. 43, 1800-1807 (2008)
- 33. Y. Huang, D. Shi, L. Liu, G. Li, S. Zheng, L. Fang, Applied Physics A 114, 891-896 (2014)
- 34. X. Sun, J. Deng, S. Liu, T. Yan, B. Peng, W. Jia, Z. Mei, H. Su, L. Fang, L. Liu, Applied Physics A 122, 864 (2016)
- 35. J. Deng, X. Sun, S. Liu, L. Liu, T. Yan, L. Fang, B. Elouadi, Journal of Advanced Dielectrics 06, 1650009 (2016)
- 36. Y. Huang, D. Shi, Y. Li, G. Li, Q. Wang, L. Liu, L. Fang, J. Mater. Sci.: Mater. Electron. 24, 1994-1999 (2012)
- 37. L. Liu, H. Fan, L. Wang, X. Chen, P. Fang, Philos. Mag. 88, 537-545 (2008)
- 38. L. Liu, L. Fang, Y. Huang, Y. Li, D. Shi, S. Zheng, S. Wu, C. Hu, J. Appl. Phys. 110, 094101 (2011)
- 39. P. Thongbai, T. Yamwong, S. Maensiri, J. Appl. Phys. 104, 074109 (2008)
- 40. L. Li, Z.W. Wang, X.M. Chen, Mater. Res. Bull. 67, 251-254 (2015)
- 41. Y. Li, L. Fang, L. Liu, Y. Huang, C. Hu, Mater. Sci. Eng. B 177, 673-677 (2012)
- 42. Y. Song, X. Wang, X. Zhang, X. Qi, Z. Liu, L. Zhang, Y. Zhang, Y. Wang, Y. Sui, B. Song, Appl. Phys. Lett. 109, 142903 (2016)
- 43. S. Zheng, D. Shi, L. Liu, G. Li, Q. Wang, L. Fang, B. Elouadi, J. Mater. Sci.: Mater. Electron. 25, 4058-4065 (2014)
- 44. F. Han, J. Deng, X. Liu, T. Yan, S. Ren, X. Ma, S. Liu, B. Peng, L. Liu, Ceram. Int. 43, 5564-5573 (2017)
- 45. R. Löhnert, B. Capraro, S. Barth, H. Bartsch, J. Müller, J. Töpfer, J. Eur. Ceram. Soc. 35, 3043-3049 (2015)
- 46. R. Löhnert, H. Bartsch, R. Schmidt, B. Capraro, J. Töpfer, A. Feteira, J. Am. Ceram. Soc. 98, 141-147 (2015)

## **CHAPTER 8**

# Preparation, Characterization, And Giant Dielectric Permittivity of (Y³+ and Nb⁵+) Co–Doped TiO<sub>2</sub> Ceramics

#### 8.1 Introduction

Giant dielectric oxides are material that exhibit very large dielectric permittivity (ɛ') values, on the order of 10³-10⁶, in the radio frequency range. These oxides have had a great impact on the progress made in recent years in the electronics industry, especially in high-energy-density storage devices. Many kinds of giant dielectric materials (e.g., oxides in a family of ACu₃Ti₄O₁₂ (where the A-site is occupied by cations with an average valance of +2) [1-5], AFe₁/₂B₁/₂O₃ (A=Ba, Sr, Ca; B=Nb, Ta, Sb) [6-8], and La₂-xSr<sub>x</sub>NiO₄ [9-11] among others) were discovered and have been intensively investigated. All giant dielectric oxides show fascinating dielectric behaviors, and studies of their properties have led to insights into their underlying mechanisms. Both classical and elegant new models have been proposed to answer questions about why these oxides show giant dielectric behaviors. These models include the internal or surface barrier layer capacitor model (IBLC or SBLC) [4, 12-15], nano-barrier layer capacitor model [16], small polaron hopping model [9, 11], and the mixed-valent structure model [3, 17] as well as the non-Ohmic sample-electrode contact model [15].

Unfortunately, unacceptably large values of the loss tangent (tanδ) of these giant dielectric oxides are one of their most serious drawbacks. Most recently, a promising giant dielectric oxide for future practical applications was reported in an In+Nb co-doped rutile- $TiO_2$  (INTO) ceramic [18]. INTO ceramics exhibited extremely high  $\varepsilon'$  values of more than 10<sup>4</sup>, depending on the dopant concentration. Notably, tanδ of INTO ceramics was very low compared to those of other giant dielectric oxides. For example, doping TiO2 with 10% (In+Nb) can result in values of  $\varepsilon' \approx 6 \times 10^4$  and  $\tan \delta \approx 0.02$  [18]. In addition to the models above, the electron-pinned defect-dipole (EPDD) model was suggested as an explanation of the fascinating giant-dielectric properties of INTO ceramics. According to the EPDD model, the aliovalent dopants used (Nb5+ and In3+) had a distinct function. The former, with higher valence state, was used to produce free electrons in the rutile-TiO<sub>2</sub> structure. The latter, with a lower valence state, was used to form local complex defect clusters that could confine free electrons [18]. It was further suggested that EPDDs can be produced in other co-doped TiO<sub>2</sub> systems [19-20]. This discovery has greatly stimulated research in the field of giant dielectric oxides [12, 14-15, 19-30]. In addition to the EPDD model, several studies have demonstrated that the giant dielectric properties of INTO ceramics originated from the IBLC or SBLC effect [13, 15, 23, 25, 27, 29].

Several co–doped TiO<sub>2</sub> systems were synthesized and their giant dielectric properties reported. The aliovalent co–dopants studied were Ga<sup>3+</sup>+Nb<sup>5+</sup> [12], Bi<sup>3+</sup>+Nb<sup>5+</sup> [19], Al<sup>3+</sup>+Nb<sup>5+</sup> [22], Bi<sup>3+</sup>+Sb<sup>5+</sup> [30], and Sm<sup>3+</sup>+Nb<sup>5+</sup> [20], among others. All of these co–doped TiO<sub>2</sub> systems showed very interesting giant dielectric behaviors. Various methodologies were used to clarify the origin of giant dielectric properties. From the point of view of capacitor applications, there is an ongoing need for a new system of co–doped TiO<sub>2</sub>. Although the giant dielectric properties of many co–doped TiO<sub>2</sub> systems have been reported, we think that it is worthwhile to develop a new co–doped TiO<sub>2</sub> system to increase the number of design options and to support a variety of applications. Thus, in the current work, a new system of (Y+Nb) co–doped TiO<sub>2</sub> was synthesized. The phase composition and microstructure were carefully characterized. The giant dielectric and

nonlinear current density–electric field (J–E) properties of (Y+Nb) co–doped TiO $_2$  ceramics were investigated. Interestingly, very large  $\varepsilon'$  values were achieved in this new co–doped TiO $_2$  system. Interestingly, sintered ceramics can exhibit J–E characteristics. The origin of the giant dielectric response is also discussed in detail.

## 8.2 Experimental details

## 2.1 Ceramic preparation

 $(Y_{1/2}Nb_{1/2})_xTi_{1,x}O_2$  ceramics with x=0.025 and 0.05 (referred as 2.5%YNTO and 5.0%YNTO ceramics, respectively) were prepared using a combustion method with glycine as a fuel. C<sub>16</sub>H<sub>28</sub>O<sub>6</sub>Ti (Sigma–Aldrich), Y(NO<sub>3</sub>)<sub>9</sub>·6H<sub>2</sub>O (Kento Chemical, >99.99%), NbCl<sub>5</sub> (Sigma-Aldrich, >99.9%), deionized water, citric acid, and glycine were used as the starting raw materials. Details of the preparation method are similar to those reported for preparation of  $(In_{1/2}Nb_{1/2})_xTi_{1-x}O_2$  ceramics [15]. First,  $Y(NO_3)_9\cdot 6H_2O$  and NbCl<sub>5</sub> were dissolved in an aqueous solution of citric acid with constant stirring at room temperature (RT). Second, a C<sub>16</sub>H<sub>28</sub>O<sub>6</sub>Ti solution was added into the solution above until a clear and transparent solution can be observed. Third, glycine powder was mixed into the metal ion solution with stirring at 150 °C until a viscous gel was obtained. Then, the gel was dried at 350 °C for 1 h using heating rate 1 °C/min. Next, the resulting dried precursors were calcined in air at 1000 °C for 6 h. The powders obtained after calcination were pressed under uniaxial compression at ≈200 MPa into pellets that were 9.5 mm in diameter and ~1.5 mm in thickness. Finally, ceramic samples with dense ceramic microstructure and no porosity were achieved by sintering in air at 1500 °C for 2 h with heating and cooling rates 2 °C/min.

## 2.2 Characterizations

The phase composition and crystal structure of the ceramic samples were characterized using X-ray diffraction (PANalytical, EMPYREAN). The microstructure of sintered ceramics was characterized using field-emission scanning electron microscopy (FE-SEM) with energy-dispersive X-ray analysis (EDS) (HITACHI SU8030, Japan). The as-fired  $(Y_{1/2}Nb_{1/2})_xTi_{1-x}O_2$  ceramics were carefully polished. Then, an obvious grain and grain boundary (GB) structure of the polished-samples was accomplished by thermally etching at 1100 °C for 30 min. Polished and etched surface was characterized by a scanning electron microscopy (SEM) (SEC, SNE4500M). The chemical states of sintered (Y<sub>1/2</sub>Nb<sub>1/2</sub>)<sub>x</sub>Ti<sub>1-x</sub>O<sub>2</sub> ceramics were analyzed using X-ray Absorption Near Edge Structure (XANES) and X-ray photoelectron spectroscopy (XPS, PHI5000 VersaProbe II, ULVAC-PHI, Japan). XANES and XPS spectra were, respectively, collected at the SUT-NANOTEC-SLRI XAS beamline (BL5.2) (electron energy of 1.2 GeV; bending magnet; beam current 80–150 mA; 1.1 to 1.7 × 10<sup>11</sup> photon s<sup>-1</sup>) and at the SUT-NANOTEC-SLRI Joint Research Facility, the Synchrotron Light Research Institute (SLRI), Nakhon Ratchasima, Thailand. Detail of the XANES characterization technique are given elsewhere [31]. The XPS spectra were fitted with PHI MultiPak XPS software using a combination of Gaussian-Lorentzian lines.

## 2.3 Dielectric and electrical measurements

For dielectric and electrical measurements, Au was sputtered onto both pellet faces at a current of 25 mA for 8 min using a Polaron SC500 sputter coating unit. The capacitance  $(C_p)$  and dispassion factor (D or  $tan\delta$ ) were measured using a KEYSIGHT E4990A

Impedance Analyzer over the frequency and temperature ranges of  $40-10^6$  Hz and -50–200 °C, respectively. Each measurement temperature was held constant with a precision of  $\pm 0.1$  °C with an oscillation voltage of 0.5 V. The nonlinear current density–electric field (*J*–*E*) behavior at RT was measured using a high voltage measurement unit (Keithley Model 247).  $E_b$  was defined as the electric field breakdown strength at which J=1 mA/cm<sup>2</sup>. The nonlinear coefficient ( $\alpha$ ) was calculated in the range of J=1-10 mA/cm<sup>2</sup>.

#### 8.3 Results and discussion

Figure 1 shows the XRD patterns of the 2.5%YNTO and 5.0%YNTO ceramics sintered at 1500 °C for 2 h. Both of the ceramic samples show a main phase consisting of rutile-TiO<sub>2</sub> (JCPDS 21-1276) with a tetragonal structure. A second phase of  $Y_2O_3$  is observed in the XRD patters of these two samples. Lattice parameters (a and c values) were calculated. a values of the 2.5%YNTO and 5.0%YNTO ceramics are, respectively, 4.596±0.001 and 4.598±0.003, while c values are 2.963±0.001 and 2.965±0.003, respectively. The a and c values of both YNTO ceramics increase with increasing codopant concentration. Lattice parameters of both of the YNTO ceramics are larger than the a (4.593 Å) and c (2.959 Å) values of the pure rutile-TiO<sub>2</sub> (JCPDS 21-1276). The enhancement of the lattice parameters may be attributed to the larger ionic radii of Y<sup>3+</sup>  $(r_6 = 0.90 \text{ Å})$  and Nb<sup>5+</sup>  $(r_6 = 0.64 \text{ Å})$  than that of the host Ti<sup>4+</sup> ion  $(r_6 = 0.605 \text{ Å})$  [32]. With regard to the low dopant concentrations of Nb5+ (1.25-2.5 at%) in both YNTO ceramics. Nb<sup>5+</sup> dopant ions can often completely enter into Ti<sup>4+</sup> sites in the rutile structure [18]. However, a secondary Y<sub>2</sub>O<sub>3</sub> phase was detected indicating that some portion or all of the Y<sup>3+</sup> could not be substituted into the Ti<sup>4+</sup> sites. Considering the greatly increased a and c values, it is likely that only some portion of the Y<sup>3+</sup> ions were substituted into the TiO<sub>2</sub> structure.

Surface morphologies of the polished–surfaces of the 2.5%YNTO and 5.0%YNTO ceramics are shown in Fig. 2. Highly dense microstructures are observed. As the codopant concentration was increased from 2.5 to 5.0 mol%, the microstructure changed slightly. The mean grain sizes of the 2.5%YNTO and 5.0%YNTO ceramics were about 15.5 $\pm$ 4.5 and 9.7 $\pm$ 4.2  $\mu$ m, respectively. Additionally, small irregularly shaped grains appeared in the triple junction of the GBs of both samples. From the XRD results, these small particles may be a  $Y_2O_3$  phase. According to the SEM-mapping and EDS results (data not shown), the major elements, Ti and O, as well as minor amounts of Nb dopant were homogeneously dispersed in the microstructure. Small irregularly shaped particles were confirmed to be  $Y_2O_3$ . Careful inspection revealed that another portion of Y dopant was homogeneously distributed throughout the microstructure, indicating that some part of Y dopant was substituted into the TiO $_2$  structure.

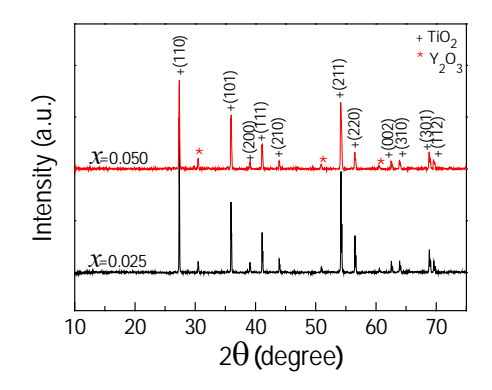


**Fig. 1** XRD patterns of  $(Y_{1/2}Nb_{1/2})_xTi_{1-x}O_2$  ceramics with x=0.025 (2.5%YNTO) and 0.05 (5.0%YNTO).

**Table 1** Lattice parameters (a and c), grain size,  $\varepsilon'$  and  $\tan\delta$  (at 40 Hz and 30 °C) and conduction activation energy of insulating regions (E<sub>a</sub>).

Sample	Lattice parameters (Å)		Grain size	ε'	tanδ	E <sub>a</sub> (eV)
	а	С	(µm)			
2.5%YNTO	4.596±0.001	2.963±0.001	15.5±4.5	17,397	0.087	0.715±0.011
5.0%YNTO	4.598±0.003	2.965±0.003	9.7±4.2	85,752	0.359	0.603±0.007

The YNTO ceramics were further characterized using XPS and XANES techniques to elucidate the influences of Y+Nb co–dopants on the formation of defects in the rutile–TiO $_2$  structure. XPS spectra of the 5.0%YNTO ceramic are shown in Figs. 3(a–d). Two peaks of Nb 3d electrons were detected with binding energies of 209.57 and 206.77 eV, corresponding to  $3d_{3/2}$  and  $3d_{5/2}$ , respectively [Fig. 3(a)]. It was observed that the splitting of the spin–orbits of these two peaks was 2.8 eV, which is quite consistent with that observed in Nb $^{5+}$  single–doped TiO $_2$  materials [18]. The fitted result revealed that an additional  $3d_{5/2}$  peak with a relatively low–binding energy (usually  $\approx$ 204.3 eV) was not found, strongly confirming the presence of only Nb $^{5+}$  in the YNTO ceramics [18]. As shown in Fig. 3(b), the binding energies of Y  $3d_{5/2}$  and Y  $3d_{3/2}$  for the 5.0%YNTO ceramics were about 157.78 and 159.63 eV, respectively, with a spin–orbit splitting of 1.85 eV. This XPS result is similar to that reported in literature, which confirmed that the oxidation state of Y dopant is primarily +3 [33].

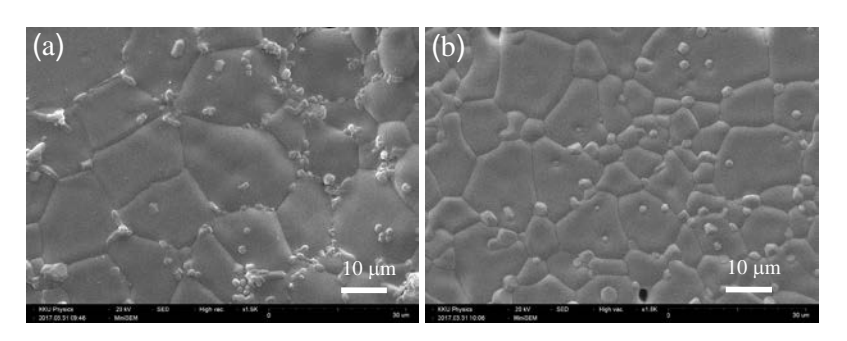


Fig. 2 SEM images of polished surfaces of (a) 2.5%YNTO and (b) 5.0%YNTO.

Generally, doping a rutile—TiO<sub>2</sub> ceramic with Nb<sup>5+</sup> can produce free electrons and eventually cause reduction of Ti<sup>4+</sup> to Ti<sup>3+</sup>, following the relationship [18]:

$$2TiO_2 + Nb_2O_5 \xrightarrow{4TiO_2} 2Ti'_{Ti} + 2Nb^{\bullet}_{Ti} + 8O_O + 1/2O_2,$$
 (1)

$$Ti^{4+} + e \rightarrow Ti^{3+}. \tag{2}$$

The XPS spectrum of Ti 2p was collected to confirm the existence of Ti<sup>3+</sup>. In Fig. 3(c), by fitting the experimental results, the main peak of Ti  $2p_{3/2}$  was observed at a binding energy of 458.42 eV, confirming the presence of a majority portion of Ti<sup>4+</sup>. Additionally, a small peak at a relatively lower binding energy (457.76 eV) was observed. This can be ascribed to Ti<sup>3+</sup> [18, 34]. The XPS spectrum of O 1s profiles was measured and shown in Fig. 3(d). Four peaks were obtained from fitting the experimental data. Two main peaks at 529.58 and 531.93 eV were ascribed to an oxygen lattice in the bulk ceramic and oxygen vacancies, respectively [14, 18]. The other two peaks at 530.73 and 533.57 eV were caused by oxygen lattices of other cation—oxygen bonds (i.e., Y—O and Nb—O bonds) and a surface hydroxyl (OH), respectively [14, 18-19]. Although, substitution of acceptor Y<sup>3+</sup> ions into TiO<sub>2</sub> can cause oxygen vacancies for charge compensation following the relation:

$$Y_2O_3 \xrightarrow{2TiO_2} 2Y'_{Ti} + V_O^{\bullet \bullet} + 3O_O,$$
 (3)

the large amount of oxygen vacancies observed (a large  $V_o^{\bullet\bullet}$  peak area) may have originated for other reasons, since only a small amount of Y<sup>3+</sup> can enter into the TiO<sub>2</sub> structure. A high concentration of oxygen vacancies may have been formed during the sintering process at 1500 °C.

Figures 3(e) and (f) illustrate normalized Ti K-edge XANES spectra of the 2.5%YNTO and 5.0%YNTO ceramics, respectively, as well as the standard samples of Ti<sub>2</sub>O<sub>3</sub> (Ti<sup>3+</sup>) and TiO<sub>2</sub> (Ti<sup>4+</sup>). The edge energy position of both samples was located between Ti<sub>2</sub>O<sub>3</sub> and TiO<sub>2</sub>, but closer to the TiO<sub>2</sub> standard, indicating that most of Ti ions were Ti<sup>4+</sup> with a relatively small amount of Ti<sup>3+</sup>. A very small shift of the edge value was caused by the presence of Ti<sup>3+</sup> in the YNTO ceramic [31]. To quantify the Ti<sup>3+</sup> and Ti<sup>4+</sup> in all ceramics, the empirical edge-shift calculation comparing with the known standard samples (Ti<sup>3+</sup>:Ti<sub>2</sub>O<sub>3</sub> and Ti<sup>4+</sup>:TiO<sub>2</sub>) was applied. The amount of Ti<sup>3+</sup> was calculated:

% of 
$$Ti^{3+}$$
 for each sample =  $\left(1 - \frac{\Delta E \text{ of sample}}{\Delta E \text{ of } Ti^{3+} \text{ and } Ti^{4+} \text{ standard}}\right) \times 100\%$ , (4)

where,  $\Delta E$  is a difference of edge value of a Ti<sup>3+</sup> standard compared with YNTO ceramic samples. The ratio of Ti<sup>3+</sup>/Ti<sup>4+</sup> in the 2.5% and 5.0%YNTO ceramics were found to be 19.3 and 13.6%, respectively. These ratios are larger than the theoretical values. This was likely originated from the existence of oxygen vacancies (i.e.,  $O^{2-}(lattice) \rightarrow 1/2O_2(g) + 2e$ ) during sintering at a high temperature. According to the XPS and XANES results, the presence of Ti<sup>3+</sup> in the YNTO ceramics was confirmed. The conduction mechanism in the YNTO ceramics was therefore caused by electron hopping between Ti<sup>4+</sup> and Ti<sup>3+</sup> sites.

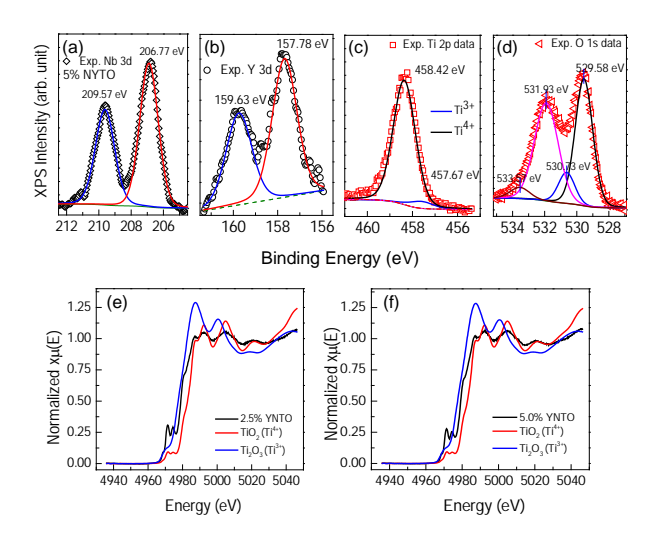


**Fig. 3** (a–d) Valence states of 2.5%YNTO from XPS spectra (open circles) and corresponding fitted results (solid lines); (a) Nb 3*d*, (b) Y 2*p*, (c) Ti 2*p*, and (d) O 1s. (e–f) Normalized X–ray absorption near–edge structure (XANES) spectra for the Ti K-edge of 2.5%YNTO and 5.0%YNTO ceramics, respectively.

The giant dielectric properties as a function of frequency at 30 °C of the 2.5%YNTO and 5.0%YNTO ceramics are illustrated in Fig. 4. Both samples exhibited ultra-high  $\epsilon'$  values, on the order of  $10^4$ – $10^5$ , over a frequency range of 40– $10^6$  Hz.  $\epsilon'$  of the 5.0%YNTO ceramic is larger than that of the 2.5%YNTO ceramic over a measured frequency range. This is similar to INTO ceramics [18]. The very large  $\epsilon'$  values of the YNTO ceramics are comparable to those observed in CCTO and related compounds [2-3, 5, 17]. The  $\epsilon'$  and tan $\delta$  values at 40 Hz of the 2.5%YNTO and 5.0%YNTO ceramics are summarized in Table 1. Interestingly, tan $\delta$  at 40 Hz of the 2.5%YNTO ceramic was low, 0.08. As demonstrated in the inset, below  $10^4$  Hz, tan $\delta$  of the 2.5%YNTO ceramic was lower than that of the 5.0%YNTO ceramic. A higher  $\epsilon'$  value was accompanied by a larger low–frequency tan $\delta$  value. This behavior is similar to that observed in other giant dielectric oxides such as CCTO [2] and (Li+Ti) co–doped NiO ceramics [35]. However, the frequency dependence of tan $\delta$  in a low–frequency range for the YNTO ceramics is completely unlike the behavior of CCTO and other giant dielectric oxides [3, 5, 7, 9, 11].

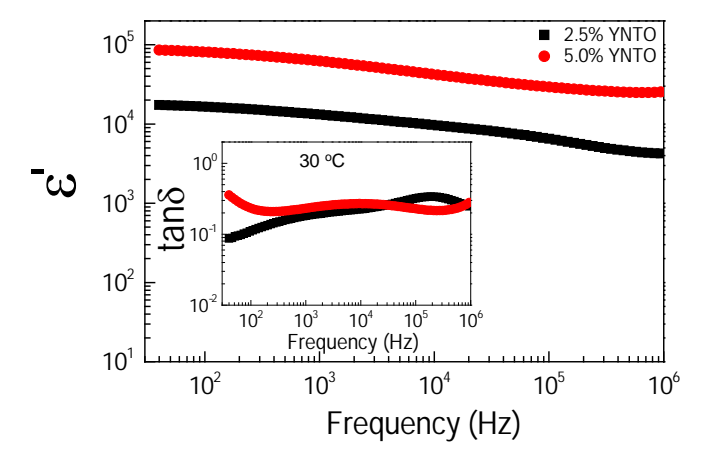


**Fig. 4** Frequency dependence of dielectric permittivity ( $\epsilon$ ') at 30 °C of 2.5%YNTO and 5.0%YNTO ceramics; inset shows tanδ at 30 °C as a function of frequency.

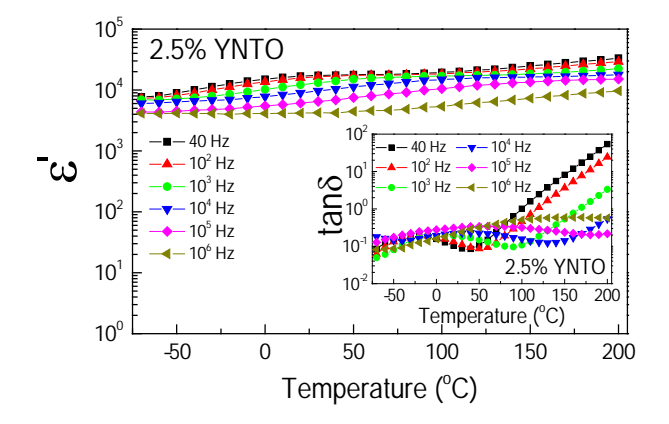


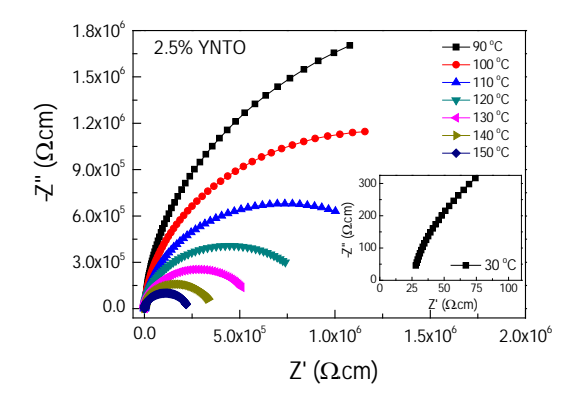
Fig. 5 Temperature dependence of dielectric permittivity ( $\epsilon$ ') at selected frequencies from 40 to 10<sup>6</sup> Hz for 2.5%YNTO ceramic; inset shows tan $\delta$  at different frequencies as a function of temperature.

Figure 5 and its inset show the temperature dependence of  $\varepsilon'$  and  $\tan\delta$  in the 2.5%YNTO ceramic at selected frequencies from 40 to  $10^6$  Hz.  $\varepsilon'$  was slightly dependent on temperature in the range from 0 to 200 °C. At temperatures higher than 100 °C, a low–frequency  $\tan\delta$  rapidly increased with increasing temperature. This observation resulted from an increase in DC conduction (i.e., the long distance movement of free charge carriers) [35]. The dielectric relaxation behavior was observed in the temperature range of -50–100 °C. This may be attributed to the polarization relaxation of trapped charges at the internal insulating GBs and/or at the interface between resistive—outer surface layers and a conductive inner core [15].

Figure 6 illustrates the impedance complex plane ( $Z^*$ ) plot of the 2.5%YNTO ceramic at different temperatures. A large semicircular arc and a nonzero intercept [inset of Fig. 6] are observed. Thus, two primary electrical responses of the insulating GBs coupled with an insulating resistive—outer surface layer and semiconducting grains were confirmed in the YNTO ceramics [1, 4]. This  $Z^*$  plot was similar to that observed for (Al+Nb) [14] and (In+Nb) co–doped TiO<sub>2</sub> ceramics [29]. As shown in Fig. 7, the temperature dependence of the total resistance of insulating parts ( $R_i$ ) followed the Arrhenius law [1, 4]:

$$R_i = R_0 \exp\left(\frac{E_a}{k_B T}\right),\tag{5}$$

where  $R_0$  is a constant value, and  $E_a$  is the activation energy required for conduction in the insulating regions. The  $E_a$  values of the 2.5%YNTO and 5.0%YNTO ceramics were found to be 0.715±0.011 and 0.603±0.007 eV, respectively.  $E_a$  for the YNTO ceramics decreased with increasing co–dopant concentration.  $E_a$  values of the YNTO ceramics were comparable to those of the conduction activation energies at the GBs of CCTO ceramics ( $E_{\rm gb} \approx 0.6$ –0.7 eV) [2, 31]. The nonzero intercept ( $R_{\rm g}$ ) shifted very slightly with changing temperature from -50 to 200 °C. Thus, the conduction activation energy inside the grains could not be calculated. Although the complex defect dipoles corresponding to EPDD model might have formed, it is more reasonable that the giant dielectric response in the YNTO ceramics is primarily caused by the interfacial polarization at the internal insulating interfaces.



**Fig. 6** Impedance complex plane plot (Z\*) at different temperatures for 2.5%YNTO ceramic; inset illustrates an expanded view of the high frequency data close to the origin, revealing a nonzero intercept.

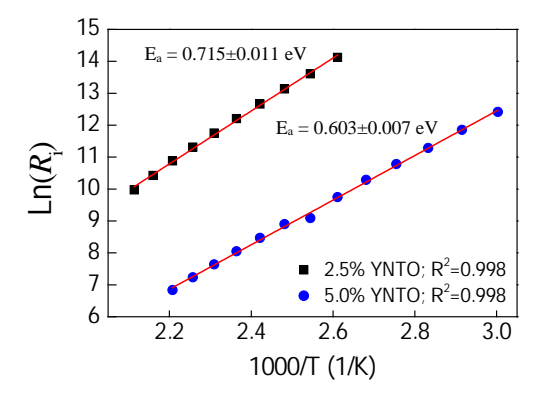


**Fig. 7** Arrhenius plot of the total resistance of insulating parts (R<sub>i</sub>) for 2.5%YNTO and 5.0%YNTO ceramics.

As shown in Fig. 8, both the 2.5%YNTO and 5.0%YNTO ceramics exhibited nonlinear J-E characteristics, as was also observed in CCTO polycrystalline ceramics [36]. E<sub>b</sub> values of the 2.5%YNTO and 5.0%YNTO ceramics are, respectively, 122.8 and 235.3 V/cm, while  $\alpha$  values are 1.9 and 4.2, respectively. Generally, non-Ohmic properties of varistor oxides and CCTO ceramics can arise from the formation of a Schottky barrier at the internal insulating interface layer, which is sandwiched by n-type semiconducting grains [1, 36]. Usually,  $\alpha$  of ceramic varistors has close relationship to the oxygen vacancy concentration. For CCTO ceramics, sintering in oxidizing atmospheres can cause an increase in the  $\alpha$  value [37]. Enhanced electrostatic barrier at GBs was suggested to be the primary origin for this observation. In the case of La-doped BiFeO<sub>3</sub> ceramics, it was found that  $\alpha$  increased with increasing oxygen partial pressure [38]. It is proposed that the electrostatic barrier was created at domain walls rather than at the GBs of BiFeO<sub>3</sub>. According to the calculated ratio of Ti<sup>3+</sup>/Ti<sup>4+</sup> using XANES spectra, the concentration of oxygen vacancies in the 5.0%YNTO ceramic was suggested to be lower than that of the 2.5%YNTO ceramic. This result is consistent with the  $\alpha$  values of these two ceramic samples. Therefore, this result strongly confirms that the origin of the giant dielectric response in YNTO ceramics was correlated with the electrical response of the internal insulating interfaces. Therefore, it is reasonably to suggest that the giant dielectric properties of YNTO ceramics were attributable to interfacial polarization due to the electrically heterogeneous microstructure of the YNTO ceramics.

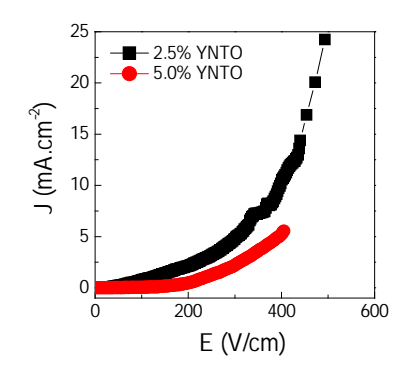


**Fig. 8** Nonlinear *J–E* characteristics at room temperature of 2.5%YNTO and 5.0%YNTO ceramics.

## 8.4 Conclusions

We successfully synthesized ( $Y^{3+}$  and  $Nb^{5+}$ ) co–doped  $TiO_2$  ceramics via a chemical combustion method using glycine as a fuel. The main phase of a rutile— $TiO_2$  structure and a secondary phase of  $Y_2O_3$  were detected in all sintered ceramics. A dense ceramic microstructure with homogeneous dispersion of O, Ti and Nb was observed. Segregation of  $Y_2O_3$  particles was observed at the GBs throughout the microstructure. This may have had an effect on the electrical response of the GBs. The n-type semiconducting grains were due to electron hopping between  $Ti^{3+}$  and  $Ti^{4+}$  sites, which was confirmed by the XPS and XENSE spectra. Very large  $\epsilon'$  values of  $\approx 10^4 - 10^5$  in the frequency range of 40– $10^6$  Hz with a low  $tan\delta \approx 0.08$  at 40 Hz were achieved. According to the impedance spectroscopy and nonlinear J-E characteristic, the giant dielectric response can be described by interfacial polarization at insulating interfaces, i.e., GBs and outer surface layers.

#### References

- [1] T. Adams, D. Sinclair, A. West, Characterization of grain boundary impedances in fine- and coarse-grained CaCu<sub>3</sub>Ti<sub>4</sub>O<sub>12</sub> ceramics, Phys. Rev. B 73 (9) (2006) 094124.
- [2] L. Liu, H. Fan, P. Fang, X. Chen, Sol–gel derived CaCu<sub>3</sub>Ti<sub>4</sub>O<sub>12</sub> ceramics: Synthesis, characterization and electrical properties, Mater. Res. Bull. 43 (7) (2008) 1800-1807.
- [3] L. Ni, X.M. Chen, Enhancement of Giant Dielectric Response in CaCu<sub>3</sub>Ti<sub>4</sub>O<sub>12</sub> Ceramics by Zn Substitution, J. Am. Ceram. Soc. 93 (1) (2010) 184-189.
- [4] R. Schmidt, M.C. Stennett, N.C. Hyatt, J. Pokorny, J. Prado-Gonjal, M. Li, D.C. Sinclair, Effects of sintering temperature on the internal barrier layer capacitor (IBLC) structure in CaCu<sub>3</sub>Ti<sub>4</sub>O<sub>12</sub> (CCTO) ceramics, J. Eur. Ceram. Soc. 32 (12) (2012) 3313-3323.
- [5] Y. Shi, W. Hao, H. Wu, L. Sun, E. Cao, Y. Zhang, H. Peng, High dielectric-permittivity properties of NaCu<sub>3</sub>Ti<sub>3</sub>Sb<sub>0.5</sub>Nb<sub>0.5</sub>O<sub>12</sub> ceramics, Ceram. Int. 42 (1, Part A) (2016) 116-121.
- [6] S. Ke, H. Fan, H. Huang, Dielectric relaxation in A<sub>2</sub>FeNbO<sub>6</sub> (A perovskite ceramics, Journal of Electroceramics 22 (1-3) (2007) 252-256.

- [7] X. Sun, J. Deng, S. Liu, T. Yan, B. Peng, W. Jia, Z. Mei, H. Su, L. Fang, L. Liu, Grain boundary defect compensation in Ti-doped BaFe<sub>0.5</sub>Nb<sub>0.5</sub>O<sub>3</sub> ceramics, Applied Physics A 122 (9) (2016) 864.
- [8] Z. Wang, X.M. Chen, L. Ni, X.Q. Liu, Dielectric abnormities of complex perovskite  $Ba(Fe_{1/2}Nb_{1/2})O_3$  ceramics over broad temperature and frequency range, Appl. Phys. Lett. 90 (2) (2007) 022904.
- [9] J. Wang, G. Liu, B.W. Jia, X.Q. Liu, X.M. Chen, Giant dielectric response and polaronic hopping in Al-substituted  $A_{5/3}Sr_{1/3}NiO_4$  (A=La, Nd) ceramics, Ceram. Int. 40 (4) (2014) 5583-5590.
- [10] A. Chouket, O. Bidault, V. Optasanu, A. Cheikhrouhou, W. Cheikhrouhou-Koubaa, M. Khitouni, Enhancement of the dielectric response through Al-substitution in La<sub>1.6</sub>Sr<sub>0.4</sub>NiO<sub>4</sub> nickelates, RSC Adv. 6 (29) (2016) 24543-24548.
- [11] K. Meeporn, N. Chanlek, P. Thongbai, Effects of DC bias on non-ohmic sample-electrode contact and grain boundary responses in giant-permittivity La<sub>1.7</sub>Sr<sub>0.3</sub>Ni<sub>1-x</sub>Mg<sub>x</sub>O<sub>4</sub> ceramics, RSC Advances 6 (94) (2016) 91377-91385.
- [12] W. Dong, W. Hu, A. Berlie, K. Lau, H. Chen, R.L. Withers, Y. Liu, Colossal Dielectric Behavior of Ga+Nb Co-Doped Rutile TiO<sub>2</sub>, ACS Applied Materials & Interfaces 7 (45) (2015) 25321-25325.
- [13] Y. Song, X. Wang, X. Zhang, Y. Sui, Y. Zhang, Z. Liu, Z. Lv, Y. Wang, P. Xu, B. Song, The contribution of doped-Al to the colossal permittivity properties of Al<sub>x</sub>Nb<sub>0.03</sub>Ti<sub>0.97-x</sub>O<sub>2</sub> rutile ceramics, Journal of Materials Chemistry C 4 (28) (2016) 6798-6805.
- [14] G. Liu, H. Fan, J. Xu, Z. Liu, Y. Zhao, Colossal permittivity and impedance analysis of niobium and aluminum co-doped TiO<sub>2</sub> ceramics, RSC Advances 6 (54) (2016) 48708-48714.
- [15] T. Nachaithong, P. Thongbai, S. Maensiri, Colossal permittivity in  $(In_{1/2}Nb_{1/2})_xTi_{1-x}O_2$  ceramics prepared by a glycine nitrate process, J. Eur. Ceram. Soc. 37 (2) (2017) 655-660.
- [16] W.C. Ribeiro, E. Joanni, R. Savu, P.R. Bueno, Nanoscale effects and polaronic relaxation in compounds, Solid State Commun. 151 (2) (2011) 173-176.
- [17] Y. Wang, L. Ni, X.M. Chen, Effects of Nd-substitution on microstructures and dielectric characteristics of  $CaCu_3Ti_4O_{12}$  ceramics, J. Mater. Sci.: Mater. Electron. 22 (4) (2011) 345-350.
- [18] W. Hu, Y. Liu, R.L. Withers, T.J. Frankcombe, L. Norén, A. Snashall, M. Kitchin, P. Smith, B. Gong, H. Chen, J. Schiemer, F. Brink, J. Wong-Leung, Electron-pinned defect-dipoles for high-performance colossal permittivity materials, Nat. Mater. 12 (9) (2013) 821-826.
- [19] X. Cheng, Z. Li, J. Wu, Colossal permittivity in ceramics of TiO<sub>2</sub> Co-doped with niobium and trivalent cation, Journal of Materials Chemistry A 3 (11) (2015) 5805-5810.
- [20] Z. Li, J. Wu, W. Wu, Composition dependence of colossal permittivity in  $(Sm_{0.5}Ta_{0.5})_xTi_{1-x}O_2$  ceramics, Journal of Materials Chemistry C 3 (35) (2015) 9206-9216.
- [21] J. Li, F. Li, Y. Zhuang, L. Jin, L. Wang, X. Wei, Z. Xu, S. Zhang, Microstructure and dielectric properties of (Nb -dopedcoutile TiO<sub>2</sub> ceramics, J. Appl. Phys. 116 (7) (2014) 074105.

- [22] W. Hu, K. Lau, Y. Liu, R.L. Withers, H. Chen, L. Fu, B. Gong, W. Hutchison, Colossal Dielectric Permittivity in (Nb+Al) Codoped Rutile TiO<sub>2</sub> Ceramics: Compositional Gradient and Local Structure, Chem. Mater. 27 (14) (2015) 4934-4942.
- [23] J. Li, F. Li, Z. Xu, Y. Zhuang, S. Zhang, Nonlinear I–V behavior in colossal permittivity ceramic: (Nb+In) co-doped rutile TiO<sub>2</sub>, Ceram. Int. 41, Supplement 1 (2015) S798-S803.
- [24] W. Tuichai, P. Srepusharawoot, E. Swatsitang, S. Danwittayakul, P. Thongbai, Giant dielectric permittivity and electronic structure in (Al + Sb) co-doped TiO<sub>2</sub> ceramics, Microelectron. Eng. 146 (2015) 32-37.
- [25] J. Li, F. Li, C. Li, G. Yang, Z. Xu, S. Zhang, Evidences of grain boundary capacitance effect on the colossal dielectric permittivity in (Nb + In) co-doped TiO<sub>2</sub> ceramics, Sci Rep 5 (2015) 8295.
- [26] J. Li, Z. Xu, F. Li, X. Zhu, S. Zhang, SiO<sub>2</sub>-Ti<sub>0.98</sub>In<sub>0.01</sub>Nb<sub>0.01</sub>O<sub>2</sub> composite ceramics with low dielectric loss, high dielectric permittivity and an enhanced breakdown electric field, RSC Advances 6 (24) (2016) 20074-20080.
- [27] Y. Song, X. Wang, Y. Sui, Z. Liu, Y. Zhang, H. Zhan, B. Song, Z. Liu, Z. Lv, L. Tao, J. Tang, Origin of colossal dielectric permittivity of rutile Ti<sub>0.9</sub>In<sub>0.05</sub>Nb<sub>0.05</sub>O<sub>2</sub>: single crystal and polycrystalline, Scientific Reports 6 (2016) 21478.
- [28] W. Tuichai, S. Danwittayakul, S. Maensiri, P. Thongbai, Investigation on temperature stability performance of giant permittivity (In + Nb) in co-doped TiO<sub>2</sub> ceramic: a crucial aspect for practical electronic applications, RSC Advances 6 (7) (2016) 5582-5589.
- [29] W. Tuichai, S. Danwittayakul, N. Chanlek, P. Srepusharawoot, P. Thongbai, S. Maensiri, Origin(s) of the apparent colossal permittivity in  $(In_{1/2}Nb_{1/2})_xTi_{1-x}O_2$ : clarification on the strongly induced Maxwell-Wagner polarization relaxation by DC bias, RSC Advances 7 (1) (2017) 95-105.
- [30] Z. Li, J. Wu, Novel titanium dioxide ceramics containing bismuth and antimony, Journal of Materiomics http://dx.doi.org/10.1016/j.jmat.2017.01.001 (2017).
- [31] J. Boonlakhorn, P. Kidkhunthod, P. Thongbai, A novel approach to achieve high dielectric permittivity and low loss tangent in  $CaCu_3Ti_4O_{12}$  ceramics by co-doping with  $Sm^{3+}$  and  $Mg^{2+}$  ions, J. Eur. Ceram. Soc. 35 (13) (2015) 3521-3528.
- [32] R.D. Shannon, Revised Effective Ionic Radii and Systematic Studies of Interatomie Distances in Halides and Chaleogenides, Acta Cryst. A32 (1976) 751-767.
- [33] B. Zhao, J. Wang, H. Li, H. Wang, X. Jia, P. Su, The influence of yttrium dopant on the properties of anatase nanoparticles and the performance of dye-sensitized solar cells, Phys. Chem. Chem. Phys. 17 (22) (2015) 14836-14842.
- [34] L.R. Sheppard, J. Holik, R. Liu, S. Macartney, R. Wuhrer, Tantalum Enrichment in Tantalum-Doped Titanium Dioxide, J. Am. Ceram. Soc. 97 (12) (2014) 3793-3799.
- [35] J. Wu, C.-W. Nan, Y. Lin, Y. Deng, Giant Dielectric Permittivity Observed in Li and Ti Doped NiO, Phys. Rev. Lett. 89 (21) (2002) 217601.
- [36] S.-Y. Chung, I.-D. Kim, S.-J.L. Kang, Strong nonlinear current–voltage behaviour in perovskite-derivative calcium copper titanate, Nat. Mater. 3 (11) (2004) 774-778.

- [37] P.R. Bueno, M.A. Ramírez, J.A. Varela, E. Longo, Dielectric spectroscopy analysis of CaCu<sub>3</sub>Ti<sub>4</sub>O<sub>12</sub> polycrystalline systems, Appl. Phys. Lett. 89 (19) (2006) 191117.
- [38] G. Dong, H. Fan, P. Ren, X. Liu, Hole conduction and nonlinear current–voltage behavior in multiferroic lanthanum-substituted bismuth ferrite, J. Alloys Compd. 615 (2014) 916-920.

## **CHAPTER 9**

## Effects of Sintering Temperature on Microstructure and Giant Dielectric Properties of (V+Ta) Co-Doped TiO<sub>2</sub> Ceramics

#### 9.1 Introduction

Recently, giant dielectric materials have been widely investigated because they can be used in electronic applications such as capacitors and memory devices, as well as in high energy–dense storage devices. Although giant dielectric materials that can exhibit very high dielectric permittivities ( $\epsilon$ ') of  $10^3$ – $10^6$ , such as CaCu<sub>3</sub>Ti<sub>4</sub>O<sub>12</sub> (CCTO) and its isostructural CCTO–type perovskites [1-6], co-doped NiO-based oxides [7], La<sub>2-x</sub>Sr<sub>x</sub>NiO<sub>4</sub> [8-11], and AFe<sub>1/2</sub>B<sub>1/2</sub>O<sub>3</sub> (A=Ba, Sr, Ca; B=Nb, Ta, Sb) [12, 13] have been widely studied, the dielectric loss tangent (tan $\delta$ ) of these giant dielectric oxides as well as CCTO ceramics are still too large. Unacceptably large values of tan $\delta$  are one of the most serious problems in developing applications for their use. Furthermore, even though tan $\delta$  can be reduced, these dielectric oxides have large variations in  $\epsilon$ ' at temperatures higher than 100 °C, which is undesirable for practical applications.

Most recently, a giant dielectric response with small variation in  $\epsilon'$  over a wide temperature range in conjunctions with a low  $\tan\delta$  was reported in (In+Nb) co–doped TiO<sub>2</sub> (INTO) ceramics [14]. Doping rutile–TiO<sub>2</sub> with 10% In<sup>3+</sup>+Nb<sup>5+</sup> enhanced its dielectric response to a value of  $\epsilon'\approx6\times10^4$ , while  $\tan\delta$  was still very low,  $\approx0.02$ , over a wide frequency range [14]. This discovery has greatly stimulated interest in the field of giant dielectric TiO<sub>2</sub>–based oxides [15-26]. The investigation of the crystal structure, phase composition, microstructure, variation in oxidation states, and the dielectric and electrical properties of other co–doped TiO<sub>2</sub> ceramics were also reported, using dopants such as  $\mathrm{Sc^{3+}}+\mathrm{Nb^{5+}}$  [20],  $\mathrm{Ga^{3+}}+\mathrm{Nb^{5+}}$  [16],  $\mathrm{Al^{3+}}+\mathrm{Ta^{5+}}$  [18], and  $\mathrm{Al^{3+}}+\mathrm{Nb^{5+}}$  [15, 17], among others. The dielectric properties of these co–doped TiO<sub>2</sub> systems are very interesting and are important for further development of giant dielectric oxides.

The formation of defects and their interaction in acceptor/donor co-doped TiO<sub>2</sub> ceramics were dependent on the ionic radius of +3 doping ions used [16]. Electron-pinned defect-dipoles (EPDDs) can be occurred in the In<sup>3+</sup>/Nb<sup>5+</sup> co-doped TiO<sub>2</sub> system because a relatively large ionic radius of  $\ln^{3+}$  ( $r_6 = 0.800 \text{ Å}$ ) compared to that of  $\ln^{4+}$  ( $r_6 = 0.605 \text{ Å}$ ) [14, 16]. Therefore, very high dielectric response in INTO ceramics was suggested to originate from EPDDs. The EPDD effect was not dominated in the Ga3+/Nb5+ co-doped  $TiO_2$  system because the ionic radius of  $Ga^{3+}$  ( $r_6 = 0.620 \text{ Å}$ ) is slightly larger than that of Ti<sup>4+</sup> [16]. Although the EPDDs might be occurred in the Sc<sup>3+</sup>/Nb<sup>5+</sup> co-doped TiO<sub>2</sub> system due to the quite large ionic radius of  $Sc^{3+}$  ( $r_6 = 0.745$  Å), we found that the high-performance giant-dielectric properties of were likely attributed to interfacial polarization at insulating layers [20]. Hu et al. [17] clearly demonstrated that the EPDDs cannot be occurred in the Al3+/Nb5+ co-doped TiO2 system due to a relatively small ionic radius of Al<sup>3+</sup> ( $r_6 = 0.535$  Å). By optimizing sintering conditions, high  $\varepsilon'$  (10<sup>3</sup>–10<sup>5</sup>) and low  $tan\delta$  (< 0.05) can be achieved in the Al<sup>3+</sup>/Nb<sup>5</sup> and Sc<sup>3+</sup>/Nb<sup>5+</sup> co-doped TiO<sub>2</sub> ceramics [17. 20]. The giant dielectric properties of these two systems were dependent on sintering conditions. For CCTO and other giant dielectric oxides, their microstructural evolution can be elucidated by varying sintering time and temperature. Studies examining the microstructural evolution of CCTO-based ceramics and their giant dielectric properties are widely published [4, 27-31]. Unfortunately, this work has never been done for co-doped TiO<sub>2</sub> ceramics. For practical applications, there is an ongoing need for a new co–doped TiO<sub>2</sub> system. Considering the ionic radius of V<sup>3+</sup> ( $r_6$  = 0.640 Å) [32], the EPDDs may unlikely be produced in the V<sup>3+</sup>/Nb<sup>5+</sup> and V<sup>3+</sup>/Ta<sup>5+</sup> co–doped TiO<sub>2</sub> systems. Nevertheless, a giant dielectric response with a low tan $\delta$  may be achieved by varying the microstructure and sintering conditions. To the best of our knowledge, the giant dielectric properties of this co–doped TiO<sub>2</sub> system has never been reported.

Therefore, in the current study,  $V^{3+}/Ta^{5+}$  co-doped rutile- $TiO_2$  ceramics were synthesized using a conventional solid state reaction method, sintering at various temperatures to obtain different microstructures. The giant dielectric response and electrical properties of the sintered  $V^{3+}/Ta^{5+}$  co-doped  $TiO_2$  ceramics with different grain sizes were investigated. In this way, dielectric properties can be optimized. The origin of the giant dielectric response behavior is described in detail.

## 9.2 Experimental details

A conventional solid state reaction (SSR) method was used to prepare  $(V_{1/2}Ta_{1/2})_{0.01}Ti_{0.99}O_2$  (1%VTTO) ceramics. This is because the SSR method has many advantages such as simple apparatus and inexpensive method. Furthermore, the SSR method can successfully be used to synthesize nanocomposite materials such as  $MoS_2/g-C_3N_4$  nanocomposites [33]. Rutile– $TiO_2$  (Sigma–Aldrich, >99.9% purity),  $Ta_2O_5$  (Sigma–Aldrich, 99.99% purity), and  $V_2O_3$  (Sigma–Aldrich, 98% purity) were used as the starting raw materials. First, a stoichiometric mixture of the starting materials corresponding to the  $(V_{1/2}Ta_{1/2})_{0.01}Ti_{0.99}O_2$  composition was mixed by ball milling in ethanol for 24 h using  $ZrO_2$  balls with  $\approx 2.0$  mm in diameter. Second, the ethanol media was evaporated at  $\approx 90$  °C. Then, a dried mixed powder was carefully ground and sieved for several times. After that, fine mixed powder was pressed into pellets (without a binder) of  $\approx 9.5$  mm in diameter and  $\approx 1.2$  mm in thickness by uniaxial compression at  $\approx 180$  MPa. To obtain 1%VTTO ceramics with different grain sizes, finally, the pellets were sintered at 1300, 1400, and 1500 °C for 5 h using heating rate 2 °C/min, followed by natural furnace–cooling to room temperature.

Phase composition and crystal structure of these samples were characterized using X-ray diffraction (PANalytical, EMPYREAN). Surface morphologies of the sintered ceramics were revealed by scanning electron microscopy (SEM) (HITACHI SU8030, Japan). Mapping the distribution of each type of ion in the 1%VTTO ceramics was performed using field-emission scanning electron microscopy (FE-SEM) with energy-dispersive X-ray analysis (EDS) (HITACHI SU8030, Japan). The oxidation states in VTTO ceramics were analyzed using X-ray photoelectron spectroscopy (XPS), PHI5000 VersaProbe II, ULVAC-PHI, Japan) at the SUT-NANOTEC-SLRI Joint Research Facility, Synchrotron Light Research Institute (SLRI), Thailand. The XPS spectra were fitted with PHI MultiPak XPS software using Gaussian-Lorentzian lines.

For dielectric measurements, two parallel electrodes were fabricated by sputtering Au on both sides of the sample surface without polishing their surfaces. The dielectric properties were measured using a KEYSIGHT E4990A Impedance Analyzer over the frequency and temperature ranges of  $40-10^6$  Hz and -60-210 °C, respectively. Each measurement temperature was kept constant with a precision of  $\pm 0.1$  °C.

#### 9.3 Results and discussion

First of all, only the 1%(V+Ta) co-doped TiO<sub>2</sub> ceramic system is discussed in this paper. This is because its  $\varepsilon'$  value was reduced by increasing the co-dopant concentration, while  $tan\delta$  increased. These are unsuitable for many applications. Sintered 1%VTTO ceramics were first characterized using an XRD technique to confirm its rutile-phase. Figure 1 demonstrates the XRD patterns of the TiO<sub>2</sub> and 1%VTTO ceramics sintered at various temperatures from 1300 to 1500 °C for 5 h. The overall XRD patterns of all co-doped 1%VTTO ceramics were similar to that observed in the pure TiO2 with no impurity phase. The main phase of rutile-TiO<sub>2</sub> (JCPDS 21-1276) was confirmed in all 1%VTTO ceramics. According to the XRD results, the lattice parameters (i.e., a and c values) were calculated. The a and c values of un-doped  $TiO_2$  were 4.593 and 2.959 Å, respectively. The a values of the 1%VTTO ceramics sintered at 1300, 1400, and 1500 °C were 4.593, 4.593, and 4.594 Å, respectively. The c values of all co-doped samples were the same, 2.961 Å. The crystalline structure of the 1%VTTO ceramics did not change as sintering temperature was increased. The a and c values of all the samples, as well as the un-doped TiO<sub>2</sub>, were comparable to literature values [14, 19, 20]. It is notable that the a and c values of TiO2 did not change by co-doping with 1%(V+Ta) due to the small co-dopant concentration.

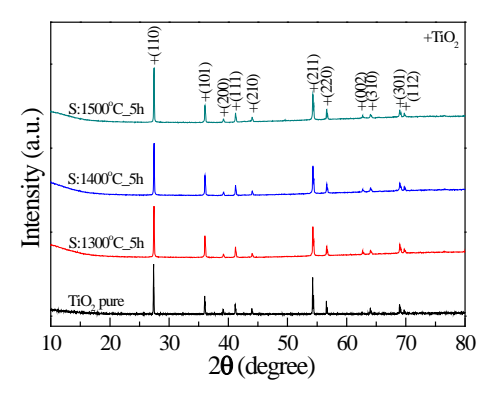


**Fig. 1** XRD patterns of  $TiO_2$  and  $(V_{1/2}Ta_{1/2})_{0.01}Ti_{0.99}O_2$  ceramics sintered at 1300-1500 °C for 5 h.

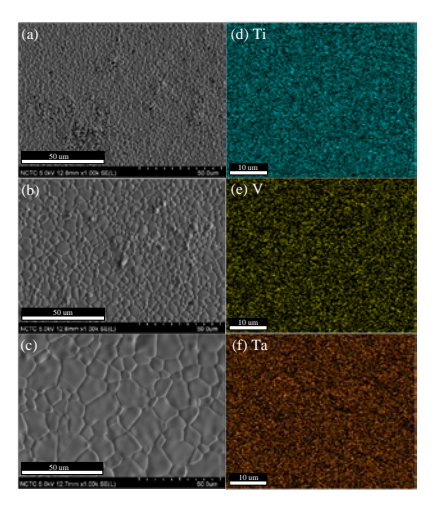


**Fig. 2** SEM images of surface morphologies of  $(V_{1/2}Ta_{1/2})_{0.01}Ti_{0.99}O_2$  ceramics sintered at (a) 1300 °C, (b) 1400 °C, and (c) 1500 °C for 5 h and SEM mapping of elements in  $(V_{1/2}Ta_{1/2})_{0.01}Ti_{0.99}O_2$  ceramic sintered at 1500 °C for 5 h; (d) Ti, (e) V, and (f) Ta.

The influence of sintering temperatures on the microstructure of the 1%VTTO ceramics is revealed in Figs. 2(a-c). Porosity was observed in only the microstructure of the ceramic sintered at 1300 °C. A highly dense microstructure with no pores was observed in the ceramics sintered at 1400 and 1500 °C. It was clearly observed that the grain size increased with increasing sintering temperature. The mean grain sizes of the ceramics sintered at 1300, 1400, and 1500 °C were about 2.1, 5.7, and 14.8 µm, respectively. It is notable that the increased grain sizes with sintering temperature was similar to that observed in other giant dielectric materials, such as CCTO-based ceramics [4, 27]. The dispersion of co-dopants and Ti elements in the 1%VTTO ceramics was revealed using the SEM mapping images in Figs. 2(d-f). Both Ta and V dopants, as well as Ti, were homogeneously dispersed in the microstructure. No segregation of dopants was observed in any specific region such as grain boundaries. Generally, the grain growth in polycrystalline materials is primary associated with the grain boundary mobility, which is controlled by the diffusion of ions, atoms, and/or charge species across the grain boundary layer [34]. This is owing to the highly defective nature of the grain boundary, and thus it is usually expected that the grain boundary diffusion is more rapid than lattice diffusion in the adjacent grains. The diffusion coefficient in a polycrystalline ceramic is usually dependent on temperature [34]. Therefore, the grain growth of the sintered 1%VTTO ceramics increases with increasing sintering temperature.

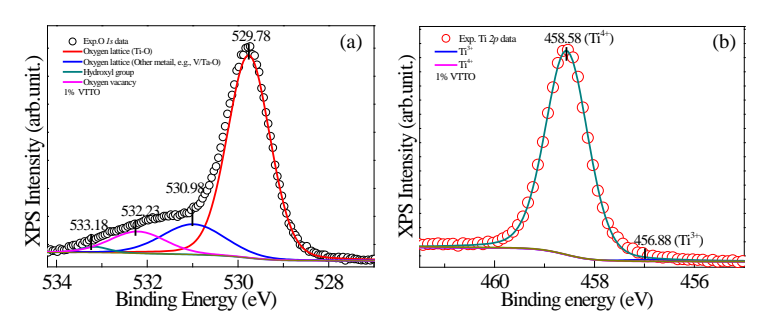


**Fig. 3** XRS spectra of the  $(V_{1/2}Ta_{1/2})_{0.01}Ti_{0.99}O_2$  ceramic sintered at 1500 °C for 5 h; (a) O 1s, and, (b) Ti 2p.

Figures 3(a) and (b) display XPS spectra of the 1%VTTO ceramic. Generally, substitution of acceptor ions (+3 ions) into  $TiO_2$  is requires oxygen vacancies for charge compensation, which have been detected in the XPS spectra of other co-doped  $TiO_2$  systems such as  $In^{3+}$ ,  $AI^{3+}$ , and  $Sc^{3+}$  [14, 15, 20]. In the current study, unfortunately, the XPS peaks of V could not be detected due to the small amount of V (0.5%) present in the ceramics. Consequently, the valence state of V could not be confirmed. However, it can be deduced that the valence state of V might be +3 because the starting raw material used was  $V_2O_3$ . Nevertheless, the presence of a large amount of oxygen vacancies in the ceramic sintered at 1500 °C was confirmed by fitting the XPS spectrum of the O 1s peak. As shown in Fig. 3(a), four peaks were achieved. The peak at 532.23 eV can generally be ascribed to the oxygen vacancies in rutile–structure [14, 20]. The main peak at 529.78 eV usually results from an oxygen lattice in the bulk Ti–O bond [14, 15], while oxygen lattices of other cation–oxygen bonds (i.e., V–O and Ta–O bonds) were identified by the peak at 530.98 eV. Another peak at 533.18 eV was ascribed to surface hydroxyl (OH) [15].

Conduction electrons (i.e., via hopping between  $Ti^{4+} \leftrightarrow Ti^{3+}$ ) in  $TiO_2$  can easily be generated by doping with electron–donors such as  $Ta^{5+}$  ion, following the relationship:

$$2TiO_2 + Ta_2O_5 \xrightarrow{4TiO_2} 2Ti'_{Ti} + 2Ta^{\bullet}_{Ti} + 8O_O + 1/2O_2$$
, (1)

$$Ti^{4+} + e \rightarrow Ti^{3+} \,. \tag{2}$$

The XPS spectrum of Ti 2p was corrected. According to the fitted result, the main peak for Ti  $2p_{3/2}$  was observed at a binding energy of 458.58 eV, confirming the majority of Ti<sup>4+</sup>. A peak at a relatively lower binding energy of 456.88 eV was also obtained, indicating the presence of Ti<sup>3+</sup> in the 1%VTTO ceramic sintered at 1500 °C [2, 14]. According to equations (2) and (3), the concentration of Ta<sup>5+</sup> dopant and induced Ti<sup>3+</sup> ions in the 1%VTTO ceramic must be the same (i.e., 0.5%). However, the Ti<sup>3+</sup>/Ti<sup>4+</sup> ratio was found to be 0.93%, which is larger than the theoretical value. A larger Ti<sup>3+</sup>/Ti<sup>4+</sup> ratio may have been caused by the presence of oxygen vacancies. Sintering at a higher temperature usually produces more oxygen vacancies and associated free electrons following the relationship:

$$O_o^x \rightarrow \frac{1}{2}O_2 + V_o^{\bullet \bullet} + 2e'.$$
 (3)

As shown in Fig. 2, the sintering temperature has a significant influence on the microstructure of 1%VTTO ceramics. This may be due to the effect of oxygen vacancies.

The effect of sintering temperature on the dielectric properties of the ceramics is demonstrated in Fig. 4.  $\varepsilon'$  increased with increasing mean grain size over the measured frequency range, which was driven by the increased sintering temperature. This behavior is similar to that observed in CCTO-based ceramics [4, 27, 31]. The  $\varepsilon'$  values of all the samples were slightly dependent on frequency from 40 Hz to  $10^6$  Hz. At  $10^2$  Hz and 30 °C, the  $\varepsilon'$  values of the 1%VTTO ceramics sintered at 1300, 1400, and 1500 °C were of approximately 381, 2663, and 7078, respectively. This behavior can be described by a simple series layer model,  $\varepsilon = \varepsilon_{gb} t_g / t_{gb}$ , where  $\varepsilon_{gb}$ ,  $t_g$ , and  $t_{gb}$  are the dielectric permittivity of the grain boundary, grain size, and thickness of the grain boundary, respectively [35]. The dielectric permittivity increases with increasing the mean grain size.

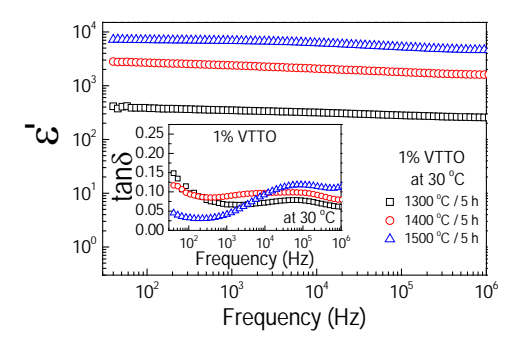


**Fig. 4** Dielectric permittivity ( $\varepsilon$ ') at 30 °C over a frequency range of 40–10<sup>6</sup> Hz for  $(V_{1/2}Ta_{1/2})_{0.01}Ti_{0.99}O_2$  ceramics sintered at different temperatures for 5 h; inset shows the loss tangent (tan $\delta$ ) as a function of frequency at 30 °C.

The frequency dependence of  $\tan\delta$  at 30 °C is shown in the inset of Fig. 4. The dielectric relaxation peaks of all the samples appeared in the frequency range of  $10^4$ – $10^6$  Hz. In contrast to the variation in  $\epsilon'$ ,  $\tan\delta$  in a low frequency range decreased with increasing mean grain size. This behavior is completely different from that observed in other giant dielectric oxides [2, 7-10, 30, 31]. At  $10^2$  Hz, the  $\tan\delta$  values of the 1%VTTO ceramics sintered at 1300, 1400, and 1500 °C were approximately 0.096, 0.093, and

0.033, respectively. Notably, good dielectric properties with high  $\epsilon' \approx 7.07 \times 10^3$  and low  $\tan \delta \approx 0.033$  were achieved in the ceramic sintered at 1500 °C for 5 h. The dielectric properties of the 1%VTTO ceramic are comparable to those observed in other co–doped  $TiO_2$  systems [16-20]. This indicates that this new (V+Ta) co–doped  $TiO_2$  ceramic system may have potential for capacitor applications.

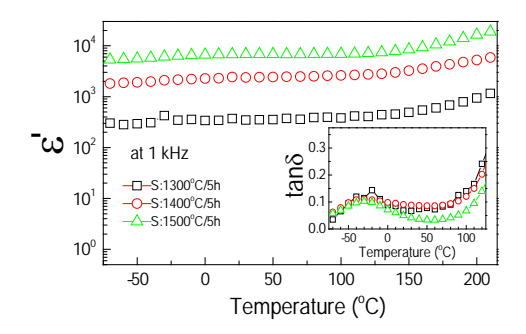


**Fig. 5** Temperature dependence of dielectric permittivity (ε') at 1 kHz for  $(V_{1/2}Ta_{1/2})_{0.01}Ti_{0.99}O_2$  ceramics sintered at different temperatures for 5 h; inset illustrates the temperature dependence of the loss tangent (tanδ) at 1 kHz.

**Table 1.** Temperature coefficient of the dielectric permittivity ( $\epsilon$ ') for  $(V_{1/2}Ta_{1/2})_{0.01}Ti_{0.99}O_2$  ceramics sintered at different temperatures.

Sintering temperature (°C)	$\Delta \varepsilon'(T)/\varepsilon'_{RT}$	$\Delta \varepsilon'(T)/\varepsilon'_{RT}$ (%)		
	90 °C	110 °C	130 °C	
1300 °C	13.25%	19.21%	26.97%	
1400 °C	8.07%	11.71%	18.30%	
1500 °C	0.66%	2.63%	8.65%	

To further explore the dielectric performance of 1%VTTO ceramics, the temperature dependence of the dielectric properties at 10<sup>3</sup> Hz was investigated. As demonstrated in Fig. 5, it is likely that  $\varepsilon'$  of all the samples was slightly dependent on temperature, even up to 150 °C. The variations of ε' values at 90, 110, and 130 °C compared to the ε' value at room temperature (i.e., the temperature coefficient of ε') were calculated and summarized in Table 1. The temperature coefficient at all temperatures decreased with increasing sintering temperature. Notably, besides very high  $\varepsilon'$  and low tan $\delta$  values of the ceramic sintered at 1500 °C, its temperature coefficient was less than ±15% at 130 °C. Therefore, a good dielectric performance was achieved in the 1%VTTO ceramic sintered at 1500 °C for 5 h. It is notable that at temperatures greater than 130 °C, the temperature coefficient values of all the samples were larger than ±15%. As shown in the inset of Fig. 5, the tanδ values at relatively high temperatures of the ceramics sintered at 1300 and 1400 °C were larger than that of the ceramic sintered at 1500 °C. In a low temperature range of -60-0 °C, the relaxation  $\tan \delta$ -peaks appeared and  $\tan \delta$  values of all the samples were nearly the sample. The observed tanδ relaxation peak at 1 kHz and -30 °C was consistent with the observed tanδ peak at 30 °C in the frequency range of 10<sup>4</sup>–10<sup>5</sup> Hz [in the inset of Fig. 4]. Compared with CCTO ceramics [2, 30, 36-39], however, the sintering temperature

of co-doped  $TiO_2$  ceramics is very high, which limits to use low temperature co-fired ceramic (LTCC) progress. A list for comparison of sintering temperature and dielectric properties between co-doped  $TiO_2$  ceramics and other giant dielectric materials is provided in Table 2.

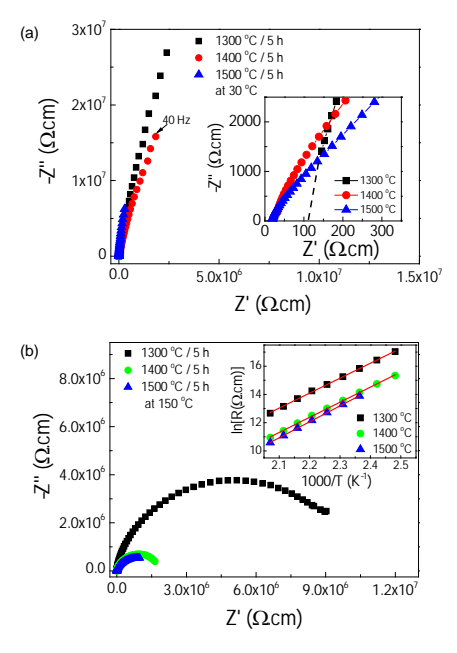


**Fig. 6** Impedance complex plane (Z\*) plots at (a) 30 °C and (b) 150 °C for  $(V_{1/2}Ta_{1/2})_{0.01}Ti_{0.99}O_2$  ceramics sintered at different temperatures. Inset of (a) shows expanded views of the impedance data at high frequencies at 30 °C. Inset of (b) illustrates an Arrhenius plot of the temperature dependence of R<sub>i</sub>.

**Table 2.** Dielectric permittivity ( $\epsilon$ ') and loss tangent ( $\tan \delta$ ) at RT and 1 kHz of co–TiO<sub>2</sub> ceramics and other giant dielectric materials sintering under different conditions.

Sintering condition	ε′	$tan\delta$
1325–1350°C / 3 h	~10 <sup>4</sup>	~0.1-0.5
1375°C / 6 h	~5.1×10 <sup>5</sup>	~0.7
1400°C / 3 h	~1.7×10 <sup>6</sup>	~1.5
1250°C / 5 h	$\sim 10^4 - 10^5$	~0.2–1.0
1020°C / 10 h (sintered in air)	~5×10 <sup>4</sup>	~0.7
$1020^{\circ}$ C / $10$ h (sintered in $O_2$ )	~0.8×10 <sup>4</sup>	~0.6
1060°C / 48 h	~10 <sup>5</sup>	~1.0
1060°C / 1 h	~104	~0.15
1060°C / 3 h	~104	~0.15
1400°C / 10 h	~6×10 <sup>4</sup>	~0.02
	1325–1350°C / 3 h  1375°C / 6 h  1400°C / 3 h  1250°C / 5 h  1020°C / 10 h (sintered in air)  1020°C / 10 h (sintered in O <sub>2</sub> )  1060°C / 48 h  1060°C / 1 h  1060°C / 3 h	$1325-1350^{\circ}C / 3 \text{ h} \qquad \sim 10^{4}$ $1375^{\circ}C / 6 \text{ h} \qquad \sim 5.1 \times 10^{5}$ $1400^{\circ}C / 3 \text{ h} \qquad \sim 1.7 \times 10^{6}$ $1250^{\circ}C / 5 \text{ h} \qquad \sim 10^{4}-10^{5}$ $1020^{\circ}C \qquad / \qquad 10 \qquad \text{h} \qquad \sim 5 \times 10^{4}$ (sintered in air) $1020^{\circ}C \qquad / \qquad 10 \qquad \text{h} \qquad \sim 0.8 \times 10^{4}$ (sintered in O <sub>2</sub> ) $1060^{\circ}C / 48 \text{ h} \qquad \sim 10^{5}$ $1060^{\circ}C / 48 \text{ h} \qquad \sim 10^{4}$ $1060^{\circ}C / 3 \text{ h} \qquad \sim 10^{4}$

[14]			
0.1-0.5%(Ga, Nb) co-doped TiO <sub>2</sub> [16]	1400–1500°C / 2–4 h	~10 <sup>3</sup> –10 <sup>5</sup>	~0.05–0.08
10%(Sc, Nb) co-doped TiO <sub>2</sub> [20]	1300-1400°C / 1-10 h	0.48-1.25×10 <sup>4</sup>	~0.05–0.09
10%(AI, Nb) co-doped TiO <sub>2</sub> [15]	1350–1500°C / 4 h	~2×10 <sup>5</sup>	~0.05
1%(V, Ta) co-doped $TiO_2$ [in this work]	1400–1500°C / 5 h	0.24-0.68×10 <sup>4</sup>	~0.04–0.08

Impedance spectroscopy was employed to separately study the electrical responses of the insulating and semiconducting parts of the VTTO ceramics to clarify the possible origin(s) of the giant dielectric properties. As demonstrated in Fig. 6(a), at 30 °C, only a linear portion of a large semicircle was observed. Additionally, a nonzero intercept was observed in Z\* plots [inset of Fig. 6(a)], which can be ascribed to the semiconducting grain response [1, 15, 20, 22, 25]. Thus, the electrical properties of the insulating parts could not be determined. The grain resistance ( $R_g$ ) of electrically heterogeneous polycrystalline ceramics is usually estimated from the nonzero intercept of Z\* plots. Actually,  $R_g$  values of all the 1%VTTO ceramics should be the same in value since the same concentration of Ta<sup>5+</sup> dopant was used to produce free electrons. However, it was found that as sintering temperature was increased from 1300 to 1400 °C,  $R_g$  was greatly reduced from ≈110 to ≈25  $\Omega$ .cm. This result may be associated with the presence of oxygen vacancies, confirmed by the XPS results [Fig. 3]. These results indicate that the sintering temperature has an influence on the electrical properties of the semiconducting grains.  $R_g$  slightly changed after the sintering temperature was further increased from 1400 to 1500 °C.

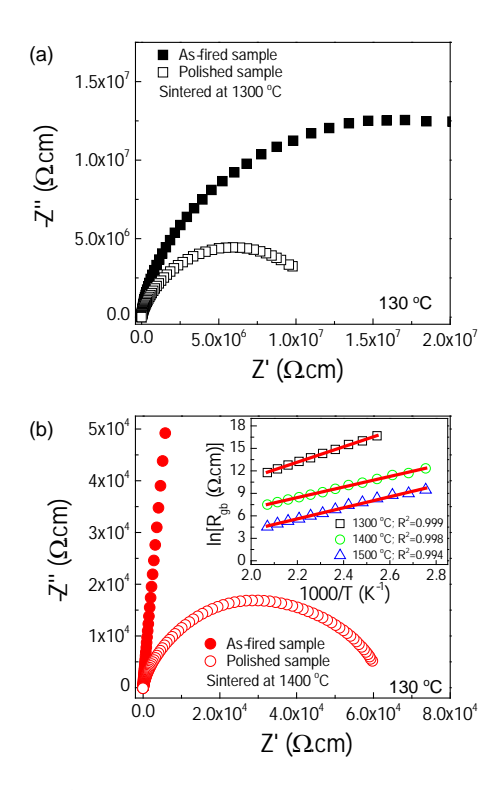


**Fig. 7** Z\* plots at 130 °C of (V<sub>1/2</sub>Ta<sub>1/2</sub>)<sub>0.01</sub>Ti<sub>0.99</sub>O<sub>2</sub> ceramics sintered at (a) 1300 and (b) 1400 °C before and after polishing resistive outer-surface layer (as-fired and

polished samples, respectively). Inset of (b) shows an Arrhenius plot of the temperature dependence of  $R_{gb}$  for the polished  $(V_{1/2}Ta_{1/2})_{0.01}Ti_{0.99}O_2$  ceramics.

The influence of sintering temperature on the electrical properties of the insulating past could not be evaluated at 30 °C and in the frequency range of 40-10<sup>6</sup> Hz because important data can only be obtained from a full semicircular arc. A full semicircle arc of codoped TiO<sub>2</sub> can be obtained if the frequency range can be reduced into the mHz region [26]. However, the lowest frequency at which the instrument can be used is only 40 Hz. To overcome this frequency limitation, measurement of impedance data at a high temperature was performed. As clearly seen in Fig. 6(b), a large semicircle arc for each sample is clearly observed in Z\* plots at 150 °C. The sintering temperature has a great effect on the electrical properties of insulating parts, which may be ascribed to the grain boundaries and/or resistive-outer surface layers. The resistance of the insulating parts (R<sub>i</sub>), which can be estimated from the diameter of a large semicircle arc in Z\* plots [1, 20, 23, 25, 40], was greatly reduced as the sintering temperature was increased from 1300 to 1400 °C. Then, R<sub>i</sub> was slightly reduced when sintered at 1500 °C. From this point of view, the giant dielectric behavior of the 1%VTTO ceramics was likely caused by Maxwell-Wagner polarization (i.e., interfacial polarization) at internal insulating interfaces. By increasing measurement temperature, R<sub>i</sub> was reduced. As shown in the inset of Fig. 6(b), the temperature dependence of R<sub>i</sub> follows the Arrhenius law,

$$R_i = R_0 \exp\left(\frac{E_i}{k_B T}\right),\tag{4}$$

where  $R_0$  is a constant value and  $E_i$  is the activation energy required for conduction in the insulating region. The  $E_i$  values can be calculated from the slope of the linear fit and was found to be 913, 920, and 942 meV for the 1%VTTO ceramics sintered at 1300, 1400, and 1500 °C, respectively. The activation energy required for conduction in the insulating region of 1%VTTO ceramics was higher than that of the conduction activation energy at the grain boundary of CCTO ceramics ( $E_{gb} \approx 600-700$  meV) [1, 3, 40].

It is important to note that the dielectric and electrical properties of the as-fired samples without polishing their surfaces were measured. Therefore, high E<sub>i</sub> values of the as-fired 1%VTTO ceramics may be caused by the combination effect of the insulating grain boundary and resistive outer-surface layer, while the total resistance of the insulating part(s) and related conduction activation energy of CCTO ceramics is primarily governed by the grain boundary only [1, 29, 31]. To separate the grain boundary and outer surface effects, both sides the outer surface layers of the as-fired 1%VTTO ceramics were removed by polishing to eliminate the outer-surface layer effect. The polished samples were coated by Au sputtering. As illustrated in Figs. 7(a) and (b), after removing the outer surface layer, Ri values are significantly reduced. This result clearly indicates that the outer surface layer of the as-fired 1%VTTO ceramics is an insulating layer. Nevertheless, the remaining resistance value for each polished sample is still very large  $(10^4-10^7 \Omega)$ cm) even at 130 °C, which can reasonably be assigned as the grain boundary response. Only R<sub>qb</sub> values at different temperatures for each polished sample can be obtained. Inset of Fig. 7(b), the temperature dependence of R<sub>ab</sub> for all polished 1%VTTO ceramics follows the Arrhenius law (Eq. 4). The  $E_{\rm gb}$  values of the 1%VTTO ceramics sintered at 1300, 1400, and 1500 °C are found to be 889, 608, and 637 meV, respectively. It is also observed that  $E_{qb}$  values of the polished 1%VTTO ceramics sintered at 1400 and 1500 °C are close to  $E_{\rm gb}$  values of CCTO ceramics, while their  $\varepsilon'$ 

values are also close to that of CCTO ceramics. It is worth noting that the interface effect of the 1%VTTO is differ from that occurred in CCTO ceramics or NiO-based ceramics. The interface effect in the 1%VTTO ceramics is caused by both of the resistive outer-surface layer and grain boundary. On the other hand, only the interface effect of the grain boundary is dominated in CCTO ceramics [1, 27, 30, 41-46].

At a high temperature, the temperature stability of the dielectric properties of the as-fired 1%VTTO ceramic sintered at 1500 °C is better than that of CCTO ceramics. A largely increased  $\varepsilon'$  value of CCTO ceramics in a high temperature range is usually reported [2-4, 27, 31, 40]. This is usually caused by the existence of interfacial polarization associated with dc conduction of free charges, which are accumulated at internal interfaces and/or defects [25]. Because of a large  $E_i$  value of the 1%VTTO ceramic, the dc conduction of free charges in the bulk 1%VTTO ceramics is hardly activated compared to that of CCTO ceramics. Therefore, changes in  $\varepsilon'$  and  $\tan\delta$  values in a high temperature range for the 1%VTTO ceramics are smaller than those of CCTO ceramics. It is important to note that the temperature stability of the dielectric properties was decreased by polishing resistive outer-surface layer. The temperature coefficient of  $\varepsilon'$  for the polished samples was much larger than that of the as-fired samples (not shown), which is unsuitable for many applications. The large  $E_i$  value is also considered as one of the most important factors for obtaining good giant dielectric properties in as-fired 1%VTTO ceramics. It is noteworthy that the R<sub>i</sub> value of the as-fired ceramic sintered at 1500 °C for 5 h was still too large (>10<sup>6</sup>  $\Omega$ .cm) even at 150 °C. This value has never been obtained in CCTO or other giant dielectric oxides.

## 9.4 Conclusions

We successfully synthesized the  $(V_{1/2}Ta_{1/2})_{0.01}Ti_{0.09}O_2$  ceramics by sintering at different temperatures for 5 h. The sintering temperature had no effect on the crystalline structure and phase formation. The mean grain size increased from 2.1–14.8 µm with increasing sintering temperature from 1300 to 1500 °C. The sintering temperature had remarkable effects on the dielectric and electrical properties of the  $(V_{1/2}Ta_{1/2})_{0.01}Ti_{0.09}O_2$  ceramics. The  $\epsilon'$  value over the measured frequency range significantly increased with increasing sintering temperature. The increased  $\epsilon'$  value was consistent with the enlarged mean grain size, while the  $\tan\delta$  values decreased. Interestingly, a low  $\tan\delta\approx0.033$  and high  $\epsilon'\approx7.07\times10^3$  with a low temperature coefficient at 130 °C were achieved in the  $(V_{1/2}Ta_{1/2})_{0.01}Ti_{0.09}O_2$  ceramics sintered at 1500 °C. The  $(V_{1/2}Ta_{1/2})_{0.01}Ti_{0.09}O_2$  ceramics were electrically heterogeneous consisting of semiconducting grains and internal insulating layers. The giant dielectric response with low  $\tan\delta$  was attributed to interfacial polarization at the highly esistive internal layers.

### References

- [1] L. Liu, H. Fan, P. Fang, X. Chen, Sol–gel derived CaCu<sub>3</sub>Ti<sub>4</sub>O<sub>12</sub> ceramics: Synthesis, characterization and electrical properties, Mater. Res. Bull. 43(7) (2008) 1800-1807.
- [2] L. Ni, X.M. Chen, Enhancement of Giant Dielectric Response in CaCu<sub>3</sub>Ti<sub>4</sub>O<sub>12</sub> Ceramics by Zn Substitution, J. Am. Ceram. Soc. 93(1) (2010) 184-189.
- [3] R. Löhnert, H. Bartsch, R. Schmidt, B. Capraro, J. Töpfer, A. Feteira, Microstructure and Electric Properties of CaCu<sub>3</sub>Ti<sub>4</sub>O<sub>12</sub> Multilayer Capacitors, J. Am. Ceram. Soc. 98(1) (2015) 141-147.
- [4] J. Li, P. Liang, J. Yi, X. Chao, Z. Yang, Phase Formation and Enhanced Dielectric Response of  $Y_{2/3}Cu_3Ti_4O_{12}$  Ceramics Derived from the Sol–Gel Process, J. Am. Ceram. Soc. 98(3) (2015) 795-803.
- [5] R. Löhnert, B. Capraro, S. Barth, H. Bartsch, J. Müller, J. Töpfer, Integration of CaCu<sub>3</sub>Ti<sub>4</sub>O<sub>12</sub> capacitors into LTCC multilayer modules, J. Eur. Ceram. Soc. 35(11) (2015) 3043-3049.
- [6] X.J. Luo, Y.S. Liu, C.P. Yang, S.S. Chen, S.L. Tang, K. Bärner, Oxygen vacancy related defect dipoles in CaCu<sub>3</sub>Ti<sub>4</sub>O<sub>12</sub>: Detected by electron paramagnetic resonance spectroscopy, J. Eur. Ceram. Soc. 35(7) (2015) 2073-2081.
- [7] Y. Li, L. Fang, L. Liu, Y. Huang, C. Hu, Giant dielectric response and charge compensation of Li- and Co-doped NiO ceramics, Mater. Sci. Eng. B 177(9) (2012) 673-677.
- [8] A. Chouket, O. Bidault, V. Optasanu, A. Cheikhrouhou, W. Cheikhrouhou-Koubaa, M. Khitouni, Enhancement of the dielectric response through Al-substitution in La<sub>1.6</sub>Sr<sub>0.4</sub>NiO<sub>4</sub> nickelates, RSC Adv. 6(29) (2016) 24543-24548.
- [9] K. Meeporn, N. Chanlek, P. Thongbai, Effects of DC bias on non-ohmic sample-electrode contact and grain boundary responses in giant-permittivity La<sub>1.7</sub>Sr<sub>0.3</sub>Ni<sub>1-x</sub>Mg<sub>x</sub>O<sub>4</sub> ceramics, RSC Advances 6(94) (2016) 91377-91385.
- [10] T.I. Chupakhina, N.I. Kadyrova, N.V. Melnikova, O.I. Gyrdasova, E.A. Yakovleva, Y.G. Zainulin, New methods for the preparation and dielectric properties of  $La_{2-x}Sr_xNiO_4$  (x = 1/8) ceramic, Mater. Res. Bull. 77 (2016) 190-198.
- [11] A. Chouket, W. Cheikhrouhou-Koubaa, A. Cheikhrouhou, V. Optasanu, O. Bidault, M. Khitouni, Structural, microstructural and dielectric studies in multiferroic LaSrNiO<sub>4-δ</sub> prepared by mechanical milling method, J. Alloys Compd. 662 (2016) 467-474.
- [12] S. Ke, H. Fan, H. Huang, Dielectric relaxation in A<sub>2</sub>FeNbO<sub>6</sub> (A perovskite ceramics, Journal of Electroceramics 22(1-3) (2007) 252-256.
- [13] X. Sun, J. Deng, S. Liu, T. Yan, B. Peng, W. Jia, Z. Mei, H. Su, L. Fang, L. Liu, Grain boundary defect compensation in Ti-doped BaFe<sub>0.5</sub>Nb<sub>0.5</sub>O<sub>3</sub> ceramics, Applied Physics A 122(9) (2016) 864.
- [14] W. Hu, Y. Liu, R.L. Withers, T.J. Frankcombe, L. Norén, A. Snashall, M. Kitchin, P. Smith, B. Gong, H. Chen, J. Schiemer, F. Brink, J. Wong-Leung, Electron-pinned defect-dipoles for high-performance colossal permittivity materials, Nat. Mater. 12(9) (2013) 821-826.
- [15] G. Liu, H. Fan, J. Xu, Z. Liu, Y. Zhao, Colossal permittivity and impedance analysis of niobium and aluminum co-doped TiO<sub>2</sub> ceramics, RSC Advances 6(54) (2016) 48708-48714.
- [16] W. Dong, W. Hu, A. Berlie, K. Lau, H. Chen, R.L. Withers, Y. Liu, Colossal Dielectric Behavior of Ga+Nb Co-Doped Rutile TiO<sub>2</sub>, ACS Applied Materials & Interfaces 7(45) (2015) 25321-25325.

= Ba, Sr,

- [17] W. Hu, K. Lau, Y. Liu, R.L. Withers, H. Chen, L. Fu, B. Gong, W. Hutchison, Colossal Dielectric Permittivity in (Nb+Al) Codoped Rutile TiO<sub>2</sub> Ceramics: Compositional Gradient and Local Structure, Chem. Mater. 27(14) (2015) 4934-4942.
- [18] Z. Li, J. Wu, D. Xiao, J. Zhu, W. Wu, Colossal permittivity in titanium dioxide ceramics modified by tantalum and trivalent elements, Acta Mater. 103 (2016) 243-251.
- [19] W. Tuichai, S. Danwittayakul, S. Maensiri, P. Thongbai, Investigation on temperature stability performance of giant permittivity (In + Nb) in co-doped TiO<sub>2</sub> ceramic: a crucial aspect for practical electronic applications, RSC Advances 6(7) (2016) 5582-5589.
- [20] W. Tuichai, S. Danwittayakul, N. Chanlek, P. Thongbai, S. Maensiri, High-performance giant-dielectric properties of rutile TiO<sub>2</sub> co-doped with acceptor-Sc<sup>3+</sup> and donor-Nb<sup>5+</sup> ions, J. Alloys Compd. 703 (2017) 139-147.
- [21] T. Nachaithong, P. Thongbai, S. Maensiri, Colossal permittivity in  $(In_{1/2}Nb_{1/2})_xTi_{1-x}O_2$  ceramics prepared by a glycine nitrate process, J. Eur. Ceram. Soc. 37(2) (2017) 655-660.
- [22] W. Tuichai, S. Danwittayakul, N. Chanlek, P. Srepusharawoot, P. Thongbai, S. Maensiri, Origin(s) of the apparent colossal permittivity in  $(In_{1/2}Nb_{1/2})_xTi_{1-x}O_2$ : clarification on the strongly induced Maxwell-Wagner polarization relaxation by DC bias, RSC Advances 7(1) (2017) 95-105.
- [23] T. Nachaithong, P. Kidkhunthod, P. Thongbai, S. Maensiri, Surface barrier layer effect in (In + Nb) co-doped TiO<sub>2</sub> ceramics: An alternative route to design low dielectric loss, J. Am. Ceram. Soc. 10.1111/jace.14688 (2017).
- [24] C. Wang, N. Zhang, Q. Li, Y. Yu, J. Zhang, Y. Li, H. Wang, Dielectric Relaxations in Rutile TiO<sub>2</sub>, J. Am. Ceram. Soc. 98(1) (2015) 148-153.
- [25] Y. Song, X. Wang, Y. Sui, Z. Liu, Y. Zhang, H. Zhan, B. Song, Z. Liu, Z. Lv, L. Tao, J. Tang, Origin of colossal dielectric permittivity of rutile Ti<sub>0.9</sub>In<sub>0.05</sub>Nb<sub>0.05</sub>O<sub>2</sub>: single crystal and polycrystalline, Scientific Reports 6 (2016) 21478.
- [26] Y.Q. Wu, X. Zhao, J.L. Zhang, W.B. Su, J. Liu, Huge low-frequency dielectric response of (Nb,In)-doped TiO<sub>2</sub> ceramics, Appl. Phys. Lett. 107(24) (2015) 242904.
- [27] L. Sun, Z. Wang, Y. Shi, E. Cao, Y. Zhang, H. Peng, L. Ju, Sol–gel synthesized pure  $CaCu_3Ti_4O_{12}$  with very low dielectric loss and high dielectric constant, Ceram. Int. 41(10, Part A) (2015) 13486-13492.
- [28] W. Wan, C. Liu, H. Sun, Z. Luo, W.-X. Yuan, H. Wu, T. Qiu, Low-toxic gelcasting of giant dielectric-constant CaCu<sub>3</sub>Ti<sub>4</sub>O<sub>12</sub> ceramics from the molten salt powder, J. Eur. Ceram. Soc. 35(13) (2015) 3529-3534.
- [29] A. Nautiyal, C. Autret, C. Honstettre, S. De Almeida-Didry, M. El Amrani, S. Roger, B. Negulescu, A. Ruyter, Local analysis of the grain and grain boundary contributions to the bulk dielectric properties of  $Ca(Cu_{3-y}Mg_y)Ti_4O_{12}$  ceramics: Importance of the potential barrier at the grain boundary, J. Eur. Ceram. Soc. 36(6) (2016) 1391-1398.
- [30] M.F. Ab Rahman, S.D. Hutagalung, Z.A. Ahmad, M.F. Ain, J.J. Mohamed, The effect of different dopant site (Cu and Ca) by magnesium onCaCu<sub>3</sub>Ti<sub>4</sub>O<sub>12</sub> dielectric properties, J. Mater. Sci.: Mater. Electron. 26(6) (2015) 3947-3956.
- [31] L. Sun, R. Zhang, Z. Wang, E. Cao, Y. Zhang, L. Ju, Microstructure, dielectric properties and impedance spectroscopy of Ni doped CaCu<sub>3</sub>Ti<sub>4</sub>O<sub>12</sub> ceramics, RSC Advances 6(61) (2016) 55984-55989.
- [32] R.D. Shannon, Revised Effective Ionic Radii and Systematic Studies of Interatomie Distances in Halides and Chaleogenides, Acta Cryst. A32 (1976) 751-767.
- [33] M.Q. Wen, T. Xiong, Z.G. Zang, W. Wei, X.S. Tang, F. Dong, Synthesis of  $MoS_2/g-C_3N_4$  nanocomposites with enhanced visible-light photocatalytic activity for the removal of nitric oxide (NO), Optics Express 24(10) (2016) 10205-10212.

- [34] M.N. Rahaman, Ceramic processing and sintering, 2nd ed., M. Dekker, New York, 2003.
- [35] A.J. Moulson, J.M. Herbert, Electroceramics: materials, properties, applications, 2nd ed., Wiley, West Sussex; New York, 2003.
- [36] L. Liu, H. Fan, P. Fang, L. Jin, Electrical heterogeneity in CaCu<sub>3</sub>Ti<sub>4</sub>O<sub>12</sub> ceramics fabricated by sol–gel method, Solid State Commun. 142(10) (2007) 573-576.
- [37] L. Liu, D. Shi, S. Zheng, Y. Huang, S. Wu, Y. Li, L. Fang, C. Hu, Polaron relaxation and non-ohmic behavior in  $CaCu_3Ti_4O_{12}$  ceramics with different cooling methods, Mater. Chem. Phys. 139(2–3) (2013) 844-850.
- [38] L. Liu, H. Fan, L. Wang, X. Chen, P. Fang, Dc-bias-field-induced dielectric relaxation and ac conduction in CaCu<sub>3</sub>Ti<sub>4</sub>O<sub>12</sub> ceramics, Philos. Mag. 88(4) (2008) 537-545.
- [39] L. Liu, L. Fang, Y. Huang, Y. Li, D. Shi, S. Zheng, S. Wu, C. Hu, Dielectric and nonlinear current–voltage characteristics of rare–earth doped CaCu<sub>3</sub>Ti<sub>4</sub>O<sub>12</sub> ceramics, J. Appl. Phys. 110(9) (2011) 094101.
- [40] L. Singh, B.C. Sin, I.W. Kim, K.D. Mandal, H. Chung, Y. Lee, J. Varela, A Novel One-Step Flame Synthesis Method for Tungsten-Doped CCTO, J. Am. Ceram. Soc. 99(1) (2016) 27-34.
- [41] L. Liu, Y. Huang, Y. Li, D. Shi, S. Zheng, S. Wu, L. Fang, C. Hu, Dielectric and non-Ohmic properties of CaCu<sub>3</sub>Ti<sub>4</sub>O<sub>12</sub> ceramics modified with NiO, SnO<sub>2</sub>, SiO<sub>2</sub>, and Al<sub>2</sub>O<sub>3</sub> additives, J. Mater. Sci. 47(5) (2012) 2294-2299.
- [42] Y. Huang, D. Shi, Y. Li, G. Li, Q. Wang, L. Liu, L. Fang, Effect of holding time on the dielectric properties and non-ohmic behavior of CaCu<sub>3</sub>Ti<sub>4</sub>O<sub>12</sub> capacitor-varistors, J. Mater. Sci.: Mater. Electron. 24(6) (2012) 1994-1999.
- [43] J. Deng, X. Sun, S. Liu, L. Liu, T. Yan, L. Fang, B. Elouadi, Influence of interface point defect on the dielectric properties of Y doped CaCu<sub>3</sub>Ti<sub>4</sub>O<sub>12</sub> ceramics, Journal of Advanced Dielectrics 06(01) (2016) 1650009.
- [44] L. Liu, H. Fan, X. Chen, P. Fang, Electrical properties and microstructural characteristics of nonstoichiometric CaCu<sub>3x</sub>Ti<sub>4</sub>O<sub>12</sub> ceramics, J. Alloys Compd. 469(1-2) (2009) 529-534.
- [45] Y. Huang, L. Liu, D. Shi, S. Wu, S. Zheng, L. Fang, C. Hu, B. Elouadi, Giant dielectric permittivity and non-linear electrical behavior in CaCu<sub>3</sub>Ti<sub>4</sub>O<sub>12</sub> varistors from the moltensalt synthesized powder, Ceram. Int. 39(6) (2013) 6063-6068.
- [46] J. Deng, L. Liu, X. Sun, S. Liu, T. Yan, L. Fang, B. Elouadi, Dielectric relaxation behavior and mechanism of Y<sub>2/3</sub>Cu<sub>3</sub>Ti<sub>4</sub>O<sub>12</sub> ceramic, Mater. Res. Bull. 88 (2017) 320-329.

## **CHAPTER 10**

# Effect of Zn<sup>2+</sup> and Nb<sup>5+</sup> Co-Doping Ions on Giant Dielectric Properties of Rutile-TiO<sub>2</sub> Ceramics

#### 10.1 Introduction

Dielectric oxide materials that can exhibit ultra–high dielectric permittivities ( $\epsilon$ ') of more than  $10^3$  in the radio frequency range have been widely studied in recent years. These oxides are generally called *giant* or *colossal* dielectric materials [1-20]. Usually, dielectric oxides with ABO<sub>3</sub> type perovskite structure (e.g., BaTiO<sub>3</sub>) can exhibit very high  $\epsilon$ ' values of about  $10^3$  [21-23]. Recently, the giant dielectric ceramics that have been widely investigated are CaCu<sub>3</sub>Ti<sub>4</sub>O<sub>12</sub> (CCTO) and its isostructural CCTO–type perovskites [2, 4, 5, 10, 13, 14, 16, 20], LaFeO<sub>3</sub> [19], co–doped NiO–based oxides [3, 9], Y<sub>2</sub>MMnO<sub>6</sub> (M = Co and Ni) [17], and  $\mathbf{AFe}_{1/2}\mathbf{B}_{1/2}\mathbf{O}_3$  ( $\mathbf{A}$ =Ba, Sr, Ca;  $\mathbf{B}$ =Nb, Ta, Sb) [1, 6]. Giant dielectric materials are considered potentially useful in applications such as multilayer ceramic capacitors and high energy–dense storage devices. Unfortunately, the dielectric loss tangent (tan $\delta$ ) values of these giant dielectric materials are still too large, especially the tan $\delta$  value in a low frequency range.

Most recently, W. Hu and co-workers reported the exciting giant dielectric properties in acceptor/donor (In<sup>3+</sup>/Nb<sup>5+</sup>) co-doped rutile-TiO<sub>2</sub> (INTO) ceramics [24]. INTO ceramics have low tanδ values of ≈0.02 and very high ε'≈6×10<sup>4</sup>. Slight temperature dependence over a wide temperature range of 80-450 K was simultaneously reported in this rutile-structure material. A new and elegant model, electron-pinned defect-dipole (EPDD), was proposed as the origin of the giant dielectric properties of INTO ceramics. Free electrons in INTO were produced by doping with Nb5+ and confined in a specially designed local structure of the In<sup>3+</sup> ionic environment [24]. Although many reports argued that the giant dielectric response in INTO ceramics arose from the classical extrinsic effect, i.e., the internal barrier layer capacitor (IBLC) effect, this report has greatly stimulated research in the field of giant dielectric materials [25-35]. Besides the giant dielectric properties, a nonlinear current current-voltage characteristic was also reported in (In3+/Nb5+) and (Al3+/Nb5+) co-doped TiO2 ceramics [28, 36]. The origin of the giant dielectric response in INTO ceramics, as well as in other co-doped TiO<sub>2</sub>-based systems, is still open to scientific debate. Therefore, the origin of the high performance dielectric properties of TiO<sub>2</sub>-based ceramics must be clarified.

Besides +3 and +5 dopants co–doped  $TiO_2$ , the giant dielectric properties of  $TiO_2$  substituted with  $Zn^{2+}$  and  $Nb^{5+}$  ions were also reported [26]. The dielectric loss of this co–doped  $TiO_2$  system was very low and is comparable to those observed in other co–doped  $TiO_2$  systems. These experimental results are very interesting and are important for further development of giant dielectric materials for capacitor applications. The giant dielectric behavior of  $(Zn^{2+}/Nb^{5+})$  co–doped  $TiO_2$  was reasonably described as originating from the EPDD. Unfortunately, theoretical calculation (*i.e.*, a first–principles study) of the possible formation of complex defect dipoles, which can support the presence of EPDDs, was not given. Additionally, the electrical properties of these  $(Zn^{2+}/Nb^{5+})$  co–doped  $TiO_2$  ceramics have never been reported. Furthermore, only results for  $(Zn_{1/3}Nb_{2/3})_{0.05}Ti_{0.95}O_2$  were reported. Also, the effects of different co–dopant  $(Zn^{2+}/Nb^{5+})$  concentrations on the microstructural evolution and giant dielectric properties have never been reported.

In this work, the effects of co–dopant concentration on the microstructure, electrical properties and giant dielectric responses of  $(Zn^{2+}/Nb^{5+})$  co–doped  $TiO_2$  (ZNTO) ceramics were systematically investigated. Dense microstructure, very high  $\epsilon'$  and low  $tan\delta$  were obtained in ZNTO ceramics. Impedance spectroscopy was used to characterize the electrical response of the semiconducting and insulating phases of these ZNTO ceramics. The origin of the giant dielectric response is discussed in detail.

## 10.2 Experimental details

ZNTO ceramics with a composition of  $(Zn_{1/3}Nb_{2/3})_xTi_{1-x}O_2$  were prepared by a solid state reaction method. ZnO (Sigma–Aldrich, 99.9% purity), Nb<sub>2</sub>O<sub>5</sub> (Sigma–Aldrich, 99.99% purity) and TiO<sub>2</sub> (Sigma–Aldrich, >99.9% purity) were used as the starting raw materials. First, stoichiometric amounts of these raw materials were weighted to produce  $(Zn_{1/3}Nb_{2/3})_xTi_{1-x}O_2$  ceramics with x=0.01, 0.025, 0.05 and 0.1 (nominally referred to as the 1%ZNTO, 2.5%ZNTO, 5%ZNTO and 10%ZNTO samples, respectively). Second, the mixture was ball milled in ethanol for 24 h using ZrO<sub>2</sub> balls. Next, the mixed slurry was heated to evaporate ethanol. Then, the dried powder was ground and pressed into pellets by uniaxial compression at 180 MPa. Finally, these pellets were sintered at 1400°C for 2 h using heating and cooling rates of 2°C/min.

A pure phase of TiO<sub>2</sub> was found in all sintered ZNTO ceramics using an X-ray diffraction technique (PANalytical, EMPYREAN). The microstructure of the sintered ceramics was characterized using scanning electron microscopy (SEM) (SEC, SNE-4500M). The microstructure and elemental distribution in the ZNTO ceramics were field-emission examined using scanning electron microscopy HITACHI SU8030, Japan). The chemical states of Ti were determined using X-ray photoelectron spectroscopy (XPS), PHI5000 VersaProbe II, ULVAC-PHI, Japan) at the SUT-NANOTEC-SLRI Joint Research Facility, Synchrotron Light Research Institute (SLRI), Thailand. The XPS spectra were fitted with PHI MultiPak XPS software using a combination of Gaussian-Lorentzian lines. To prepare the electrodes, surfaces of the unpolished sintered ceramics were coated with Au for 8 min at 25 mA using a Polaron SC500 sputter coating unit. Their dielectric properties were measured using a KEYSIGHT E4990A Impedance Analyzer over the frequency range of 40-10<sup>6</sup> Hz with an oscillation voltage of 0.5 V. The dielectric properties as a function of temperature were measured in the temperature range of -60 to 210 °C.

## 10.3 Results and discussion

The XRD patterns of the ZNTO ceramics with a variety of co–dopant concentrations are given in Fig. 1, confirming that the main phase is rutile– $TiO_2$  (JCPDS 21–1276). These XRD patterns are similar to those reported in literature [28, 33, 37]. No impurity phase is detected in these XRD patterns. Lattice parameters (a and c values) are calculated from the XRD patterns and summarized in Table 1. Both the a and c values of all co–doped ZNTO ceramics are larger than those of pure rutile– $TiO_2$ , with a = 4.593 and c = 2.959 Å (JCPDS 21–1276). The a and c values of the co–doped ZNTO ceramics increase with increasing co–dopant concentration. The enlarged lattice parameters likely resulted from the larger ionic radii of  $Zn^{2+}$  ( $r_6$  = 0.74 Å) and  $Nb^{5+}$  ( $r_6$  = 0.64 Å) than that of

the host  $Ti^{4+}$  ion ( $r_6 = 0.605 \text{ Å}$ ) [38]. This indicates that both of the  $Zn^{2+}$  and  $Nb^{5+}$  dopants could enter the Ti sites of the rutile– $TiO_2$  lattice structure.

Figure 2 reveals the surface morphologies of 5%ZNTO and 10%ZNTO ceramics sintered at 1400°C for 2 h. The grains and grain boundary structures are clearly observed with grain sizes of  $\approx 5-10~\mu m$ . A highly dense microstructure with no pores was obtained in all of the samples. The concentration of Zn and Nb co–dopant had a slight effect on the microstructural evolution of ZNTO ceramics. Moreover, it was found that the microstructure of ZNTO ceramics was not significantly changed by increasing the sintering temperature from 1400 to 1450°C (data not shown). It is worth noting that no abnormal grain growth was observed, indicating good dispersion of dopants in the microstructure [39]. To further characterize the distribution of elements in these ZNTO ceramics, elemental mapping of Ti, O, Zn, and Nb was done. As revealed in Fig. 3, both the Zn and Nb dopants as well as the major element, Ti, are homogeneously dispersed in the grains and grain boundaries. Segregation of the dopants at the grain boundaries or in other regions is not detected. The percentages of Ti, Nb, and Zn measured in the selected area in Fig. 3(a) are of  $\approx 48.6$ ,  $\approx 7.3$ , and  $\approx 2.6$  wt%, respectively.

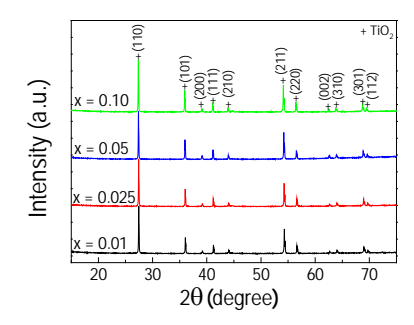


Fig. 1 XRD patterns of  $(Zn_{1/3}Nb_{2/3})_xTi_{1-x}O_2$  ceramics sintered at 1400°C for 2 h.

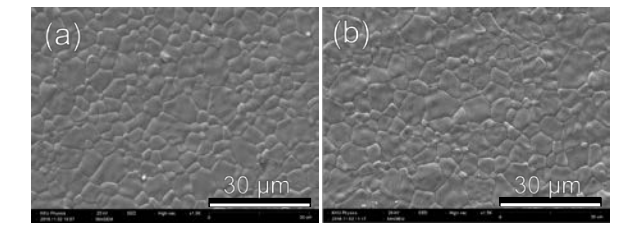
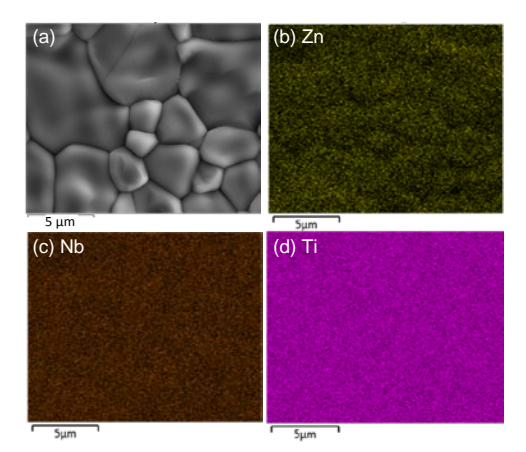


Fig. 2 SEM images of surface morphologies for  $(Zn_{1/3}Nb_{2/3})_xTi_{1-x}O_2$  ceramics; (a) x = 0.5 and (b) x = 0.1.

**Table 1** Lattice parameters (a and c) and conduction activation energy of insulating phases  $(E_i)$  of  $(Zn_{1/3}Nb_{2/3})_xTi_{1-x}O_2$  ceramics.

х	a (Å)	c (Å)	E <sub>i</sub> (eV)
0.01 (1%ZNTO)	4.5977	2.9641	0.714
0.025 (2.5%ZNTO)	4.5998	2.9659	0.682
0.05 (5%ZNTO)	4.6049	2.9690	0.661
0.10 (10%ZNTO)	4.6125	2.9748	0.648



**Fig. 3** Elemental mapping of the  $(Zn_{1/3}Nb_{2/3})_xTi_{1-x}O_2$  ceramic with x = 0.1 sintered at 1400°C for 2 h; (a) selected area for mapping, (b) Zn, (c) Nb and (d) Ti.

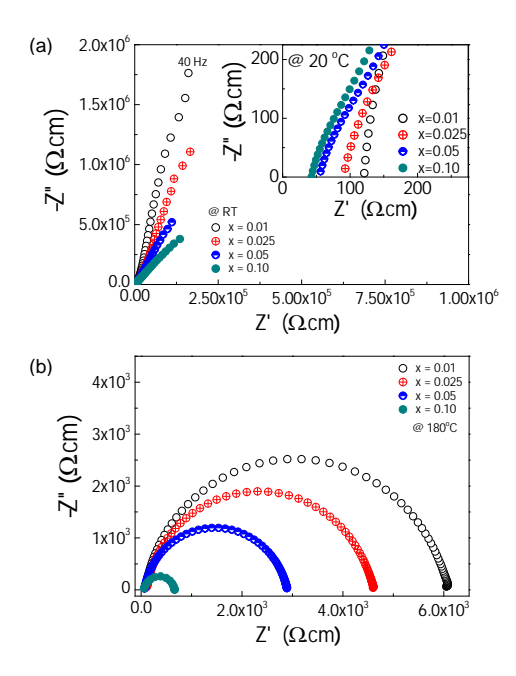


**Fig. 4** (a) Impedance complex plane plot ( $Z^*$  plot) at RT for  $(Zn_{1/3}Nb_{2/3})_xTi_{1-x}O_2$  ceramics with different co–dopant concentrations (x=0.01–0.10); inset shows an expanded view near the origin at 20°C. (b)  $Z^*$  plots of ZNTO ceramics at 180°C.

To study the effects of co-dopants on the electrical properties of the semiconducting and relative insulating parts of the microstructure of ZNTO ceramics, an impedance spectroscopy was performed. At room temperature (RT), only a linear portion of the semicircular arcs can be observed in  $Z^*$  plots for all of the ZNTO ceramics, Fig. 4(a). It is likely that the total resistance of the insulating phase(s) (R<sub>i</sub>) of the ZNTO ceramics, which is usually estimated from the diameter of a large semicircular arc [31, 32], decreases with increasing co-dopant concentration. The variation in R<sub>i</sub> is more evident at a higher temperature, as shown in Fig. 4(b). In the inset of Fig. 4(a), a nonzero intercept on the Z' axis (at  $20^{\circ}$ C) is observed in the  $Z^*$  plot, indicating the electrical response of the semiconducting phase (i.e., semiconducting grains). The grain resistance (R<sub>g</sub>) of the ZNTO ceramics, which can be estimated from the nonzero intercept, decreases with

increasing co-dopant concentration. The concentration of free electrons in  $Nb^{5+}$ -doped  $TiO_2$  is generally proportional to the  $Nb^{5+}$  dopant concentration, following the equations [24]:

$$2TiO_2 + Nb_2O_5 \xrightarrow{4TiO_2} 2Ti'_{Ti} + 2Nb^{\bullet}_{Ti} + 8O_O + 1/2O_2,$$
 (1)

$$Ti^{4+} + e \to Ti^{3+}$$
 (2)

Thus,  $R_g$  of the ZNTO ceramics should be reduced by increasing the concentration of Nb<sup>5+</sup>. The decrease in  $R_i$  (e.g., grain boundary and/or outer surface layer resistance) was also associated with the Nb<sup>5+</sup> dopant concentration. Higher numbers of charge carriers in ZNTO ceramics can cause a decrease in its total resistance. It is worth noting that the total resistance of ZNTO ceramics was still much larger than that of the Nb<sup>5+</sup> single–doped TiO<sub>2</sub> ceramics [30]. Therefore, the acceptor–Zn<sup>2+</sup> dopant had an influence on formation on the insulting properties of ZNTO ceramics.

 $R_i$  values at different temperatures can easily be calculated from the -Z''-frequency plots,  $R=2Z''_{max}$ .  $Z''_{max}$  decreased with increasing temperature, indicating a decrease in the total resistance, as shown in Fig. 5. At 80°C, the R value was about  $6.3\times10^5~\Omega$ .cm, which is value is a typical value of the insulating phase. Thus, this set of Z'' peaks can be attributed to the electrical response of the insulating phases of ZNTO ceramics. As illustrated in the inset of Fig. 5, the temperature dependence of  $R_i$  follows the Arrhenius law:

$$R_i = R_0 \exp\left(\frac{E_i}{k_B T}\right),\tag{3}$$

where  $\sigma_0$  is a constant value,  $E_i$  is the activation energy required for conduction in the insulating phases. The  $E_i$  values were calculated from the slopes of the fitted lines and summarized in Table 1. The  $E_i$  values of the 1%ZNTO, 2.5%ZNTO, 5%ZNTO and 10%ZNTO samples are of about 0.714, 0.682, 0.661, and 0.648 eV, respectively. These  $E_i$  values are comparable to the conduction activation energies at the grain boundary for CaCu<sub>3</sub>Ti<sub>4</sub>O<sub>12</sub> ceramics ( $E_{gb} \approx 0.6$ –0.7 eV) [4, 10], Al<sub>0.03</sub>Nb<sub>0.03</sub>Ti<sub>0.94</sub>O<sub>2</sub> ceramics ( $E_{gb} \approx 0.6$ 9 eV) [27], and 2 wt% B<sub>2</sub>O<sub>3</sub> doped (1 mol%) INTO ceramics (0.71 eV) [33]. However, the  $E_i$  values of the ZNTO ceramics were lower than those of other systems, such as (Ga<sup>3+</sup>/Ta<sup>5+</sup>) and (Sc<sup>3+</sup>/Nb<sup>5+</sup>) co–doped TiO<sub>2</sub> ceramics [31, 32].

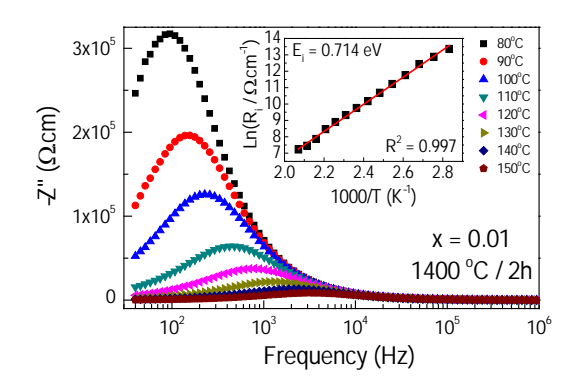


**Fig. 5** Frequency dependence of -Z" at various temperatures of the  $(Zn_{1/3}Nb_{2/3})_xTi_{1-x}O_2$  ceramic with x = 0.01; inset shows the Arrhenius plots of the resistance of insulating components (R<sub>i</sub>).

The giant dielectric properties at RT of as-fired ZNTO ceramics are represented in Fig. 6(a) and its inset. As can be clearly seen, all of the samples exhibit very high  $\varepsilon'$  values of  $\approx 10^4 - 10^5$ , which can be comparable to those reported in literature for other giant dielectric oxides [1, 2, 6, 9, 11, 16, 40]. At 40 Hz, ε' increases with increasing co-dopant concentration. According to the Z\* plot, the giant dielectric properties of ZNTO ceramics are correlated with the interfacial polarization due to the existence of semiconducting and insulating phases. Under an applied electric field, free charges inside the grains or inner core of the sample accumulated at the insulating interface layers (i.e., the grain boundary and resistive-outer surface layer), producing a strong interfacial polarization. This can be responsible for the observed giant dielectric response in ZNTO ceramics. With increasing Nb<sup>5+</sup> dopant concentration, more charge carriers are produced, which is confirmed by a decrease in R<sub>a</sub>. More trapped charges produced a greater polarization, leading to a larger low-frequency ε' value. This result is similar to that observed in (Li, Ti) co-doped NiO ceramics [9]. As shown in the inset of Fig. 6. a low-frequency  $tan\delta$  increases with increasing co-dopant concentration, corresponding to a decrease in R<sub>i</sub> [Fig. 4]. This is a general characteristic of a giant dielectric material. Its giant dielectric response originates from interfacial (Maxwell-Wagner) polarization. Notably, the 1%ZNTO ceramic exhibits good dielectric properties, with  $\varepsilon' \approx 5 \times 10^4$  and a very low  $\tan \delta \approx 0.03$  at 40 Hz and RT. In such a low-frequency range, a low tanδ value has never achieved in other giant dielectric oxides such as CaCu<sub>3</sub>Ti<sub>4</sub>O<sub>12</sub> and related oxides, A<sub>2</sub>FeNbO<sub>6</sub> (A co-doped NiO [1-4, 6, 9, 11-15]. Figure 6(b) demonstrates the temperature dependence of  $\varepsilon'$  at various frequencies (40–10<sup>6</sup> Hz) of the  $(Zn_{1/3}Nb_{2/3})_xTi_{1-x}O_2$  ceramic with x = 0.10. Strong dispersion of  $\varepsilon'$  is observed in a high temperature range, especially at high frequencies. The step-like decrease in  $\varepsilon'$  is observed in the temperature range from -20 to 20 °C, which is likely resulted from the interfacial polarization effect. It is important to note that the temperature dependence behaviors of  $\varepsilon'$  for all the samples with x = 0.01-0.10are similar.

Figure 7 shows the XPS spectra of the 10%ZNTO ceramic. The XPS spectrum of Ti 2p is shown in Fig. 7(a). Using Gaussian-Lorentzian profile fitting, the main peak of Ti  $2p_{3/2}$  was obtained at a binding energy of 458.13 eV, indicating the presence of Ti<sup>4+</sup> [41]. The small peak at relatively lower binding energy of 457.39 eV confirmed the existence of Ti<sup>3+</sup> in the 10%ZNTO ceramic [24, 41]. Thus, it is reasonable to infer that the semiconducting grains of ZNTO ceramics are primarily originated by electron hopping between Ti<sup>3+</sup> ↔Ti<sup>4+</sup> [42]. Ti<sup>3+</sup>/Ti<sup>4+</sup> ratios were found to be ≈6%, which is slightly larger than the theoretical value determining from the starting composition. This result indicates that Ti<sup>3+</sup> primarily originated by inclusion of Nb<sup>5+</sup> doping ions following equations (1) and (2). Furthermore, the presence of Ti<sup>3+</sup> may also have been promoted by oxygen vacancies during sintering at high temperature. The XPS spectrum of O 1s profiles was also corrected, as shown in Fig. 7(b). Four peaks were observed in the fitted data. The primary peak at a binding energy of 529.49 eV is ascribed to the oxygen lattice of TiO<sub>2</sub> (i.e., Ti-O bond) [24, 36]. The relatively lower peaks at 530.2, 531.5 and 532.6 eV can be respectively ascribed to oxygen lattices of other metal ions (i.e., Zn-O and Nb-O), oxygen vacancies and surface hydroxyls (OH) [24, 36]. The concentration of oxygen vacancies was higher than the theoretical value determined from the starting compositions of the ceramics. Figure 7(c) illustrates the XPS spectrum of Nb 3d. The binding energies of Nb 3d at 209.1 and 206.49 eV indicate the  $3d_{3/2}$  and  $3d_{5/2}$  electrons, respectively. The splitting of the spin-orbit was ≈2.61 eV, confirming the presence of only Nb<sup>5+</sup> in the ZNTO ceramics [24].

= Ba, Sr, and Ca),

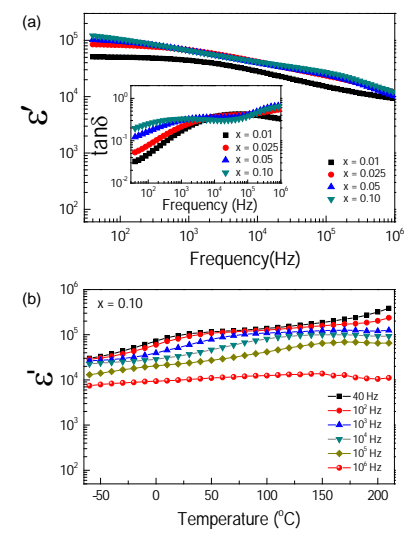


**Fig. 6** (a) Frequency dependence of ε' at RT for  $(Zn_{1/3}Nb_{2/3})_xTi_{1-x}O_2$  ceramics with various co–dopant concentrations (x=0.01–0.1); inset shows frequency dependence of tanδ at RT. (b) Temperature dependence of ε' at various frequencies (40–10<sup>6</sup> Hz) of the  $(Zn_{1/3}Nb_{2/3})_xTi_{1-x}O_2$  ceramic with x = 0.10.

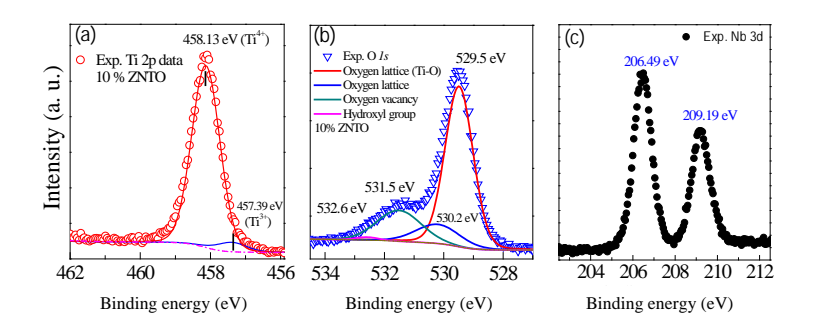


Fig. 7 XRS spectra of the  $(Zn_{1/3}Nb_{2/3})_xTi_{1-x}O_2$  ceramic with x = 0.1 sintered at 1400°C for 2 h; (a) Ti 2p, (b) O 1s and (c) Nb 3d.

## 10.4 Conclusions

 $(Zn_{1/3}Nb_{2/3})_xTi_{1-x}O_2$  ceramics with x=0.01-0.1 were successfully synthesized via a conventional solid state reaction method. The microstructure of sintered ceramics was obtained with highly dense microstructure and good homogeneous dispersion of  $Zn^{2+}$  and  $Nb^{5+}$  dopants. The  $(Zn_{1/3}Nb_{2/3})_xTi_{1-x}O_2$  ceramics with x=0.01 exhibited remarkable dielectric properties with  $\epsilon'$  of  $\epsilon 5\times 10^4$  and a very low  $\epsilon'$  on  $\epsilon'$  on  $\epsilon'$  and RT. The giant dielectric response of the ZNTO ceramics can be well described by the internal barrier layer capacitor effect at the grain boundaries and/or resistive outer–surface layer.

### References

[1] S. Ke, H. Fan, H. Huang, Dielectric relaxation in A<sub>2</sub>FeNbO<sub>6</sub> (A perovskite ceramics, Journal of Electroceramics 22(1-3) (2007) 252-256.

- = Ba, Sr, and Ca)
- [2] L. Ni, X.M. Chen, Dielectric relaxations and formation mechanism of giant dielectric constant step in CaCu<sub>3</sub>Ti<sub>4</sub>O<sub>12</sub> ceramics, Appl. Phys. Lett. 91(12) (2007) 122905.
- [3] Y. Li, L. Fang, L. Liu, Y. Huang, C. Hu, Giant dielectric response and charge compensation of Li- and Co-doped NiO ceramics, Mater. Sci. Eng. B 177(9) (2012) 673-677.
- [4] Q. Zheng, H. Fan, C. Long, Microstructures and electrical responses of pure and chromium-doped CaCu<sub>3</sub>Ti<sub>4</sub>O<sub>12</sub> ceramics, J. Alloys Compd. 511(1) (2012) 90-94.
- [5] Y. Shi, W. Hao, H. Wu, L. Sun, E. Cao, Y. Zhang, H. Peng, High dielectric-permittivity properties of NaCu<sub>3</sub>Ti<sub>3</sub>Sb<sub>0.5</sub>Nb<sub>0.5</sub>O<sub>12</sub> ceramics, Ceram. Int. 42(1, Part A) (2016) 116-121.
- [6] S. Ke, H. Huang, H. Fan, H.L.W. Chan, L.M. Zhou, Colossal dielectric response in barium iron niobate ceramics obtained by different precursors, Ceram. Int. 34(4) (2008) 1059-1062.
- [7] A. Nautiyal, C. Autret, C. Honstettre, S. De Almeida-Didry, M. El Amrani, S. Roger, B. Negulescu, A. Ruyter, Local analysis of the grain and grain boundary contributions to the bulk dielectric properties of  $Ca(Cu_{3-y}Mg_y)Ti_4O_{12}$  ceramics: Importance of the potential barrier at the grain boundary, J. Eur. Ceram. Soc. 36(6) (2016) 1391-1398.
- [8] Z. Wang, M. Cao, Q. Zhang, H. Hao, Z. Yao, Z. Wang, Z. Song, Y. Zhang, W. Hu, H. Liu, Dielectric Relaxation in Zr-Doped SrTiO<sub>3</sub> Ceramics Sintered in N<sub>2</sub> with Giant Permittivity and Low Dielectric Loss, J. Am. Ceram. Soc. 98(2) (2015) 476-482.
- [9] J. Wu, C.-W. Nan, Y. Lin, Y. Deng, Giant Dielectric Permittivity Observed in Li and Ti Doped NiO, Phys. Rev. Lett. 89(21) (2002) 217601.
- [10] J. Boonlakhorn, P. Kidkhunthod, P. Thongbai, A novel approach to achieve high dielectric permittivity and low loss tangent in CaCu<sub>3</sub>Ti<sub>4</sub>O<sub>12</sub> ceramics by co-doping with Sm<sup>3+</sup> and Mg<sup>2+</sup> ions, J. Eur. Ceram. Soc. 35(13) (2015) 3521-3528.
- [11] J. Jumpatam, P. Thongbai, T. Yamwong, S. Maensiri, Effects of Bi<sup>3+</sup> doping on microstructure and dielectric properties of CaCu<sub>3</sub>Ti<sub>4</sub>O<sub>12</sub>/CaTiO<sub>3</sub> composite ceramics, Ceram. Int. 41, Supplement 1 (2015) S498-S503.
- [12] X.W. Wang, P.B. Jia, X.E. Wang, B.H. Zhang, L.Y. Sun, Q.B. Liu, Calcining temperature dependence on structure and dielectric properties of CaCu<sub>3</sub>Ti<sub>4</sub>O<sub>12</sub> ceramics, J. Mater. Sci.: Mater. Electron. (2016) 1-7.
- [13] Y. Liu, X. Zhao, C. Zhang, Dielectric and impedance characteristics of  $Na_{1/3}Ca_{1/3}Y_{1/3}Cu_3Ti_4O_{12}$  ceramic prepared by solid-state reaction method, J. Mater. Sci.: Mater. Electron. 27(11) (2016) 11757-11761.
- [14] L. Yang, X. Chao, L. Wei, N. Zhao, Z. Yang, Dielectric responses of  $Na_{0.65}Bi_{0.45}Cu_3Ti_4O_{12}$  ceramics based on the composition design of changing the Na/Bi ratio, J. Mater. Sci.: Mater. Electron. 27(3) (2015) 2221-2227.
- [15] T.C. Porfirio, E.N.S. Muccillo, Influence of lithium disilicate addition on the dielectric properties of chemically synthesized CaCu<sub>3</sub>Ti<sub>4</sub>O<sub>12</sub>, J. Mater. Sci.: Mater. Electron. 26(6) (2015) 3970-3975.
- [16] L. Singh, B.C. Sin, I.W. Kim, K.D. Mandal, H. Chung, Y. Lee, J. Varela, A Novel One-Step Flame Synthesis Method for Tungsten-Doped CCTO, J. Am. Ceram. Soc. 99(1) (2016) 27-34.
- [17] V. Katari, P.D. Babu, S.K. Mishra, R. Mittal, S. Bevara, S.N. Achary, S.K. Deshpande, A.K. Tyagi, Effect of Preparation Conditions on Magnetic and Dielectric Properties of  $Y_2MMnO_6$  (M = Co, Ni), J. Am. Ceram. Soc. 99(2) (2016) 499-506.

- [18] C. Wang, W. Ni, X. Sun, L. Wang, C. Wang, K. Jin, Relaxor-like behaviors in  $Na_{1/2}Bi_{1/2}Cu_3Ti_4O_{12}$  ceramics, J. Am. Ceram. Soc. 100(5) (2017) 2016-2023.
- [19] W. Ni, J. Ye, Y. Guo, C. Cheng, Z. Lin, Y. Li, H. Wang, Y. Yu, Q. Li, S. Huang, Z. Shao, C. Wang, Decisive role of mixed-valence structure in colossal dielectric constant of LaFeO<sub>3</sub>, J. Am. Ceram. Soc. (2017) DOI: 10.1111/jace.14860.
- [20] W. Hao, H. Wu, P. Xu, Y. Shi, S. Yang, M. Wang, L. Sun, E. Cao, Y. Zhang, Influence of Sb-doping on dielectric properties of NaCu<sub>3</sub>Ti<sub>3</sub>TaO<sub>12</sub> ceramics and relevant mechanism(s), Ceram. Int. 43(4) (2017) 3631-3638.
- [21] J. Zhang, Y. Hou, M. Zheng, W. Jia, M. Zhu, H. Yan, The Occupation Behavior of  $Y_2O_3$  and Its Effect on the Microstructure and Electric Properties in X7R Dielectrics, J. Am. Ceram. Soc. 99(4) (2016) 1375-1382.
- [22] A. Khare, S.S. Yadava, K.D. Mandal, N.K. Mukhopadhyay, Effect of sintering duration on the dielectric properties of 0.9BaTiO<sub>3</sub>-0.1CaCu<sub>3</sub>Ti<sub>4</sub>O<sub>12</sub> nanocomposite synthesized by solid state route, Microelectron. Eng. 164 (2016) 1-6.
- [23] T. Xu, C.-A. Wang, Effect of two-step sintering on micro-honeycomb BaTiO₃ ceramics prepared by freeze-casting process, J. Eur. Ceram. Soc. 36(10) (2016) 2647-2652.
- [24] W. Hu, Y. Liu, R.L. Withers, T.J. Frankcombe, L. Norén, A. Snashall, M. Kitchin, P. Smith, B. Gong, H. Chen, J. Schiemer, F. Brink, J. Wong-Leung, Electron-pinned defect-dipoles for high-performance colossal permittivity materials, Nat. Mater. 12(9) (2013) 821-826.
- [25] C. Wang, N. Zhang, Q. Li, Y. Yu, J. Zhang, Y. Li, H. Wang, Dielectric Relaxations in Rutile TiO<sub>2</sub>, J. Am. Ceram. Soc. 98(1) (2015) 148-153.
- [26] X. Wei, W. Jie, Z. Yang, F. Zheng, H. Zeng, Y. Liu, J. Hao, Colossal permittivity properties of Zn,Nb co-doped TiO<sub>2</sub> with different phase structures, Journal of Materials Chemistry C 3(42) (2015) 11005-11010.
- [27] Y. Song, X. Wang, X. Zhang, Y. Sui, Y. Zhang, Z. Liu, Z. Lv, Y. Wang, P. Xu, B. Song, The contribution of doped-Al to the colossal permittivity properties of  $AI_xNb_{0.03}Ti_{0.97-x}O_2$  rutile ceramics, Journal of Materials Chemistry C 4(28) (2016) 6798-6805.
- [28] T. Nachaithong, P. Thongbai, S. Maensiri, Colossal permittivity in  $(In_{1/2}Nb_{1/2})_xTi_{1-x}O_2$  ceramics prepared by a glycine nitrate process, J. Eur. Ceram. Soc. 37(2) (2017) 655-660.
- [29] B. Shang, P. Liang, F. Li, X. Chao, L. Wei, Z. Yang, Dielectric response of TiO<sub>2</sub> ceramics: The crucial role of Ta<sub>2</sub>O<sub>5</sub>, J. Alloys Compd. 704 (2017) 64-69.
- [30] W. Tuichai, S. Danwittayakul, N. Chanlek, P. Srepusharawoot, P. Thongbai, S. Maensiri, Origin(s) of the apparent colossal permittivity in  $(In_{1/2}Nb_{1/2})_xTi_{1-x}O_2$ : clarification on the strongly induced Maxwell-Wagner polarization relaxation by DC bias, RSC Advances 7(1) (2017) 95-105.
- [31] W. Tuichai, S. Danwittayakul, N. Chanlek, P. Thongbai, S. Maensiri, High-performance giant-dielectric properties of rutile TiO<sub>2</sub> co-doped with acceptor-Sc<sup>3+</sup> and donor-Nb<sup>5+</sup> ions, J. Alloys Compd. 703 (2017) 139-147.
- [32] W. Tuichai, N. Thongyong, S. Danwittayakul, N. Chanlek, P. Srepusharawoot, P. Thongbai, S. Maensiri, Very low dielectric loss and giant dielectric response with excellent temperature stability of Ga<sup>3+</sup> and Ta<sup>5+</sup> co-doped rutile-TiO<sub>2</sub> ceramics, Materials & Design 123 (2017) 15-23.
- [33] X. Zhu, L. Yang, J. Li, L. Jin, L. Wang, X. Wei, Z. Xu, F. Li, The dielectric properties for (Nb,In,B) co-doped rutile TiO<sub>2</sub> ceramics, Ceram. Int. 43(8) (2017) 6403-6409.
- [34] Z. Li, X. Luo, W. Wu, J. Wu, Niobium and Divalent-Modified Titanium Dioxide Ceramics: Colossal Permittivity and Composition Design, J. Am. Ceram. Soc. (2017) 10.1111/jace.14850.

- [35] X.-g. Zhao, P. Liu, Dielectric and electric relaxations induced by the complex defect clusters in (Yb+Nb) co-doped rutile TiO2 ceramics, J. Am. Ceram. Soc. (2017) 10.1111/jace.14861.
- [36] G. Liu, H. Fan, J. Xu, Z. Liu, Y. Zhao, Colossal permittivity and impedance analysis of niobium and aluminum co-doped TiO<sub>2</sub> ceramics, RSC Advances 6(54) (2016) 48708-48714.
- [37] J. Zhang, Z. Yue, Y. Zhou, B. Peng, X. Zhang, L. Li, Temperature-dependent dielectric properties, thermally-stimulated relaxations and defect-property correlations of TiO<sub>2</sub> ceramics for wireless passive temperature sensing, J. Eur. Ceram. Soc. 36(8) (2016) 1923-1930.
- [38] R.D. Shannon, Revised Effective Ionic Radii and Systematic Studies of Interatomie Distances in Halides and Chaleogenides, Acta Cryst. A32 (1976) 751-767.
- [39] M.N. Rahaman, Ceramic processing and sintering, 2nd ed., M. Dekker, New York, 2003.
- [40] L. Singh, I.W. Kim, B.C. Sin, K.D. Mandal, U.S. Rai, A. Ullah, H. Chung, Y. Lee, Dielectric studies of a nano-crystalline  $CaCu_{2.90}Zn_{0.10}Ti_4O_{12}e$ electro-ceramic by one pot glycine assisted synthesis from inexpensive  $TiO_2$  for energy storage capacitors, RSC Adv. 4(95) (2014) 52770-52784.
- [41] L.R. Sheppard, J. Holik, R. Liu, S. Macartney, R. Wuhrer, Tantalum Enrichment in Tantalum-Doped Titanium Dioxide, J. Am. Ceram. Soc. 97(12) (2014) 3793-3799.
- [42] A. Marzec, M. Radecka, W. Maziarz, A. Kusior, Z. Pędzich, Structural, optical and electrical properties of nanocrystalline TiO<sub>2</sub>, SnO<sub>2</sub> and their composites obtained by the sol–gel method, J. Eur. Ceram. Soc. 36(12) (2016) 2981-2989.

## CHAPTER 1

## Abnormally Enhanced Dielectric Permittivity in Poly(vinylidene fluoride)/Nanosized-La<sub>2</sub>NiO<sub>4-δ</sub> Films

#### 1.1 Introduction

In recent years, flexible–polymeric dielectric materials with large dielectric permittivity ( $\epsilon'$ ) have been intensively investigated due to their potential for many applications, especially for embedded capacitor technology [1-12]. Thus, high  $\epsilon'$  value of a dielectric polymer is required for capacitor applications [1, 13]. Unfortunately,  $\epsilon'$  of polymer is very low compared to those of many dielectric ceramics. Poly(vinylidene fluoride) (PVDF) is often chosen as a polymer matrix because of its high  $\epsilon'$  value [2-7, 10, 14-16]. The excellent mechanical properties of polymer and high–performance electrical properties of ceramics are usually required for fabricating polymer–ceramic composites with good mechanical and electrical properties. An insulating properties of the polymer matrix used was strongly decreased as loading content of filler increased. In this case, the conductivity and dielectric loss tangent (tan $\delta$ ) will also be increased, which is undesirable for capacitor applications [10].

Lead-zirconate-titanate [17],  $Ba_{0.6}Sr_{0.4}TiO_3$  [4],  $CaCu_3Ti_4O_{12}$  [15, 18, 19] and BaTiO<sub>3</sub> [2, 7, 8, 12, 14, 16, 20] are often used as fillers in polymeric composites due to their high  $\varepsilon'$  values. A ceramic filler with large particle sizes ( $\sim 1-10~\mu m$ ) lead to the degradation of dielectric properties due to the existence of pores and poor dispersion in the polymer composites [10], especially when filler loading is close to 50 vol%. For example, filling 52 vol% CaCu<sub>3</sub>Ti<sub>4</sub>O<sub>12</sub> with sizes of 0.5–1.5 μm into PVDF matrix resulted in the existence of a large amount of pores [19]. Moreover, micro-sized powder limit the thickness of the polymer composite films used for embedded capacitor applications. Thus, polymer matrix composites filled with ceramic nanoparticles are highly desirable. Dang et al. [3] reported the strong increase in interfacial polarization intensity of BaTiO<sub>3</sub>/PVDF nanocomposite prepared by a solution processing method increased with decreasing BaTiO<sub>3</sub> particle size from 500 to 100 nm. This resulted in an increase in a low-frequency ε' value. It was also found that the dielectric response in CaCu<sub>3</sub>Ti<sub>4</sub>O<sub>12</sub>/PVDF composites was extensively increased ( $\epsilon' \approx 10^5$  at 1 kHz) by using CaCu<sub>3</sub>Ti<sub>4</sub>O<sub>12</sub> nanoparticles with sizes of about 200 nm as a filler material, while the ε' value of the micro-sized CaCu<sub>3</sub>Ti<sub>4</sub>O<sub>12</sub> powder/PVDF composite with 52 vol% was ≈40 at 1 kHz [19]. This was resulted from the strongly improved interfacial polarization caused by reduction in filler particles. Unfortunately, tanδ of such CaCu<sub>3</sub>Ti<sub>4</sub>O<sub>12</sub>/PVDF nanocomposites was greatly increased as well.

Usually, greatly enhanced  $\varepsilon'$  value of many polymer–ceramic composite systems mentioned above can successfully be obtained by filling with large volume fractions of ceramic fillers (f > 0.4) [2, 14-16, 19]. This has a great influence on the mechanical properties of the fabricated polymeric nanocomposites. Furthermore,  $\varepsilon'$  values of most 2–phase polymer–ceramic composite systems were found to be lower than 100 at 1 kHz and room temperature (RT) because  $\varepsilon'$  values of ceramic fillers are not large enough ( $\varepsilon' \approx 10^3 - 10^4$ ). High  $\varepsilon'$  and low  $\tan \delta$  in a polymer–ceramic composite containing low ceramic filler loading are difficult to accomplish. Recently,  $La_{2-x}Sr_xNiO_4$  has become one of the most interesting dielectric ceramics due to its extremely large  $\varepsilon' \approx 10^5 - 10^6$  [21]. Such a high  $\varepsilon'$  of  $La_{2-x}Sr_xNiO_4$  can be observed in a GHz region. Note that  $La_2NiO_{4-\delta}$  can also exhibit

large  $\varepsilon'$  due to presence of Ni<sup>2+</sup> and Ni<sup>3+</sup>. The giant dielectric response was attributed to the adiabatic small polaronic hopping process of Ni<sup>2+</sup> and Ni<sup>3+</sup> [22]. Unfortunately, this high-permittivity ceramic has never been used for incorporating in PVDF polymer.

Thus, the aim of this work is to represent a novel high–performance polymeric nanocomposite system. Good dielectric properties were achieved in PVDF/La<sub>2</sub>NiO<sub>4</sub> nanocomposite films. We found that greatly enhanced dielectric properties with  $\epsilon' \approx 431.17$  and  $\tan \delta \approx 0.43$  were successfully achieved in the PVDF/La<sub>2</sub>NiO<sub>4</sub> nanocomposite film incorporating with 25 vol% La<sub>2</sub>NiO<sub>4</sub>. The effect of filler particle size was also investigated.

## 1.2 Experimental details

## 2.1 Preparation of La<sub>2</sub>NiO<sub>4</sub> powders

La<sub>2</sub>NiO<sub>4</sub> (LNO) nanocrystalline powder was prepared by a combustion method using urea as a fuel for reaction initiation. The starting raw materials consisted of Ni(NO<sub>3</sub>)<sub>2</sub>·6H<sub>2</sub>O (99.0%, Kanto Chemical), La(NO<sub>3</sub>)<sub>3</sub>·6H<sub>2</sub>O (99.99%, Sigma–Aldrich), deionized water, citric acid (C<sub>6</sub>H<sub>8</sub>O<sub>7</sub>.H<sub>2</sub>O, 99.7%), and urea (CH<sub>4</sub>N<sub>2</sub>O, 99.0%). First, stoichiometric amounts of Ni(NO<sub>3</sub>)<sub>2</sub>·6H<sub>2</sub>O and La(NO<sub>3</sub>)<sub>3</sub>·6H<sub>2</sub>O were dissolved in an aqueous solution of citric acid. Second, urea powder was added into the mixed solution with stirring at 200 °C until a viscous gel appeared. Then, the gel was dried at 300 °C for 0.5 h. Finally, the resulting dried porous precursor was ground and calcined at 1000 °C for 6 h to form pure phase of nano–sized LNO powder. Micro–sized LNO powder was prepared by a solid state reaction method. The mixture of starting powders was ball milled in ethanol for 24 h. The mixed powder was calcined at 1200 °C for 12 h to achieve pure phase of micro–sized LNO powder.

## 2.2 Preparation of PVDF/LNO nanocomposite films by a solution processing method

In this work, PVDF (Sigma–Aldrich Co., France) polymer was used as a matrix. PVDF/LNO nanocomposite films with different loading LNO volume fractions ( $f_{LNO}=0.05$  to 0.45). First, an appropriate amount of PVDF was dissolved in N,N dimethylformamide (DMF). Second, LNO nanoparticles were added into the above solution under constant stirring for 4 h. The PVDF/LNO mixture solution was further stirred by means of ultrasonic action for 1 h in order to drive the dispersion of LNO nanoparticles. Then, the mixture was kept in an oven at 100 °C for 6 h to completely evaporate the DMF solvent. Finally, the obtained polymer nanocomposite films with 100  $\mu$ m in thickness were cut into a disc–shape with 12 mm in diameter and molded by hot–pressing at a temperature of 200 °C and 10 MPa for 30 min.

#### 2.3 Characterization techniques and Electrical measurements

X-ray diffraction (XRD) (PANalytical, EMPYREAN) and scanning electron microscopy (SEM) (SEC, SNE4500M) were used to characterize the phase composition and microstructure of PVDF/LNO nanocomposite films. Transmission electron microscopy (TEM, ZEISS EM902) was used to reveal the LNO micro and nanoparticles. For the dielectric measurements, silver paint was used as electrodes and painted on surfaces of composite samples. The dielectric properties were measured using an Agilent 4294A Precision Impedance Analyzer over the frequency range of 10<sup>2</sup> to 10<sup>6</sup> Hz at RT with an oscillation voltage of 500 mV. Thermo gravimetric (TG) analyses were performed using the Pyris Diamond TG/DTA (Perkin Elmer Instrument), with alumina as the reference

material. The experiments were carried out at a heating rate of 10  $^{\circ}$ C/min in flowing N<sub>2</sub> atmosphere (flow rate: 100 cm³/min). To reveal the oxidation states of Ni atoms, X-ray photoelectron spectroscopy (ULVAC-PHI, Japan) analysis and X-ray Absorption Near Edge Structure (XANES) spectra were collected at the SUT-NANOTEC-SLRI XAS beamline (BL5.2) (electron energy of 1.2 GeV; bending magnet; beam current 80 – 150 mA; 1.1 to 1.7  $\times$  10<sup>11</sup> photon s<sup>-1</sup>) at the Synchrotron Light Research Institute (SLRI), Nakhon Ratchasima, Thailand.

#### 1.3 Results and discussion

Figs. 1(a) and (b) show the SEM images of nano-sized and micro-sized LNO powders, respectively. It is clearly seen that the particle-size distributions of these LNO powders are narrow with average sizes of  $\approx$ 200 nm and  $\approx$ 1.0  $\mu$ m, respectively. The cross-section SEM images of the PVDF/LNO nanocomposite films with  $f_{LNO}=0$ , 0.1, 0.2, 0.25, and 0.3 are respectively shown in Figs. 1(c)–(g), revealing the dispersion of LNO particles in the PVDF polymer matrix. As shown in Fig. 1(c), the PVDF polymer matrix forms a continuous phase. The dispersion of LNO nanoparticles is quite well. However, a slight inhomogeneity of the filler distribution in the PVDF matrix is still observed, as indicated in circle areas. Nevertheless, the 0–3 connectivity pattern is clearly to exist in all nanocomposites because LNO nanoparticles are randomly surrounded by the PVDF matrix [23]. The thickness values of PVDF/LNO nanocomposite films are in the range of 90–150  $\mu$ m [insets of Figs. 1(d)–(g)], while the thickness of pure PVDF film is  $\approx$ 300  $\mu$ m. Interestingly, the PVDF/LNO nanocomposites with  $f_{LNO} \leq 0.25$  show good flexibility, as demonstrated in Fig. 1(h).

The phase formation of pure PVDF and LNO nanopowder are represented in Fig. 2. It is found that the existence of  $\alpha$ -phase of PVDF was confirmed [24]. It is confirmed that the prepared LNO nanopowder is pure in phase without any possible impurity (JCPDS 32–1241). All XRD peaks are perfectly indexed as a tetragonal structure. Fig. 3 illustrates the XRD patterns of PVDF/LNO nanocomposite films with different loading contents of filler. XRD peak of PVDF was observed in the composites with low loading content of filler. The XRD patterns of LNO are unchanged for all compositions. The intensities of  $\alpha$ -phase diffraction peaks slightly decrease and become amorphous phase with increasing LNO content in the nanocomposites.

Fig. 4 reveals the thermo gravimetric analyses (TGA) of the PVDF/LNO nanocomposite films to study the thermal stability of the polymer and the composites. It is observed that the degradation of pure PVDF polymer occurred at around  $\approx$ 500 °C. This is similar to that observed in literature [15, 25]. The thermal degradation behavior of the PVDF/LNO composites is similar to that pure PVDF. The residual weight in the composites at 800 °C are 22.1, 30.03, 44.11, 57.04, and 67.45 wt% for pure PVDF and nanocomposite films with  $f_{\text{LNO}}$ =0.1, 0.2, 0.3, and 0.4, respectively. The composition obtained from the experimental results is slightly lower than that of theoretical calculation results. This may be caused by a slight inhomogeneity of filler distribution in the PVDF matrix [25], as clearly seen in the circle areas of Figs. 1(d)–(g).

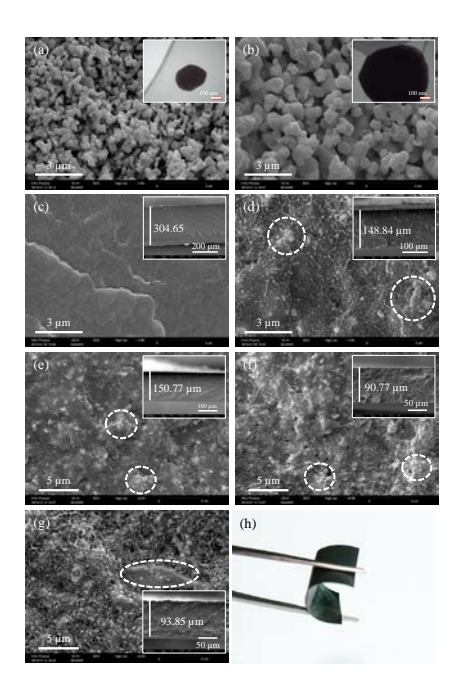


**Fig. 1** (a–b) SEM images of nano–sized and micro–sized LNO powders, respectively; insets show their TEM images of nano–sized and micro–sized LNO particles. (c–g) SEM images of cross section of PVDF/LNO nanocomposite films with  $f_{\rm LNO}$ =0, 0.10, 0.20, 0.25, and 0.3, respectively; insets are their SEM images with low magnification for revealing the thickness of polymer nanocomposite films. (f) Photo image of the PVDF/LNO nanocomposite film with  $f_{\rm LNO}$ =0.25.

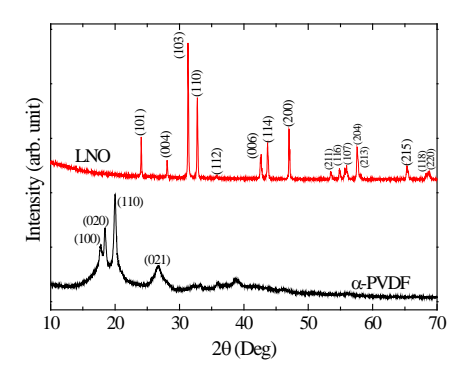


**Fig. 2** XRD patterns of pure PVDF polymer and nano–sized LNO powder prepared by a combustion method and calcined at 1000 °C for 6 h.

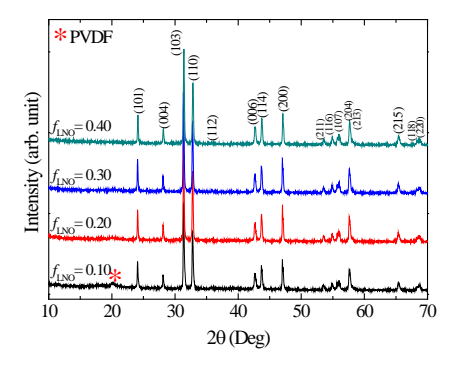


**Fig. 3** XRD patterns of PVDF/LNO nanocomposite films with various  $f_{LNO}$ .

The dielectric properties of the PVDF/LNO nanocomposite films are demonstrated in Figs. 5 and 6.  $\varepsilon'$  of PVDF/LNO nanocomposites increases with increasing  $f_{\text{LNO}}$ .  $\varepsilon'$  of PVDF/LNO nanocomposites with  $f_{\text{LNO}} \leq 0.2$  is nearly independent on frequency in the range of  $10^2 - 10^6$  Hz. It is observed that  $\varepsilon'$  of the PVDF/LNO nanocomposite with  $f_{\text{LNO}} = 0.25$  linearly decreases with increasing frequency. This evidently indicates that the dielectric response is primarily caused by the interfacial polarization effect. The frequency–dependent behavior of this composition is totally different from other samples. For the PVDF/LNO nanocomposites with  $f_{\text{LNO}} \geq 0.30$ ,  $\varepsilon'$  is slightly dependent on frequency in the range of  $10^2 - 10^5$  Hz. For the interfacial polarization mechanism in the insulator–conductor composite system, when the distance between the adjacent conductive particles is shorten by increasing filler content and/or the density of free charges in the conductive particles is sufficiently large, the frequency range of sensitivity for the interfacial polarization can usually extend into higher frequency range. Thus, this means that the intensity of interfacial polarization become stronger when the  $f_{\text{LNO}}$  increased.

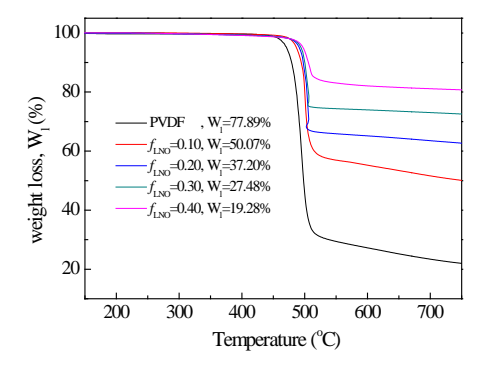


**Fig. 4** Thermal analysis (TG) for pure PVDF and PVDF/LNO nanocomposite films with  $f_{LNO} = 0.1-0.4$ .

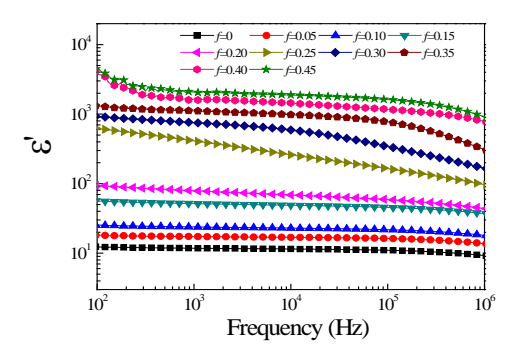
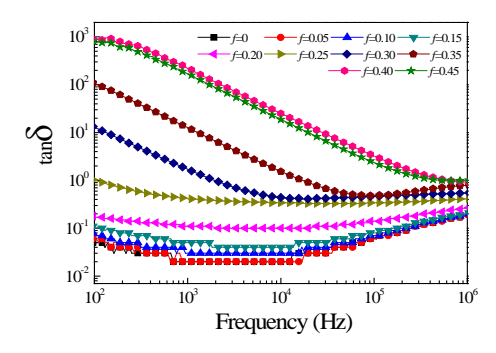


Fig. 5  $\epsilon'$  at RT as a function of frequency for PVDF and PVDF/LNO nanocomposite films.

Usually, high dielectric response in materials caused by the interfacial polarization is accompanied with a large  $\tan\delta$  in a low–frequency range, resulting from high dc conductivity [26, 27]. In this case, the signified characteristic is that a low–frequency  $\tan\delta$  will strongly decrease with increasing frequency [28]. As shown in Fig. 6, a low–frequency  $\tan\delta$  of PVDF/LNO nanocomposites with  $f_{\text{LNO}} \ge 0.30$  decreases with increasing frequency  $\tan\delta$  increases with increasing

 $f_{\rm LNO}$  from 0.25 to 0.45. These results clearly indicate that a large dielectric response in PVDF/LNO nanocomposites with  $f_{\rm LNO} \geq 0.30$  is attributed to the strong interfacial polarization. Interestingly,  $\tan\delta$  of PVDF/LNO nanocomposites with  $f_{\rm LNO} \leq 0.25$  is slightly dependent on frequency.  $\tan\delta$  values at 1 kHz of these samples are lower than 1.0 at RT. It is important to note that the frequency–dependent behavior of microcomposites is similar to that of the nanocomposites.



**Fig. 6** tanδ at RT as a function of frequency for PVDF and PVDF/LNO nanocomposite films

Fig. 7 displays the dielectric properties at 1 kHz and RT of PVDF/LNO composites as a function of loading content of fillers. The drastic increases in  $\varepsilon'$  and  $\tan\delta$  were observed in both PVDF/LNO micro and nanocomposites. Normally, dramatic changes in metal–insulator matrix composites in the critical region are caused by the percolation effect [29, 30]. A rapid increase in effective dielectric constant ( $\varepsilon'_{eff}$ ) of the composites can be well described by the power law [30]:

$$\varepsilon'_{eff} = \varepsilon'_{matrix} \left| \frac{f_c - f_f}{f_c} \right|^{-q}, \tag{1}$$

where  $\varepsilon'_{matrix}$  is the dielectric constant of the insulator matrix,  $f_c$  is the percolation threshold,  $f_f$  is the volume fraction of conductive filler, and q is a critical component. By using Eq. (1), it was found that  $f_c$  values of the nanocomposites and microcomposites were found to be 0.26 and 0.38, respectively, while q values were 1.03 and 1.05, respectively. In the case where conductive fillers were in spherical form,  $f_c$  of the two-phase random composite was theoretically calculated to be 0.16 with the lower limit of the normal range ( $q \approx 0.8$ -1) [30]. Deviation of  $f_c$  from percolation theory may be due to non-spherical form and semiconductive nature of both micro and nano-sized powders. As shown in Figs. 1(a) and (b), the agglomeration of filler particles can also cause an increase in  $f_c$  [31]. High  $f_c \approx 0.38$  of the microcomposites is comparable to  $f_c \approx 0.4$  for the PVDF/giant-permittivity Li<sub>0.1</sub>(Ti<sub>0.02</sub>Ni<sub>0.98</sub>)<sub>0.9</sub>O composites [32].

Obviously,  $\epsilon'$  and  $\tan\delta$  of the PVDF/LNO microcomposites are higher than that of the nanocomposite. Higher  $\epsilon'$  of the nanocomposites is attributed to the stronger polarization intensity. To clarify this, the dielectric properties of sintered LNO ceramics were investigated. Fig. 7(b) shows the frequency dependence of dielectric properties at RT of the sintered LNO ceramics. Both of the sintered LNO ceramics fabricated from

nano–sized and micro–sized powders (referred as nano–LNO and micro–LNO ceramics, respectively) exhibit giant  $\epsilon'$  values over the frequency range of  $10^2$ – $10^7$  Hz. This giant dielectric response may be attributed to the adiabatic small polaronic hopping process [33] and/or sample–electrode contract response [34]. As clearly seen, both  $\epsilon'$  and  $\tan\delta$  values of the micro–LNO ceramic are larger than the values of the nano–LNO ceramic. This result is not consistent with the dielectric properties of PVDF/LNO composite films as demonstrated in Fig. 7(a). Thus, it is likely that the dielectric properties of the PVDF/LNO composite films are associated with the extrinsic factors (e.g., interfacial area, inter–particle distance, and particle sizes) rather than the intrinsic–dielectric properties inside the LNO particles.

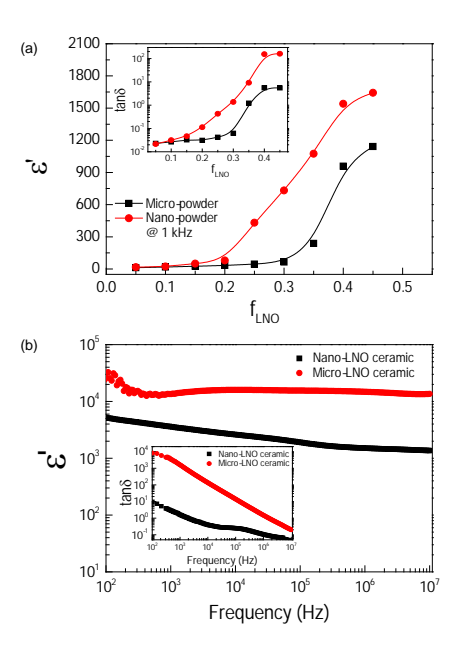
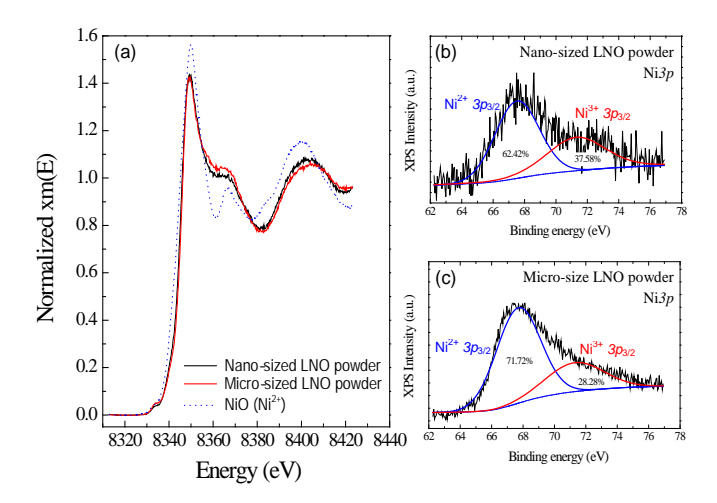


Fig. 7 (a)  $\varepsilon'$  at 1 kHz and RT as a function of with  $f_{\text{LNO}}$  for PVDF/LNO micro and nanocomposite films; inset shows  $\tan\delta$  as a function of  $f_{\text{LNO}}$ . (b) Frequency dependence of  $\varepsilon'$  at 1 kHz and RT of the LNO ceramics sintered at 1400 °C for 6 h using nano–sized and micro–sized LNO powders.

The interfacial polarization in composite materials is usually associated with both of conductivity of filler used and amount of active internal interfaces [30]. The smaller  $f_c$  value of the nanocomposites clearly indicates a higher conductivity and better distribution of filler nanoparticles. Besides the effect of interfacial area, the inter–particle distance is also important for the insulator–conductor composite system. It was demonstrated that the percolation network can be created as the inter–particle distance between fillers approached to  $\approx$ 250 nm ( $d_{fc}$ ) [35]. Since the distance between inter–particles of conducting phase is very short, the energy required for electron transport between the conducting particles is negligibly reduced. This gives rise to a frequency independent conductivity and  $\varepsilon'$  value. According to the frequency–dependent behavior of the PVDF/LNO nanocomposite with  $f_{\text{LNO}} = 0.25$ , the frequency dependence of  $\varepsilon'$  in the range of  $10^2$ – $10^6$  Hz may also be due to the fact that the inter–particle distance is still larger than  $d_{fc}$ , since  $f_c$  of this nanocomposite system is 0.26.



**Fig. 8** (a) Normalized X–ray absorption near edge structure (XANES) spectra for Ni *K*–edge of NiO and LNO powders. (b–c) Ni3*p* XPS data of nano–sized and micro–sized LNO powders.

It is likely that nano-sized LNO powder prepared by a combustion method may have more defects, especially on the surfaces, than that of the micro-sized LNO powder prepared by a solid state reaction method. This can cause an increase in the conductivity. To clarify this, the nano-sized and micro-sized LNO powers were characterized by XANES and XPS techniques. Fig. 8(a) shows the XANES spectra for Ni K-edge of NiO and LNO powders, confirming the presence of Ni3+ ions in both of the nano and micro-sized LNO powers. The XPS spectra of Ni 3p regions of both powders are illustrated in Figs. 8(b) and (c), showing coexistence of Ni<sup>2+</sup> and Ni<sup>3+</sup>. The main Ni 3p peaks (Ni<sup>2+</sup>) of the nano and micro-powders appear at 67.48 and 67.70 eV, respectively. These are consistent with the reported literature results for approximately 67-68 eV [36]. The corresponding Ni<sup>3+</sup> peak appears at ≈ 71.30 eV for both powders, which is consistent with that reported in literature (≈ 71 eV) [37]. It was found that the amount of Ni<sup>3+</sup> in the nano-powder (≈ 37.85%) is greater than in the micro-powder (≈ 28.28%). This indicates that the conductivity of nano-sized LNO particle as a result of charge hopping between Ni<sup>3+</sup>↔Ni<sup>2+</sup> is higher than that of the micro-sized particle. According to the combustion method, one of the most advantages for this method is very high-energy efficiency with fast heating rates because the reactions occurring during ignition are highly explosive [38]. Thus, the prepared LNO powders have subjected to very high-energy with rapid increase in heating. Under an applied electric field, more free charges on the surfaces of nano-sized LNO particles are responsible for the observed strong interfacial polarization at the interface between insulating PVDF matrix and semiconducting LNO particle. It is reasonable to suggest that the distribution of nano-sized LNO particles in PVDF is better than that of the micro-sized LNO particles. Therefore, the formation of percolation network of semiconductive LNO nanoparticles is easily to form, resulting in a low  $f_c$ value.

It is worth noting that the optimized dielectric properties with large  $\varepsilon' \approx 431.17$  and low  $\tan \delta \approx 0.43$  were achieved in the PVDF/LNO nanocomposite with  $f_{LNO} = 0.25$ . This may have resulted from the existence of micro-capacitance structure [39]. For the PVDF/giant-permittivity Li<sub>0.1</sub>(Ti<sub>0.02</sub>Ni<sub>0.98</sub>)<sub>0.9</sub>O composite system [32], although a high  $\varepsilon' \approx$ 

600 was obtained in the 40 vol% of filler loading sample, it was accompanied with high  $\tan\delta\approx 2.0$ . For PVDF/(55 vol%)CaCu<sub>3</sub>Ti<sub>4</sub>O<sub>12</sub> and PVDF/(50 vol%)Na<sub>0.5</sub>Bi<sub>0.5</sub>Cu<sub>3</sub>Ti<sub>4</sub>O<sub>12</sub> composites, low  $\epsilon'$  values of 80 and 79.8 at 1 kHz were achieved [15]. Notably, the PVDF/LNO nanocomposite system should be one of the most interesting polymeric materials embedded capacitor technology due to its high  $\epsilon'$  and low  $\tan\delta$ . Moreover, good mechanical property of the PVDF/LNO nanocomposite films is also obtained due to a low filler loading usage.

#### 1.4 Conclusions

In conclusion, PVDF/LNO composite films were successfully fabricated by a solution processing method. It was found that particle size of LNO filler has an effect on the dielectric properties of PVDF/LNO composite films. It was found that  $f_c$  value of the nanocomposite was lower than that of the microscomposite, whereas  $\epsilon'$  of the nanocomposite was larger. Abrupt increase in  $\epsilon'$  was observed in the neighborhood of  $f_c$  for both of micro and nanocomposite films. Interestingly, the PVDF/(f=0.25)LNO nanocomposite film exhibited high  $\epsilon'\approx 431.17$  and low  $\tan\delta\approx 0.43$ , while the microcomposite film had a high  $\tan\delta$ . Improved dielectric properties of the PVDF/LNO nanocomposite were due to the formation of micro–capacitors in the polymer matrix.

#### References

- [1] Z.-M. Dang, J.-K. Yuan, J.-W. Zha, T. Zhou, S.-T. Li, G.-H. Hu, Prog. Mater. Sci. 57 (2012) 660-723.
- [2] Z.-M. Dang, H.-Y. Wang, Y.-H. Zhang, J.-Q. Qi, Macromol. Rapid Commun. 26 (2005) 1185-1189.
- [3] Z.-M. Dang, H.-P. Xu, H.-Y. Wang, Appl. Phys. Lett. 90 (2007) 012901.
- [4] K. Li, H. Wang, F. Xiang, W. Liu, H. Yang, Appl. Phys. Lett. 95 (2009) 202904.
- [5] A. Baji, Y.-W. Mai, Q. Li, Y. Liu, Composites Science and Technology 71 (2011) 1435-1440.
- [6] B.-H. Fan, J.-W. Zha, D. Wang, J. Zhao, Z.-M. Dang, Appl. Phys. Lett. 100 (2012) 012903.
- [7] S. Luo, S. Yu, R. Sun, C.-P. Wong, ACS Applied Materials & Interfaces 6 (2013) 176-182.
- [8] S.A. Paniagua, Y. Kim, K. Henry, R. Kumar, J.W. Perry, S.R. Marder, ACS Applied Materials & Interfaces 6 (2014) 3477-3482.
- [9] X. Huang, P. Jiang, Adv. Mater. (2014) DOI: 10.1002/adma.201401310.
- [10] L. Gao, J. He, J. Hu, Y. Li, The Journal of Physical Chemistry C 118 (2013) 831-838.
- [11] Z.-M. Dang, T. Zhou, S.-H. Yao, J.-K. Yuan, J.-W. Zha, H.-T. Song, et al., Adv. Mater. 21 (2009) 2077-2082.
- [12] M.A. Alam, M.H. Azarian, M.G. Pecht, J. Mater. Sci.: Mater. Electron. 23 (2012) 1504-1510.
- [13] A.J. Moulson, J.M. Herbert, Electroceramics : materials, properties, applications, 2nd ed., Wiley, West Sussex; New York, 2003.
- [14] Z.-M. Dang, H.-Y. Wang, H.-P. Xu, Appl. Phys. Lett. 89 (2006) 112902.
- [15] P. Thomas, K.T. Varughese, K. Dwarakanath, K.B.R. Varma, Composites Science and Technology 70 (2010) 539-545.
- [16] Q. Xiao, L. Li, B. Qing Zhang, X. Ming Chen, Ceram. Int. 39 (2013) S3-S7.

- [17] A.K. Zak, W.C. Gan, W.H.A. Majid, M. Darroudi, T.S. Velayutham, Ceram. Int. 37 (2011) 1653-1660.
- [18] C. Yang, H.-s. Song, D.-b. Liu, Composites Part B: Engineering 50 (2013) 180-186.
- [19] W. Yang, S. Yu, R. Sun, R. Du, Acta Mater. 59 (2011) 5593-5602.
- [20] R.K. Goyal, S.S. Katkade, D.M. Mule, Composites Part B: Engineering 44 (2013) 128-132.
- [21] S. Krohns, P. Lunkenheimer, C. Kant, A.V. Pronin, H.B. Brom, A.A. Nugroho, et al., Appl. Phys. Lett. 94 (2009) 122903.
- [22] X.Q. Liu, B.W. Jia, W.Z. Yang, J.P. Cheng, X.M. Chen, J. Phys. D: Appl. Phys. 43 (2010) 495402.
- [23] Z. Wang, M. Fang, H. Li, Y. Wen, C. Wang, Y. Pu, Composites Science and Technology 117 (2015) 410-416.
- [24] P. Martins, A.C. Lopes, S. Lanceros-Mendez, Prog. Polym. Sci. 39 (2014) 683-706.
- [25] Y.-I. Su, C. Sun, W.-q. Zhang, H. Huang, J. Mater. Sci. 48 (2013) 8147-8152.
- [26] W. Hu, Y. Liu, R.L. Withers, T.J. Frankcombe, L. Norén, A. Snashall, et al., Nat. Mater. 12 (2013) 821-826.
- [27] S. Vangchangyia, E. Swatsitang, P. Thongbai, S. Pinitsoontorn, T. Yamwong, S. Maensiri, et al., J. Am. Ceram. Soc. 95 (2012) 1497-1500.
- [28] K. Meeporn, T. Yamwong, S. Pinitsoontorn, V. Amornkitbamrung, P. Thongbai, Ceram. Int. 40 (2014) 15897-15906.
- [29] C. Pecharromán, F. Esteban-Betegón, J.F. Bartolomé, S. López-Esteban, J.S. Moya, Adv. Mater. 13 (2001) 1541-1544.
- [30] C.W. Nan, Y. Shen, J. Ma, Annu. Rev. Mater. Res. 40 (2010) 131-151.
- [31] W. Tuichai, S. Somjid, B. Putasaeng, T. Yamwong, A. Chompoosor, P. Thongbai, et al., Nanoscale Research Letters 8 (2013) 1-6.
- [32] Z.M. Dang, J.B. Wu, L.Z. Fan, C.W. Nan, Chem. Phys. Lett. 376 (2003) 389-394.
- [33] X.Q. Liu, C.L. Song, Y.J. Wu, X.M. Chen, Ceram. Int. 37 (2011) 2423-2427.
- [34] M. Li, D.C. Sinclair, J. Appl. Phys. 111 (2012) 054106.
- [35] K.S. Deepa, M.T. Sebastian, J. James, Appl. Phys. Lett. 91 (2007) 202904.
- [36] J.F. Marco, J.R. Gancedo, J. Ortiz, J.L. Gautier, Appl. Surf. Sci. 227 (2004) 175-186.
- [37] M. Burriel, S. Wilkins, J.P. Hill, M.A. Munoz-Marquez, H.H. Brongersma, J.A. Kilner, et al., Energy & Environmental Science 7 (2014) 311-316.
- [38] M.N. Rahaman, Ceramic processing and sintering, 2nd ed., M. Dekker, New York, 2003.
- [39] Z.-M. Dang, S.-H. Yao, J.-K. Yuan, J. Bai, The Journal of Physical Chemistry C 114 (2010) 13204-13209.

## **CHAPTER 2**

Greatly Enhanced Dielectric Permittivity in La<sub>1.7</sub>Sr<sub>0.3</sub>NiO<sub>4</sub>/Poly(vinylidene fluoride) Nanocomposites that Retained a Low Loss Tangent

#### 2.1 Introduction

Nowadays, dielectric polymer materials have been intensively investigated due to their unique advantages, such as process compatibility, light weight, flexibility and high breakdown strength. However,  $\varepsilon'$  of these polymers is still very low ( $\varepsilon'$ <10) compared to those of ceramic oxides ( $\varepsilon'$ <10³-10⁵). Thus, incorporating of various types of materials (*i.e.*, insulating dielectric oxides or conducting materials) into a polymer to enhance the  $\varepsilon'$  value was widely investigated. Generally, the dielectric properties of a polymer composite are determined by the polymer matrix used and its filler. The most widely used polymers are poly(vinylidene fluoride) (PVDF) and its copolymers. This is because PVDF has been found a superior dielectric material for capacitor applications due to its relatively high  $\varepsilon'$  values ( $\approx$ 10), high energy density, high electric breakdown field, low-dielectric loss tangent ( $\tan \delta$ ), low cost and high reliability. High electric breakdown field, low-dielectric loss

One of the most common and promising strategies to increase the  $\varepsilon'$  value of PVDF is to incorporate ceramic oxide particles that exhibit a large  $\varepsilon' > 10^3.^{2-4, \ 11-16}$  This capitalizes upon the idea that a combination of a very large  $\varepsilon'$  value of inorganic ceramic particles coupled with excellent flexibility and good dielectric strength of polymers<sup>1, 11-12</sup> can be used to produce suitable polymeric dielectric materials. From the point of view of capacitor applications, although significant efforts have been made to increase the  $\varepsilon'$  of ferroelectric–ceramic/polymer composites, their  $\varepsilon'$  values are difficult to significantly enhance to more than 100 even though the filler contents as high as 50 vol% (or  $f_{\text{filler}}$ =0.5) were used.<sup>3, 17-18</sup> Furthermore, ferroelectric ceramics usually exhibit an electromechanical effect (*i.e.*, a piezoelectric effect). This can cause a mechanical resonance in the device during charging and discharging, resulting in a reliability limit of the device.<sup>11</sup>

Non–ferroelectric ceramics that can exhibit very high  $\epsilon'$  values of  $\approx 10^4-10^5$ , such as CaCu<sub>3</sub>Ti<sub>4</sub>O<sub>12</sub> and isostructural CaCu<sub>3</sub>Ti<sub>4</sub>O<sub>12</sub>—oxides (e.g., Na<sub>0.5</sub>Bi<sub>0.5</sub>Cu<sub>3</sub>Ti<sub>4</sub>O<sub>12</sub> and Na<sub>1/3</sub>Ca<sub>1/3</sub>Bi<sub>1/3</sub>Cu<sub>3</sub>Ti<sub>4</sub>O<sub>12</sub>), <sup>12-13, 15, 19</sup> (Li+Ti) co–doped NiO (LTNO) particles, <sup>2</sup> and Ba(Fe<sub>0.5</sub>Nb<sub>0.5</sub>)O<sub>3</sub><sup>4</sup> are considered promising fillers for greatly enhancing the  $\epsilon'$  value of PVDF polymers. Non–ferroelectric ceramic/polymer composite systems have been intensively developed to overcome the limitation of ferroelectric–ceramic/polymer composites. Accordingly, a number of excellent research studies have been done. At the same volume fraction, the  $\epsilon'$  value these composite systems was larger than that of ferroelectric–ceramic/polymer composites. However, the  $\epsilon'$  values of these non–ferroelectric ceramic/PVDF composites were difficult to enhance to values larger than 100 (at 10<sup>3</sup> Hz), even when a large volume fraction of filler was used ( $f_{\text{filler}} \geq 0.5$ ). <sup>4, 12-14, 20</sup> Although a large value of  $\epsilon' \approx 600$  at (100 Hz) could be obtained in LTNO/PVDF composite with  $f_{\text{LTNO}} = 0.4$ ,  $\tan \delta$  of this composite was also large ( $\tan \delta > 1.0$  at 2 kHz). <sup>2</sup>

It has been generally observed that the low  $\varepsilon'$  values (<10<sup>2</sup>) of these ceramic/PVDF composites are much lower than those of sintered bulk ceramics ( $\varepsilon' \approx 10^4 - 10^5$ ) by 2–3 orders of magnitude. This may have occurred since the very high  $\varepsilon'$  values of many giant dielectric oxides originated from the extrinsic effect, *i.e.*, strong interfacial polarization at the grain boundaries. When calcined a ceramic powder or a powder that was obtained by grinding a sintered ceramic was incorporated into polymer matrix, there were no grain

boundary layers. Only interfacial polarization at the interface between ceramic particles and polymer occurred, while the dielectric response contributed by intrinsic polarizations inside ceramic particles (usually,  $\epsilon' \approx 10^2$  for CCTO<sup>21</sup>) and polymer matrix (usually,  $\epsilon' \approx 10$  for PVDF) were very low.

Most recently, incorporation of FeTiNbO<sub>6</sub> ceramic particles into PVDF was used successfully increase the  $\varepsilon'$  value of a composite with f = 0.4 to  $\approx 181$  (at 100 Hz). This was due to a very high  $\varepsilon'$  of  $\approx 4 \times 10^3$  of a FeTiNbO<sub>6</sub> ceramic, in which its high  $\varepsilon'$  originated from the intrinsic effect inside the grains (or particles). This opened a new way for using giant dielectric material as a filler to enhance  $\varepsilon'$  of a polymer matrix. A dielectric ceramic, where the origin of the giant  $\varepsilon'$  was caused by an intrinsic effect, is more suitable than that of a giant dielectric ceramic whose high  $\varepsilon'$  value originated from an extrinsic mechanism at the grain boundaries. Among several giant dielectric materials that were reported in recent years, La<sub>2-x</sub>Sr<sub>x</sub>NiO<sub>4</sub> has become one of the most interesting dielectric ceramics due to its extremely large  $\varepsilon' \approx 10^5 - 10^6$ . It can also exhibit a very high  $\varepsilon' \approx 10^4$  even when the frequency is increased into the GHz region.<sup>23</sup> The origin of the giant dielectric response in La<sub>2</sub>. <sub>x</sub>Sr<sub>x</sub>NiO<sub>4</sub> ceramics was intrinsically caused by the adiabatic small polaronic hopping process of Ni<sup>2+</sup> and Ni<sup>3+</sup>.<sup>24-27</sup> Therefore, La<sub>2-x</sub>Sr<sub>x</sub>NiO<sub>4</sub> is an important candidate for making high ε' flexible polymeric composites for various applications. Unfortunately, to our best knowledge, this high-permittivity La<sub>2-x</sub>Sr<sub>x</sub>NiO<sub>4</sub> ceramic has rarely been incorporated into a PVDF polymer to enhance its  $\varepsilon'$  value.<sup>28</sup>

The aim of this work was to enhance the dielectric response in a PVDF polymer by incorporating La<sub>1.7</sub>Sr<sub>0.3</sub>NiO<sub>4</sub> nanoparticles (LSNO–NPs). A novel high–performance polymeric nanocomposite system of LSNO–NPs/PVDF composites was fabricated. It was found that  $\varepsilon'$  of LSNO–NPs/PVDF composites can be greatly enhanced while retaining a low tan $\delta$  value. At  $f_{\rm LSNO}=0.35$ , the composite showed a very large  $\varepsilon'\approx3595$  with low tan $\delta<1.0$ . The mechanisms of improvement of the dielectric properties of LSNO–NPs/PVDF composites are discussed in detail.

#### 2.2 Experimental details

## 2.1 Preparation of La<sub>1.7</sub>Sr<sub>0.3</sub>NiO<sub>4</sub> nanoparticles

La<sub>1.7</sub>Sr<sub>0.3</sub>NiO<sub>4</sub> nanocrystalline powders were prepared via a chemical combustion method using urea as fuel for reaction initiation. The starting raw materials consisted of Ni(NO<sub>3</sub>)<sub>2</sub>·6H<sub>2</sub>O (99.0%, Kanto Chemical), La(NO<sub>3</sub>)<sub>3</sub>·6H<sub>2</sub>O (99.99%, Sigma–Aldrich), Sr(NO<sub>3</sub>)<sub>2</sub> (99.0%, Sigma–Aldrich), deionized water, citric acid (C<sub>6</sub>H<sub>8</sub>O<sub>7</sub>.H<sub>2</sub>O, 99.7%), and urea (CH<sub>4</sub>N<sub>2</sub>O, 99.0%). Details of the preparation method are given in elsewhere.<sup>29</sup> To obtain LSNO–NPs, the dried porous precursor was calcined at 1000 °C for 6 h.

## 2.2 Preparation of LSNO-NPs/PVDF composites

LSNO–NPs/PVDF composites with different volume fractions of LSNO–NPs ( $f_{LSNO}$ =0, 0.05, 0.1, 0.15, 0.2, 0.25, 0.3, 0.35 and 0.4) were prepared using a liquid–phase assisted dispersion method.<sup>1, 15, 17</sup> First, the prepared LSNO–NPs and purchased PVDF (Sigma–Aldrich) were mixed by ball–milling in absolute ethanol for 5 h using ZrO<sub>2</sub> balls. Second, the mixture was further dried to evaporate the absolute ethanol. Finally, the dried powders were molded by hot–pressing them at about 200 °C and  $\approx$ 10 MPa for 30 min.

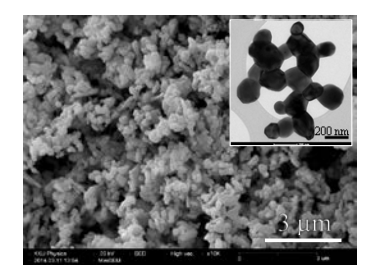
The final LSNO-NPs/PVDF composite samples had a disc-shape that was 12 mm in diameter and 1 mm in thickness.

#### 2.3 Characterization techniques and Dielectric measurements

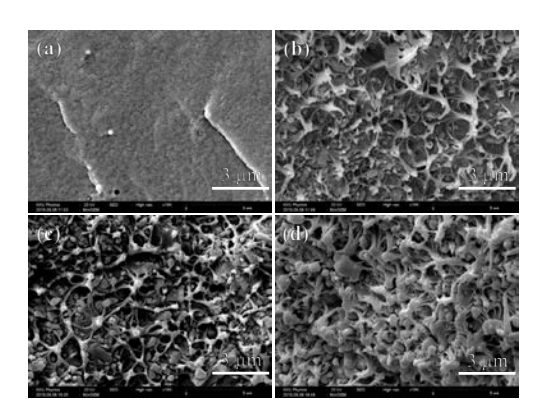
Transmission electron microscopy (TEM) (FEI Tecnai  $G^2$ , Eindhoven, Netherlands) was used to reveal the morphologies of LSNO–NPs. X–ray diffraction (XRD) (PANalytical, EMPYREAN) and scanning electron microscopy (SEM) (SEC, SNE4500M) were used to characterize the phase composition and microstructure of LSNO powder and LSNO–NPs/PVDF composites, respectively. Prior to characterizing the microstructure using SEM, polymer nanocomposite samples were initially immersed in liquid  $N_2$  and fractured. The cross–sections of the samples were coated by Au sputtering. Thermogravimetric analyses (TGA) were performed using a Pyris Diamond TGA/DTA (Perkin Elmer Instrument) with alumina as the reference material. The experiments were carried out at a heating rate of 10  $^{\circ}$ C/min in a flowing  $N_2$  atmosphere (flow rate: 100 cm $^{3}$ /min). The dielectric properties were measured using a KEYSIGHT E4990A Impedance Analyzer over the frequency range of  $10^{2}$  to  $10^{6}$  Hz at room temperature (RT) with an oscillation voltage of 500 mV. Ag paint was used as an electrode material.

#### 2.3 Results and discussion

Fig. 1 and its inset reveal the SEM and TEM images of LSNO–NPs prepared by a combustion method and calcined at 1000  $^{\circ}$ C for 6 h. Particle sizes of LSNO–NPs with nearly spherical shape had diameters of about 100–200 nm. Using an XRD technique [Fig. 3], only one phase of LSNO (JCPDS 32–1241) with a tetragonal structure was detected in the XRD pattern of the calcined LSNO powder and it showed no impurity phases. According to the analyses of phase composition and powder morphologies, this synthesized LSNO powder is suitable for incorporation into PVDF polymer to enhance its  $\epsilon'$  value.

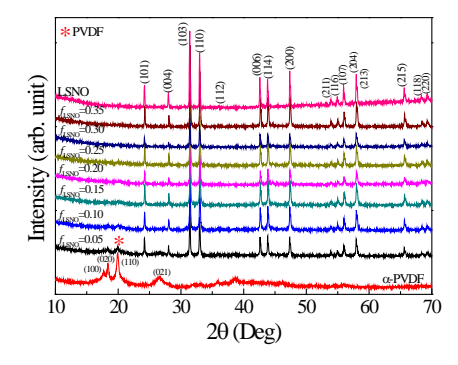


**Fig. 1** SEM image of LSNO nanoparticles obtained using a combustion method. The inset is a TEM image of LSNO nanoparticles calcined at 1000 °C for 6 h.



**Fig. 2** (a) SEM images of fracture cross section of pure PVDF polymer, (b) LSNO/PVDF nanocomposites with  $f_{LSNO}$  = 0.15 (c) 0.25, and (d) 0.30.

Fig. 2 shows the SEM images of the fractured cross–section of pure PVDF polymer and LSNO–NPs/PVDF composites with various volume fractions of LSNO filler ( $f_{LSNO}$ =0.15, 0.25 and 0.30). In Fig. 2(a), the PVDF polymer sample prepared *via* a liquid–phase assisted dispersion and hot–pressing method formed a continuous phase. As shown in Figs. 2(b–d), LSNO–NPs were homogeneously dispersed in the PVDF polymer matrix. Furthermore, a 0–3 type composite structure was confirmed in the LSNO–NPs/PVDF composites, in which LSNO–NPs were randomly distributed and surrounded by a PVDF matrix. With increasing  $f_{LSNO}$ , a small number of pores and small aggregates of LSNO–NPs were observed, as can be seen in Fig. 2(d). With regard to the effect of filler dispersion on the dielectric properties of polymer composites, <sup>17</sup> we found that good dispersion of ceramic filler in the polymer matrix improved its dielectric properties.



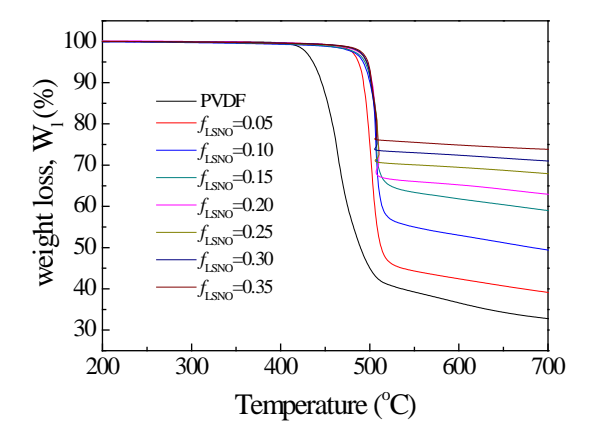
**Fig. 3** XRD patterns of LSNO nanoparticles, pure PVDF polymer and LSNO/PVDF nanocomposites with various  $f_{LSNO}$  values.

Fig. 3 illustrates the XRD patterns of LSNO powder, pure PVDF and LSNO-NPs/PVDF composites with different loading contents of LSNO ( $f_{\rm LSNO}$ =0–0.35). The existence of an  $\alpha$ -phase of PVDF was confirmed. With increasing  $f_{\rm LSNO}$ , the peak height of PVDF decreased. XRD peaks of PVDF were not observed in the composites with  $f_{\rm LSNO}$  > 0.25. This was due more to the presence of a volume fraction of LSNO-NPs than to that of a semi-crystalline PVDF phase. PVDF and LSNO phases were found, but no impurity phase was detected. It is notable that the XRD patterns of a LSNO-NPs phase were the same for all compositions. Generally, it would be suitable to evaluate and quantify the  $\beta$ -phase content, as it is the most relevant phase of PVDF for a large number of applications. Unfortunately, an  $\beta$ -phase of PVDF cannot be detected in the XRD patterns. This may be due to a small amount of this phase in pure PVDF and LSNO-NPs/PVDF composites.

The thermal stability of the PVDF matrix as a result of incorporating LSNO–NPs was investigated. The TGA curves of PVDF and LSNO–NPs/PVDF composites are shown in Fig. 4. In the temperature range of  $200-700\,^{\circ}$ C, the degradation behaviors of all the samples had a similar trend. Incorporation of LSNO–NPs into the PVDF polymer had no significant effect on its structure when compared to pure PVDF. The influence of LSNO–NPs on the thermal stability of PVDF–based composites was similar to that observed in Ba(Fe $_{1/2}$ Nb $_{1/2}$ )O $_3$ /PVDF nanocomposites. $^4$  The thermal stability of LSNO–NPs/PVDF

composites was better than that of the pure PVDF polymer. Homogeneous distribution of LSNO-NPs may inhibit the decomposition of the PVDF polymer.

Generally, the  $\varepsilon'$  values of composites with a low filler loading content (f < 0.3) for various ceramic/PVDF polymeric composites such as (Li+Ti) co-doped NiO/PVDF, BaTiO<sub>3</sub>/PVDF, CaCu<sub>3</sub>Ti<sub>4</sub>O<sub>12</sub>/PVDF, and Ba(Fe<sub>1/2</sub>Nb<sub>1/2</sub>)O<sub>3</sub>/PVDF composite systems were still lower than 50 at RT and 10  $^2$  Hz.  $^{3\text{-4},\ 12,\ 14,\ 34}$  For example, the  $\epsilon'$  values at 1 kHz of CCTO/PVDF composites with  $f_{\text{CCTO}} = 0.2$  and 0.3 were  $\approx$ 25 and  $\approx$ 45, respectively <sup>12</sup>. For Ba(Fe<sub>1/2</sub>Nb<sub>1/2</sub>)O<sub>3</sub>/PVDF nanocomposites with  $f_{BFN} = 0.2$  and 0.3, the  $\varepsilon'$  values at 100 Hz were reported to be 25 and 40, respectively. With increasing f > 0.5, the  $\varepsilon'$  values at RT and 10<sup>2</sup> Hz of these composites were still lower than 100. These results may be primarily caused by two factors: (1)  $\varepsilon'$  values of these high-permittivity fillers used were not sufficiently large  $(\epsilon' \approx 10^3 - 10^4)^{12, 35-36}$  and (2) large  $\epsilon'$  values in these ceramics were generally associated with the insulating grain boundary response, 21, 36 and thus, there were no (or less) grain boundaries in ceramic particles incorporated into PVDF matrix. As illustrated in Fig. 5, low-frequency  $\varepsilon'$  values at RT of sintered LSNO ceramics were extremely large (10<sup>5</sup>-10<sup>6</sup>) and they were nearly independent of frequency in the range of  $10^2$ – $10^5$  Hz. The extremely large  $\varepsilon'$  value of LSNO was intrinsically attributed to a small polaronic hopping mechanism in the grain interiors or inside particles.<sup>23, 25-27</sup> Therefore. such a large  $\varepsilon'$  value is usually accompanied by large values of tan $\delta$  and DC conductivity, as shown in the inset of Fig. 5. In addition to a small polaronic hopping mechanism inside the LSNO-NPs, it is expected that the dielectric response in LSNO-NPs/PVDF composites could arise the interfacial polarization of the interface between an insulting PVDF polymeric phase and semiconducting LSNO particles.



**Fig. 4** TGA curves of pure PVDF polymer and LSNO/PVDF nanocomposites with various  $f_{LSNO}$  values.

Regarding the essential properties of LSNO ceramics, the enhanced dielectric response in LSNO–NPs/PVDF composites may be larger than those of other ceramic/PVDF composites. As depicted in Fig. 6(a),  $\varepsilon'$  of the LSNO–NPs/PVDF composites greatly increased with increasing loading content of LSNO–NPs. The  $\varepsilon'$  value of pure PVDF polymer was slightly higher than 10 over the measured frequency range.  $\varepsilon'$  of LSNO–NPs/PVDF composites continuously increased with increasing  $f_{LSNO}$  from 0.10 to 0.25 over the measured frequency range. Interestingly, incorporating only 25 vol% of LSNO–NPs ( $f_{LSNO} = 0.25$ ) into PVDF can cause a great increase in  $\varepsilon'$  of  $\approx$ 205.9 and  $\approx$ 158.8 at 100 Hz and 1 kHz, respectively, while the associated  $\tan\delta$  values were 0.33 and

0.24, respectively. With further increases in  $f_{LSNO} > 0.25$ ,  $\epsilon'$  at 100 Hz greatly increased with increasing  $f_{LSNO}$ . Notably, at  $f_{LSNO} = 0.35$ , the  $\epsilon'$  values at 100 Hz and 1 kHz of the nanocomposites were 5,523.6 and 3,285.3, respectively, while tan $\delta$  at 1 kHz was 0.83. It is worth noting that the large increase in  $\epsilon'$  of LSNO–NPs/PVDF composites can be comparable to that observed in the multi walled carbon nanotube/poly(vinylidene fluoride) composite system.<sup>37</sup>

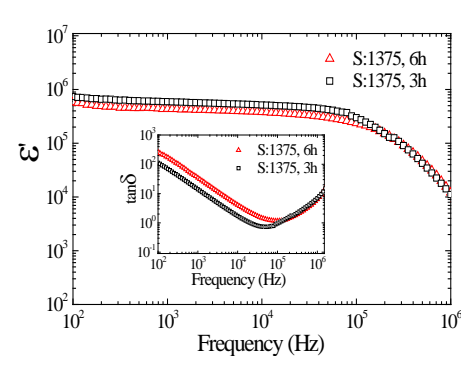
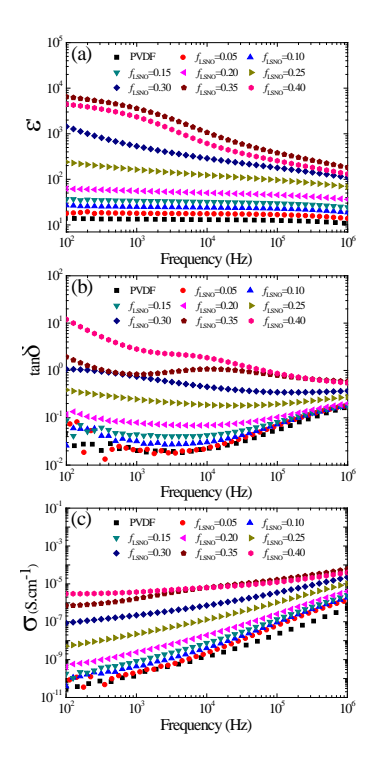


Fig. 5 Frequency dependence of dielectric permittivity ( $\epsilon'$ ) at room temperature of LSNO ceramic samples; the insets show the dielectric loss tangent (tan  $\Box$ ) as a function of frequency at room temperature.

Fig. 6(b) shows  $\tan\delta$  as a function of frequency. For the LSNO–NPs/PVDF composites with  $f_{LSNO} \leq 0.25$ , the frequency–dependent behaviors of  $\tan\delta$  were similar for all the samples. The increase in  $\tan\delta$  in a high frequency range was attributed to the relaxation process of the PVDF polymer.<sup>10</sup> At a low frequency,  $\tan\delta$  of the LSNO–NPs/PVDF composites increased with increasing  $f_{LSNO}$ . Usually, the large values of low–frequency  $\tan\delta$  of a dielectric material are associated with a long–range motion of free charge carriers, *i.e.*, DC conduction and/or interfacial polarization of the accumulated charges at internal interfaces.<sup>38</sup> This was confirmed by the observed increase in the low–frequency conductivity ( $\sigma$ ) as the LSNO–NPs loading was increased [Fig. 6(c)].

Two distinct frequency–dependent dielectric behaviors of LSNO–NPs/PVDF composites were observed, as shown in Fig. 6(a). At  $f_{\rm LSNO}=0$ –0.25,  $\varepsilon'$  was nearly independent of frequency over the measured frequency range. In contrast, at  $f_{\rm LSNO}=0.3$ –0.4, a strong frequency dependence of  $\varepsilon'$  was observed. For the composites with  $f_{\rm LSNO}=0.35$  and 0.4, plateaus of  $\varepsilon'$  were observed in the frequency range of  $10^2$ – $10^3$  Hz. A step–like decrease in  $\varepsilon'$  was observed in the range of  $10^3$ – $10^5$  Hz, corresponding to an apparent  $\tan\delta$  peak in this range. This indicates that dielectric relaxation behavior occurred rather than a dielectric response in a low–frequency range due to conductivity. The enhanced dielectric response in a low–frequency range may be correlated to strong interfacial polarization. Therefore, the greatly enhanced  $\varepsilon'$  values in a low–frequency range when  $f_{\rm LSNO} \geq 0.25$  should be attributed to strong interfacial polarization. In contrast,  $\varepsilon'$  values in a relatively high–frequency range for all samples ( $f_{\rm LSNO}=0$ –0.4) may be primarily attributed to the largely intrinsic  $\varepsilon'$  values of LSNO–NPs.



The volume fraction dependence of  $\varepsilon'$  at 1 kHz of LSNO–NPs/PVDF composites was studied by fitting the experimental  $\varepsilon'$  values with several appropriate models. This was performed to explain mechanisms of the overall dielectric behaviors for all filler volume fractions over the measured frequency range. Each technique used to understanding dielectric responses in LSNO–NPs/PVDF composites with different levels of  $f_{\rm LSNO}$  is described as follows. In first step, the experimental  $\varepsilon'$  values were fitted using the effective medium theory (EMT) and Lichtenecker's logarithmic (LL) models following their respective relations:<sup>1,5</sup>

$$\varepsilon_{eff} = \varepsilon_{PVDF} \left[ 1 + \frac{f_{LSNO} \left( \varepsilon_{LSNO} - \varepsilon_{PVDF} \right)}{\varepsilon_{PVDF} + n \left( 1 - f_{LSNO} \right) \left( \varepsilon_{LSNO} - \varepsilon_{PVDF} \right)} \right]$$
 (1)

$$\varepsilon_{eff} = f_{LSNO} \ln \varepsilon_{LSNO} + (1 - f_{LSNO}) \ln \varepsilon_{PVDF}$$
 (2)

where  $\varepsilon_{\it eff}$  is the effective dielectric permittivity of the composite. n is the filler morphology fitting factor.  $\varepsilon_{\it PVDF}$  and  $\varepsilon_{\it LSNO}$  are, respectively, the dielectric permittivities of the PVDF matrix and LSNO–NPs, which were set to 13 and 2.2×10<sup>5</sup>, respectively. To obtain the theoretical prediction curves, a very large number of  $f_{\it LSNO}$  values were input into these equations with a step-increase of 0.0025 in  $f_{\it LSNO}$  from 0–0.4. According to the fitted curve using equation (1), the n value was 0.09, which is very close to that obtained for KTa<sub>0.5</sub>Nb<sub>0.5</sub>O<sub>3</sub>/PVDF composites with n = 0.088  $^{5}$ . It is noteworthy that these two models were selected because  $\varepsilon_{\it eff}$  was theoretically predicted by considering the intrinsic dielectric permittivities of the matrix and filler without considering any of the interactions between these two materials. As illustrated in Fig. 7(a), the theoretical prediction curves of

 $\varepsilon'$  values deviated greatly from the experimental value when  $f_{LSNO} > 0.3$ , there should be another source of polarization. As clearly illustrated in the inset of Fig. 7(a), the experimental result was in very good agreement with these two models only when  $f_{LSNO} \le$ 0.2.  $\varepsilon'$  of the composite with  $f_{LSNO} = 0.25$  significantly deviated from the theoretical prediction curves calculated using equations (1) and (2). When an experimental  $\varepsilon'$  value was lower than that of a theoretical value, inhomogeneous dispersion of incorporated particles and the existence of pores are usually cited.<sup>4-5</sup> In contrast, when the experimental  $\epsilon'$  value was higher than the theoretical value, the contribution may be from additional polarization, interfacial polarization. e.g., frequency-dependent behavior of  $\varepsilon'$  of the LSNO-NPs/PVDF composites with  $f_{ISNO} \ge 0.3$ coupled with their deviations of  $\varepsilon'$  from the theoretical values, largely enhanced  $\varepsilon'$  values should be correlated with interfacial polarization in the composites.

An abrupt change in the  $\varepsilon'$  value of LSNO–NPs/PVDF composites was observed at around  $f_{LSNO} = 0.3$ –0.35, which might have been caused by the formation of a percolation network of semiconducting LSNO–NPs in the PVDF matrix. Usually, a dramatic change in electrical and dielectric properties of metal (or semiconductor)–insulator composites in a critical volume fraction of filler is caused by the percolation effect.<sup>39</sup> Thus, in second step, the rapid increase in the experimental  $\varepsilon'$  values as well as the continuous increase in  $\varepsilon'$  in a low  $f_{LSNO}$  range was fitted using the power law of the percolation theory (PT):<sup>39</sup>

$$\varepsilon_{eff} = \varepsilon_{PVDF} \left| \frac{f_c - f}{f_c} \right|^{-q} \tag{3}$$

where  $f_c$  is the percolation threshold and f is the volume fraction of conducting (or semiconducting) filler. The best fitting curve was achieved by adjusting  $f_c \approx 0.355$  and  $q \approx 1.0$ , as illustrated in Fig. 7(b). Nevertheless, it is likely that the percolation theory was unsuitable for describing the overall dielectric behavior of the LSNO-NPs/PVDF composites. As clearly seen in the inset of Fig. 7(b), the experimental  $\varepsilon'$  value began to deviate from the theoretical prediction curve at  $f_{LSNO}$ =0.1 and a large deviation was observed when  $f_{\rm LSNO}$  was increased. According to the percolation theory, <sup>39</sup> a large  $\epsilon'$  value of the composite can be achieved only when f is very close to  $f_c$  ( $f \rightarrow f_c^-$ ). When  $f < f_c$ ,  $\epsilon'$  increases very slowly at low concentrations as demonstrated by the red curve in the range of  $f_{LSNO} = 0-0.25$  [inset of Fig. 7(b)]. Experimentally, the  $\varepsilon'$  value of the LSNO-NPs/PVDF composites did not slowly increase, but continuously increased as  $f_{LSNO}$ was increased from 0 to 0.2, following conventional mixed models (i.e., EMT and LL models) for dielectric-ceramic/PVDF composites. The overall dielectric properties of the LSNO-NPs/PVDF composites cannot be fully described by the percolation theory or any of the conventional mixed models. The loading content-dependent behavior of  $\varepsilon'$  for the LSNO-NPs/PVDF composite system with low loading content was similar to that observed in other ceramic/polymer composites (e.g., Ba(Fe<sub>1/2</sub>Nb<sub>1/2</sub>)O<sub>3</sub>/PVDF<sup>4, 14</sup> and  $CaCu_3Ti_4O_{12}/PVDF$  composites<sup>12</sup>), but its  $\varepsilon'$  value was larger. For 20 vol% filler (f=0.2), the ε' values at RT and 100 Hz of the Ba(Fe<sub>1/2</sub>Nb<sub>1/2</sub>)O<sub>3</sub>/PVDF and CaCu<sub>3</sub>Ti<sub>4</sub>O<sub>12</sub>/PVDF composites were 25 and ≈30, respectively, 4, 12 while ε' of the LSNO-NPs/PVDF composite was 60.48. This larger ε' value of the LSNO-NPs/PVDF composite was primarily attributed to the greater value of  $\varepsilon'$  of the LSNO filler.

-shaped m

It was observed that the EMT and PT models can describe the dielectric behavior of LSNO–NPs/PVDF composites only in cases of low and high filler loading, respectively. Therefore, a combination of these two models may be better than either model alone. In final step, the effective medium percolation theory model (EMPT) was used to fit the dielectric behavior of LSNO–NPs/PVDF composites.  $\varepsilon_{\it eff}$  of the EMPT model is expressed as follows:<sup>40</sup>

$$\varepsilon_{eff} = \varepsilon_{PVDF} \left[ 1 + \frac{f_{LSNO} \left( \varepsilon_{LSNO} - \varepsilon_{PVDF} \right)}{\varepsilon_{PVDF} + n \left( 1 - f_{LSNO} \right) \left( \varepsilon_{LSNO} - \varepsilon_{PVDF} \right)} \right] \left| \frac{f_c - f}{f} \right|^{-q}$$
(4)

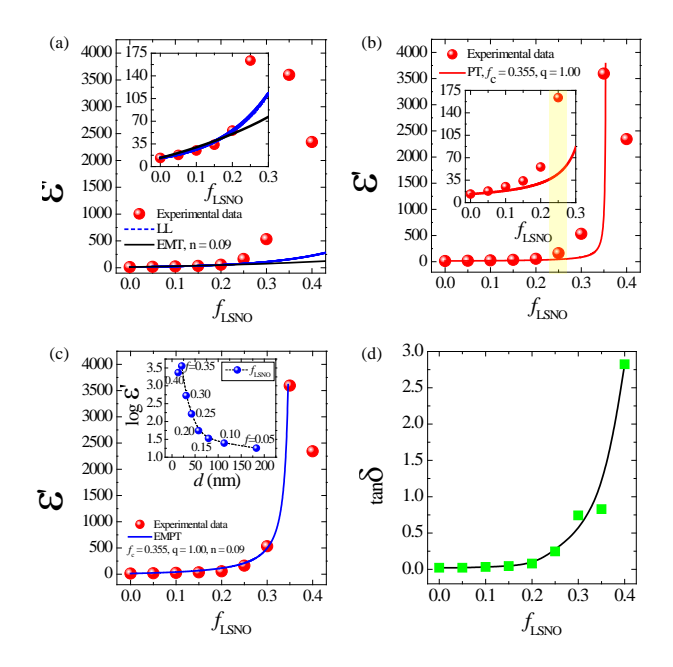
Using the same fitting conditions in the EMT and PT models, the fitted result of EMPT model nearly matches the experimental  $\varepsilon'$  values over filler loading contents ranging from  $f_{\rm LSNO}=0$  to 0.4 [Fig. 7(c)]. The best fitting parameters for the EMPT model were  $f_c=0.355$ , n=0.09, and q=1.0. Theoretically,  $f_c$  of a spherical is about 0.16, which is much smaller than  $f_c=0.355$  for the LSNO-NPs/PVDF composites. Usually,  $f_c$  increases with decreasing conductivity of the fillers. A large  $f_c$  value was therefore due to the semiconducting property of the LSNO-NPs. According to the fitted results using the EMPT model, it is likely that more than one mechanism had a significant influence on the dielectric responses of LSNO-NPs/PVDF composites. All possible mechanisms in the distinct loading contains of filler can be described as follows.

For the composites with  $f_{LSNO}=0-0.2$ , the continuous increase in  $\varepsilon'$  in with low filler loading contents was dominated by the intrinsic polarization inside the LSNO-NPs. Interfacial polarization at the interface between semiconducting LSNO-NPs and insulating PVDF layers had an effect on the dielectric response in this range, but it was small because of a low polarized interfacial area. The average distance (d) between neighboring particles in the PVDF matrix for various filler volume fractions can be calculated from the relation  $d = r \left[ \left( 4\pi / 3 f_{LSNO} \right)^{1/3} - 2 \right]$ , where r is the average radius of LSNO-NPs. <sup>41-42</sup> As shown in the inset of Fig. 7(c), the interparticle distance was larger than 50 nm when  $f_{LSNO}$ ≤ 0.2. It is likely that the formation of microcapacitors in the LSNO-NPs/PVDF composites with  $f_{LSNO}=0-0.2$  was not dominate due to the large distance between neighboring LSNO-NPs. Consequently, electromagnetic coupling between particles was very weak, and hence the local electric field and ε' value were very low. Generally, a low-frequency  $tan\delta$  value of a dielectric is correlated with a long range transfer of electrons. Conduction in a composite can occur by electron transfer between the conducting particles in intimate contact and/or by tunneling of electrons between the uncontacted particles at distances of less than 10 nm. 41-42 As illustrated in Fig. 7(d),  $tan\delta$  slightly increased with increasing  $f_{LSNO}$ in the range of 0-0.2. All composites exhibited a very small tanδ<0.1 at 1 kHz. This is because the LSNO-NPs were separated from each other and roughly thought to be completely surrounded by a thick layer of an insulating PVDF matrix (> 50 nm). So, contact between particles and tunneling of electrons could not occur.

For the composites with  $f_{LSNO}=0.25-0.35$ , the drastic increase in  $\varepsilon'$  may have been caused by the percolation effect. Although the increase in  $\tan\delta$  was more dominant than that of the composites with  $f_{LSNO}\leq0.2$ ,  $\tan\delta$  slightly increased when  $f_{LSNO}$  was increased from 0.3 to 0.35. Thus, formation of a percolation network was unlikely occurred,

corresponding to the theoretical fitted value for  $f_c = 0.355$ . Furthermore, when  $f_{LSNO}$  was increased from 0.25 to 0.35, the interparticle distance was reduced from ≈44 to ≈22 nm. Thus, tunneling of electrons between particles with a large distance from each other (>10 nm) still could not happen, allowing these materials to retain their low tan $\delta$  values (< 1.0 at RT and 1 kHz). With increasing filler loading of LSNO-NPs in a PVDF matrix, the interfacial area, which can be roughly estimated to be equal to the total surface area of LSNO-NPs, greatly increased. This is one of the most important factors contributing to the enhanced  $\varepsilon'$  value.<sup>41</sup> Another important cause is that the interparticle distance was lessened, but the LSNO-NPs were still separated by a PVDF layer. When the thickness of the PVDF layer between LSNO-NPs was sufficiently reduced to nearly 10 nm, an overlapping of diffused double layer charge clouds, i.e., Debye length, around the semiconducting LSNO-NPs may have formed. 41, 43 The electromagnetic coupling between semiconducting LSNO-NPs surfaces became stronger, thereby increasing the local electric field strength. In this case, it can be expected that the electric field strength was sufficiently strong to orientate the dipoles in PVDF layer of neighboring particles. Both the charge ordering polarization inside LSNO-NPs and dipolar polarization in the PVDF layers can cause a sudden increase in  $\varepsilon'$ . This explanation from the viewpoint of a microcapacitor structure can be reasonably described as follows. Under an applied external electric field, induced surface charges of neighboring LSNO-NPs behaved as electrode-like plates, in which they were separated by an insulating PVDF dielectric-layer. With increasing  $f_{LSNO}$ , a large number of microcapacitors were produced in the PVDF matrix. The capacitance of each microcapacitor was enhanced because the thickness of the PVDF layer was reduced, resulting from shorter interparticle distances. The explanation of the results in terms of a microcapatior network in a conductive/polymer composite was clearly demonstrated by Simoes et al.44 The numerical model was developed and successfully compared to the experimental result. They have demonstrated that below the percolation threshold, highly dispersed conductive fillers can form capacitor networks in the polymer matrix. Furthermore, it was shown that  $\varepsilon'$  and the dielectric strength of the conductive/polymer composite were greatly dependent on the distribution of fillers, leading to high deviations of the electrical properties.

When a filler load of LSNO–NPs was incorporated into PVDF at levels higher than  $f_c$  ( $\approx$ 0.355),  $\epsilon'$  of the LSNO–NPs/PVDF composite greatly decreased [Fig. 7(c)], while  $\tan\delta$  significantly increased [Fig. 7(d)]. As depicted in the inset of Fig. 7(c), when  $f_{\rm LSNO}$ =0.4, the calculated interparticle distance was  $\approx$ 14 nm, which is very close to the lower theoretical limit thickness of the PVDF layer (10 nm) necessary to inhibit conduction of free charges. Therefore, the possibility of electron tunneling between the uncontacted particles separated by a thin layer of LSNO–NPs was very high. The percolation threshold was  $\approx$ 0.355. Thus, conduction between particles in intimate contact could occur in composites with very high LSNO–NP filler loading. The interparticle distance was very much shortened, and the energy required for electron movement between the conducting phases across a PVDF layer can be negligible, giving rise to a frequency independent conductivity, as shown in Fig. 6(c).<sup>41</sup>



## 2.4 Conclusions

The dielectric properties of PVDF polymer were successfully enhanced by incorporating it with LSNO-NPs, which were easily synthesized using a combustion method. Liquid-phase assisted dispersion and hot-pressing methods were successfully used to prepare LSNO-NPs/PVDF composites with good dispersion of filler. Interstingly, incorporation of LSNO-NPs can cause improved thermal properties of a PVDF polymer. The greatly enhanced dielectric response, ε'≈3,285 at 1 kHz, was accomplished by incorporating 35 vol% LSNO-NPs into a PVDF polymer, while a low tanδ≈0.83 was obtained. The overall \( \varepsilon' \) values were well described by the EMPT model, indicating that there were several mechanisms contributing to the dielectric properties of the composites with different volume fractions of filler. For the composites with  $f_{LSNO} \leq 0.2$ , the observed continuous increase in  $\varepsilon'$  was primarily attributed to the very large  $\varepsilon'$  of the LSNO-NP filler. The dramatically enhanced  $\varepsilon'$  of LSNO–NPs/PVDF composites in the range of  $f_{LSNO}$ > 0.25-0.35 resulted from the large interfacial area between the semiconducting filler and insulating PVDF matrix combined with a very short interparticle distance between the LSNO-NPs (≈20-30 nm) separated by a thin layer of PVDF, creating largely capacitive microcapacitors in the composites.

#### References

- 1 Z.-M. Dang, J.-K. Yuan, J.-W. Zha, T. Zhou, S.-T. Li and G.-H. Hu, *Prog. Mater. Sci.*, 2012, **57**, 660-723.
- 2 Z. M. Dang, J. B. Wu, L. Z. Fan and C. W. Nan, *Chem. Phys. Lett.*, 2003, **376**, 389-394.
- 3 Z.-M. Dang, H.-Y. Wang and H.-P. Xu, Appl. Phys. Lett., 2006, 89, 112902.
- 4 Z. Wang, M. Fang, H. Li, Y. Wen, C. Wang and Y. Pu, *Composites Science and Technology*, 2015, **117**, 410-416.
- 5 G. Chen, X. Wang, J. Lin, W. Yang, H. Li and Y. Wen, *The Journal of Physical Chemistry C*, 2016, **120**, 28423-28431.
- 6 J. Bi, Y. Gu, Z. Zhang, S. Wang, M. Li and Z. Zhang, Materials & Design, 2016, 89, 933-940.
- 7 L. Zhang, R. Gao, P. Hu and Z.-M. Dang, *RSC Advances*, 2016, **6**, 34529-34533.
- 8 Q. Huang, H. Luo, C. Chen, X. Zhou, K. Zhou and D. Zhang, *J. Alloys Compd.*, 2017, **696**, 1220-1227.
- 9 U. Yagoob and G.-S. Chung, *J. Alloys Compd.*, 2017, **695**, 1231-1236.
- 10 X. Jiang, X. Zhao, G. Peng, W. Liu, K. Liu and Z. Zhan, *Current Applied Physics*, 2017, **17**, 15-23.
- 11 M. Arbatti, X. Shan and Z. Y. Cheng, Adv. Mater., 2007, 19, 1369-1372.
- 12 P. Thomas, K. T. Varughese, K. Dwarakanath and K. B. R. Varma, *Composites Science and Technology*, 2010, **70**, 539-545.
- 13 Y.-I. Su, C. Sun, W.-q. Zhang and H. Huang, J. Mater. Sci., 2013, 48, 8147-8152.
- 14 M. Fang, Z. Wang, H. Li and Y. Wen, Ceram. Int., 2015, 41, Supplement 1, S387-S392.
- 15 P. Kum-onsa, P. Thongbai, S. Maensiri and P. Chindaprasirt, *J. Mater. Sci.: Mater. Electron.*, 2016, **27**, 9650-9655.
- 16 K. Meeporn, S. Maensiri and P. Thongbai, *Appl. Surf. Sci.*, 2016, **380**, 67-72.
- 17 K. Silakaew, W. Saijingwong, K. Meeporn, S. Maensiri and P. Thongbai, *Microelectron. Eng.*, 2015, **146**, 1-5.
- 18 R. K. Goyal, S. S. Katkade and D. M. Mule, *Composites Part B: Engineering*, 2013, **44**, 128-132.
- 19 B. Shri Prakash and K. B. R. Varma, *Composites Science and Technology*, 2007, **67**, 2363-2368.
- 20 C. Yang, H.-s. Song and D.-b. Liu, Composites Part B: Engineering, 2013, 50, 180-186.
- 21 R. Schmidt, M. C. Stennett, N. C. Hyatt, J. Pokorny, J. Prado-Gonjal, M. Li and D. C. Sinclair, *J. Eur. Ceram. Soc.*, 2012, **32**, 3313-3323.
- 22 J. Fu, Y. Hou, Q. Wei, M. Zheng, M. Zhu and H. Yan, J. Appl. Phys., 2015, 118, 235502.
- 23 S. Krohns, P. Lunkenheimer, C. Kant, A. V. Pronin, H. B. Brom, A. A. Nugroho, M. Diantoro and A. Loidl, *Appl. Phys. Lett.*, 2009, **94**, 122903.
- 24 J. Wang, G. Liu, B. W. Jia, X. Q. Liu and X. M. Chen, Ceram. Int., 2014, 40, 5583-5590.
- 25 A. Chouket, O. Bidault, V. Optasanu, A. Cheikhrouhou, W. Cheikhrouhou-Koubaa and M. Khitouni, *RSC Adv.*, 2016, **6**, 24543-24548.
- 26 K. Meeporn, N. Chanlek and P. Thongbai, RSC Advances, 2016, 6, 91377-91385.
- 27 X. Q. Liu, S. Y. Wu and X. M. Chen, *J. Alloys Compd.*, 2010, **507**, 230-235.
- 28 R. Kumar, A. M. Goswami and M. Kar, AIP Conf. Proc., 2016, 1728, 020580.
- 29 K. Meeporn, T. Yamwong and P. Thongbai, Jpn. J. Appl. Phys., 2014, 53, 06JF01.
- 30 Z. D. Liu, Y. Feng and W. L. Li, RSC Advances, 2015, 5, 29017-29021.
- 31 P. Martins, A. C. Lopes and S. Lanceros-Mendez, Prog. Polym. Sci., 2014, 39, 683-706.
- 32 A. C. Lopes, C. M. Costa, R. S. i. Serra, I. C. Neves, J. L. G. Ribelles and S. Lanceros-Méndez, *Solid State Ionics*, 2013, **235**, 42-50.
- 33 S. F. Mendes, C. M. Costa, C. Caparros, V. Sencadas and S. Lanceros-Méndez, *J. Mater. Sci.*, 2012, **47**, 1378-1388.
- 34 Z.-M. Dang and C.-W. Nan, Ceram. Int., 2005, **31**, 349-351.
- 35 A. R. West, T. B. Adams, F. D. Morrison and D. C. Sinclair, *J. Eur. Ceram. Soc.*, 2004, **24**, 1439-1448.
- 36 X. Sun, J. Deng, S. Liu, T. Yan, B. Peng, W. Jia, Z. Mei, H. Su, L. Fang and L. Liu, *Applied Physics A*, 2016, **122**, 864.

- 37 P. Costa, J. Silva and S. Lanceros Mendez, *Composites Part B: Engineering*, 2016, **93**, 310-316.
- 38 P. Lunkenheimer, S. Krohns, S. Riegg, S. G. Ebbinghaus, A. Reller and A. Loidl, *The European Physical Journal Special Topics*, 2010, **180**, 61-89.
- 39 C. W. Nan, Y. Shen and J. Ma, *Annu. Rev. Mater. Res.*, 2010, **40**, 131-151.
- 40 C. Li, S. Yu, S. Luo, W. Yang, Z. Ge, H. Huang, R. Sun and C.-P. Wong, *RSC Advances*, 2016, **6**, 36450-36458.
- 41 K. S. Deepa, M. T. Sebastian and J. James, Appl. Phys. Lett., 2007, 91, 202904.
- 42 J. I. Hong, L. S. Schadler, R. W. Siegel and E. Mårtensson, *Appl. Phys. Lett.*, 2003, **82**, 1956-1958.
- 43 F. Claro, Phys. Rev. B, 1982, 25, 7875-7876.
- 44 S. Ricardo, S. Jaime, V. Richard, S. Vítor, C. Pedro, G. João and L.-M. Senentxu, *Nanotechnology*, 2009, **20**, 035703.

## **CHAPTER 3**

#### 

#### 3.1 Introduction

High -permittivit their important applications in the electrical and electronic industries, especially for high energy storage devices [1-6]. Ferroelectric oxides such as BaTiO<sub>3</sub>, Ba<sub>x</sub>Sr<sub>1-x</sub>TiO<sub>3</sub> and Pb(Zr,Ti)O<sub>3</sub>, as well as perovskite 3 TikeO422 Ceramics can exhibit high dielectric permittivity ( $\varepsilon' \approx 10^3 - 10^5$ ), but they are brittle, require high processing temperatures and have a low dielectric strength [1, 2, 7-10]. The uses of these ceramics may be limited in some electronics applications. Alternatively, polymers are flexible, easy to process and have a high dielectric strength as well as low dielectric loss tangent ( $tan\delta$ ) [8, 9, 11-13]. The only disadvantage of a dielectric polymer is its low  $\varepsilon'$  compared to those of ceramic oxides. Therefore, investigations on the enhancement of  $\epsilon'$  values of polymers have been widely conducted in recently years [8, 9, 11-23]. A conventional method is to incorporate e/perarhuteis, it follows in oic so im tentioly anders to enh mixture rules. This method is an effective and promising way to overcome the disadvantage of dielectric polymers. It is expected that ceramic -polymer c be a better alternative and offer excellent material characteristics, including flexibility, low- temperature manufacture and good dielectric properties.

Generally, poly(vinylidene fluoride) (PVDF) is used as a polymer matrix because of its high  $\epsilon'$  value of  $\approx 10$  - 12 at robreakdown field, low  $\tan \delta$ , low cost and high reliability [3, 13, 24, 25]. High -permittivity dielectric ceramics, including BaTiO<sub>3</sub>, Ba<sub>x</sub>Sr<sub>1-x</sub>TiO<sub>3</sub>, Pb(Zr,Ti)O<sub>3</sub>, CaCu<sub>3</sub>Ti<sub>4</sub>O<sub>12</sub> and (Li, Ti) co-doped NiO (LNTO), have often been used as a filler material in the polymer matrix to enhance the  $\epsilon'$  of polymer matrix [1, 3, 5, 8, 9, 13, 24]. Although many excellent studies have been done, there still exists some limitations, especially with regard to attaining low  $\epsilon'$  values and/or high  $\tan \delta$  (> 1.0 at 1 kHz) of these composite systems.  $\epsilon'$  values of some composite systems were quite high and can be as high as  $\approx 100$  at  $10^3$  Hz even when the loading of a filler was  $\geq 50$  vol%. The polymer composite loses its flexibility at high ceramic contents. Therefore, it is crucial to choose suitable high -permittivity ceramic fillers.

Recently, extremely high  $\epsilon'$  values of  $\approx 10^5$  –  $10^6$  at room temperature were observed in Ln<sub>2-x</sub>Sr<sub>x</sub>NiO<sub>4</sub> ceramics (Ln = La<sup>3+</sup>, Sm<sup>3+</sup>, and Nd<sup>3+</sup>) in the radio frequency range. The  $\epsilon'$  values were still too large ( $\approx 10^4$ ) even when the frequency was increased into the GHz region [26]. However,  $\tan \delta$  values of these Ln<sub>2-x</sub>Sr<sub>x</sub>NiO<sub>4</sub> ceramics were too large (> 10) [26-29], which is one of the most serious obstacles to their use in practical applications. In considering these Ln<sub>2-x</sub>Sr<sub>x</sub>NiO<sub>4</sub> ceramics for use as filler materials in polymeric composites, the very high  $\tan \delta$  of these ceramics may cause an extreme increase in the  $\tan \delta$  of Ln<sub>2-x</sub>Sr<sub>x</sub>NiO<sub>4</sub>/polymer composites. Thus, improved dielectric properties of Ln<sub>2-x</sub>Sr<sub>x</sub>NiO<sub>4</sub> ceramics should be obtained before attempting to use these ceramics in polymer composites.

In the current study, reduction of  $tan\delta$  with retaining the high  $\epsilon'$  value of  $La_{2-x}Sr_xNiO_4$  (LSNO) ceramics was first done by doping with  $Mg^{2+}$  ions. This Mg

-doped LS

was expected to be suitable for use as a filler material in a PVDF matrix to obtain enhanced  $\varepsilon'$  value, while retaining appropriate  $\tan \delta$  values of the polymer composites.

#### 3.2 Experimental details

#### 2.1 Preparation of Mg- doped La<sub>2-x</sub>Sr<sub>x</sub>NiO<sub>4</sub> particles

In this work, La<sub>1.9</sub>Sr<sub>0.1</sub>Ni<sub>0.6</sub>Mg<sub>0.4</sub>O<sub>4</sub> (LSNMO) powder was prepared by a combustion method using urea as a fuel for reaction initiation. The starting raw materials consisted  $La(NO_3)_3 \cdot 6H_2O$ (99.99%, Sigma- Aldrich),  $Sr(NO_3)_2$ Sigma-Aldrich),  $Ni(NO_3)_2 \cdot 6H_2O$  (99.0%, Kanto Chemical),  $Mg(NO_3)_2 \cdot 6H_2O$  (99%, Sigma- Aldrich), deionized water, citric acid (C<sub>6</sub>H<sub>8</sub>O<sub>7</sub>.H<sub>2</sub>O, 99.7%) and urea (CH<sub>4</sub>N<sub>2</sub>O, 99.0%). First, stoichiometric amounts of Ni(NO<sub>3</sub>)<sub>2</sub>·6H<sub>2</sub>O, La(NO<sub>3</sub>)<sub>3</sub>·6H<sub>2</sub>O, Sr(NO<sub>3</sub>)<sub>2</sub> and Mg(NO<sub>3</sub>)<sub>2</sub>·6H<sub>2</sub>O were dissolved in an aqueous solution of citric acid with constant stirring at room temperature until a transparent clear solution was obtained. Second, 0.7 g of urea powder was added into the mixed solution with stirring at 200 °C until a viscous gel formed. Then, the gel was dried at 300 °C for 0.5 h yielding a dried porous precursor. Finally, the resulting dried porous precursor was ground and calcined at 1000 °C for 6 h to form a pure LSNMO phase. A portion (0.35 g) of the calcined LSNMO powder was pressed into pellets having dimensions of 9.5 mm in diameter and ≈1.2 mm in thickness by uniaxial compression at 200 MPa. This green body was sintered in air at 1375 °C for 6 h and used for studying the dielectric properties of its bulk ceramic.

## 2.2 Preparation of LSNMO/PVDF composites

LSNMO/PVDF composites were prepared using a liquid -phase assisted dispersion method [30]. First, the prepared LSNMO particles and commercially obtained PVDF (Sigma -Aldrich Co., France using ZrO<sub>2</sub> balls. Second, the mixture was further dried to evaporate the ethanol. Finally, the dry mixture of LSNMO and PVDF powders was molded by hot \$\frac{9}{2}\text{press}\text{sing at 200}\$ 30 min. The resulting composite samples had a disc- shape that was 12 mm in diameter and \$\approx 1\text{ mm in thickness.}\$

#### 2.3 Characterization techniques and Electrical measurements

X-ray diffraction (XRD) (PANalytical, EMPYREAN) and scanning electron microscopy (SEM) (SEC, SNE4500M) were used to characterize the phase composition and microstructure of pure PVDF, LSNMO- NPs and LSNMO/PVDF composites. The dielectric properties were measured using a KEYSIGHT E4990A Impedance Analyzer over the frequency range of 10<sup>2</sup> to 10<sup>6</sup> Hz at room temperature with an oscillation voltage of 500 mV. Silver paint was used as an electrode material.

## 3.3 Results and discussion

Figure 1 shows the XRD patterns of the LSNMO powder, pure PVDF and LSNMO/PVDF composites with different volume fractions of LSNMO (f). A single phase of LSNO with a tetragonal structure was found in the LSNMO powder, which was used as a ceramic filler in the PVDF polymer matrix. All diffraction peaks of the LSNMO powder were indexed to the tetragonal crystal structure (JCPDS 32 -1241). No impurity was detected in the XRD patterns of the LSNMO powder. Even the Mg -coxiated phase was absent. This may indicate that Mg<sup>2+</sup> dopant was completely substituted into the

Ni sites in the LSNO structure. The XRD pattern is similar to those reported in the literature for LSNO ceramics [31, 32]. As shown in Fig. 2(a), particle sizes of the LSNMO powder were of about 1  $-3 \mu m$ .

The XRD pattern of PVDF indicates the presence of a semi- crystalline structure. The shape peaks were observed at  $2\theta \approx 17.69$ , 18.36, 19.93 and  $26.61^{\circ}$ . These were respectively attributed to diffraction at the (100), (020), (110) and (021) planes of the  $\alpha$  [33]as The XRDD Fpeaks of PVDF were only observed in the LSNMO/PVDF composites with low loadings of LSNMO filler (at f < 0.2). For the composites with high volume fractions of LSNMO, no diffraction peaks of PVDF were seen. This was due to the shielding effect of relatively high intensity of the diffraction peaks of the LSNMO ceramic.

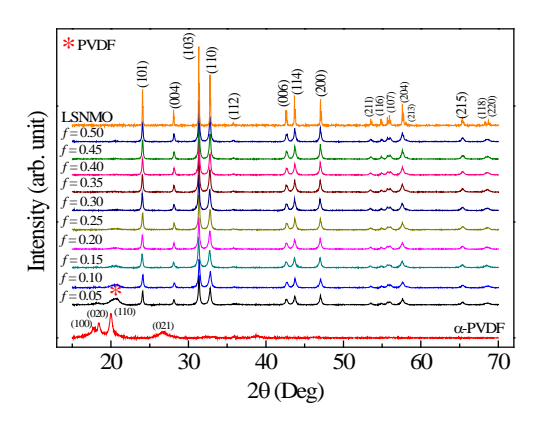


**Fig. 1** XRD patterns of LSNMO nanoparticles, pure PVDF and LSNMO/PVDF composites with different volume fractions of LSNMO.

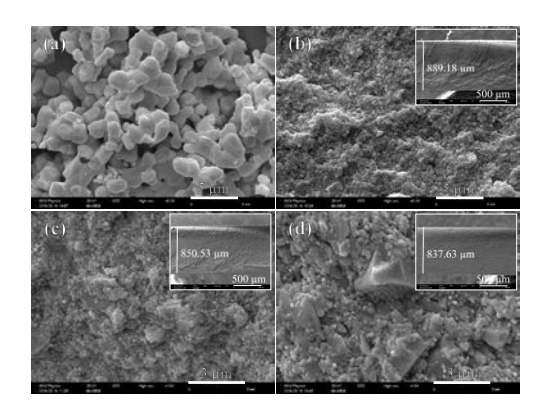


**Fig. 2** (a) SEM image of LSNMO nanoparticles. (b–d) SEM images of cross sections of LSNMO/PVDF composites with f = 0.20, 0.40 and 0.50, respectively; insets are their SEM images with low magnification to determine the thickness of the polymer composites.

Figures 2(b) -(d) show composites films with f = 0.20, 0.40 and 0.50, respectively, revealing good dispersion of LSNMO particles in the PVDF polymer matrix. The 0 -3 connect composites was observed. This is because LSNMO nanoparticles were randomly surrounded by a PVDF matrix. Interestingly, only a small number of pores were observed in the composites, even though the volume fraction of filler was as high as 50 vol% ( $f = \frac{1}{2}$ ) show the composite of the properties of the properties

0.5). The thickness of LSNMO/PVDF composites was in the range of 0.83 - 0.89 mm [insets of Figs. 2(b)

-(d)]. Generally, the

has a great effect on the dielectric properties of polymeric composites. Thus, good dispersion of LSNMO particles is expected to contribute to the improved dielectric properties of PVDF polymer composites.

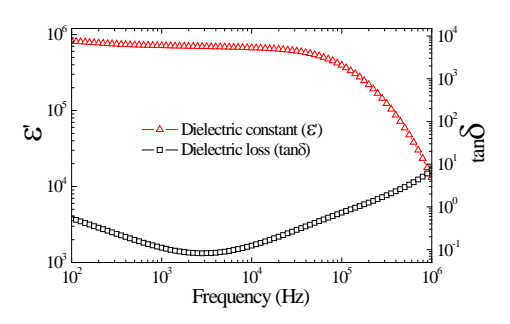


**Fig. 3** Frequency dependence of of ε' and tan the LSNMO ceramic sintered at 1375 °C for 6 h.

☐ (measured at ro

The dielectric properties of the sintered LSNMO ceramics are shown in Fig. 3. As clearly seen,  $\epsilon'$  showed a weak frequency dependence in the range of  $10^2$  –  $10^5$  Hz, while  $\tan\delta$  was lower than 1.0 under this condition. Usually,  $\tan\delta$  values of un —doped LSNO ceramics are larger than 10 over a wide frequency range [31, 32]. Thus, the LSNMO ceramic particles may be suitable for use as filler due to their low  $\tan\delta$  and very high  $\epsilon'$ .

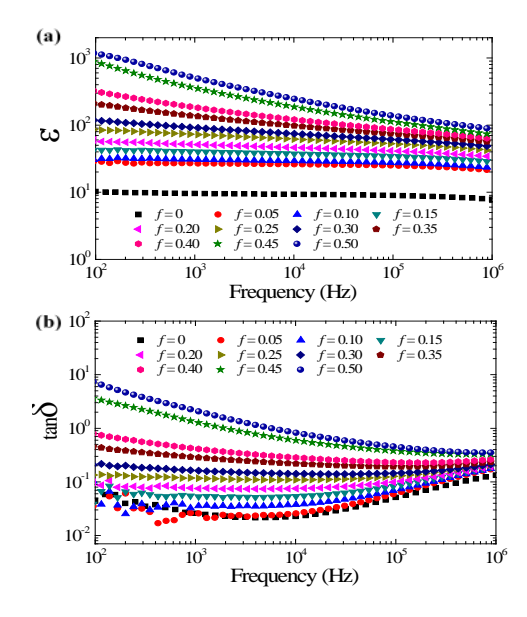


**Fig. 4** Frequency dependence of (a) ε' and (b) tanδ at room temperature for LSNMO/PVDF composites with various volume fractions of LSNMO (f).

The frequency dependencies of  $\epsilon'$  and  $\tan\delta$  measured at room temperature for LSNMO/PVDF composites with various loadings of LSNMO filler are shown in Fig. 4. As expected,  $\epsilon'$  and  $\tan\delta$  increased with increasing LSNMO content in PVDF.  $\epsilon'$  of pure PVDF and the composites with  $f \leq 0.30$  showed a relatively stable frequency dependence in the range of  $10^2$  –  $10^6$  Hz. Over this frequency range,  $\epsilon'$  of the LSNMO/PVDF composites increased with increasing LSNMO content. However, an obvious frequency dependence

of  $\varepsilon'$  was observed with further increases in the volume fraction of LSNMO in the range of f = 0.35 for f = 0.35

dependence of  $\epsilon'$  in a low

-frequency

polarization and/or long range motion of charges. The  $\epsilon'$  values of all the LSNMO/PVDF composites were higher than that of pure PVDF, but much lower than that of the sintered LSNMO ceramic. As demonstrated in Fig. 1, only the  $\alpha$ -phase of PVDF was detected, which is a non—lapophase [33]. The constrained polymer chain inhibited the electrical polarization in the composite system [12]. Therefore, the  $\epsilon'$  value of the LSNMO/PVDF composites was much lower than that of the LSNMO ceramic [12]. Interestingly, strongly enhanced  $\epsilon' \approx 10^3$  at  $10^2$  Hz was obtained for the LSNMO/PVDF composite with f = 0.5, which was  $\approx 100$  times higher than that of pure PVDF.

As shown in Fig. 4(b),  $\tan \delta$  of PVDF and the composites with f = 0.05-0.30increased with increasing frequency from 10<sup>4</sup> to 10<sup>6</sup> Hz. This signifies the appearance of a relaxation peak of  $tan\delta$ , which is indicative of dielectric relaxation behavior. This dielectric relaxation can be referred to  $\alpha_a$  relaxation and it is due to dipole polarization of PVDF [16]. For high volume fractions of LSNMO ( $f \ge 0.35$ ), a bw  $\delta$ --orfelg8 bHM $\phi$ /12MDF composites increased with increasing LSNMO loading. This low -frequency response of the LSNMO/PVDF composites can be caused by the DC conduction behavior inside the composites and/or the low rélia sparté on cyprocess [1]. To confirm this, the AC conductivity of the composites was studied. As shown in Fig. 5, the low -frequency conductivity of the composite gradually increased as the LSNMO volume fraction increased from in the range of f < 0.4. When f > 0.4, the low -frequency LSNMO/PVDF composite was greatly enhanced and it was nearly independent of frequency in the range of 10<sup>2</sup> - 10<sup>3</sup> Hz. These results clearly indicate the dominate effect of DC conduction in the composites.

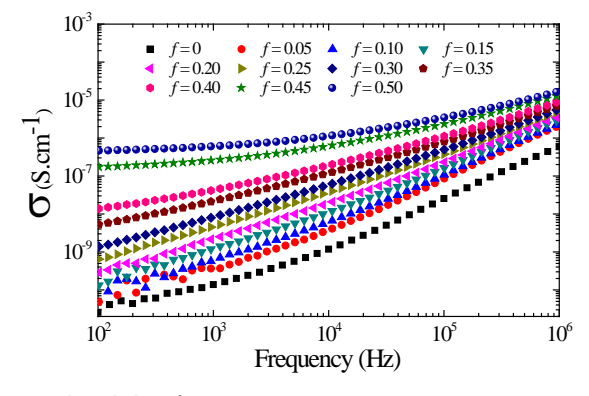


**Fig. 5** AC conductivity ( 0.5).

(t) Qt-room tempe

To clearly understand the possible mechanisms of the dielectric response in the composites over the range of LSNMO loadings, the volume —fraction decelectric properties ( $\varepsilon'$  and  $\tan\delta$ ) and conductivity ( $\sigma$ ) of the LSNMO/PVDF composites at room temperature (at 1 kHz) was studied. As shown in Fig. 6, variations in  $\varepsilon'$ ,  $\tan\delta$  and  $\sigma$  as a function of LSNMO loading show a similar trend. The  $\varepsilon'$ ,  $\tan\delta$  and  $\sigma$  [inset of Fig. 6b] values gradually increased with increasing volume fraction of LSNMO for f < 0.4. Interestingly, with further increases in the LSNMO volume fraction above f = 0.4, the  $\varepsilon'$ ,  $\tan\delta$  and  $\sigma$  values dramatically increased. When the LSNMO volume fraction was 0.40, good dielectric properties were achieved. At 1 kHz,  $\varepsilon'$  was  $\approx$ 183, which is  $\approx$ 18 times larger

than that of pure PVDF ( $\approx$ 10), while its tan $\delta$  was lower than 0.5. At f = 0.5,  $\epsilon'$  was as high as 503.73, which is  $\approx$ 50 times higher than that of PVDF.

-polymer composite

As discussed above, the overall dielectric and electrical properties likely obeyed the percolation theory, which is usually found in conductive However, another important observation with a relatively low volume fraction of filler (f < 0.4) should be carefully considered. The  $\varepsilon'$  and  $\tan\delta$  values of the LSNMO/PVDF composites continuously increased with increasing filler concentration (Fig. 6a and the inset of Fig. 6b). These behaviors are totally different from that observed in the conductive **rpolympe**sites, where  $\varepsilon'$  and  $\sigma$  rise very slowly at low concentrations of filler (or at a filler concentration lower than the percolation threshold). At f < 0.4, it was observed that the variation in  $\epsilon'$  and  $\sigma$  was similar to that observed in other modely composites such as CaCu<sub>3</sub>Ti<sub>4</sub>O<sub>12</sub>/PVDF [12] and BaTiO<sub>3</sub>/PVDF ceramic composites [16]. Thus, the overall dielectric and electrical properties of the LSNMO/PVDF composites cannot be fully described by the percolation theory or any conventional mixed model. In contrast, the combination of these two models may be suitable for describing the dielectric behavior of LSNMO/PVDF composites.

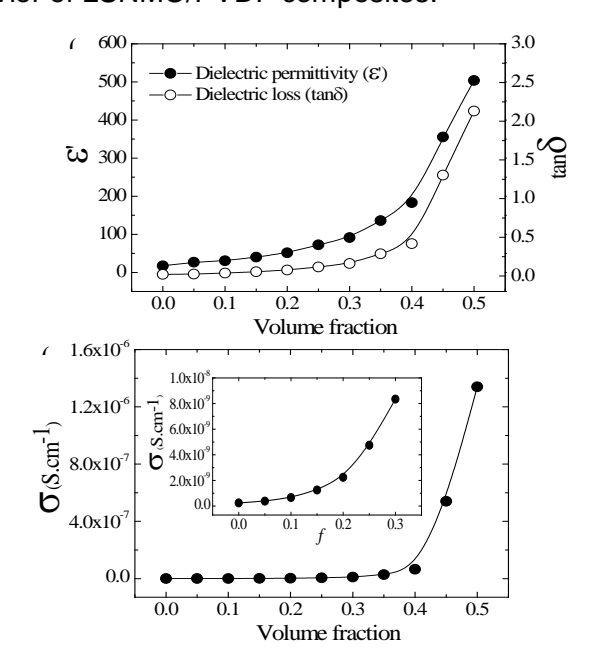


**Fig. 6** (a) Dependence of  $\varepsilon'$  and tanδ values (at 1 kHz and room temperature) on the volume fraction of LSNMO filler. (b) AC conductivity (σ) of LSNMO/PVDF composites as a function of LSNMO volume fraction (f) measured at 1 kHz and room temperature; inset shows the enlarged scale in the range of f = 0 - 0.3.

To better understand the dielectric behavior of the LSNMO/PVDF composites, the effective medium percolation theory model (EMPT) was developed [5, 14]. This model is the combination of the effective medium theory (EMT) model and the percolation model [14]. The effective dielectric permittivity ( $\mathcal{E}_{r}$ ) of the EMPT model is expressed as follows:

$$\varepsilon_r = \varepsilon_1 \left[ 1 + \frac{f_{\rm CST}(\varepsilon_2 - \varepsilon_1)}{\varepsilon_1 + n(1 - f_{\rm CST})(\varepsilon_2 - \varepsilon_1)} \right] |(f_c - f_{\rm CST})/f_{\rm CST}|^{-q} \tag{1}$$

where  $f_{\varepsilon}$  is the percolation threshold of the conductive or semi-conductive filler.  $\varepsilon_1$  and  $\varepsilon_2$  are dielectric permittivity values of polymer matrix and filler ( $\varepsilon_1 = 10$  and  $\varepsilon_2 = 7.13 \times 10^5$ ).

 $f_{cer}$  is the volume fraction of the ceramic semi-conductive filler. n and q are the ceramic morphology fitting factor and the critical exponent, respectively. As illustrated in Fig. 7, according to the fitted result using the EMPT model and compared to the EMT or percolation theory model, the fitted result of EMPT closely matches the experimental data over a filler loading content (f = 0 - 0.5). The EMT model cannot fit the data in the range of f > 0.4, while the fitting results are in good accordance with the experimental data in the range of f < 0.4. Alternatively, percolation theory cannot fit the data when f < 0.4 where the fitted data deviate from the experimental data. At f > 0.4, the experimental data can be well fitted by percolation theory.

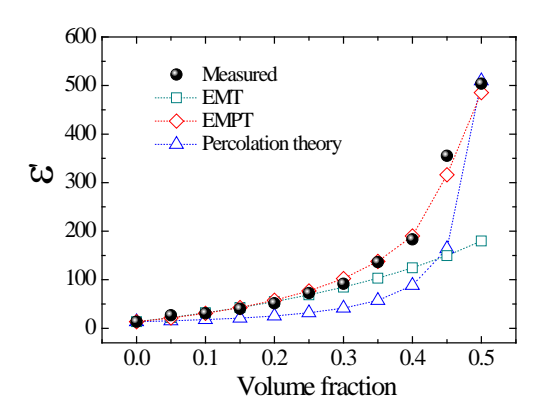


Fig. 7 Experimental data and theoretical  $\epsilon'$  values from different models of LSNMO/PVDF composites with different volume fractions of LSNMO at 1 kHz and room temperature.

Therefore, at least two mechanisms are responsible for the observed overall dielectric behavior in the LSNMO/PVDF composites. The best fitting parameters for the EMPT model are  $f_{\rm c}$  = 0.54, n = 0.10 and q = 0.50. The filler morphology fitting factor n and the critical exponent q are similar to that reported by Fang et al. [5]. It is notable that  $f_e$  of the LSNMO/PVDF composites was much higher than the theoretical percolation threshold of **Lyppo**er composite, which is about  $f_c = 0.16$  for conductive a conductive -filler with spherical shape [34]. It was clearly shown that  $f_{\rm c}$  increased with increasing conductivity of the fillers [4, 17, 35]. Therefore, the obtained high  $f_c$  value is attributed to the semiconductor properties of the LSNMO ceramic filler. At f = 0.05- 0.035, L particles are separated from another and surrounded by an insulating PVDF matrix. Thus, the continuously enhanced dielectric response in the LSNMO/PVDF composites arose from the giant  $\varepsilon'$  values of the LSNMO particles and the strong interfacial polarization between the insulating PVDF matrix and semiconducting LSNMO particles. At f = 0.350.5, a rapid increase in  $\varepsilon'$  was observed. This is typically caused by the formation of a percolation network [34]. This is evidenced by the observed increase in both the conductivity and  $tan \delta$ .

#### 3.4 Conclusions

The LSNMO/PVDF polymeric composites with volume fractions of LSNMO filler from f = 0 - 0.5 were fabricated to enhance the dielectric response in PVDF polymer. LSNMO particles were homogeneously dispersed in the PVDF matrix, confirming the formation of

a 0–3 composite.  $\varepsilon'$  and  $\tan\delta$  of the composites increased with increasing filler loading. For the composite with f=0.5, interestingly, largely increased  $\varepsilon'\approx 10^3$  and  $\approx 500$  at  $10^2$  and  $10^3$  Hz, respectively, were achieved. The variation in dielectric properties as a function of filler volume fraction for the LSNMO/PVDF composites was well fitted and obeyed the combined model of the percolation theory and EMT model, which was referred to the effective medium percolation theory (EMPT) model. At a low filler loading, a continuous increase in  $\varepsilon'$  was caused by strong interfacial polarization and a very high  $\varepsilon'$  value of LSNMO particles. At a relatively high volume fraction, the dramatic increase in  $\varepsilon'$  was due to the formation of a percolation network throughout the PVDF polymer matrix, increasing both of  $\varepsilon'$  and the conductivity of the composites.

#### References

- 1. M. Arbatti, X. Shan, Z.Y. Cheng, Adv. Mater. 19, 1369-1372 (2007)
- 2. L. Xie, X. Huang, K. Yang, S. Li, P. Jiang, Journal of Materials Chemistry A 2, 5244-5251 (2014)
- 3. Z. Wang, M. Fang, H. Li, Y. Wen, C. Wang, Y. Pu, Composites Science and Technology 117, 410-416 (2015)
- 4. Z.M. Dang, J.B. Wu, L.Z. Fan, C.W. Nan, Chem. Phys. Lett. 376, 389-394 (2003)
- 5. F. Fang, W. Yang, S. Yu, S. Luo, R. Sun, Appl. Phys. Lett. 104, 132909 (2014)
- 6. D. Wang, T. Zhou, J.-W. Zha, J. Zhao, C.-Y. Shi, Z.-M. Dang, Journal of Materials Chemistry A 1, 6162-6168 (2013)
- 7. Z.-M. Dang, J.-K. Yuan, J.-W. Zha, T. Zhou, S.-T. Li, G.-H. Hu, Prog. Mater. Sci. 57, 660-723 (2012)
- 8. E.-Q. Huang, J. Zhao, J.-W. Zha, L. Zhang, R.-J. Liao, Z.-M. Dang, J. Appl. Phys. 115, 194102 (2014)
- 9. J. Fu, Y. Hou, M. Zheng, Q. Wei, M. Zhu, H. Yan, ACS Applied Materials & Interfaces 7, 24480-24491 (2015)
- 10. K. Yu, H. Wang, Y. Zhou, Y. Bai, Y. Niu, J. Appl. Phys. 113, 034105 (2013)
- 11. X.-J. Zhang, G.-S. Wang, Y.-Z. Wei, L. Guo, M.-S. Cao, Journal of Materials Chemistry A 1, 12115-12122 (2013)
- 12. P. Thomas, K.T. Varughese, K. Dwarakanath, K.B.R. Varma, Composites Science and Technology 70, 539-545 (2010)
- 13. S. Liu, S. Xue, W. Zhang, J. Zhai, G. Chen, Journal of Materials Chemistry A 2, 18040-18046 (2014)
- 14. Prateek, V.K. Thakur, R.K. Gupta, Chemical Reviews 116, 4260-4317 (2016)
- Y.-I. Su, C. Sun, W.-q. Zhang, H. Huang, J. Mater. Sci. 48, 8147-8152 (2013)
- 16. S. Luo, S. Yu, R. Sun, C.-P. Wong, ACS Applied Materials & Interfaces 6, 176-182 (2014)
- 17. Z.-M. Dang, T. Zhou, S.-H. Yao, J.-K. Yuan, J.-W. Zha, H.-T. Song, J.-Y. Li, Q. Chen, W.-T. Yang, J. Bai, Adv. Mater. 21, 2077-2082 (2009)
- 18. Z.-M. Dang, B. Peng, D. Xie, S.-H. Yao, M.-J. Jiang, J. Bai, Appl. Phys. Lett. 92, 112910 (2008)
- 19. Z.-M. Dang, C.-W. Nan, Ceram. Int. 31, 349-351 (2005)
- 20. M. Yao, S. You, Y. Peng, Ceram. Int. 43, 3127-3132 (2017)
- 21. M. Fang, Z. Wang, H. Li, Y. Wen, Ceram. Int. 41, Supplement 1, S387-S392 (2015)
- 22. P. Kum-onsa, P. Thongbai, S. Maensiri, P. Chindaprasirt, J. Mater. Sci.: Mater. Electron. 27, 9650-9655 (2016)
- 23. K. Meeporn, S. Maensiri, P. Thongbai, Appl. Surf. Sci. 380, 67-72 (2016)
- 24. M.-F. Lin, P.S. Lee, Journal of Materials Chemistry A 1, 14455-14459 (2013)
- 25. H. Tang, H.A. Sodano, Nano Lett. 13, 1373-1379 (2013)
- 26. S. Krohns, P. Lunkenheimer, C. Kant, A.V. Pronin, H.B. Brom, A.A. Nugroho, M. Diantoro, A. Loidl, Appl. Phys. Lett. 94, 122903 (2009)

- 27. T. Park, Z. Nussinov, K. Hazzard, V. Sidorov, A. Balatsky, J. Sarrao, S.W. Cheong, M. Hundley, J.-S. Lee, Q. Jia, J. Thompson, Phys. Rev. Lett. 94, 017002 (2005)
- 28. X.Q. Liu, B.W. Jia, W.Z. Yang, J.P. Cheng, X.M. Chen, J. Phys. D: Appl. Phys. 43, 495402 (2010)
- 29. B.W. Jia, W.Z. Yang, X.Q. Liu, X.M. Chen, J. Appl. Phys. 112, 024104 (2012)
- 30. K. Silakaew, W. Saijingwong, K. Meeporn, S. Maensiri, P. Thongbai, Microelectron. Eng. 146, 1-5 (2015)
- 31. K. Meeporn, N. Chanlek, P. Thongbai, RSC Advances 6, 91377-91385 (2016)
- 32. K. Meeporn, T. Yamwong, P. Thongbai, Jpn. J. Appl. Phys. 53, 06JF01 (2014)
- 33. P. Martins, A.C. Lopes, S. Lanceros-Mendez, Prog. Polym. Sci. 39, 683-706 (2014)
- 34. C.W. Nan, Y. Shen, J. Ma, Annu. Rev. Mater. Res. 40, 131-151 (2010)
- 35. J. Fu, Y. Hou, Q. Wei, M. Zheng, M. Zhu, H. Yan, J. Appl. Phys. 118, 235502 (2015)

## CHAPTER 1

# Effects of DC Bias on Non-Ohmic Sample–Electrode Contact and Grain Boundary Responses in Giant–Permittivity La<sub>1.7</sub>Sr<sub>0.3</sub>Ni<sub>1-x</sub>Mg<sub>x</sub>O<sub>4</sub> Ceramics

#### 1.1 Introduction

An  $Ln_{2-x}Sr_xNiO_4$  (Ln = La, Nd, and Sm) ceramic system is one of the most interesting giant dielectric materials investigated in recent years. This is because of its very high dielectric permittivity ( $\varepsilon' \approx 10^5 - 10^6$ ). For La<sub>1.875</sub>Sr<sub>0.125</sub>NiO<sub>4</sub> single crystal, high values of  $\varepsilon' \approx 10^4$  can be obtained even when the frequency is increased into the GHz range.<sup>2</sup> The origin of the giant dielectric response (GDR) in Ln<sub>2-x</sub>Sr<sub>x</sub>NiO<sub>4</sub> ceramics has been intensively investigated. 1-5, 15 It has been widely proposed that the GDR is attributable to the small polaronic hopping process in  $Ln_{2-x}Sr_xNiO_4$  ceramics.<sup>1-4</sup> Accordingly, the dielectric response has been directly linked to the concentration and size of small polarons and the hopping process is directly correlated to the charge ordering. Three mechanisms reflect the existence of the small polaronic hopping process: First, the  $\varepsilon'$ value increases with increasing concentrations of small polarons. 16 Second, the critical response frequency, at which a sudden drop in  $\varepsilon'$  occurs, shifts to lower frequencies as the polaronic size is increased, since the bigger polaron will have a larger effective mass.<sup>6</sup>, 17-18 It was demonstrated that the polaronic size of Ln<sub>2-x</sub>Sr<sub>x</sub>NiO<sub>4</sub> can be increased by decreasing Sr2+ concentration and by partially doping this ceramic material with Al3+ ions into Ni<sup>3+</sup> sites.<sup>6, 18-19</sup> Lastly, the long-range hopping of small polarons gives rise to electrical conductivity, leading to a large increase in the low-frequency tanδ value.<sup>11</sup>

In addition to the intrinsic origin, it was suggested that the giant  $\epsilon'$  values of  $Ln_{2-x}Sr_xNiO_4$  ceramics were primarily associated with an extrinsic non–Ohmic sample–electrode contact effect. Furthermore, the grain boundary (GB) (i.e., Maxwell–Wagner effect) response was also suggested to have an effect on the GDR in  $La_{2-x}Sr_xNiO_4$  (LSNO) thin films. The GDR in  $SiO_2/LSNO$  composite ceramics was described and attributed to a combination of small polaronic hopping and the GB response. Although all of these explanations are reasonable, a significant controversy concerning the precise mechanism of GDR in  $Ln_{2-x}Sr_xNiO_4$  ceramic systems remains. Perhaps, none of these models can completely describe the GDR. Further studies are needed to clarify the relevant mechanisms and each of their contributions.

For  $Ln_{2-x}$ Sr<sub>x</sub>NiO<sub>4</sub> ceramics, the grain resistance ( $R_g \approx 0.1~\Omega$ ) (or bulk resistance) and GB resistance ( $R_{gb} \approx 17.5~\Omega$ ) at RT are very small.<sup>1, 7</sup>  $R_{gb}$  is much smaller than for other giant dielectric materials (e.g., CCTO) by at least 3–4 orders of magnitude.<sup>20-21</sup> As a result, the grain and GB responses in  $Ln_{2-x}$ Sr<sub>x</sub>NiO<sub>4</sub> ceramics cannot be analyzed using impedance spectroscopy (IS), even if the measurements are performed at 10 K.<sup>15</sup> According to an equivalent circuit consisting of three parallel RC elements connected in series (*i.e.*, grain, GB, and electrode responses),<sup>22</sup> it was theoretically demonstrated that when  $R_{gb} << R_e$  (resistance of sample–electrode contact), the high  $\epsilon$ ' plateau in a low–frequency range is dominated by the electrode effect at RT. When  $R_{gb} >> R_e$  and  $R_g$ , a high  $\epsilon$ ' value in a low–frequency range is dominated by the GB response (high GB capacitance,  $C_{gb}$ ).<sup>23</sup> In this case, the electrode effect is concealed by the GB effect. Furthermore, the electrode effect would not be dominant if the semiconducting surface becomes an insulating surface, *i.e.*, the conductivity of the grains was greatly enhanced.  $R_{gb}$  of other giant dielectric materials (e.g.,  $CaCu_3Ti_4O_{12}$ ) can generally enhanced by

doping with  $Mg^{2+}$ .  $^{24-27}$  Doping  $Mg^{2+}$  ions into LSNO may increase its  $R_{gb}$ . Thus, the electrical responses of the grain, GB, and electrode contact contributing to the GDR in an  $Ln_{2-x}Sr_xNiO_4$  ceramic system can be easily characterized. Dielectric measurements under a DC bias have given important clues to understand the GB and electrode responses.  $^{22, 28-30}$ 

In this work, Mg<sup>2+</sup> doped–LSNO ceramics were prepared to demonstrate the dominant effects of the GB response and non–Ohmic sample–electrode contact. The effects of DC bias on the GDR in Mg<sup>2+</sup> doped–LSNO ceramics were investigated to clarify the underlying mechanism(s) of the GDR in LSNO ceramics. Details of each contribution to the GDRs in different temperature and frequency ranges are discussed.

## 1.2 Experimental details

A chemical combustion was used to synthesize nanosized  $La_{1.7}Sr_{0.3}Ni_{1-x}Mg_xO_4$  (x=0, 0.3, 0.4 and 0.5) powders. The starting raw materials used as metal-ion sources were  $Ni(NO_3)_2 \cdot 6H_2O$  (99.0%, Kanto Chemical), La( $NO_3$ )<sub>3</sub>· $6H_2O$  (99.99%, Sigma-Aldrich), Sr(NO<sub>3</sub>)<sub>2</sub> (99.0%, Sigma-Aldrich) and Mg(NO<sub>3</sub>)<sub>2</sub>·6H<sub>2</sub>O (99.999%, Sigma-Aldrich). Urea  $(CH_4N_2O, 99.0\%)$  was used as a fuel. For  $La_{1.7}Sr_{0.3}Ni_{1-x}Mg_xO_4$  with x=0, first, 3.6806 g of  $La(NO_3)_3.6H_2O$ , 0.3147 g of  $Sr(NO_3)_2$  and 1.4540 g of  $Ni(NO_3)_2.6H_2O$  were dissolved in 80 mL of aqueous solution of citric acid (2.5 wt%) at RT with constant stirring using a magnetic bar on a hotplate. For La<sub>1.7</sub>Sr<sub>0.3</sub>Ni<sub>1.x</sub>Mg<sub>x</sub>O<sub>4</sub> with x=0.3, 0.4 and 0.5, 1.0178 g of  $Ni(NO_3)_2 \cdot 6H_2O$  and 0.3846 g of  $Mg(NO_3)_2 \cdot 6H_2O$ , 0.8724 g of  $Ni(NO_3)_2 \cdot 6H_2O$  and 0.5128 g of Mg(NO<sub>3</sub>)<sub>2</sub>·6H<sub>2</sub>O, and 0.7270 g of Ni(NO<sub>3</sub>)<sub>2</sub>·6H<sub>2</sub>O and 0.6410 g of Mg(NO<sub>3</sub>)<sub>2</sub>·6H<sub>2</sub>O were used, respectively. Second, 0.7 g of CH<sub>4</sub>N<sub>2</sub>O was mixed into the metal ion solution with constant stirring at 200 °C for 2 h. When a transparent viscous gel was observed, then the viscous gel was dried in a furnace at 300 °C for 30 min using heating rate 10 °C/min. On heating, a fast and strong combustion was observed when the temperature increased to ≈200–210 °C. To obtain a single phase of La<sub>1.7</sub>Sr<sub>0.3</sub>Ni<sub>1-x</sub>Mg<sub>x</sub>O<sub>4</sub> powders, the dried porous precursors were ground and calcined in a furnace in air at 1000 °C for 6 h using heating rate 5 °C/min. The resulting nanosized powders were pressed by uniaxial compression at ≈200 MPa into a pellet shape of 9.5 mm in diameter and ~1-2 mm in thickness. Finally, these pellets were sintered in air at 1375 °C for 6 h with a heating rate 5 °C/min followed by natural furnace cooling to room temperature (RT). The atmospheric pressure was ≈758 mmHg.

The particle size and shape of nanosized–La<sub>1.7</sub>Sr<sub>0.3</sub>Ni<sub>1-x</sub>Mg<sub>x</sub>O<sub>4</sub> powders were determined using transmission electron microscopy (TEM; FEI Tecnai G²). Structure and phase composition of the sintered La<sub>1.7</sub>Sr<sub>0.3</sub>Ni<sub>1-x</sub>Mg<sub>x</sub>O<sub>4</sub> ceramics were characterized using an X–ray diffraction (XRD) technique (PANalytical, EMPYREAN). Rietveld quantitative phase analysis was carried out using the X'Pert High Score Plus v3.0e software package by PANalytical. Polished–surface morphologies of the sintered La<sub>1.7</sub>Sr<sub>0.3</sub>Ni<sub>1-x</sub>Mg<sub>x</sub>O<sub>4</sub> ceramics were characterized using scanning electron microscopy (SEM) (LEO 1450VP, UK). The chemical states of Ni were analyzed using X–ray photoelectron spectroscopy (XPS), PHI5000 VersaProbe II, ULVAC–PHI, Japan) at the SUT–NANOTEC–SLRI Joint Research Facility, Synchrotron Light Research Institute (SLRI), Thailand. All binding energies of the samples were calibrated with the C1s peak at 284.8 eV. The XPS spectra were fitted with PHI MultiPak XPS software using a combination of Gaussian–Lorentzian lines.

Prior to dielectric and electrical measurements, Au electrodes were sputtered onto each polished–face at a current of 25 mA for 8 min using a Polaron SC500 sputter coating unit. The dielectric properties were measured using a KEYSIGHT E4990A Impedance Analyzer over the frequency range of 100 Hz – 1 MHz under different DC bias voltages. An oscillation voltage of 500 mV was used.

#### 1.3 Results and discussion

The XRD patterns of the sintered La<sub>1.7</sub>Sr<sub>0.3</sub>Ni<sub>1.x</sub>Mg<sub>x</sub>O<sub>4</sub> (M–LSNO) ceramics, where x = 0, 0.3, 0.4 and 0.5, are shown in Fig. 1(a), confirming the formation of an LSNO phase (JCPDS 32–1241) with a tetragonal structure. The identified crystal structure and the detected XRD patterns were similar to those reported in previous studies. <sup>6-7, 9, 11-14, 31</sup> No impurity phase diffraction peak was observed. Rietveld refinement profile fits were performed, as illustrated in Fig. 1(b). Accordingly, lattice parameters of La<sub>1.7</sub>Sr<sub>0.3</sub>Ni<sub>1.x</sub>Mg<sub>x</sub>O<sub>4</sub> ceramics with x = 0, 0.3, 0.4 and 0.5 were obtained to be a = 3.8306 and c = 12.7115 Å, a = 3.8371 and c = 12.7234 Å, a = 3.8463 and c = 12.7429 Å and a = 3.8653 and c = 12.8225 Å, respectively. These values are comparable to JCPDS 32–1241 for a = 3.817 and c = 12.766 Å and literature values [a = 3.8167 and c = 12.7410 Å]. <sup>9-10, 15, 18-19</sup> The effect of Mg<sup>2+</sup> dopant on the crystal structure of LSNO ceramics is demonstrated in Fig. 1 (c). Both of a and c values of the La<sub>1.7</sub>Sr<sub>0.3</sub>Ni<sub>1-x</sub>Mg<sub>x</sub>O<sub>4</sub> ceramics increases with increasing Mg<sup>2+</sup> dopant (x). The increased lattice parameters were primarily attributed to the larger ionic radius of the Mg<sup>2+</sup> dopant (r<sub>4</sub> = 0.57 Å) compared to that of the host Ni<sup>2+</sup> ion (r<sub>4</sub> = 0.55 Å). The crystal structure of La<sub>1.7</sub>Sr<sub>0.3</sub>Ni<sub>1-x</sub>Mg<sub>x</sub>O<sub>4</sub> is illustrated in Fig. 1(d).

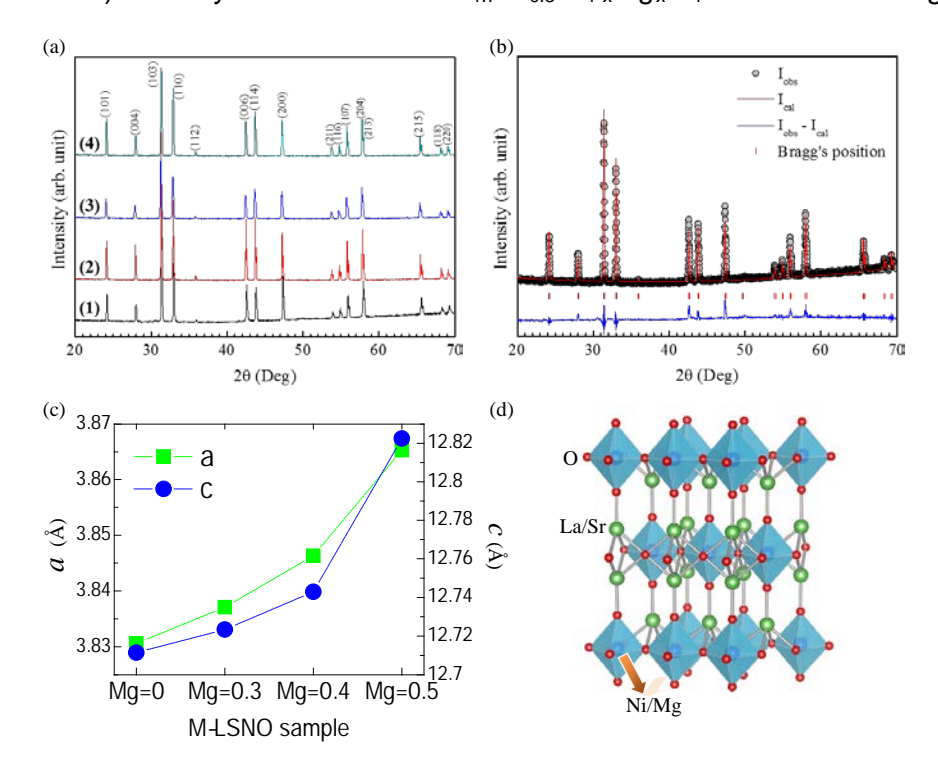


Fig. 1 (a) XRD patterns of La<sub>1.7</sub>Sr<sub>0.3</sub>Ni<sub>1-x</sub>Mg<sub>x</sub>O<sub>4</sub> ceramics with (1) x = 0, (2) x = 0.3, (3) x = 0.4, and (4) x = 0.5. (b) Profile fits for the Rietveld refinement of the undoped La<sub>1.7</sub>Sr<sub>0.3</sub>NiO<sub>4</sub> ceramic. (c) Lattice parameters (a and c) of La<sub>1.7</sub>Sr<sub>0.3</sub>Ni<sub>1-x</sub>Mg<sub>x</sub>O<sub>4</sub> ceramics with x = 0-0.5. (d) The schematic of La<sub>1.7</sub>Sr<sub>0.3</sub>NiO<sub>4</sub> structure.

Nanosized–La<sub>1.7</sub>Sr<sub>0.3</sub>Ni<sub>1-x</sub>Mg<sub>x</sub>O<sub>4</sub> powders (x=0 and 0.4) with grain sizes of about 200–400 nm are shown in Fig. 2(a) and (b). The polished–surfaces of the sintered ceramics using these powders are shown in Fig. 2(c)–(f). The grain size of the sintered LSNO ceramics was slightly enlarged by doping with Mg<sup>2+</sup> ions with x=0–0.4. However, the grain size of the La<sub>1.7</sub>Sr<sub>0.3</sub>Ni<sub>1-x</sub>Mg<sub>x</sub>O<sub>4</sub> ceramic with x=0.5 was significantly reduced. A large number of pores were observed in the microstructure of undoped–LSNO ceramics, while the La<sub>1.7</sub>Sr<sub>0.3</sub>Ni<sub>1-x</sub>Mg<sub>x</sub>O<sub>4</sub> ceramics with x=0.3–0.5 had a dense microstructure with no pores. The relative densities of the La<sub>1.7</sub>Sr<sub>0.3</sub>Ni<sub>1-x</sub>Mg<sub>x</sub>O<sub>4</sub> ceramics with x=0, 0.3, 0.4 and 0.5 were calculated using the Archimedes method and found to be ≈73, ≈87, ≈86, and ≈90%, respectively. It is likely that doping with Mg<sup>2+</sup> ions caused an increase in densification of LSNO ceramics.

The giant dielectric properties in the frequency range of 10<sup>2</sup>-10<sup>6</sup> Hz for the sintered La<sub>1.7</sub>Sr<sub>0.3</sub>Ni<sub>1-x</sub>Mg<sub>x</sub>O<sub>4</sub> ceramics were studied at RT, as shown in Fig. 3. All of the ceramics exhibited giant  $\varepsilon'$  values of about  $10^5-10^6$  in a low-frequency range. At  $10^2$  Hz, the  $\varepsilon'$ values of the  $La_{1.7}Sr_{0.3}Ni_{1-x}Mg_xO_4$  ceramics with x = 0-0.4 were nearly identical [Fig. 3(a)]. The  $\varepsilon'$  value at 1 kHz increased from  $\approx 4.3 \times 10^5$  to  $\approx 5.1 \times 10^5$  as x increased from 0-0.5. The difference in the frequency dependence of ε' and tanδ for the La<sub>1.7</sub>Sr<sub>0.3</sub>Ni<sub>1.5</sub>  $_{x}$ Mg $_{x}$ O $_{4}$  ceramics with different x values was observed. In the frequency range of  $10^{2}-10^{5}$ Hz,  $\varepsilon'$  of the La<sub>1.7</sub>Sr<sub>0.3</sub>Ni<sub>1.x</sub>Mg<sub>x</sub>O<sub>4</sub> ceramic with x = 0 was independent of frequency.  $\varepsilon'$ began to decrease to a lower value when the frequency was increased to 106 Hz. A step-like decrease in ε' (or a critical response frequency) of La<sub>1.7</sub>Sr<sub>0.3</sub>Ni<sub>1.x</sub>Mg<sub>x</sub>O<sub>4</sub> ceramics shifted to lower frequencies as x increased. This result is similar to that observed in Al-doped LSNO<sup>10</sup> and Al-doped Sm<sub>1.5</sub>Sr<sub>0.5</sub>NiO<sub>4</sub><sup>32</sup> ceramics. As shown in Fig. 3(b),  $tan\delta$  of the undoped-LSNO ceramic (x=0) increased sharply, by about two orders of magnitude, as the frequency was decreased from 10<sup>4</sup> to 10<sup>2</sup> Hz. This behavior is generally considered the effect of DC conduction in the bulk ceramics and/or the effect of non-Ohmic sample-electrode contact. 33-35 It was also found that, for the ceramics with x =0-0.4, tanδ increased sharply with increasing frequency in a high frequency range, corresponding to a rapid decrease in  $\varepsilon'$ . For the ceramic with x = 0.5, the critical response frequency was the lowest and a corresponding tanδ-peak appeared. This behavior indicated that a dielectric relaxation mechanism exists in the bulk ceramic under an applied AC electric field. According to the small polaronic model, 11, 19, 32 the decrease in a critical response frequency of the M-LSNO ceramic with x = 0.5 can be ascribed to the effect of polaronic size, which may be increased by doping with a high concentration of Mg<sup>2+</sup> ions. Alternatively, it is possible but unlikely that this dielectric relaxation behavior can be described based on the electrode effect or that the electrode effect may be quite small in M-LSNO ceramics with high concentrations of Mg<sup>2+</sup> ions.

To clarify the effect of  $Mg^{2+}$  doping ions on the small polaronic hopping behavior in LSNO ceramics, all the sintered ceramics were characterized by XPS. Fig. 4 shows the XPS spectra of Ni 3p regions of the sintered  $La_{1.7}Sr_{0.3}Ni_{1-x}Mg_xO_4$  (M–LSNO) ceramics with x=0, 0.3, 0.4 and 0.5. The Ni 3p peaks of all sintered ceramics can be deconvoluted into three main peaks. The peaks at  $\approx$ 67.2–67.5 eV are assigned to  $Ni^{2+}$ ,  $^{36}$  while the peaks at  $\approx$ 68.7–69.0 eV are attributed to  $Ni^{3+}$ . The peaks at  $\approx$ 73.0–73.3 eV are assigned to a satellite peak associated with  $Ni^{2+}$ . This observation is consistent with that reported in literature. The result confirms the coexistence of  $Ni^{2+}$  and  $Ni^{3+}$  in the samples. The presence of  $Ni^{3+}$  indicated that the conductivity was attributable to charge hopping between  $Ni^{3+} \leftrightarrow Ni^{2+}$ . As shown in Fig. 4, the ratios of  $Ni^{3+}/Ni^{2+}$  in the undoped–LSNO

ceramic and M–LSNO ceramics with x = 0.3, 0.4 and 0.5 changed slightly. This means that Mg<sup>2+</sup> ions preferentially substituted into Ni<sup>2+</sup> sites. It is reasonable to suggest that the small polaronic concentration the M–LSNO ceramics should not significantly change. This result is consistent with the observed GDR in M–LSNO ceramics, in which the  $\varepsilon'$  value in a low frequency range was not decreased by Mg<sup>2+</sup> doping. Changes in the critical response frequency were likely due to an increase in polaronic sizes, just as was proposed in Al–doped LSNO ceramics.<sup>6</sup>

The small polaronic hopping mechanism or the electrode effect is now the most likely origin of the GDR in LSNO ceramics. 10, 15, 32 Electrical conduction inside the grains is therefore considered the primary factor. In the M-LSNO ceramics, however, the GB response may be another important factor. This is because the large decrease in tanδ may have been caused by the dominant effect of the GB response. Impedance spectroscopy is a powerful tool for separating the electrical responses of grains, GB and the electrode effect. 22, 28-29 It was used to determine the total resistance, which can be estimated from a large semicircular arc. Total resistance increases with increasing Mg<sup>2+</sup> dopant concentration [Fig. 5]. A  $Z^*$  plot of the M-LSNO ceramic with x=0(undoped-LSNO) cannot be seen in Fig. 5 and inset (a). This was due to its very low total resistance compared to that of the other ceramics [inset (b)]. Furthermore, a nonzero intercept on the Z' axis was observed, indicating that there exists some component of the ceramic with relatively low conductivity, which may be the grains. Usually, R<sub>a</sub> values at RT of LSNO ceramics are about 0.1-2.5 Ω.cm.32 This is quite consistent with the value obtained from the observed nonzero intercept, which corresponds to Rq. The total resistance is usually governed by R<sub>ab</sub> or R<sub>ab</sub>+R<sub>e</sub>. Generally, the grain (bulk), GB, and electrode responses can each be described by a parallel R-C element, whereas the macroscopic dielectric response is usually represented by a series connection of two R-C elements.<sup>38</sup> To clarify, impedance data were fitted to a single R-C parallel circuit for a Z<sup>\*</sup> plot,

$$Z^* = \frac{R}{1 + (i\omega RC)},\tag{1}$$

where R and C are the resistance and capacitance of each element, and  $\omega$  is the angular frequency of an applied electric field. As shown in the inset (b) of Fig. 5, two overlapping arcs in Z\* plot of the undoped–LSNO ceramic are observed and fitted by Eq. (1). The observed small and large arcs in the relatively high and low–frequency ranges can be ascribed to be the electrical responses of the GBs  $(R_{gb}C_{gb})$  and non–Ohmic sample–electrode contact  $(R_eC_e)$ , respectively.<sup>29</sup>

It is notable that the capacitance of the non–Ohmic sample–electrode contact ( $C_e=1/2\pi f_{max}R_e$ ) was  $\approx 4.8\times 10^{-8}$  F, which was lower than that of the apparent capacitance of the sample ( $\approx 1.2\times 10^{-7}$  F at 1 kHz). This indicates that there is another source of polarization contributing to the overall GDR in the undoped–LSNO ceramic. Interfacial polarization at the GBs can be ruled out because  $R_{gb}$  ( $\approx 5.34~\Omega$ .cm) was just slightly larger than  $R_g$  ( $\approx 2.65~\Omega$ .cm). Thus, the polaronic hopping process is the most probable factor contributing to the overall GDR in the undoped–LSNO ceramic coupled with the electrode effect, but its intensity was too great. In inset (a) of Fig. 5, a relatively small semicircular arc was observed in the  $Z^*$  plot of the M–LSNO ceramic with x=0.5 that could be ascribed to the grain response with  $R_g \approx 1120~\Omega$ .cm (at RT). This value is comparable to  $R_g \approx 1100$ 

 $\Omega$  (at 300 K) for Sm<sub>1.5</sub>Sr<sub>0.5</sub>Ni<sub>0.5</sub>Al<sub>0.5</sub>O<sub>4</sub> ceramic<sup>32</sup> and R<sub>g</sub> $\approx$ 2663  $\Omega$  (at 300 K) for La<sub>1.75</sub>Sr<sub>0.25</sub>Ni<sub>0.7</sub>Al<sub>0.3</sub>O<sub>4</sub> ceramic.<sup>6</sup> According to the Z\* plot of the M–LSNO ceramic with x=0.5, the large semicircular arc can be ascribed to the R<sub>gb</sub>C<sub>gb</sub> response, since the R<sub>e</sub>C<sub>e</sub> response was less dominant due to large increases in R<sub>g</sub> and R<sub>gb</sub>. <sup>22-23</sup> Thus, it is reasonable that R<sub>g</sub> and R<sub>gb</sub> of the M–LSNO ceramics increased with increasing Mg<sup>2+</sup> dopant concentration, as shown in Fig. 6.

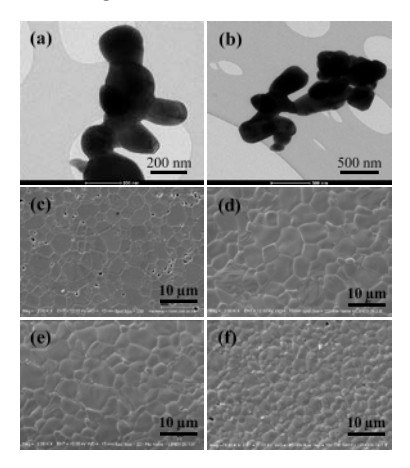


**Fig. 2** (a-b) TEM images of  $La_{1.7}Sr_{0.3}Ni_{1-x}Mg_xO_4$  powders with x=0 and 0.4. (c-f) SEM images of polished-surfaces of sintered  $La_{1.7}Sr_{0.3}Ni_{1-x}Mg_xO_4$  ceramics with x=0, 0.3, 0.4 and 0.5, respectively.

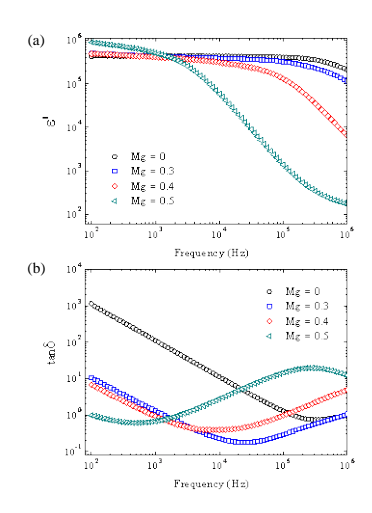


**Fig. 3** Frequency dependence of (a) ε' and (b) tanδ at RT for  $ta_{1.7}Sr_{0.3}Ni_{1-x}Mg_xO_4$  ceramics.

The R<sub>g</sub> values of the M–LSNO ceramics with x=0.3, 0.4 and 0.5 were, respectively, enhanced by factors of  $\approx$ 2,  $\approx$ 21 and  $\approx$ 422 compared to that of the undoped–LSNO ceramic. As represented in Fig. 4, giving a real overall composition of La<sub>1.7</sub>Sr<sub>0.3</sub>(Ni<sup>2+</sup>,Ni<sup>3+</sup>)<sub>1-x</sub>Mg<sub>x</sub>O<sub>4</sub>, the amount of both Ni<sup>2+</sup> and Ni<sup>3+</sup> ions decreased with increasing Mg<sup>2+</sup> dopant concentration because of a slight change in the ratios of Ni<sup>3+</sup>/Ni<sup>2+</sup> for all ceramics. The conductivity of M–LSNO ceramics, which was primarily caused by charge hopping between Ni<sup>3+</sup> $\leftrightarrow$ Ni<sup>2+</sup> ions, was decreased due to reduction in concentration of charge carriers. It is notable that the total amount of Ni<sup>2+</sup> and Ni<sup>3+</sup> ions and the amount of Mg<sup>2+</sup> dopant ions are the same in value for the M–LSNO ceramic with x = 0.5. Therefore, the

long range motion of hopping charges inside the grains was also strongly inhibited by Mg<sup>2+</sup> ions.

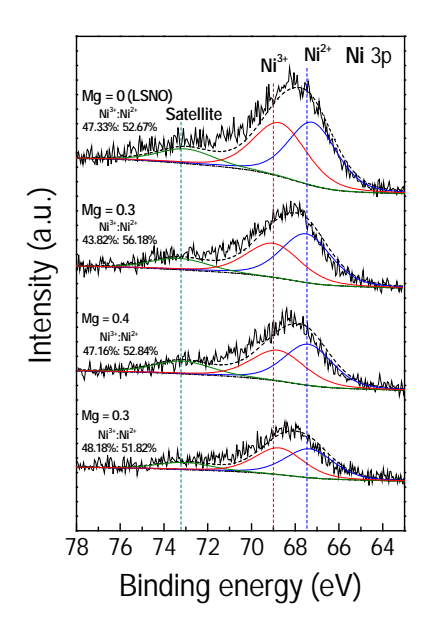


Fig. 4 XPS spectra of  $La_{1.7}Sr_{0.3}Ni_{1-x}Mg_xO_4$  ceramics with x = 0, 0.3, 0.4 and 0.5.

It was also observed that the  $R_{gb}$  value of the M–LSNO ceramic with x=0.5 was much larger than that of the ceramics with x=0.3 and 0.4. The GB response in M–LSNO ceramics was dominant and the total resistance is therefore governed by  $R_{gb}$ . Substitution of  $Mg^{2+}$  into LSNO ceramics can cause a great increase in  $R_{gb}$ . Usually, both of the intrinsic and geometric factors have an influence on the electrical properties of the GBs. As clearly shown in the SEM images, the grain size of the M–LSNO ceramic with x=0.5 was significantly reduced. This is the primary cause of the remarkable increase in  $R_{gb}$  due to the increase in insulating GB layers. Accordingly, the significant decrease in tanbla in a low–frequency range for M–LSNO ceramics was clearly due to the large increase in  $R_{gb}$ .

Generally, investigation of the electrical and dielectric properties under different DC bias voltages can be done to analyze the electrical responses of GB and electrode effects. As shown in Fig. 7(a), the observed semicircular arc of the undoped–LSNO ceramic decreased with increasing DC bias. As previously discussed, such a semicircular arc may have been due to the  $R_eC_e$  response. This was confirmed using a Mott–Schottky plot of  $1/C^2$  vs. DC bias voltage, as shown in the inset of Fig. 8(a). It showed a linear response, i.e., variation in the capacitance value with DC bias obeys the Mott–Schottky law for the formation Schottky barrier between metal electrodes and a semiconducting surface. Semiconducting surface.

In Figs. 7(b) and (c), the semicircular arc of the M–LSNO ceramics with x=0.3 and 0.4 decreased with increasing DC bias voltage, while the nonzero intercept did not change as shown in the insets. The R<sub>gb</sub> values of the M–LSNO ceramics with x=0.3 and 0.4 were enhanced by factors of  $\approx$ 930 and  $\approx$ 1200, respectively, compared that of the undoped–LSNO ceramic. These R<sub>gb</sub> values were much larger than that of R<sub>e</sub> of the undoped–LSNO ceramic. When R<sub>gb</sub>>>of R<sub>e</sub>, the electrode effect was dominant in these samples.  $^{22}$ 

Fig. 5 Impedance complex plane plot ( $Z^*$ ) at RT for La<sub>1.7</sub>Sr<sub>0.3</sub>Ni<sub>1-x</sub>Mg<sub>x</sub>O<sub>4</sub> ceramics with x = 0–0.5. Inset (a) shows an expanded view of the high–frequency data close to the origin. Inset (b) shows an expanded view of the inset (a), revealing the electrical responses of grain, GBs, and sample–electrode contact.

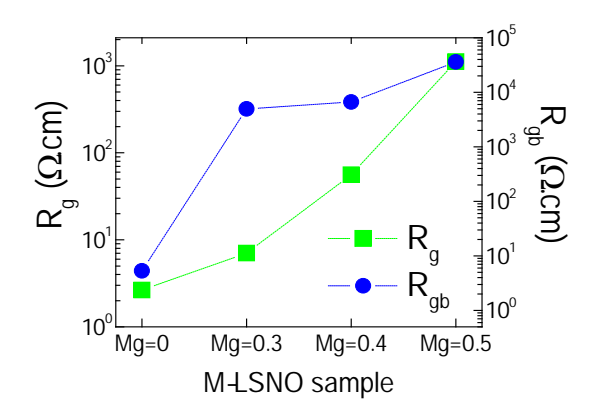


**Fig. 6** R<sub>g</sub> and R<sub>gb</sub> values of La<sub>1.7</sub>Sr<sub>0.3</sub>Ni<sub>1-x</sub>Mg<sub>x</sub>O<sub>4</sub> ceramics with different doping concentrations.

In Fig. 7(d) and its inset, the  $R_{gb}$  of the M–LSNO ceramic with x=0.5 was greatly reduced from 36 k $\Omega$ .cm to 222  $\Omega$ .cm by increasing the DC bias from 0 to 13 V, while  $R_g$  decreased slightly from 1120 to 1009  $\Omega$ .cm. The reduction in  $R_g$  may have been caused by injected electrons, which were trapped by oxygen vacancies or other defects<sup>39</sup>. A Mott–Schottky plot of  $1/C^2$  (extracted from the large arc in the  $Z^*$  plots) vs. DC bias voltage showed a nonlinear response (inset of Fig. 8(c)). Therefore, the electrode effect can be excluded as the origin of this electrical response. The GB capacitance of the M-LSNO ceramic with x=0.5 was extracted from  $Z^*$  plots ( $C_{gb}$ =1/2 $\pi f_{max}R_{gb}$ ) and found to be  $\approx 7.5 \times 10^{-8}$  F. This was lower than that of the apparent capacitance value of the sample ( $\approx 1.2 \times 10^{-7}$  F at 1 kHz). In contrast to the undoped–LSNO ceramic, further contribution from the electrode effect can be ignored because  $R_{gb}$ >> $R_e$ . The polaronic hopping process is also hypothesized as another important factor contributing to the GDR in the M-LSNO ceramic with x=0.5 as well as in the x=0.3 and 0.4 samples.

As illustrated in Figs. 8(a) and (b), the  $\varepsilon'$  value over the measured frequency range of the undoped–LSNO ceramic decreased as the DC bias was increased from 0–1.5 V, while  $\tan\delta$  increased. These results were due to the decrease in Schottky barrier height at the sample-electrode contact as a result of the effect of DC bias. When the DC bias was increased to 2 V, an overload limited measurement occurred. The overload DC bias was at 15 V. This tended to occur in the M–LSNO ceramic with x=0.5, but only in the frequency range below  $10^4$  Hz. However, the mechanisms in these two cases were totally

different. The mechanisms in the former and later ceramics were correlated with the electrical responses at the sample-electrode contact and GBs, respectively.

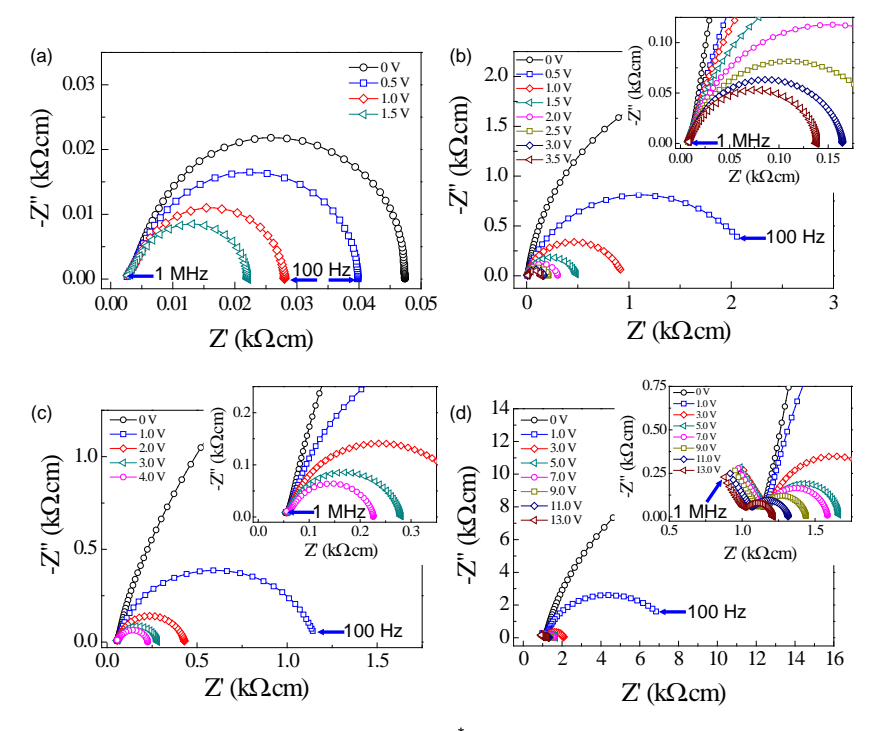


Fig. 7 Impedance complex plane plot ( $Z^*$ ) at RT under different DC bias voltages for La<sub>1.7</sub>Sr<sub>0.3</sub>Ni<sub>1-x</sub>Mg<sub>x</sub>O<sub>4</sub> ceramics with x = 0 (a), x = 0.3 (b), x = 0.4 (c), and x = 0.5 (d), insets of (a–c) show an expanded view of the high–frequency data close to the origin.

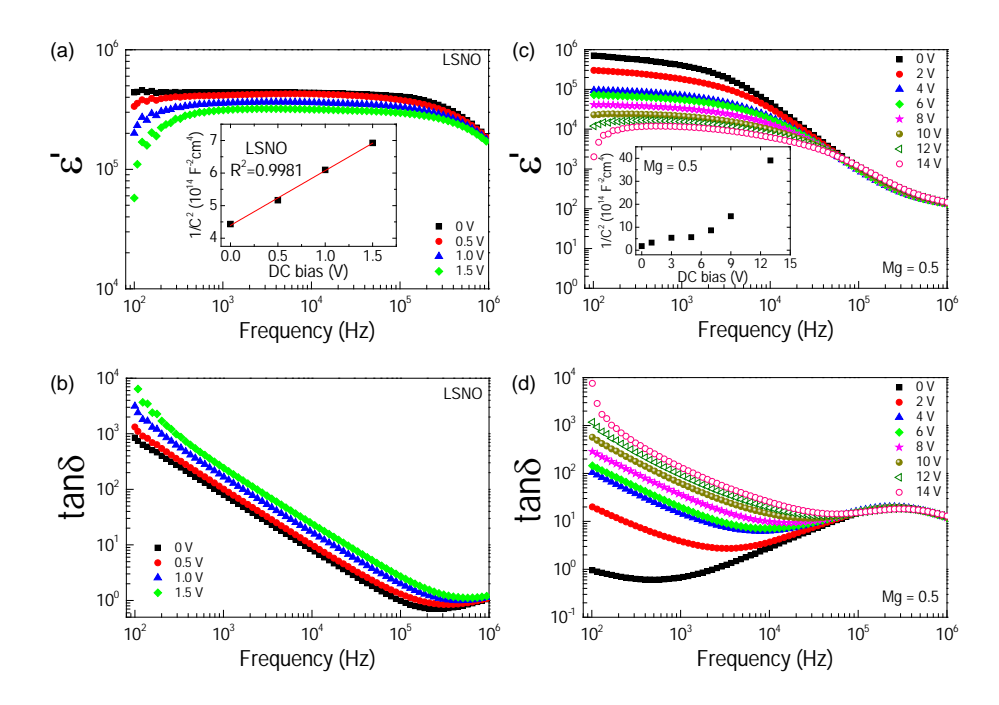


Fig. 8 Frequency dependence of  $\varepsilon'$  and  $\tan\delta$  at RT under different DC bias voltages for La<sub>1.7</sub>Sr<sub>0.3</sub>Ni<sub>1-x</sub>Mg<sub>x</sub>O<sub>4</sub> ceramics with x=0 (a-b) and x=0.5 (c-d); insets (a) and (c) demonstrate their  $1/C^2$  vs V plots, revealing the possible formation of a Schottky–Mott barrier height due to the electrode effect.

#### 1.4 Conclusions

The origins of the giant dielectric responses in LSNO ceramics were demonstrated via DC bias measurements. For the undoped–LSNO ceramic, the giant  $\epsilon'$  and  $R_e$  values decreased with increasing DC bias over the measured frequency range, while  $\tan\delta$  linearly increased. Furthermore, the decreased C values with increasing DC bias voltage were found to follow the Mott–Schottky law, confirming the dominant electrode effect. By comparing the apparent C value of the sintered ceramic with  $C_e$  value extracted from IS analysis, the giant  $\epsilon'$  response in the undoped–LSNO ceramic can be attributed to the electrode effect and the small polaronic hopping mechanism. For M–LSNO ceramics, changes in  $\epsilon'$ ,  $R_{gb}$  and  $\tan\delta$  were similar to those observed in an undoped–LSNO ceramic. However, a linear Mott–Schottky plot of  $1/C^2$  vs. DC bias voltage was not obtained, indicating that the electrode effect was not dominant in the M–LSNO ceramics due to a large increase in  $R_{gb}$ . The origins of the giant  $\epsilon'$  behavior in M–LSNO ceramics can be well described based on the Maxwell–Wagner polarization at insulating GBs and the small polaronic hopping mechanism.

#### References

- 1 X. Q. Liu, S. Y. Wu, X. M. Chen and H. Y. Zhu, J. Appl. Phys., 2008, **104**, 054114.
- 2 S. Krohns, P. Lunkenheimer, C. Kant, A. V. Pronin, H. B. Brom, A. A. Nugroho, M. Diantoro and A. Loidl, *Appl. Phys. Lett.*, 2009, **94**, 122903.
- 3 X. Q. Liu, Y. J. Wu and X. M. Chen, Solid State Commun., 2010, 150, 1794-1797.
- 4 B. W. Jia, W. Z. Yang, X. Q. Liu and X. M. Chen, J. Appl. Phys., 2012, 112, 024104.
- 5 A. Podpirka and S. Ramanathan, J. Appl. Phys., 2011, 109, 014106.
- 6 X. Q. Liu, S. Y. Wu and X. M. Chen, J. Alloys Compd., 2010, 507, 230-235.
- 7 X. Q. Liu, Y. J. Wu, X. M. Chen and H. Y. Zhu, *J. Appl. Phys.*, 2009, **105**, 054104.
- 8 P. Thongbai, T. Yamwong and S. Maensiri, *Mater. Lett.*, 2012, **82**, 244-247.
- 9 K. Meeporn, T. Yamwong and P. Thongbai, Jpn. J. Appl. Phys., 2014, 53, 06JF01.
- 10 A. Chouket, O. Bidault, V. Optasanu, A. Cheikhrouhou, W. Cheikhrouhou-Koubaa and M. Khitouni, *RSC Adv.*, 2016, **6**, 24543-24548.
- 11 X. Q. Liu, G. Liu, P. P. Ma, G. J. Li, J. W. Wu and X. M. Chen, *Journal of Electroceramics*, 2016.
- 12 T. I. Chupakhina, N. I. Kadyrova, N. V. Melnikova, O. I. Gyrdasova, E. A. Yakovleva and Y. G. Zainulin, *Mater. Res. Bull.*, 2016, **77**, 190-198.
- 13 A. Chouket, W. Cheikhrouhou-Koubaa, A. Cheikhrouhou, V. Optasanu, O. Bidault and M. Khitouni, *J. Alloys Compd.*, 2016, **662**, 467-474.
- 14 A. Chouket, V. Optasanu, O. Bidault, A. Cheikhrouhou, W. Cheikhrouhou-Koubaa and M. Khitouni, *J. Alloys Compd.*, 2016.
- 15 M. Li and D. C. Sinclair, *J. Appl. Phys.*, 2012, **111**, 054106.
- 16 E. Winkler, F. Rivadulla, J. S. Zhou and J. B. Goodenough, Phys. Rev. B, 2002, 66, 094418.
- 17 G. Liu, X. Q. Liu and X. M. Chen, Applied Physics A, 2014, 116, 1421-1427.
- 18 G. Liu, T. T. Chen, J. Wang, X. Q. Liu and X. M. Chen, J. Alloys Compd., 2013, 579, 502-506.
- 19 J. Wang, G. Liu, B. W. Jia, X. Q. Liu and X. M. Chen, Ceram. Int., 2014, 40, 5583-5590.
- 20 X. Huang, H. Zhang, J. Li and Y. Lai, J. Mater. Sci.: Mater. Electron., 2016, 1-7.
- 21 S. Wu, P. Liu, Y. Lai, W. Guan, Z. Huang, J. Han, Y. Xiang, W. Yi and Y. Zeng, *J. Mater. Sci.: Mater. Electron.*, 2016, 1-6.
- 22 M. Li, D. C. Sinclair and A. R. West, J. Appl. Phys., 2011, 109, 084106.
- 23 M. Li, Z. Shen, M. Nygren, A. Feteira, D. C. Sinclair and A. R. West, *J. Appl. Phys.*, 2009, **106**, 104106.
- 24 L. Sun, R. Zhang, Z. Wang, E. Cao, Y. Zhang and L. Ju, J. Alloys Compd., 2016, 663, 345-350.
- 25 A. Nautiyal, C. Autret, C. Honstettre, S. De Almeida-Didry, M. El Amrani, S. Roger, B. Negulescu and A. Ruyter, *J. Eur. Ceram. Soc.*, 2016, **36**, 1391-1398.
- 26 J. Boonlakhorn and P. Thongbai, Jpn. J. Appl. Phys., 2015, 54, 06FJ06.

- 27 J. Boonlakhorn, P. Kidkhunthod and P. Thongbai, J. Eur. Ceram. Soc., 2015, 35, 3521-3528.
- 28 T. Adams, D. Sinclair and A. West, *Phys. Rev. B*, 2006, **73**, 094124.
- 29 M. Li, A. Feteira and D. C. Sinclair, J. Appl. Phys., 2009, 105, 114109.
- 30 P. Thongbai, T. Yamwong and S. Maensiri, Appl. Phys. Lett., 2009, 94, 152905.
- 31 C. L. Song, Y. J. Wu, X. Q. Liu and X. M. Chen, J. Alloys Compd., 2010, 490, 605-608.
- 32 X. Q. Liu, B. W. Jia, W. Z. Yang, J. P. Cheng and X. M. Chen, *J. Phys. D: Appl. Phys.*, 2010, **43**, 495402.
- 33 K. Meeporn, T. Yamwong, S. Pinitsoontorn, V. Amornkitbamrung and P. Thongbai, *Ceram. Int.*, 2014, **40**, 15897-15906.
- 34 J. Boonlakhorn and P. Thongbai, *J. Electron. Mater.*, 2015, **44**, 3687-3695.
- 35 B. Wen Jia, X. Qiang Liu and X. Ming Chen, J. Appl. Phys., 2011, 110, 064110.
- 36 A. N. Mansour, Surface Science Spectra, 1994, 3, 231-238.
- 37 A. N. Mansour, Surface Science Spectra, 1994, 3, 279-286.
- 38 R. Schmidt, M. C. Stennett, N. C. Hyatt, J. Pokorny, J. Prado-Gonjal, M. Li and D. C. Sinclair, J. Eur. Ceram. Soc., 2012, 32, 3313-3323.
- 39 Y. Song, X. Wang, Y. Sui, Z. Liu, Y. Zhang, H. Zhan, B. Song, Z. Liu, Z. Lv, L. Tao and J. Tang, Scientific Reports, 2016, 6, 21478.

## **Output & Research Honors and Awards**

### Output

- **1.** Boonlakhorn J, Kidkhunthod P, <u>Thongbai P</u>, Maensiri S. Colossal dielectric permittivity and electrical properties of grain boundary of  $Ca_{1-3x/2}Yb_xCu_{3-y}Mg_yTi_4O_{12}$  (x = 0.05, y=0.05 and 0.30). Ceram. Int. 2016; 42: 8567-8572. (IF2016 = 2.986, Q1 ISI)
- 2. Meeporn K, Santi Maensiri S, <u>Thongbai P</u>. Abnormally enhanced dielectric permittivity in poly(vinylidene fluoride)/nanosized-La<sub>2</sub>NiO<sub>4-δ</sub> films. Applied Surface Science. 2016; 380: 67-72 (IF2016 = 3.387, Q1 ISI)
- 3. Tuichai W, Danwittayakul S, Maensiri S, <u>Thongbai P</u>. Investigation on Temperature Stability Performance of Giant Permittivity (In+Nb) in Co-doped TiO<sub>2</sub> Ceramic: A Crucial Aspect for Practical Electronic Applications. RSC Advances. 2016; 6:5582-5589. (IF2016 = 3.108, Q2 ISI)
- **4.** Boonlakhorn J, Putasaeng B, Kidkhunthod P, <u>Thongbai P</u>. Significantly Improved Dielectric Properties of (Y+Mg) co-doped CaCu<sub>3</sub>Ti<sub>4</sub>O<sub>12</sub> Ceramics by Simultaneously Controlling Geometric and Intrinsic Properties of Grain Boundaries. <u>Materials and design</u>. 2016; 92:494-498. (IF2016 = 4.364, Q1 ISI)
- 5. Jumpatam J, Putasaeng B, Yamwong T, <u>Thongbai P</u>, Maensiri S. Microstructural evolution and strongly enhanced dielectric response in Sndoped CaCu<sub>3</sub>Ti<sub>4</sub>O<sub>12</sub>-CaTiO<sub>3</sub> ceramic composites. Mater. Res. Bull. 2016; 77:178-184. (IF2016 = 2.446, Q2 ISI)
- 6. Tuichai W, Danwittayakul S, Chanlek N, Srepusharawoot P, <u>Thongbai P</u>, Maensiri S, Origin(s) of apparent colossal permittivity in (In<sub>1/2</sub>Nb<sub>1/2</sub>)<sub>x</sub>Ti<sub>1-x</sub>O<sub>2</sub>: Clarification on the extremely induced Maxwell-Wagner polarization relaxation in by DC bias, RSC Advances 2017; 7: 95. (IF2016 = 3.108, Q2 ISI)
- 7. Boonlakhorn J, Kidkhunthod P, Putasaeng B, <u>Thongbai P</u>, Significantly improved non–Ohmic and giant dielectric properties of CaCu<sub>3-x</sub>Zn<sub>x</sub>Ti<sub>4</sub>O<sub>12</sub> ceramics by enhancing grain boundary response, Ceramics International 2017; 43: 2705–2711. (IF2016 = 2.986, Q1 ISI)
- 8. Jumpatam J, Mooltang A, Putasaeng B, Kidkhunthod P, Chanlek N, <u>Thongbai P</u>, Maensiri S, Effects of Mg<sup>2+</sup> doping ions on giant dielectric properties and electrical responses of Na<sub>1/2</sub>Y<sub>1/2</sub>Cu<sub>3</sub>Ti<sub>4</sub>O<sub>12</sub> ceramics, <u>Ceramics International</u> 2016; 42: 16287–16295. (IF2016 = 2.986, Q1 ISI)

- 9. Jumpatam J, Somphan W, Boonlakhorn J. Putasaeng B, Kidkhunthod P, <u>Thongbai P</u>, Maensiri S, Non–Ohmic properties and electrical responses of grain and grain boundaries of Na<sub>1/2</sub>Y<sub>1/2</sub>Cu<sub>3</sub>Ti<sub>4</sub>O<sub>12</sub> ceramics, <u>Journal of the American Ceramic Society</u> 2017; 100: 157-166. (IF2016 = 2.841, Q1 ISI)
- 10. Nachaithong T, Kidkhunthod P, <u>Thongbai P</u>, Maensiri S, Surface barrier layer effect in (In+Nb) co-doped TiO<sub>2</sub> ceramics: An alternative route to design low dielectric loss, <u>Journal of the American Ceramic Society</u> 2017; 100:1452–1459. (IF2016 = 2.841, Q1 ISI)
- **11.** Nachaithong T, <u>Thongbai P</u>, Maensiri S, Colossal permittivity in  $(In_{1/2}Nb_{1/2})_xTi_{1-x}O_2$  ceramics prepared by a glycine nitrate process, Journal of the European Ceramic Society 2017; 37: 655–660. (IF2016 = 3.441, Q1 ISI)
- **12.** Jumpatam J, <u>Thongbai P</u>, Enhanced Dielectric and Non-Ohmic Properties in CaCu<sub>3</sub>Ti<sub>4</sub>O<sub>12</sub>/CaTiO<sub>3</sub> Nanocomposites Prepared by a Chemical Combustion Method, <u>Journal of Materials Science</u>: <u>Materials in Electronics</u> 2016; 27: 12085–12090. (IF2016 = 2.019, Q2 ISI)
- 13. Meeporn K, Chanlek N, <u>Thongbai P</u>, Effects of DC bias on non-ohmic sample-electrode contact and grain boundary responses in giant permittivity La<sub>1.7</sub>Sr<sub>0.3</sub>Ni<sub>1-x</sub>Mg<sub>x</sub>O<sub>4</sub> ceramics, RSC Advances 2016; 6: 91377-91385. (IF2016 = 3.108, Q2 ISI)
- 14. Boonlakhorn J, Kidkhunthod P, Chanlek N, <u>Thongbai P</u>, Effects of DC bias on dielectric and electrical responses in (Y+Zn) co-doped CaCu<sub>3</sub>Ti<sub>4</sub>O<sub>12</sub> perovskite oxides, <u>Journal of Materials Science</u>: <u>Materials in Electronics</u> 2017; 28: 4695–4701. (IF2016 = 2.019, Q2 ISI)
- **15.** Jumpatam J, Putasaeng B, Chanlek N, Kidkhunthod P, <u>Thongbai P</u>, Maensiri S, Chindaprasirt P, Improved giant dielectric properties of CaCu<sub>3</sub>Ti<sub>4</sub>O<sub>12</sub> via simultaneously tuning the electrical properties of grains and grain boundaries by F<sup>-</sup> substitution, RSC Advances 2017; 7: 4092. (IF2016 = 3.108, Q2 ISI)
- **16.** Tuichai W, Danwittayakul S, Chanlek N, <u>Thongbai P</u>, Maensiri S, High-performance giant-dielectric properties of rutile TiO<sub>2</sub> co-doped with acceptor-Sc<sup>3+</sup> and donor-Nb<sup>5+</sup> ions, <u>Journal of Alloys and Compounds 2017</u>; 703: 139-147. (IF2016 = 3.133, Q1 ISI)
- **17.** Jumpatam J, Somphan W, Putasaeng B, Chanlek N, Kidkhunthod P, <u>Thongbaid P</u>, Maensiri S, Nonlinear electrical properties and giant dielectric response in Na<sub>1/3</sub>Ca<sub>1/3</sub>Y<sub>1/3</sub>Cu<sub>3</sub>Ti<sub>4</sub>O<sub>12</sub> ceramic, <u>Materials Research Bulletin</u> 2017; 90: 8–14. (IF2016 = 2.446, Q2 ISI)

- 18. Boonlakhorn J, Thongbai P, Putasaeng, Kidkhunthod P, Maensiri S, Chindaprasirt P, Microstructural Evolution, Non-Ohmic Properties and Giant Dielectric Response in CaCu<sub>3</sub>Ti<sub>4-x</sub>Ge<sub>x</sub>O<sub>12</sub> Ceramics, Journal of the American Ceramic Society 2017; 100:3478–3487. (IF2016 = 2.841, Q1 ISI)
- **19.** Tuichai W, Thongyong N, Danwittayakul S, Chanlek N, Srepusharawoot P, <u>Thongbai P</u>, Maensiri S, Very low dielectric loss and giant dielectric response with excellent temperature stability of Ga<sup>3+</sup> and Ta<sup>5+</sup> co-doped rutile-TiO<sub>2</sub> ceramics, <u>Materials and Design 2017</u>; 123: 15-23. (IF2016 = 4.364, Q1 ISI)
- 20. Meeporn K, Thongbai P, Yamwong T, Maensiri S, Greatly enhanced dielectric permittivity in La<sub>1.7</sub>Sr<sub>0.3</sub>NiO<sub>4</sub>/poly(vinylidene fluoride) nanocomposites that retained a low loss tangent, RSC Advances 2017; 7: 17128. (IF2016 = 3.108, Q2 ISI)
- 21. Nachaithong T, <u>Thongbai P</u>, Preparation, characterization, electrical properties and giant dielectric response in (In + Nb) co-doped TiO<sub>2</sub> ceramics synthesized by a urea chemical-combustion method, <u>Journal of Materials Science</u>: <u>Materials in Electronics</u> 2017; 28: 10914–10920. (IF2016 = 2.019, Q2 ISI)
- **22.** Meeporn K, <u>Thongbai-P</u>, Maensiri S, Chindaprasirt P, Improved dielectric properties of PVDF composites by employing Mg-doped La<sub>1.9</sub>Sr<sub>0.1</sub>NiO<sub>4</sub> particles as a filler, <u>Journal of Materials Science</u>: <u>Materials in Electronics</u> 2017; 28:11762–11768. (IF2016 = 2.019, Q2 ISI)
- 23. Nachaithong T, Tuichai W, Kidkhunthod P, Chanlek N, <u>Thongbai P</u>, Maensiri S, Preparation, characterization, and giant dielectric permittivity of(Y<sup>3+</sup> and Nb<sup>5+</sup>) co-doped TiO<sub>2</sub> ceramics, <u>Journal of the European Ceramic Society</u> 2017; 37: 3521–3526. (IF2016 = 3.441, Q1 ISI)
- 24. Jumpatam J, Moontang A, Putasaeng B, Kidkhunthod P, Chanlek N, <u>Thongbai P</u>, Preparation, characterization, and dielectric properties of CaCu<sub>3</sub>Ti<sub>4</sub>O<sub>12</sub>-related (Na<sub>1/3</sub>Ca<sub>1/3</sub>Y<sub>1/3</sub>)Cu<sub>3</sub>Ti<sub>4</sub>O<sub>12</sub> ceramics using a simple sol-gel method, Journal of Materials Science: Materials in Electronics 2017; 28: 14839–14847. (IF2016 = 2.019, Q2 ISI)
- 25. Boonlakhorn J, <u>Thongbai P</u>, Enhanced non-Ohmic properties and giant dielectric response of (Sm+Zn) co-doped CaCu<sub>3</sub>Ti<sub>4</sub>O<sub>12</sub> ceramics, Ceramics International 2017; 43: 12736-12741. (IF2016 = 2.986, Q1 ISI)
- **26.** Boonlakhorn J, Kidkhunthod P, Chanlek N, <u>Thongbai P</u>, (Al<sup>3+</sup>, Nb<sup>5+</sup>) co–doped CaCu<sub>3</sub>Ti<sub>4</sub>O<sub>12</sub>: An extended approach for acceptor–donor heteroatomic

- substitutions to achieve high–performance giant–dielectric permittivity, Journal of the European Ceramic Society 2018; 38: 137–143. (IF2016 = 3.441, Q1 ISI)
- **27.** Thongyong N, Tuichai W, Chanlek N, <u>Thongbai P</u>, Effect of Zn<sup>2+</sup> and Nb<sup>5+</sup> codoping ions on giant dielectric properties of rutile-TiO<sub>2</sub> ceramics, Ceramics International 2017; 43: 15466–15471. (IF2016 = 2.986, Q1 ISI)
- **28.** Tuichai W, Danwittayakul S, Chanlek N, <u>Thongbai P</u>, Effects of sintering temperature on microstructure and giant dielectric properties of (V+Ta) codoped TiO<sub>2</sub> ceramics, Journal of Alloys and Compounds 2017; 725: 310-317. (IF2016 = 3.133, Q1 ISI)

# **Research Honors and Awards**

• 2017 TWAS (The World Academy of Sciences (TWAS) for the advancement of science in developing countries) in Physics